IUTAM Symposium on

Chaotic Dynamics and Control of Systems and Processes in Mechanics

Proceedings of the IUTAM Symposium held in Rome, Italy, 8–13 June 2003

Edited by

G. REGA

Università di Roma 'La Sapienza', Rome, Italy

and

F. VESTRONI

Università di Roma 'La Sapienza', Rome, Italy

Springer

A C.I.P. Catalogue record for this book is available from the Library of Congress.

ISBN 1-4020-3267-6 (HB)
ISBN 1-4020-3268-4 (e-book)

Published by Springer,
P.O. Box 17, 3300 AA Dordrecht, The Netherlands.

Sold and distributed in North, Central and South America
by Springer,
101 Philip Drive, Norwell, MA 02061, U.S.A.

In all other countries, sold and distributed
by Springer,
P.O. Box 322, 3300 AH Dordrecht, The Netherlands.

Printed on acid-free paper

Printed in Great Britain by MPG Books Ltd., Bodmin, Cornwall.

CONTENTS

(KL – Key Lecture, P – Poster Presentation)

Group picture of some of the participants

1. W. Wedig, 2. P. Goncalves, 3. S. Shaw, 4. O. Gottlieb, 5. G. Rega, 6. S. Wustrack, 7. T. Kapitaniak, 8. D. van Campen, 9. R. Leine, 10. R. Plaut, 11. D. Bernardini, 12. N. Sri Namachchivaya, 13. I. Georgiou, 14. M. Thompson, 15. F. Romeo, 16. D. Chelidze, 17. F. Vestroni, 18. F. Chernousko, 19. F. Moon, 20. F. Pfeiffer, 21. A. Nayfeh, 22. J. Hogan, 23. R. Ibrahim, 24. A. Bajaj, 25.J. Wauer, 26. J. Cusumano, 27. W. Schiehlen, 28. R. Masiani, 29. K. Hedrih, 30. H. Troger, 31. V. Beletski, 32. E. Kreuzer, 33. G. Domokos, 34. E. Karaesmen, 35. H. Yabuno, 36. M. di Bernardo, 37. M. Wiercigroch, 38. E. Pavlovskaia, 39. U. Galvanetto, 40. A. Kovaleva, 41. W. Lacarbonara, 42. G. Stépan, 43. A. Fradkov, 44. B. Balachandran, 45. F. Lakrad, 46. A. Luo, 47. P. Kowalczyk, 48. A. Vakakis, 49. L. Manevitch.

a. Mrs. Van Campen, b. Mrs. Pfeiffer, c. Miss Raimondi, d. Mrs. Belloni, e. Mrs. Bianconi, f. Mrs. Wedig, g. Mrs. Wustrack, h. Mrs. Thompson, i. Mrs. Moon, j. Mrs. Schiehlen, k. Mrs. Wauer.

PREFACE

The interest of the applied mechanics community in *chaotic dynamics of engineering systems* has exploded in the last fifteen years, although research activity on nonlinear dynamical problems in mechanics started well before the end of the Eighties. It developed first within the general context of the classical theory of *nonlinear oscillations*, or nonlinear vibrations, and of the relevant engineering applications. This was an extremely fertile field in terms of formulation of mechanical and mathematical models, of development of powerful *analytical* techniques, and of understanding of a number of basic nonlinear phenomena. At about the same time, meaningful theoretical results highlighting new solution methods and new or complex phenomena in the dynamics of deterministic systems were obtained within *dynamical systems* theory by means of sophisticated *geometrical* and *computational* techniques.

In recent years, careful *experimental* studies have been made to establish the actual occurrence and observability of the predicted dynamic phenomena, as it is vitally needed in all engineering fields. Complex dynamics have been shown to characterize the behaviour of a great number of nonlinear mechanical systems, ranging from aerospace engineering applications to naval applications, mechanical engineering, structural engineering, robotics and biomechanics, and other areas.

The International Union of Theoretical and Applied Mechanics grasped the importance of such complex phenomena in the Eighties, when the first IUTAM Symposium devoted to the general topic of nonlinear and chaotic dynamics in applied mechanics and engineering was held in Stuttgart (1989). Starting with that meeting, mechanics people began thinking of nonlinear vibration problems within the more modern framework of *Nonlinear Dynamics*. Two successive IUTAM Symposia in the same fields were held in London (1993) and Ithaca, NY (1997). Though these three Symposia dealt with a variety of more and more intriguing problems in nonlinear and chaotic dynamics of mechanical systems, one could say, at the risk of being

G. Rega and F. Vestroni (eds.),
IUTAM Symposium on Chaotic Dynamics and Control of Systems and Processes in Mechanics, xvii–xx.

too schematic, that their respective focuses were on *computational* techniques (Stuttgart), *geometrical* tools (London), and *experimental* investigations (Ithaca), reflecting the interests and the specific expertise developed in the Schools of the symposium organizers.

Today, it seems generally accepted that nonlinear vibration problems should be cooperatively addressed through the combined use of *analytical, computational, geometrical* and *experimental* approaches, each of them giving fundamental and complementary contributions to the overall understanding of the problem.

Further important related issues have attracted the attention of the mechanics community in the last decade. First, the *interaction* between *nonlinear dynamics and control*, which plays an important role in advanced engineering systems in order to obtain desired dynamic behaviour and improved reliability during operation. It was the subject of a IUTAM Symposium held in Eindhoven (1996). Second, topics related to methods and applications of *control of chaos*, which primarily developed within the physics and dynamical systems communities but have recently received increasing attention by the nonlinear mechanics community.

This volume evolves from a further international event in the field, namely the IUTAM Symposium on *Chaotic Dynamics and Control of Systems and Processes in Mechanics*, held in Rome, Italy, on 8–13 June 2003. It was aimed at diving deep both into theory and recent applications to mechanics of nonlinear and chaotic dynamics, and into their control, by at the same time furthering the exchange of scientific ideas within the group of scholars – as well as friends – from various research teams, that had been established in the last fifteen years.

By now, the new and revolutionary dynamic phenomena of some years ago have become increasingly popular in the scientific community, as witnessed even by the overabundance of chaos software and pictures available on books and websites; they are known to characterize many theoretical systems and engineering applications. So, what is the present research framework in the field?

One can identify two main general issues: (i) the need to overcome the limitations inherent in the archetypal single- or few-degree-of-freedom systems mostly considered in the past, and (ii) the increased interest towards control of chaos – or more generally – of nonlinear dynamics in mechanical systems. The aim is to develop more reliable models for the analysis of high-dimensional systems and processes encountered in most technical applications; to obtain further meaningful hints from experimental investigations; to generalize techniques for the analysis of new complex behaviours; to explore implications of chaos in design and operating conditions of advanced systems, as well as needs and features for their

control. It is important to remember how difficult and involved is the passage from simple models to actual engineering systems.

For the Symposium, an International Scientific Committee was appointed by the Bureau of IUTAM with the following members: G. Rega (Italy, Chair), F. Vestroni (Italy, Co-Chair), F. L. Chernousko (Russia), E. Kreuzer (Germany), F. C. Moon (USA), G. Stepan (Hungary), J. M. T. Thompson (UK), H. Troger (Austria) and D. H. van Campen (The Netherlands)

This Committee selected the papers to be presented at the Symposium and 51 papers were presented in lecture and poster-discussion sessions. There were 63 registered participants from engineering, physics and applied mathematics communities regularly attending the Technical Sessions; they came from 20 different countries according to the following geographical distribution: Austria (1), Brazil (1), Canada (1), Czech Republic (1), China (1), Denmark (1), Germany (6), Greece (3), Hungary (2), Israel (1), Italy (13), Japan (1), Morocco (1), Poland (1), Russia (5), Serbia-Montenegro (1), the Netherlands (2), Turkey (1), U.K. (8), U.S.A. (12). A number of Italian PhD students and University scientists also attended some scientific sessions.

Papers derived from nearly all of the Symposium presentations are now published in the present volume, after undergoing review by members of the Scientific Committee, or other participants to the Symposium, aimed at achieving a standard of Proceedings comparable to that of refereed journals in the field.

Though most papers are related to more than one topic, it seemed suitable to group them within 7 main areas:

I. Bifurcation, Chaos and Control
II. Mechanical Systems
III. Structural Systems
IV. Nonsmooth Dynamics
V. Delay and Random Systems
VI. Control of Systems and Processes
VII. Chaos Control and Synchronization.

Meaningful scientific achievements are highlighted mostly as regards the following topics:

(i) Complex systems and processes for classical and innovative applications
(ii) Features of nonlinear interactions in mechanical systems
(iii) Patterns of novel bifurcations, with special emphasis on non-smooth systems
(iv) Dimensionality and reduced-order models of continuous systems
(v) Exploitation of dynamical system properties for applications
(vi) Implications of chaos for design and operating conditions
(vii) Control of spatio-temporal dynamics.

The four keynote lectures of the Symposium, and the relevant lectures and poster presentations, are indicated in the Table of Contents.

We thank both the participants to the Symposium and the authors of the papers for their valuable contributions.

The Symposium was held in the 15th-century cloister of the Faculty of Engineering of the University of Rome "La Sapienza", in the very centre of the city. The opening remarks were given by G. Rega, F. Vestroni (Head, Structural Engineering Department), T. Bucciarelli (Faculty Dean), and W. Schiehlen (Vice President, IUTAM). Within a rich cultural and social programme, we also took the opportunity to recognize the contributions to the area of nonlinear dynamics and control of three world class scientists, Professors Felix Chernousko, Werner Schiehlen, and Michael Thompson, by celebrating their respective 65th birthdays during the Symposium banquet.

The success of the Symposium would not have been possible without the work of the local Organizing Committee established at the Department of Structural and Geotechnical Engineering of the University of Rome "La Sapienza", whose members were as follows: G. Rega (Chair), F. Vestroni (Co-Chair), F. Romeo (Secretary), D. Bernardini, P. Casini, W. Lacarbonara, R. Masiani, A. Paolone.

A special acknowledgment has to be given to Dr. Francesco Romeo for his hard and valuable effort, and the continuous care spent for the success of both the Symposium and this Proceedings volume.

The financial support of the University of Rome "La Sapienza", of the IUTAM, and of a significant number of Italian companies from the area of civil engineering is most gratefully acknowledged.

Finally, many thanks are due to Kluwer Academic Publishers, especially to Ms. Nathalie Jacobs, for their support and efficient cooperation with this Proceedings volume.

Giuseppe Rega
Fabrizio Vestroni
University of Rome "La Sapienza", Italy
July 2004

WELCOME ADDRESS
BY THE VICE-PRESIDENT OF IUTAM

Professor Bucciarelli, Professor Vestroni
Dear Professor Rega,
Dear Colleagues from all over the world,
Ladies and Gentlemen,

It is my honor and pleasure to welcome all of you on behalf of the International Union of Theoretical and Applied Mechanics, here in Italy. As we have learnt, the University of Rome "La Sapienza" (which means "Wisdom") is the oldest university in town, founded in 1303 by Pope Boniface the Eighth. Today, the university is well-known within the mechanics community due to its outstanding academic and scientific strength in nonlinear dynamics. Further, most of us know also the International Journal of the Italian Association of Theoretical and Applied Mechanics, published by Kluwer and called simply *MECCANICA*. This Journal is edited by Professor Giuseppe Rega here at the Department of Structural and Geotechnical Engineering.

Let me use this Opening Ceremony for a short look on the past and present activities of IUTAM. Organized meetings between scientists in the field of mechanics were initiated 80 years ago, namely in 1922, when Professor Theodore von Kármán from Germany and Professor Tullio Levi-Civita from Italy organized the world's first conference in hydro- and aero-mechanics. Two years later, in 1924, the First International Congress was held in Delft, The Netherlands, encompassing all fields of mechanics, that means analytical, solid and fluid mechanics, including their applications. From then on, with exception of the year 1942, international congresses on mechanics have been held every four years.

The disruption of international scientific cooperation caused by the Second World War was deeper than that caused by the First World War, and the need for re-knotting ties seemed stronger than ever before, when the

G. Rega and F. Vestroni (eds.),
IUTAM Symposium on Chaotic Dynamics and Control of Systems and Processes in Mechanics, xxi–xxiii.

mechanics community reassembled in Paris for the Sixth Congress in 1946. Under these circumstances, at the Sixth Congress in Paris, it seemed an obvious step to strengthen bonds by forming an international union, and as a result IUTAM was created and statutes were adopted. After one year, in 1947, the Union was admitted to ICSU, the International Council for Science. This council coordinates activities among various other scientific unions to form a tie between them and the United Nations Educational, Scientific and Cultural Organization, well known as UNESCO.

Today, IUTAM forms the international umbrella organization of more than 50 national Adhering Organizations representing mechanics in many nations around the globe. Each Adhering Organization of IUTAM, like the Italian Association of Theoretical and Applied Mechanics, is represented by a number of scientists in IUTAM's General Assembly. In particular, the Italian representatives are:

Professor Carlo Cercignani and Professor Giulio Maier, from the Politecnico di Milano,

Professor Paolo Podio-Guidugli, from the University of Rome "Tor Vergata", and

Professor Furio Vatta, from the Politecnico di Torino.

Furthermore, a large number of international scientific organizations of general or more specialized branches of mechanics are connected with IUTAM as Affiliated Organizations. As a few examples, let me mention: the European Mechanics Society (EUROMECH), the International Association of Computational Mechanics (IACM), and the International Association for Vehicle System Dynamics (IAVSD).

Within IUTAM, the only division used so far is related to solid and fluid mechanics as indicated by our two Symposia Panels. But last year the General Assembly of IUTAM approved and established Working Parties devoted to specific areas of mechanics. These areas are:

- Non-Newtonian Fluid Mechanics and Rheology,
- Dynamical Systems and Mechatronics, which is our topic, too,
- Mechanics of Materials,
- Material Processing,
- Computational Fluid and Solid Mechanics.

And in addition, with potential links to other International Unions the following subjects were chosen:

- Biomechanics,
- Nano- and Microscale Phenomena in Mechanics,
- Geophysical and Environmental Mechanics,
- Education in Mechanics and Capacity Building.

These Working Parties may be developed into Standing Scientific Committees, too, in the future.

Since 1949 there have been held more than 260 IUTAM symposia worldwide. Out of them, 6 symposia were organized in Italy, but our symposium is the first one to be held in Rome. It is worthwhile to mention that the second IUTAM Symposium ever held took place in Pallanza, Lago Maggiore back in 1950 with 27 participants from 11 countries.

The present Symposium is exceptionally interesting because it deals with new developments in dynamics. IUTAM found that the proposal of Professors Rega and Vestroni for such a symposium was not only very timely, but also very well founded in the outstanding research carried out in this field at the University of Rome "La Sapienza". Thus, the proposal for the Symposium was readily accepted and granted by the General Assembly of IUTAM in the year 2000. There is no doubt that IUTAM considers nonlinear dynamics as an important field of mechanics. Successful IUTAM symposia on chaos and control have been held since 1989 in Stuttgart, London, Eindhoven and at Cornell. Nevertheless, IUTAM does not offer series of symposia. Thus, the titles are always adapted to the latest developments.

As I mentioned before, IUTAM organizes not only symposia but also international congresses in all part of the world. These quadrennial congresses are also considered as the Olympics of Mechanics. With 1500 participants the Chicago Congress was the central millennium event in mechanics to celebrate the turn of the century, too. The Twenty-first International Congress of Theoretical and Applied Mechanics will be held in Warsaw, Poland, from 15 to 21 August 2004, which means in one year's time. Announcements of this forthcoming congress will be widely distributed and published in many scientific journals. Please visit also IUTAM's very informative website designed and maintained by the Secretary-General Dick van Campen, who is with us this week, too.

On behalf of IUTAM, I wish to express my sincere thanks to the Department of Structural and Geotechnical Engineering, and in particular to Professor Giuseppe Rega, for the invitation to host this significant scientific event. I thank all participants for their readiness to come and to contribute to the Symposium with presentations, posters and scientific discussions.

It is up to you now, Ladies and Gentlemen, to harvest the fruits of the Organizers' work. Contribute your share to make this IUTAM Symposium a meeting that will be long remembered. On behalf of IUTAM, I greet you all and wish you a symposium crowned by success!

Werner Schiehlen
Professor of Mechanics
University of Stuttgart, Germany

OBITUARY

It is very sad to note that one of the contributors to this volume, Professor František PETERKA, died just three months after attending the IUTAM Symposium in Rome, due to an unexpected and incredible event.

With his important and updated research activity in the field of nonlinear impacting dynamics, Professor Peterka was an assiduous protagonist of a great number of scientific events that occurred in the last decade in the general area of mechanical applications of nonlinear and chaotic dynamics.

For his scientific work, as well as for being a man of great humanity, mildness, tolerance and generosity, Professor Peterka was credited with great esteem, appreciation and friendship within the overall group of scholars in nonlinear dynamics who interacted with him during the years.

I believe I fully interpret the feelings of all of his scientific friends and colleagues from different countries by including in this volume, which is one of the very last volumes he contributed to, a short résumé of Professor Peterka's scientific activity kindly prepared by his colleague Professor Ladislav Pust.

Giuseppe Rega

Ing. František PETERKA, Dr. Sc., was born on November 26, 1939 in *Týn nad Vltavou* in South Bohemia. From his mother, a teacher of mathematics, he inherited a talent for the natural and technical sciences. In 1962, he graduated with honour in applied mechanics from the Faculty of Mechanical Engineering of the Czech Technical University, Prague. Thereafter he began his scientific activity at the Institute of Thermomechanics of the Czechoslovak Academy of Sciences. His research was focused on the dynamics of mechanical systems, particularly on the problems of dynamics of strongly nonlinear systems with impacts. In 1968, he defended his PhD thesis *Theory of dynamical impact damper with two degrees of freedom*.

G. Rega and F. Vestroni (eds.),
IUTAM Symposium on Chaotic Dynamics and Control of Systems and Processes in Mechanics, xxv–xxvi.

He was the author and co-author of more then 150 papers and lectures, and five books. Using both theory and analogue computer simulation he studied the problems of periodic and chaotic impact motions, and the optimisation of parameters of impact systems with viscous and dry friction. He was one of the first researchers who discovered chaotic phenomena in nonlinear mechanical systems. He worked also on the experimental verification of theoretical results by means of physical models of mechanical impact-systems. His last larger contribution to the theory of vibration is the chapter *Vibration Impact Systems* in the *Encyclopedia of Vibration*, published by Academic Press, London in 2001. With industrial enterprises he collaborated on the development of mechanical hammers for metal scrap compacting equipment, pneumatic drill hammers, and on the modelling of the oscillation of the nuclear reactor fuel rods under aeroelastic and seismic excitation. He elaborated a new principle of forming impact machines. However, the prototype of the patented forming machine remains unfinished.

He was the Head of the Laboratory of Non-linear Systems Dynamics in the Institute of Thermomechanics, Academy of Sciences of the Czech Republic. His scientific work was supported from 1991 in five grant projects by Grant Agency of the AS CR, Grant Agency of the CR and by the Ministry of the Education, Youth and Sport of the CR within the European action COST P-4. He was the Chairman of the Czech National Committee of the IFToMM (International Federation for the Theory of Machines and Mechanisms) and the Secretary of the IFToMM Technical Committee *Non-linear Oscillations*. He was the member of the permanent Euromech (European Society for Mechanics) Non-Linear Oscillations Conferences Committee. As a secretary of the 2nd European Nonlinear Oscillations Conference (ENOC ‘96) in Prague 1996, he contributed to a great degree to its success.

His spare time he devoted mainly to his family, a daughter, two sons and four grandchildren, and to music; he played violin and sang in the church orchestra and choir.

Ladislav Pust
Institute of Thermomechanics
Academy of Sciences of the Czech Republic, Prague

I.

BIFURCATION, CHAOS AND CONTROL

Bifurcation and *chaos* are important nonlinear phenomena in many engineering systems and processes, which need to be *controlled* for several practical purposes. The focus of the first part of the Proceedings is on some relevant paradigmatic topics. The Key Lecture of the Symposium given by Francis Moon of Cornell University, Ithaca, USA, is the lead paper of this part, whereas the rest of the papers are compiled alphabetically, based on the last name of the first author.

Francis Moon addresses two problems in the dynamics of machines: the nature of noise and the evolution of noisy dynamics over several generations of machine design. The dynamics of clock escapements are examined from experimental, historical and analytical points of view, by assuming them as a paradigm for the evolution of noise in machines, and by developing a theoretical model of chaotic clocks.

Bajaj et al. investigate the nonlinear local and global dynamics of a resonantly excited linear oscillator coupled to an array of weakly coupled pendulums under 1:2 internal resonance with the primary system. The method of averaging is used, and local bifurcation analysis is performed. The global dynamics is formulated in action-angle variables, and the numerical simulations show the occurrence of complex dynamics even for the unforced system.

Efimov and Fradkov deal with the design of adaptive nonlinear observers, and develop new applicability conditions which provide partial observation of uncertain nonlinear affine plant with estimation of unknown parameters. Applicability of results to time-varying chaotic systems is demonstrated.

In the paper by Hedrih, some aspects of the nonlinear dynamics of a heavy material particle moving along a circle with coupled rotation are presented, together with the effect of a relevant optimal control.

G. Rega and F. Vestroni (eds.),
IUTAM Symposium on Chaotic Dynamics and Control of Systems and Processes in Mechanics, 1–2.

Lenci and Rega present a unified theoretical framework for controlling bifurcation and chaos in mechanical systems. Attention is paid to investigating how a generic dynamical property, i.e. the occurrence of homo/heteroclinic bifurcations, entails a system-independent approach to optimal control, as well as generic solutions. Numerical simulations highlight the effectiveness of the method in controlling a number of meaningful bifurcational events.

Manevitch et al. present the results of analytical and numerical studies of random vibrations in nonlinear one-dimensional oscillatory chains which model significant mechanical and physical systems. The dependence of wave existence and propagation on the properties of nonlinear normal modes is investigated, and the occurrence of localized nonlinear vibrations (breathers) and chaotic thermal vibrations is shown.

In the last paper of Part I, van der Heijden and Thompson examine the patterns of various bifurcations governing the 1:2 internal resonance of an archetypal two-degree-of-freedom forced oscillator, relevant to a large class of mechanical problems. A knowledge of these bifurcations allows the counter-intuitive suppression and control of escape by internal modal interactions. Attention is focused on the effect that a symmetry-breaking imperfection has on the suppression of escape.

CHAOTIC CLOCKS: A PARADIGM FOR THE EVOLUTION OF NOISE IN MACHINES

Francis C. Moon
Cornell University, Ithaca, New York, USA
fcm3@cornell.edu

Abstract: This paper addresses two problems in the dynamics of machines; the nature of noise in machines and the evolution of noisy dynamics over several generations of machine design. To present a concrete example we examine the dynamics of clock escapements from experimental, historical and analytical points of view. This model is shown to exhibit a strange attractor in the structural vibration of the clock. Finally we introduce a theory and mathematical model for the evolution of noise in machine dynamics over several generations of design.

Key words: Noise, machine dynamics, clocks, chaos

1. Introduction

All machines exhibit a certain level of noise. The question arises as to whether a certain level of noise is natural or inevitable in a complex assembly of mechanical or electromechanical devices? In the early history of the steam turbine for example, Charles Parsons patented a mechanical oscillator in 1895 to break the friction in servo control valves (Conway [1]). Such designed noise in control systems is sometimes called 'dither'. However here we examine the question of whether engineers unknowingly admit noise in successive generations of design of machines. After two decades of research in nonlinear dynamics of machine elements, there are well documented examples of chaotic vibrations in bearings, gears, ball bearings and linkages. (See e.g. Moon [2])

G. Rega and F. Vestroni (eds.),
IUTAM Symposium on Chaotic Dynamics and Control of Systems and Processes in Mechanics, 3–16.

I have chosen to examine noise in the mechanical clock for several reasons. First it has a long and documented history of about five centuries. Second, although there have been many books written on the clock, there are very few that describe the complete nonlinear dynamics. Finally, the clock is a machine in which most people would assume the absence of noise and that establishing the existence of deterministic noise in clocks might give credence to the broader claim of natural chaos in complex machines.

2. Part I: Models for Chaotic Clocks

Early mechanical clocks from the 13th to the 17th century had an escapement without an oscillator. Post Huygens clocks (1657) have either a pendulum or a balance wheel and spring as the basic oscillator. Energy is supplied each cycle from either a falling weight or a wound elastic spring, through an escapement mechanism. [Figure 1.] The energy in most escapements is transmitted from the escape wheel to one or two pallets through impact forces. These forces propagate vibrations through the supporting structure and we posit that these impulse forces play a role in unlocking static friction in the gear train.

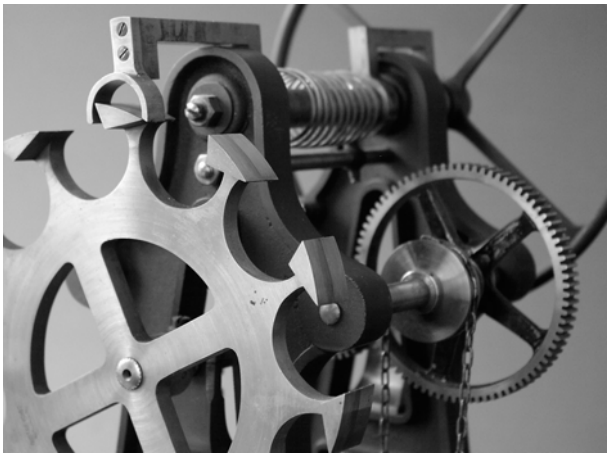

Figure 1. Reuleaux escapement model showing a cylinder escapement arm that drives the balance wheel in the background.(See Reuleaux (1893) [3])

The torque from the falling weight is delivered through a train of gears that acts in the opposite direction from most gear transmissions. The motion is driven from slow speed (falling weight) to the higher speeds of the clock hands. Thus it generally takes a large torque to deliver a small torque to the pendulum through the pallet arms of the escapement. In many theoretical

papers on clock dynamics, the gear train is not treated. However we will show that the static friction in the gear train is a key element in the existence of internal, chaotic noise in the clock.

2.1 Historical Review

The first pendulum clock is attributed to Huygens in 1657. The Huygens clock is a combination of the verge and the pendulum. Huygens [4] recognized that the period increased with the amplitude and designed a cycloidal shaped clamp for the pendulum that decreased the effective length of the swinging bob that led to a constant period independent of amplitude.

The next major improvement was the invention of the *anchor escapement* that replaced the verge with a two arm device in the shape of and anchor. This invention is often attributed to Robert Hooke but other sources give credit to a clockmaker William Clement in 1670. The anchor, like its predecessor the verge, served to regulate the amount of energy or torsional impulse imparted to the pendulum from the falling weight in each cycle. One fault of this device was the recoil that occurred when one of the two anchor pallets impacted the escape wheel teeth. This was corrected by the invention of the so-called *deadbeat escapement* invented by clock and instrument maker George Clement in 1715. This improvement redesigned the shape of the anchor pallet arms as well as the escape wheel so as to prevent recoil on impact.

The English clockmaker John Harrison (1693-1776) on the design of accurate clocks for marine travel and the determination of longitude is discussed in the popular book by Sobel and Andrewes [5]. Without listing all the improvements that he made, clock accuracy went from seconds per day to seconds per month during the Harrison dynasty. Despite this progress, the historical record is replete with evidence and discussion in the literature of the irregularities, inaccuracies and unpredictabilities in the mechanical clock.

Early works on the dynamics of clocks include George Biddell Airy (1826) [6], James Mackenzie Bloxam (1854) [7], and Edmond Beckett Denison (Lord Grimthorpe) (1868) [8]. Other important mathematical analyses in the 20th century were those of the Russians Andronov et al [9]. There have appeared a series of papers on the mathematical analysis of escapement dynamics such as, Kauderer in 1958 [10], Kesteven [11], Lepschy et al [12], Bernstein [13] and Roup and Bernstein et al [14].

2.2 Historical Evidence for Irregular Dynamics in Clocks

The quotes below, while anecdotal, are not based on controlled experiments as regards irregularity in clocks. However they do represent

typical data and observations of actual complex machines, in this case mechanical clocks. Lacking controlled experiments, the historical record from respected clock designers contains data, that although is course, is better than no data at all.

The following quotations are taken from a paper by Bloxam [7], published by the Royal Astronomical Society. This work was cited by another clock designer in a later paper by Lord Grimthorpe [8]. Bloxam combined both mathematical analysis with practical experience in addressing the sources of irregularities in clocks. The mathematics here is essentially sensitivity analysis of the clock period for various physical parameters in the clock. The paper starts on page 103 and quotations are in page order.

> Page 109 "It is usual with theorists to consider this force [of the impulse which the train transmits from the going weight to the pendulum], as constant during each impulse, but this assumption is too incorrect to be admitted, at least without examination, --"

> Page 121 "It is well known that the force transmitted by clock trains is far from constant. Small defects in the forms of the teeth of the wheels, and of the leaves of the pinions, and also in the depths to which they are set into each other, cause considerable irregularity in the force transmitted from each wheel to the next; and the accidental combinations of these irregularities in a train of four or five wheels makes the force transmitted from each to the last exceedingly variable."

> Page 128 "the theory of this escapement [the dead beat escapement], however perfect it may be by itself, must be rendered practically imperfect by the mechanical imperfections which we cannot estimate."

Denison (1868) (Lord Grimthorpe) later, in a book about clocks, also wrote about the unpredictability in clocks especially the gravity escapement;

> Page 153 "there is one position of the lever in which it jams against the teeth and stops the clock for good, --. Sometimes too, the click sticks and it sometimes slips, even if made rightly."

2.3 Experiments on Clock Escapements

To investigate the role of noise in clock escapements, dynamic experiments were made on several escapement models from the Reuleaux kinematic collection at Cornell University. This 19th century collection of 220 iron and brass models contains 10 clock escapement models. [Moon

[15]] One model is shown in Figure 1. This model is of a cylinder escapement that drives a balance wheel and torsional spring oscillator. This escapement was used in pocket watches. The second escapement is a three tooth device that is very old and drives a pendulum oscillator. In order to measure the internal vibrations, an accelerometer was placed on the half cylindrical arm on the cylinder escapement and on the pendulum arm on the three-tooth escapement.

In each model, the torque was generated by a falling weight acting through a single stage pinion and gear mechanism with the driving torque applied to the large diameter gear wheel. Thus torque flows from the falling weight through the pinion and is transferred to the oscillator by impact between the escapement arm that is connected to the pendulum or balance wheel. This impact generates vibration in the clock structure that is measured by the accelerometer.

The models were designed for demonstration and the falling weights only operated for a limited time so that it was not possible to obtain long time data and Poincaré maps.

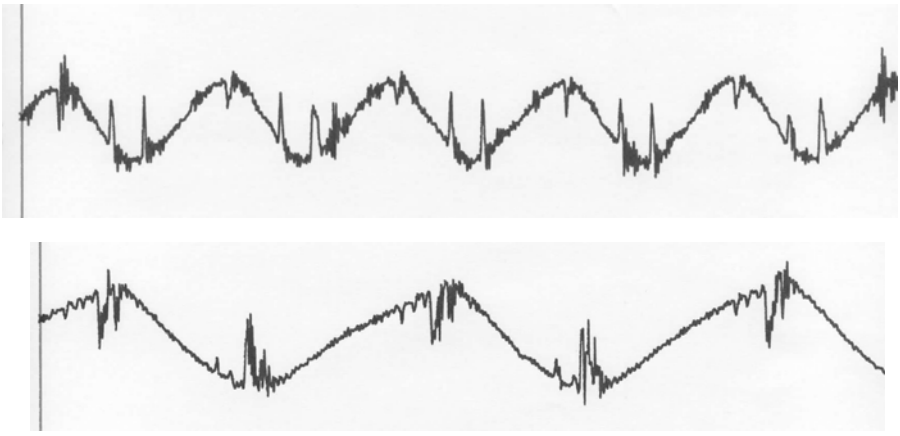

Figure 2 [Top] Experimental acceleration measurements on a clock escapement from the Cornell Reuleaux collection of kinematic models. Three tooth gravity escapement, Model X3. Reuleaux.
[Bottom] Experimental acceleration measurements on a clock cylinder escapement, Model X2. Reuleaux (1893).

The experimental data on clock escapements show the existence of non-periodic noise as shown in Figure 2. The vibrations clearly show the low frequency balance wheel or pendulum vibrations that are used to measure the time in seconds and minutes. However riding on top of these motions are non-periodic vibrations associated with the impact of the escapement wheel with the drive arm.

Friction in Gear Trains: Gear trains are used in clocks to change the very slow motion of the falling weight into motions associated with hours, minutes and seconds. A clock gear train is driven in the opposite direction than a speed reducer. Small friction torques in the pinion require large torques in the large gear. Thus it is possible for clock gear trains to lock up. Because of this friction large weights are sometimes required to maintain reliable running of a clock. For example an 8-day longcase clock might require 12-16 lbf weight. A month to three month clock required a weight of 40 lbf. (Bruton [16])

It is known however that motion in the gears can reduce the friction loss by up to 80%. Evidence for this can be found in the classic book on gears by Buckingham [17] in which he reported on experiments by the ASME that showed a dramatic drop in friction loss with gear speed (Figure 3). Following Parsons (Conway [1]), we postulate that a similar phenomenon occurs due to vibration in the gear transmission system. In the clock this vibration is self-induced by the 'tick tock' impact of the escapement.

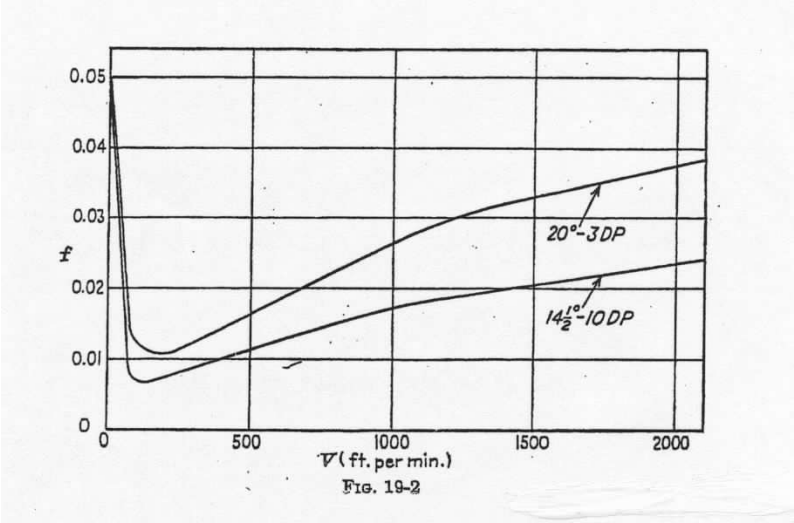

Figure 3. Friction in pinion and spur gear pairs versus velocity based on ASME tests 1931 [From Buckingham (1963) [17]]

2.4 Theoretical Model for Clock Chaos

To avoid the difficulties in the detailed analysis of specific escapements, we construct a generic model or prototype model, which it is hoped captures the essential features that the author claims is responsible for chaos in complex machines such as clocks. The model will incorporate the following assumptions and features.

a) the pendulum will be modeled by a linear harmonic oscillator with light damping;
b) the impact dynamics in the escapement and the propagation of structural dynamics through bearings with gaps will be modeled by a cubic oscillator of the Duffing type linearly coupled to the pendulum equation;
c) the driving gear train torque and static friction lockup is modeled by a threshold condition of structural impact as measured by the Duffing oscillator;
d) the driving torque from the weight driven gear train, when released by the Duffing oscillator, acts to add energy through the escapement pallet when the pendulum velocity is positive.

The first assumption a) is based on the fact that pendula in clocks rotate through a very small amplitude such that the nonlinear effects are not important. The second assumption b) is based on research by groups such as Pao et al [19] on the propagation of stress waves in structures. Both experimental and theoretical research show that a single impact or a step input load on a structure leads to complex wave patterns through reflections and dispersion which excite many modes in the structure. Thus this energy redistribution can propagate into the gear train and break the friction and prevent lockup. These assumptions lead to the following equations of motion for the coupled pendulum, structural dynamics and driving train. This fourth order model employs a vibration sensitive torque to capture the escapement impact;

$$\ddot{x}_1 + \beta_1 \dot{x}_1 + \omega_1^2 x_1 + \alpha_1 x_3 = tq(\dot{x}_3) sign(\dot{x}_1); \quad \text{[Clock Escapement]}$$

$$\ddot{x}_3 + \beta_2 \dot{x}_3 + \omega_2^2 x_3 + \kappa x_3^3 + \alpha_2 x_1 = 0; \quad \text{[Clock Structure]}$$

where

$tq(\dot{x}_3) = T_0$; if $\dot{x}_3^2 > \delta$ and $0 < x_1 < \Delta$;

$tq(\dot{x}_3) = 0$, otherwise.

Here $x_1(t)$, represents the motion of the pendulum or balance wheel oscillator; $x_3(t)$, represents the motion of the structural connection between the escapement and the driving train; the cubic term is a nonlinear surrogate for the gaps between bearings and gear teeth. The torque dependence on structural velocity is an attempt to capture the static friction in the drive train and its dependence on the structural vibration.

2.5 Simulation Results of Clock Proto-Model

The coupled oscillator equations of motion were numerically integrated using MATLAB software. A few of the results are shown in Figures 4,5. Figure 4-left shows a near limit cycle oscillation in the primary clock variable while Figure 4-right shows a more chaotic-looking signal in the coupled structural state variable. A low dimensional model might neglect the structural 'noise', but an analysis of the problem shows that the noise is self generated and is essential to providing the trigger for the escapement torque in order to drive the nearly periodic oscillator. The trigger in this model is included as a mechanism for the friction-breaking 'dither' in real machines.

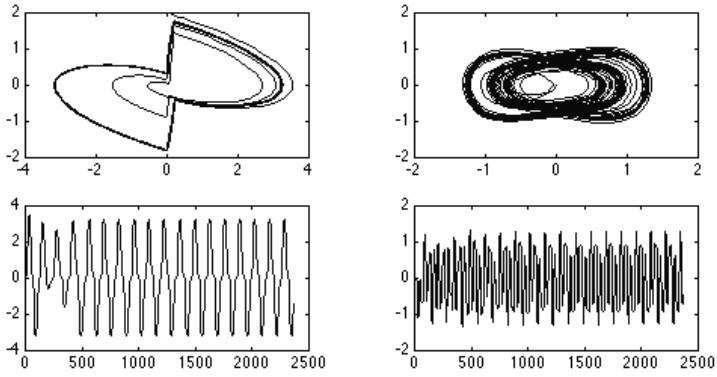

Figure 4. Numerical simulation of dynamic model of a clock escapement. Right pair is the clock oscillator. Left pair shows the structure oscillator dynamics.

A Poincaré map (Moon [2]) is used to show the existence of a fractal strange attractor as shown in Figure 5, and provides evidence for chaotic vibrations in the clock. In the simulation, the Poincaré map is generated when the clock variable $x_1(t)$ crosses a certain level. The map is plotted in the phase space variables of the structural oscillator. The resulting Poincaré map has a fractal-like structure. This is rather remarkable since the attractor lies in a four dimensional state space. However the 2D map shows the dynamical decoupling that occurs in this model between the near periodic clock oscillator and its structural linkage.

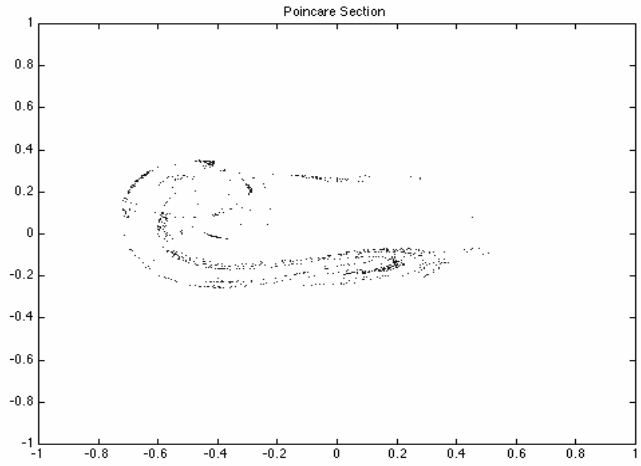

Figure 5. Poincaré map of the clock model; $\dot{x}_3$ vs x_3; when x_1=0, $\dot{x}_1$>0.

3. Part II: A Proto-Model for Machine Evolution

In our discussion of the history of clocks and their dynamic modeling several characteristics of clock evolution emerged. First, most clock designs evolved from earlier designs in which a small number of components are changed at each design generation. Second as precision in the clock increases, the number of parts and/or their complexity increases. Thirdly we learned in the dynamic model of the clock escapement that a small amount of noise may be desired to break friction in the drive train. We propose a mathematical model that incorporates these properties of clock design evolution. The idealized model cannot hope to predict actual part changes. Our goal however is to develop a model that will predict the evolutionary behavior of the clock dynamics over several design generations. We call this a prototype model or proto-model.

This proto-model will have two time scales; the machine or clock time and the design generation time. In the machine time, the clock model must exhibit a near periodic solution over all design generations; otherwise it fails as a clock. Also the model must account for the existence of noise and maintain the near periodic behavior in the presence of noise and through successive design cycles.

At each generation, the increase in parts or complexity is modeled by the addition of new state variables. At the same time, an optimization principle must be established to assign parameters to the new model so that some cost function or performance measure is minimized or maximized to improve

some aspect of the dynamical behavior. This optimization model differs from classical techniques that often are applied to a fixed dimensional state space. (Haug and Arora, [19]) In our problem however the dimension of the state space grows as the complexity of the machine evolves. For simplicity and to illustrate the methodology we chose a discrete time or iterated map for the clock. This map is not too far from the real clock machine if one imagines a mapping based on the escapement impact with the pendulum or balance wheel.

For every proto-model of machine evolution we posit a '*primitive machine dynamics'*. In the case of the ideal clock, we chose as our primitive mapping the logistic equation. This map is autonomous, nonlinear and exhibits periodic solutions like the clock. It also exhibits near periodic solutions in the presence of small random noise. We denote the state of machine by the vector x^a_n ; where the superscript indicates the design generation cycle and the subscript 'n' denotes the discrete clock time, not unlike the 'tick-tock' time. For the form of the logistic map we write;

$$x^o_{n+1} = \lambda_1 x^o_n (1 - x^o_n) + r_n$$

where λ is a control parameter and r_n, represents a random or chaotic noise in the machine. [See e.g. Nayfeh and Balachandran [20] for properties of the logistic map.] As an example we choose the control parameter λ equal to 3.0 such that the map has a period-two cycle. Under a small amount of random noise, $\{ r_n \}$, a return map shows a distribution function about the two cyclic points of *x*.

To create a design iteration map, or the next generation machine, we add another state variable with linear coupling to the primary machine as illustrated below;

$$\begin{bmatrix} x^1_1 \\ x^1_2 \end{bmatrix}_{n+1} = \begin{bmatrix} \lambda_1 x^1_1 (1 - x^1_1) \\ 0 \end{bmatrix}_n + \begin{bmatrix} r_n \\ 0 \end{bmatrix} + \begin{bmatrix} a_{11} & a_{12} \\ a_{21} & a_{22} \end{bmatrix} \begin{bmatrix} x^1_1 \\ x^1_2 \end{bmatrix}_n$$

where,

$$A = [a_{ij}] = \begin{bmatrix} 0 & \varepsilon \\ \varepsilon & \lambda_2 \end{bmatrix}$$

$\varepsilon << 1$, and $0 < \lambda_2 < 1$.

To simplify this model further and to insure that the new 'clock' remains ticking near a period two cycle, we chose the A matrix to have the special form given above. When there is no coupling between the primitive machine and the new state variable x_2 , $(\varepsilon = 0)$, the system exhibits a linear map in

the additional state variable. Restricting the control parameter between zero and one guarantees an asymptotically stable fixed point with monotonic dynamics. We choose λ_2 equal to 0.2 in our numerical example. [A discussion of two and higher dimensional maps may be found in Devaney [21].]

We chose ε to be small and to try to optimize a cost or performance function. The addition of the extra state variable and the coupling matrix A has two effects on the map dynamics; the first is to change the width of the PDF of the map around the cycle-two points. The second effect is to increase the separation between the two fixed points. A plot of these two measures of performance (Figure 6) shows that the complex 'machine' {A and ε} can produce a minimum in the noise induced PDF of the dynamics. Thus the added complexity of the 'machine' can optimize the dynamic performance.

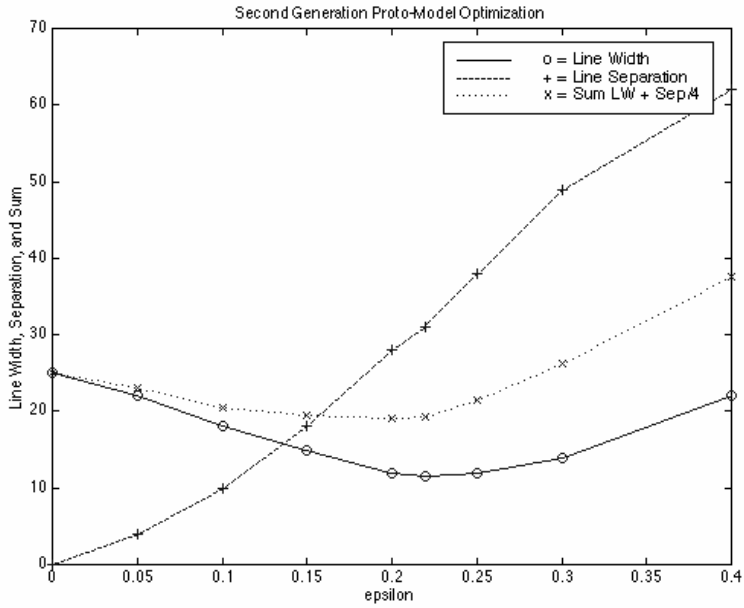

Figure 6. Three dynamic cost functions for the second generation logistic map 'machine'; Line width of histogram, Separation of near periodic orbit points, Weighted sum of the first two cost functions.

This process can be extended to a third generation machine as defined by the third order mapping;

$$\begin{bmatrix} x_1^{(2)} \\ x_2^{(2)} \\ x_3^{(2)} \end{bmatrix}_{n+1} = \begin{bmatrix} \lambda_1 x_1^{(2)}(1-x_1^{(2)}) \\ 0 \\ 0 \end{bmatrix}_n + \begin{bmatrix} r_n \\ 0 \\ 0 \end{bmatrix} + [A] \begin{bmatrix} x_1^{(2)} \\ x_2^{(2)} \\ x_3^{(2)} \end{bmatrix}_n$$

$$[A] = \begin{bmatrix} 0 & \varepsilon_1 & \varepsilon_3 \\ \varepsilon_1 & \lambda_2 & \varepsilon_2 \\ \varepsilon_3 & \varepsilon_2 & \lambda_3 \end{bmatrix}$$

where ε_1 and λ_2 are chosen from the second generation machine. The new parameter λ_3 {=0.1} is again restricted between zero and one for stability while the new coupling parameters ε_2 and ε_3 are chosen to optimize the cost function again, which is the sum of the widths of the noise broadened period-two motion.

Such a process of machine dynamics evolution raises several interesting questions about both the mathematical model as well as the evolution of actual machines. For example, will such a process lead to a '*limit machine'*? By a limit machine we mean one where the increase in the complexity of the machine dynamics does not result in further performance enhancement. This limit might be asymptotic or a finite limit.

Another question is the possibility of the design iteration process leading to multiple solutions. For example in the third generation model above there exist two minima in the cost function leading to two fourth generation machines. This would constitute *design branching* or bifurcation in the design generation tree leading to different families of the same primitive machine.

The evolution model for the development of machines differs substantially from that in biology that is based on the coexistence of many species competing for changing resources. It also differs from the genius-inventor theory of technical progress popular in the nonacademic literature. Our theory is based on a primitive machine or kernel from which all other branches derive based on added complexity and performance optimization.

These questions are clearly speculative, yet may be prescient about the future development of machines. There is already research on the use of computer models to 'invent' new mechatronic machines through optimization techniques. What this paper suggests is that if such a direction is inevitable then dynamic modeling of machines and their evolution may play a part in this new world of machines.

4. General Remarks and Conclusions

We have presented a clock dynamics model with gear friction released by structural vibration as an example of 'good chaos' in machines. It is the author's belief that an examination of real machine systems will reveal low levels of noise which in many cases may have beneficial effects on the dynamic machine performance.

We have also used the clock paradigm to postulate an evolution model for the development of complexity as a way to optimize noise in the design of machines over several generations. Using optimization of a cost function for the dynamic performance we have shown how multiple solutions in the design solutions can naturally occur. This speculative model may provide a paradigm for the role of nonlinear dynamics and chaotic noise in the design evolution of machines.

5. References

[1] H. G. Conway, "Origins of mechanical servo mechanisms", *The Newcomen Society,* Vol. XXIX, 1953-54, 1954-55.
[2] F. C. Moon, *Chaotic and Fractal Dynamics*, J. Wiley, New York, 1992.
[3] F. Reuleaux, *The Constructor*, 4th Edition, Translated by H. Suplee, 1893.
[4] C. Huygens, *Horologium,* 1658.
[5] D. Sobel and W. J. H. Andrewes, *The Illustrated Longitude,* Walker and Company, N.Y, 1998.
[6] G. B. Airy, (1826) "On the disturbances of pendulums and balances and the theory of escapements", *Trans. Cambridge Phil. Soc.* Vol III Part I, 105-128, Pl. 2, 1830.
[7] J. M. Bloxam, "On the mathematical theory and practical defects of clock escapements, with a description of a new escapement; and some observations for astronomical and scientific purposes", *Memoirs of the Royal Astronomical Society*, Vol. XXII, 103-150, 1854.
[8] E. B. Denison, (a.k.a. Lord Grimthorpe), *A Rudimentary Treatise on Clocks and Watches and Bells,* 1868.
[9] A. A. Andronov, A. A. Vitt and S. E. Khaikin, *Theory of Oscillators*, Pergamon Press, Oxford. Dover Publ., 1987.
[10] H. Kauderer, *Nichtlineare Mechanik,* Springer-Verlag, Berlin. Second part, Section 4, pp. 415-423, 1958.
[11] M. Kesteven, "On the mathematical theory of clocks", *Am. J. Phys*. 46(2), pp 125-129, 1978.
[12] A. M. Lepschy, G. A. Mian and U. Viaro, "Feedback control in ancient water and mechanical clocks", *IEEE Trans. Edu.*, Vol. 35, No.1, pp. 3-10, 1992.
[13] D. Bernstein, *Escapements, Governors, Ailerons, Gyros, and Amplifiers: Feedback Control and the History of Technology*, Michigan St. Univ. Report, 2000.
[14] A.V. Roup, D. S. Bernstein, S. G. Nersesov, W. M. Haddad and V. Chellaboina, *Limit Cycle Analysis of the Verge and Foliot Clock Escapement Using Impulsive Differential Equations and Poincaré Maps*, Michigan St. Univ. Report, 2001.

[15] F. C. Moon, "Franz Reuleaux; Contributions to 19th century kinematics and theory of machines", *Applied Mechanics Reviews,* Vol. 56, No. 2, pp. 261-285, 2003.
[16] E. Bruton, *The Longcase Clock*, F.A. Praeger, N.Y., 1968.
[17] E. Buckingham, *Analytical Mechanics of Gears,* 1949.
[18] Y-H. Pao, D-C. Keh and S. Howard, "Dynamic response and wave propagation in plane trusses and frames", *AIAA J.* Vol. 37, No. 5, pp. 594-603, 1998.
[19] E. J. Haug and J. S. Arora, *Applied Optimal Design*, J. Wiley, N.Y.
[20] A. Neyfeh and B. Balachandran, *Applied Nonlinear Dynamics,* J. Wiley, N.Y., 1995.
[21] R. L. Devaney, *An Introduction to Chaotic Dynamical Systems,* 2nd Edition, Addison-Wesley, Reading, Mass., 1989.

EXPLORATIONS INTO THE NONLINEAR DYNAMICS OF A SINGLE DOF SYSTEM COUPLED TO A WIDEBAND AUTO-PARAMETRIC VIBRATION ABSORBER

Anil K. Bajaj, Ashwin Vyas and Arvind Raman
School of Mechanical Engineering, Purdue University
West Lafayette, IN 47907-2088, U.S.A
bajaj@ecn.purdue.edu

Abstract: The nonlinear dynamics of a resonantly excited linear oscillator coupled to an array of weakly coupled nonlinear pendulums is investigated under 1:1:...:1:2 internal resonance between the pendulums and the linear oscillator. In the first part of the work, periodic solutions and bifurcations under harmonic excitation of the linear oscillator are investigated. In the second part of the work, numerical simulations of the unperturbed Hamiltonian are presented to demonstrate the complex dynamics of the system even in the absence of external excitation.

Key words: Autoparametric system, vibration absorber, internal resonances, Hamiltonian.

1. Introduction

Autoparametric two degree-of-freedom nonlinear systems coupled by quadratic nonlinearities exhibit saturation phenomenon under 1:2 internal resonance [1, 2]. This property of quadratically coupled systems has been utilized in developing an autoparametric vibration absorber modelled as a secondary system (pendulum) coupled to a resonantly excited primary system (linear oscillator). The secondary system is tuned to a frequency nearly half that of the primary system for attenuating resonant response of the primary system [3]. Recently, Vyas and Bajaj [4] introduced the concept and working principle of a wideband autoparametric vibration absorber consisting of an array of n slightly mistuned *uncoupled* pendulums that were attached to the primary system. It was shown that the effective bandwidth of absorber action can

G. Rega and F. Vestroni (eds.),
IUTAM Symposium on Chaotic Dynamics and Control of Systems and Processes in Mechanics, 17–26.

be substantially increased by using pendulums with non-uniformly distributed mistunings.

The present work investigates the nonlinear dynamics of a resonantly excited primary system coupled to an array of weakly coupled pendulums under 1:2 internal resonance with the primary system. The amplitude and phase equations, obtained using the method of averaging [1], are studied for equilibrium solutions. Local bifurcation analysis is performed using AUTO [5] and the effects of coupling the pendulums are explored. To investigate global behavior for amplitude and phase variables, a Hamiltonian formulation is introduced. This analysis is restricted to the case of uncoupled pendulums. Some equilibrium solutions are determined and their stability analysis is performed to help guide numerical investigations. Numerical simulations of the Hamiltonian averaged system are performed to demonstrate the complex dynamics of the system.

2. System Equations and Averaging

Figure 1 shows the primary system consisting of a linear spring-mass-damper and the secondary system consisting of an array of n weakly coupled ideal pendulums. The block is excited by a harmonic external force $P_0\ cos(\omega t)$. The non-dimensional equations of motion for the system, assuming only linear coupling between the pendulums, are [4]:

$$\eta'' + 2\hat{\xi}_b\alpha\eta' + \alpha^2\eta - \sum_{i=1}^{n}\frac{r_i\nu_i R}{1+R}(\theta_i''\sin\theta_i + \theta_i'^2\cos\theta_i) = F\alpha^2\cos\tau, \quad (1)$$

$$\begin{aligned}
&\theta_i'' + 2\xi_i\alpha\hat{\beta}_i\theta_i' + \alpha^2\beta_{3i}^2\theta_i + (\alpha^2\beta_{2i}^2 - \frac{\eta''}{\nu_i})\sin\theta_i = \\
&\quad + \frac{\kappa_{(i-1)i}}{r_i}(\theta_i - \frac{\nu_{(i-1)}}{\nu_i}\theta_{(i-1)}) + \frac{\kappa_{i(i+1)}}{r_i}(\theta_i - \frac{\nu_{(i+1)}}{\nu_i}\theta_{(i+1)}) = 0, \\
&i = 1,\ldots,n;\ \ \kappa_{01} = \kappa_{n(n+1)} = 0;\ \ \nu_0 = \nu_{n+1} = \theta_0 = \theta_{n+1} = 0,
\end{aligned} \quad (2)$$

where

$$\kappa_{j(j+1)} = \frac{K_{j(j+1)}}{(1 + (l(\nu_j - \nu_{(j+1)})/L_{j(j+1)})^2)}, \qquad j = 1, 2, \ldots, (n-1). \quad (3)$$

Here, r_j is the "mass fraction" of the j^{th} pendulum, ν_j is the "length fraction" of the j^{th} pendulum, $\sum_{i=1}^{n} r_i = 1$ and $\sum_{i=1}^{n}\nu_i^2 = 1$. Also, $\kappa_{i(i+1)}$ is the coupling stiffness between the i^{th} and the $(i+1)^{th}$ pendulum. All other non-dimensional variables are as defined in [4].

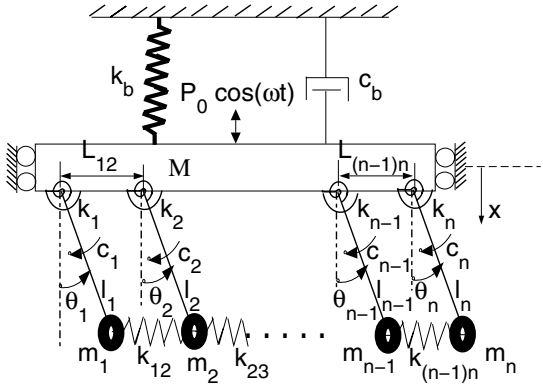

Figure 1. A linear SDOF system with n attached weakly coupled pendulums.

Formulation and the Averaged Equations: The dynamics of the system under investigation is controlled by Equations (1) and (1). These equations are transformed to a standard form for applying the method of averaging by defining the following scale changes:

$$\eta = \epsilon\hat{\eta}, \quad \theta_i = \epsilon\hat{\theta}_i, \quad \overline{\theta}_i = \frac{1}{2}\sqrt{\frac{R}{2(1+R)}}\,\hat{\theta}_i, \quad F = \epsilon^2\hat{F},$$

$$\hat{\xi}_b = \epsilon\overline{\xi}_b, \quad \xi_i = \epsilon\hat{\xi}_i, \quad i = 1, 2, \ldots, n,$$

$$K_{j(j+1)} = \epsilon\hat{K}_{j(j+1)}, \quad \kappa_{j(j+1)} = \epsilon\hat{\kappa}_{j(j+1)} \quad j = 1, 2, \ldots, n-1, \tag{4}$$

where ϵ is some arbitrary scaling parameter such that $0 < \epsilon << 1$. Also, we introduce external and internal mistunings:

$$\alpha^2 = 1 + 2\epsilon\sigma_b, \quad p_i^2 = \frac{1}{4} + \epsilon\sigma_i, \quad d_i = \sigma_b - 2\sigma_i, \quad i = 1, 2, \ldots, n, \tag{5}$$

where σ_b is the detuning between the excitation frequency and the locked-pendulum natural frequency, σ_i, $i = 1, 2, \ldots, n$, are the mistunings from perfect 1:2 resonance between the linear natural frequencies of the uncoupled pendulums and the frequency of excitation, and d_i defines the detuning from exact internal resonance between the linear natural frequency of the locked-pendulum motion and the natural frequency of the i^{th} uncoupled pendulum.

The averaged equations for the system are then [4]:

$$a_b' = [-\frac{1}{2}\hat{F}\sin\beta_b - a_b\xi - \sum_{i=1}^{n} r_i v_i a_i^2 \sin(2\beta_i - \beta_b)],$$

$$a_b\beta_b' = [-\frac{1}{2}\hat{F}\cos\beta_b + a_b\sigma_b + \sum_{i=1}^{n} r_i v_i a_i^2 \cos(2\beta_i - \beta_b)],$$

$$a_i' = [\frac{1}{2\nu_i} a_b a_i \sin(2\beta_i - \beta_b) - a_i \bar{\xi}_i + C_{p1i}],$$
$$a_i \beta_i' = [\frac{1}{2\nu_i} a_b a_i \cos(2\beta_i - \beta_b) + a_i \sigma_i + C_{p2i}],$$
$$i = 1, 2, \ldots, n, \tag{6}$$

where

$$C_{p1j} = -\frac{\hat{\kappa}_{(j-1)j}}{r_j} \frac{\nu_{(j-1)}}{\nu_j} a_{(j-1)} \sin(\beta_j - \beta_{(j-1)})$$
$$-\frac{\hat{\kappa}_{j(j+1)}}{r_j} \frac{\nu_{(j+1)}}{\nu_j} a_{(j+1)} \sin(\beta_j - \beta_{(j+1)}),$$
$$C_{p2j} = \frac{\hat{\kappa}_{(j-1)j}}{r_j} (a_j - \frac{\nu_{(j-1)}}{\nu_j} a_{(j-1)} \cos(\beta_j - \beta_{(j-1)}))$$
$$+\frac{\hat{\kappa}_{j(j+1)}}{r_j} (a_j - \frac{\nu_{(j+1)}}{\nu_j} a_{(j+1)} \cos(\beta_j - \beta_{(j+1)})),$$
$$j = 1, 2, \ldots, n; \quad \kappa_{01} = \kappa_{n(n+1)} = 0; \nu_0 = \nu_{n+1} = 0, \tag{7}$$

and a prime now denotes derivative with respect to the slow time.

Here, (a_b, β_b) represent the amplitude and phase of the block motion with locked pendulums, and (a_i, β_i) are the amplitudes and phases of pendulum motions.

3. Steady-State Periodic Motions

It can be shown [4] that the averaged equations are exactly solvable for equilibrium solutions in the absence of coupling springs. In the presence of coupling springs [6], this can be achieved only for special parameter combinations. In general, the equilibrium solutions have to be numerically determined. The results presented here focus on the effect of coupling on the steady-state solutions. These solutions are obtained numerically using the continuation and bifurcation analysis software AUTO [5]. Figure 2 shows the response of a system with two pendulums for different coupling stiffnesses $\hat{K}_{12} = 0$, $\hat{K}_{12} = 0.05$ and $\hat{K}_{12} = 0.1$. The other parameters for this system are: the mass fractions $r_1 = r_2 = 0.5$; the length fractions $\nu_1 = \nu_2 = \frac{1}{\sqrt{2}}$; the internal mistunings $d_1 = 1$ and $d_2 = -1$; and the scaled dampings $\bar{\xi}_1 = \bar{\xi}_2 = 0.25$. The forcing amplitude $\hat{F}$ is set equal to 2.0.

For the case of uncoupled pendulums ($\hat{K}_{12} = 0$), it is seen in the figure that the locked-pendulums response of the system ($a_1 = a_2 = 0$) exists at all frequencies. This response becomes unstable by pitchfork bifurcation [7] at frequencies denoted by a '□'. For excitation frequencies between the two

pitchfork points where the locked-pendulums response is unstable, stable motions only have one of the pendulums oscillating along with the block. There is a degeneracy in the solutions at which the stable non-zero pendulum response switches from one pendulum to the other and a manifold of equilibria exists at the switching frequency, leading to a change in stability of the pendulum motions [4]. This frequency is characterized by the point where the amplitude of block motions in the two distinct solution branches with non-zero motion of one or the other pendulum coincide.

For the coupled pendulums system ($\hat{K}_{12} \neq 0$), both the pendulums are now in motion for frequencies between the pitchfork points; however, interestingly one of the pendulums has much larger amplitude compared to the other. This phenomenon of mode-localization has also been observed [8] in the response of cyclic periodic systems. Hopf-bifurcation points [7] also appear for $\hat{K}_{12} = 0.1$, as shown by solid square in the figure. This is a result of coupling in the pendulums leading to additional mistuning in the system. It is shown in [6] that the manifolds of equilibria joining solution branches in the pendulum motions persist even in the presence of coupling if the two pendulums have equal length fractions and damping. Figure 3 shows the steady-state amplitudes a_1 and a_2 for a system with unequal length fractions ($\nu_1 = \sqrt{\frac{1}{5}}$, $\nu_2 = \sqrt{\frac{5}{6}}$), demonstrating an unfolding of the degenerate manifold into distinct stable and unstable branches. The mode-localization effect is still visible with one pendulum oscillating at much larger amplitude compared to the other over a large frequency interval. As the excitation frequency is varied, the response of the pendulum then switches rapidly, though continuously, to a small amplitude in the vicinity of a certain value of σ_b.

4. Global Dynamics of the Averaged System

The global dynamics of the averaged system (5) for general two DOF systems, including the present system with only one pendulum, was investigated in [9]. A global perturbation analysis technique was used such that the forced system was considered as a perturbation of a completely integrable Hamiltonian system. This was accomplished by assuming the external excitation to be small compared to nonlinearities in the system. Due to the complete integrability of the reduced Hamiltonian system, the phase plane behavior provided the whole picture of dynamics, including the homoclinic and heteroclinic invariant manifolds. Melnikov analysis then showed that saddle connections in the reduced phase space are most susceptible and lead to chaotic motions under perturbation. Thus, Hamiltonian dynamics can form a basis for global dynamic analysis.

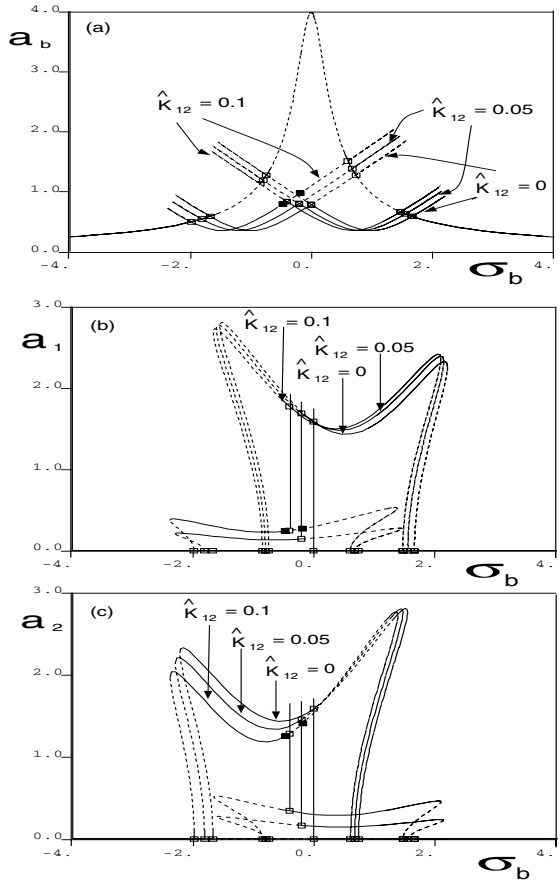

Figure 2. Effect of the coupling stiffness $\hat{K}_{12}$ on the response of the system with two pendulums. $\xi = \bar{\xi}_1 = \bar{\xi}_2 = 0.25$; $d_1 = 1.0$, $d_2 = -1.0$; $r_1 = r_2 = 0.5$; $\nu_1 = \nu_2 = \frac{1}{\sqrt{2}}$. Amplitude of response for (a) Primary system, a_b; (b) First pendulum, a_1; (c) Second pendulum, a_2.

The approximate Hamiltonian (upto O(3)) of the system with n uncoupled pendulums, simplified by Canonical transformations and averaged over time [10, 11], results in the following averaged Hamiltonian equations:

$$
\begin{aligned}
&P_E' = -\delta\hat{F}\sqrt{2P_b}\sin 2Q_E,\\
&Q_E' = \frac{\sigma_b}{2} + \sum_{i=1}^{n}\frac{P_i}{4\nu_i\sqrt{2P_b}}\cos 2Q_i - \frac{\delta\hat{F}}{4\sqrt{2P_b}}\cos 2Q_E,\\
&P_j' = \frac{P_j\sqrt{2P_b}}{\nu_j}\sin 2Q_j,\\
&Q_j' = -\frac{d_j}{2} + \frac{\sqrt{2P_b}\cos 2Q_j}{2\nu_j} - \sum_{i=1}^{n}\frac{P_i\cos 2Q_i}{4\nu_i\sqrt{2P_b}} + \frac{\delta\hat{F}}{4\sqrt{2P_b}}\cos 2Q_E,\\
&j = 1, 2, \ldots, n; \qquad P_b = 0.5(P_E - \sum_{i=1}^{n} P_i),
\end{aligned}
\tag{8}
$$

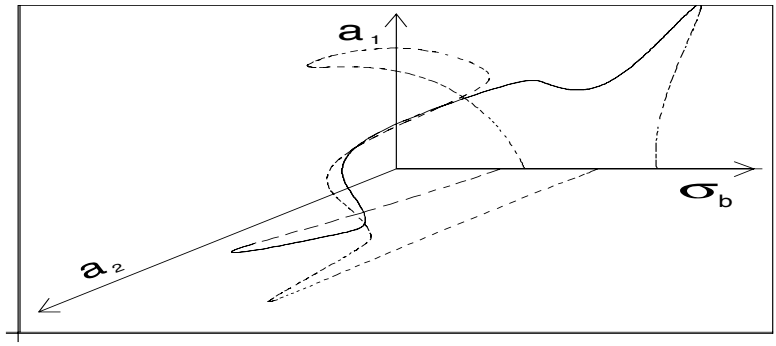

Figure 3. Pendulum amplitudes as a function of σ_b showing the unfolding of manifolds of equilibria. $\xi = \bar{\xi}_1 = \bar{\xi}_2 = 0.25$; $d_1 = 1.0$, $d_2 = -1.0$; $r_1 = r_2 = 0.50$; $\nu_1 = \frac{1}{\sqrt{5}}$, $\nu_2 = \sqrt{\frac{5}{6}}$; $\hat{K}_{12} = 0.05$.

where (P_j, Q_j) represent the action and phase variables for the j^{th} pendulum, P_E is an invariant of motion (total energy) for the unperturbed system (δ=0) and the Hamiltonian is cyclic in phase Q_E. Further, for the unperturbed system, dynamics in the (P_j, Q_j) space are independent of σ_b. The Hamiltonian for the unperturbed (zero external excitation) system is:

$$H_0(P_E, Q_E, P_j, Q_j) = \frac{\sigma_b P_E}{2} + \sum_{j=1}^{n} \frac{P_j}{2\nu_j}(-\nu_j d_j + \sqrt{2P_b}\cos 2Q_j). \quad (9)$$

Consider the system with two pendulums. Then, (P_1,Q_1) and (P_2,Q_2) are invariant planes. The orbits in the (P_1,Q_1) plane for the unperturbed system (δ=0) with $d_1 = 0.18$ and $P_E = 1$ are shown in Figure 4. The value of P_E is set to 1.0 for all the results of unperturbed system. There exist centers and saddles, periodic motions and heteroclinic orbits. When perturbed by external excitation ($\delta = 0.17$ and $\sigma_b = 1.5$), the system with one pendulum ($P_2 = 0$) exhibits complex dynamics, as is illustrated in Figure 5 (see also [9]).

For an unperturbed system with two pendulums that are in perfect internal resonance (d_j=0) and equal length fractions, the equilibrium solutions in (P_1, Q_1, P_2, Q_2) space (for $P_E = 1.0$) are located at $\{(P_1, 0, (2/3) - P_1, 0), (P_1, \pi/2, (2/3) - P_1, \pi/2)\}$ (center and a pair of zero eigenvalues), $\{(0, 0, 2/3, 0), (0, \pi/2, 2/3, \pi/2)\}$, (a pair of zero eigenvalues and center), $\{(2/3, 0, 0, 0), (2/3, \pi/2, 0, \pi/2)\}$, (center and a pair of zero eigenvalues), and (0, $\pi/4$ or $3\pi/4$, 0, $\pi/4$ or $3\pi/4$) (saddle-saddle). This provides a qualitative picture of the trajectories in the 4-D phase space. Numerical simulations of the system with initial conditions in the vicinity of heteroclinic orbits are then of interest in exploring complex (chaotic) dynamics arising from the transverse intersections of stable and unstable manifolds [9].

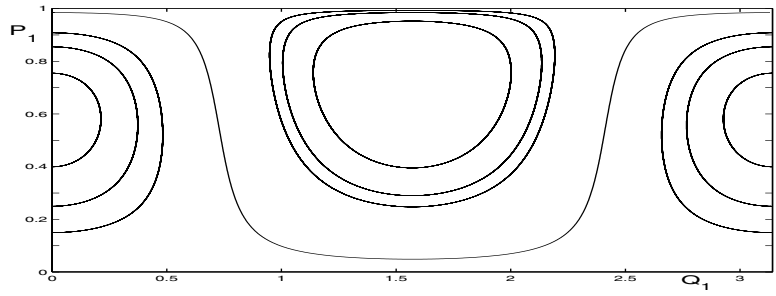

Figure 4. Orbits in the invariant (P_1, Q_1) plane for the unforced single pendulum system. $d_1 = 0.18$, $\delta = 0.0$, $P_E = 1$.

Figure 6 shows the Poincare section in the (P_1, Q_1) plane, at $\cos(2Q_2) = -0.9$. The system has unequal length fractions with $\nu_1 = \sqrt{5/6}$ and internal mistunings $d_1 = 0.18$ and $d_2 = 0$. The equilibrium solutions of the system (for $P_E = 1.0$) are $\{E1 = (0, 0.703, 0, \pi/4)\,,\ E2 = (0, 0.703, 0, 3\pi/4)\}$ (saddle-saddle) and $\{E3 = (0.597, 0, 0, 0.616),\ E4 = (0.724, \pi/2, 0, 1.099)\}$ (center-saddle). The initial conditions are chosen near the equilibrium points of the system. For the initial condition near the saddle-saddles, the stochastic motion occupies a larger region of the phase space as compared to the other two initial conditions near center-saddles. Figures 7(a) and 7(b) show P_2 as a function of time τ when the initial conditions are chosen near the equilibrium point $E4$ (center-saddle) and $E1$ (saddle-saddle), respectively.

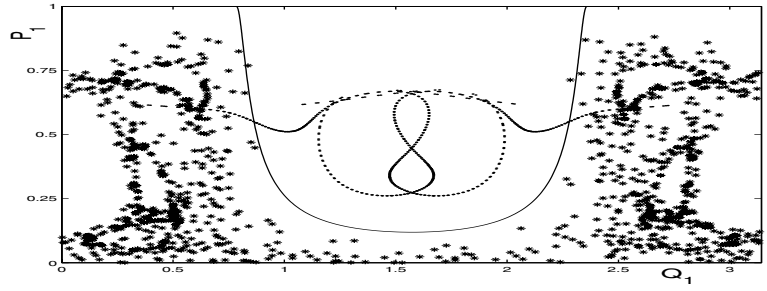

Figure 5. Poincare sections at $\cos Q_E$=0.75 for two orbits started with different initial conditions for the externally excited system with a single pendulum: near a center (.) and near a saddle (*). Solid curve shows the heteroclinic orbit. d_1=0.18, $\sigma_b = 1.5$, $\delta = 0.17$, $\hat{F} = 2.0$.

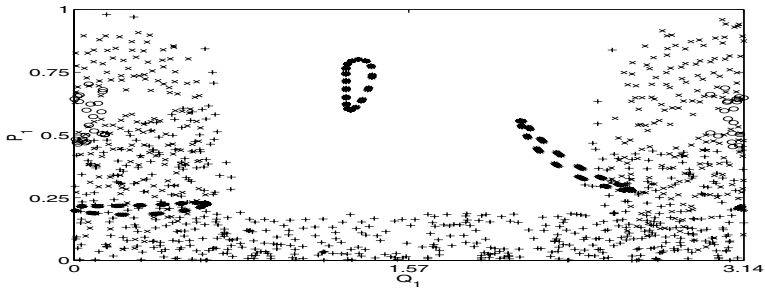

Figure 6. (P_1, Q_1) plane projection of Poincare sections at $\cos 2Q_2$=-0.9 for solutions with four different initial conditions: near two center-saddles (o and *), near two saddle-saddles (+ and x). $d_1 = 0.18$, $d_2 = 0$; $\nu_1 = \sqrt{\frac{5}{6}}$, $\nu_2 = \sqrt{\frac{1}{6}}$; P_E=1.

5. Summary

In this work, the nonlinear local and global dynamics of a resonantly excited linear oscillator coupled to an array of nonlinear pendulums are investigated. The pendulum frequencies are tuned so that the pendulums are coupled to the linear oscillator through autoparametric 1:2 internal resonances. For the forced nonlinear system, effect of linear coupling between the pendulums is investigated. In particular, it is shown that for the uncoupled pendulums case, only one stable periodic motion exists at each excitation frequency. At discrete frequencies, stable motion switches from one pendulum to the other. A manifold of solutions exists at such switching frequencies. In the presence of

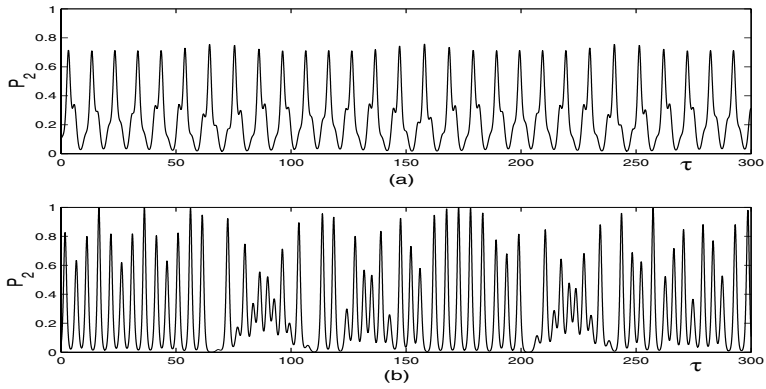

Figure 7. Trajectory of pendulum 2 action P_2 as a function of time τ. $d_1 = 0.18$, $d_2 = 0$; $\nu_1 = \sqrt{\frac{5}{6}}$, $\nu_2 = \sqrt{\frac{1}{6}}$; P_E=1. (a) Motion started near the center-saddle represented by * in Figure 6, (b) Motion started near the saddle-saddle represented by + in Figure 6.

linear coupling among pendulums, this manifold and degenerate behavior is destroyed. The global dynamics of the amplitude equations is then formulated in action-angle variables, and numerical simulations show complex dynamics even for the unforced system.

References

[1] A.H. Nayfeh and D.T. Mook, *Nonlinear Oscillations*. Wiley Interscience, New York, 1979.

[2] P.R. Sethna, "Vibrations of dynamical systems with quadratic nonlinearities," *Journal of Applied Mechanics*, 32:576–582, 1965.

[3] R.S. Haxton and A.D.S. Barr, "The autoparametric vibration absorber," *Journal of Engineering for Industry*, 94:119–225, 1972.

[4] A. Vyas and A.K. Bajaj, "Dynamics of autoparametric vibration absorbers using multiple pendulums," *Journal of Sound and Vibration*, 246:115–135, 2001.

[5] E. Doedel, Auto: Software for continuation and bifurcation problems in ordinary differential equations. Report, Department of Applied Mathematics, California Institute of Technology, Pasadena, CA, 1986.

[6] A. Vyas, A.K. Bajaj, and A. Raman, "Dynamics of flexible structures with wideband autoparametric vibration absorbers - theory," *Proceedings of the Royal Society of London*, 460(2046):1547–1581, 2004.

[7] S. Wiggins, *Introduction to Applied Nonlinear Dynamical Systems and Chaos*. Springer Verlag, New York, 1990.

[8] A. Vakakis, T. Nayfeh, and M. King, "A multiple-scales analysis of nonlinear, localized modes in a cyclic periodic system," *Journal of Applied Mechanics*, 60:388–397, 1993.

[9] B. Banerjee and A.K. Bajaj, "Amplitude modulated chaos in two degree-of-freedom systems with quadratic nonlinearities," *Acta Mechanica*, 124:131–154, 1997.

[10] F.A. McRobie, A.A. Popov, and J.M.T. Thompson, "Auto-parametric resonance in cylindrical shells using geometric averaging," *Journal of Sound and Vibration*, 227(1):65–84, 1999.

[11] P. Holmes, "Chaotic motions in a weakly nonlinear model for surface waves," *Journal of Fluid Mechanics*, 162:365–388, 1986.

ADAPTIVE PARTIAL OBSERVERS WITH APPLICATION TO TIME-VARYING CHAOTIC SYSTEMS

D. V. Efimov and A. L. Fradkov
Institute of Problems of Mechanical Engineering, Control of Complex Systems Laboratory
fradkov@mail.ru

Abstract: New applicability conditions for adaptive nonlinear observer are developed, which provide partial observation of uncertain nonlinear affine plant with estimation of unknown parameters. Applicability of the proposed results to time-varying chaotic systems is demonstrated by examples of Brusselator and Duffing systems. Computer simulation results are presented.

Key words: Adaptive observer, partial stability, synchronization, information transmission.

1. Introduction

Adaptive observers design for nonlinear systems was extensively studied during last decade. Such an interest was mainly motivated by possible application of adaptive observers to information encoding and transmission. Typically a chaotic dynamical system is used as a transmitter and its output signal is changed by modulating its parameters [1], [2], [3]. It was shown in [4] that it is possible to build a receiver based on adaptive observer, which can track output of transmitter and estimate transmitter parameters under some mild conditions. Potentialities of fast information transmission in the presence of noise in such systems were demonstrated in [5], [6], [7]. Several techniques were previously used to design receivers [8], [9], [4], [10], [11], [12], [13], most of them being based on passifiability property of transmitter under assumption that relative degree of transmitter is equal to zero or one. Other solutions can be found in [14], [15], where a state feedback was used for adaptive observer construction and robust properties of proposed schemes were not investigated. Recent paper [16] overcame the relative degree limitation for adaptive observer-based communication systems and

G. Rega and F. Vestroni (eds.),
IUTAM Symposium on Chaotic Dynamics and Control of Systems and Processes in Mechanics, 27–35.

extended them to a class of nonpassifiable systems. The result of [16] is based on a new canonical form of nonlinear adaptive observers [17], [18].

In the present paper the result of [16] is extended to the case of partial observation when exact estimation of only a part of the transmitter state variables is needed. For such a case the applicability conditions are obtained, which allow to enlarge class of transmitter systems. Unlike previous results, our results allow to use time-varying systems for both transmitter and receiver. For example, the proposed results are applicable to chaos generators with external periodic excitation, nevertheless, it is worth to note, that the solution is applicable for not necessary chaotic dynamical systems. In the paper the obtained results are demonstrated by example of practical importance: the Duffing system excited by harmonic signals.

In Section 2 the problem and the Duffing system is introduced. In Section 3 an adaptive observer scheme is designed under assumptions covering case of the systems from the previous section. Computer simulation results are presented in Section 4. Conclusion in Section 5 finishes the paper.

2. Statement of the Problem

In the literature on chaos and its applications two main classes of chaotic systems are usually considered: autonomous (time-invariant) and non-autonomous (time-varying) (see, e.g.[19]). However, in applications to information transmission in most cases only the former ones are used [1], [2], [3]. At the same time time-varying systems are sometimes easier to implement, or, they can be modeled by using other physical principles [20]. A typical example of nonlinear time-varying system where chaos is generated by means of applying a harmonic excitation signal is Duffing system, used in many studies in mechanics.

We will use the equations of Duffing's system in the following form [19]:

$$\begin{aligned} &\dot{x}_1 = x_2;\ y = x_1; \\ &\dot{x}_2 = -a x_1 + \theta x_1^3 + B\cos(\omega t), \end{aligned} \tag{1}$$

where x_1 and x_2 are state variables; y is measured output; $\theta \in \Omega_\theta = [0.5, 1.5]$ is "transmitted" parameter; model parameters $a = B = \omega = 1$.

The problem is to design a dynamical system (adaptive observer), some variables of which provide estimates of a specified part of variables and parameters of the transmitter (system (1)) using only measurements of output y (if time derivative of output, variable x_2, would be known this task can be solved in more simpler way). Since the system is time-varying, it is not always possible to achieve zero estimation error. Therefore, we will be

interested in achieving bounded and sufficiently small asymptotic value of the estimation error.

3. Design of Adaptive Observers

As in [16] we will investigate the following model of transmitter system:

$$\dot{\mathbf{x}} = \mathbf{A}(\mathbf{y})\mathbf{x} + \varphi(\mathbf{y}) + \mathbf{B}(\mathbf{y})\theta\,,\ \mathbf{y} = \mathbf{C}\mathbf{x}\,, \tag{2}$$

where $\mathbf{x} \in R^n$ is state space vector of transmitter; $\mathbf{y} \in R^m$ is output vector; $\theta \in \Omega_\theta \subset R^p$ is vector of "unknown" parameters of transmitter, or, better to say, it is transmitted vector, which values belonged to some known compact set Ω_θ should be estimated by receiver basing on current measurements of transmitter output $\mathbf{y}$. Vector function φ and columns of matrix functions $\mathbf{A}$ and $\mathbf{B}$ are locally Lipschitz continuous, $\mathbf{C}$ is some constant matrix of appropriate dimension. Thus, for any initial condition $\mathbf{x}_0 \in \Omega_x \subset R^n$ and any $\theta \in \Omega_\theta$ (where Ω_x some known, probably compact, set), solution of (2) $\mathbf{x}(t, \mathbf{x}_0, \theta)$ is well defined at the least locally (further we will omit dependence of $\mathbf{x}_0$ and θ if it is clear from the context and will simply write $\mathbf{x}(t)$). For transmitter it is naturally to suppose [16], that its solution is bounded and defined for all $t \geq 0$.

Assumption 1. *For any initial conditions* $\mathbf{x}_0 \in \Omega_x$ *and any* $\theta \in \Omega_\theta$, *solution of (2)* $\mathbf{x}(t, \mathbf{x}_0, \theta)$ *is an essentially bounded function of time:*

$$|\mathbf{x}(t, \mathbf{x}_0, \theta)| \leq \sigma_0(|\mathbf{x}_0|),\ \sigma_0 \in \mathcal{K} \text{ for almost all } t \geq 0\,. \qquad \blacksquare$$

As usually, it is said, that function $\rho: R_{\geq 0} \to R_{\geq 0}$ belongs to class $\mathcal{K}$, if it is strictly increasing and $\rho(0)=0$; $\rho \in \mathcal{K}_\infty$ if $\rho \in \mathcal{K}$ and $\rho(s) \to \infty$ for $s \to \infty$ (radially unbounded). Function $\mathbf{x}: R_{\geq 0} \to R^n$ is essentially bounded, if

$$\|\mathbf{x}\| = ess\sup\{|\mathbf{x}(t)|, t \geq 0\} < +\infty\,,$$

where $|\cdot|$ denotes usual Euclidean norm. Such assumption is valid for class of system (2) with so-called chaotic dynamics. The next two assumptions deal with stabilizability property of linear part of transmitter system (2).

Assumption 2. *There exists continuous matrix function* $\mathbf{K}: R^m \to R^{n \times m}$, *such, that there exists function* $V: R^n \to R_{\geq 0}$,

$$\alpha_1(|\mathbf{C}\mathbf{x}|) \leq V(\mathbf{x}) \leq \alpha_2(|\mathbf{C}\mathbf{x}|),\ |\partial V / \partial \mathbf{x}| \leq \rho(|\mathbf{x}|)\,;$$

$$\partial V(\mathbf{x})/\partial \mathbf{x}\, \mathbf{G}(\mathbf{y})\mathbf{x} \le -\alpha_3(|\mathbf{C}\mathbf{x}|)+\alpha_4(|\mathbf{x}|),$$

for any $\mathbf{y}\in R^m$ *and* $\mathbf{x}\in R^n$, *where* α_1, α_2, α_3 *are some functions from class* $\mathcal{K}_\infty$ *and* α_4, ρ *are functions from class* $\mathcal{K}$, *matrix* $\mathbf{G}(\mathbf{y})=\mathbf{A}(\mathbf{y})-\mathbf{K}(\mathbf{y})\mathbf{C}$. ■

Assumption 3. *For any initial conditions* $\mathbf{s}_0\in R^n$ *solution of system*

$$\dot{\mathbf{s}}=\mathbf{G}(\mathbf{y})\mathbf{s}+\mathbf{r}, \tag{3}$$

is bounded for any essentially bounded inputs $\mathbf{r}$ *and* $\mathbf{y}$:

$$|\mathbf{s}(t,\mathbf{s}_0,\mathbf{r})| \le \sigma_1(|\mathbf{s}_0|)+\sigma_1(\|\mathbf{r}\|),\ \sigma_1\in\mathcal{K}\ \textit{for almost all}\ t\ge 0.$$ ■

By itself Assumption 2 means nothing, but with combination with Assumption 3 they provide for system (3) ultimate boundedness of signal $\mathbf{C}\mathbf{s}$. Indeed, Assumption 3 implies existence of finite norm $\|\mathbf{s}\|$ for state vector of system (3), then inequality for time derivative of function V from Assumption 2 takes form:

$$\dot{V} \le -\alpha_3\circ\alpha_2^{-1}(V(\mathbf{s}))+\alpha_4(\sigma_1(|\mathbf{s}_0|)+\sigma_1(\|\mathbf{r}\|)).$$

Then the following output asymptotic gain can be obtained:

$$\lim_{t\to+\infty}|\mathbf{C}\mathbf{s}(t)| \le \lambda_1(|\mathbf{s}_0|)+\lambda_2(\|\mathbf{r}\|),\ \lambda_1(s)=\alpha_4(2\sigma_1(s))+0.5\rho(2\sigma_1(s))^2,$$

$$\lambda_2(s)=0.5s^2+\alpha_4(2\sigma_1(s))+\rho(2\sigma_1(s))^2 s.$$

Then the desired asymptotic bound for signal $\mathbf{C}\mathbf{s}$ can be assigned by appropriate choice of design matrix function $\mathbf{K}$ in gain function α_4.

It is worth to stress, that comparing with [16] Assumptions 2 and 3 enlarge the class of models for transmitter systems, since they do not suppose global asymptotic stability property of system (3) uniformly with respect to input $\mathbf{y}$ and $\mathbf{r}=0$, as it was done in [16]. Before we prove our main result we should introduce a new useful property.

Definition 1. *Function* $a: R_{\ge 0}\to R$ *is called* (μ,Δ)*–positive in average (PA), if for any* $t\ge 0$ *and any* $\delta\ge\Delta$, $\mu>0$,

$$\int_t^{t+\delta} a(\tau)d\tau \ge \mu\delta.$$ ■

In other words, time function $a(t)$ is (μ,Δ)–PA, if its average value a_{av} on any large enough time interval $[t,t+\delta]$, $\delta\ge\Delta$,

$$a_{av} = \frac{1}{\delta}\int_{t}^{t+\delta} a(\tau)d\tau$$

is not smaller than some positive constant μ. Note, that function $a(t)=\sin(t)+\alpha$ admits this property for any strictly positive constant α, thus, function a should not be positive for all $t\geq 0$. We will need the following lemma that can be easily proved by integration.

L e m m a 1. *Let us consider time-varying linear dynamic system*

$$\dot{p} = -a(t)p + b(t),\ t_0 \geq 0, \tag{4}$$

where $p\in R$, $p(t_0)\in R$ *and functions* $a: R_{\geq 0}\to R$, $b: R_{\geq 0}\to R$ *are Lebesgue measurable and essentially bounded. Then*:

A. *Solution of system (4) is defined for all* $t\geq t_0$:

$$|p(t)| \leq \left[|p(t_0)| + \|b\| e^{\|a\|t}\right] e^{\|a\|(t-t_0)}.$$

B. *If function* a *is* (μ,Δ)*–PA for some* $\mu>0$, $\Delta>0$, *then this solution is bounded and the following upper estimate holds*:

$$p(t) \leq \begin{cases} \left[|p(t_0)| + \|b\| e^{\|a\|(t_0+\Delta)}\right] e^{\|a\|\Delta} \ \text{if}\ t\leq t_0+\Delta; \\ p(t_0)e^{-\mu(t-t_0)} + \mu^{-1}\|b\| e^{-\mu(\Delta+t_0)} + \\ \quad + \|a\|^{-1}\|b\| e^{-\|a\|(t-\Delta)} \ \text{if}\ t\geq t_0+\Delta, \end{cases}$$

additionally, if $b(t)\to 0$ *for* $t\to+\infty$, *then also* $p(t)\to 0$ *asymptotically.* ■

In this work we will use the same adaptive observer equations as in [16]:

$$\dot{\mathbf{z}} = \mathbf{A}(\mathbf{y})\mathbf{z} + \varphi(\mathbf{y}) + \mathbf{B}(\mathbf{y})\hat{\theta} + \mathbf{K}(\mathbf{y})(\mathbf{y}-\hat{\mathbf{y}}),\ \hat{\mathbf{y}} = \mathbf{C}\mathbf{z}; \tag{5}$$

$$\dot{\boldsymbol{\eta}} = \mathbf{G}(\mathbf{y})\boldsymbol{\eta} - \boldsymbol{\Omega}\dot{\hat{\theta}}; \tag{6}$$

$$\dot{\boldsymbol{\Omega}} = \mathbf{G}(\mathbf{y})\boldsymbol{\Omega} + \mathbf{B}(\mathbf{y}); \tag{7}$$

$$\dot{\hat{\theta}} = \gamma\boldsymbol{\Omega}^T\mathbf{C}^T(\mathbf{y}-\hat{\mathbf{y}}+\mathbf{C}\boldsymbol{\eta}), \tag{8}$$

where $\mathbf{z}\in R^n$ is vector of estimates of nonmeasurable state space vector of system (2); $\hat{\mathbf{y}}\in R^m$ is vector of on-line measurable output $\mathbf{y}$ estimates; vector $\boldsymbol{\eta}\in R^n$ and matrix $\boldsymbol{\Omega}\in R^{n\times p}$ are auxiliary variables, which help to overcome high relative degree obstruction; $\hat{\theta}\in R^p$ is vector of estimates of "transmitted" vector θ; $\gamma>0$ is a design parameter.

Theorem 1. *If Assumptions 1, 2 and 3 hold and function* $|\mathbf{C}\,\mathbf{\Omega}(t)|^2$ *satisfies* (μ,Δ)*–PA condition for some* $\mu>0$, $\Delta>0$, *then closed-loop system consisting of transmitter (2), adjustable receiver (5), scheme of augmentation (6), (7) and adaptation algorithm (8) provides boundedness property of the system solution for any initial conditions and any* $\gamma>0$, *additionally*

$$\lim_{t\to+\infty}\left|\boldsymbol{\theta}-\hat{\boldsymbol{\theta}}(t)\right|\le\sqrt{\mu^{-1}e^{-\gamma\mu\Delta}}\,\lambda\left(|\boldsymbol{\delta}_0|\right).$$

Proof. We will denote $\mathbf{e}=\mathbf{x}-\mathbf{z}$ as state estimation error of proposed observer (5). Let $\boldsymbol{\varepsilon}=\mathbf{y}-\bar{\mathbf{y}}$ be corresponding measurable output error. The behavior of error $\mathbf{e}$ can be rewritten as follows:

$$\dot{\mathbf{e}}=\mathbf{G}(\mathbf{y})\mathbf{e}+\mathbf{B}(\mathbf{y})\left(\boldsymbol{\theta}-\hat{\boldsymbol{\theta}}\right),\ \boldsymbol{\varepsilon}=\mathbf{C}\mathbf{e}. \tag{9}$$

Let us introduce the auxiliary error signal $\boldsymbol{\delta}=\mathbf{e}+\boldsymbol{\eta}-\mathbf{\Omega}\left(\boldsymbol{\theta}-\hat{\boldsymbol{\theta}}\right)$, which dynamics coincides with auxiliary system (3) with zero input $\mathbf{r}$:

$$\dot{\boldsymbol{\delta}}=\mathbf{G}(\mathbf{y})\boldsymbol{\delta}. \tag{10}$$

Hence, according to previous discussion, signal $\boldsymbol{\delta}$ is bounded and signal $\mathbf{C}\boldsymbol{\delta}$ is ultimately bounded. Let us analyze the following Lyapunov function candidate with respect to part of variables [21] $W\left(\hat{\boldsymbol{\theta}}\right)=\gamma^{-1}\left(\boldsymbol{\theta}-\hat{\boldsymbol{\theta}}\right)^T\left(\boldsymbol{\theta}-\hat{\boldsymbol{\theta}}\right)$, its time derivative for system (8) takes form:

$$\begin{aligned}\dot{W}&=-2\left(\boldsymbol{\theta}-\hat{\boldsymbol{\theta}}\right)^T\mathbf{\Omega}^T\mathbf{C}^T\mathbf{C}\left(\boldsymbol{\delta}+\mathbf{\Omega}\left(\boldsymbol{\theta}-\hat{\boldsymbol{\theta}}\right)\right)\le\\&\le-|\mathbf{C}\,\mathbf{\Omega}|^2\left|\boldsymbol{\theta}-\hat{\boldsymbol{\theta}}\right|^2+|\mathbf{C}\boldsymbol{\delta}|^2=-\gamma|\mathbf{C}\,\mathbf{\Omega}|^2W+|\mathbf{C}\boldsymbol{\delta}|^2.\end{aligned}$$

According to Lemma 1 solution of the last linear time-varying inequality is bounded, if functions $\gamma|\mathbf{C}\,\mathbf{\Omega}(t)|^2$ and $|\mathbf{C}\boldsymbol{\delta}(t)|^2$ are. But these two conditions are satisfied, due to form of systems (7), (10) (they are in class of system (3)) and Assumptions 1 and 3, signals $\mathbf{\Omega}$ and $\boldsymbol{\delta}$ are bounded and:

$$\gamma|\mathbf{C}\,\mathbf{\Omega}(t)|^2\le\gamma|\mathbf{C}|^2\left(\sigma_1(|\mathbf{\Omega}_0|)+\sigma_1\left(B_{\max}(\mathbf{x}_0)\right)\right)^2<+\infty,$$

$$|\mathbf{C}\,\boldsymbol{\delta}(t)|^2\le|\mathbf{C}|^2\sigma_1(|\boldsymbol{\delta}_0|)^2<+\infty,$$

where $B_{\max}(\mathbf{x}_0)=\sup\{|\mathbf{B}(\mathbf{C}\mathbf{x})|,\ |\mathbf{x}|\le\sigma_0(|\mathbf{x}_0|)\}$ and expression $|\mathbf{C}|$ for some matrix $\mathbf{C}=\{c_{i,j}\}$, $i=\overline{1,m}$, $j=\overline{1,n}$ ($c_{i,j}$ are corresponding elements of matrix $\mathbf{C}$) should be understood in the following sense:

$$|\mathbf{C}| = \sqrt{\sum_{i=1}^{m}\sum_{j=1}^{n} c_{i,j}^2}\ .$$

From Lemma 1, the following estimate asymptotically holds with $t_0 = 0$:

$$\lim_{t\to+\infty} W(t) \le \gamma^{-1}\mu^{-1}\lambda(|\boldsymbol{\delta}_0|)^2\, e^{-\gamma\mu\Delta},$$

and parameter error boundedness $\boldsymbol{\theta} - \hat{\boldsymbol{\theta}}(t)$ is also obtained. Note, that system (9) has form of system (3) too with input $\mathbf{B}(\mathbf{y})(\boldsymbol{\theta} - \hat{\boldsymbol{\theta}})$. Therefore, the boundedness of signal $\boldsymbol{\varepsilon}$ follows from Assumption 3. Finally, signal $\boldsymbol{\eta}$ is bounded because it forms bounded signal $\boldsymbol{\delta}$, and all other signals, which also form signal $\boldsymbol{\delta}$, are bounded. Therefore, boundedness of the system solution is established. ■

Note, that the result of the last theorem does not guarantee attractivity property of output estimation error $\boldsymbol{\varepsilon}$ for an adaptive observer. In general only asymptotic convergence of $\boldsymbol{\varepsilon}$ and parameter error $\boldsymbol{\theta} - \hat{\boldsymbol{\theta}}(t)$ to some compact set is provided. In fact, for information transmitting purposes only parameter error convergence is necessary, and output error estimation is not needed.

It is worth noticing that asymptotic estimate for parameter error $\boldsymbol{\theta} - \hat{\boldsymbol{\theta}}(t)$, presented in the Theorem, can be evaluated with some difficulties, since the initial condition $\boldsymbol{\delta}_0$ itself depends on unmeasured discrepancy $\boldsymbol{\theta} - \hat{\boldsymbol{\theta}}(0)$, but this estimate helps to understand mechanisms for parameter error decreasing (for example, increasing coefficient γ or decreasing gain function λ).

4. Applications

To exclude explicit time dependence and to generate needed sinusoidal signal we should introduce auxiliary variables x_3 and x_4 in model (1):

$$\begin{aligned} &\dot{x}_1 = x_2;\ y = x_1;\\ &\dot{x}_2 = -a x_1 + \theta x_1^3 + B x_3;\\ &\dot{x}_3 = \omega x_4;\\ &\dot{x}_4 = -\omega x_3. \end{aligned} \qquad (11)$$

For some bounded set of initial conditions $|x_1(0)| \le 1$ and $|x_2(0)| \le 1$ this system produces bounded solution (initial conditions for auxiliary variables $x_3(0)$ and $x_4(0)$ are chosen to guarantee desired sinusoidal signal on the

input of Duffing's model). Model (11) for such initial conditions satisfies all Assumptions 1 – 3.

The result of computer simulation of proposed observer system is shown in Fig. 1. All initial conditions for simulations were taken zero except $x_1(0)=1$, $x_2(0)=1$, $x_3(0)=\Omega_3(0)=\eta_3(0)=1$ and parameters $K=\gamma=1$. In Fig. 1,a state space trajectories are presented for transmitter model and observer, in Fig. 1,b output and parameter estimation errors time graphics are shown.

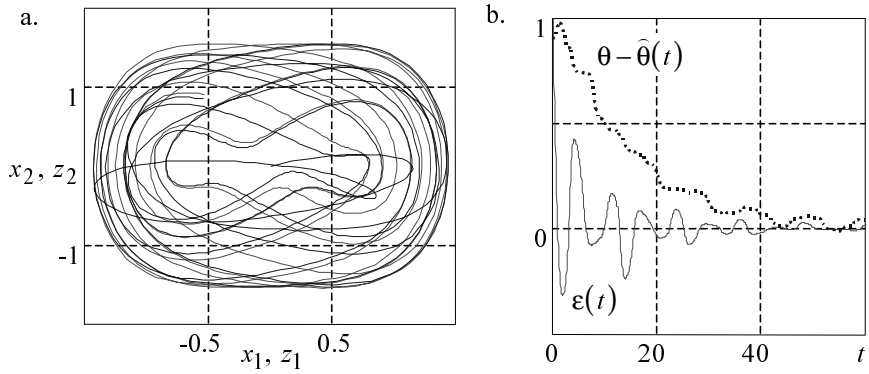

Figure 1. Simulation result for Duffing's model

5. Conclusion

Set of applicability conditions for a scheme of adaptive observer, proposed in [16], is introduced and substantiated. These new conditions weaken requirements imposed on adaptive observer scheme in [16]. Such a weakening allows to enlarge class of admissible transmitter systems. The main advantage of these conditions consists in specializing of "estimation" goals for adaptive observer system, i.e. proposed in paper [16] requirement of output estimation error asymptotic convergence was replaced to simple boundedness.

References

[1] *IEEE Trans. on Circuits and Systems*, **44**, 10. Special issue "Chaos control and synchronization" / Eds. M. Kennedy, M. Ogorzalek, 1997.

[2] *International Journal of Circuit Theory and Applications*, **27**,6. Special issue "Communications, information processing and control using chaos / Eds. M. Hasler, J. Vandewalle, 1999.

[3] M. P. Kennedy and G. Kolumban, "Digital communications using chaos," in: *Controlling chaos and bifurcations in engineering systems* / Ed. G. Chen, CRC Press, pp. 477–500, 1999.

[4] A. L. Fradkov, H. Nijmeijer, and A. Markov, "Adaptive observer-based synchronisation for communications," *Intern. J. of Bifurcation and Chaos*, **10**, 12, pp. 2807–2814, 2000.

[5] B. R. Andrievsky, "Information transmission by adaptive identification with chaotic carrier," in *Proc. 2nd Int. Conf. "Control of Oscillation and Chaos"*, St. Petersburg, 5 – 7 July, **1**, pp. 115–117, 2000.

[6] B. R. Andrievsky, "Adaptive synchronization methods for signal transmission on chaotic carriers," *Mathem. and Computers in Simulation*, 2002.

[7] B. R. Andrievsky and A. L. Fradkov, "Information transmission by adaptive synchronisation with chaotic carrier and noisy channel," in *Proc. 39th IEEE Conf. Decision and Control*, Sydney, 12 –15 Dec, pp. 1025–1030., 2000.

[8] A. L. Fradkov, "Adaptive synchronisation of hyper-minimum-phase systems with nonlinearities," in *Proc. of 3rd IEEE Mediterranean Symp. on New Directions in Control*. Limassol, **1**, pp. 272–277, 1995.

[9] A. L. Fradkov and A. Yu. Markov, "Adaptive synchronisation of chaotic systems based on speed gradient method and passification," *IEEE Trans. on Circuit and Systems*-I, **44**, 10, pp. 905–912, 1997.

[10] R. Marino, "Adaptive observers for single output nonlinear systems,' *IEEE Trans. Aut. Contr.*, **AC–35**, pp. 1054 – 1058, 1990.

[11] A. Yu. Markov and A. L. Fradkov, "Adaptive synchronisation of coupled chaotic systems," *Proc. Int. Conf. "Fractals and Chaos in Chemical Engineering"*, Rome, Sept. 2–5, pp. 153–154, 1996.

[12] H. Nijmeijer and I. M. Y. Mareels, "An observer looks at synchronization," *IEEE Trans. on Circuit and Systems*-I, **44**, 10, pp. 882–890, 1997.

[13] C. Wu, Y. Yang, and L. Chua, "On adaptive synchronisation and control of nonlinear dynamical systems," *Intern. J. of Bifurcation and Chaos*, **6**, pp. 455–471, 1996.

[14] S. S. Ge and C. Wang, "Adaptive control of uncertain Chua circuits," *IEEE Trans. on Circuit and Systems*-I, **47**, 9, pp. 1397–1402, 2000.

[15] H. Huijberts, H. Nijmeijer, and R. Willems, "System identification in communication with chaotic systems," *IEEE Trans. on Circuit and Systems*-I, **47**, 6, pp. 800–808, 2000.

[16] A. L. Fradkov, V. O. Nikiforov, and B. R. Andrievsky, "Adaptive observers for nonlinear nonpassifiable systems with application to signal transmission," in *Proc. 41th IEEE Conf. Decision and Control*, Las Vegas, pp. 4706–4711, 10 –13 Dec. 2002.

[17] A. L. Fradkov, I. V. Miroshnik, and V. O. Nikiforov, *Nonlinear and Adaptive Control of Complex Systems*. Kluwer Academic Publishers, 528 p, 1999.

[18] V.O. Nikiforov and K.V. Voronov, "Adaptive backstepping with high-order tuner," *Automatica*, **37**, pp. 1953 – 1960, 2001.

[19] F. Moon, *Chaotic and Fractal Dynamics. An Introduction for Applied Scientists and Engineers*. Wiley, 1992.

[20] G. Nikolis and I. R. Prigogine, *Self-Organization in Non-Equilibrium Systems*. Wiley, New York, 1977.

[21] V.V. Rumyantsev and A.S. Oziraner, *Stability and stabilization of motion with respect to part of variables*. Moscow, Nauka. P. 263, 1987, (in Russian).

NONLINEAR DYNAMICS OF A HEAVY MATERIAL PARTICLE ALONG A CIRCLE WHICH ROTATES AND OPTIMAL CONTROL

Katica (Stevanovic) Hedrih
Faculty of Mechanical Engineering, University of Nis, Nis, Serbia-Montenegro
katica@masfak.ni.ac.yu

Abstract: In this paper some research results of fascinating nonlinear dynamics of a heavy material particle along circles with coupled rotations, with many different properties of nonlinear dynamics and optimal control of this dynamics, are presented. By using MathCad software, visualizations of nonlinear dynamical processes in such rheonomic systems are made.

Key words: Nonlinear dynamics, coupled rotation, material particle, optimal control, homoclinic orbit, trigger, coupled singularities, bifurcation, phase plane portrait, separatrix layering, separatrix in the form of number eight.

1. Introduction

Dynamics of coupled rotors is a very old engineering problem with many different research results and discoveries of new nonlinear phenomena (see Refs. [1], [2] and [3]), and of stationary and nonstationary vibrations regimes (see Ref. [4]) with different kinetic parameters of the dynamical system. However, even nowadays many researchers pay attention to this problem, and again arises interest in doing research on nonlinear dynamics of coupled rotors (see Refs. [5], [6], [7], [8]) by using new analytical, numerical and experimental methods to discover properties of nonlinear dynamics and finer possibilities for controlling nonlinear phenomena, instabilities and non stationary regimes as well as the appearance of chaotic-like and stochastic-like processes. One of the reasons for researching on this problem by means of analytical and numerical methods applied to a not too complicated model is that it is already very good for pointing out the complexity of multifrequency regimes in nonlinear systems, since it undergoes many different regimes with sensitive dependence of dynamical system properties and nonstationary processes on the system kinetic

G. Rega and F. Vestroni (eds.),
IUTAM Symposium on Chaotic Dynamics and Control of Systems and Processes in Mechanics, 37–45.

parameters. By changing the distribution of the deviation material particles on the coupled rotors, we can build a nonlinear model of the dynamical system with many varieties of kinetic states of the coupled rotor dynamics.

In one classical monograph [1] by A. A. Andronov, A. A. Witt and S. E. Hajkin, which has a great number of editions, besides the general theory of nonlinear oscillations, some classical examples of oscillatory motion and phase portraits of nonlinear systems with one degree of freedom are presented, and such examples can also be found in the books by J. J. Stoker [9] and by D.P. Rašković [10]. Especially in the monograph by Guckenheimer, J. and Holmes, Ph. [3], results of research on nonlinear systems and properties of various kinds of bifurcation are pointed out. A series of monographs by *Mitropolyskiy, Yu. A* [4] deals with theory, methods and problems of asymptotic theory of non-steady nonlinear oscillations of nonlinear systems.

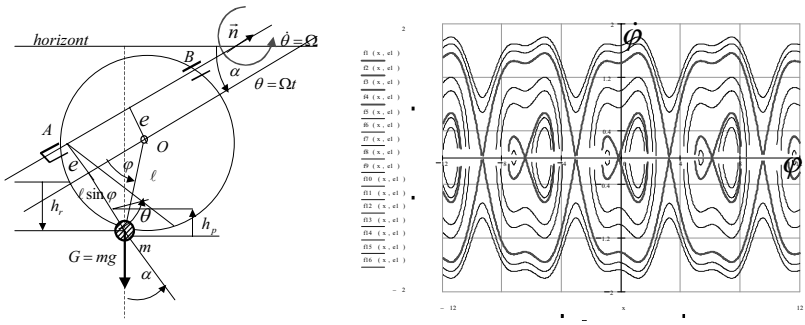

Figure 1. Motion of the heavy material particle along a circle which rotates about a fixed axis. Simple model of the nonlinear dynamics. Phase portrait of the nonlinear dynamics of basic model.

2. Motion of the Heavy Material Particle Along Circles

We will consider a discrete system (see Fig. 1.) of a heavy material particle with mass m along a circle which rotates around a skew positioned (angle α to the horizontal direction) axis oriented by unit vector $\vec{n}$, in the case that the eccentricity is either zero or different from zero ($e=0$ or $e\neq 0$).

The relative position of the material particle along the circle with radius ℓ is determined by the angle φ as a generalized coordinate. The rheonomic coordinate $\theta=\Omega t$ is the angle of circle's rotation around the axis oriented by the unit vector $\vec{n}$.

Using the notation in Fig.1, the rate of potential energy change $\mathbf{E}_P$, expressed by the generalized coordinate φ and the rheonomic coordinate θ, can be written in the following form:

$$\mathbf{E}_p = mgh = mg\ell\left[\sin\alpha\left(1-\cos\varphi\right)-\sin\varphi\cos\alpha\cos\theta+e\cos\alpha\left(1-\cos\theta\right)\right] \tag{1}$$

The expression of kinetic energy $\mathbf{E_k}$ of the system is:

$$\mathbf{E_k} = \frac{1}{2} m\ell^2 \left[\dot{\varphi}^2 + \dot{\theta}^2 \left(\sin\varphi + \frac{e}{\ell} \right)^2 \right] \tag{2}$$

Introducing the following notation

$$\dot{\theta} = \Omega\,, \quad \lambda = \frac{g\sin\alpha}{\ell\Omega^2}\,, \quad \varepsilon = \frac{e}{\ell} \quad \text{and} \quad \Omega_{rez}^2 = \frac{g\sin\alpha}{2\ell}\,, \tag{3}$$

the differential equation of the relative motion of the heavy material particle can be written in the following form:

$$\ddot{\varphi} + \Omega^2(\lambda - \cos\varphi)\sin\varphi - \Omega^2\varepsilon\cos\varphi = \Omega^2\lambda ctg\alpha\cos\varphi\cos\Omega t \tag{4}$$

From the extended Lagrange's system equation for the rheonomic coordinate θ (see [11]), we can obtain the expression of the corresponding couple M_θ:

$$\mathrm{M}_\theta = m\ell^2 \left\{ \frac{d}{dt}\left[(\varepsilon + \sin\varphi)^2 \Omega \right] + \frac{g}{\ell}\sin\theta\cos\alpha(\varepsilon + \sin\varphi) \right\} \tag{5}$$

3. Linearized Approximation

Now, let us consider the special cases of heavy material particle dynamics with $e = 0$. To start with, we consider small oscillations around the stable relative equilibrium position of the homogenous differential equation (4) for the cases: 1*: $\lambda > 1$, $\varphi = 0$, $e = 0$ and 2*: $\lambda < 1$, $\varphi = \pm\arccos\lambda$, $e = 0$, and when $ctg\alpha$ is small.

1*: For the case $\lambda > 1$, we study small oscillations around stable relative equilibrium position $\varphi = 0$, by using the corresponding linearization of the differential equation in the form of:

$$\ddot{\varphi} + \Omega^2(\lambda - 1)\varphi \approx \Omega^2\lambda ctg\alpha\cos\Omega t \tag{6}$$

when we make the approximations: $\sin\varphi \approx \varphi + \ldots$ and $\cos\varphi \approx 1 + \ldots$. We can conclude that these small oscillations around $\varphi = 0$ for $\lambda > 1$ are simple forced two frequency oscillations with the following frequencies: the "own" frequency $\omega \approx \Omega\sqrt{\lambda - 1}$, and the forced frequency Ω with amplitudes depending on initial conditions and forced excitation amplitude $\Omega^2\lambda ctg\alpha$ as function of the axis angle α, and that $ctg\alpha$ is small. We can conclude that in this case the resonance regime is possible when $\Omega = \Omega_{rez}$ and for $\lambda = 2$, then $\lambda > 1$, and that the angular velocity of the circle is critical. But this conclusion is in contrast with the assumption that the oscillations are of small amplitude. In that case, the linearization is not correct.

In the resonant case, for the approximate solution of small relative forced oscillations of the heavy material particle around relative stable position $\varphi = 0$ when Ω_{rez}^2 and $\lambda = 2$, $\lambda > 1$, and for a short period of time, we can write:

$$\varphi(t) \approx \varphi_0\cos\frac{\omega_0 t\sqrt{2}}{2} + \frac{\sqrt{2}\dot{\varphi}_0}{\omega_0}\sin\frac{\omega_0 t\sqrt{2}}{2} + \left[\frac{\omega_0 t\sqrt{2}}{2}\sin\frac{\omega_0 t\sqrt{2}}{2} \right] ctg\alpha \tag{7}$$

where $\Omega_{rez}^2 = \frac{g\sin\alpha}{2\ell} = \frac{\omega_0^2}{2}$, $\omega_0^2 = \frac{g\sin\alpha}{\ell}$, $\lambda = \frac{\omega_0^2}{\Omega^2}$, $\lambda_{rez} = 2$.

2*: For the case when $\lambda < 1$, we study the small oscillations around the stable relative equilibrium position $\varphi_s = \pm\arccos\lambda$ by applying the corresponding linearization of the differential equation, and by changing the generalized coordinate φ to $\varphi_s + \varphi$. We obtain the following linearized equation:

$$\ddot{\varphi} + \Omega^2\left(1-\lambda^2\right)\left[1 + \frac{\lambda\, ctg\alpha}{\sqrt{1-\lambda^2}}\cos\Omega t\right]\varphi \approx \Omega^2 \lambda ctg\alpha \cos\Omega t \tag{8}$$

which is of Mathieu-Hill type. From this linearized differential equation we can conclude that these small oscillations around $\varphi_s = \pm\arccos\lambda$ for $\lambda < 1$ are not simple forced two frequency oscillations, but are of the type of Mathieu parametric and forced oscillations. In this case, we can point out possibilities of appearance of parametric resonance. In the first linearized approximation, around the relative equilibrium position $\varphi_s = \pm\arccos\lambda$ for $\lambda < 1$ the small oscillations are described by the Mathieu's oscillator in the form of the following equation:

$$\frac{d^2\varphi}{d\tau^2} + \left(\tilde{\lambda} + \tilde{\gamma}\cos\tau\right)\varphi = h\cos\tau \tag{9}$$

with circular frequency and parameters:

$\omega = \Omega\sqrt{\left(1-\lambda^2\right)}$, $\tilde{\lambda} = 1-\lambda^2$ i $\tilde{\gamma} = \lambda\sqrt{1-\lambda^2}\, ctg\alpha = h\sqrt{\tilde{\lambda}}$, $\tau = \Omega t$, external forced excitation amplitude $h = \lambda\, ctg\alpha$, and frequency equal to the angular velocity of the rotation of the circle.

For the general solution of *Mathieu's differential equation*, see Ref. [12] or *Floquet, Annales de l'Ecole Normale*, 1883. Based on these references, we can write $\varphi(t) = Ae^{\mu t}p_1(t) + Be^{-\mu t}p_2(t)$, where A and B are integral constants, μ is a characteristic exponent, and $p_i(t), i = 1,2$ are periodic functions with period 2π depending on parameters $\tilde{\lambda}$ and $\tilde{\gamma}$. The main problem is the investigation of the stability of solutions (see Refs. [10], [12] and [13]). Following Ince and Strutt, the domains of stability and instability are graphically presented in the form of Ince-Strutt's stability charts for different values of the parameters $\tilde{\lambda}$ and $\tilde{\gamma}$.

4. Optimal Control of Nonlinear Dynamics

For controlling the motion of the nonlinear system at hand, we consider one parameter control by one generalized force corresponding to the generalized system coordinate. Accordingly, we transform the differential equation of motion (4) in the form of a system of differential equations of first order:

$$\begin{aligned} &\varphi' = v && v = \frac{\varphi}{\Omega}; \qquad \tau = \Omega t \\ &v' = -(\lambda - \cos\varphi)\sin\varphi + \varepsilon\cos\varphi + ctg\alpha\cos\varphi\cos\tau \end{aligned} \tag{10}$$

For the optimal control of the nonlinear dynamics of the system defined by the nonlinear equation (4), we can introduce two phase coordinates in the state space x_1 and x_2, and transform the second order differential equation into two nonlinear differential equations of first order in the following form:

$$\begin{aligned} &\dot{x}_1 = x_2 && x_1 = \varphi; \quad x_2 = v; \quad t(=)\tau \\ &\dot{x}_2 = -(\lambda - \cos x_1)\sin x_1 + \varepsilon\cos x_1 + ctg\alpha\cos x_1\cos\tau + u(t) && -\tilde{u}_0 \le \tilde{u}(t) \le +\tilde{u}_0 \end{aligned} \tag{11}$$

with the following initial conditions: $x_1(0) = \varphi(0) = \varphi_0$ and $x_2(0) = v(0) = \frac{\varphi_0}{\Omega}$.

The optimal control task for the defined dynamical system is as follows: By using a controlling force $\tilde{u}(t)$ acting on the system, the transfer from the initial state of the nonlinear dynamics of the system, defined by $x_1(0) = x_{01}$ and $x_2(0) = x_{02}$, to the final state of the nonlinear dynamics, defined by $x_1(T) = x_{T1}$ and $x_2(T) = x_{T2}$, where T is the minimal time for optimal control, has to be performed. Then we can write two new nonlinear differential equations of first order for the optimal control task in the form (11) with following initial and final conditions:

$$\begin{aligned} &x_1(0) = x_{01} && x_1(T) = x_{T1} \\ &x_2(0) = x_{02} && x_2(T) = x_{T2} \end{aligned} \tag{12}$$

Pontrijagin's maximum principle (see Ref. [11]) is used. For minimizing the time T, we add to the previous system dynamics equations the following functional

$$\mathbf{I} = \int_0^T 1 \cdot dt \tag{13}$$

as a criterion of optimality or "*criterion of quality*". In addition, constraints of the controlling force $\tilde{u}(t)$ in the form $-\tilde{u}_0 \le \tilde{u}(t) \le +\tilde{u}_0$ hold.

The concept of controllability of motion (or system dynamics) implies the possibility that the mechanical system motion (or dynamics) is realized according to a given program under the action of special generalized forces. The controlling force $\tilde{u}(t)$ of the motion or the dynamics is herein considered as a generalized force of controllability corresponding to the generalized coordinate of the system. The phrase "*system motion or system dynamics control*" implies the process of realizing a given motion or programmed dynamics. Programs can be of a great variety. This study includes the program of pathways and the program of velocities.

The concept of optimal motion of system dynamics implies here motion or dynamics of the mechanical system whose particular attributes are the extreme values with respect to some parameters of the dynamics.

Now, let's determine the force $\tilde{u}(t)$ that can control the dynamics of the system in accordance with the defined control tasks (11)-(13). By using the theory, we can write the following Hamilton function:

$$\mathrm{H} = 1 + p_1 x_2 + p_2\left[-(\lambda - \cos x_1)\sin x_1 + \varepsilon \cos x_1 + ctg\alpha \cos x_1 \cos\tau + u(t)\right] \tag{14}$$

and describe the optimal dynamics by the following equations:

$$\dot{x}_i = \frac{\partial \mathrm{H}}{\partial p_i}; \quad \dot{p}_i = -\frac{\partial \mathrm{H}}{\partial x_i}; \quad \frac{\partial \mathrm{H}}{\partial u} = 0; \quad -u_0 \le u(t) \le u_0; \quad \mathrm{H}\big|_{t=T} = 0; i = 1,2. \tag{15}$$

We have the case of control by using a force with constant value by with change of the direction (bing-bang solution). In this system, the control force occurs linearly and, in accordance with the maximum principle, it attains its upper and/or lower bounds in the general case. Solution of the task is obtained by solving the basic system of differential equations and getting corresponding particular solutions which contain the state of the defined dynamics at the initial moment and the final moment of time T. At the moment t_C, we must change the control force direction.

In the considered case, the dynamics of the system is described by nonlinear differential equations, and is not possible to solve the problem in analytical form. But it is convenient to use phase plane methods for a qualitative analysis by using the basic scleronomic holonomic conservative system corresponding to the rheonomic and forced excited system. By following a representative point in the phase plane along phase trajectories and the transformation of structure of phase portrait when using the control force, it is possible to learn about the nonlinear dynamics in the optimal control case. Families of constant energy curves of the system are also a tool to learn the controllability properties of the nonlinear system.

For the control of the relative motion of the heavy material particle along a circle which rotates about a fixed axis with a corresponding number of rotations in one and in the opposite direction, we can use phase plane methods and visualization of the numerical MathCad experiment. Visualization of the phase portrait of the basic holonomic scleronomic conservative system gives us information about the existence of a trigger of coupled singularities as well as of a homoclinic orbit in the form of number eight. Also, we can see in Fig. 2 that the structure of the phase portrait changes under the influence and excitation of the control force.

The equations of the phase trajectories passing through the initial point state $(t_0 = 0, x_{01}, x_{02})$ and the final point state $(t_T = T, x_{T1}, x_{T2})$ are in the form:

$$x_2 = \pm\sqrt{x_{02}^2 + 2\lambda(\cos x_1 - \cos x_{01}) - \frac{1}{2}(\cos 2x_1 - \cos 2x_{01}) + 2\varepsilon(\sin x_1 - \sin x_{01}) \pm 2u_0(x_1 - x_{01})}$$

$$x_2 = \pm\sqrt{x_{T2}^2 + 2\lambda(\cos x_1 - \cos x_{T1}) - \frac{1}{2}(\cos 2x_1 - \cos 2x_{T1}) + 2\varepsilon(\sin x_1 - \sin x_{T1}) \mp 2u_0(x_1 - x_{T1})} \quad (16)$$

For solving the problem, it is necessary to find the cross section $(t_C = T_C, x_{C1}, x_{C2})$ (mutual phase state) between the previous phase trajectories in which the control force changes direction. The initial branch of the phase trajectory contains the representative point $(t_0 = 0, x_{01}, x_{02})$, and the final branch of the phase trajectory contains the point $(t_T = T, x_{T1}, x_{T2})$.

By using phase trajectories of the nonlinear dynamics, we can find the time moment T_C in which we must change the control force direction and the final minimal time for optimal control motion:

$$T = \int_{x_{01}}^{x_{C1}} \frac{dx_1}{\sqrt{\dot{x}_{01}^2 + 2\lambda(\cos x_1 - \cos x_{01}) - \frac{1}{2}(\cos 2x_1 - \cos 2x_{01}) + 2\varepsilon(\sin x_1 - \sin x_{01}) + 2u_0(x_1 - x_{01})}} + \\ + \int_{x_{C1}}^{x_{T1}} \frac{dx_1}{\sqrt{\dot{x}_{T1}^2 + 2\lambda(\cos x_1 - \cos x_{T1}) - \frac{1}{2}(\cos 2x_1 - \cos 2x_{T1}) + 2\varepsilon(\sin x_1 - \sin x_{T1}) - 2u_0(x_1 - x_{T1})}} \quad (17)$$

5. Concluding Remarks

Optimal control of the nonlinear dynamics of a heavy material particle moving without friction along a circle which rotates about a fixed axis has been studied by using a variational method combined with the phase plane method. Many different properties of the nonlinear dynamics have been highlighted. Transformation of trajectories in phase portrait under the influence of the control force and comparison with the basic nonlinear system dynamics have been pointed out.

Acknowledgment

Parts of this research were supported by the Ministry of Sciences, Technologies and Development of Republic Serbia through Mathematical Institute SANU Belgrade Grants No. 1616 and Faculty of Mechanical Engineering University of Niš Grant No. 1828.

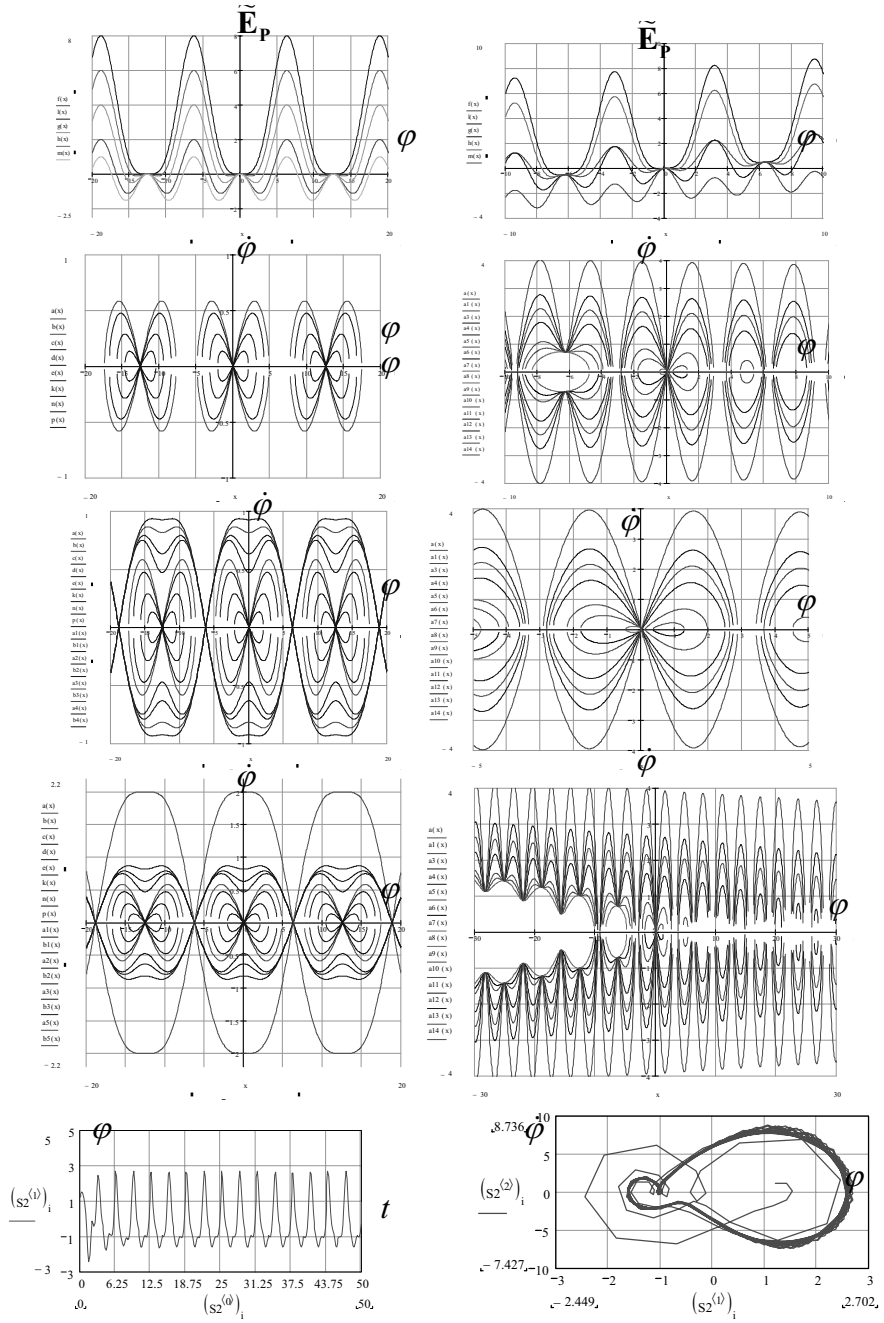

Figure 2. Phase trajectories for the corresponding basic nonlinear discrete system dynamics (see Fig. 1. a*) of the heavy material particle with mass m along a circle which rotates around a skew positioned axis, with angle α to the horizon, oriented by the unit vector $\vec{n}$, in the case where the eccentricity is equal to zero, $e = 0$. Different values of system parameters and control basic system with control force (right size). Transformation of the structure of phase portrait by control force (right size). The system parameters λ and Ω are varied in the Figures.

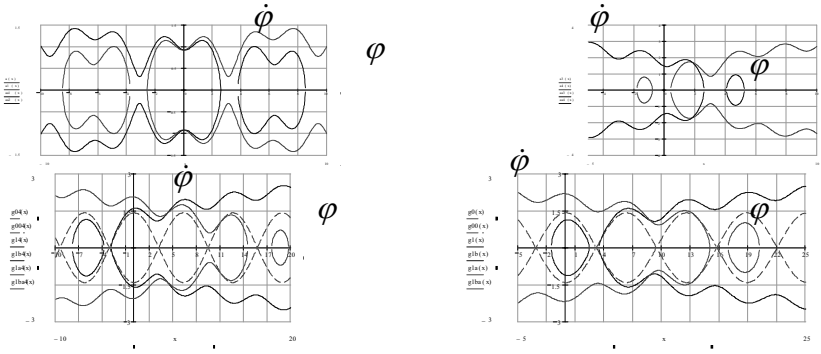

Figure 3. Phase trajectories for the basic nonlinear discrete system dynamics (see Fig. 1. a*) with control force and with opposite directions. Graphical presentation of the cross section between trajectories with opposite direction of the control force.

References

[1] A.A. Andronov, A.A. Vitt, and S.E. Haykin, *Teoriya Kolebaniy,* Nauka, Moskva., pp. 568, 1981.

[2] I. Gerard and J. Daniel, *Elementary Stability and BIfurcation Theory*, Springer Verlag, 1980.

[3] J. Guckenheimer and Ph. Holmes, *Nonlinear Oscillations, Dynamical Systems, and Bifurcations of Fields* , Springer-Verlag, pp. 461, 1983.

[4] A. Yu Mitropolyskiy, *Problemi Asimptoticheskoy Teorii Nestashionarnih Kolebaniy*, Nauka Moskva, pp. 431, 1964.

[5] K. Hedrih (Stevanović), *"*Trigger of coupled singularities" (invited plenary lecture)*, Dynamical Systems - Theory and Applications*, Edited By J. Awrejcewicz and all, Lodz, pp. 51-78, 2001.

[6] K. Hedrih (Stevanović), "Nonlinear Dynamics of a Gyrorotor, and Sensitive Dependence on initial Conditions of a Heav Gyrorotor Forced Vibration/Rotation Motion," *Proceedings of COC*, Ed. F.L. Chernousko and A.I. Fradkov, vol. 2, pp. 259-266, 2000.

[7] K. Hedrih (Stevanović), "On rheonomic systems with equaivalent holonomic conservative system*,*" *Int. Conf. ICNM-IV*, Ed. W. Chien and all. Shanghai, pp. 1046-1054, 2002.

[8] K. Hedrih (Stevanović), *The Vector Method of the Heavy Rotor Kinetic Parameter Analysis and Nonlinear Dynamics*, Monograph, University of Niš, pp. 252., YU ISBN 86-7181-046-1, 2001.

[9] J.J. Stoker, *Nonlinear Vibrations,* Interscience Publishers, New Yor, pp.273, 1950.

[10] D. Rašković, *Teoirija Oscilacija* (*Theory of Oscillations*) Naučna knjiga, Beograd, pp. 504, 1965.

[11] V.A. Vujičić, *Preprinciples of Mehanics*, Mathematical Institute SANU, Beograd, p. 223, 1999.

[12] E. Mathieu*, Cours de Physique Mathématique*, Paris, 1873.

[13] M.J. O. Strutt, *Lamésche, Mathieusche und verwandle Funktionen in Physik und Technik*, Berlin,1932.

BIFURCATION AND CHAOS IN MECHANICAL APPLICATIONS: A DYNAMICAL SYSTEMS APPROACH TO THEIR CONTROL

Stefano Lenci
Istituto di Scienza e Tecnica delle Costruzioni
Università Politecnica delle Marche, 60131 ANCONA, Italy
Lenci@univpm.it

Giuseppe Rega
Dipartimento di Ingegneria Strutturale e Geotecnica
Università di Roma "La Sapienza", 00197 ROMA, Italy
Giuseppe.Rega@uniroma1.it

Abstract: This work reviews in an unified context some previous independently developed works by the authors related to a method for controlling nonlinear dynamics and chaos in mechanical oscillators based on optimal elimination of homo/heteroclinic bifurcations.

Key words: Homo/heteroclinic bifurcations, chaos, optimal control, mechanical oscillators.

1. Introduction

Control of nonlinear dynamics and chaos has increasingly attracted the attention of researchers in various fields of science and engineering. This interest relies on the need to eliminate the chaotic features of systems dynamics or, more recently, on the wish to exploit the peculiarities of chaos for practical purposes (so-called *anti-control of chaos*).

After the pioneering work of Ott, Grebogi & Yorke [7], several different methods have been proposed. Some are based on the dynamical characteristics of the systems, and are usually theoretically well founded [6]; others are more or less empirical, though with various degree of skillfulness [8], all

G. Rega and F. Vestroni (eds.),
IUTAM Symposium on Chaotic Dynamics and Control of Systems and Processes in Mechanics, 47–57.

of them have been shown to be able to eliminate chaotic characteristics to a certain extent. However, while most are simply aimed at *suppressing* chaos, irrespective of the employed tools and of the system characteristics, others are indeed aimed at *exploiting* chaos for its control, even if, incidentally, they may not succeed in eliminating the chaotic attractor. A control method recently proposed by the authors [1] [2] [3] [4] [5] belongs to this latter class, and its investigation is the subject of this work.

The method consists in eliminating homo/heteroclinic intersections embedded in system dynamics and responsible for unwanted events, such as fractal basin boundaries, transient and (possibly) steady chaos, safe basin erosion, escape, overturning, single-well to cross-well chaos transition, scattered impacting dynamics, and so on. These goals can be achieved in various ways, and to date they have been obtained by *varying the shape* of the excitation in an *optimal way*.

Recent works by the authors [1] [2] [3] [4] [5] aimed at applying control separately to different models, are reconsidered in a unified context with the aim of better understanding the control procedure. Indeed, it is expected that some characteristics are shared by all systems, due to the application of the same control method, whereas other characteristics are different, due to the different nature of the oscillators. More precisely, attention is paid to investigating how a *generic* dynamical property, namely the structure of the distance of the invariant manifolds governing homo/heteroclinic bifurcations, entails a *generic* approach to control consisting in the system independence of the relevant optimization problems and their solutions. This reveals the generic nature of the method.

The work consists in a theoretical part devoted to the design of controlled excitations, and a numerical part devoted to verifying theoretical predictions and checking practical performances of the method.

2. The Considered Single-d.o.f. Oscillators

In this paper the following four different single-degree-of-freedom mechanical systems are considered in a unified context:

$$\ddot{x} + \epsilon\delta\dot{x} - x + x^2 = \epsilon\gamma_1 \sum_{j=1}^{N} \frac{\gamma_j}{\gamma_1} \sin(j\omega t + \Psi_j), \tag{1}$$

$$\begin{aligned} &\ddot{x} + \epsilon\delta\dot{x} - \tfrac{x}{2} + \tfrac{x^3}{2} = \epsilon\gamma_1 \textstyle\sum_{j=1}^{N} \frac{\gamma_j}{\gamma_1} \sin(j\omega t + \Psi_j), \\ &\ddot{x} + 0.164\dot{x} - 0.2x + x^3 = A[sin(t) + c_1 sin(nt + c_2), \end{aligned} \tag{2}$$

$$\begin{cases} \ddot{x} + 2\epsilon\delta\dot{x} - x = \epsilon\gamma_1 \sum_{j=1}^{N} \frac{\gamma_j}{\gamma_1} \sin(j\omega t + \Psi_j), & |x| < 1, \\ \dot{x}(t^+) = -r\dot{x}(t^-), & |x| = 1, \end{cases} \tag{3}$$

$$\begin{cases} \ddot{x} + \epsilon\delta\dot{x} - x \pm \alpha = \epsilon\gamma_1 \sum_{j=1}^{N} \frac{\gamma_j}{\gamma_1} \sin(j\omega t + \Psi_j - \pi/2), & x \overset{<}{>} 0, \\ \dot{x}(t^+) = r\dot{x}(t^-), & x = 0. \end{cases} \tag{4}$$

Systems (1) and (2) are the Helmholtz [2] and the Duffing [3] [4] oscillators, respectively. The two versions (2_a) and (2_b) differ by a rescaling, and are used in the analytical and numerical approach to control. Equations (3) and (4), on the other hand, describe the dynamics of an inverted pendulum between lateral walls [1], and of a slender rigid block on an oscillating foundation [5].

All considered systems are Hamiltonian (the unperturbed phase portraits are depicted in Fig. 1) plus perturbations caused by damping $\epsilon\delta$ and *generic* periodic external excitation of amplitude $\epsilon\gamma_1$. Furthermore, as emphasized by Fig. 1, all have at least one homo or heteroclinic loop in the unperturbed dynamics. The strong nonlinearities and smoothness of (1) & (2) vs the

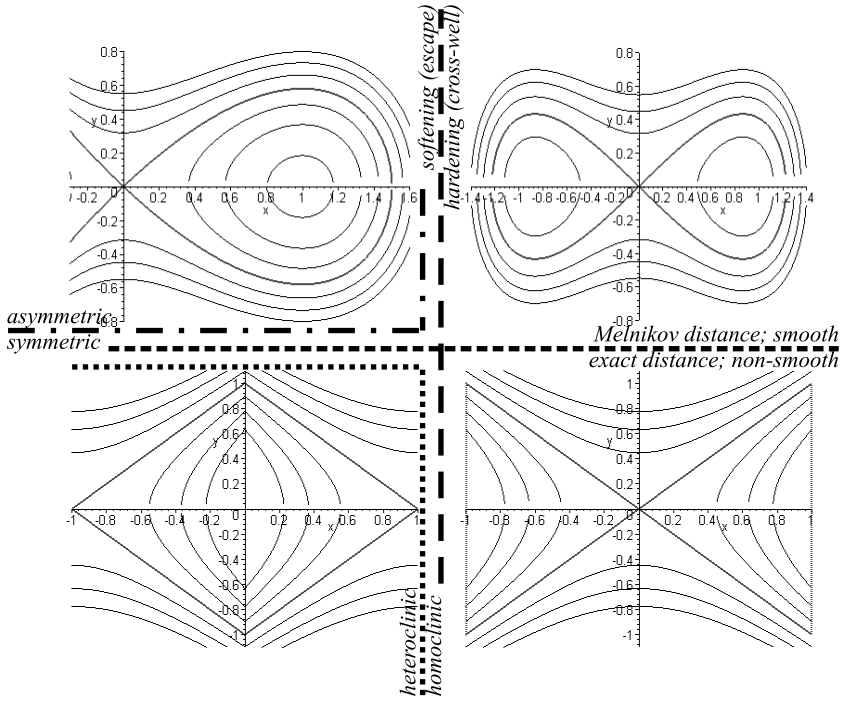

Figure 1. The phase portraits of the four considered oscillators. In clockwise sense from the upper left: Helmholtz, Duffing, Inverted pendulum and Rigid block.

piece-wise linearities and non-smoothness of (3) & (4) constitute meaningful dynamical and mechanical differences; they further entail a difference in the computation of the distances between perturbed manifolds, as the former are computed by the perturbative Melnikov method while the latter exactly.

A different comparison can be made in terms of hardening (eqs. (2) & (3)) vs softening (eqs. (1) & (4)) behaviour, which is another key mechanical property. The asymmetric vs symmetric dichotomy is also considered by comparing (1) with (2), (3) & (4), as well as the fact that (1) & (4) have only one potential well, while (2) & (3) have two wells.

From a dynamical system point of view we note that in (1), (2) & (3) there are homoclinic loops, while in (4) there are heteroclinic solutions. Moreover, while (1) has only one loop, (2), (3) & (4) have two homo/heteroclinic orbits. This entails a difference from a control point of view, as in the first case we have only *one-side* control (see Sect. 4), while in the latter we have *one-side* and *global* controls.

Another considered point is the comparison of theoretically (numerically) detected homoclinic bifurcations of the hilltop (non-hilltop) saddles through eq. (2_a) (eq. (2_b)).

The previous considerations, which are summarized in Fig. 1, show that the selected oscillators are a limited but comprehensive series of sample cases permitting the discussion of the main mechanical, dynamical systems and control points, and highlighting the generality of the control method. Other single-d.o.f. oscillators (e.g., the Helmholtz-Duffing), and infinite-dimensional systems have also been considered by the authors; they involve further theoretical work, and are not addressed in this paper.

3. Detecting Homo/Heteroclinic Bifurcations

Central for the development of control is the detection of the distance between perturbed stable and unstable manifolds. The detailed computations are reported in the quoted works, and here we just note that it consists of a constant part, due to the damping, plus an oscillating part due to the excitation:

$$d(\tau)=\epsilon\delta a_0+\epsilon\gamma_1 a_1(\omega)h(\tau), \quad h(\tau)=\sum_{j=1}^{N}\frac{\gamma_j a_1(j\omega)}{\gamma_1 a_1(\omega)}\cos(j\tau+\chi_j(\Psi_j)). \quad (5)$$

The structure of the distance is always the same, so that it is *system-independent* and *universal*. The coefficients a_0, χ_j and $a_1(\omega)$ are instead *system-dependent*, and take into account the differences between the various cases. The function $h(\tau)$ depends only on the shape of the excitation, and reduces to $cos(\tau+\chi_1)$ for harmonic excitation.

As long as the minimum $d = min_\tau d(\tau)$ is positive, the manifolds remain disjoint; when $d < 0$ there is intersection in some points. Thus, the condition for homo/heteroclinic bifurcation is $d = 0$, which yields

$$\epsilon\gamma_{1,cr} = \frac{\epsilon\delta a_0}{a_1(\omega)M}, \qquad M = M(\gamma_j, \Psi_j) = -min_\tau h(\tau). \tag{6}$$

Equation (6) is sufficient for the Helmholtz oscillator, which has only one homoclinic loop. For the other systems we have one critical threshold for each homo/heteroclinic loop. They have the same structure of (6_a), the only difference being in the definition of the various numbers M. Thanks to the symmetry, we have

$$M^{right} = -min_\tau h(\tau), \quad M^{left} = max_\tau h(\tau), \quad \text{(Duffing+Inverted pend.)} \tag{7}$$

$$M^{up} = -min_\tau h(\tau), \quad M^{low} = max_\tau h(\tau), \quad \text{(Rigid block)} \tag{8}$$

For the harmonic excitation all Ms are equal to 1. For generic excitations, on the other hand, we can have $M < 1$, i.e., $\epsilon\gamma_{1,cr}^{gen.} > \epsilon\gamma_{1,cr}^{harm.}$, and we are able to increase the excitation amplitude critical threshold for the occurence of the global bifurcation. The region between $\epsilon\gamma_{1,cr}^{harm.}$ and $\epsilon\gamma_{1,cr}^{gen.}$, which has homo/heteroclinic intersections with harmonic excitation and no intersections with generic excitation, is the zone of parameters space where the control is theoretically effective. It is called the *saved region* and is depicted in Fig. 2 for the four considered cases.

4. The Optimization Problem

To measure the improvement of generic excitation with respect to harmonic excitation, the *gain* is defined as follows [1] [2] [4] [5]:

$$G = \frac{\epsilon\gamma_{1,cr}^{generic}}{\epsilon\gamma_{1,cr}^{harmonic}} = \frac{1}{M}, \tag{9}$$

so that the saved region can also be defined as $\epsilon\gamma_{1,cr}^{harm.} < \epsilon\gamma_1 < G\epsilon\gamma_{1,cr}^{harm.}$.

It is now clear that if we want to optimize the excitation shape, a point which is the second keystone of the control method, we have to solve the following optimization problem:

Maximize G by varying the excitation shape. (10)

The previous problem is sufficient for the Helmholtz oscillator. In the presence of more homo/heteroclinic loops, two alternative strategies can be

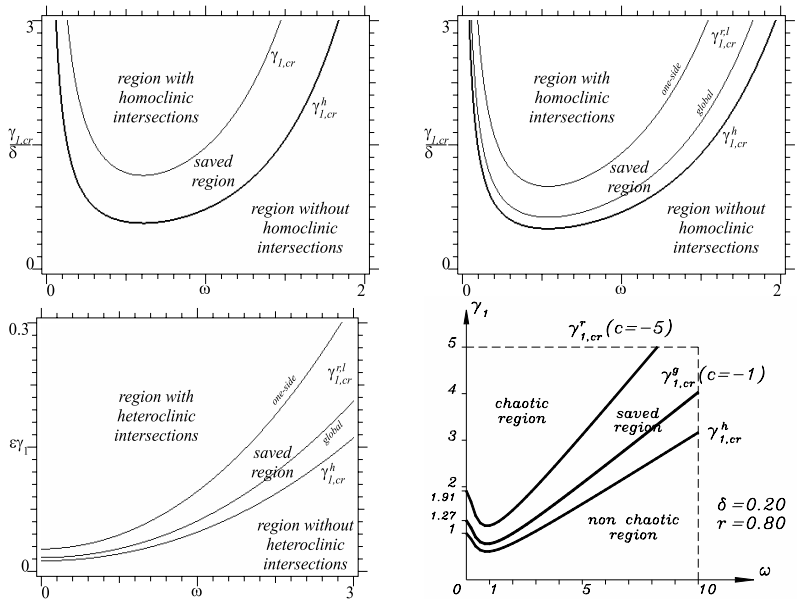

Figure 2. The critical thresholds and the saved regions. In clockwise sense from the upper left: Helmholtz, Duffing, Inverted pendulum and Rigid block.

followed: (i) we can control *only one* homo/heteroclinic bifurcation, irrespective of what happens to the other, or (ii) we can control *simultaneously* both homo/heteroclinic bifurcations. The former choice (called one-side control) is aimed at obtaining a topologically localized control, and reduces to solving problem (10) for a specific loop, whereas the latter (called global control) is aimed at controlling, on average, the whole phase space, and requires solving, e.g.,

$$\textit{Maximize min } \{G^{right}, G^{left}\} \textit{ by varying the excitation shape.} \tag{11}$$

In has been shown [1] [2] [3] [4] [5] that: (i) problem (11) is actually a constrained version of problem (10), so that the global control gain is less than the one-side; (ii) the maximum gains, which are obtained with an infinite number of superharmonics, are 2 and 1.2732, respectively; (iii) the solution of problem (11) has only even superharmonics, a property shared by theoretical [4] and numerical [3] controls; (iv) both problems (10) and (11), and their solutions, are *system-independent*, thus further emphasing the generic nature of the control method.

Problems (10) and (11) have been solved in various forms: reduced, constrained, reduced and contrained solutions have been obtained [2]. Among these, of particular interest are the reduced solutions, obtained with a finite

number of superharmonics, which provide sufficiently high theoretical gains and are relatively easy to reproduce in practice. Their expressions are reported in the original works, and they will be used in the remaining part of this work, where systematic numerical simulations are addressed (i) to confirm theoretical predictions and (ii) to check the feasibility and the actual performances of the technique.

5. Reducing Fractal Basin Erosion

In this section we focus on the safe basin erosion, which is known to occur through incursion of fractal fingers [10] and is the triggering phenomenon for escape from potential wells. Being able to eliminate the fractal basin boundaries, the controls are *a fortiori* able to eliminate basin erosions.

An isolated example of reduction of basin erosion is reported in Fig. 3, which clearly shows how for fixed parameters and excitation amplitude, the optimal excitation significatively enlarges the safe basin. This is also quantitatively confirmed by the Safe Integrity Factor (S.I.F.) [2] [9] which passes from 26.3% to 95.3% by adding control superharmonics.

A more systematic investigation is summarized in Fig. 4, which reports the S.I.F. versus the excitation amplitude for both Helmholtz and Duffing oscillators. In both cases, the excitation frequency is close to the vertex of the relevant V-shaped regions of unwanted phenomena (escape for Helmholtz [2], cross-well chaos for Duffing [4]).

Figure 4 shows how the optimal excitations are able to shift toward larger amplitudes the so-called *Dover Cliff* erosion profiles [2] [4] [9]. In turn, the starting points of erosion are just ahead of the homoclinic bifurcations thresholds (marked by vertical segments), thus showing good agreement between theoretical prediction and practical performances.

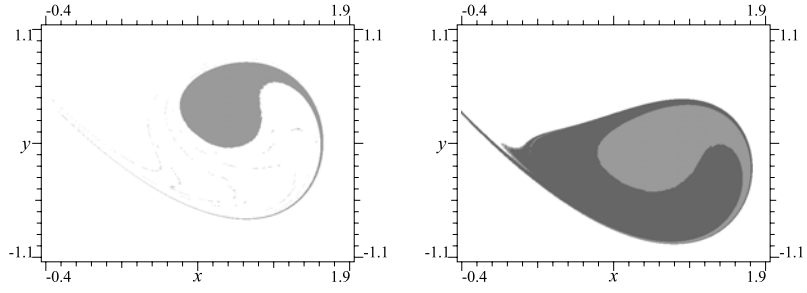

Figure 3. Basins of attraction of the Helmholtz oscillator. Left: harmonic excitation. Right: optimal excitation with two superharmonics.

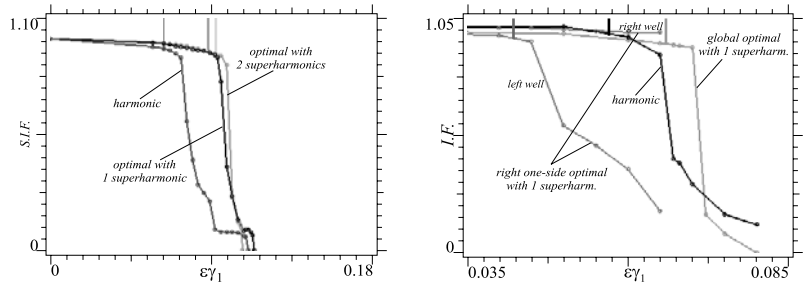

Figure 4. The basin erosion profiles for the Helmholtz (left) and Duffing (right) oscillator. The vertical segments denote the respective homoclinic bifurcations.

For the rigid block and the inverted pendulum it is found that the erosion profiles are *not* sharp (Dover Cliff-like), so its shifting is less important from a practical point of view and is not investigated; we conjecture that this is due to the absence of a resonance frequency.

6. Effects of Control on Out-of-well Phenomena

Other practical performances discussed in this work are the control induced modifications on the out-of-well phenomena. For the Helmholtz oscillator, this is the sudden approach to infinity of the trajectories, a feature commonly known as *escape* [2] [9]. The systematic effectiveness of control in increasing the escape threshold around the most dangerous excitation frequency is shown in Fig. 5_{left}.

For the other softening system, the rigid block, the out-of-well phenomenon is the overturning of the rest position, which is a very important aspect of the dynamics especially in conjunction with earthquakes. The sample response in Fig. 5_{right} illustrates how the control may eliminate the toppling of the block.

The counterpart of escape for hardening oscillators is the onset of cross-well chaos, or, more generally, of scattered dynamics. This question is investigated in Fig. 6, which reports both theoretical and numerical controls. We remark that there are very different expectations for the two cases. In fact, the theoretical control is not expected to be able to shift the appearance of scattered chaotic attractors, because the homoclinic bifurcation of the hill-top saddle does not *directly* influence the attractors' scenario. The numerical control, on the other hand, has been designed just to shift the occurrence of cross-well chaos, which is thus expected not to occur with optimal excitations.

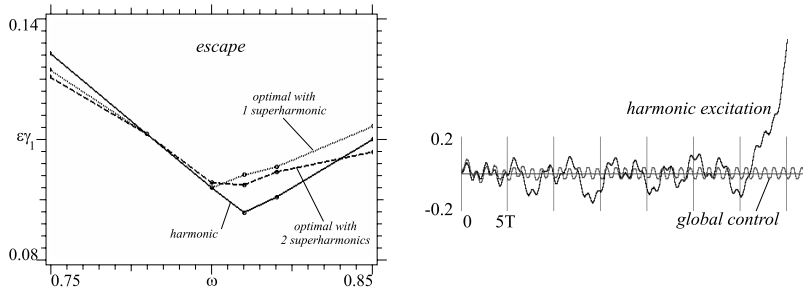

Figure 5. Left: The escape regions of the Helmholtz oscillator. Right: Time histories of the rigid block starting from the rest position.

The latter prediction is actually confirmed by numerical simulations, both for one-side (see Fig. 6_{low}) and global (non reported) controls: the theoretical one-side control is unexpectedly able to shift cross-well chaos (see Fig. 6_{up}).

Finally, bifurcation diagrams for the optimal control of hilltop saddles have been constructed for the inverted pendulum also. They show an overall

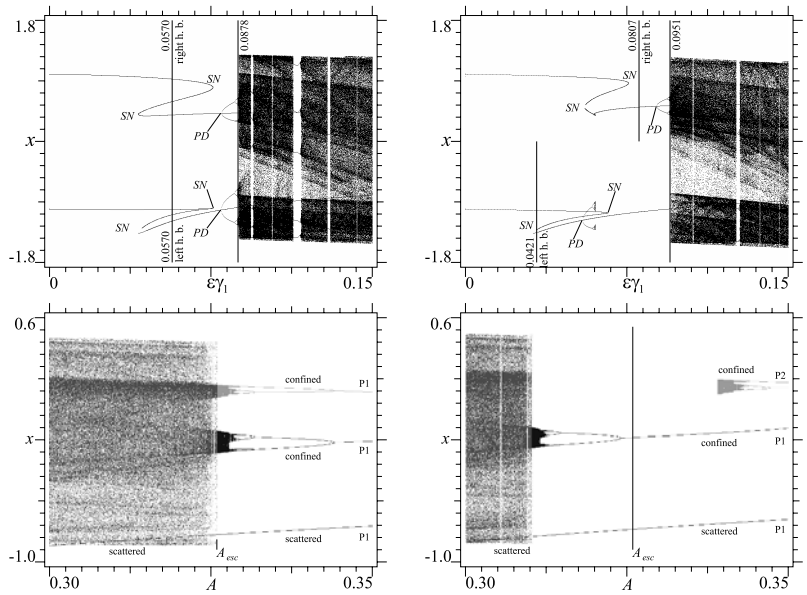

Figure 6. Bifurcation diagram for the Duffing oscillator. Up: Theoretical control of the hilltop saddle. Low: numerical control of a non-hilltop saddle. Left: Harmonic excitations. Right: one-side control excitations with one superharmonic.

resemblance to the previous ones, accompanied by some phenomenological differences, and are not reported in this paper.

7. Conclusions

A method based on exploiting nonlinear dynamics for control of mechanical systems has been reconsidered with the double aim of placing previous works in a unified context and illustrating the similarities and differences between controls for different systems.

In the first part, the theoretical aspects of control were discussed, by computing the *system-independent* distances between stable and unstable manifolds, and the homo/heteroclinic bifurcation thresholds, and then by formulating and solving the *system-independent* optimization problems which provide the best excitations.

In the second part, extended numerical simulations aimed at checking the theoretical predictions and the practical performances of control, were summarized. It was shown that it is effective in reducing safe basin erosion, and has a meaningful influence also on the out-of-well phenomena. The optimal excitations have been shown to be effective, where required, in increasing the excitation critical threshold for escape, and to be extremely efficient in shifting cross-well chaos in parameters space when properly designed. Surprisingly enough, they are possibly effective also when designed for different purposes.

References

[1] S. Lenci and G. Rega, "Controlling nonlinear dynamics in a two-well impact system. Parts I & II," *Int. J. Bif. Chaos*, 8, 2387-2424, 1998.

[2] S. Lenci and G. Rega, "Optimal control of homoclinic bifurcation: Theoretical treatment and practical reduction of safe basin erosion in the Helmholtz oscillator," *J. Vibr. Control*, 9, 281-316, 2003.

[3] S. Lenci and G. Rega, "Optimal numerical control of single-well to cross-well chaos transition in mechanical systems," *Chaos Sol. & Fract.*, 15, 173-186, 2003.

[4] S. Lenci and G. Rega, "Optimal control of nonregular dynamics in a Duffing oscillator," *Nonlin. Dynam.*, 33, 71-86, 2003.

[5] S. Lenci and G. Rega, "Heteroclinic bifurcations and optimal control in the nonlinear rocking dynamics of generic and slender rigid blocks," in press on *Int. J. Bifur. Chaos*, 2003.

[6] R. Lima and M. Pettini, "Suppression of chaos by resonant parametric perturbations," *Phys. Rev. A*, 41, 726-733, 1990.

[7] E. Ott, C. Grebogi and J.A. Yorke, "Controlling chaos," *Phys. Rev. Lett. E*, 64, 1196-1199, 1990.

[8] K. Pyragas, "Continuous control of chaos by self-controlling feedback," *Phys. Letters A*, 170, 421-428, 1992.

[9] J.M.T. Thompson, "Chaotic phenomena triggering the escape from a potential well," *Proc. R. Soc. London A*, 421, 195-225, 1989.

[10] J.M.T. Thompson and H.B. Stewart, *Nonlinear Dynamics and Chaos*, John Wiley, Chichester, Second Edition, 2002.

NONLINEAR NORMAL MODES AND CHAOTIC MOTIONS IN OSCILLATORY CHAINS

Leonid I. Manevitch
N. N. Semenov Institute of Chemical Physics, Russian Academy of Sciences, 117977 Moscow, Russia
lmanev@center.chph.ras.ru

Oleg V. Gendelman
N. N. Semenov Institute of Chemical Physics, Russian Academy of Sciences, 117977 Moscow, Russia
ovgend@center.chph.ras.ru

Alexander V. Savin
N. N. Semenov Institute of Chemical Physics, Russian Academy of Sciences, 117977 Moscow, Russia
asavin@center.chph.ras.ru

Abstract: We present the results of analytical and numerical study of the random vibrations in several nonlinear one-dimensional oscillatory chains which model significant mechanical and physical systems. It is shown that existence and propagation of the random excitations in the considered models is strongly dependent on the properties of nonlinear normal modes. In particular, nonlinear vibrations in attenuation zone of linearized system initiated by global random excitations, correspond to localized nonlinear normal modes – breathers. In the localization region periodic contraction-extension of interparticle bonds occurs which is accompanied by decrease-increase of angles between the bonds. It is shown that the breathers present in thermalized chain and their contribution dependent on temperature has been revealed.

Process of heat conduction in the chain with periodic potential of nearest-neighbor interaction is investigated by means of computer simulation. It is demonstrated that the periodic potential of nearest-neighbor interaction allows to obtain normal heat conductivity in isolated one-dimensional chain with conserved momentum. The system exhibits transition from infinite to normal heat conductivity with growth of its temperature. The physical reason for normal heat conductivity is excitation of high-frequency stationary localized rotational modes. These modes absorb the momentum and facilitate locking of the heat

G. Rega and F. Vestroni (eds.),
IUTAM Symposium on Chaotic Dynamics and Control of Systems and Processes in Mechanics, 59–68.

flux. Concentration and lifetime of the localized modes grow with the growth of the temperature and the heat conductivity monotonically decreases.

The process of heat conduction in one-dimensional lattice with on-site potential is also studied by means of numerical simulation. Using the discrete Frenkel-Kontorova, ϕ^4 and sinh-Gordon models we demonstrate that contrary to previously expressed opinions the sole anharmonicity of the on-site potential is insufficient to ensure the normal heat conductivity in these systems. The character of the energy transfer is determined by the spectrum of nonlinear excitations peculiar for every given model and therefore depends on the concrete potential shape and a temperature of the lattice. The reason is that the peculiarities of the nonlinear excitations and their interactions prescribe the energy scattering mechanism in each model. For sine-Gordon and ϕ^4 models, linear waves (phonons) are scattered at a dynamical lattice of topological solitons; for sinh-Gordon and for ϕ^4 in a different parameter regime the phonons are scattered at localized high-frequency breathers (in the case of ϕ^4 the scattering mechanism switches with the growth of the temperature).

Key words: Nonlinear normal modes, breathers, heat transfer.

1. Introduction

Existence and manifestation of the random excitations in nonlinear oscillatory chains is of major practical significance in many mechanical problems, but is scantily known. When using the notion "random" or "chaotic" excitation we mean elementary (preserving their form) excitations in fully thermalized system. Within context of this problem a deep difference exists between linear and nonlinear models of mechanical systems. While in the former case characteristics of the excitations action and spreading are similar to those for harmonic linear waves (and of course can be examined by common spectral methods), in the latter case the significant peculiarities arise. They can be qualitatively described if translating the problem to the language of thermodynamics and statistical mechanics. From such alternative point of view, e.g. random vibrations and localized random excitations of the chain correspond to global thermal action, and local heating of the chain respectively. Then random excitations spreading (mechanical energy transfer) along the chain can be associated with a heat conduction process. Historically this problem is closely related to famous Fermi-Pasta-Ulan numerical experiment [1] which has been undertaken in order to substantiate Pierls model of heat conduction in dielectrics [2]. The model states that the heat conduction is related to so called Umklapp processes of weakly nonlinear waves (phonons) interaction insuring partial transfer of momentum to the lattice. Still, the numerical experiment failed to verify this mechanism (but lead to discovery of solitons). The problem of finite heat conductivity in dielectrics in many extents remains to be unresolved issue.

It is easy to understand why a linear model of the chain does not allow simulating well-known experimental features of this process, such as the presence of vibration modes in the attenuation zone. And above all the rate of spreading in linear chains will be related to sound velocity rather than to substantially less value corresponding to thermal diffusion process. Even in nonlinear models the special conditions have to be satisfied to provide a similarity of dynamic process to thermal conductivity. Normally the processes of random vibrations and heat conduction involve various agents of energy transfer (periodic waves, solitons etc.) as well as a scattering mechanism of these agents insuring the equipartition of the energy over all degrees of freedom.

Accordingly the clue for constructing the relevant model of the nonlinear oscillatory chain is that two types of random excitations should be distinguished. The excitations of the first type are qualitatively similar to those in linear case and may be named as the fast ones (they are abnormal from thermodynamic viewpoint). Second type of behavior (slow excitations) is rather common in thermodynamic and statistical mechanics. To provide understanding of the regularities of chaotic excitation manifestation in nonlinear oscillatory chains two key problems have to be solved:

1 characterization of specific nonlinear normal modes in the attenuation and propagation zones of the oscillatory chain and study of their possible roles in the random vibration and scattering of elastic waves;

2 clarifying the conditions of slow and fast propagation of random excitations via dynamical (nonlinear normal modes) and statistical autocorrelation function characteristics of the oscillatory chain.

Both these problems are described in application to several modes of one dimensional oscillatory chains including the chains with translational invariants (zigzag chains with asymmetric nonlinearity, rotator chain with symmetric nonlinearity) as well as the chains with on-site potential (oscillatory chain on symmetric nonlinear substrate).

2. Short Wavelength Normal Modes (Breathers) in Zigzag Oscillatory Chain

The structure of planar zigzag oscillatory chain is schematically plotted at figure 1.

Let us introduce the local coordinate system presented on this figure. Then the Hamiltonian function of the chain in the case of planar dynamics can be written as follows.

$$H = \sum_n \frac{1}{2} M \left(\dot{u}_n^2 + \dot{v}_n^2 \right) + V(\rho_n) + U(\theta_n) \tag{1}$$

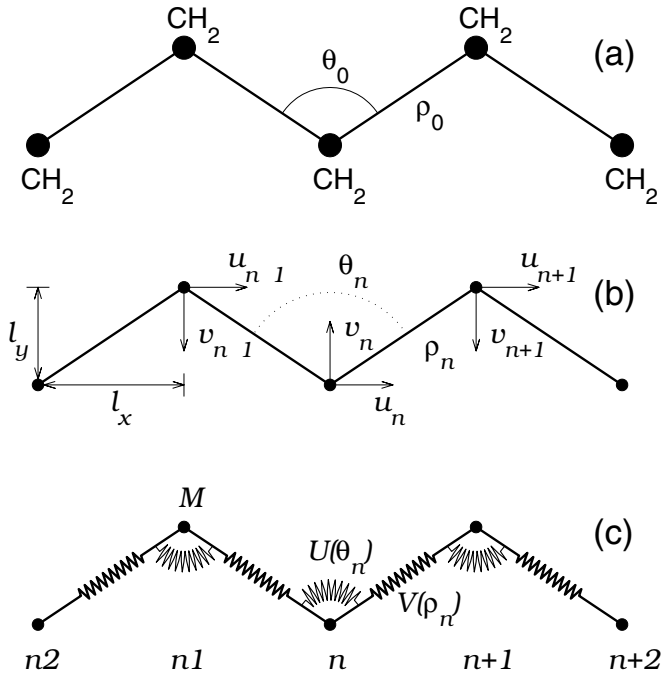

Figure 1.
(a) Structure of the polyethylene molecule (CH2),
(b) selection of local coordinate systems,
(c) flat mechanical model of macro-molecule.

where the first term describes the kinetic energy of the n-th particle (M is the mass of every particle), the second – the deformation energy of the n-th bond between n-th and $(n+1)$-th particles, and the last term – the deformation energy of the n-th angle between $(n-1)$ and n-th bonds.

The length of the n-th bond is

$$\rho_n = \left(a_{n,1}^2 + a_{n,2}^2\right)^{1/2}, \tag{2}$$

where $a_{n,1} = u_{n+1} - u_n + l_x$, $a_{n,2} = \upsilon_n + \upsilon_{n+1} - l_y$, ($l_x = \rho_0 \sin(\theta_0/2)$ and $l_y = \rho_0 \cos(\theta_0/2)$ are the transversal and longitudinal steps of the zigzag chain respectively).

The cosine of the n-th angle is

$$\cos\theta_n = (a_{n-1,1}a_{n,1} - a_{n-1,2}a_{n,2})/\rho_{n-1}\rho_n. \tag{3}$$

Potentials of the bonds and angles are accepted in the form

$$V(\rho_n) = \frac{1}{2}K_1(\rho_n - \rho_0)^2, \quad U(\theta_n) = \frac{1}{2}\gamma\,(\cos\theta_n - \cos\theta_0)^2, \tag{4}$$

where force constant $K_1 = 405.5$ N/m, $\gamma = 130.1$ kJ/mol.

Small-amplitude vibrations of isolated transzigzag were considered in [3–5] and vibrations with account of interaction with immobile surrounding chains – in [6].

Small-amplitude vibrations can be divided to planar (in the zigzag plane) and transversal ones. In turn, the plane motions are divided to low- frequency acoustic and high-frequency optic vibrations. Accordingly, one can separate three dispersion curves corresponding to 1) plane acoustic phonons $\omega = \omega_a(q)$, 2) transversal phonons $\omega = \omega_t(q)$, 3) plane optic phonons $\omega = \omega_o(q)$. These curves with account of interchain interaction are presented at Fig. 2 (a).

Let us consider the long wavelength modulation waves in weakly nonlinear limiting case when one can find the following main nonlinear continuum approximations for $\Delta\rho_n$ and $\Delta\theta_n$ with respect to small ratio of interparticle space and characteristic wavelength of the process (the smallness of this ratio is supposed to be similar to ratio of cubic and quadratic (as well as quarter and cubic terms) in Hamiltonian

$$\Delta\rho = \rho_n - \rho_0 = \cos\frac{\theta_0}{2}\left(2u + l_z\frac{\partial v}{\partial z} + \frac{1}{2}l_x^2\frac{\partial^2 v}{\partial z^2}\right) + \sin\frac{\theta_0}{2}l_x\frac{\partial u}{\partial z} + \frac{2}{\rho_0}\sin^2\frac{\theta_0}{2}v^2, \tag{5}$$

$$\Delta\theta = \theta_n - \theta_0 = \frac{4}{\rho_0}\sin^2\frac{\theta_0}{2}v + \frac{2}{\rho_0}\cos\frac{\theta_0}{2}l_x\frac{\partial u}{\partial z} + \frac{8}{\rho_0^2}v^2. \tag{6}$$

Besides, it is taken into account that linear analysis reveals smallness of longitudinal displacement with respect the transversal one for considered type of motion. In this approximation the equations of motion after certain transformations can be reduced to nonlinear partial equation:

$$\frac{\partial^2 U}{\partial\tau^2} - \varepsilon^2 c^2\frac{\partial^2 U}{\partial\zeta^2} + U - 4\alpha\varepsilon U^2 + 8\beta\varepsilon^2 U^3 = 0, \tag{7}$$

where

$$\varepsilon U = \frac{u}{\rho_0}\ ;\quad \tau = \frac{2}{\sqrt{m}}\sqrt{K_1\cos^2\frac{\theta_0}{2} + 4\frac{K_2}{\rho_0^2}\sin^2\frac{\theta_0}{2}}\,t\ ;$$

$$\zeta = \frac{\varepsilon z}{l_z};\quad c^2 = -\frac{K_1\rho_0^2\sin^2\theta_0}{16\left(K_1\cos^2\frac{\theta_0}{2} + 4\frac{K_2}{\rho_0^2}\sin^2\frac{\theta_0}{2}\right)}\times\ ;$$

$$\times\left(\frac{\cos\theta_0 + 2\frac{K_2}{K_1\rho_0^2}\sin^2\frac{\theta_0}{2}}{1 + 2\frac{K_2}{K_1\rho_0^2} + \left(1 - 2\frac{K_2}{K_1\rho_0^2}\right)\cos\theta_0}\right)\ ;$$

$$4\alpha = \frac{\sin\theta_0\sin\frac{\theta_0}{2}\left(3K_1 + \frac{8K_2}{\rho_0^2}\right)}{2\left(K_1\cos^2\frac{\theta_0}{2} + \frac{4K_2}{\rho_0^2}\sin^2\frac{\theta_0}{2}\right)}\ ;$$

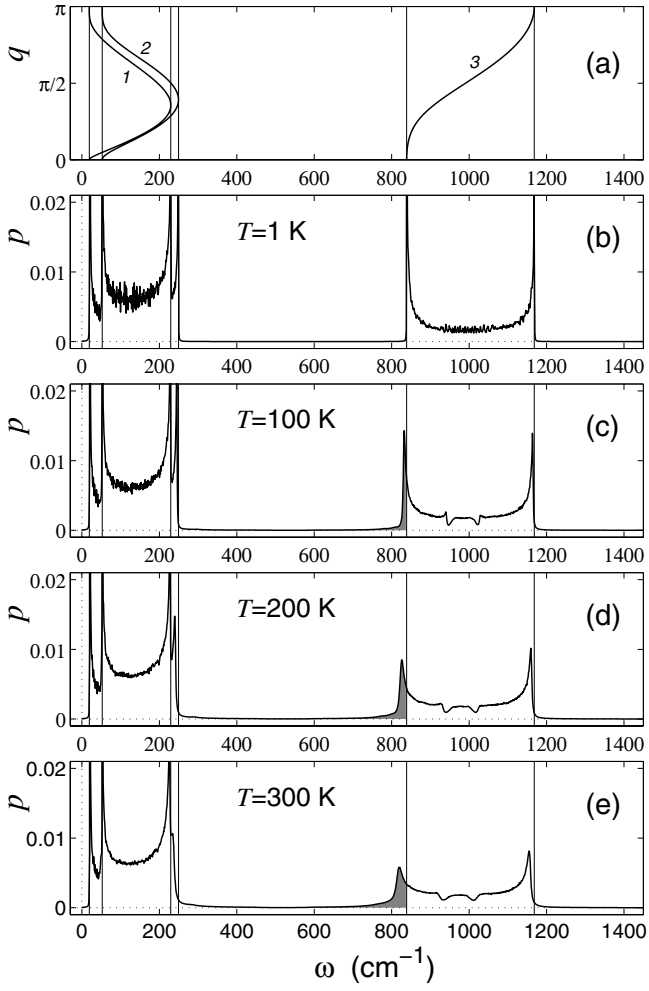

Figure 2. Dispersion curves $\omega = \omega_a(q)$, $\omega = \omega_t(q)$, $\omega = \omega_o(q)$ (curves 1, 2, 3) for trans-zigzag interacting with immobile surrounding chains (a). Density of energy distribution p on frequencies ω for thermal vibrations with temperature T = 1 K (b), T = 100 K (c), T = 200 K (d), and T = 300 K (e). Gray color corresponds to frequencies region in which the discrete breathers occur.

$$8\beta = \frac{8}{\rho_0^2}\left(K_1 \sin^4\frac{\theta_0}{2} + 2\frac{K_2}{\rho_0^2}\sin^2\theta_0\right) .$$

Let us introduce the complex functions [7, 8]:

$$\psi(\zeta,\tau) = V + iU, \quad \psi^*(\zeta,\tau) = V - iU \tag{8}$$

where $V = \partial U/\partial\tau$. Partial equation is equivalent to the system of two equations

$$\begin{aligned} \frac{\partial V}{\partial\tau} &= \varepsilon^2 c^2 \frac{\partial^2 U}{\partial\zeta^2} - U + 4\alpha\varepsilon U^2 - 8\beta\varepsilon^2 U^3 , \\ \frac{\partial U}{\partial\tau} &= V . \end{aligned} \tag{9}$$

After substitution of (8) into (8) and certain transformation one can obtain

$$\frac{\partial \psi}{\partial \tau} = -i\psi + i\varepsilon^2 c^2 \frac{\partial^2 (\psi - \psi^*)}{\partial \zeta^2} + \alpha\varepsilon \left(\psi - \psi^*\right)^2 - i\beta\varepsilon^2 \left(\psi - \psi^*\right)^3 = 0 .$$

The change of variables $\psi = e^{i\tau}\varphi\,(\zeta, \tau)$ leads to equation

$$\frac{\partial \varphi}{\partial \tau} + i\varepsilon^2 c^2 \frac{\partial^2 \left(\varphi - \varphi^* e^{-i\tau}\right)}{\partial \zeta^2} + \alpha\varepsilon \left(\varphi e^{i\tau} - \varphi^* e^{-i\tau}\right)^2 e^{-i\tau} - i\beta\varepsilon^2 \left(\varphi e^{i\tau} - \varphi^* e^{-i\tau}\right)^3 e^{-i\tau} = 0 . \tag{10}$$

Then we introduce, alongside with fast time $\tau = \tau_0$, the slow times

$$\tau_1 = \varepsilon\tau_0,\ \tau_2 = \varepsilon^2\tau_0 \ldots \tag{11}$$

and power expansion

$$\varphi = \varphi_0 + \varepsilon\varphi_1 + \varepsilon^2\varphi_2 + \cdots \tag{12}$$

After substitution of the expansion (12) into (9) with taking into account (11) and selecting the terms of similar order with respect to small parameter one can find

$$\frac{\partial \varphi_0}{\partial \tau_0} = 0,$$

$$\frac{\partial \varphi_1}{\partial \tau_0} + \frac{\partial \varphi_0}{\partial \tau_1} + \varphi_0^2 e^{i\tau_0} - 2\alpha\,|\varphi_0|^2 e^{-i\tau_0} + \alpha \left(\varphi_o^*\right)^2 e^{-3i\tau_0} = 0$$

$$\frac{\partial \varphi_2}{\partial \tau_0} + \frac{\partial \varphi_1}{\partial \tau_1} + \frac{\partial \varphi_0}{\partial \tau_2} + ic^2 \frac{\partial^2 \varphi_0}{\partial \xi^2} + 2\alpha\varphi_0\varphi_1 e^{i\tau_0} - 2\alpha\varphi_0^*\varphi_1^* e^{-3i\tau_0} - 2\alpha\varphi_0\varphi_1^* e^{-i\tau_0} - 2\alpha\varphi_0^*\varphi_1 e^{-i\tau_0} + i\beta \left[\varphi_0^3 e^{2i\tau_0} - 3\,|\varphi_0|^2 \varphi_0 + 3\,|\varphi_0|^2 \varphi_0^* e^{-2i\tau_0} + \left(\varphi_0^*\right)^3 e^{-4i\tau_0}\right] = 0$$

The condition of absence of secular terms in first two equations of this system leads to relations $\varphi_0 = \varphi_0\,(\tau_1, \tau_2, \ldots)$, $\frac{\partial \varphi_0}{\partial \tau_1} = 0$, consequently $\varphi_0 = \varphi_0\,(\tau_2, \tau_3, \ldots)$. Then the solution of the second equation can be written as follows

$$\varphi_1 = i\alpha\varphi_0^2 e^{i\tau_0} + 2i\alpha\,|\varphi_0|^2 e^{-i\tau_0} - \frac{1}{3}\alpha \left(\varphi_o^*\right)^2 e^{-3i\tau_0}$$

The condition of absence of secular terms in third equation may be presented in the form

$$\frac{\partial \varphi_0}{\partial \tau_2} + ic^2 \frac{\partial^2 \varphi_0}{\partial \zeta^2} + i\left(\frac{16}{3}\alpha^2 - 3\beta\right)|\varphi_0|^2 \varphi_0 = 0 \tag{13}$$

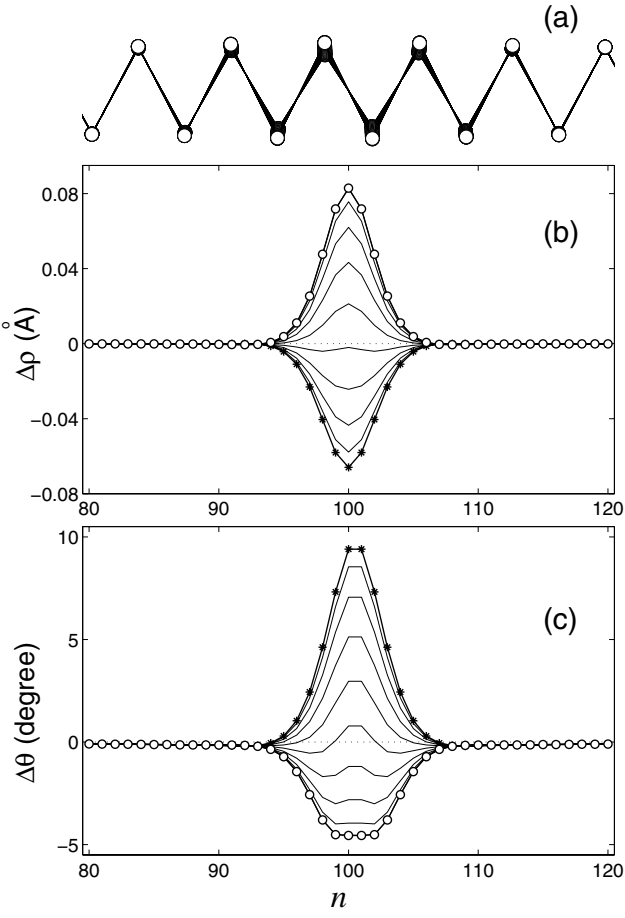

Figure 3.
Localized planar periodic vibrations of trans-zigzag. Vibrations are schematically shown, the thickness of line corresponds to amplitude (a). The magnitudes of valence bonds ρ_n (b) and angles θ_n (c) are presented for ten different instants. The frequency of breather $\omega = 820.5$ cm^{-1}, energy $E = 26.4$ kJ/mol, width $L = 4.28$

So we come to well known exactly integrable nonlinear Schrodinger equation (NSE). If

$$\nu = \left(\frac{16}{3}\alpha^2 - 3\beta\right) > 0, \tag{14}$$

this equation possess localized soliton-like solution (envelope soliton)

$$\varphi_0(\zeta, \tau_2) = \left(\frac{2S}{\nu}\right)^2 \exp\left(i\frac{\zeta v}{2c} + i\omega\tau_2\right) \times \\ \times \operatorname{sech}\left[S^{1/2}\left(\frac{\zeta}{c} + v\tau_2\right)\right] \tag{15}$$

where

$$\omega = \frac{v^2}{4} - S, \tag{16}$$

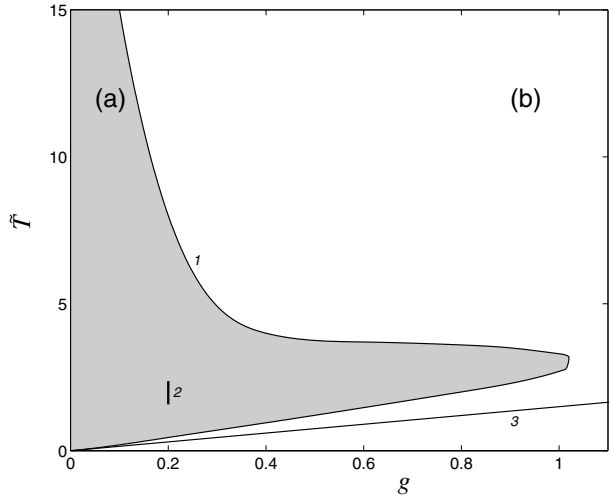

Figure 4.
The zone in the space of parameters $(g, \tilde{T})$, where for finite chains of length $N \leq 640$ with periodic on-site potential he heat conductivity converges (a, grey zone) and may be diverges (b, white zone) [10]. Curve 1 divides these two zones. Interval 2 corresponds to the parameters used in [11]. For finite chains ($N \leq 640$) with on-site potential ϕ^4 finite heat conductivity is detected above line 3.

To check the assumptions accepted for derivation of the equation (14) a numerical study of the problem has been performed.

3. Numerical Study of Localized Nonlinear Vibrations and Chaotic Motion of the Chain

The results of numerical simulation of the chaotic thermal vibrations in zigzag chain consisting of 200 particles lead to conclusion that oscillations in attenuation zone are observed (Fig. 2) and they can be identified with discrete breathers, plotted at Fig. 3. So, at Fig. 3 we present spatial characteristics of localized excitations (breather), while at Fig. 2 the densities of energy distribution corresponding, in particular, breathers are shown. We have shown also that localized normal modes play a significant role in the process of chaotic excitations propagation (thermal conductivity), being simultaneously scattering agents for periodic waves.

The performed investigation demonstrates that the conductivity of any concrete model of chains without and with on-site potentials depends on peculiar nonlinear excitations, which determine the process of the heat transfer and phonon scattering. Three typical agents of the phonon scattering were revealed: localized modes (chain without one-site potential [9]) in the paper – thermalized soliton superlattice (discrete sine-Gordon and ϕ^4 models [10]) and discrete high-frequency breathers (ϕ^4 and sinh-Gordon models [10]). Phonon scattering mechanism may switch with the change of the temperature (ϕ^4 model).

For the discrete Frenkel-Kontorova model the zone of the converging heat conductivity for given chain length is limited by low and high temperatures and by high cooperativeness. The numerical possibilities available up to date does not allow us to establish unambiguously the character of the heat conductivity outside the zone designated at Fig. 4. Still there is a reason to suggest that an infinite chain has diverging heat conductivity for certain parameters, although the zone corresponding to finite heat conductivity will be larger than computed above. The same is relevant for two other models considered. Still, the transition from exponential to power-like decrease rate of the autocorrelation function is observed in every case. This observation supports the suggestions related to the switches of physical mechanisms responsible for the character of the heat transport.

4. Conclusion

Stable localized nonlinear vibrations, which are discrete breathers, can exist in attention zone of the zigzag oscillatory chain. They are planar vibrations of zigzag with periodic deformation of the longitudinal and angular springs. The breathers present in thermalized chain and their contribution to general vibration energy may be essential.

The investigation presented above demonstrates that energy transfer in any concrete model of chain without or with on-site potentials depends on peculiar nonlinear localized excitations which determine the process of the their propagation and scattering.

The authors are grateful to Russian Foundation of Basic Research (grant No. 01-03- 33122) and to RAS Commission for Support of Young Scientists (6th competition, grant No.123) for financial support. O.V.G. is grateful to Russian Science Support Foundation for financial support

References

[1] E. Fermi, J. Pasta, and S. Ulam, Los Alamos Report No. LA-1940, 1955.
[2] R.E. Peierls, *Quantum theory of solids*, Oxford University Press, London 1955.
[3] J.G. Kirkwood, *J Chem. Phys.* **7** (7) 506, 1939.
[4] K. Pitzer, *J Chem. Phys.* **8** (8) 711, 1940.
[5] L.I. Manevitch, and A.V. Savin, *Phys. Rev. E* **55** 4713, 1997.
[6] A.V. Savin, and L.I. Manevitch, *Phys. Rev. B* **58** (17) 11386, 1998.
[7] L.I. Manevitch, *Nonlinear Dynamics* **25** 95-109, 2001.
[8] L.I. Manevitch, *Polymer Science C* **4**(2) 117-181, 2001.
[9] O.V. Gendelman, and A.V. Savin, *Phys. Rev. Lett.* **84** 2381, 2000.
[10] A.V. Savin, and O.V. Gendelman, *Phys. Rev. E* **67** 041205, 2003.
[11] B. Hu, B. Li, and H. Zhao, *Phys. Rev. E* **57** 2992, 1998.

PATTERNS OF BIFURCATION SUPPRESSING ESCAPE AT INTERNAL RESONANCE

G.H.M. van der Heijden and J.M.T. Thompson
Centre for Nonlinear Dynamics
University College London
London WC1E 6BT, UK
g.heijden@ucl.ac.uk

Abstract: For an archetypal two-degree-of-freedom forced oscillator, relevant to a large class of mechanical problems, we examine the patterns of bifurcation that govern the internal 1:2 resonance of the system. A knowledge of these bifurcations allows the counter-intuitive suppression and control of escape by internal modal interactions. The bifurcations examined include symmetry-breaking pitchforks, Neimark bifurcations (secondary Hopf bifurcations) to a toroidal attractor, and chaotic crises which trigger dangerous large-amplitude excursions. We particularly focus on the effect that a symmetry-breaking imperfection has on the suppression of escape.

Key words: Suppression of escape, 2 DOF forced oscillator, symmetry breaking, 1:2 resonance, Neimark bifurcation, unfolding.

1. Introduction

Engineering failures are often triggered when an underlying dynamical system escapes from a potential well. Electrical systems, for example, can slip out of synchronisation. With power generators this can result in a blackout in the supply grid to an entire city; in the electronic phase-locked loop of a receiver, a slip from the locked configuration can result in loss of communication; while if a synchronous motor slips under excessive load, time keeping will be lost. In civil and aerospace engineering slender and thin-walled structures can buckle elastically under compressive loading, resulting in collapse. In naval architecture recent activity is directed towards an improved understanding of the capsize of vessels, including off-shore oil production facilities and roll-on-roll-off ferries. Escape from a potential well is likewise a

G. Rega and F. Vestroni (eds.),
IUTAM Symposium on Chaotic Dynamics and Control of Systems and Processes in Mechanics, 69–78.

universal problem in the natural sciences, from activation energies of molecular dynamics to the gravitational collapse of massive starts.

Useful information about the escape process can be gained from mathematical models with periodic excitation. In man-made technological systems such forcing is in fact not uncommon. Sinusoidal electric currents and out-of-balance forces from rotating machinery supply quite precise periodic excitation. Even if the real-world excitation is not expected to be periodic, it is often valid to represent it as periodic in a model or simulation. This is the case in capsize studies, where periodic excitation from ocean waves can be visualised as a worst-case scenario and one that might form the basis of a standardised and repeatable test of the capsizability of a hull [1, 2].

Since most real problems have more than one degree of freedom, we consider here escape from a two-dimensional well using the archetypal model derived in [3]. The model consists of a pair of coupled nonlinear oscillators, whose potential well allows escape to infinity over a pair of symmetrically disposed saddles. Under direct excitation of one of the degrees of freedom, we study the nonlinear coupling with the other. An internal tuning parameter allows us to induce internal resonance where an interesting and counterintuitive suppression of escape is uncovered. Applied to the resonant rolling of ships in beam seas, our results suggest that when the heave frequency is twice the frequency of wave encounter, capsize is significantly suppressed. We particularly concentrate on the effect on this suppression of a bias in the forced degree of freedom.

2. The System

We consider the following coupled system of nonlinear oscillators derived in [3]:

$$\begin{aligned} &\ddot{x} + 2\zeta\dot{x} + x - 2xy - b = F\sin\omega t, \\ &(2/R^2)(\ddot{y} + 2\zeta R\dot{y}) + 2y - x^2 = 0. \end{aligned} \tag{1}$$

Note that b is a symmetry-breaking imperfection. For $b = 0$ the system is invariant under the following transformation

$$\omega t \to \omega t + \pi, \qquad x \to -x, \qquad y \to y. \tag{2}$$

This symmetry is an example of what the authors in [4] call spatio-temporal symmetry since it involves both the phase space variables and time. Period-1 solutions of (1) (i.e., periodic solutions of frequency equal to the frequency of forcing) that are invariant under (2) are examples of what they call discrete rotating waves: they have discrete spatial symmetry (D_2 symmetry), while this (reflection) symmetry is equivalent to a time shift by $T/2$, where $T = 2\pi/\omega$ is the period of the forcing. The authors of [4] consider bifurcations

in systems with spatio-temporal symmetry. In particular, for Hopf bifurcation they classify the types of motion on the bifurcating invariant torus. They treat several cases in detail, but our case ((D_2, D_2) in their classification) is not one of them.

The underlying conservative system is obtained by setting $\zeta = F = 0$:

$$\begin{aligned} &\ddot{x} + x = 2xy + b, \\ &(2/R^2)\ddot{y} + 2y = x^2. \end{aligned} \tag{3}$$

It is described by the potential energy function

$$V(x, y) = \frac{1}{2}x^2 + y^2 - x^2 y - bx, \tag{4}$$

which is illustrated graphically in Fig 1 for both the symmetric and non-symmetric case.

In ship capsize, x is a measure for the roll angle, while y represents the amplitude of heave motion.

The equations (3) with $b = 0$ also describe the free lateral vibrations in a two-mode Rayleigh-Ritz discretisation of the cylindrical Von Kármán-Donnell shell near 1:2 resonance [5, 6]. The two degrees of freedom are then the chequerboard mode with $2n$ panels circumferentially (some integer n) and 2 panels axially (x) and the concertina mode (y). These two modes are known to have a significant *static* nonlinear interaction in the post-buckling of axially compressed cylinders, leading to a breaking of the in-out symmetry exhibited by each of the modes individually [7]. In the dynamical setting this leads to preferred vibration patterns with larger deflections inwards than outwards (cf. Fig. 2). The parameter b corresponds to an initial imperfection in the chequerboard mode.

A further system whose dynamics near 1:2 resonance is described by (3) is the planar spring pendulum. The autoparametric resonance phenomena in this sytem have been widely studied (see, e.g., [8, 9] and references therein). The swinging mode of the pendulum is analogous to the chequerboard mode of the shell, while the bouncing mode of the pendulum is analogous to the concertina mode of the shell; so at resonance the spring motion has twice the frequency of the swing motion.

We should emphasise that in both the shell and the pendulum the condition of resonance is important. It is only sufficiently close to resonance that the dynamics is described (to leading order in a perturbation analysis) by the cubic energy function $V(x, y)$ above. The full two-mode model leads to a quartic energy function that does not feature the saddle points present in the contour plots of $V(x, y)$ in Figs 1(b,c). Motions of (3) involving deflections approaching those of the saddle solutions are therefore of limited relevance to the unloaded shell or pendulum. Note, though, that at high axial compression the potential energy of the shell *will* have the form of (3), with the possibility of the shell buckling dynamically over the saddles [3].

In studying the dynamics of (1) we shall take $R = 1.6$, $\zeta = 0.05$ throughout this paper. In ship stability this corresponds to the situation in which the natural frequency in heave is roughly twice the natural frequency in roll. Such a frequency ratio was considered by Froude [10] to have undesirable

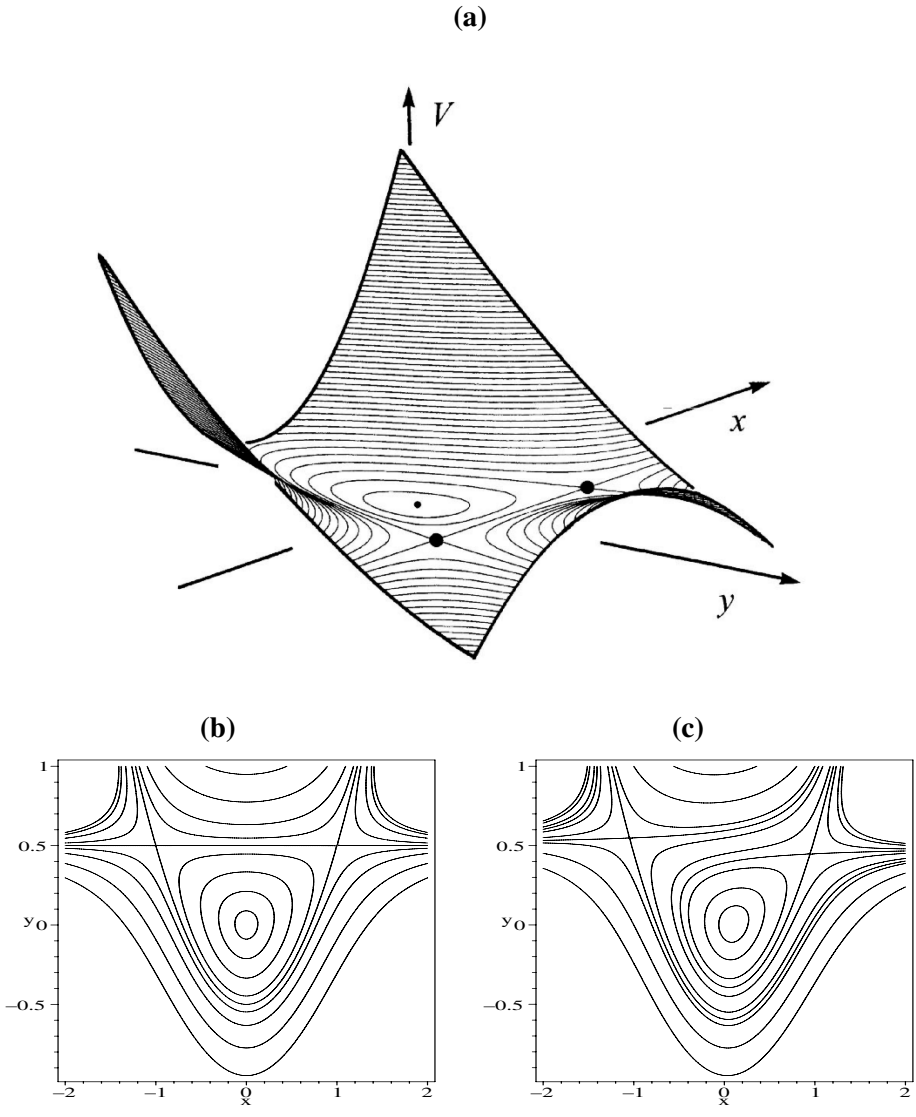

Figure 1. (a,b) Energy surface and contour plot for the symmetric well $V(x, y)$ with $b = 0$. (c) Contour plot for the non-symmetric well with $b = 0.1$. (Figure in (a) provided by Atanas Popov.)

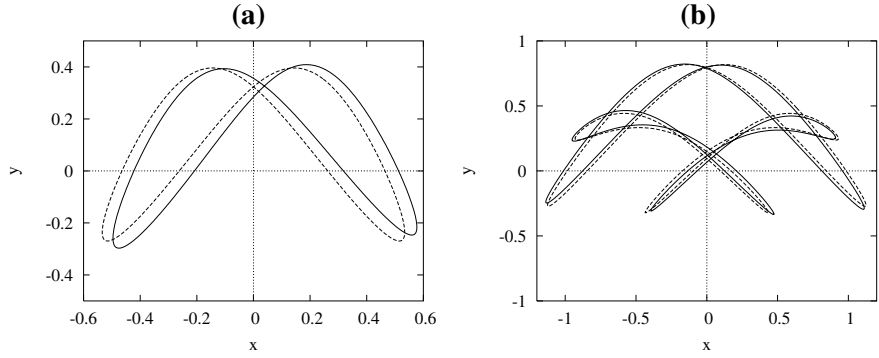

Figure 2. (a) Stable resonant solutions for $b = 0.02$ (solid) and $b = 0$ (dashed) at $\omega = 0.87$. (b) Symmetric and symmetry-broken resonant solutions for $b = 0.02$ (solid) and $b = 0$ (dashed) at $\omega = 1$. The solutions sloping up towards the right are located on the upper branches in Fig. 3. ($R = 1.6$, $\zeta = 0.05$, $F = 0.25$.)

sea-keeping characteristics. The reason for this has been explored, for the case $b = 0$, in [11] using perturbation analysis for weakly nonlinear motions, concentrating on internal autoparametric coupling between pitch and roll. Here we are interested in the case $b \neq 0$. Standard perturbation approaches fail in this case as the constant term b would not survive any reduction based on averaging. Therefore, in order to study the strongly nonlinear motions of the system, we resort to numerical techniques informed by advanced results from bifurcation theory describing the generic underlying dynamics.

Typical stable symmetric and non-symmetric period-1 solutions for $F = 0.25$ and $\omega = 0.87$ are shown in Fig. 2(a). A bifurcation diagram for these solutions under variation of ω is depicted in Fig. 3. The phase space function plotted along the vertical axis has been carefully chosen to obtain a symmetric picture and to give the value zero for solutions which themselves are invariant under (2). The $b = 0$ solution loses stability in a torus (or Neimark) bifurcation under decreasing ω and a subcritical pitchfork bifurcation under increasing ω. At the latter, two branches of non-symmetric solutions bifurcate which rejoin later in a supercritical pitchfork at $\omega = 1.12$. Solutions along these branches are shown in Fig. 2(b). Meanwhile, the $b = 0.02$ solution loses stability in a torus bifurcation under decreasing ω and a period-doubling bifurcation under increasing ω. This period-doubling bifurcation is already present on the bifurcating unstable branch for $b = 0$ and it passes around the limit point as b is increased (see the triangles in Fig. 3).

Curves of the bifurcations through which the resonant periodic solution loses stability are shown in Fig. 4. In the symmetric case (a) the stable period-1

solution eventually disappears in a codimension-two combined torus-pitchfork bifurcation at $F \approx 2$. In the non-symmetric case (b), stability is finally lost in a combined torus-period doubling bifurcation (denoted by N in the diagram). In this event two eigenvalues pass through -1, making it an instance of the strong 1:2 resonance of the Neimark bifurcation [12]. The dotted curves in Fig. 4 are curves of crises where a chaotic attractor suddenly disappears.

Notice how sensitive the suppression of escape is to b: for a b as small as 0.001 the maximum F with stable solutions (reachable from low F along a connected path), $F_{\max}$, drops to 1.042, about half its value at $b = 0$. This behaviour is further explored in Fig. 5 which gives $F_{\max}$ as a function of b.

An analytical study of (1) in the neighbourhood of the torus-period doubling bifurcation (provided it were feasible), would proceed along the following four steps.

1 Take a Poincaré section to obtain a fixed point of a 4D map.

2 At the codimension-2 point the linearisation of this map at the fixed point will have two eigenvalues equal to -1. Do a centre manifold reduction to a 2D map corresponding to these non-hyperbolic eigenvalues.

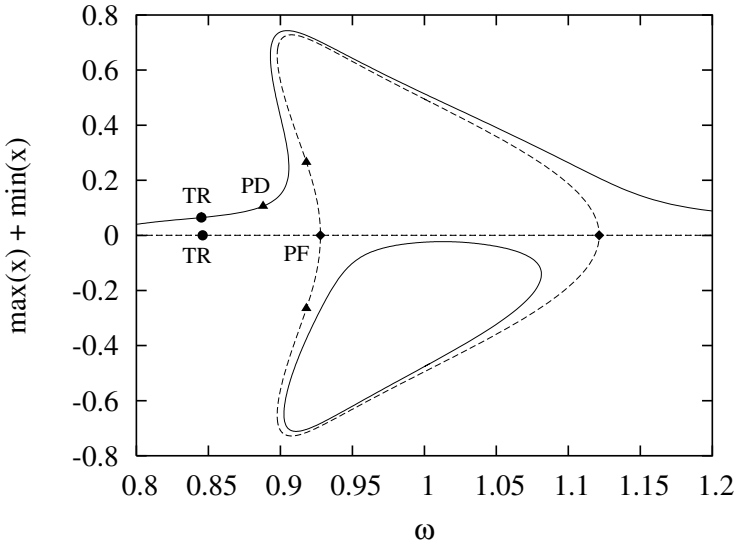

Figure 3. Bifurcation diagram for $b = 0.02$ (solid) and $b = 0$ (dashed), showing the unfolding of the sub- and supercritical pitchforks (PF, indicated by diamonds). Circles indicate torus bifurcations (TR); triangles indicate period-doubling bifurcations (PD). Stable solutions occur between TR and PD for b=0.02, and between TR and the nearest PF for b=0. (R=1.6, ζ=0.05, F = 0.25.)

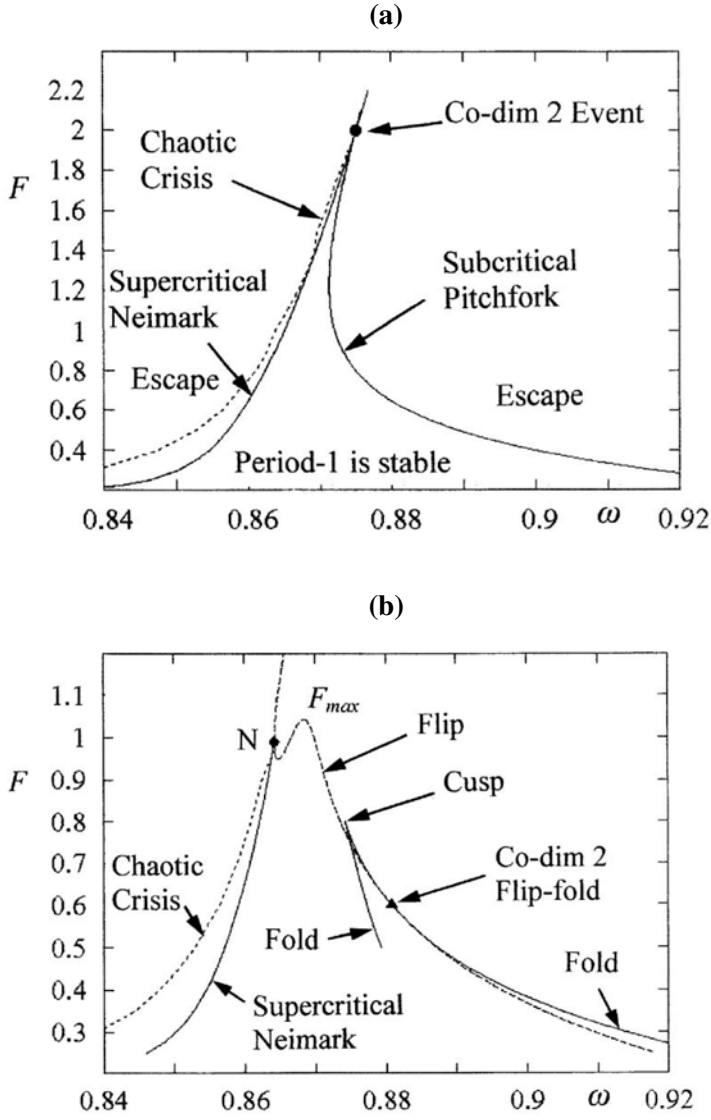

Figure 4. Bifurcation curves for the (a) symmetric ($b = 0$) and (b) non-symmetric ($b = 0.001$) case ($\zeta = 0.05$, $R = 1.6$).

3 Consider the square of the resulting map and approximate it by an interpolating flow, i.e., view this square map as the time-one map of a flow. This can be done up to all finite orders.

4 Study the bifurcations of this 2D flow and interpret the results back to the original driven oscillator system.

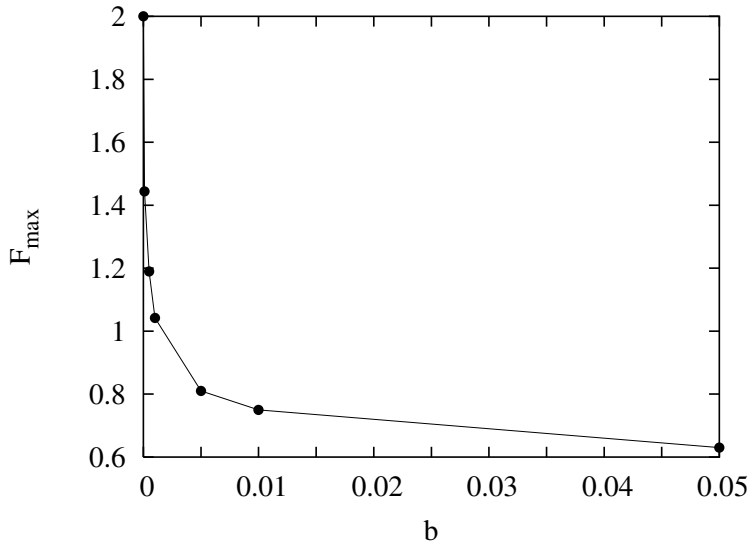

Figure 5. Sensitivity to symmetry breaking: plot against ω of the maximum forcing $F_{\max}$ at which a stable period-1 solution survives (reachable along a connected path). In Fig. 4(b) this maximum corresponds to the local maximum of the PD/flip curve. ($\zeta = 0.05,\ R = 1.6$.)

For the present 1:2 resonance the final 2D flow obtained from the above programme can be written (possibly after time reversal) as:

$$\begin{aligned} \dot{u} &= v, \\ \dot{v} &= \mu_1 u + \mu_2 v + \sigma u^3 - u^2 v, \end{aligned} \tag{5}$$

where $\sigma = \pm 1$ [12]. The parameters μ_1 and μ_2 are unfolding parameters which parametrise our ω-F control space. The two cases $\sigma = 1$ and $\sigma = -1$ have clearly distinct phase portraits. It is impossible to carry out the above programme explicitly (especially step 1) and thereby determine the parameters σ, μ_1 and μ_2 in terms of the parameters in (1), but numerical analysis close to the codimension-2 event reveals (through the sole existence of subcritical period-doubling bifurcations) that we are dealing with the $\sigma = 1$ case. We illustrate this case in Fig. 6, from which it is seen that the invariant torus in the dynamics of (1) is destroyed in a heteroclinic tangle.

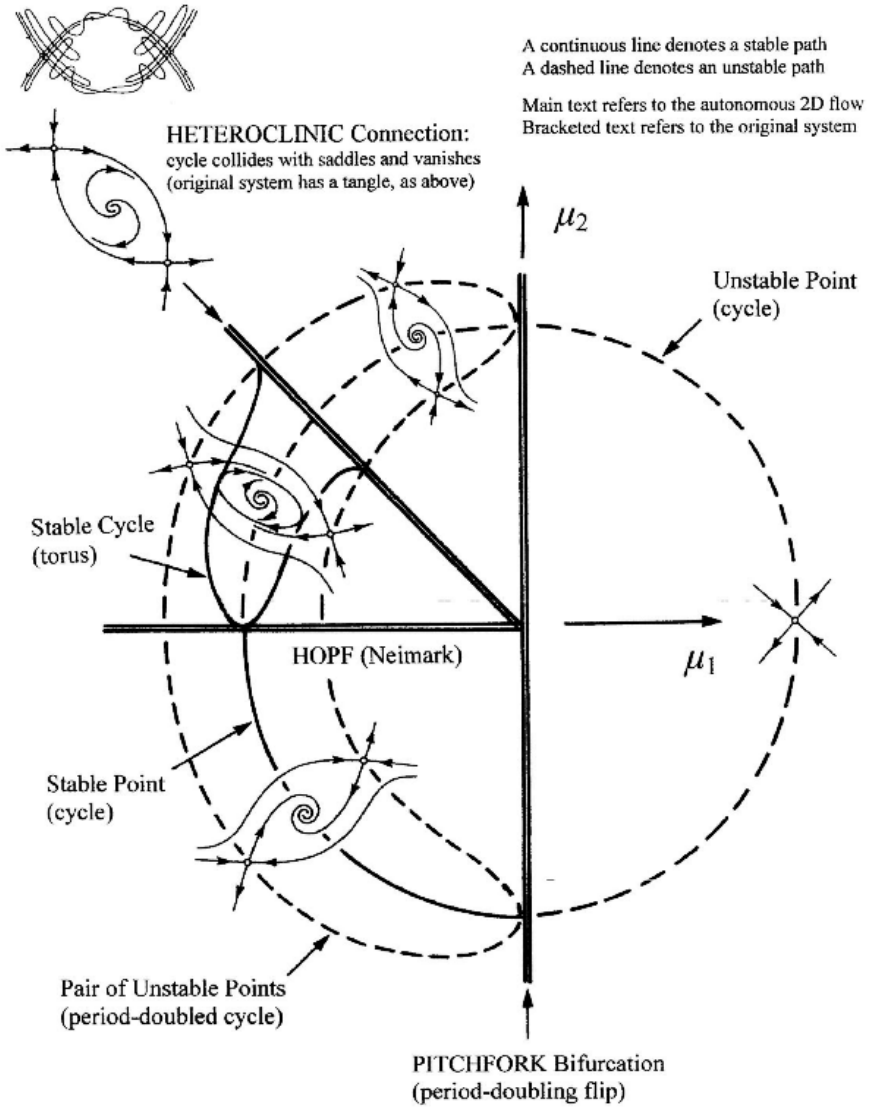

Figure 6. Unfolding of the codimension-2 Neimark bifurcation at 1:2 resonance for the case $\sigma = 1$.

3. Conclusion

We have shown that the codimension-2 bifurcation governing suppression of escape in the non-symmetric case is a 1:2 resonant Neimark bifurcation. The symmetry-breaking imperfection is found to reduce the suppression of escape, but there is still a considerable effect left, as shown by the plateau in Fig. 5.

References

[1] R.C.T. Rainey and J.M.T. Thompson, "The transient capsize diagram – a new method of quantifying stability in waves," *J. Ship Res.* 35, 58-62, 1991.

[2] J.M.T. Thompson, "Designing against capsize in beam seas: recent advances and new insights," *Appl. Mech. Rev.* 50, 307-325, 1997.

[3] J.M.T. Thompson and J.R. de Souza, "Suppression of escape by resonant modal interactions: in shell vibration and heave-roll capsize," *Proc. R. Soc. Lond. A* 452, 2527-2550, 1996.

[4] J.S.W. Lamb and I. Melbourne, "Bifurcation from discrete rotating waves," *Arch. Rat. Mech. Anal.* 149, 229-270, 1999.

[5] F.A. McRobie, A.A. Popov and J.M.T. Thompson, "Auto-parametric resonance in cylindrical shells using geometric averaging," *J. Sound Vibr.* 227, 65-84, 1999.

[6] A.A. Popov, J.M.T. Thompson and F.A. McRobie, "Chaotic energy exchange through auto-parametric resonance in cylindrical shells," *J. Sound Vibr.* 248, 395-411, 2001.

[7] G.W. Hunt, K.A.J. Williams and R.G. Cowell, "Hidden symmetry concepts in the elastic buckling of axially-loaded cylinders," *Int. J. Solids Struct.* 22, 1501-1515, 1986.

[8] E. Breitenberger and R.D. Mueller, "The elastic pendulum: a nonlinear paradigm," *J. Math. Phys.* 22, 1196-1210, 1981.

[9] J.P. van der Weele and E. de Kleine, "The order-chaos-order sequence in the spring pendulum," *Physica A* 228, 245-272, 1996.

[10] W. Froude, "Remarks on Mr. Scott Russell's paper on rolling," *Trans. Inst. Naval Architects* 4, 232-275, 1863.

[11] A.H. Nayfeh, D.T. Mook and L.R. Marshall, "Nonlinear coupling of pitch and roll modes in ship motions," *J. Hydronautics* 7, 145-152, 1973.

[12] Y.A. Kuznetsov, *Elements of Applied Bifurcation Theory* (Springer-Verlag, New York), 1995.

II.

MECHANICAL SYSTEMS

Bifurcation and chaos in *mechanical systems* are the focus of the second part of the Proceedings, which opens with the Key Lecture of the Symposium given by Friedrich Pfeiffer of the Technische Universität Munchen, Germany. The rest of the papers are compiled alphabetically, based on the last name of the first author.

Friedrich Pfeiffer deals with chains of continuous variable transmissions in automotive systems, and presents mechanical and mathematical models together with some applications. The need for a 3D-theory for chain design is highlighted. Proper modelling accounts for a large number of rigid and elastic degrees-of-freedom, as well as of unilateral contacts, to be addressed within the context of the dynamics of multibody systems and the numerical treatment of nonsmooth systems of high dimension.

A group of papers in this part deals with nonlinear dynamic phenomena in somehow *classical* mechanical applications. Giagopulos et al. investigate the dynamics of a simple but representative gear-pair model supported by bearings with rolling elements. Both regular and chaotic response of the system is examined through computer simulations. Attention is also focused on issues related to parametric identification and fault detection of geared systems.

Schweizer and Wauer investigate the vibrations of a rigid rotor supported in short MHD journal bearings with time-dependent electric fields, and examine the oscillations of slider bearings. The equations for the fluid film are solved analytically, whereas those for the shaft and the slider are solved numerically. Applications are envisaged in several fields, in micro devices amongst others.

Stépán et al. investigate dynamic phenomena in high-speed milling, which nowadays is one of the most efficient cutting processes. The nonlinear vibrations occurring in highly interrupted low immersion milling in the case of period doubling are investigated and compared to the well-known

G. Rega and F. Vestroni (eds.),
IUTAM Symposium on Chaotic Dynamics and Control of Systems and Processes in Mechanics, 79–80.

subcritical nature of Hopf bifurcations in turning processes. Global period-two and chaotic oscillations are determined through analytical predictions, and confirmed by numerical simulations.

Nonlinear dynamics and chaos in a simple model of a railway freight wagon wheelset with dry friction damping are investigated in the paper by True and Trzepacz. A realistic modelling of the rail-wheel geometry is pursued, which entails interesting nonperiodic oscillations ensuing also from the nonlinear stick-slip of the dry friction forces, and the impacts between the axleboxes and the side bearings.

Nonlinear dynamic phenomena arising in definitely *innovative* applications such as microelectromechanical systems (MEMS) are dealt with in the last three papers. Balachandran and Li study the nonlinear oscillations of clamped-clamped microelectromechanical filters which are important components in mobile communication systems, signal processing, and flow control applications. The considered resonators are based on the piezoelectric effect. Experimental observations and analytical investigation are presented. In turn, Shaw et al. describe the dynamics of MEMS oscillators to be used as frequency filters based on parametric resonance for frequency selection, as opposed to the usual linear resonance. MEMS oscillators that overcome some of the undesirable features arising in parametric resonance from the standpoint of filter performance are described. Their design is made possible by the highly tunable nature of MEMS devices, which allows one to build in system features to achieve desired performance. Finally, Gottlieb and Champneys formulate a nonlinear boundary-value problem describing the thermoelastic dynamics of a microbeam that is subject to a localized electrodynamic actuation, and is operating in an ultra-vacuum environment. The focus of the investigation is on the possible existence of global bifurcations and chaotic transients in a projected low-order modal dynamical system which reveals a homoclinic structure.

SPATIAL MOTION OF CVT-CHAINS

Friedrich Pfeiffer
Lehrstuhl für Angewandte Mechanik
Technische Universität München
85748 Garching, Germany
pfeiffer@amm.mw.tum.de

Abstract: Mainly due to geometric incompatibilities all CVT-chains do not perfectly move in a plane but show also out-of-plane effects, which cannot be neglected. In addition the elastic behaviour of all components play a crucial role concerning three-dimensional motion. With respect to modeling this increases the number of degrees of freedom considerably leading to growing simulation times. On the other hand design or design improvements of chains are only possible applying a 3D-theory. Paper presents mechanical and mathematical models together with some applications.

Key words: CVT-Chains, friction, force reduction, multibody system.

1. Introduction

Power transmission in automotive systems is classically carried out by gear trains, which transmit power by form-closure. In recent times an increasing number of continuous variable transmissions (CVT) are applied. They transmit power by friction, and at the time being they try to establish some competition with respect to gear trains. The advantage of gear trains consists in a better efficiency, the disadvantage in an only stepwise approximation of the drag-velocity hyperbola. The advantage of CVT consists in a perfect adaptation to this hyperbola, the disadvantage in a lower efficiency due to the friction transmission. Moreover, CVT-gears can be shifted without any unsteady effects, which avoids jerk.
For both types of transmission systems intensive research and development is being performed generating six- and seven-stage automated gears on the gear train side and leading to significant improvements of the design performance on the CVT-chain side. This paper gives a contribution to the improvements of CVT-chains, where already very small geometrical modifications result in

G. Rega and F. Vestroni (eds.),
IUTAM Symposium on Chaotic Dynamics and Control of Systems and Processes in Mechanics, 81–95.

remarkable large changes in performance. For optimising the chain layout a threedimensional theory is needed, which will be presented in the following. Figure 1 depicts a typical configuration of a CVT-chain V-belt drive. According to [1] the vibrational behavior of a V-belt CVT is dominated by the dynamics of its force transmitting belt. The dynamics of the chain belt is characterized by its discrete structure, causing a polygonal excitation and entrance impacts. Hence, the mechanical model of the CVT chain represents a multibody system, taking into consideration each link, containing one pair of rocker pins and plenty of plates. In [2, 3] only the in-plane motion of the chain was modeled. But even a small pulley misalignment, mainly kinematically induced by the variation of the transmission ratio, leads to significant tensile forces. Therefore, we propose a chain model which takes spatial effects of the chain V-belt CVT into consideration.

2. Components of the CVT

A complete CVT gear consists of the force transmitting belt and two pairs of discs with hydraulically shifted sheaves. Rocker pin chains represent one typical belt design. Figure 2 shows the main parts and their assemblage. In the following we shall focus on a chain of the PIV-type, system Reimers (Figure 2). This chain consists of rocker pins connected by plates. The rocker pin design coming out with two parts rolling on each other within the joint motion results in lower friction losses due to rolling instead of sliding friction, suitable contours anticipated. The plate arrangement and the plate number influence the tensile forces and their distribution. Clasp plates stabilize the direction of the rocker pins. We have chains with and without clasp plates. For a 3D-theory all chain elements must be modelled elastically. The same is true for the sheaves of the two discs, the elastic deformations of which influence

Figure 1. CVT Chain Drive System

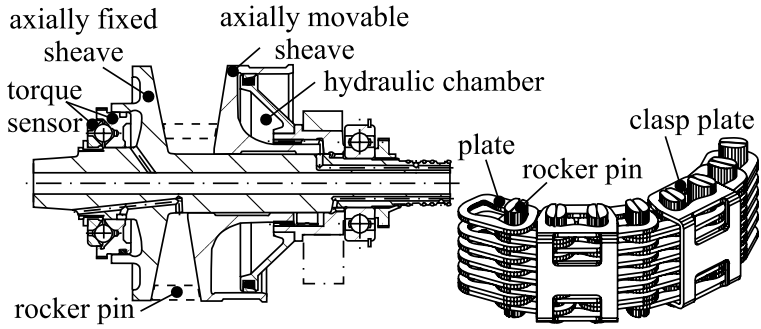

Figure 2. CVT Chain Drive Components

considerably the forces between disc and rocker pins. The axially movable sheaves slide on an elastic shaft. In addition we have some backlash between sheave and shaft, which allows some angular motion in form of a sheave inclination.
For the sensor and control system based on hydraulics suitable models are established, which will not be discussed here.

3. Mechanical Model

The multibody system of the above described gear consists of two movable and two fixed sheaves and $n_L = 63$ chain link bodies. The sheaves as well as the links are elastic. The bodies are interconnected by force elements.

Pulley Set

The contact forces between the chain and the pulleys cause a considerable deformation of the pulley's sheaves. The eigenfrequency of the sheaves is much higher than the operating frequencies. According to [2, 3] the mass forces of the elastic deformations can be neglected in this case. Using the degrees of freedom ($\Delta\vartheta_{F/M}$, $\gamma_{0,F/M}$) the lateral buckling of the movable sheaves may be approximated by a sine function $\Delta\vartheta_{F/M}\sin(\gamma_{c,F/M} - \gamma_{0,F/M})$. The magnitude $\Delta\vartheta$ is the angle of inclination of the sheaves including rigid and elastic parts. The gliding angle γ describes the difference of the pin's motion along the disc and the exact circumferential direction. The indices F and M denote the fixed and the movable sheave, respectively and $\gamma_{c,F/M}$ the contact location. The amplitude $\Delta\vartheta_{F/M}$ consists of a backlash s_{skew} and an elastic deformation between the movable sheave and the shaft, Figure 3. With a FEM-analysis the sheave deformation can be calculated with the Reciprocal Theorem of Elasticity (Betti/Maxwell). Together with Hooke's law applied at the pin this results in a Linear Complementary Problem (LCP) in a standard

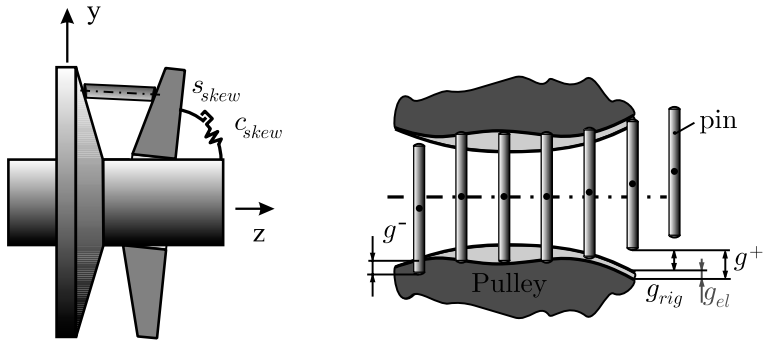

Figure 3. Lateral Buckling and Pulley Deformation

form (1). The meaning is clear: If the pins get into contact, we have constraint forces, otherwise not (Fig. 3). Both pulley sets have one rotational (φ), two translational in-plane (x, y) and one axial out-of-plane (z_M) degree of freedom. The pulley misalignment Δz mainly depends on the transmission ratio i and the length of the chain ([4] and Figure 4). In order to limit the contact pressure between pins and sheaves the disc curvature radius R must have a lower bound, which in our example is $1.7m$. All degrees of freedom can be collocated in $\boldsymbol{q}_P = (x, y, z_M, \varphi, \Delta\vartheta_F, \gamma_{0,F}, \Delta\vartheta_M, \gamma_{0,M})^T$.

$$
\begin{aligned}
g_i &= g_{rig,i} + g_{el,i} = g_i^+ - g_i^- \\
g_i^+ &= \sum_j w_{ij} F_{rp,j} + c_{rp}^{-1} F_{rp,i} + g_{rig,i} \Longleftarrow \left\{ \begin{array}{c} g_i^- = c_{rp}^{-1} F_{rp,i} \\ g_{el,i} = \sum_j w_{ij} F_{rp,j} \end{array} \right. \\
\boldsymbol{g}^+ &= \boldsymbol{W}\boldsymbol{F}_{rp} + \boldsymbol{g}_{rig}, \quad \boldsymbol{F}_{rp} \geq \boldsymbol{0}, \quad \boldsymbol{g}^+ \geq \boldsymbol{0}, \quad \boldsymbol{F}_{rp}\boldsymbol{g}^+ = \boldsymbol{0}
\end{aligned}
\tag{1}
$$

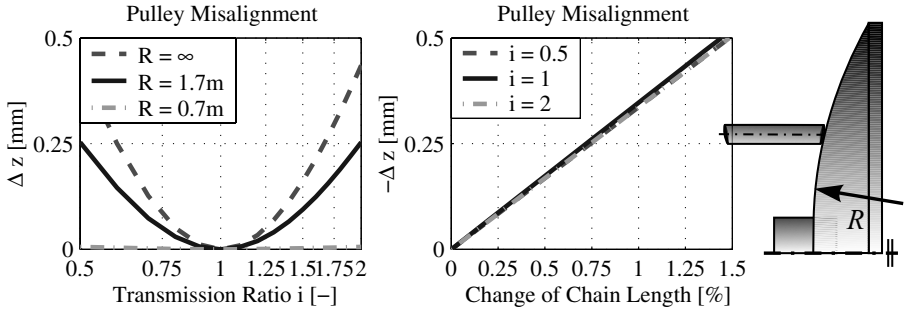

Figure 4. Reason for Pulley Misalignment

Chain Link

Each link represents an elastic body, having three translational rigid body and in addition the elastic degrees of freedom. The angles β_L and γ_L, shown in Figure 5, kinematically depend on the translational position of the successor link. In order to describe the orientation and elastic deformation of a pin some more degrees of freedom $\boldsymbol{q}_{el} = (\boldsymbol{q}_{el,x}^T \ \boldsymbol{q}_{el,y}^T)^T$ have to be introduced. We discern the radial (y) and azimuthal (x) directions. Thus the set of generalized coordinates can be written as $\boldsymbol{q}_L = (x_L \ \ y_L \ \ z_L \ \ \boldsymbol{q}_{el}^T)^T$. The links are kinematically interconnected between pairs of rocker pins. The elasticity and the translational damping of the joint is taken into account by the link force element whereas the rotational damping and the axial friction between the pair of pins is considered in the joint force element. In the link force element each plate is taken into account as a spring. The effect of moving contact points relative to the plate spring reference points between a rocker pin and an adjoining plate are modeled as a contact torque. In order to improve the performance of the software the axial high-frequency vibration in the V-groove can be neglected by a structure variant model regarding only the axial chain oscillations in the strands. Even if only one side of the pin gets in contact with a sheave the transition conditions to stick are complied with.

Chain Pulley Contact

In the experimental results of [5] it is shown that an edge bearing between the ends of the pins and the sheaves occurs. This is not only because of the shear and torsional deformation of the chain belt but also because of the

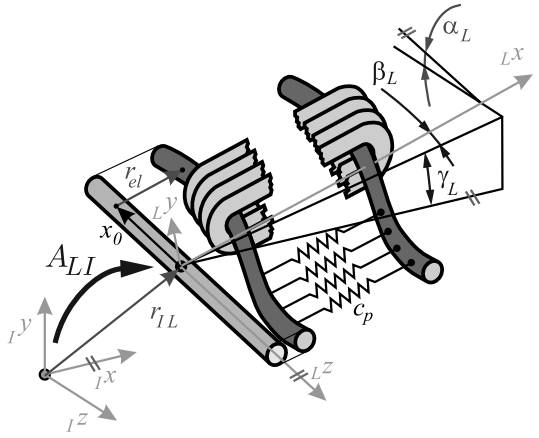

Figure 5. Chain Link Model

bending of the rocker pins. Therefore the elasto-hydrodynamic oil film is quickly squeezed out of the contact zone and mixed friction appears. Altogether it turned out that Coulomb's friction law represents a good approximation. In order to take into account Hertzian deformation a nonlinear spring law in the chain pulley contact will be introduced.

4. Mathematical Description

Applying the principle of virtual power (Jourdain) the following equations of motion for a rigid body as well as for an elastic body can be derived:

$$\boldsymbol{M}\,\ddot{\boldsymbol{q}} = \boldsymbol{h}(\boldsymbol{q}, \dot{\boldsymbol{q}}, t)\ . \tag{2}$$

The matrix $\boldsymbol{M}$ represents the positive definite mass matrix with respect to the minimal coordinates $\boldsymbol{q}$. The vector $\boldsymbol{h}$ of the right hand side contains active forces from all adjoining force elements as well as the external torque in the case of the sheaves.

Rigid Bodies

In order to derive the equations of motion for a rigid body in the form of (2) we start with the equations of momentum and the equations of moment of momentum.

$$\boldsymbol{J}^T \begin{pmatrix} m\boldsymbol{E} & m\tilde{\boldsymbol{r}}_{BS} \\ m\tilde{\boldsymbol{r}}_{BS} & \boldsymbol{I}_B \end{pmatrix} \boldsymbol{J}\ddot{\boldsymbol{q}} + \boldsymbol{J}^T \begin{pmatrix} m\tilde{\Omega}\tilde{\Omega}\tilde{\boldsymbol{r}}_{BS} \\ \tilde{\Omega}\boldsymbol{I}_B\Omega \end{pmatrix} = \boldsymbol{J}^T \begin{pmatrix} \boldsymbol{F} \\ \boldsymbol{T} + \tilde{\boldsymbol{r}}_{BF}\boldsymbol{F} \end{pmatrix} \tag{3}$$

$$\boldsymbol{J}^T = \left(\boldsymbol{J}_T^T\ \boldsymbol{J}_R^T\right) = \left(\left(\frac{\partial \boldsymbol{v}_B}{\partial \dot{\boldsymbol{q}}}\right)^T \left(\frac{\partial \Omega}{\partial \dot{\boldsymbol{q}}}\right)^T\right) \tag{4}$$

These equations of motion refer to a point B of the rigid body. The point S marks the center of mass. The vector $\boldsymbol{r}_{BS}$ points from B to S. $\boldsymbol{I}_B$ denotes the matrix of moments of inertia, m the mass, Ω the rotational speed, $\boldsymbol{v}_B$ the velocity, $\boldsymbol{F}$ the active forces and $\boldsymbol{T}$ the active torques. The Jacobian $\boldsymbol{J}$ transforms the equations of motion from the space of rigid body motion to the hyper-spaces orientated tangential to the constraint surface called configuration space. The rigid body degrees of freedom of the pulleys are determined by equations (3). The rigid body motion is superposed by elastic deformations.

Elastic Bodies

Starting from an inertial reference the vector to a mass point of a deformed body is composed by rigid parts ($\boldsymbol{r}_{IL} + \boldsymbol{x}_0$) and by the elastic deformation

parts $\boldsymbol{r}_{el}$. The vector $\boldsymbol{r}_{IL}$ denotes the distance from the inertially fixed point I to the origin of the reference system of coordinates L, $\boldsymbol{x}_0$ denotes the vector from this origin to a mass element dm in the undeformed configuration and $\boldsymbol{r}_{el}$ the elastic displacement vector. Assuming small displacements one can introduce a Ritz approach for the elastic deformation in a time and space separated formulation.

$$\boldsymbol{r} = \boldsymbol{r}_{IL} + \boldsymbol{x}_0 + \boldsymbol{r}_{el}, \quad \boldsymbol{r}_{IL} = (x_L \;\; y_L \;\; z_L)_i^T \quad \boldsymbol{A}_{IR_i} = \begin{pmatrix} \cos\gamma_L & -\sin\gamma_L \\ \sin\gamma_L & \cos\gamma_L \end{pmatrix}_i \tag{5}$$

$$\boldsymbol{r}_{el} = \left[\left(\boldsymbol{A}_{IR} \left(\boldsymbol{w}_x^T(\boldsymbol{x}_0)\boldsymbol{q}_{el,x}(t) \;\; \boldsymbol{w}_y^T(\boldsymbol{x}_0)\boldsymbol{q}_{el,y}(t) \right)^T \right)^T \;\; \boldsymbol{0} \right]_i^T \tag{6}$$

The equations of motion for an elastic body may be derived from d'Alemberts principle in the version of Lagrange (Jourdain). $\boldsymbol{a}$ absolute acceleration, $\boldsymbol{f}$ applied forces:

$$\int \left(\frac{\partial \boldsymbol{v}}{\partial \dot{\boldsymbol{q}}} \right)^T (\boldsymbol{a} - \boldsymbol{f})\, dm = \int \left[\boldsymbol{J}_T^T + \boldsymbol{J}_R^T(\tilde{\boldsymbol{x}}_0 - \tilde{\boldsymbol{r}}_{el}) + \left(\frac{\partial \dot{\boldsymbol{r}}_{el}}{\partial \dot{\boldsymbol{q}}} \right) \right] (\boldsymbol{a} - \boldsymbol{f})\, dm = 0 \tag{7}$$

After some tedious calculations equation (6) can be formulated in the form of equation (2).

The equations of motion can be simplified and to a certain extend decoupled by the fact, that the out-of-plane motion is very small compared to the nominal motion. Nevertheless it should be noted, that this refers to kinematics not to forces. Very small geometric changes produce very large changes in the forces, especially contact forces. Details of these equations may be found in [10].

Contact Forces

The contact forces between the sheaves and the front faces of the rocker pins are determined by the geometrical gap function $g(\boldsymbol{q})$ which is defined in the axial direction of the undeformed rocker pin. A system of coordinates C is introduced on the cone surface in the middle of the rocker pin end, defined by the triple of circumferential, radial and normal direction (t, r, n), their forces $(F_t, \; F_r, \; F_n)$:

$$F_{rp,i} = -c_{rp}(g_i^-)\, g_i^-$$

$${}_R\boldsymbol{F}_{F/M,i} = \begin{pmatrix} * \\ * \\ F_{rp} \end{pmatrix}_{F/M,i} = \boldsymbol{A}_{RiC_{F/M,i}} \boldsymbol{F}_{n,F/M,i} \begin{pmatrix} \mu \frac{v_t}{v} \\ \mu \frac{v_r}{v} \\ 1 \end{pmatrix}_{F/M,i} \tag{8}$$

where c_{rp} denotes the nonlinear axial stiffness of a rocker pin pair, $\boldsymbol{A}_{RC_{F/M}}$ is the transformation matrix from the $C_{F/M}$- to the reference R-system of a link and μ is the friction coefficient.

Thus the forces in the direction of the generalized coordinates $\boldsymbol{q}_{el+,i}$ are:

$$\boldsymbol{Q}_{F/M} = \left(\boldsymbol{w}_{+,x}(\xi = \pm 1)\, {}_R\boldsymbol{F}_{F/M}(1) \quad \boldsymbol{w}_{+,y}(\xi = \pm 1)\, {}_R\boldsymbol{F}_{F/M}(2) \right)^T \tag{9}$$

Contact Torques

Considering the motion of the contact points, we introduce contact torques in an exponential approximation as a function "con" of the normal force F_c, the distance l_e of the edge of a contact body to the reference point, the radius r_c of the contact surface, the rotational contact stiffness c_c and the relative rotational displacement φ_c. By increasing the contact forces F_c over the limit $c_{c,max}/r_c$ the contact area reaches the cross section area, see Figure 6. Then the stiffness is independent from the contact radius r_c and becomes the constant value of $c_{c,max}$. Thus the projected torques $\boldsymbol{T}_{F/M,i}$ and $\boldsymbol{T}_{pl,i}$ between a rocker pin pair i and a sheave (F/M) and between the plates (pl) and the pin i are

$$\boldsymbol{T}_{F/M,i} = -2 \begin{pmatrix} \boldsymbol{w}_x' \boldsymbol{A}_{IC_{F/M}} \cdot \mathrm{con}(F_n/2, l_h/2, c_h, \vartheta_c) \\ \boldsymbol{w}_y' \boldsymbol{A}_{IC_{F/M}} \cdot \mathrm{con}(F_n/2, l_w/2, c_w, \vartheta_c) \\ 0 \end{pmatrix}_i, \tag{11}$$

$$\vartheta_c \approx \vartheta_0 + (\Delta\vartheta \sin(\gamma_c - \gamma_0))_{F/M} \mp \alpha_L, \quad \psi_c \approx \pm(\Delta\vartheta \cos(\gamma_c - \gamma_0))_{F/M} \pm \psi_L, \tag{12}$$

$$\boldsymbol{T}_{pl,i} = \int_{-1}^{+1} \boldsymbol{w}_x'(\xi)(\mathrm{con}(f_i, \frac{b_{pl}}{2}, \frac{c_{pl}}{l_{rp}}, \beta_{L,i} - \psi_i) - \mathrm{con}(f_{i-1}, \frac{b_{pl}}{2}, \frac{c_{pl}}{l_{rp}}, \beta_{L,i-1} - \psi_i))d\xi \tag{13}$$

respectively, where (l_h, l_w) denote the height and width of a single pin and (c_h, c_w) the contact stiffness in their rotational direction. In equation (12) the

$$\mathrm{con}(F_c, l_e, c_c, \varphi_c) = F_c l_e \mathrm{sign}(\varphi_c)\left(1 - \exp\left[-\frac{|\varphi_c| c_c}{F_c l_e}\right]\right); \tag{10}$$

$$c_c = \begin{cases} c_{c,max} & \forall F_c : c_{c,max} < F_c r_c \\ F_c r_c & \forall F_c : c_{c,max} \geq F_c r_c \end{cases}$$

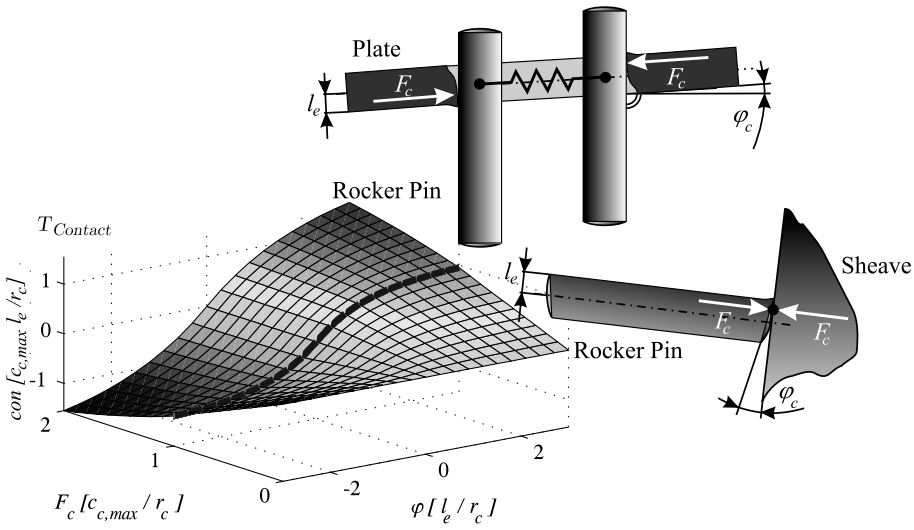

Figure 6. Torque Contact Caused by Relative Angle Displacement

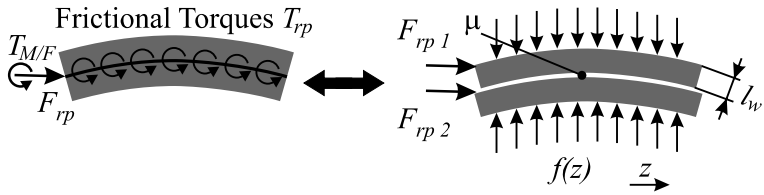

Figure 7. Contact Reactions acting on the Rocker Pin Pair

elastic pin deformations are neglected. To take into account the friction forces between the pair of rocker pins i we calculate the torque

$$\boldsymbol{T}_{rp,i} = -\mu l_w \int_{-1}^{+1} \boldsymbol{w}_x'(\xi) f_i(\xi) \text{sign}(\boldsymbol{w}_x'^T \dot{\boldsymbol{q}}_{el,x,i}) d\xi \;\; with \;\; f_i(\xi) = \frac{c_L}{l_{rp}} (a_{el,i}(\xi) - a_i) \quad (14)$$

as the line load of the pin. The parameter a_i is the kinematically unstressed and $a_{el,i}$ is the kinematically stressed length of a link. The forces and torques are visualized in Figure 7. In order to take into account the position of the contact line between a pin pair, we have to add an in-plane bending torque T_γ. Regarding the clasp plate stiffness c_{clasp}, we have to project the shear torque T_{clasp} into the configuration space of a link containing a clasp plate. Figure 8 shows the joint kinematics and their parameters.

Distinguishing between the reference point and the contact point the link length and contact torque are determined. The rocker pin radius r_{rp} can change according to equation (15) with regard to the angle $\Delta\gamma$.

$$T_\gamma = c_L(a_{el} - a)\Delta y = F_{Chain}\Delta y\,; \quad T_{clasp,\beta} = -T_{clasp,\psi} = c_{clasp}(\psi_L - \beta_L) \quad (15)$$

$$r_{rp} = r_{rp,0} + \frac{\partial r_{rp}}{\partial \Delta\gamma}\Delta\gamma \quad (16)$$

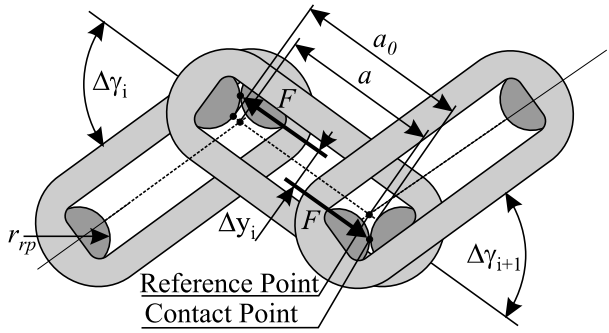

Figure 8. Joint Kinematics

5. Results

Due to the lateral buckling of the sheaves and the elastic deformation of sheaves and pins we get in addition to belt creep and azimuthal belt slip a radial movement between the chain and the sheaves. Introducing the sliding angle γ we can define the direction of the relative velocity between pins and sheaves. The sliding angle determines the equilibrium between the two pulley clamping forces and also the chain forces. Thus a comparison of the sliding angle is suitable for the verification of chain models. Figure 9 depicts the sliding angle of the discrete dynamic model and the continous steady state model of Sattler [2]. In the dynamic model the contact arcs are longer than by the model of Sattler where they are 180 Grad. In the continuous model the polygonal excitation is missing. Only for low rotational speeds the comparison is good. For high speeds the continuous model does not describe all effects. The results of the dynamic model presented in the following are computed for an uniform motion with constant driving speed n_1 and an external output torque T_2. Figures 11 and 12 show the tensile force of an outer plate of a chain with clasp plates for two different pulley misalignments ($T = 150Nm$, $n = 600rpm$, $i = 1$). The comparison of simulation and measurement [7] confirms the mechanical model. Due to the bending forces the misalignment induces a large gradient of the tensile forces in the spans. Entering a pulley the shape of a pin changes abruptly because of

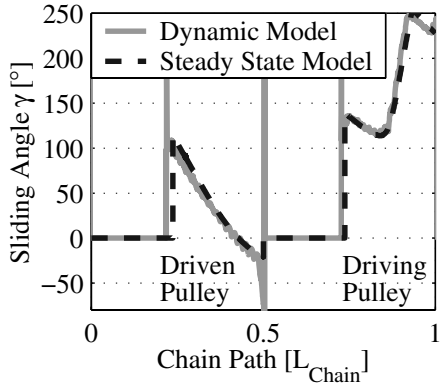

Figure 9. Model Comparison

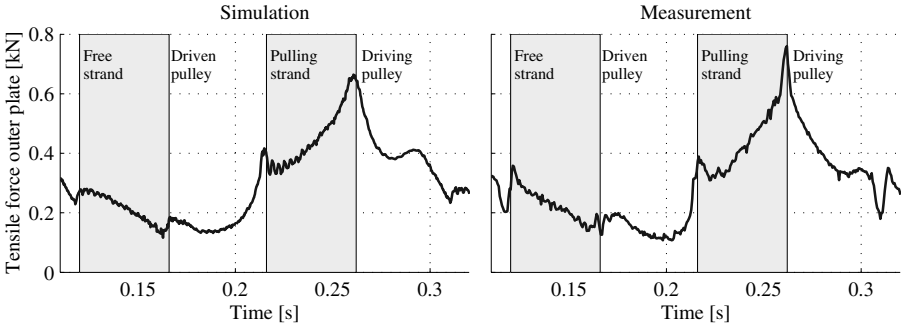

Figure 10. Tensile Force of an Outer Plate with Clasp Plate; $\Delta z = 1.5mm$

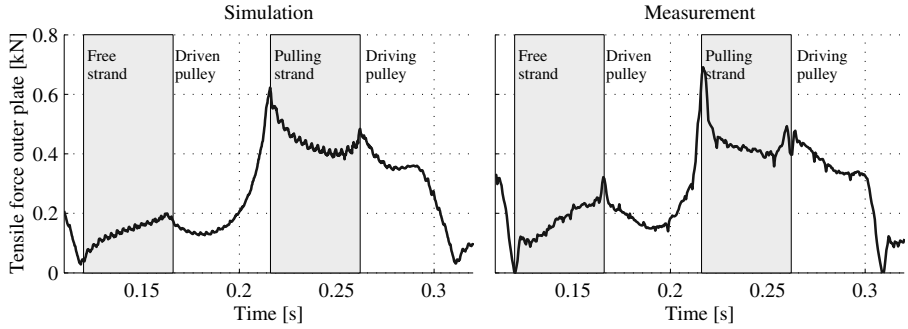

Figure 11. Tensile Force of an Outer Plate with Clasp Plate; $\Delta z = -0.5mm$

the sudden growing contact forces. Thus especially at the beginnings and the ends of the pulling spans great force peaks appear.

In the following we consider some parameterstudies with the goal to show the possibility of influencing the chain performance significantly by even small changes of chain component geometry. For this purpose we concentrate only on the forces of the outer plates, which are the most stressed plates on one side, but represent also a good measure of the chain performance on the other side. With longer rocker pins and more plates the tensile forces of a plate can be reduced because of a load splitting on more plates. But with the same cross section of the pins due to the pin bending the load splitting on the plates becomes worse. Thus the gain connected with more plates is not large (Figure 12). By changing the design of a plate without altering the tensile strength we influence the stiffness $c_L(\pm 20\%)$ and the mass $m_L(\pm 10\%)$ of a link. The resistance to the pin bending with low stiffness c_L is dominated by the bending stiffness of the pin. As a result the static components of the tensile forces of both outer

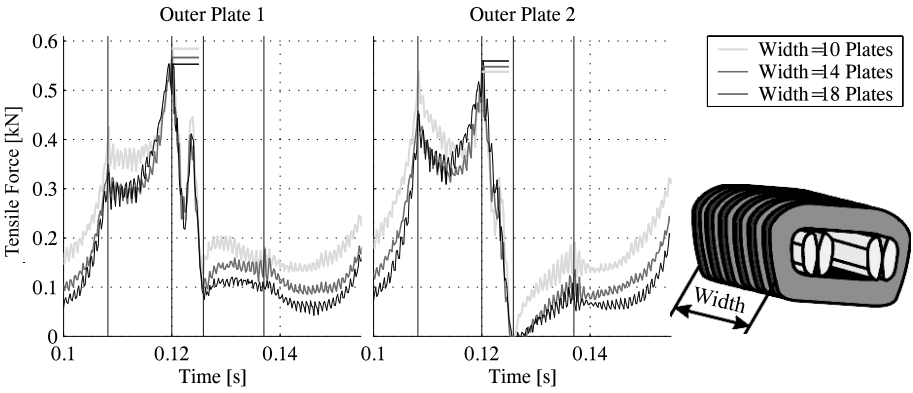

Figure 12. Variation of the Number of Plates of Each Link
($i_{red} = 1, i_{CVT} = 2.3, n_1 = 4000rpm$)

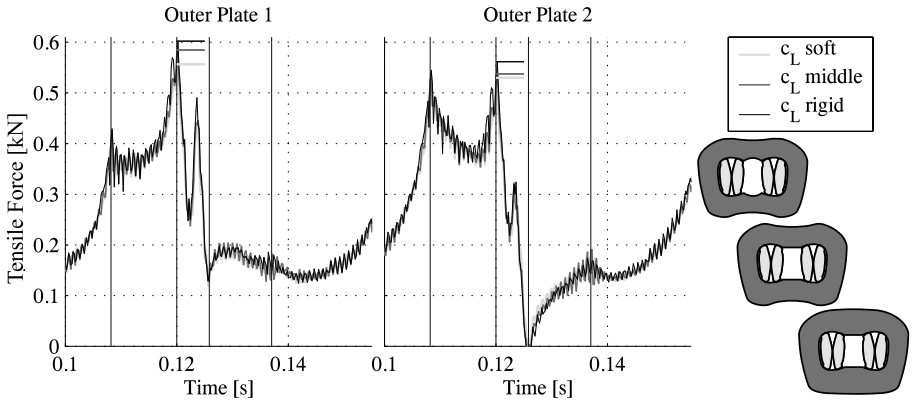

Figure 13. Variation of the Chain Link Stiffness c_L
($i_{red} = 1, i_{CVT} = 2.3, n_1 = 4000rpm$)

plates become smaller with softer plates, see Figure 13. Additionally the dynamic and centrifugal force components get smaller because of the lower link mass m_L. The previous calculation in the figures above are executed with no specification of the assemblage of the plates and thus with a continuously approximation. In Figure 14 we have three chains with different assemblages of the plates. But in each chain the link configuration is repeated after the third following link. In Figure 14 the brightest, middle and darkest link is link number 1, 2 and 3, respectively. In both cases examined with a symmetric link configuration pattern the load on all outer plates are nearly equal, whereas the maximum tensile force of the right outer plate of link 2 is larger in the case of the asymmetric traditional arrangement than the highest plate forces of the links with symmetric configuration patterns. There are even more design parameters than discussed above. For example for a greater axle-base the tensile forces of the chain are smaller [8]. By enlarging the curvature of the pin ends

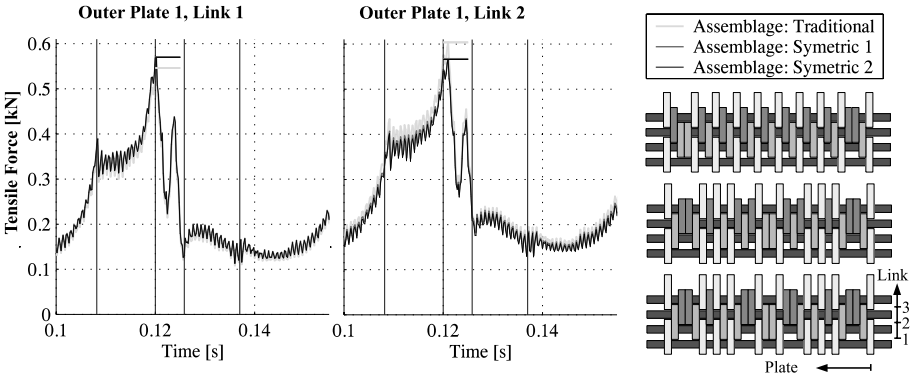

Figure 14. Variation of the Assemblage of the Plates
($i_{red} = 1, i_{CVT} = 2.3, n_1 = 4000rpm$)

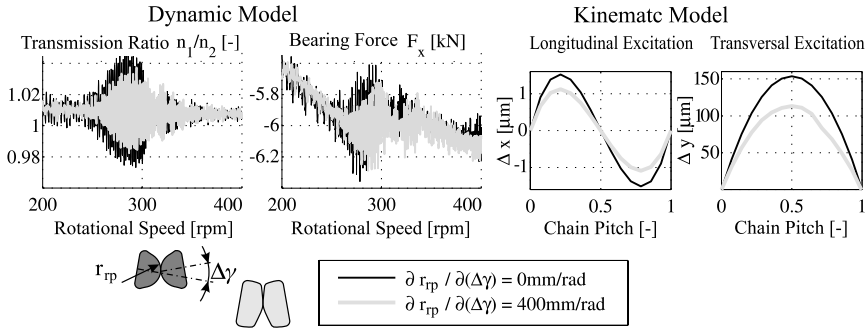

Figure 15. Influence of the Rocker Pin Kinematics

and lowering the contact stiffness between pins and plates the outer plate tensile forces can be reduced [9].
The polygonal excitation causes some resonance of the chain drive. Altering the kinematics of the excitation we influence the resonance. On the right hand side of Figure 15 we see the excitation at the entrance and the exit areas of the sheaves assuming the contact arc as an ideal circle. On the left hand side the dynamic response of the excitation with all details of the model is illustrated. The oscillation of the transmission induces rotational vibration in the drive train whereas the vibrating bearing forces impair the gear acoustic. With low torques the ratio of the axial clamping forces is near one, because there is nearly no difference between the driving and driven pulley. At adequate torques the ratio is high due to different direction of the lateral buckling of the sheaves. Near the slipping border the radial friction forces vanish and therefore the ratio decreases. At high torques before the slippage of the chain the losses of the gear including the bearing and excluding the hydraulics are low in comparison with the gear power. The pulley thrust ratio in Figure 17 is changing with the pulley misalignment because of axial components of the chain tensile forces, whereas the efficiency shows no influence. At transient operating state the global behavior of the gear, the forces, thrust ratio and the

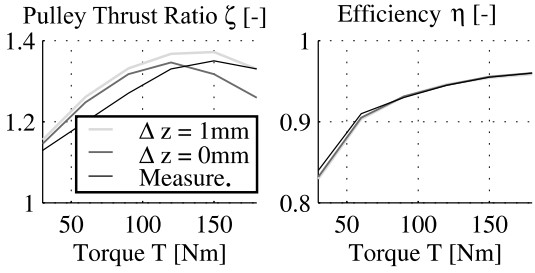

Figure 16. Global Parameters Influenced by Pulley Misalignment

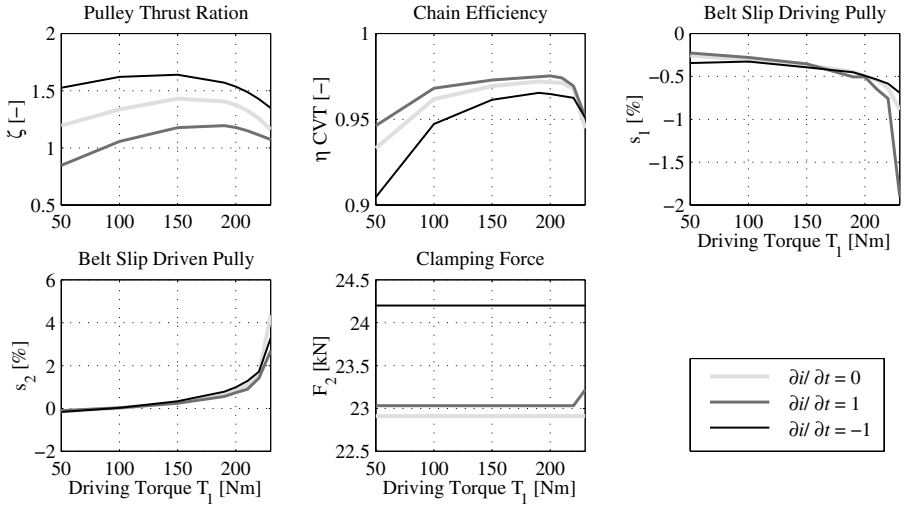

Figure 17. Global Parameters Influenced by a Transient Transmission Ratio ($i_{CVT} = 1, n_1 = 2000rpm$)

efficiency change. In Figure 17 the effects are illustrated for a transient transmission ratio i of the CVT. It is obvious that the pulley forces have to differ to induce a large gradient of the transmission ratio. At a positive gradient the great losses due to the clamping effect at the chain exit of the driving pulley becomes significantly smaller. As a result the CVT-efficiency increases. Due to this clamping effect the slip at the driving pulley is smaller than at the driven pulley.

6. Summary

Chains and belts of continuous variable transmissions (CVT) define at the time being a limit of modeling in dynamics. The extremely large number of rigid and elastic degrees of freedom in connection with just as well a large number of unilateral contacts resulting in additional problems of complementarity character end up with two questions of considerable complexity. One concerns the question of modeling itself, the transmission of reality into a reasonable mechanical model without neglecting important physical features. The other one concerns the numerical treatment of a non-smooth system of high dimensions. It is not only the large number of degrees of freedom and problems like order-n-algorithms and similar methods, it is also the solution of high-order linear and nonlinear complementary problems, where a variety of methods exist, but all involving questions of numerical stability and computing time. Paper can only indicate, what has been done in the last ten years

comprising several dissertations, many diploma-thesis and continuous cooperation with industry.
The presented model of a continuously variable chain drive provides detailed insight into the influence of construction parameters on the dynamics of the gear. It was shown that with an adequate transmission ratio of the gear reducer unit, with more plates in a link, with lower stiffness of a plate and with a symmetric assemblage of the plates the maximal tensile force of the outer plates can be significantly reduced. The quality of the developed mechanical model is verified by measurements. Influences on the polygonal excitation, the pulley thrust ratio and the efficiency were investigated.

Acknowledgement

The research presented is based on the dissertation of Dr.-Ing. Martin Sedlmayr. It has been supported by the Germain Research Foundation (Deutsche Forschungsgemeinschaft, Sonderforschungsbereich 365 “Umweltfreundliche Antriebstechnik für Fahrzeuge”)

References

[1] F. Pfeiffer, “Dynamics of chains – To the bounds of modeling,” *9th German–Japanese Seminar: Nonlinear Problems in Dynamical Systems – Theory and Applications*, August 20–23, 2000.
[2] H. Sattler, Stationäres betriebsverhalten stufenlos verstellbarer Metallumschlingungsgetriebe. Dissertation, Universität Hannover, 1999.
[3] J. Srnik and F. Pfeiffer, Dynamics of CVT Chain Drives. In: *International Journal of Vehicle Design*, Special Edition, 1999.
[4] G. Nitescu, “Geometrische verhältnisse in stufenlos verstellbaren keilscheibenumschlingungsgetrieben,” In *Antriebstechnik* Vol.23 Nr.7, S. 54–56, 1984.
[5] V. Hirschmann, Tragfähigkeitsuntersuchungen an stufenlosen Umschlingungsgetrieben. Dissertation, FZG, TU München, 1997.
[6] M. Sedlmayr and F. Pfeiffer, “Spatial contact mechanics of CVT chain drives, “*18th ASME Bien. Conf. on Mech. Vibration and Noise* DETC01/VIB. 2001.
[7] G. Sauer, “Grundlagen und betriebsverhalten eines zugketten-umschlingungsgetriebes,” *Fortschritt-Berichte VDI*, Reihe 12, Nr. 293, VDI-Verlag, 1996.
[8] U. Wagner, A. Teubert and T. Endler, “Entwicklung von CVT-Ketten für pkw-anwendungen bis 400Nm,” *VDI-Berichte* 1610, S. 223–242, 2001.
[9] M. Sedlmayr and F. Pfeiffer, “Spurversatz bei CVT-Ketten,” *VDI-Berichte* 1630 “Schwingungen in Antrieben 2001”, p.117–136, 2001.
[10] M. Sedlmayr, Räumliche Dynamik von CVT-Keilkettengetrieben, Dissertation TU-München, Lehrstuhl für Angewandte Mechanik, 2003.
[11] M. Campanelli and A.A. Shabana, “Chain vibration and dynamic stress in three-dimensional multibody tracked vehicles,” *Multibody System Dynamics* 2: p.277-316, Kluwer Academic Publisher, 1998.
[12] D.W. Lee and C.K. Sung, “On the efficiency analysis and improved design of a rubber V-belt, “*Int. J. of Vehicle Design*, Vol.18, No.2, pp 119-131, 1997.

NONLINEAR PHENOMENA IN MICROELECTROMECHANICAL RESONATORS

B. Balachandran and H. Li
Department of Mechanical Engineering, University of Maryland College Park, MD 20742-3035, USA
balab@eng.umd.edu

Abstract: Nonlinear oscillations of clamped-clamped microelectromechanical filters are studied in this effort. Piezoelectric actuation is used to excite these structures on the input side and piezoelectric sensing is carried out on the output side. Experimental observations of nonlinear phenomena are presented and nonlinear analysis being carried out to explain the experimental observations is briefly discussed.

Key words: Clamped-clamped structures, piezo actuation, MEMS resonators, buckling.

1. Introduction

Oscillations of microelectromechanical resonators fabricated as clamped-clamped composite structures are studied here. These resonators, which are used as micromechanical filters, are important for mobile communication systems, signal processing applications (e.g., Fourier transform computations) and microjets for flow control applications. The considered resonators are based on the piezoelectric effect, as shown in Figure 1. The elastic substrate is a SiO_2 layer, on the top of which a platinum electrode layer is deposited throughout the length of the structure. There is a thin layer of sol-gel piezoelectric film on the top of this electrode layer. To complete the structure, another platinum layer on the top of this piezoelectric film extends over one quarter of the length from each anchor and the mid-section of the resonator structure is free from this platinum electrode layer [1], [2].

G. Rega and F. Vestroni (eds.),
IUTAM Symposium on Chaotic Dynamics and Control of Systems and Processes in Mechanics, 97–106.

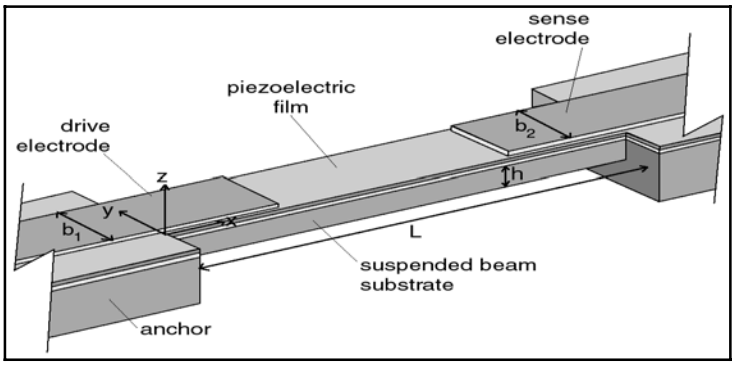

Figure 1. Piezoelectric resonator structure [1].

Due to the asymmetry of the cross-section, the position of the piezoelectric layer is offset from the neutral axis, and in addition, (tensional) residual stress may also be introduced in each layer during the manufacturing process. The resonators considered here typically range in lengths from 100 μm to 400 μm, and the thickness of each platinum electrode is in the range of 90 nm to 180 nm. In some typical uses of this resonator, the structure is driven close to its first resonance frequency with the input at the drive electrode having a DC bias in addition to the harmonic excitation.

2. Experimental Observations

In this section, different experimental observations that are illustrative of the nonlinear behavior of the microresonator structures are presented. A sketch of the experimental arrangement is shown in Figure 2.

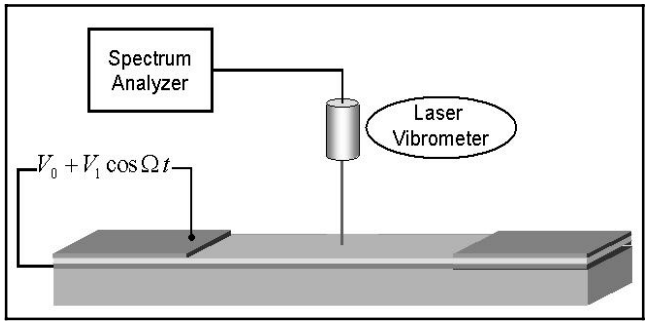

Figure 2. Experimental arrangement showing the positioning of a laser vibrometer for measuring the transverse vibrations of a resonator. The resonator is excited by electrical signals provided to the drive electrode located at the left-end of the structure.

In Figure 3, a representative spatial distribution of a 200μm resonator observed in the experiments is shown [2]. This spatial distribution was measured by using a scanning laser vibrometer. The scanning was carried out along the longitudinal axis of the considered resonator. The excitation signal into the drive electrode of the resonator was a combination of a sinusoidal signal at the first resonance frequency and a DC bias input. In other experiments conducted with similar microresonator structures, similar spatial patterns, which are different from the spatial pattern of the first mode of a clamped-clamped structure, have been observed.

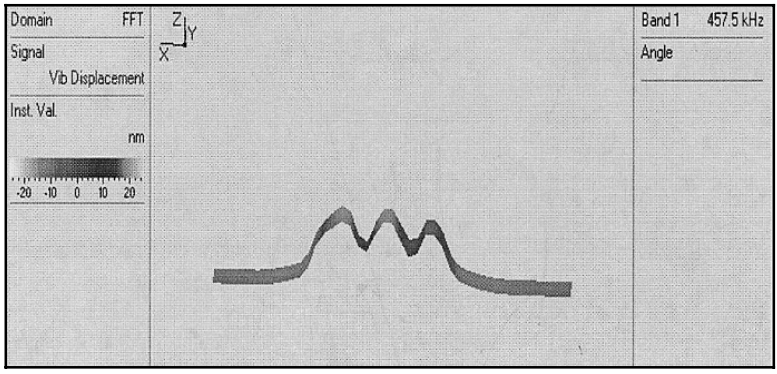

Figure 3. Laser vibrometer measurement of a spatial pattern observed in a forced oscillation experiment. The presence of spatial harmonics distorts the spatial pattern from the typical mode shape associated with the fundamental mode of vibration of a clamped-clamped structure [2]. Typical values of the AC component of the drive signal used in this and other experiments is in the mV range and the DC component of the signal is of the order of 10 Volts.

In Figure 4, the nonlinear response observed in experiments conducted at a fixed sinusoidal excitation amplitude is shown. The excitation frequency is used as a control parameter in the neighborhood of the first natural frequency of the resonator, and the velocity-amplitude data recorded during the forward and backward sweeps of this control parameter are shown. The presence of a hardening type of response and a jump is clear from this data. Only single point measurements where carried out during these experiments.

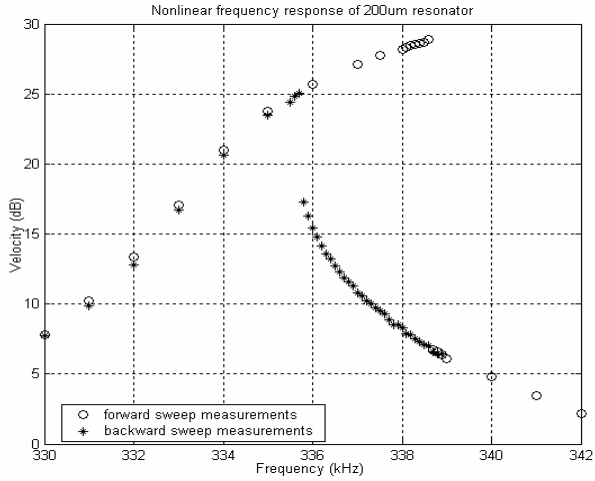

Figure 4. Frequency response of a 200μm resonator: excitation amplitude 224mV with a 0V DC offset.

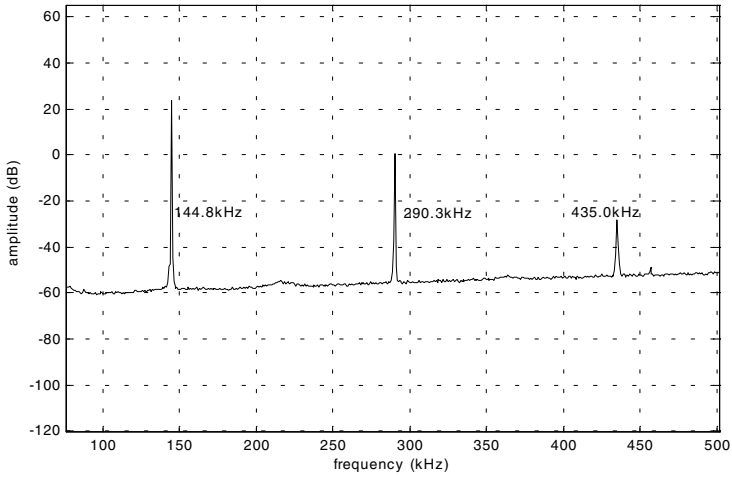

Figure 5. Response spectrum of a 400μm resonator when excited close to its first natural frequency. The drive signal consisted of an AC component and a zero voltage DC component.

In Figure 5, the response spectrum of another resonator is shown. The response shows components at the excitation frequency and second and third harmonics of this frequency. To explain the nonlinear responses observed in the experiments, the analysis being undertaken is briefly discussed following the nomenclature provided below.

3. Nomenclature

ϕ_n	n^{th} static buckling mode shape
Φ	Mode shape of dynamic deflection
A	Area of the cross section
b	Normalized buckling level
E	Young's modulus
EI	Bending stiffness of the beam
I	Area moment of inertia of the beam cross section
l	Length of the beam
m	Mass per unit length of the beam
$\hat{P}$	Axial force
P	Nondimensional form of the axial force
$\hat{p}$	Amplitude of the external excitation force
p	Nondimensional form of the amplitude of the external excitation force
$\hat{\Omega}$	External excitation frequency
Ω	Nondimensional form of the external excitation frequency
$\hat{\mu}$	Damping coefficient
μ	Nondimensional form of the damping coefficient
$\hat{W}$	Beam displacement
W	Nondimensional form of displacement

4. Analytical Development, Results, and Discussion

One possible hypothesis is that the experimentally observed data shown in Figure 3 is due to oscillations about a non-flat equilibrium position. Based on studies that have been conducted with large-scale structures [3]—[5], it is conjectured that this non-flat equilibrium position occurs due to buckling caused by axial loads that arise due to residual stresses and the DC voltage input into the drive electrode. The rest of this section is based on material borrowed from the earlier work of the authors [7]—[9], and it is aimed at explaining some of the qualitative aspects of the forced response.

4.1 Analytical Development

In Figures 6 and 7, a sketch map of the resonator on the input side, and the buckled beam configuration that will be used for developing the model

are shown, respectively. With external actuation and damping terms, the governing system can be written as

$$m(\hat{x})\frac{\partial^2 \hat{W}(\hat{x},\hat{t})}{\partial \hat{t}^2}+2\hat{\mu}\frac{\partial \hat{W}(\hat{x},\hat{t})}{\partial \hat{t}}+\frac{\partial^2}{\partial \hat{x}^2}\left[EI(\hat{x})\frac{\partial^2 \hat{W}(\hat{x},\hat{t})}{\partial \hat{x}^2}\right]$$
$$+\left[\hat{P}_2(\hat{t})-\frac{EA}{2l}\int_0^l\left[\frac{\partial \hat{W}(\hat{x},\hat{t})}{\partial \hat{x}}\right]^2 d\hat{x}\right]\frac{\partial^2 \hat{W}(\hat{x},\hat{t})}{\partial \hat{x}^2}=\frac{\partial^2[\hat{P}_1(\hat{t})\,\hat{h}(\hat{x})]}{\partial \hat{x}^2} \tag{1}$$

$$\hat{W}(\hat{x},\hat{t})=0 \text{ and } \frac{\partial \hat{W}(\hat{x},\hat{t})}{\partial \hat{x}}=0 \text{ at } \hat{x}=0 \text{ and } \hat{x}=l.$$

In Eqs. (1), $\hat{P}_1(\hat{t})=\hat{P}_{dc}+\hat{p}\cos\hat{\Omega}\hat{t}$ is the dynamic actuation force in the piezoelectric layer, $\hat{P}_{dc}$ is the force due to the DC offset, $\hat{P}_2(\hat{t})=\hat{P}_0+\hat{P}_1(\hat{t})$, $\hat{P}_0$ is the force due to the residual stress in the beam, $\hat{h}$ is the height above the neutral axis at which the actuation force $\hat{P}_1(\hat{t})$ is applied as shown in Figure 6, $\hat{h}(\hat{x})=\hat{h}[u(\hat{x})-u(\hat{x}-\hat{x}_0)]$, $u(\hat{x})$ is the Heaviside step function, m is the mass per unit length, $\hat{\mu}$ is the damping factor, and l is the length of the beam. The microresonator is modeled as a composite beam with step-wise characteristics and appropriate boundary conditions [6]—[9].

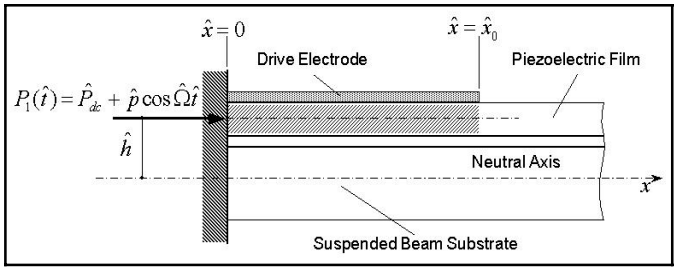

Figure 6. A sketch map of the microresonator at the input port.

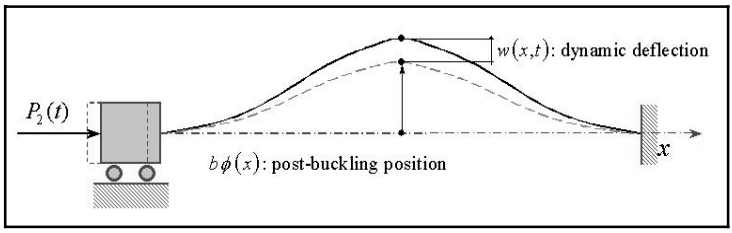

Figure 7. Buckled beam configuration.

After using the nondimensional quantities

$$x=\frac{\hat{x}}{l},\quad W=\frac{\hat{W}}{l},\quad h=\frac{\hat{h}}{l},\quad t=\sqrt{\frac{(EI)_{avg}}{m_{avg}l^4}}\,\hat{t},\quad \Omega=\sqrt{\frac{m_{avg}\,l^4}{(EI)_{avg}}}\,\hat{\Omega} \tag{2}$$

where $(EI)_{avg}$ and m_{avg} are spatially averaged values. Eqs. (1) can be rewritten in the following form:

$$\begin{aligned}&\ddot{W}+2\mu\,\dot{W}+W^{IV}+\left[P_0+P_{dc}+p\cos\Omega t-\frac{Al^2}{2I}\int_0^1\left(W'\right)^2dx\right]W''\\&=\left(P_{dc}+p\cos\Omega t\right)\,h\left[\delta'(x)-\delta'(x-x_0)\right]\end{aligned} \tag{3}$$

$$W(x,t)=0 \text{ and } \frac{\partial W(x,t)}{\partial x}=0 \text{ at } x=0 \text{ and } x=1.$$

In Eqs. (3), the overdot indicates the derivative with respect to the nondimensional time t, the prime indicates the derivative with respect to x, and

$$P_0=\frac{\hat{P}_0\,l^2}{(EI)_{avg}},\quad P_{dc}=\frac{\hat{P}_{dc}\,l^2}{(EI)_{avg}},\quad p=\frac{\hat{p}\,l^2}{(EI)_{avg}},\quad \text{and } \mu=\frac{\hat{\mu}\,l^2}{\sqrt{m_{avg}\,(EI)_{avg}}} \tag{4}$$

During undamped free oscillations, a solution of the following form is sought

$$w(x,t) = b\phi(x) + \upsilon(x,t) \tag{5}$$

where b is the normalized buckling level factor, $\upsilon(x,t)$ is the dynamic deflection, and $b\phi(x)$ is the static post-buckling position [7]—[9]. Further details regarding the analysis can be found in these references.

4.2 Free Oscillation Results for a Buckled Microresonator and Discussion

As a representative case, a resonator with the following dimensions is chosen: 200 μm in length, 20 μm in width, and 2 μm in thickness. The thickness of the piezoelectric layer is 0.53 μm and the dimensions of the top electrode over the beam are 50 μm in length, 20 μm in width and about 170 nm in thickness. The predicted pattern for this 200μm resonator in the 5th static buckling mode is shown in Figure 8. This spatial pattern obtained during the undamped free oscillations is in good agreement with the spatial pattern obtained during forced oscillations close to the first natural frequency of the system, suggesting that the spatial pattern observed in Figure 3 may be explained as a "buckling" induced nonlinear behavior. As representative results, in Figures 9 and 10, the spatial patterns corresponding to different

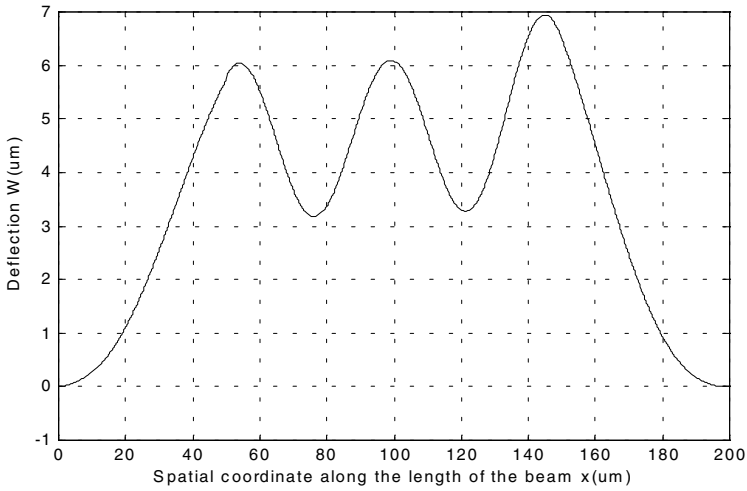

Figure 8. Predicted spatial pattern of a 200mm beam through the free vibration model [7].

buckling modes are shown. The different spatial patterns observed are a function of the buckling level b as in other studies carried with "large-scale" structures [3]. Experiments have not been carried out to examine if this type of behavior is possible in the considered microresonators. The agreement

between the analysis and experimental data indicates that for clamped-clamped piezoelectric resonators, buckling effects can be important to consider. As discussed in earlier work [7], the authors' work provides the first evidence of such phenomenon in microscale structures. Forced oscillation analysis [8],[9] has been initiated and the predicted responses are in qualitative agreement with the results shown in this article.

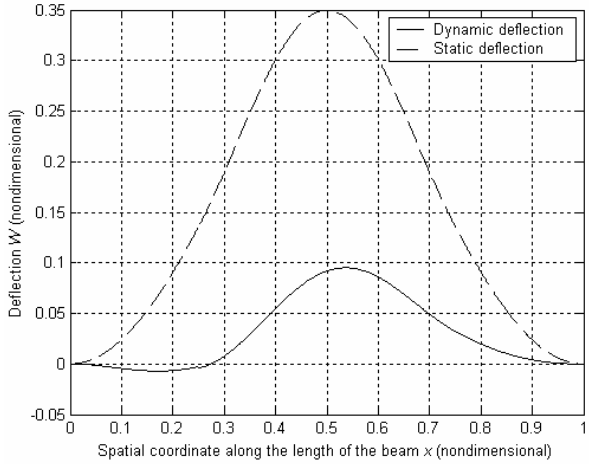

Figure 9. Mode shapes when $b = 0.5$

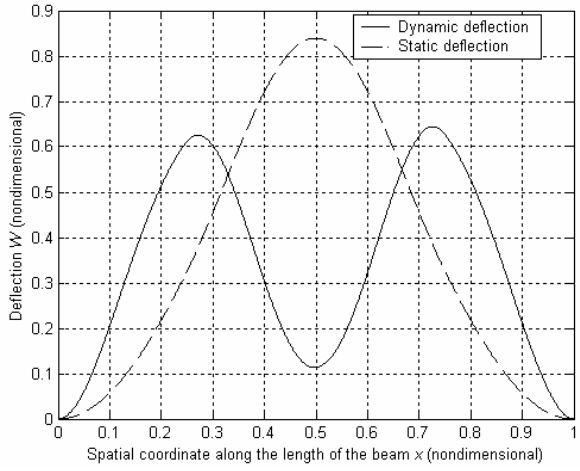

Figure 10. Mode shapes when $b = 1.2$

Acknowledgement

Support received for this work through DARPA Grant F3060202C0016 and AFOSR Grant F496200310181 is gratefully acknowledged. Professor Don DeVoe is thanked for his valuable input and Mr. Daniel Volkmann and Ms. Lihua Li are thanked for their help in collecting the experimental data.

References

[1] D. L. DeVoe, "Piezoelectric Thin Film Micromechanical Beam Resonators," *Sensors and Actuators A (Physical)*, Vol. 88, pp. 263-272, 2001.

[2] L. Currano, *Experimental and Finite Element Analysis of Piezoelectrically Driven MEMS Actuators*, M.S. Thesis, Department of Mechanical Engineering, University of Maryland, College Park, 2002.

[3] A. H. Nayfeh and W. Lacarbonara, "On the Discretization of Spatially Continuous Systems with Quadratic and Cubic Nonlinearities," *JSME International Journal, Series C*, Vol. 41(No. 3), pp. 510-531, 1998.

[4] A. H. Nayfeh, W. Kreider, and T. J. Anderson, "Investigation of Natural Frequencies and Mode Shapes of Buckled Beams," *AIAA Journal*, Vol. 33 (No. 6), pp. 1121-1126, June 1995.

[5] A. H. Nayfeh and D. T. Mook, *Nonlinear Oscillations*, Wiley, New York, pp. 56-59, 1979.

[6] R. Seshadri, *Active Vibration Control of Beams Using Piezoelectric Actuators*, M.S. Scholarly Paper, Department of Mechanical Engineering, University of Maryland, College Park, 1994.

[7] H. Li and B. Balachandran, "Buckling Induced Nonlinear Phenomenon in a Micro-electromechancial Resonator," *Proceedings of ASME International Mechanical Engineering Congress and Exposition*, New Orleans, LA, 2002.

[8] H. Li and B. Balachandran, "Nonlinear Oscillations of Microelectromechanical Resonators," *Proceedings of ASME International Design Engineering Technical Conferences*, Chicago, IL, 2003.

[9] S. Preidikman, H. Li, and B. Balachandran, "Forced Oscillations of Microelectro-mechanical Resonators," *Proceedings of ASME International Mechanical Engineering Congress and Exposition*, Washington, DC, 2003.

DYNAMICS AND PARAMETRIC IDENTIFICATION OF GEARED ROTORDYNAMIC SYSTEMS

D. Giagopulos, C. Salpistis and S. Natsiavas
Department of Mechanical Engineering Aristotle University, 54 124 Thessaloniki, Greece
natsiava@auth.gr

Abstract: In the first part of this study, dynamic response and stability characteristics of gear-pair systems supported on bearings with rolling elements is investigated. The resulting mechanical models possess strongly nonlinear characteristics, accounting for gear backlash and bearing stiffness nonlinearities. The emphasis is first put on obtaining periodic steady state motions and the results illustrate the effect of selected system parameters on the dynamics. The results obtained indicate that for some parameter combinations, there appear frequency intervals where only branches of unstable periodic motions are captured, generated through a Hopf bifurcation. By performing direct integration of the equations of motion, it is demonstrated that quasiperiodic and chaotic responses emerge inside these intervals. Finally, the attention is focused on issues related to parametric identification. In particular, a Bayesian statistical framework is adopted to estimate the optimal values of the gear and bearing model parameters. This is achieved by combining experimental information from vibration measurements with theoretical information built into a parametric mathematical model of the system.

Key words: Nonlinear dynamics, parametric identification, rotordynamics.

1. Introduction

Research on the dynamics of systems involving gear mechanisms has been performed continuously, especially during the last few decades (e.g., [1-5]). Previous studies have focused on a large variety of topics. Among all the factors affecting the response, the presence of gear backlash plays a dominant role. On the other hand, it introduces serious difficulties because the resulting equations of motion become strongly nonlinear. These

G. Rega and F. Vestroni (eds.),
IUTAM Symposium on Chaotic Dynamics and Control of Systems and Processes in Mechanics, 107–116.

difficulties are further intensified by the variation in the number of gear teeth pairs, which are in contact at a given time, causing a variation of the equivalent gear meshing stiffness. Similar difficulties are also related to the nonlinearities associated with the supporting bearing. Some of the earlier studies have already shown that these complications are responsible for complicated dynamics (e.g., [2-5]).

The main objective of the present study is twofold. First, the emphasis is directed towards investigating the dynamics of a simple but representative gear-pair model supported by bearings with rolling elements. Both regular and chaotic response of the system is examined. The second objective is to focus on issues related to parametric identification and fault detection of geared systems. A Bayesian statistical framework is adopted to estimate the optimal values of the gear and bearing model parameters and their associated uncertainties, using measured dynamic data [6].

The mechanical model and the accompanying equations of motion are presented in the following section, while the basic steps of the parametric identification methodology are briefly described in the third section. Then, numerical results are presented in the fourth section. The initial effort is focused on long time response of the nonlinear system examined. The final set of results was obtained by applying the parametric identification methodology for selected combinations of system parameters.

2. Mechanical Model

The geared system examined is shown in Figure 1. It consists of a spur gear-pair with masses m_n, mass moments of inertia I_n and base radii R_n ($n = 1,2$). Both gears are supported on bearings with rolling elements and the corresponding equations of motion are first cast in the general form

$$I_1\ddot{\varphi}_1 + R_1 f_g(\varphi_1,\varphi_2,u,\dot{u}) = M_1, \quad I_2\ddot{\varphi}_2 - R_2 f_g(\varphi_1,\varphi_2,u,\dot{u}) = -M_2,$$

$$m_1\ddot{u}_1 + f_1(u_1,\dot{u}_1) + f_g = F_{b1}, \qquad m_2\ddot{u}_2 + f_2(u_2,\dot{u}_2) - f_g = F_{b2}.$$

The quantities $M_n(t,\varphi_n,\dot{\varphi}_n)$ represent the driving and resisting external moments, while F_{bn} refer to pretension radial forces applied to the gear centers. Moreover, this model takes into account the static transmission error, $e(\varphi_1,\varphi_2)$, representing geometrical errors of the gear teeth profile and spacing. In addition, the quantity

$$u = R_1\varphi_1 - R_2\varphi_2 + u_1 - u_2 - e(\varphi_1,\varphi_2) \tag{1}$$

is known as the dynamic transmission error. Also, the damping mechanisms in both the gear mesh and the bearings are assumed to be linear, so that the corresponding forces are expressed in the form

$$f_g(\varphi_1,\varphi_2,u,\dot{u}) = c_g\dot{u} + f_g(u,\varphi_1,\varphi_2) \quad \text{and} \quad f_n(u_n,\dot{u}_n) = c_n\dot{u}_n + f_n(u_n),$$

respectively. Furthermore, taking into account the gear backlash, the gear meshing restoring force component appears in the form $f_g(u,\varphi_1,\varphi_2) = k_g(\varphi_1,\varphi_2)f_g(u)$, where the function $k_g(\varphi_1,\varphi_2)$ represents the gear mesh stiffness, while the function $f_g(u)$ represents the gear backlash [5]. Likewise, the restoring forces developed in the n-th rolling element bearing is expressed either in the linear form $f_n(u_n) = k_n u_n$, or in a more complicated but accurate nonlinear form, taking into account the diametral clearance, and the bearing characteristics and loading conditions [2, 5, 7].

Next, the total rotation angle of each gear is assumed in the form $\varphi_n = \omega_n t + \theta_n$, where ω_n are constant and θ_n represent small vibration of the mating gear teeth [2-5]. Then, both the gear mesh stiffness and the static transmission error become time-periodic functions, with fundamental frequency equal to the gear meshing frequency $\omega_M = n_1\omega_1 = n_2\omega_2$. Moreover, after setting $\underline{w}(t) = (u \quad u_1 \quad u_2)^T$ and employing relation (1), the equations of motion of the system can be put in the form

$$M\ddot{\underline{w}} + C\dot{\underline{w}} + \underline{k}(\underline{w}) = \underline{f}_b + \underline{f}(t). \tag{2}$$

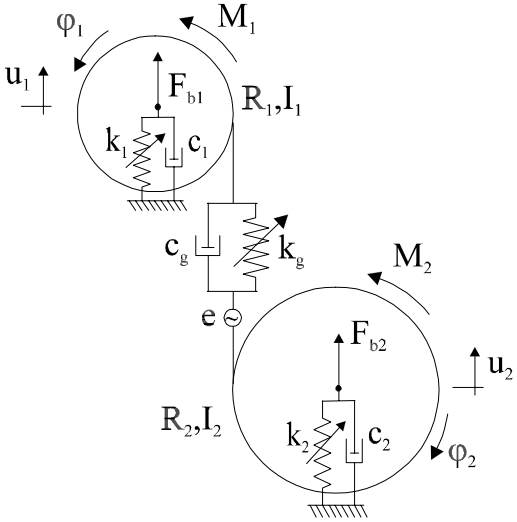

Figure 1. Mechanical *model*

3. Identification and Fault Detection Method

First, consider a parameterised class of gear-pair models representing the system examined and let $\underline{\theta}$ be a vector including the set of parameters to be identified. The values of these parameters are indicative of the condition of the system. Originally, these values are unknown. Also, let $\underline{z}(n\Delta t,\underline{\varphi})$, with $n=1,\ldots,N$, be the measured excitation time history at N_e locations and $\underline{\ddot{y}}(n\Delta t,\underline{\varphi})$ be the measured response history at R degrees of freedom of the model, where N is the number of time samples taken at a constant rate Δt. Moreover, let $\underline{\varphi}$ be a set of parameters related to the excitation. Likewise, let $\underline{\ddot{x}}(n\Delta t,\underline{\theta},\underline{\varphi})$ be the sampled acceleration response predictions at N_d degrees of freedom of the model due to the excitation $\underline{z}(n\Delta t,\underline{\varphi})$, computed for a particular model corresponding to a specific value of $\underline{\theta}$. Due to modelling error and measurement noise, the response predictions from each model will be different from the measured response data. The difference between the measured response data $\underline{\ddot{y}}(n\Delta t,\underline{\varphi})$ and the corresponding prediction $\underline{\ddot{x}}(n\Delta t,\underline{\theta},\underline{\varphi})$ at the measured locations is denoted by $\underline{e}(n)$.

In order to update the values of the parameter set and their associated uncertainty, a proper statistical system identification formulation is adopted, using the measured data set $D=\{\underline{\ddot{y}}(n\Delta t,\underline{\varphi}),\underline{z}(n\Delta t,\underline{\varphi}),\quad n=1,\ldots,N\}$. The errors $e_i(n)$ at different degrees of freedom $i=1,\ldots,R$ are chosen to be independent, zero-mean, Gaussian, discrete, white noise processes with variance σ^2. This variance, along with the parameters $\underline{\theta}$ of the model class, constitutes the set of system parameters to be identified from the measured data. Also, parameter uncertainties are quantified by modelling the parameters as random variables with probability density function specifying the relative plausibility of each of the models in the class used to describe the system behavior and prediction errors. Using Bayes theorem, the uncertainty in the model parameters $\underline{\theta}$ and the variance σ^2, taking into account the measured data set D, is quantified by the updated probability density function

$$p\left(\underline{\theta},\sigma^2|D,\underline{\delta},\underline{\varphi}\right)=\frac{c}{\left(2\pi\sigma^2\right)^{NR/2}}\exp\left(-\frac{NR}{2}\frac{J(\underline{\theta},\underline{\delta},\underline{\varphi},D)}{\sigma^2}\right)\pi(\underline{\theta},\sigma^2). \tag{3}$$

The function $\pi(\underline{\theta},\sigma^2)$ represents the prior probability density function of the model parameters, allowing engineering judgment to be incorporated in the analysis, while c is a normalizing constant. Finally, J is given by

$$J(\underline{\theta},\underline{\delta},\underline{\varphi},D)=\frac{1}{N\cdot R}\sum_{n=1}^{N}\left\|\underline{\ddot{y}}(n\Delta t,\underline{\varphi})-L_0(\underline{\delta})\underline{\ddot{x}}(n\Delta t;\underline{\theta},\underline{\varphi})\right\|^2. \tag{4}$$

The uncertainty in the model parameters $\underline{\theta}$ is obtained by computing the marginal probability density function of the parameters $\underline{\theta}$, defined to be the integral of $p(\underline{\theta},\sigma^2 \mid D,\underline{\delta},\underline{\varphi})$ with respect to the parameter σ^2. The updated probability density function $p(\underline{\theta},\mid D,\underline{\delta},\underline{\varphi})$ gives a complete description of the uncertainty in the estimates of the model parameters. Finally, the optimal model $\hat{\underline{\theta}}$, corresponds to the most probable model, which is obtained by maximizing $p(\underline{\theta},\mid D,\underline{\delta},\underline{\varphi})$ or, equivalently, by minimizing $J(\underline{\theta},\underline{\delta},\underline{\varphi},D)$.

4. Numerical Results

The results presented in the first part of this section refer to regular and irregular dynamics of the system examined. Then, results obtained by applying the parametric identification methodology are presented. For convenience, the following parameters are first introduced

$$\zeta_g = \frac{c_g}{2\sqrt{m_0 k_0}}, \quad \zeta_n = \frac{c_n}{2m_n\omega_0}, \quad b_n = \frac{b_{bn}}{b}, \quad r_n = \frac{R_n}{b}, \quad v(\tau) = \frac{u(t)}{b},$$

$$v_n(\tau) = \frac{u_n(t)}{b}, \quad J_n = \frac{I_n}{m_0 R_n^2}, \quad \mu_n = \frac{m_n}{m_0}, \quad f_{bn} = \frac{F_{bn}}{k_0 b}, \quad \kappa_n = \frac{\hat{k}_n b^{\nu-1}}{k_0},$$

$$\kappa_g(\psi_1) = \frac{k_g(\varphi_1)}{k_0}, \quad \hat{e}(\psi_1) = \frac{e(\varphi_1)}{b},$$

where $\omega_0 = \sqrt{k_0/m_0}$ and $\tau = \omega_0 t$. In all cases, the driving and the resisting moments are chosen to have constant magnitude. The response diagrams of Fig. 2 were determined by applying a numerical code, which locates branches of periodic motions, together with their stability and bifurcation properties [8]. These diagrams show the amplitude of the center translation of the driven gear as a function of the gear meshing frequency. Here, the gear mesh stiffness is assumed to be constant, while the static transmission error is harmonic with $\hat{e}_{c1} = 0.05$. In addition, the results of Fig. 2a correspond to linear bearings with normalized stiffness $\kappa_1 = \kappa_2 = 1$, while Fig. 2b shows results for nonlinear bearings.

Among other things, the results presented in the previous diagrams indicate that there appear extensive frequency ranges where only unstable periodic motions are captured. For instance, consider the branch of Fig. 2a covering the frequency interval $\Omega \approx 0.97 - 1.43$. This branch is generated via a Hopf bifurcation at both of its ends. In order to investigate the dynamics of the system within this frequency range, results obtained by direct integration of the equations of motion are presented next in Fig. 3, in the form of Poincare sections. The unstable periodic motions are first replaced by quasiperiodic response [9]. Moreover, moving away from the bifurcation point, these motions repeatedly undergo transitions from quasiperiodic or large order periodic to chaotic motions and vice versa [10].

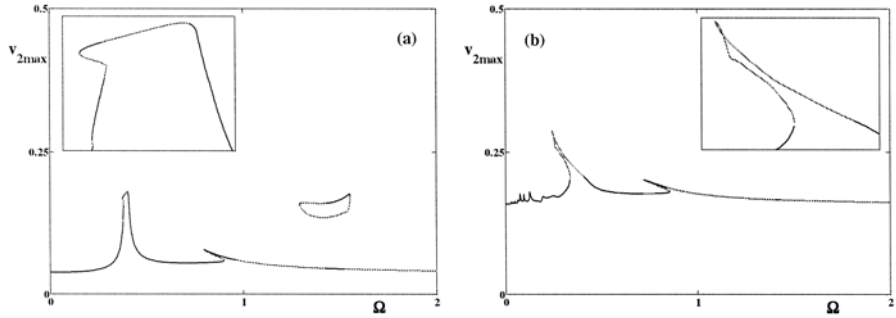

Figure 2. Frequency-response diagram for a gear-pair system with: (a) linear and (b) nonlinear bearings.

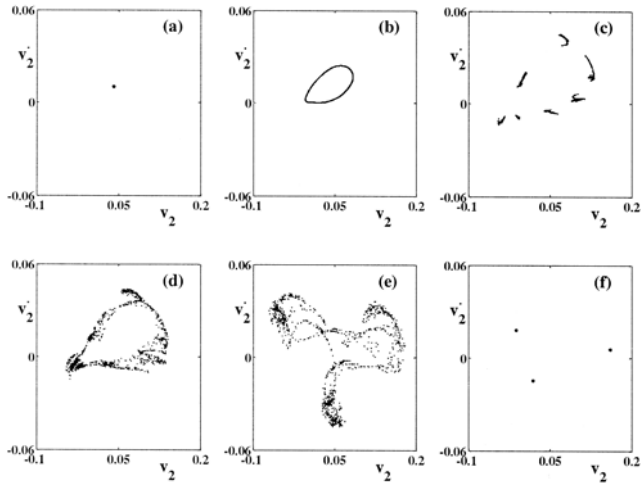

Figure 3. Poincare sections for a model with linear bearings at: (a) $\Omega = 1.43$,(b) $\Omega = 1.39$, (c) $\Omega = 1.37$, (d) $\Omega = 1.35$, (e) $\Omega = 1.1$ and (f) $\Omega = 1.0$.

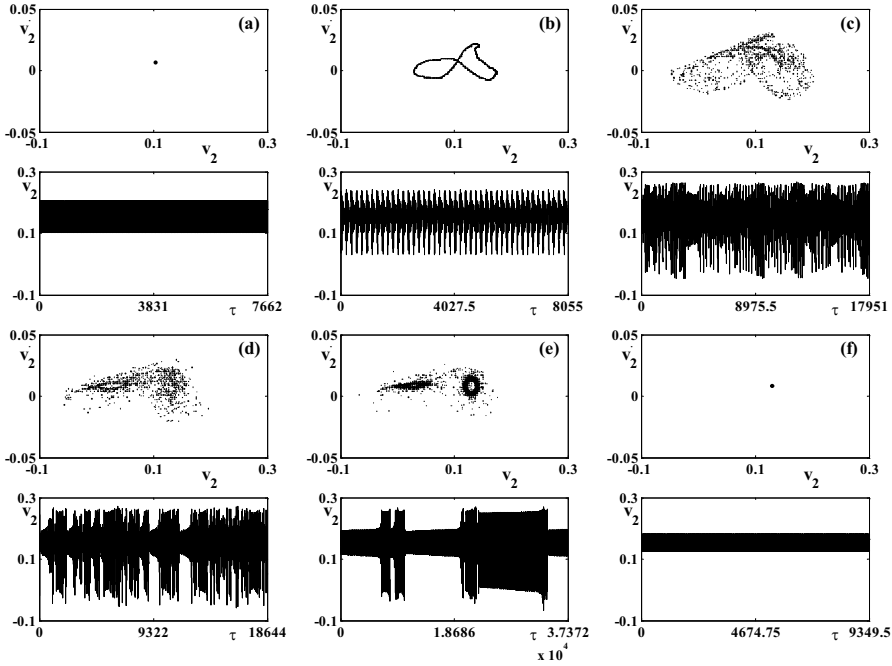

Figure 4. Response history and Poincare sections for a model with nonlinear bearings at: (a) $\Omega = 0.41$,(b) $\Omega = 0.39$, (c) $\Omega = 0.35$, (d) $\Omega = 0.337$, (e) $\Omega = 0.33625$ and (f) $\Omega = 0.336$.

A similar situation was found to occur for parameter combinations leading to the response diagram of Fig. 2b. In that case, the roller bearing nonlinearity causes a bending to the left even of the first resonance branch. On this branch, there appears a Hopf bifurcation point. Figure 4 presents Poincare sections and the corresponding histories for the translation of the driven gear, illustrating the evolution of the motions resulting after that point. The rapid qualitative change in the response is very probably affected significantly by the simultaneous loss of contact at all the bearing rollers, which occurs for bearing displacement less than 0.1. These motions are characterized by substantially greater amplitudes than the coexisting unstable periodic motions. Finally, Figure 4d demonstrates that the chaotic motions are attracted eventually by the coexisting lower amplitude stable periodic motions.

The numerical results presented next were obtained by applying the identification methodology described in section 3. In particular, the results of Table 1 were obtained by measuring the displacement of the driven gear only. The first column indicates the forcing amplitude and the meshing frequency. The second column shows the level of white noise added in the

simulated data, expressed as a percentage of the standard deviation of the model response, while the third column includes the values of the parameters to be identified. Finally, the last two columns include the estimated optimal values for the parameters and the corresponding relative error. The presence of a fault in the gear teeth or the bearings is indicated by a reduction in the value of the corresponding stiffness parameter.

Critical examination and comparison of the results presented in Table 1 demonstrates that the methodology applied provides an effective and practical way of detecting the type and severity of faults in the base of the gear teeth and the bearing supports. This was found to be the case even in the presence of relatively large levels of measurement noise. However, the identification methodology encountered difficulties for parameter combinations leading to chaotic dynamics of the gear-pair system. These identification problems are very probably associated with the sensitivity of the response on the parameter values and therefore on the evaluation of the derivatives needed in the optimisation process for those parameter combinations. To alleviate some of these difficulties, Table 2 shows results obtained by measuring response at both gears, for the cases shown in Table 1 with the larger error in the identification predictions.

Finally, Table 3 and Table 4 present results obtained by considering cases involving model error. More specifically, for all the identification cases examined so far, the response was obtained for gear-pair models with linear bearing characteristics and periodic gear mesh stiffness and static transmission error. For the results shown in Table 3, the model was assumed to have a constant gear mesh stiffness. The measurement data were referring to v_1 and v_2. Likewise the results of Table 4 were obtained for the same model by measuring v_1, v_2 and v.

Table 1. Identification of Bearing Stiffness (measurement of v_2)

M_{10}/Ω	$M.N$ (%)	$\underline{\theta} = (\kappa_1 \quad \kappa_2)^T$		$\underline{\tilde{\theta}}$		$\frac{\tilde{\theta}-\theta}{\theta}100(\%)$	
0.1 / 0.6	0	1	1	0.999	0.999	0.1	0.1
0.1 / 0.8	0	1	1	0.998	0.999	0.2	0.1
0.1 / 1.35	0	1	1	0.200	2.000	80	100
0.0375 / 0.6	0	1	1	0.997	0.999	0.3	0.1
0.1 / 0.6	5	1	1	1.010	0.980	1	2
0.1 / 0.6	10	1	1	1.020	1.010	2	1
0.1 / 0.6	10	1	0.9	1.020	0.896	2	0.44
0.1 / 0.6	10	0.8	0.9	0.920	0.900	15	0
		$\underline{\theta} = (\hat{\kappa}_1 \quad \hat{\kappa}_2)^T$					
0.1 / 0.6	0	0.3594	0.3594	0.3594	0.3597	0	0.0083
0.1 / 0.6	10	0.3594	0.3594	0.3590	0.3591	0.1112	0.0083

Table 2. Identification of Bearing Stiffness (measurement of v_1, v_2)

M_{10}/Ω	$M.N$ (%)	$\underline{\theta} = (\kappa_1 \quad \kappa_2)^T$		$\underline{\tilde{\theta}}$		$\frac{\tilde{\theta}-\theta}{\theta}100(\%)$	
0.1 / 0.6	0	1	1	0.999	1.000	0.1	0
0.1 / 0.8	0	1	1	1.000	1.000	0	0
0.1 / 1.35	0	1	1	0.400	1.700	60	70
0.0375 / 0.6	0	1	1	0.999	0.999	0.1	0.1
0.1 / 0.6	5	1	1	1.000	1000	0	0
0.1 / 0.6	10	1	1	0.999	1.000	0.1	0
0.1 / 0.6	10	1	0.9	0.999	0.899	0.1	0.11
0.1 / 0.6	10	0.8	0.9	0.800	0.899	0	0.11
		$\underline{\theta} = (\hat{\kappa}_1 \quad \hat{\kappa}_2)^T$					
0.1 / 0.6	0	0.3594	0.3594	0.3594	0.3594	0	0
0.1 / 0.6	10	0.3594	0.3594	0.3595	0.3593	0.0278	0.0278

Table 3. Model Error (Model: Periodic Stiffness, Simulated Data: Constant Stiffness), (measurement of v_1, v_2)

M_{10}/Ω	$M.N$ (%)	$\underline{\theta} = (\kappa_1 \quad \kappa_2 \quad \kappa_o)^T$			$\underline{\tilde{\theta}}$			$\frac{\tilde{\theta}-\theta}{\theta}100(\%)$		
0.1 / 0.6	0	1	0.9	1	1.00	0.90	1.90	0	0	90
0.1 / 0.6	10	1	0.9	1	0.99	0.90	3.00	1	0	200
0.1 / 0.25	0	1	0.9	1	1.00	0.90	2.00	0	0	100

Table 4. Model Error (Model: Periodic Stiffness, Simulated Data: Constant Stiffness), (measurement v, v_1, v_2)

M_{10}/Ω	$M.N$ (%)	$\underline{\theta} = (\kappa_1 \quad \kappa_2 \quad \kappa_o)^T$			$\underline{\tilde{\theta}}$			$\frac{\tilde{\theta}-\theta}{\theta}100(\%)$		
0.1 / 0.6	0	1	0.9	1	1.000	0.900	0.980	0	0	2
0.1 / 0.6	10	1	0.9	1	0.998	0.900	0.979	0.2	0	2.1
0.1 / 0.25	0	1	0.9	1	1.000	0.900	0.982	0	0	1.8

5. Summary

In the first part of this study, a mechanical model of a gear-pair system was developed. This model takes into account the gear mesh variable stiffness and backlash, the static transmission error and deformability effects from bearings with rolling elements. The emphasis was first put on locating periodic steady state motions in an effort to demonstrate the effect of some system parameters on the dynamics. For some parameter combinations, frequency intervals were captured where only branches of unstable periodic motions exist, emanating through Hopf bifurcation points. Performing direct integration of the equations of motion, it was illustrated that the unstable

periodic response inside these branches gives its place to quasiperiodic and chaotic responses, which may possess much higher amplitudes.

The information extracted from the dynamic analysis was then utilized in explaining results obtained by the application of an appropriate parametric identification methodology. These results demonstrated that the methodology applied provides an effective way of detecting the type, location and severity of faults in the gear teeth and the bearing supports. This was found to be the case even in the presence of relatively large model errors and measurement noise. However, it was observed that the identification methodology encountered difficulties for parameter combinations leading to chaotic dynamics of the gear-pair system.

Acknowledgments

This research was funded by the Greek Ministry of Development (YEET) and the European Union, through the PENED 2001 program (01 ΕΔ 330).

References

[1] H.N. Ozguven and D.R. Houser, "Mathematical models used in gear dynamics - a review," *Journal of Sound and Vibration,* **121**, 383-411, 1988.

[2] A. Kahraman and R. Singh, "Nonlinear dynamics of a geared rotor-bearing system with multiple clearances," *Journal of Sound and Vibration,* **144**, 469-506, 1991.

[3] F. Pfeiffer and C. Glocker, *Multibody Dynamics with Unilateral Contacts,* New York: Wiley-Interscience, 1996.

[4] C.-S. Chen, S. Natsiavas and H.D. Nelson, "Coupled lateral-torsional vibration of a gear-pair system supported by a squeeze film damper," *ASME Journal of Vibration and Acoustics,* **120**, 860-867, 1998.

[5] S. Theodossiades and S. Natsiavas, "Periodic and chaotic dynamics of motor-driven gear-pair systems with backlash", *Chaos, Solitons and Fractals,* **12**, 2427-2440, 2001.

[6] L.S. Katafygiotis, C. Papadimitriou and H.F. Lam, "A probabilistic approach to structural model updating," *International Journal of Soil Dynamics and Earthquake Engineering,* **17**, 495-507, 1998.

[7] T.A. Harris, *Rolling Bearing Analysis*. New York: John Wiley, 1966.

[8] E. Doedel, *AUTO: Software for Continuation and Bifurcation Problems in Ordinary Differential Equations*, California Institute of Technology, Pasadena, California, 1986.

[9] A.H. Nayfeh and B. Balachandran, *Applied Nonlinear Dynamics.* New York: John Wiley & Sons, 1995.

[10] D.G. Aronson, M.A. Chory, G.R. Hall and R.P. McGehee, "Bifurcations from an invariant circle for two parameter families of maps of the plane: a computer assisted study," *Communications in Mathematical Physics,* **83**, 303-354, 1982.

GLOBAL BIFURCATIONS OF NONLINEAR THERMOELASTIC MICROBEAMS SUBJECT TO ELECTRODYNAMIC ACTUATION

O. Gottlieb[1] and A.R. Champneys[2]
[1]*Department of Mechanical Engineering, Technion – Israel Institute of Technology, Israel;*
[2]*Department of Engineering Mathematics, University of Bristol, UK.*
oded@techunix.technion.ac.il

Abstract: In this paper we formulate a nonlinear boundary-value problem describing the thermoelastic dynamics of a microbeam that is subject to a localized electrodynamic actuation and is operating in an ultra-high vacuum environment. A modal Galerkin projection reveals a planar homoclinic structure describing escape from a potential well that is perturbed by both thermoelastic damping and modulated periodic actuation. This structure is investigated via Melnikov analysis to shed light on possible existence of global bifurcations and chaotic transients.

Key words: Thermoelastic microbeams, electrodynamic actuation, global bifurcation.

1. Introduction

Microbeams are the fundamental structural elements employed in the growing domain of micro- and nano- electromechanical systems (MEMS/NEMS). These slender elements (with length, breadth, and height on the order of 100*10*1 microns, respectively) serve as components in resonant sensors and actuators governed by attractive forces proportional to an inverse power of the displacement. The forces acting on the various elements differ in their amplitudes in accordance with their operating range. Electrostatic/electrodynamic attraction in MEMS devices appears in the form of a distributed force controlling displacements on the order of microns, whereas atomic interactions govern localized forces of dynamic

G. Rega and F. Vestroni (eds.),
IUTAM Symposium on Chaotic Dynamics and Control of Systems and Processes in Mechanics, 117–126.

sensors that resolve nanometric scales via sharp tips in scanning probe microscopy (SPM),or nanoresonator response in NEMS devices.

Examples include constrained microbeams with immovable boundaries (resulting in mid-plane stretching) designed as rate sensors and strain gauges and microcantilevers (with negligible mid-plane stretching) that are the key elements in SPM systems. The generalized forces acting on these elements also include distributed loads such as squeeze-film damping in air [1] and coupled thermoelastic damping in ultra-high vacuum [2]. These damping loads are typically quantified by a linear equivalent damping parameter or quality factor (Q). Thermoelastic damping in Silicon microbeams decreases sharply with decreasing temperature ($10^4 < Q < 10^9$ between 300°K and 20°K [2]). The exciting mechanisms may also differ for each application. An immovable electrodynamic sensor is excited by combined external and parametric excitation proportional to the square of the input voltage [1], whereas a SPM microcantilever can resonate by direct base excitation [3] or an applied moment induced via a piezoelectric layer [4].

While microbeams can be very different in their shape, form and material properties, they share a common phenomenological structural instability when placed in an attractive field, where for a small enough gap, the beam will be pulled into the substrate. This instability is due to the nonlinear force balance between the elastic restoring force of the microbeam and the attractive force where the threshold (i.e. 'pull-in' in MEMS and 'jump-to-contact' in SPMs) denotes the upper limit where the elastic restoring force cannot resist the attractive force. The bifurcation point separates two distinct domains of operation: i) below a critical distance there exists a unique equilibrium where the microbeam collapses onto the substrate, and ii) above a certain distance (also corresponding to below a critical voltage in electrostatic resonators) there exist an additional stable equilibrium that is separated from its counterpart on the substrate by an unstable saddle. The latter domain is governed by a global homoclinic connection that is an typical of an asymmetric configuration describing escape from a unique potential well [5].

The dynamic model that will be considered here is that of a MEMS sensor subject to an asymmetric and localized nonlinear electrodynamic actuation. We extend the boundary-value problem to include nonlinear membrane stiffness and a thermoelastic field corresponding to operation in an ultra-high vacuum environment. The model structure is that of a perturbed nonlinear Hamiltonian microbeam that is governed by elastic nonlinearities and the autonomous part of a generalized electrodynamic force. The perturbation originates from the time dependent electrodynamic force and from both viscoelastic structural damping and thermoelastic dissipation. The focus of our investigation is on possible descriptions of the global unperturbed homoclinic connections in the projected low-order modal

dynamical system. The perturbation of the fundamental homoclinic structure is demonstrated via Melnikov's method and complemented by numerical simulation of the dynamical system.

2. The Dynamical System

We consider a boundary-value problem for a fixed thermoelastic microbeam (with length L, width B, height H) which incorporates possible residual stresses modeled as an axial load [1], and a geometric nonlinearity due to membrane stiffness [6]. The electrodynamic interaction is modeled as a concentrated load at mid span which is proportional to the inverse second power of the relative displacement [1], and the elastic field is augmented by the heat equation [2].

The nondimensional $(s = x/L, \tau = \omega_s t, \omega_s^2 = EI/(\rho AL^4))$ equation for the elastic field $V(s,\tau)$, is accurate to cubic order and incorporates electrodynamic excitation $Q(V,\tau)$, an elastic restoring force $R(V)$, and a structural damping force $S(U,V)$. The latter includes a linear viscoelastic term and a thermal moment of inertia that is a function of the nondimensional $(r=y/B)$ relative temperature field $U(r,s,\tau)$, which represents the difference between current temperature and that of the unstrained and unstressed beam:

$$V_{\tau\tau} = Q(V,\tau) - R(V) - S(U,V) \tag{1}$$

where

$$Q = \delta(s-1/2)\hat{\Gamma}(1+\hat{\eta}\sin\hat{\Omega}\tau)^2(\hat{\gamma}-V)^{-2}, R = V_{ssss} + V_{ss}\left(\hat{\kappa}_1 - \hat{\kappa}_3\int_0^1 V_s^2 ds\right),$$

$$S = \hat{\mu}_1 V_{sss\tau} + \hat{\mu}_2\left(\int_{-1/2}^{1/2} rUdr\right)_{ss}$$ and subscripts denote partial differentiation with respect to nondimensional space (s) and time (τ).

The parameters governing the elastic field in Eq. (1) are $\hat{\kappa}_1 = GL^2/(EI), \hat{\kappa}_3 = 6(L/H)^2$, which correspond to residual stress induced in the manufacturing process and nonlinear stiffness respectively. The nondimensional parameters governing the electrodynamic excitation incorporate the gap height $\hat{\gamma} = g/L$, and magnitude of interaction defined by a bias (DC) input voltage $\hat{\Gamma} = 6\varepsilon_0 v_{DC}^2/(EH^3)$. The latter is perturbed

by an oscillating harmonic (AC) voltage that consists of an amplitude and frequency of excitation $\hat{\eta} = v_{AC} / v_{DC}, \hat{\Omega} = \Omega_{AC} / \omega_s$ respectively.

The equation for the relative nondimensional temperature field is:

$$U_\tau = \hat{\chi} U_{rr} + \hat{\sigma} r V_{ss\tau} \tag{2}$$

where the relative dimensional temperature has been normalized by the unstrained and unstressed equilibrium temperature (T_0). The nondimensional parameters governing the temperature field in Eq. (2) include thermal diffusivity, $\hat{\chi} = \chi/(H^2\omega_s)$, and a function of relaxation strength (Δ_E) of the elastic Young's modulus, $\hat{\sigma} = 12\Delta_E/\hat{\mu}_2$. The latter is inversely proportional to the material thermal expansion coefficient (α), and the equilibrium temperature $\hat{\mu}_2 = 12\alpha T_0 L/H$. We note that the linear form of Eq. (2), which is valid to order Δ_E^2, is based on two simplifications [7]: i) small differences between equilibrium and response temperature, and ii) thermal gradients in the plane of the cross-section along the vertical direction are much larger than the gradients along the beam.

We employ an assumed mode Galerkin procedure which enables reduction of the boundary value problem described Eq. (1) and Eq. (2) to two coupled ordinary differential equations describing dynamics near primary resonance of the thermoelastic microbeam. The spatial mode shape selected for the elastic field corresponds to that of a linear undamped microbeam with fixed boundary conditions at both ends: $\phi_n = [\cosh z_n s - \cos z_n s - C_n(\sinh z_n s - \sin z_n s)]$, where the modal frequencies, $\omega_n = z_n^2$, are determined from $\cos hz_n \cos z_n = 1$. The spatial mode shape of the temperature field is obtained by solving the non homogeneous Eq. (2) with no flow of heat across the boundaries (e.g. $U_r(\pm 1/2) = 0$), to yield $\psi = \hat{\sigma}\phi_{nss}[r - \sin(k_n r)/k_n \cos(k_n/2)]$, where the wavelength is a function of the nondimensional diffusivity: $k_n = (\omega_n/\hat{\chi})^{1/2}$ [8]. We note that comparison of this modal approximation to the exact result obtained by [2] is excellent for $k_1 < 7$ (e.g. Figure 2 in [2] for $\xi < 5$). We focus here on the lowest (bending) mode primary resonance (e.g. n=1: q=q_1, p=p_1) so the resulting equations of motion for the modal amplitudes are:

$$\begin{aligned} &J_1 q_{\tau\tau} + (J_4 + \hat{\kappa}_1 J_2) q - \hat{\kappa}_3 J_3 q^3 = \\ &\quad = \hat{\Gamma}\phi_1(1/2)(1 + \hat{\eta}\sin\hat{\Omega}\tau/(\hat{\gamma} - \phi_1(1/2)q)^{-2} - \hat{\mu}_1 J_4 q_\tau - \hat{\mu}_2 J_5 p \end{aligned} \tag{3}$$

$$J_6 p_\tau = \hat{\chi} J_7 p + \hat{\sigma} J_8 q_\tau \tag{4}$$

where J_i (i=1,8) are constants determined by integration over the domain [8]. We note that $J_{1,4,6}>0$, $J_{2,3,7}<0$ and $J_{5,8}$ can change sign as a function of wave number (e.g. $k_1<\pi$: $J_5>0$, $J_8<0$ and vice versa for $\pi<k_1<7$). Consequently, the beam natural frequency for pure bending is $\omega_1=(J_4/J_1)^{1/2}$, and that possible residual stress reduce the natural frequency ($J_2<0$). Furthermore, while the elastic membrane stiffness is hardening ($J_3<0$), the contribution of the electrostatic force (e.g. $\hat{\eta}=0$) is softening.

Finally, we rescale the modal amplitudes and time ($x=q\phi_1(1/2)/\hat{\gamma}$, $z=p\phi_1(1/2)/\hat{\gamma}$, $t=\omega_1\tau$) to yield the dynamical system:

$$\begin{aligned} x' &= y \\ y' &= \gamma(1+\eta\sin\Omega t)^2(1-x)^{-2}-\alpha x-\beta x^3-\mu_1 y-\mu_2 z \\ z' &= -\nu z+\sigma y \end{aligned} \tag{5}$$

where (') denotes the derivative with respect to the rescaled time. The parameters that govern Eq. (5) include: i) linear and cubic elastic stiffness terms $\alpha=1-\hat{\kappa}_1|J_2|/(J_1\omega_1^2), \beta=\hat{\kappa}_3|J_3|\hat{\gamma}^2/(J_1\omega_1^2\phi_1^2(1/2))$, ii) viscoelastic damping $\mu_1=\hat{\mu}_1 J_4/\omega_1$, iii) electrostatic magnitude $\gamma=\hat{\Gamma}\phi_1(1/2)^2/(J_1\omega_1^2\hat{\gamma}^3)$, iv) electrodynamic amplitude and frequency $\eta=\hat{\eta}, \Omega=\hat{\Omega}/(\omega_1)$, and v) thermoelastic damping parameter defined by $\mu_2=\hat{\mu}_2 J_5/(J_1\omega_1^2)$ augmented by $\nu=\hat{\chi}|J_7|/(J_6\omega_1), \sigma=\hat{\sigma}J_8/J_6$. We note that the hardening nonlinear cubic stiffness is proportional to $(g/H)^2$, where g/H is the ratio between the gap and the microbeam height.

The third order dynamical system in Eq. (5) consists of a time independent Hamiltonian subsystem (α, β, γ), that is perturbed by visco and thermoelastic damping (μ, σ, ν), and by combined external and parametric excitation (η,Ω). We note that the thermoelastic damping is proportional to $\hat{\mu}_2\hat{\sigma}=12\Delta_E$. Consequently, as the relaxation strengths Δ_E are typically very small [2], we focus on two limiting configurations: i) $\mu_2 \sim O(1)$ and σ, ν small, and ii) $\mu_2 \sim O(\varepsilon)$ where σ and ν are large. The latter enables freezing the z velocity component in Eq. (5c) to yield a second order system.

The corresponding third order system is:

$$\begin{aligned} x' &= f_1(y) \\ y' &= f_2(x,z)+\varepsilon g_2(x,t) \\ z' &= \varepsilon g_3(y,z) \end{aligned} \tag{6}$$

where $f_1 = y, f_2 = \gamma(1-x)^{-2} - \alpha x - \beta x^3 - \mu_2 z$, and the perturbation is $\varepsilon g_2 = \gamma\eta \sin\Omega t(2+\eta\sin\Omega t)(1-x)^{-2} - \mu_1 y, \varepsilon g_3 = \sigma y - \nu z$.

The limiting second order system is:

$$\begin{aligned} x' &= f_1(y) \\ y' &= f_2(x) + \varepsilon g_2(x,y,t) \end{aligned} \tag{7}$$

where $f_1 = y, f_2 = \gamma(1-x)^{-2} - \alpha x - \beta x^3$, and the perturbation is $\varepsilon g_2 = \gamma\eta \sin\Omega t(2+\eta\sin\Omega t)(1-x)^{-2} - (\mu_1 + \mu_2\sigma/\nu)y$.

We focus here on total damping governed by $(\mu_1\nu + \mu_2\sigma) > 0$, which ensures that both limiting cases are indeed dissipative. Note that the third order system in Eq. (6) corresponds to the form described by [9] where perturbed homoclinic orbits in three dimensional flow may exhibit transverse intersections that are portrayed via length transients and possible strange attractors. Examples of the latter include a periodically forced Duffing equation with weak feed back [9] and a slender beam rotating about is longitudinal axis [10]. Both examples are of slowly varying oscillators with a pair of homoclinic orbits corresponding to a quartic double well potential. However, this dynamical system incorporates a single well that portrays stable periodic dynamics when the response is confined within its bounds and escape when a certain threshold is exceeded. Furthermore, we note that the second order system in Eq. (7) is similar to that analyzed for lumped mass [3] and continuous [4] microbeam models for noncontacting atomic force microscopy.

3. The Hamiltonian System

We consider the planar, undamped, and unforced subset of Eq. (5) which is Hamiltonian with:

$$H = y^2/2 + \alpha x^2/2 + \beta x^4/4 - \gamma(1-x)^{-1} \tag{8}$$

and note that below a critical threshold (e.g. pull-in) it has two physical fixed points corresponding to an elliptic center and a hyperbolic saddle. Beyond this threshold there are no fixed points and all solutions escape to the substrate (e.g. x=1). The homoclinic orbit that separates periodic and escaping orbits is deduced from Eq. (8):

$$y_s(x) = \pm\left[\alpha(x_S^2 - x^2) + \beta(x_S^4 - x^4)/2 - 2\gamma((1-x_S)^{-1} - (1-x)^{-1})\right]^{1/2} \tag{9}$$

where x_S is the value of the saddle fixed point. The separatrix in Eq. (9) can be reduced to the following form by matching coefficients of like powers:

$$y_s(x) = \pm\left(\frac{\beta}{2}\right)^{1/2}(x - x_S)\left[\frac{(x - x_E)(x - A)(x - B)}{1 - x}\right]^{1/2} \tag{10}$$

where x_E is the intersection of the separatrix with the horizontal axis and that A and B are the complex conjugate roots of the quadratic equation:

$$x^2 + b_1 x + b_2 = 0, b_1 = (2x_S - x_E - 1), b_2 = (2\frac{\alpha}{\beta}(1 - 2x_S) + {x_S}^2(3 - 4x_S))/x_E.$$

Integration of Eq. (10) enables an implicit form for the homoclinic orbit:

$$\left(\frac{\beta}{2}\right)^{1/2}(t - t_0) = \int_{x_E}^{x} \frac{1}{(x - x_S)}\left[\frac{1 - x}{(x - x_E)(x^2 - 2\mathrm{Re}[A] + |A|^2)}\right]^{1/2} dx \tag{11}$$

We note that for negligible membrane stiffness $(\beta \to 0, g \ll H)$,, the integral form in Eq. (11) reduces to an implicit al form where $x_E = 1 - 2x_S$:

$$\alpha^{1/2}(t - t_0) = -\arcsin\left(\frac{x + x_S - 1}{x_S}\right) - \frac{\pi}{2}$$
$$+\left(\frac{1 - x_S}{x_S - x_E}\right)^{1/2} \ln\left[\frac{((1 - x_S)(x_S - x_E)(1 - x)(x - x_E))^{1/2} - (2x_S - 1)(x + x_S - 1)}{x_S(x_S - x)}\right] \tag{12}$$

A similar form to Eq. (12) was obtained for an interaction potential of a lumped mass model of an atomic force microscope [3].

Finally, we estimate the homoclinic orbit in Eq. (9) by construction of an equivalent cubic potential which exactly reproduces the saddle (x_S) and phase plane intersection (x_E):

$$H = y^2/2 + \alpha_0 x + x^2/2 - \alpha_2 x^3/3 \tag{13}$$

where $\alpha_0 = -\frac{x_S(x_S + 2x_E)}{2(2x_S + x_E)}, \alpha_2 = \frac{3}{2(2x_S + x_E)}$. In this case the homoclinic orbit can be integrated in closed form to yield an explicit expression:

$$x(t) = x_S - (x_S - x_E)\sec h^2((x_S - x_E)^{1/2} t/2) \tag{14}$$

A comparison of the quadratic estimate and the original homoclinic orbit (corresponding to a microbeam with a gap equal to the beam height [1] and

no residual stress $\alpha = \beta = 1, \gamma = 0.05248$), reveals in Figure 1, that the former slightly reduces the domain of periodic solutions and as anticipated, does not portray the physical limit of the substrate at x=1.

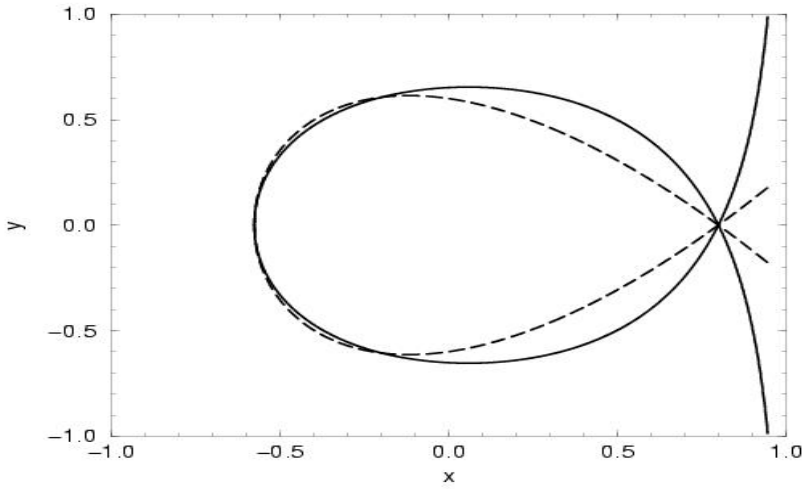

Figure 1. Hamiltonian system phase plane [Eq.(8) - solid line] and its quadratic estimate [Eq. (13) – dashed line]: $\alpha = \beta = 1, \gamma = 0.05248$.

4. A Global Bifurcation

We consider the limiting case proposed by Eq. (6) and augment the planar Hamiltonian in Eq. (8) with $\mu_2 xz$. Following [9], we formulate the Melnikov integral:

$$M(t_0) = \int_{-\infty}^{\infty} \left(f_1 g_2 + \frac{\partial H}{\partial z} g_3 \right)(q_0, \bar{z}, t + t_0)dt - \frac{\partial H}{\partial z} \int_{-\infty}^{\infty} g_3(q_0, \bar{z}, t + t_0)dt \quad (15)$$

where the bracketed terms are to be evaluated along the unperturbed homoclinic orbit (q_0=(x(t),y(t) on the z level corresponding to x_S of the averaged field) which can be computed numerically from Eq. (11) or Eq. (12). The limiting case proposed by Eq. (7) yields a similar integral for small modulation amplitude:

$$M(t_0) = \int_{-\infty}^{\infty} \left(2\gamma\tilde{\eta} y \sin\Omega(t + t_0) - \left(\frac{\tilde{\mu}\sigma}{\nu} \right) y^2 \right) dt \quad (16)$$

The integral in Eq. (16) has been computed numerically (along the homoclinic orbit in Eq. (12)) [3], to reveal a standard form which includes both bias (I_1) and modulation (I_2) that depend on damping and modulation amplitude respectively [11]:

$$M(t_0) = I_1 + I_2 \sin \Omega t_0 \tag{17}$$

Consequently, for a given small equivalent damping level, zeros of Eq. (17) describe a curve in parameter space defined by forcing amplitude versus frequency $(\eta = \eta(\Omega))$. Solutions below the curve are stable periodic orbits whereas above the curve, solutions are anticipated to exhibit chaotic transients corresponding to transverse intersections of the stable and unstable manifolds of the perturbed homoclinic orbit. Furthermore, we note that the quadratic approximation of the homoclinic orbit in Eq. (14) enables derivation of an explicit form for the components of the Melnikov integral. This yields a simple closed form estimate of the Melnikov stability curve [5].

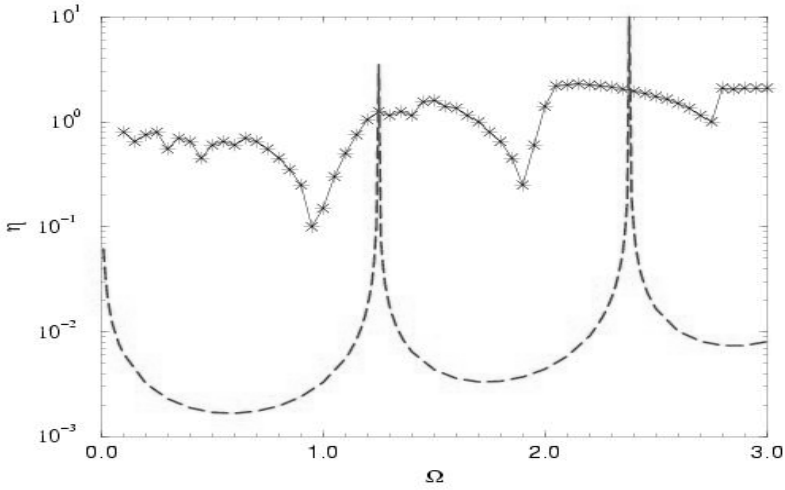

Figure 2. Escape boundaries for the dynamical system [Eq. (5) - solid line] and approximate Melnikov stability curve [Eq. (17) - dashed line] with parameters of Figure 1 and $(\mu_1 + \mu_2 \sigma / \nu) = 10^{-3}$.

Numerical simulations of the dynamical system in Eq. (7) with maximal thermoelastic damping ($Q = 10^3$ corresponding to $\nu / \mu_2 \sigma$ for $k_1 \ll \pi$), reveal a complex wedge like structure in the amplitude-frequency parameter space describing the escape boundary to the confining substrate at x=1. While a

dense grid of initial conditions is required to accurately map the escape boundary, we employed several combinations of initial displacement beginning with the stable equilibrium until escape and repeated the process for several initial velocities. The corresponding approximate Melnikov stability curve consists of a lower bound as its validity is limited to small excitation ($\eta \sim Q^{-1}/2\gamma = 10^{-2}$). A similar structure has been recorded for a damped, forced single cubic potential well [5] where the minimas of the wedge correspond to ultra-sub-harmonic resonance frequencies (e.g. $\Omega \sim n\omega_0/m$, where ω_0 is the system natural frequency, m,n=1,2,3,...) and where chaotic transitions were found only near the period-doubling flip boundaries. We note that for smaller thermoelastic damping, the wedge like structure becomes dense and the Melnikov analysis is then valid for comparably very low exciting amplitudes (e.g. $\eta \sim 10^{-4}$ for $Q \sim 10^5$).

Acknowledgments

The authors are grateful to EPSRC for promoting the authors collaboration. OG also acknowledges support from the Israel Science Foundation and the Technion Fund for Promotion of Research. We also thank Professor K. Yagasaki for his comments and insight on the numerical Melnikov estimate.

References

[1] E.S. Hung and S.D. Senturia, *IEEE J. MEMS*, 8, 280-289, 1999.
[2] R. Lifshitz and M.L. Roukes, *Phys. Rev. B*, 61, 5600-5609, 2000.
[3] M. Ashab, M.V. Salapaka, M. Daleh, and I. Mezic, *Automatica*, 35, 1663-1670, 1999.
[4] W. Wolf and O. Gottlieb, *J. App. Phys.*, 92, 4701-4709, 2002.
[5] J.M:T. Thompson, *Proc. R. Soc. Lond. A* 421, 195-225, 1989.
[6] A.H. Nayfeh, *Nonlinear Interactions*, Wiley, 2000.
[7] L.D. Landau and E.M. Lifshitz, *Theory of Elasticity*, Pergamon, 1959.
[8] O. Gottlieb and A.R.C. Champneys, preprint, 2004.
[9] S. Wiggins and P.J. Holmes, *SIAM J. Math Anal.* 18, 612-629,1987.
[10] S.W. Shaw, *J. Sound Vib.*, 124, 329-343, 1988.
[11] J. Guckenheimer and P.J. Holmes, *Nonlinear Oscillations, Dynamical Systems and Bifurcations of Vector Fields*, Springer, 1983.

NONLINEAR INTERACTION IN MHD BEARINGS UNDER OSCILLATING ELECTRIC FIELDS

Bernhard Schweizer and Jörg Wauer
Institut für Technische Mechanik, Universität Karlsruhe,
D–76126 Karlsruhe, Germany
wauer@itm.uni-karlsruhe.de

Abstract: Nonlinear oscillations in connection with magnetohydrodynamic journal and slider bearings are discussed. It is assumed that the externally applied magnetic field is constant and uniform, the applied electric field is uniform but harmonically oscillating. Using electrically conducting fluids as lubricant and applying electric and magnetic fields, it is possible to produce pressure even if the shaft does not rotate and the bearing is fixed. The equations of motion for a rigid shaft supported in short MHD journal bearings are derived and solved numerically. By a similar analysis the slider bearing is examined.

Key words: Nonlinear oscillations, MHD journal bearings, slider bearings, electric field.

1. Introduction

The load capacity of bearings using electrically conducting fluids as lubricant can be influenced by applying electric and magnetic fields. There exist a great deal of investigations on MHD journal and slider bearings (see e.g. [1,2,3].

In some recent work of the authors [4,5], infinitely short journal bearings were considered the first time to obtain analytical solutions of the magnetohydrodynamic form of Reynolds' bearing equation. Based on this, the stiffness and damping properties of such bearings can be computed to examine their stability.

Referring to that, in the present study it will be shown that it is possible to produce pressure even if the shaft does not rotate and the bearing is fixed where two general cases concerning the orientation of the applied electromagnetic fields are investigated. The key idea is to apply oscillating electric fields giving

G. Rega and F. Vestroni (eds.),
IUTAM Symposium on Chaotic Dynamics and Control of Systems and Processes in Mechanics, 127–136.

rise to nonlinear self-excited vibrations of the movable part in journal or slider bearings.

In order to calculate the oscillations of the shaft and the slider, respectively, it is on the one side necessary to calculate the pressure distribution in the lubrication gap. Knowing the pressure field and hence by integration the total force, one has on the other side in the case of the journal bearing to solve the equations of motion for the shaft and in the case of the slider bearing the equation of motion for the slider.

To determine the pressure field, one has to solve the magnetohydrodynamic basic equations, namely the Navier-Stokes equations, the continuity equation, Maxwell's equations, the conservation of charge and Ohm's generalized law. Approximate analytical solutions for the pressure distribution can be derived by applying the short bearing hypothesis [6,7]. To simplify the problem, in addition to the short bearing hypothesis the ordinary assumptions of lubrication theory are applied. Moreover, the flow is assumed to be isothermal. To reduce Maxwell's equations, induction effects are neglected, i. e., the magnetic Reynolds number is assumed to be zero. Both, the journal and the slider are considered as rigid bodies. With these assumptions, the pressure field and therefore the total load can be calculated analytically. Hence, the equations of motion for the shaft and the slider can be derived and solved numerically.

2. Journal Bearing

A sketch of the assembly is shown in Figure 1. The radius of the journal is denoted by r and the inner radius of the bearing by R. The eccentricity is termed as e, the breadth of the journal in z-direction is $b = 2a$. The film

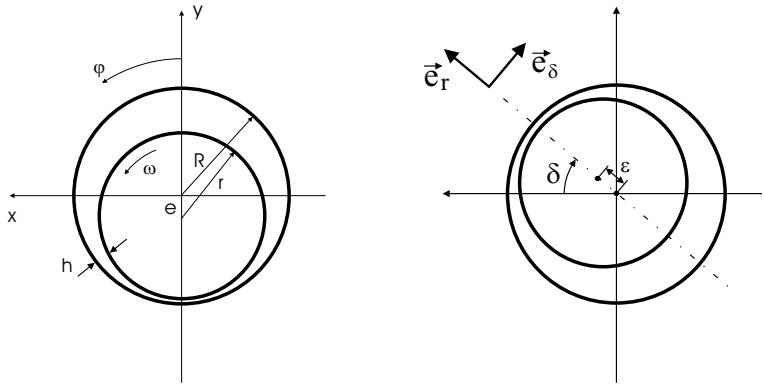

Figure 1. Bearing geometry

thickness $h(\varphi)$ is due to the eccentricity a function of $\varphi = x/R$. It is assumed that the bearing is fixed and that in contrast to the conventional case the shaft does not rotate, i.e., $\omega = 0$.

As a first case, an externally applied constant magnetic field is oriented in radial direction. The electric field is applied in z-direction and is harmonically oscillating: $E_z = \hat{E}_z \cos(\Omega t)$. Both, the journal and the bearing are assumed to be ideal conductors. Due to the electric field, a periodic current is generated in the lubrication film. Because of the magnetic field, a Lorentz force is induced and generates a flow in the gap. Therefore the journal starts to move. Due to this motion, two hydrodynamic damping forces are produced. The tangential motion, defined by the angular velocity $\dot{\delta}$, creates the hydrodynamic force $S_{\dot{\delta}}$. The radial motion with $\dot{\epsilon}$ generates the hydrodynamic squeezing force S_V. The rotation of the shaft due to shear forces will be neglected.

Under the assumptions mentioned in the introductory chapter, the balance of momentum in tangential and axial direction are reduced to (see [2-5,6])

$$\varphi: \quad 0 = -\frac{1}{R}\frac{\partial p}{\partial \varphi} + \eta \frac{\partial^2 u}{\partial y^2} - j_z B_y, \qquad z: \quad 0 = -\frac{\partial p}{\partial z} + \eta \frac{\partial^2 w}{\partial y^2}. \tag{1}$$

Ohm's law in z-direction is given by

$$j_z = \sigma \left(E_z + u B_y\right). \tag{2}$$

p is the pressure, u and w are the tangential and axial velocities, j_z is the current density in axial direction, η is the viscosity and σ the conductivity of the fluid.

We introduce dimensionless variables (denoted by an overbar) and parameters [4] where M_y is the well–known Hartmann number and ψ, ϵ correspond to $R - r, e$. Integration of the balance of momentum in φ-direction leads in connection with Eq. (2) and the boundary conditions $\bar{u}(\bar{y} = 0) = 1$ and $\bar{u}(\bar{y} = \bar{h}) = 1$ ($\bar{h} = 1 + \epsilon \cos(\varphi)$ describes the dimensionless film thickness) to the velocity component

$$\begin{aligned} \bar{u}(\varphi, \bar{y}) \;=\; & \left[\frac{1}{M_y^2}\frac{\partial \bar{p}}{\partial \varphi} + \frac{\bar{E}_z}{M_y}\right]\Bigg[\cosh(M_y\bar{y}) - \sinh(M_y\bar{y})\coth(M_y\bar{h}) \\ & + \frac{\sinh(M_y\bar{y})}{\sinh(M_y\bar{h})} - 1\Bigg] + \cosh(M_y\bar{y}) \\ & - \sinh(M_y\bar{y})\coth(M_y\bar{h}) + \frac{\sinh(M_y\bar{y})}{\sinh(M_y\bar{h})}. \end{aligned} \tag{3}$$

Integrating $\bar{u}$ in y-direction, yields the flow rate $\bar{q}_\varphi = \int_0^{\bar{h}} \bar{u}\, d\bar{y}$. Differentiating $\bar{q}_\varphi$ with respect to φ and expanding the result into a Taylor series with respect to M_y yields an approximation

$$\frac{\partial \bar{q}_\varphi}{\partial \bar{\varphi}} \approx M_y \bar{E}_z \left[-\frac{1}{4}\bar{h}^2 + \frac{1}{24} M_y^2 \bar{h}^4 \right] \bar{h}' + \left[1 - \frac{1}{12} M_y^2 \bar{h}^2 \right] \bar{h}'. \tag{4}$$

for small Hartmann numbers M_y. With the boundary conditions $\bar{w}(\bar{y}=0)=0$ and $\bar{w}(\bar{y}=\bar{h})=0$, the integration of the balance of momentum in z-direction leads to

$$\bar{w}(\varphi, \bar{y}) = \frac{1}{2} \left[\frac{R}{a} \frac{\partial \bar{p}}{\partial \bar{z}} + M\ \bar{j}_y \right] \left(\bar{y}^2 - \bar{h}\ \bar{y} \right). \tag{5}$$

The dimensionless flow rate $\bar{q}_z$ is found to be

$$\bar{q}_z = \int_0^{\bar{h}} \bar{w}\, d\bar{y} = -\frac{\bar{h}^3}{12} \left[\frac{R}{a} \frac{\partial \bar{p}}{\partial \bar{z}} + M\ \bar{j}_y \right]. \tag{6}$$

The continuity equation requires

$$\frac{a}{R} \frac{\partial \bar{q}_\varphi}{\partial \varphi} + \frac{\partial \bar{q}_z}{\partial \bar{z}} = 0. \tag{7}$$

Making use of the short bearing approximation $\frac{\partial \bar{p}}{\partial \varphi} \ll \frac{\partial \bar{p}}{\partial z}$ (see e.g. [6]), an integration in z-direction of the continuity equation with the boundary conditions $\bar{p}(\bar{z}=1) = \bar{p}(\bar{z}=-1) = 0$ results in the pressure field

$$\bar{p} = \left(\frac{a}{R}\right)^2 \frac{6}{\bar{h}^3} \frac{\partial \bar{q}_{\varphi,1}}{\partial \bar{\varphi}} (\bar{z}^2 - 1) + \left(\frac{a}{R}\right)^2 \frac{6}{\bar{h}^3} \frac{\partial \bar{q}_{\varphi,2}}{\partial \bar{\varphi}} (\bar{z}^2 - 1). \tag{8}$$

The first summand $\bar{p}_1$ is the pressure generated by the electric field and the second one, $\bar{p}_2$, is the pressure created by the tangential motion with $\dot{\delta}$. By integrating $\bar{p}_1$ over the bearing surface, one gets the tangential and radial component of the dimensionless load

$$\begin{aligned} S_{E,\delta} &= \frac{1}{4} \int_0^{\pi} \int_{-1}^{1} \bar{p}_1\ \sin(\varphi)\, d\bar{z}\, d\varphi \\ &= \frac{\pi}{2} \left(\frac{a}{R}\right)^2 \frac{M_y \bar{E}_z(\bar{t})}{\epsilon \left(1-\epsilon^2\right)^{\frac{3}{2}}} \left[\left(1-\epsilon^2\right)^2 - \left(1-\epsilon^2\right)^{\frac{3}{2}} \right], \end{aligned} \tag{9}$$

$$S_{E,r} = \frac{1}{4}\int_0^{\pi}\int_{-1}^{1} \bar{p}_1 \cos(\varphi)\, d\bar{z}\, d\varphi = \frac{1}{36}\left(\frac{a}{R}\right)^2 \frac{M_y \bar{E}_z(\bar{t})}{\epsilon\left(1-\epsilon^2\right)^2}\Bigg[72\epsilon^3 - 18\left(1-\epsilon^2\right)^2 \ln\frac{(1-\epsilon)}{(1+\epsilon)} - 36\epsilon\left(1-\epsilon^2\right)^2\Bigg]. \quad (10)$$

Similarly, the tangential and radial component of the dimensionless load due to $\bar{p}_2$ are derived:

$$S_{\dot{\delta},\delta} = \frac{1}{4}\int_0^{\pi}\int_{-1}^{1} \bar{p}_2 \sin(\varphi)\, d\bar{z}\, d\varphi = \frac{\pi}{24}\left(\frac{a}{R}\right)^2 \frac{1}{\epsilon\left(1-\epsilon^2\right)^{\frac{3}{2}}}\Bigg[12\epsilon^2 + 6M_y^2\left(1-\epsilon^2\right)^2 - 6M_y^2\left(1-\epsilon^2\right)^{\frac{3}{2}}\Bigg], \quad (11)$$

$$S_{\dot{\delta},r} = \frac{1}{4}\int_0^{\pi}\int_{-1}^{1} \bar{p}_2 \cos(\varphi)\, d\bar{z}\, d\varphi = \frac{1}{36}\left(\frac{a}{R}\right)^2 \frac{1}{\epsilon\left(1-\epsilon^2\right)^2}\Bigg[72\epsilon^3 - 9M_y^2\left(1-\epsilon^2\right)^2 \ln\frac{(1-\epsilon)}{(1+\epsilon)} - 18M_y^2\epsilon\left(1-\epsilon^2\right)^2\Bigg]. \quad (12)$$

The pressure distribution due to the radial motion of the shaft with $\dot{\epsilon}$ is in the case of the short bearing not affected by the electric and magnetic field. As shown in [4,5], the dimensionless load S_V is given by

$$S_V^+ = -\frac{4(a/R)^2}{\left(1-\epsilon^2\right)^{\frac{5}{2}}}\left[\frac{3\epsilon}{2}\sqrt{1-\epsilon^2} + (1+2\epsilon^2)\left(\frac{\pi}{2} - \arctan\sqrt{\frac{1-\epsilon}{1+\epsilon}}\right)\right] \quad (13)$$

for $\dot{\epsilon} > 0$ and

$$S_V^- = -\frac{4(a/R)^2}{\left(1-\epsilon^2\right)^{\frac{5}{2}}}\left[\frac{-3\epsilon}{2}\sqrt{1-\epsilon^2} + (1+2\epsilon^2)\arctan\sqrt{\frac{1-\epsilon}{1+\epsilon}}\right] \quad (14)$$

for $\dot{\epsilon} < 0$. Now, the equations of motion for the shaft can be derived. Note that the radial components $S_{E,r}$ and $S_{\dot{\delta},r}$ are always oriented in negative $\vec{\mathbf{e}}_r$-direction. The direction of $S_{E,\delta}$ oscillates according to the external electric field. The tangential load $S_{\dot{\delta},\delta}$ acts like a damping force and therefore against the tangential motion. We assume that gravitation acts in negative y-direction. The equations of motion in radial and tangential direction are then given by [4]

$$r: \quad \epsilon'' - \epsilon\cdot\delta'^2 = -\nu\left[|S_{E,r}| + |S_V^{\pm}|\cdot\epsilon' + |S_{\dot{\delta},r}|\cdot|\delta'|\right] - \bar{g}\cdot\sin\delta, \quad (15)$$

$$\delta: \quad \epsilon\cdot\delta'' + 2\epsilon'\cdot\delta' = -\nu\left[S_{E,\delta} + |S_{\dot{\delta},\delta}|\cdot\delta'\right] - \bar{g}\cdot\cos\delta \quad (16)$$

with $\nu = \dfrac{4aR\eta}{\psi^2 m\Omega e}$ and $\bar{g} = \dfrac{g}{\Omega^2 e}$, where m is the mass of the shaft and g the constant of gravitation.

The equations (14) and (15) are coupled, nonlinear ordinary differential equations with time-dependent coefficients. There exists no rest position $\epsilon = \delta = 0$. A linearization and a classical stability analysis is therefore impossible. Hence, the system has been solved numerically using the Runge-Kutta-Fehlberg-4(5)-method. Figure 2 shows the results of the simulation. As can be seen, the trajectory reaches a stable limit cycle which shape resembles the horizontal number 8. Simulations have been carried out for various parameter data. For realistic system parameters, the trajectories always reached stable limit cycles. Instabilities or chaotic vibrations have only been detected for unrealistic data.

As a second case, the externally applied magnetic field is now oriented in axial direction. The journal and the bearing are assumed to be ideal conductors, $V_y(t) = \hat{V}_y \cos(\Omega t)$ is the externally applied terminal voltage between the journal and the bearing. As shown in [5], the balance of momentum in φ- and z-direction are now given by

$$\varphi : 0 = -\frac{1}{R}\frac{\partial p}{\partial \varphi} + \eta \frac{\partial^2 u}{\partial y^2} + j_y B_z, \qquad z : 0 = -\frac{\partial p}{\partial z} + \eta \frac{\partial^2 w}{\partial y^2}, \tag{17}$$

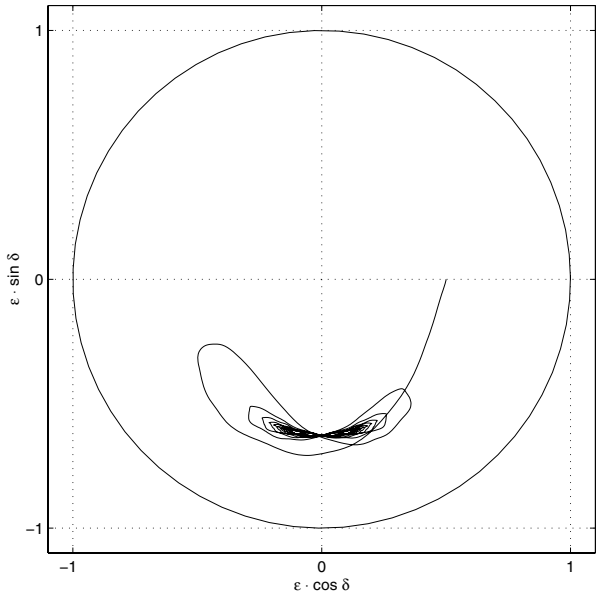

Figure 2. Shaft motion under axial oscillating electric field; trajectory of the center of the shaft; parameters: $\hat{\bar{E}}_z = 2$, $M_y = 0.5$, $\frac{a}{R} = \frac{1}{8}$, $\nu = 0.775$, $\bar{g} = 0.013$.

and Ohm's law in y-direction reads

$$j_y = \sigma \left(E_y - u\ B_z \right). \tag{18}$$

A similar analysis as in the previous section leads to the components of the dimensionless load

$$S_{E,\delta} = -\left(\frac{a}{R}\right)^2 \frac{\pi M_z \bar{V}_y(\bar{t})}{3\epsilon \left(1-\epsilon^2\right)^{\frac{3}{2}}} \left[\left(1-\epsilon^2\right) + \left(1-\epsilon^2\right)^{\frac{3}{2}} \right], \tag{19}$$

$$S_{E,r} = \left(\frac{a}{R}\right)^2 \frac{M_z \bar{V}_y(\bar{t})}{3\epsilon \left(1-\epsilon^2\right)^2} \left[\left(1-\epsilon^2\right)^2 \ln \frac{(1-\epsilon)}{(1+\epsilon)} + 2\epsilon \left(1-\epsilon^2\right) \right], \tag{20}$$

$$S_{\dot{\delta},\delta} = \frac{\pi (a/R)^2}{4\epsilon \left(1-\epsilon^2\right)^{\frac{3}{2}}} \left[2\epsilon^2 + M_z^2 \left(1-\epsilon^2\right) - M_z^2 \left(1-\epsilon^2\right)^{\frac{3}{2}} \right], \tag{21}$$

$$S_{\dot{\delta},r} = -\left(\frac{a}{R}\right)^2 \frac{1}{4\epsilon \left(1-\epsilon^2\right)^2} \left[8\epsilon^3 + M_z^2 \left(1-\epsilon^2\right)^2 \ln \frac{(1-\epsilon)}{(1+\epsilon)} + 2M_z^2 \epsilon \left(1-\epsilon^2\right)^2 \right]. \tag{22}$$

The equations of motion are given by (14) and (15). As in the case of the axial electric field, the trajectory reaches a stable limit cycle. Compared with the result for the first case, the amplitude is smaller.

3. Slider Bearing

In this section, we consider the slider bearing shown in Figure 3. The bearing is fixed and the slider can only move in y-direction.

In a first case, slider and bearing are assumed to be perfect insulators. The magnetic field is applied in y-direction, the harmonically oscillating electric field $E_z = \hat{E}_z \cos(\Omega t)$ is oriented in z-direction. According to the journal bearing, the film thickness is assumed to be $h = \Delta r + e \cos\varphi$, so that results from the chapter before (case 1) can be used. The slider has the length $L = 2\pi R$ and the breadth $b = 2a$. Again, appropriate dimensionless variables and parameters are introduced. The balance of momentum in φ- and z-direction and Ohm's law in z-direction are given by Eq. (1) and Eq. (2). Integration with respect to the boundary conditions $\bar{u}(\bar{y}=0) = 0$ and $\bar{u}(\bar{y}=\bar{h}) = 0$ yields the velocity component $\bar{u}$. Integration of $\bar{u}$ over $\bar{y}$ leads to the dimensionless flow rate in φ-direction

$$\bar{q}_\varphi = \frac{1}{M_y^3} \left[\frac{\partial \bar{p}}{\partial \varphi} + M_y\ \bar{E}_z(t) \right] \left[2\frac{\left(\cosh(M_y\bar{h}) - 1\right)}{\sinh(M_y\bar{h})} - (M_y\bar{h}) \right]. \tag{23}$$

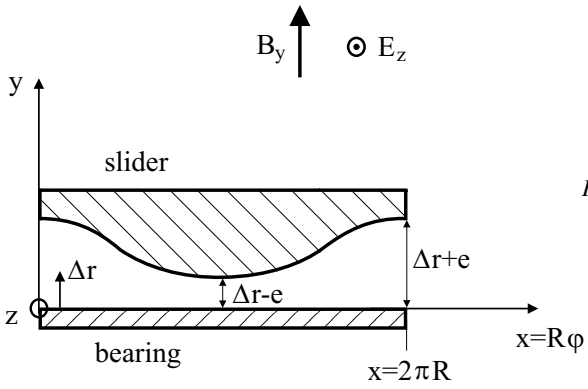

Figure 3. Slider bearing

A Taylor series expansion with respect to M_y leads for small Hartmann numbers M_y the approximation

$$\frac{\partial \bar{q}_\varphi}{\partial \bar{\varphi}} \approx M_y \bar{E}_z(t) \left[-\frac{1}{4}\bar{h}^2 + \frac{1}{24} M_y^2 \bar{h}^4 \right] \bar{h}'. \tag{24}$$

The dimensionless flow rate in z-direction is given by Eq. (6). With the continuity equation (7) and the boundary conditions $\bar{p}(\bar{z} = -1) = \bar{p}(\bar{z} = 1) = 0$, the pressure distribution is found to be

$$\bar{p} = \left(\frac{a}{R}\right)^2 \frac{6}{\bar{h}^3} \frac{\partial \bar{q}_\varphi}{\partial \varphi} (\bar{z}^2 - 1). \tag{25}$$

The dimensionless load is then determined by

$$S_y = \int_0^\pi \int_{-1}^{1} \bar{p}\, d\bar{z}\, d\varphi = 2 \left(\frac{a}{R}\right)^2 M_y \bar{E}_z(t) \left[\ln \frac{(\bar{\Delta}r - 1)}{(\bar{\Delta}r + 1)} + \frac{1}{3} M_y^2 \bar{\Delta}r \right]. \tag{26}$$

Since the fluid is assumed to be incompressible, negative pressure is physically impossible. Hence, we integrate only over the possitive part of $\bar{p}$, i.e., from 0 to π. S_y is the load due to the oscillating electric field. Next, we consider the load due to the motion of the slider in y-direction, i.e., the load due to squeezing. The calculation for the slider bearing is similar to that for the journal bearing. Details can be found in [4]. The result is given by

$$S_{y,V} = 16 \left(\frac{a}{R}\right)^2 \bar{\Delta}r' \frac{\pi (2\bar{\Delta}r^2 + 1)}{(\bar{\Delta}r^2 - 1)^{5/2}} \quad \text{with} \quad \bar{\Delta}r' = \frac{\partial \bar{\Delta}r}{\partial \bar{t}}. \tag{27}$$

Formula (27) is only valid for $\bar{\Delta}r' < 0$, i.e., for the motion of the slider in negative y-direction. For $\bar{\Delta}r' > 0$, $S_{y,V}$ is assumed to be zero. With these results, the equation of motion for the slider reads

$$\bar{\Delta}r'' - \kappa \left[|S_y(\bar{\Delta}r', \bar{t})| + |S_{y,V}| \frac{(|\bar{\Delta}r'| - \bar{\Delta}r')}{2\bar{\Delta}r'} \right] - \bar{G} = 0 \tag{28}$$

with the dimensionless parameters $\kappa = \dfrac{\eta Ra}{\psi^2 me\Omega}$ and $\bar{G} = \dfrac{g}{e\Omega^2}$, where m is the mass of the slider.

An analytical solution of the ordinary differential equation (27) cannot be found. Since the coefficients of this differential equation are time-dependent, there exists no rest position $\Delta r = const$. As in the case of the journal bearing, a numerical integration is necessary. The numerical integration shows a stable limit cycle. Simulations with other parameters also lead to a periodic limit cycle. Instabilities have not been detected.

The magnetic field is now applied in z-direction. Journal and bearing are assumed to be ideal conductors. $V_y(t) = \hat{V}_y \, cos(\Omega t)$ is the terminal voltage between the journal and the bearing. The balance of momentum in φ- and z-direction and Ohm's law in z-direction are given by the equations (17) and (18). The calculation of the dimensionless load resembles the calculation for the first case in this section and leads to the same equation of motion for the slider. The dimensionless load due to the oscillating terminal potential is now found to be

$$S_y = \int_0^{\pi} \int_{-1}^{1} \bar{p} \, d\bar{z} \, d\varphi = \frac{4}{9} \left(\frac{a}{R}\right)^2 \frac{M_z \bar{V}_y(t)}{(\bar{\Delta} r^2 - 1)} \left[-6 + M_z^2 (\bar{\Delta} r^2 - 1)\right]. \qquad (29)$$

$S_{y,V}$ is again given by (27). As in the case of the applied axial electric field, the trajectory reaches a stable limit cycle, no instabilities occur. Figure 4 shows a numerical result for case 2.

4. Conclusions

Vibrations of a rigid rotor supported in short MHD journal bearings with time-dependent electric fields were investigated. Furthermore, the oscillations of slider bearings have been examined. The equations for the fluid film were solved analytically. The oscillations of the shaft and the slider, respectively, were reduced to a system of nonlinear inhomogeneous ordinary differential equations with time-dependent coefficients. There exist no equilibrium positions so that a linearization and a classical stability analysis is impossible. The system is solved numerically. Basically, the dynamic system is capable to exhibit chaotic vibrations but for realistic system data, there exist stable oscillations with periodic limit cycles.

The analysis shows the possibility of a hydrodynamic levitation without a rotating shaft or tangentially moving slider, which is in the framework of the ordinary bearing theory not possible. Due to the simple controlling of the assembly, applications can be seen in several fields, among others in micro devices.

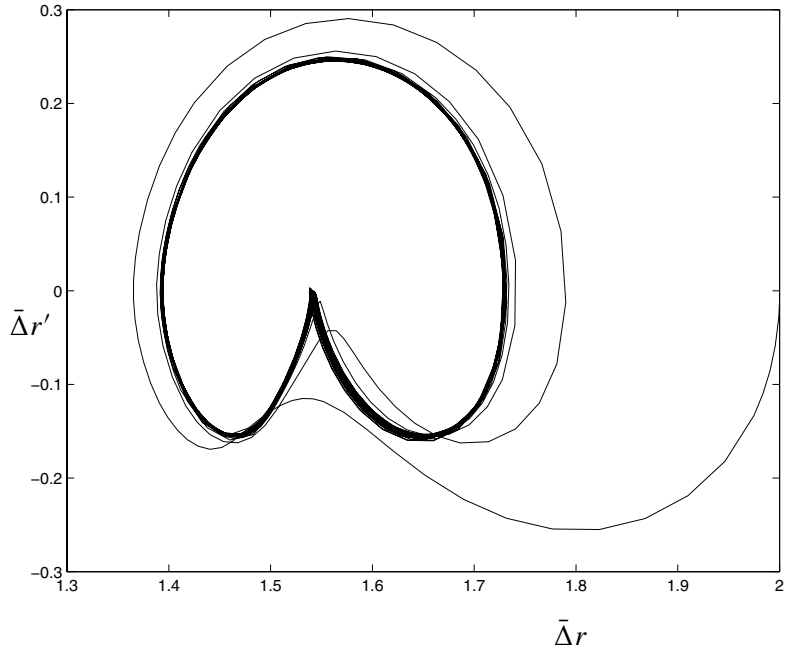

Figure 4. Slider bearing under oscillating transverse electric field; parameters: $\hat{\bar{V}}_y = 2$, $M_z = 0.5$, $\kappa = 2$, $\frac{a}{R} = \frac{1}{8}$, $\bar{G} = 0.88$.

References

[1] S.J. Dudzinsky, F.J. Young, and W. F. Hughes, "On the load capacity of the MHD journal bearing." *ASME* Paper No. 67-Lub-H.

[2] W.F. Hughes and F.J. Young, *The Electromagnetodynamics of Fluids*. Robert E. Krieger Publishing Company, Malabar, Florida, 1989.

[3] S. Kamiyama, "Magnetohydrodynamic journal bearing," *ASME* Paper No. 68-Lub-6.

[4] B. Schweizer, *Magnetohydrodynamische Schmierspaltströmung bei unendlich schmaler Lagergeometrie*, PhD thesis, Universität Karlsruhe, 2002.

[5] J. Wauer and B. Schweizer, "Analysis of short magnetohydrodynamic journal bearings," *Proceedings Iscorma-1, International Symposium on Stability Control of Rotating Machinery*, Lake Tahoe, 2001.

[6] A. Cameron, *The Principles of Lubrication*, London: Longmans Green 1966.

[7] F.W. Ocvirk, *Short Bearing Approximation for Full Journal Bearings*, NACA Technical Note 2808 (1952).

PARAMETRICALLY EXCITED MEMS-BASED FILTERS

Steven W. Shaw[1], Kimberly L. Turner[2], Jeffrey F. Rhoads[1], and Rajashree Baskaran[2]
[1]*Department of Mechanical Engineering, Michigan State University;* [2]*Department of Mechanical and Environmental Engineering, University of California - Santa Barbara*
shawsw@msu.edu

Abstract: In this paper we describe the dynamics of MEMS oscillators that can be used as frequency filters. The unique feature of these devices is that they use parametric resonance, as opposed to the usual linear resonance, for frequency selection. However, their response in the parametric resonance zone has some undesirable features from the standpoint of filter performance, most notably that their bandwidth depends on the amplitude of the input and the nonlinear nature of the response. Here we provide a brief background on filters, a MEMS oscillator that overcomes some of the deficiencies, and we offer a description of how one might utilize a pair of these MEMS oscillators to build a band-pass filter with nearly ideal stopband rejection. These designs are made possible by the fact that MEMS devices are highly tunable, which allows one to build in system features to achieve desired performance.

Key words: MEMS, parametric resonance, filters.

1. Introduction

As the demand for wireless communications technology continues to increase, so too does the demand for effective and efficient band-pass filters, as these devices, which pass signals with frequency components inside a specific bandwidth while attenuating those outside of it, are often integral components of such technology. While much research has been done on the design and performance of conventional electrical band-pass filters (for example, [1]), and their mechanical analogs (for example, [2]), the aforementioned demand for increased performance has led to a search for other alternatives. One that has shown early promise is to create microelectromechanical systems (MEMS) filters [3]. These micro-scale

G. Rega and F. Vestroni (eds.),
IUTAM Symposium on Chaotic Dynamics and Control of Systems and Processes in Mechanics, 137–146.

components are more desirable than their more conventional counterparts primarily due to their size, low power consumption, and ease of integration with electrical systems. Equally important is the fact that MEMS filters have been shown to exhibit quality (Q) factors as high as 80,000 (as reported in [4]). More relevant to the present work are the inherent parametric resonances that occur in certain types of MEMS, which are shown here to be potentially advantageous in filtering applications.

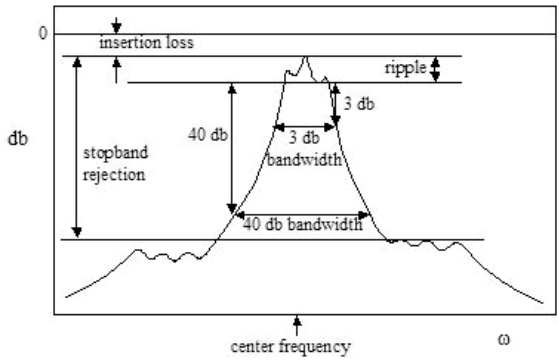

Figure 1. Key features of the transmission frequency response of a band-pass filter. (Adapted from [4])

2. Filter Basics

Here we highlight the key features to consider when designing a band-pass filter. Ideally, one would like a device that transmits a harmonic signal essentially intact if its frequency is in a prescribed bandwidth, and completely attenuates the signal if it is outside of the bandwidth. Virtually all filter designs make use of a chain of linear resonators, either electrical [1] or mechanical [2]. Figure 1 depicts a sample frequency response transmission function for such a filter, where the following features are noted:

– The center frequency of the passband.
– The bandwidth of the passband – the range of frequencies to be passed through the filter.
– The stopband attenuation – the amount by which the signal is reduced outside of the passband.
– The insertion loss – the drop-off in signal amplitude as it passes through the filter.

– The sharpness of the roll-off – the width of the frequency range between the edges of the passband and the stopband.
– The flatness of the passband response, which typically has ripples.

3. Parametric Resonance for Filtering

As previously mentioned, one of the interesting features of MEMS oscillators is that, when driven by non-interdigitated comb drives, such as those shown in Figure 2, they exhibit parametric resonances [5]. The existence of such resonances can be traced to the fact that the electrostatic driving and restoring forces acting on such a device result in a fluctuating effective stiffness. While the parametric instability caused by such fluctuations may be undesirable in many applications, the nearly instantaneous jumps that occur in the response amplitude when the parametric resonance is activated may prove to be highly beneficial for filtering, since they result in *nearly ideal stopband rejection* as well as an *extremely sharp response roll-off* outside of the resonance zone. Of course, the use of parametric instability for filtering is not without difficulties. Among the most obvious drawbacks are:
– The bandwidth depends on the excitation amplitude.
– There can exist non-trivial responses outside of the passband.
– There is a nonlinear input/output relationship.
– Higher order resonances may occur.

Fortunately, by employing a novel tuning scheme in conjunction with a specific logic implementation, the effects of most of these drawbacks can be largely overcome. We begin by describing the tuning for a single MEMS oscillator, and then turn to a design that makes use of two such devices.

4. Analysis of a Single MEMS Oscillator

In an attempt to gain a better understanding of the benefits and drawbacks of a parametrically excited MEMS band-pass filter, as well as how the drawbacks can be overcome, consider the response of a single DOF MEMS oscillator, such as the one depicted in Figure 2. This device consists of a backbone (essentially, the mass) suspended by folded beam springs which is activated by a pair of non-interdigitated comb drives, very similar to the devices considered in [6], [7] and [8].

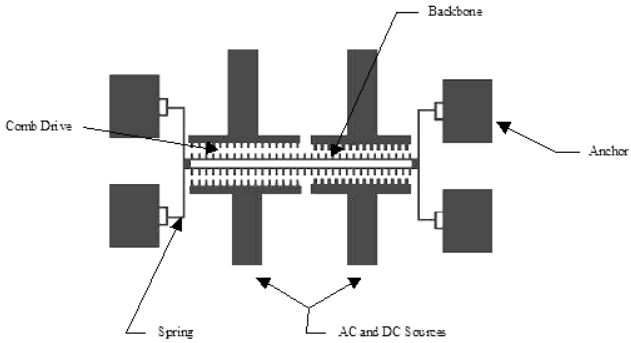

Figure 2. CAD drawing of a parametrically excited MEMS filter device.

The equation of motion for this device can be expressed as [7]:

$$m\ddot{x} + c\dot{x} + F_r(x) + F_{es}(x,t) = 0\,.$$

The elastic restoring force can be accurately modeled by a cubic function $F_r(x) = k_1 x + k_3 x^3$, where typically the system is mechanically hardening ($k_3 > 0$). The electrostatic driving and restoring forces are assumed to be generated by two separate, essentially frictionless, non-interdigitated comb drives, one providing a DC input voltage V_0 and the other driven by a square-rooted AC signal of amplitude V_A. Again, cubic functions in displacement, proportional to the square of the applied voltage, provide an accurate model [7]:

$$F_{es}(x,t) = \left(r_{10}x + r_{30}x^3\right)V_0^2 + \left(r_{1A}x + r_{3A}x^3\right)V_A^2\left(1+\cos(\omega t)\right).$$

Note that one can design combs such that any combination of signs on the r coefficients is possible (although their magnitudes are limited). Time is rescaled according to $\tau = \omega_0 t$, where $\omega_0 = (k_1/m)^{1/2}$, and the displacement is rescaled by a characteristic displacement, x_0, (for example, the length of the oscillator backbone), such that $\varepsilon^{1/2} z = x/x_0$, where ε is a scaling parameter introduced for the analysis. The result is a non-dimensional equation of motion for the oscillator of the form

$$z'' + 2\varepsilon\zeta z' + z\left(1 + \varepsilon\nu_1 + \varepsilon\lambda_1\cos(\Omega\tau)\right) + \varepsilon z^3\left(\chi + \nu_3 + \lambda_3\cos(\Omega\tau)\right) = 0$$

where $(\bullet)'$ denotes $d(\bullet)/d\tau$ and the nondimensional parameters are defined in a manner consistent with the above scaling. With this non-dimensional equation, the oscillator's response can be examined as system parameters

and inputs are varied. For example, the parametric resonance instability zone that exists in the V_A versus Ω parameter space is shown in Figure 3 (it is the boundary designated by $\rho = 0$) as created using both perturbation analysis (described below) and simulations.

As Figure 3 shows, the instability zone that exists for this particular oscillator is a 'wedge of instability' with its apex centered at a non-dimensional frequency of 2. In this case, the zero response is stable 'outside' of the wedge, while 'inside' of the wedge the trivial response is unstable, thereby leading to a non-zero response amplitude that is determined by the system nonlinearity. Of course, the response outside of the wedge may be zero or non-zero, depending on the damping, whether the system is hardening or softening, and on initial conditions. Another important feature to note here is that the frequency at which the filtering takes place is at *twice* the natural frequency of the device, and therefore one gets double the filter frequency as compared with using the same device as a filter using direct excitation. We now turn to addressing the amplitude dependent nature of the bandwidth.

5. Tuning for Constant Frequency Instability

As shown, the frequency at which the oscillator is activated depends on the amplitude of the alternating voltage. However, this can be overcome by employing the following tuning scheme, wherein the natural frequency of the oscillator is made to depend on the amplitude of the excitation, by varying the linear electrostatic stiffness. To begin, a proportionality constant, α, is defined that relates the DC voltage input to the AC voltage amplitude, such that $V_0 = \alpha V_A$, which results in a linear electrostatic stiffness that depends on α, the r_1's, k_1, and the input voltage V_A. Substituting this, as well as the other redefined coefficients, back into the non-dimensional equation of motion results in a modified equation of motion for the oscillator,

$$z'' + z = -\varepsilon\left(2\varsigma z' + zA\left(\rho + \cos(\Omega t)\right) + z^3\left(\chi + \nu_3 + \lambda_3 \cos(\Omega\tau)\right)\right)$$

where the linear excitation amplitude is redefined such that $A = \lambda_1$ and a new tuning parameter ρ is introduced which relates the effective electrostatic linear stiffness to the amplitude of excitation. It is related to the designer-selected parameters via,

$$\rho = \frac{\nu_1}{\lambda_1} = 1 + \frac{r_{10}\alpha^2}{r_{1A}}.$$

This parameter allows for the distortion of the instability zone, by changing the linear natural frequency $\omega_n = (1+\varepsilon\rho A)^{1/2}$ in a manner that depends on A. The result of this tuning is a rotation of the wedge of instability; see Figure 3. In particular, for $\rho > 0$ the wedge rotates clockwise and for $\rho < 0$ it rotates counterclockwise. Also, perturbation theory and simulations, created using design parameters similar to those in [6-8], have verified that by selecting $\rho = 1/2$ the left stability boundary becomes essentially vertical, as shown in Figure 3, and, similarly, by selecting $\rho = -1/2$ the right stability boundary becomes essentially vertical.

The $\rho = 1/2$ case makes the oscillator behave like a high pass switch, while the $\rho = -1/2$ case constitutes a low pass switch. However, one must take into account the nonlinear nature of the response, and the fact that there may exist nontrivial responses outside of the instability zone. Also, the response, once activated, may not exist for all frequencies above or below the desired switch frequency. These issues, which depend on the system nonlinearities, are considered subsequently. Also note that the presence of damping creates a threshold voltage level above which the device will function, due to the parametric instability. This is not a major concern here, though, since the damping levels of these devices are anticipated to be very low (with Q's in the thousands). The main point here is that this tuning capability makes it theoretically possible to create amplitude independent switches over a reasonable range of input voltages.

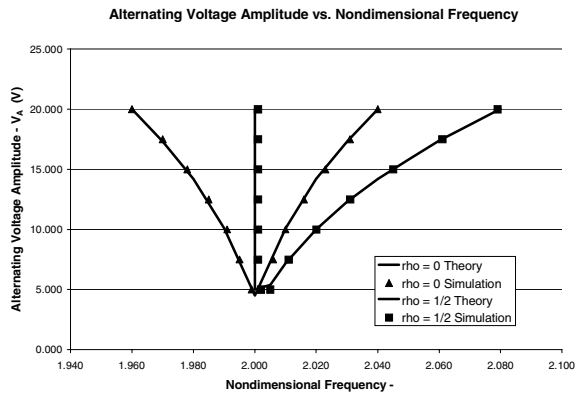

Figure 3. Region of parametric instability in the A - Ω parameter space; $\rho = 0$ and $\rho = 1/2$.

6. Tuning the Nonlinearity

Another desirable feature of MEMS devices is that one can tune the system nonlinearity using the nonlinear nature of the electrostatic forces exerted by the comb drives [6, 7]. This is crucial for achieving the desired behavior of non-trivial solutions outside of the passband. Specifically, the cubic nonlinearity of each oscillator can be specified, and it is desired that the high pass oscillator (with $\rho = 1/2$) have a hardening behavior, so that no nontrivial responses exist below the switch frequency. Similarly, the low pass oscillator (with $\rho = -1/2$) should have softening behavior. In order to consider these responses, we turn to the equations of motion and examine the response using a perturbation method.

The system's averaged equations are given by

$$a' = \frac{1}{8} a\varepsilon\left[-8\varsigma + \left(2A + a^2\lambda_3\right)\sin(2\psi)\right]$$

$$\psi' = \frac{1}{8}\varepsilon\left[3a^2(\chi + \nu_3) + 4A\rho - 4\sigma + 2\left(A + a^2\lambda_3\right)\cos(2\psi)\right]$$

where a is the response amplitude of the averaged solution, ψ is the phase of the averaged solution, and σ is a detuning parameter defined such that $\Omega_0 = 2+\varepsilon\sigma$. Note that the form of these equations is not the typical nonlinear Mathieu equation, due to the presence of the parametric excitation that acts on the nonlinearity, which affects the nature of the nonlinear responses. Using these equations the theoretical instability curves shown in Figure 3 were generated. Likewise, these equations can be solved to produce approximate analytical response curves, examples of which are shown in Figure 4 for a $\rho = 1/2$ oscillator with a hardening nonlinearity. Simulation data is also shown, verifying the accuracy of the response predictions, which is especially good at low input voltages. The key feature here is that the system behaves like a high pass filter with a very sharp transition at a frequency that is independent of the input voltage amplitude. Note that no secondary instabilities that would lead to more complicated dynamics, such as chaos, are predicted by analysis or seen in simulations. If this occurred, an upper bound on the input voltage may need to be imposed. In addition, it should be noted that any difficulties that may arise due to the overlapping of the nontrivial response branch and a stable trivial solution are negated through the logic implementation described below.

As shown in previous works [6-8] the aforementioned nonlinear tuning can be accomplished by varying the oscillator's cubic electrostatic stiffness. In the proposed design this may be done in a couple of ways: by altering the AC/DC voltage relationship (although the parameter α is used here to set the

value of ρ, and thus another set of combs may be required), or by selective design of the combs to achieve the desired values for the nonlinear electrostatic coefficients (r_{3O} and r_{3A}). These are current research topics under consideration.

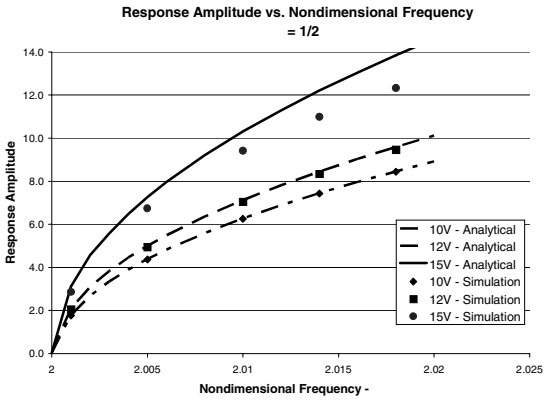

Figure 4. Sample response curves – amplitude vs. frequency.

7. Combining Two Oscillators into a Band-Pass Filter

A possible implementation scheme for a band-pass filter is represented in Figure 5. In this system, the idea is to generate a band-pass filter with a center frequency of Ω_0 and a bandwidth of $\Delta\Omega_0$, where Δ represents a small number that prescribes the bandwidth to a percentage of the center frequency. To accomplish this, two oscillators, which are ideally isolated to avoid internal resonances, are employed, one with $\rho = 1/2$ and a hardening nonlinearity, which will be designated as 'H', for high pass, and another with $\rho = -1/2$ and a softening nonlinearity, which will be designated as 'L', for low pass. To develop the specified bandwidth in the final system, these oscillators must be specially tuned so that the apexes of each of the respective wedges are slightly shifted. Specifically, the zero-voltage linear frequencies are designed such that the H oscillator's frequency is $\Delta\Omega_0/2$ below the center frequency and L's is $\Delta\Omega_0/2$ above it.

We now take the two oscillators, tuned using the electrostatic linear and nonlinear tunings described previously, and also tune their zero-voltage frequencies as described immediately above, so that the desired 'H' and 'L' characteristics are achieved. These are then incorporated into a MEMS with the logic indicated in Figure 5 below.

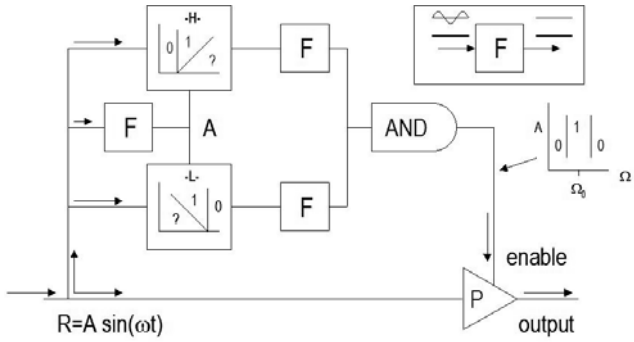

Figure 5. Hardware implementation scheme.

This filter system is designed to work as follows. A harmonic signal R is input into the system. This input is used to drive the two oscillators, and, in addition, its amplitude A is determined using block F (an AC to DC converter). A is used as an input to tune the oscillators through the parameters $\rho = \pm 1/2$. The oscillators are designated by blocks H and L, each of which shows a simple logic diagram in A - Ω space, showing 0 where the response must be trivial, 1 where it must be nontrivial, and ? where it may be either, depending on parameters and initial conditions. After each oscillator does its respective filtering, its output is sent to another block F which converts the output signal into a constant voltage, say unity or zero, depending on the results of the filtering. The two resulting voltages are then fed into an AND block which produces a zero voltage unless the frequency is in the desired passband. The output of the AND block provides a signal to an enabling device P which allows the signal to pass only if it sees a nonzero enabling signal. The amplitude dependent linear tuning makes the edges of the stopbands independent of the voltage amplitude (above a certain small threshold), and the nonlinear tuning and the logic ensure that the output of the AND gate is as desired. This produces a MEMS filter with ideal stopband rejection and essentially infinitely sharp roll-off characteristics.

8. Conclusion

This paper outlines a means of achieving a band-pass filter using parametric resonance in MEMS. The main features of the system are achieved through the highly tunable nature of these devices. However, several topics remain to be resolved for the final realization of such a filter. First, the input/output relationship for parametric resonance is nonlinear; while the logic shown in Figure 5 may overcome this obstacle, simpler logic may be possible if one can somehow ‘linearize’ this relationship. Also, the

existence of higher order parametric resonances remains an issue [5], although this issue may be addressed by specifying the damping level such that they do not occur over operational ranges of voltage. In addition, the insertion loss of such a device must be considered to ensure that the overall signal drop-off is acceptable. Finally, since the input considered here is idealized, future works will need to consider more realistic inputs, including those which feature noise. The implementation of the linear and nonlinear tuning described herein in an actual device is currently underway. The ultimate goal is, of course, the integration of the two MEMS oscillators, with the described tuning features, and the logic of Figure 5 onto a single filter chip.

Acknowledgements

This work is supported by the AFOSR under contract F49620-02-1-0069.

References

[1] J.T. Taylor and Q. Huang. (eds.), *CRC Handbook of Electrical Filters*, CRC Press, Boca Raton, 1997.

[2] R.A. Johnson, M. Borner, and M. Konno, "Mechanical Filters – A Review of Progress," *IEEE Transactions of Sonics and Ultrasonics,* SU-18, 3, 1971.

[3] C.T.-C. Nguyen, "Micromechanical Filters for Miniaturized Low-Power Communications," *Proceedings of SPIE*: Smart Structures and Materials (Smart Electronics and MEMS), Newport Beach, California, March 1-5, 1999.

[4] K. Wang, and C.T.-C. Nguyen, "High-Order Micromechanical Electronic Filters," *Proceedings, 1997 IEEE International Micro Electro Mechanical Workshop*, Nagoya, Japan, 25-30.

[5] K.L. Turner, S.A. Miller, P.G. Hartwell, N.C. MacDonald, S.H. Strogatz, and S.G. Adams, "Five Parametric Resonances in a Microelectromechanical System," *Nature*, 396, 149-152, 1998.

[6] S.G. Adams, F. Bertsch, and N.C. MacDonald, "Independent Tuning of Linear and Nonlinear Stiffness Coefficients," *Journal of Microelectromechanical Systems,* 7 (2), 172-180, 1998.

[7] W. Zhang, R. Baskaran, and K.L. Turner, "Effect of Cubic Nonlinearity on Auto-parametrically Excited MEMS Mass Sensor," *Sensors & Actuators A*, 3758, 2002.

[8] W. Zhang, R. Baskaran, and K.L. Turner, "Tuning the Dynamic Behavior of Parametric Resonance in a Micro Mechanical Oscillator," *Applied Physics Letters*, 82, 130, 2003.

THE CHAOTIC OSCILLATIONS OF HIGH-SPEED MILLING

G. Stépán*, R. Szalai*, S. J. Hogan**
** Department of Applied Mechanics, Budapest University of Technology and Economics*
Budapest H-1521, Hungary
stepan@mm.bme.hu, szalai@mm.bme.hu
***Department of Engineering Mathematics, University of Bristol*
Bristol BS8 1LN, England
S.J.Hogan@bristol.ac.uk

Abstract: In case of highly interrupted machining, the ratio of time spent cutting to not cutting can be considered as a small parameter. In these cases, the classical regenerative vibration model playing an essential role in machine tool vibrations breaks down to a simplified discrete mathematical model. The linear analysis of this discrete model leads to the recognition of the doubling of the so-called instability lobes in the stability charts of the machining parameters. This kind of lobe doubling is related to the appearance of period doubling vibration or flip bifurcation. This is a new phenomenon occurring primarily in low-immersion high-speed milling along with the classical self-excited vibrations or secondary Hopf bifurcations. The present work investigates the nonlinear vibrations in case of period doubling and compares this to the well-known subcritical nature of the Hopf bifurcations in turning processes. Also, the appearance of chaotic oscillation 'outside' the unstable period-two oscillation is proved for low-immersion high-speed milling processes.

Key words: Flip bifurcation, high-speed milling, time delay.

G. Rega and F. Vestroni (eds.),
IUTAM Symposium on Chaotic Dynamics and Control of Systems and Processes in Mechanics, 147–158.

1. Introduction

High-speed milling is one of the most efficient cutting processes nowadays. In the process of optimizing this technology, it is a challenging task to explore its special dynamical properties, including the stability conditions of the cutting process, and the nonlinear vibrations that may occur near to the stability boundaries. These dynamical properties are mainly related to the underlying regenerative effect in the same way as it is in case of the classical turning process having complicated but well-studied and understood stability properties. Still, some new phenomena appear for low-immersion milling as predicted by Davies et al. (2000, 2002) and Bayly et al. (2001). Insperger and Stépán (1999, 2000a,b) also described these phenomena in case of milling independently from the immersion or speed characteristic of the milling processes.

High-speed milling has specific properties like small tool diameter, low number of milling teeth (2, 3 or 4), and high cutting speed. Together, all these lead to the so-called highly interrupted cutting. This means that, most of the time, none of the tool cutting edges is in contact with the work-piece, while cutting occurs during those short time-intervals only when one of the teeth hits the workpiece. Actually, the time spent cutting to not cutting may be less than 10%, so it can often be considered as a small parameter.

For the case of highly interrupted cutting, the short contact periods between the tool and the workpiece can be described as kind of impacts, where the linear impulse coming from the cutting force contains, again, a past-effect, i.e., the regenerative effect still has a central role, even in high-speed milling. The corresponding mathematical model is similar to that of an impact oscillator, but it also involves time delay. The governing equations of the tool free-flights and the subsequent impacts can be solved analytically, and a closed form nonlinear Poincare mapping can be constructed.

In the subsequent sections, the simplest possible, but still nonlinear highly interrupted cutting model is described. The resulting discrete mathematical model is two-dimensional and nonlinear. The linear stability analysis is presented in the same form as it appears in the specialist literature. The bifurcation analysis is carried out along the stability limit related to period doubling bifurcation. This requires center manifold reduction and normal form transformation. The tedious algebraic work can be carried out in closed form and it leads to a phenomenon similar to the one experienced in the case of the Hopf bifurcation in the turning process.

It is suspected that chaotic oscillations may occur for those technological parameters of turning where the stationary cutting is unstable, or unstable periodic orbits arise ‘around’ stable stationary cutting (Stépán, 2000). In a similar way, chaotic oscillations are experienced also for high-speed milling. The existence and the structure of these chaotic oscillations are proved and explained for the introduced nonlinear discrete model of high-speed milling

in those parameter domains where the stationary cutting loses its stability via period doubling bifurcation.

2. Mechanical Model

The simplest possible one degree-of-freedom (DOF) model of highly interrupted cutting is presented in Figure 1 (for a 2 DOF model see Altintas and Budak, 1995). Here, the number of the cutting edges is one only, and it is in contact with the workpiece material periodically with time period τ. The time it spends in contact is $\rho\tau$ where $\rho<<1$ is the ratio of time spent cutting to not cutting. Clearly, the time delay τ is the time period of the tool revolution over the number z of cutting edges for cases of more edges than one. If Ω denotes the tool angular velocity then $\tau=2\pi/(z\Omega)$.

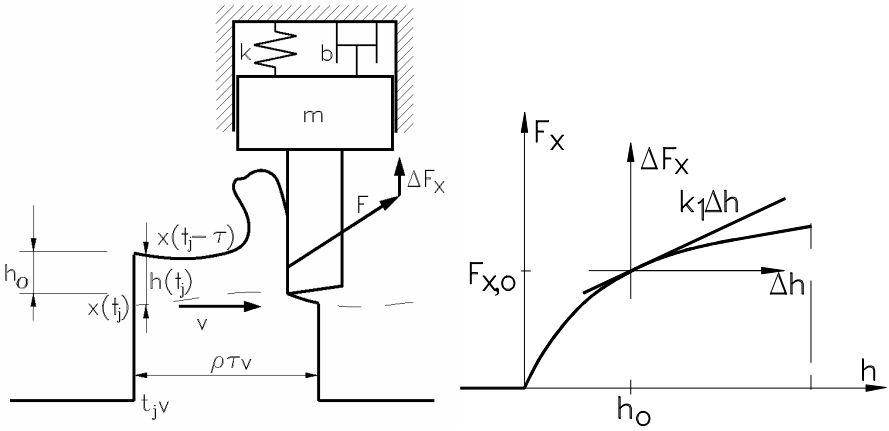

Figure 1. Mechanical model of highly interrupted cutting, and nonlinear cutting force

The elastic tool is characterized by the angular natural frequency $\omega_n = \sqrt{k/m}$, the relative damping factor $\varsigma = b/(2m\omega_n)$, and the frequency $\omega_d = \omega_n\sqrt{1-\zeta^2}$ of the damped oscillation.

The theoretical chip thickness is h_0. The actual chip thickness is either zero for no contact, or

$$h(t_j) = h_0 + x(t_j - \tau) - x(t_j)\ , \tag{1}$$

where $t_j - \rho\tau$ is the initial time instant of the j^{th} contact period between the tool and the workpiece (j=1,2,…). We consider that the contact time $\rho\tau$ is so

short that the position of the tool, and also the chip thickness, does not change during this time. This approximation is analyzed and justified by Davies et al. (2001), and confirmed experimentally by Bayly et al. (2001).

Thus, the equations of motion can be constructed for the two parts of the tool motion in the following way. For the free flight of the tool, we have

$$\ddot{x}(t) + 2\zeta\omega_n \dot{x}(t) + \omega_n^2 x(t) = 0, \quad t \in [t_j - \tau\,, t_j - \rho\tau) \tag{2}$$

with initial conditions

$$x_{j-1} = x(t_{j-1}) \approx x(t_{j-1} - \rho\tau), \quad v_{j-1} = \dot{x}(t_{j-1})\,, \tag{3}$$

where, again, we consider that the position of the tool does not change much during the short contact period. For the contact period, we have

$$\begin{aligned} m\ddot{x}(t) = -c\dot{x}(t) - kx(t) + F(x(t), x(t-\tau)) \approx \\ \approx F(x(t), x(t-\tau)) \end{aligned}, \quad t \in [t_j - \rho\tau\,, t_j) \tag{4}$$

where the usual condition of the classical impact theory is applied: all the forces except the contact ones (actually, except the cutting force) are negligible. The initial conditions are as follows

$$x_j = x(t_j - \rho\tau) \approx x(t_j), \quad v_j^- = \dot{x}(t_j - \rho\tau)\,. \tag{5}$$

The nonlinear cutting force can be calculated in accordance with the experimentally verified ¾ rule:

$$\begin{aligned} F(x(t), x(t-\tau)) = Kwh^{3/4}(t) = Kw(h_0 + x(t-\tau) - x(t))^{3/4} \approx \\ \approx Kw(h_0 + x_{j-1} - x_j)^{3/4}\,, \end{aligned} \tag{6}$$

where w is the chip width and K is an experimentally identified parameter. The Taylor series of this cutting force with respect to the chip thickness deviation $x_{j-1} - x_j$ assumes the form

$$\begin{aligned} F(x(t), x(t-\tau)) \approx F_0 + k_1(x_{j-1} - x_j) - \frac{1}{8h_0} k_1 (x_{j-1} - x_j)^2 + \\ + \frac{5}{96h_0^2} k_1 (x_{j-1} - x_j)^3 \end{aligned}$$

where the stationary cutting force F_0 and the so-called cutting coefficient k_1 assume the form

$$F_0 = Kwh_0^{3/4}, \quad k_1 = \frac{3}{4}\frac{Kw}{h_0^{1/4}}. \tag{7}$$

In addition, the nonlinear cutting force characteristics shown in Fig. 1 have an important non-smooth property for large oscillations: the cutting force becomes zero at negative chip thickness values. This means, that the delay-effect is switched off when the tool actually leaves the workpiece.

3. Nonlinear Discrete Map

The solution of the impact equation (4) for the time interval $\rho\tau$ assumes the form $m(v_j - \bar{v_j}) = \rho\tau F$, that is

$$v_j = \frac{\rho\tau}{m}F_0 + \frac{\rho\tau}{m}k_1(x_{j-1} - x_j) + \bar{v_j} - \frac{\rho\tau}{8mh_0}k_1(x_{j-1} - x_j)^2 + \\ + \frac{5\rho\tau}{96mh_0^2}k_1(x_{j-1} - x_j)^3, \tag{8}$$

where x_j and $\bar{v_j}$ can be calculated as a linear function of x_{j-1} and v_{j-1} by means of the well-known solution of the equation of motion (2) of the free damped oscillation of the tool with the initial conditions (3).

With the above-determined coefficients we can construct the nonlinear discrete model

$$\begin{bmatrix} x_j \\ v_j \end{bmatrix} = \mathbf{A}\begin{bmatrix} x_{j-1} \\ v_{j-1} \end{bmatrix} + \begin{bmatrix} 0 \\ \sum\limits_{h+k=2,3;\ h,k\geq 0} b_{hk}x_{j-1}^h v_{j-1}^k \end{bmatrix} + \begin{bmatrix} 0 \\ \frac{\rho\tau}{m}F_0 \end{bmatrix}, \tag{9}$$

where the coefficients b_{hk} are determined from Eqns. (2), (3) and (8), and

$$\mathbf{A} = \begin{bmatrix} \frac{e^{-\zeta\omega_n\tau}}{\sqrt{1-\zeta^2}}\cos(\omega_d\tau - \varepsilon) & \frac{e^{-\zeta\omega_n\tau}}{\omega_n\sqrt{1-\zeta^2}}\sin(\omega_d\tau) \\ -\frac{\omega_n e^{-\zeta\omega_n\tau}}{\sqrt{1-\zeta^2}}\sin(\omega_d\tau) + \frac{\rho\tau k_1}{m}\left(1 - \frac{e^{-\zeta\omega_n\tau}}{\sqrt{1-\zeta^2}}\cos(\omega_d\tau - \varepsilon)\right) & \frac{e^{-\zeta\omega_n\tau}}{\sqrt{1-\zeta^2}}\left(\cos(\omega_d\tau + \varepsilon) - \frac{\rho\tau k_1}{m\omega_n}\sin(\omega_d\tau)\right) \end{bmatrix}.$$

In the above formula, the phase angle satisfies $\tan\varepsilon = \zeta/\sqrt{1-\zeta^2}$.

4. Stability Chart

The linear stability analysis of stationary cutting is based on the characteristic equation of the linear part of the difference equation (9):

$$\det(\lambda\mathbf{I} - \mathbf{A}) = 0\,. \tag{10}$$

In stable cases, the characteristic multipliers $\lambda_{1,2}$ are located in the open unit disc of the complex plane. The stability boundaries in the stability chart of Fig. 2 are calculated from the condition

$$\left|\lambda_{1,2}\right| = 1\,. \tag{11}$$

The analysis of (10) with (11) shows that there are two kinds of loss of stability. The stability conditions are constructed with respect to the dimensionless parameters

$$z\tilde{\Omega} = z\frac{\Omega}{\omega_n} = \frac{2\pi}{\tau\omega_n}, \quad \tilde{w} = \frac{\rho k_1}{k} = \frac{\rho k_1}{m\omega_n^2} = \frac{3}{4}\frac{K\rho}{k\sqrt[4]{h_0}}w\ . \tag{12}$$

Neimark-Sacker (or secondary Hopf) bifurcation occurs when $\lambda_{1,2} = \exp(\pm i\varphi)$ at

$$\tilde{w}\big|_{cr} = \frac{\rho k_1\big|_{cr}}{m\omega_n^2} = -2\frac{\sqrt{1-\varsigma^2}}{\omega_n\tau}\frac{sh(\zeta\omega_n\tau)}{\sin(\omega_d\tau)}, \quad \omega_n\tau = \frac{2\pi}{z\tilde{\Omega}}. \tag{13}$$

Period doubling (or flip) bifurcation occurs when $\lambda_1 = -1$ at

$$\tilde{w}\big|_{cr} = \frac{\rho k_1\big|_{cr}}{m\omega_n^2} = \frac{\omega_d}{\omega_n^2\tau}\frac{ch(\zeta\omega_n\tau) + \cos(\omega_d\tau)}{\sin(\omega_d\tau)}, \quad \omega_n\tau = \frac{2\pi}{z\tilde{\Omega}}\ . \tag{14}$$

The bifurcations along the stability limits can be distinguished with the help of the dimensionless vibration frequencies of the self-excited vibrations above the stability chart of Fig. 2. The full structure of these frequencies is presented in Insperger et al. (2003) experimentally, too.

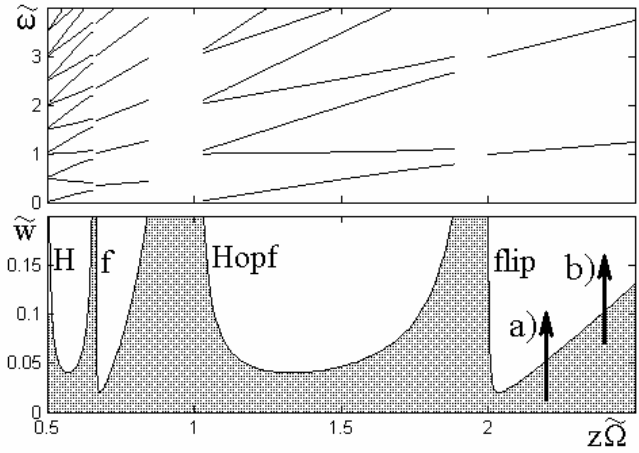

Figure 2. Stability chart of high-speed milling

5. Subcritical Bifurcations

At the stability boundary of period doubling vibrations, the eigenvalues of the coefficient matrix **A** are $\lambda_1 = -1, \quad \lambda_2 = \mathrm{e}^{-\zeta\omega_n\tau}\left(sh(\zeta\omega_n\tau) + \cos(\omega_d\tau)\right)$. With the help of the corresponding critical eigenvectors $\mathbf{s}_1$ and $\mathbf{s}_2$ of the matrix **A**, and the 2nd degree approximation of the center manifold, the perturbed 3rd degree normal form of the iteration restricted to the 1-dimensional center manifold can be determined in the scalar form

$$u_{j+1} = \left(-1 + \left.\frac{\mathrm{d}\lambda_1}{\mathrm{d}w}\right|_{w=w_{\mathrm{cr}}} (w - w_{\mathrm{cr}}) \right) u_j + \delta u_j^3 . \tag{16}$$

The implicit differentiation of the characteristic equation (10) with respect to the chip width w results

$$\left.\frac{\mathrm{d}\lambda_1}{\mathrm{d}w}\right|_{w=w_{\mathrm{cr}}} = -\frac{2\tau}{\omega_d} \frac{\sin(\omega_d\tau)}{\cos(\omega_d\tau) + ch(\varsigma\omega_n\tau) + 2sh(\varsigma\omega_n\tau)} < 0 , \tag{17}$$

which means that the characteristic root crosses the unit circle at –1 with negative speed as the chip width increases. This corresponds well to the stability chart in Fig. 2 that shows instability for increasing chip width.

The result of a long algebraic calculation gives

$$\delta = -\frac{5}{12h_0^2}\frac{\sin^2(\omega_d\tau)\left(\cos(\omega_d\tau)+ch(\varsigma\omega_n\tau)\right)}{\cos(\omega_d\tau)+ch(\varsigma\omega_n\tau)+2sh(\varsigma\omega_n\tau)}<0\,.$$

Since the sign of δ is always negative, the flip bifurcation is *subcritical*. This means that unstable period-2 motion exists locally around the stable period-1 motion (which is the stable fix point of the iteration). This bifurcation can also be found in the numerically constructed bifurcation diagram of Fig. 3 at the dimensionless chip width about 0.06.

The numerical solutions present, however, stable period two oscillations, too, and their further bifurcations into chaotic oscillations. These stable 2-period oscillations cannot be found with the local bifurcation analysis. Still, these oscillations can be given in closed form as explained in the subsequent section.

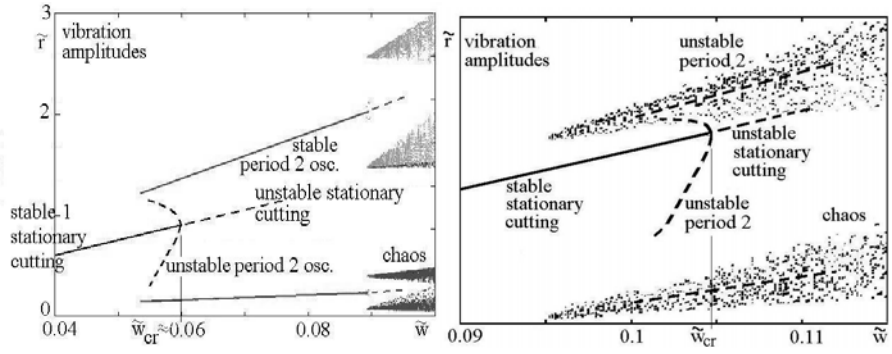

Figure 3. Bifurcation diagrams at $z\tilde{\Omega} = 2.2$ and 2.4, see section a) and b) in chart Fig. 2

6. Global Period-Two Oscillation

It is likely, that 'outside' this unstable limit cycle, there is a region where the tool leaves the workpiece, more exactly, it does not enter the workpiece at each revolution. The recognition of this kind of structure of the oscillation is quite obvious from the structure of the global attractor of the turning process (see Stépán, 2001). The new period two motion can be found by analyzing another discrete map obtained from the chaining of 2-period-long free-flights and one impact. This discrete map will have a very similar structure to that of the one in (9), but its linear part assumes the form:

$$\mathbf{A}_{(2)} = \begin{bmatrix} \frac{\mathrm{e}^{-2\zeta\omega_n\tau}}{\sqrt{1-\zeta^2}}\cos(2\omega_d\tau-\varepsilon) & \frac{\mathrm{e}^{-2\zeta\omega_n\tau}}{\omega_n\sqrt{1-\zeta^2}}\sin(2\omega_d\tau) \\ -\frac{\omega_n\mathrm{e}^{-2\zeta\omega_n\tau}}{\sqrt{1-\zeta^2}}\sin(2\omega_d\tau)+\frac{\rho\tilde{\kappa}_1}{\sqrt[3]{2}m}\left(1-\frac{\mathrm{e}^{-2\zeta\omega_n\tau}}{\sqrt{1-\zeta^2}}\cos(2\omega_d\tau-\varepsilon)\right) & \frac{\mathrm{e}^{-2\zeta\omega_n\tau}}{\sqrt{1-\zeta^2}}\left(\cos(2\omega_d\tau+\varepsilon)-\frac{\rho\tilde{\kappa}_1}{\sqrt[3]{2}m\omega_n}\sin(2\omega_d\tau)\right) \end{bmatrix}$$

This formula clearly shows the change in the linear part of the mapping (9): all the time periods are doubled to 2τ, and one impact period is added as before. The fixed point of this mapping does not reflect necessarily the existence of the corresponding period two oscillation: it has to be checked whether the amplitude of the oscillation is really greater than h_0 at every second round, that is it really misses the workpiece. The detailed algebraic analysis of this condition can be found in Szalai (2002), and the result agrees with that of the simulation in Fig. 3. For example, it exists for $\tilde{w} \geq 0.053$ where one branch of the dimensionless vibration amplitudes is at $\tilde{r} = r/h_0 > 1$ (the cutting edge misses the workpiece), indeed, while the other branch of the same period two motion runs much below 1.

Szalai (2002) also investigated analytically the stability of these period two solutions as the fix points of the linear map given by $\mathbf{A}_{(2)}$. For example, this 'global' period two oscillation loses stability at about $\tilde{w} \geq 0.09$ via a subcritical Neimark-Sacker bifurcation. As the simulation results show, further bifurcations lead to chaotic oscillations. This cascade of bifurcations could not be followed further analytically, but still, the existence of the chaotic oscillation can be proved at section b) of the stability chart in Fig. 2. Again, numerical simulation helped to construct the 2nd bifurcation diagram of Fig. 3 at the given parameter point. This is analyzed in the next section.

7. The Chaotic Oscillation

Numerical simulations presented in Fig. 3 clearly confirm the analytical predictions about the existence and stability of stationary cutting and period doubling vibrations. For example, there is a parameter region at about $\tilde{w} \approx 0.107$ where both existing period one and two oscillations are unstable. The simulation shows that the actual motion is quite random 'around' them. We will prove in this section, that the present dynamics is isomorphic to a subshift of finite type on the space of two-symbol bi-infinite sequences.

The construction is as follows. The map in Fig. 4 is constructed from every 2nd iterate of the dynamics, and the so-called switching line separates two domains of the phase space of displacement and velocity. Above the switching line the tool actually misses the contact with the workpiece at every 2nd round, while below this line, the tool hits the workpiece at each period. Clearly, the inner unstable period one oscillation is then represented by the fixed point P_1, while the outer unstable period two oscillation having

two free-flights and one impact is represented by the fixed point P_2. They are both saddle like.

So we take the second iterate of the general map, and we call it *f*. This means that the originally orientation reversing fixed point P_1 will become orientation preserving. The 'outer' period two point P_2 remains orientation reversing for its unstable manifold $W^u_{P_2}$, because it is originally defined for every contact, which is in every second period while we remain above the switching line. This property is responsible for the attractive feature of the invariant Cantor set, because points above the switching line sooner or later will be mapped below this line.

The unstable manifolds $W^u_{P_{\{1,2\}}}$ and the stable ones $W^s_{P_{\{1,2\}}}$ of the two periodic points are presented in Fig. 4, whose orientation is essential. For regularity, we need the contracting direction to be somewhat parallel to the switching line, and the expanding direction needs to be perpendicular to that. In addition, we fit rectangles along the stable manifolds in a way that there is enough space around them. The intersection points of the unstable manifolds with the switching line are denoted by *A* and *D*. So the condition, which guarantees the regularity, is that the first intersection of stable manifolds with the switching line should not be between the points *A* and *D*.

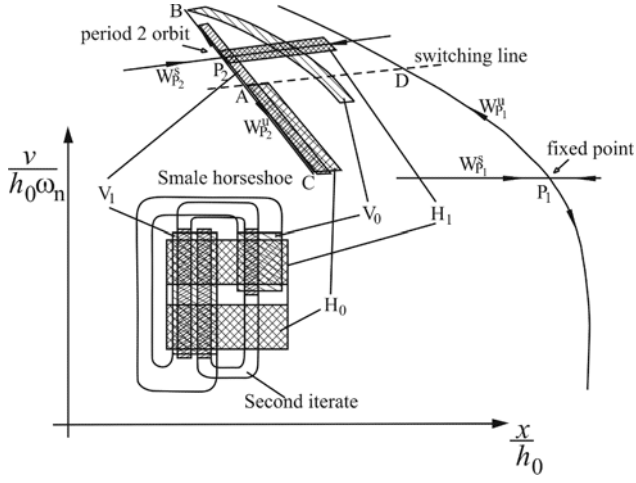

Figure 4. The chaotic iteration between two saddle points of two unstable oscillations

The map takes *A* into *B*, *B* into *C*, i.e., $B=f(A)$ and $C=f(f(A))$. We put a rectangle H_0 along $W^u_{P_2}$ between *A* and *C* with width sufficiently small to have its lower horizontal boundary mapped below $W^s_{P_2}$. Since we choose a

sufficiently thin rectangle it suffices that $f(C)$ is below $W^s_{P_2}$. From regularity and the orientation reversing property of P_2, it follows that the image of the corresponding rectangle V_0 transversally intersects the stable manifold of the period two point. The other rectangle H_1 is placed along $W^s_{P_2}$, which should be thin and long enough to be mapped into V_1 after a finite number of iteration. V_1 must intersect both horizontal rectangles ($H_{\{0,1\}}$) transversally.

Check also that the map is homeomorphism on each $H_i \cap V_j$, $i, j \in \{0,1\}$. This can be shown by a straightforward application of the inverse function theorem. Clearly, there is an invariant Cantor set

$$I = \bigcap_{n=-\infty}^{\infty} f^n \left(\bigcup_{i,j\in\{0,1\}} H_i \cap V_j \right) \subset \bigcup_{i,j\in\{0,1\}} H_i \cap V_j ,$$

such that the dynamics on I is isomorphic to the left shift on the symbol space restricted by the transition matrix

$$\begin{pmatrix} 0 & 1 \\ 1 & 1 \end{pmatrix}.$$

This matrix is irreducible. Consequently (see Wiggins, 1988), the periodic points in I are dense, there is also a dense orbit in I, and the dynamics is topologically transitive, ergodic and mixing in I. This may complete the proof of the existence of the chaotic oscillation.

8. Conclusion

The non-linear analysis of the highly interrupted low immersion milling showed that the period doubling bifurcation is subcritical, similar to the Hopf bifurcation results of Stépán and Kalmár Nagy (1997) or Kalmár-Nagy et al. (2001) obtained for regenerative machine tool vibrations in case of turning. The approximate amplitude of the unstable period two vibration was also determined in closed form. This gives a useful estimation for the domain of attraction of stable stationary cutting in case of high-speed milling.

Also, the existence and the stability of another, global period two oscillation was shown and determined. In those parameter domains of cutting speed and chip width, where both the local and the global period two oscillations as well as the stationary cutting are unstable, the existence of chaotic oscillations were proved. The analytical predictions were supported and also confirmed by numerical simulation.

Acknowledgement

This research was supported by the Hungarian National Science Foundation under grant no. OTKA T043368/03, and also by the Slovenian-Hungarian Joint Fund for Research in Technology under grant no. TeT SLO-02/01, the Research Group on Dynamics of Machines and Vehicles, Hungarian Academy of Sciences. Special thanks to Daniel Bachrathy for some of the simulation work.

References

[1] Y. Altintas and E. Budak, "Analytical prediction of stability lobes in milling," *Annals of the CIRP*, 44 (1), pp. 357–362, 1995.

[2] P.V. Bayly, J.E. Halley, B.P. Mann, and M.A. Davies, "Stability of interrupted cutting by temporal finite element analysis," *19th Biennial Conference on Mechanical Vibration and Noise, ASME 2001 Design Engineering Technical Conferences (Pittsburgh),* **DETC2001/VIB-21581**, 2001.

[3] M.A. Davies, J.R. Pratt, B. Dutterer, and T.J. Burns, "The stability of low immersion milling," *Annals of the CIRP,* **49**, pp. 37-40, 2000.

[4] M.A. Davies, J.R. Pratt, B. Dutterer, and T.J. Burns, "Stability prediction for low radial immersion milling," *J. Manuf. Sci. & Eng.*, **124**(2), pp. 217-225, 2002.

[5] J. Guckenheimer and P. Holmes, *Nonlinear Oscillation, Dynamical Systems and Bifurcation of Vector Fields*, Springer-Verlag, New-York, 1986.

[6] T. Insperger and G. Stépán, "Regenerative vibration of milling process," in *Proceedings of Dynamics and Control of Mechanical Processing,* pp. 75-79, 1999.

[7] T. Insperger and G. Stépán , "Stability of high-speed milling," in *Proceedings of ASME Symposium on Nonlinear Dynamics and Stochastic Mechanics, (Orlando)* **AMD-241**, pp. 119-123, 2000a.

[8] T. Insperger and G. Stépán, "Vibration frequencies in high-speed milling processes," submitted to the *Journal of Manufacturing Science and Engineering*, 2000b.

[9] T. Insperger, G. Stépán, P.V. Bayly, and B.P. Mann, "Multiple chatter frequencies in milling processes," *Journal of Sound and Vibration*, 2003, in press.

[10] T. Kalmár-Nagy, G. Stépán, and F.C. Moon, "Subcritical Hopf bifurcation in the dely equation model for machine tool vibrations," *Nonlinear Dyn.,* **26**, pp. 121-142, 2001.

[11] S. Wiggins, *Global Bifurcations and Chaos*, Springer-Verlag, New-York, 1988.

[12] G. Stépán, T. Kalmár-Nagy, "Nonlinear regenerative machine tool vibration," *Proceedings of the 17th Biennial Conference on Mechanical Vibration and Noise, ASME Design Engineering Technical Conferences*, **DETC97/VIB-4021**, 1-11, 1997.

[13] G. Stépán, "Modelling non-linear regenerative effects in metal cutting," *Philosophical Transactions of the Royal Society,* **359**, pp. 739-757, 2001.

[14] R. Szalai, *Nonlinear Vibrations of Interrupted Cutting Processes,* MSc thesis, Budapest University of Technology and Economics, 2002.

ON THE DYNAMICS OF A RAILWAY FREIGHT WAGON WHEELSET WITH DRY FRICTION DAMPING

Hans True and Lars Trzepacz[1]
[1] *Technical University of Denmark*
Informatics and Mathematical Modelling
DK-2800 Lyngby
Denmark
ht@imm.dtu.dk

Abstract: We consider a simple model of a wheelset that supports one end of a railway freight wagon by springs with linear characteristics and dry friction dampers.

We extend our earlier results to more realistic models, so in this presentation the linear kinematic contact relation in an earlier paper [True and Asmund, 2002] is replaced by the nonlinear rail/wheel contact geometry between a UIC60 rail and an S 1002 wheel profile. In addition we add a linear restoring force to control the yaw motion and finally add the axle side bearings to limit the maximum amplitude of the yaw oscillations. Stick-slip and hysteresis are included in our model of the dry friction.

The resulting dynamics is nonperiodic and most likely chaotic. A bifurcation diagram and some interesting types of apparently chaotic motion are presented and discussed.

Key words: Chaos, nonlinear dynamics, railway vehicle dynamics.

1. Introduction

True and Asmund [True and Asmund, 2002] investigated the dynamics of a simplified model of a wheelset of a freight wagon. The wagon runs on an ideal, straight and level track with constant speed. They investigated the lateral dynamics of the wheelset in dependence on the speed, which is the bifurcation parameter in the problem. The wheels had a conical profile, no flanges and ran on a rail profile which was shaped as an arc of a circle. The wagon is supported horizontally by linear springs and dry friction dampers. It turned out that the wheelset derailed in large speed intervals. In this article the

G. Rega and F. Vestroni (eds.),
IUTAM Symposium on Chaotic Dynamics and Control of Systems and Processes in Mechanics, 159–168.

dynamical model will be improved in steps until the wheelset stops derailing. In this way we shall gain insight into the functions of each of the single components in the suspension and their dynamical interactions. At the same time we shall explore some interesting nonperiodic oscillations that are created by the interactions between the nonlinear contact geometry, the nonlinear rail/wheel contact forces, the nonlinear stick-slip of the dry friction forces and the impacts between the axleboxes and the side bearings.

2. The Vehicle Model

The original dynamical multibody system was formulated by True and Asmund [True and Asmund, 2002] see figure 1. It is assumed that all elements with exception of the suspension elements are ideally rigid and that the springs have linear characteristics. A new model for the dry friction dampers was formulated in the article by True and Asmund [True and Asmund, 2002]. The bogie frame can turn horizontally in a frictionless pivot in the bottom of the car body.

In this article the rails are UIC60 rails with a cant of 1/40 and the wheels have DSB 97-1 wear profiles. The contact is assumed to be Hertzian. Since we only investigate the horizontal dynamics it is assumed that the normal forces are equally distributed. The equations of motion are formulated in a coordinate system, that moves along the centre axis of the track with the constant speed of the wagon. Since we are interested in the lateral and yaw motions we assume that the normal forces are constant and the wheels and the rails remain in

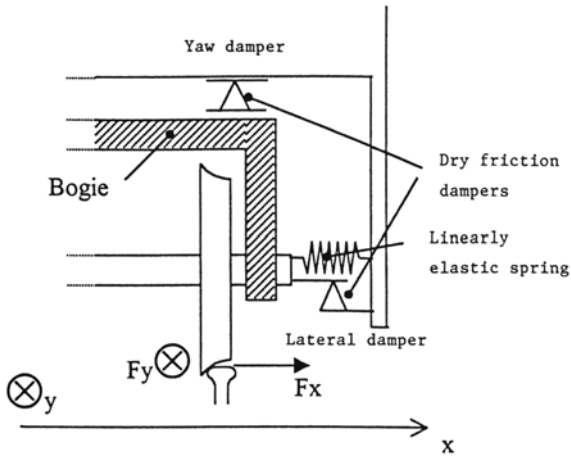

Figure 1. A diagram of the single-axle bogie model.

contact. We use the approximation by Shen, Hedrick and Elkins [Shen et al., 1984] for the calculation of the creep forces. The creep forces depend nonlinearly with a decreasing gradient on the creepage and for high creepage they reach a saturation value, which corresponds to pure Coulomb friction. The wheel-rail contact points are calculated by W. Kik's routine RSGEO.

We have included stick-slip and hysteresis in our model of the dry friction and assume that Coulomb's friction law holds during the slip phase. We focus on the lateral dynamics so we neglect vertical springs and dampers. We thus have three important nonlinearities in our problem: The nonlinear creep-creep force relation, the nonlinear kinematic contact condition and the hysteresis with stick-slip of the dry friction dampers.

The model system has three degrees of freedom: Lateral (x-) translation of the car body and the wheelset and yaw of the bogie around the frictionless pivot in the bottom of the car body.

The nonlinear dynamical system becomes a system of a six first order differential equations with time t as the independent variable. The dependent variables in our problems are:

x_1 The lateral translation of the wheelset

x_2 The lateral speed of the wheelset

x_3 The yaw angle of the wheelset

x_4 The speed of the yaw rotation

x_5 The lateral translation of the car body

x_6 The lateral speed of the car body

As an example of the calculation of the forces we show the calculation of the lateral forces that act upon a wheelset.

$$F_{wheel} = F_{wheel,l} \cdot sech[(x_2 - x_6)\alpha] + F_{wheel,h} \cdot (1 - sech[(x_2 - x_6)\alpha]);$$
$$F_{wheel,l} = F_{in} - \nu N \cdot sign F_{in} + F_{in} m_{wheel}/(m_K + m_{wheel}) \text{ for } |F_{in}| > \nu N;$$
$$F_{wheel,l} = F_{in}/(m_b + m_{wheel}) \text{ for } |F_{in}| < \nu N;$$
$$F_{wheel,h} = F_{in} - \mu N \cdot sign(x_2 - x_6);$$
$$F_{in} = -2 \cdot F_x - F_F;$$
$$F_F = k_F(x_1 - x_5).$$

Here are

F_F The spring force

k_F The spring constant 10^6 m/N

F_x The lateral creep force

N The normal force (constant)

ν The static adhesion coefficient of the lateral damper ($\nu N = 923$ N)

μ The dynamical coefficient of friction of the lateral damper ($\mu N = 773$ N)

$F_{wheel,l}$ The resulting force when the damper sticks

$F_{wheel,h}$ The resulting force when the damper slips

m_{wheel} The mass of the wheelset 1022 kg

m_b The active mass of the car body 10000 kg

α A constant in the dry friction law - here equal to 50

The dynamical system is solved numerically with appropriate initial conditions. We use a Runge/Kutta/Cash/Karp 5/6 order solver with adaptive steplength and error control. The program is implemented in C++. The speed of the calculations is then 1000 times higher than a MATLAB program. However MATLAB was used for the post processing.

3. Some Results

In the work by True and Asmund [True and Asmund, 2002] we found that the dynamics is very sensitive to infinitesimal disturbances in the initial conditions or the parameters. As an example we show on Figure 2 two curves of the lateral oscillations with the same initial conditions but with an infinitesimal speed difference. At the speed 10.00 m/s the wheelset stays in the track but at 10.05 m/s the wheelset derails within 38 seconds.

We now introduce the realistic wheel-rail geometry into the model. On figure 3 we plot the time until derailment versus the vehicle speed. If the time is longer than 200 s we assume that the wheelset will not derail. We have plotted the results for the realistic wheel-rail geometry together with the results from True and Asmund [True and Asmund, 2002] in the same diagram. The black curves and points correspond to the realistic wheel-rail geometry and the gray points and curves illustrate for comparison the results from True and Asmund. The realistic wheel-rail geometry does stabilize the motion in two large speed intervals, but between 20 m/s (72 km/h) and 40 m/s (144 km/h) the wheelset will derail within a few seconds.

In a realistic axlebox side bearing the lateral motions will be limited. We now introduce a lateral play of 20 mm as it is described in the standards for

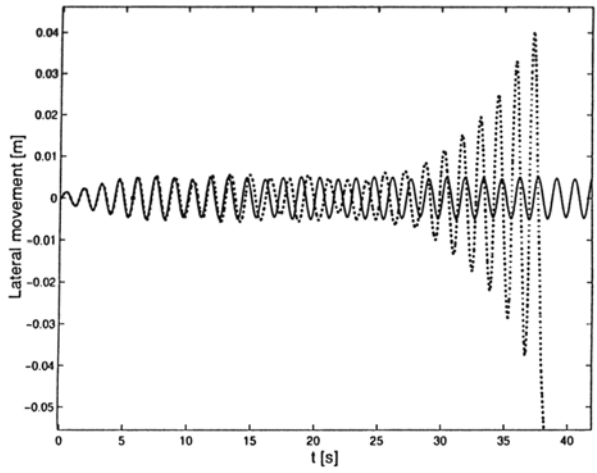

Figure 2. The sensitivity to changes in the vehicle speed. The lateral oscillations versus time for $V = 10.00$ m/s (full line) and at $V = 10.05$ m/s (broken line).

the UIC suspension or in the book by Hanneforth and Fischer p.36 [Hanneforth and Fischer, 1986]. Through the impact of the axlebox the side bearing will deform. The restoring force is modelled as a linearly elastic spring with a spring constant of 1500 kN/m. The calculations show that the lateral guidance *has no effect* on the lateral oscillations.

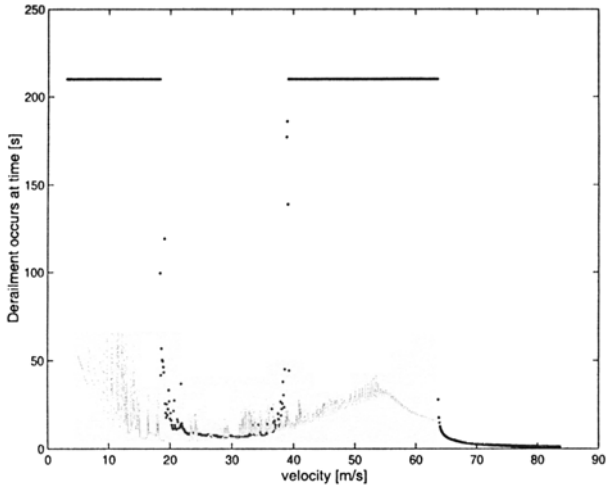

Figure 3. Comparison of the times until derailment versus the vehicle speed for realistic wheel-rail geometry (black) and conical profile without flanges (gray).

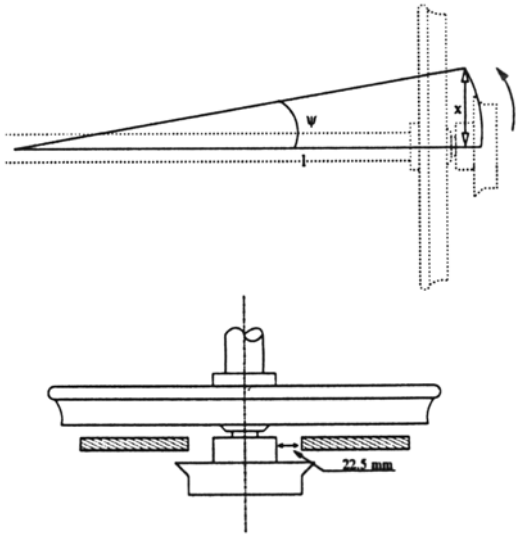

Figure 4. The longitudinal play and the maximum yaw angle of the wheelset.

We finally fix the bogie frame in the car body and give the axlebox a longitudinal play of 22.5 mm. Again the value is taken from Hanneforth and Fischer p.36 [Hanneforth and Fischer, 1986]. With the distance 1 = 1000 mm (see figure 4) it is easy to calculate the maximum yaw angle of the wheelset. The restoring force is very big in this case and the assumption of an elastic impact with $E=2.1 \cdot 10^{11}$ makes the dynamical system so stiff that the calculation time becomes unacceptably high. We therefore approximate the impact by an ideally elastic one where the yaw speed of the wheelset is the same before and after impact but the direction of the motion changes. We have compared some results of computations under each of the two assumptions and they agree very well.

As seen on figure 5 we have now finally achieved what we wanted: *The wheelset derails no more*.

Figure 5 shows the maximum amplitudes of the lateral oscillations versus the speed of the vehicle when as well lateral as longitudinal plays are present. The limit on the yaw motion stabilizes the motion of the wheelset but due to the impacts with the side bearings the motion is apparently chaotic in the entire speed range.

On figure 5 the different forms of motion are clearly seen. After the big oscillations at 0 m/s $<$ V $<$ 5 m/s follow small oscillations at 5 m/s $<$ V $<$ 10 m/s. Then a range 10 m/s $<$ V $<$ 19 m/s follows with big chaotic oscillations followed by an interval 19 m/s $<$ V $<$ 25 m/s where we must investigate the motion more carefully. The motion is not clearly chaotic. In the speed

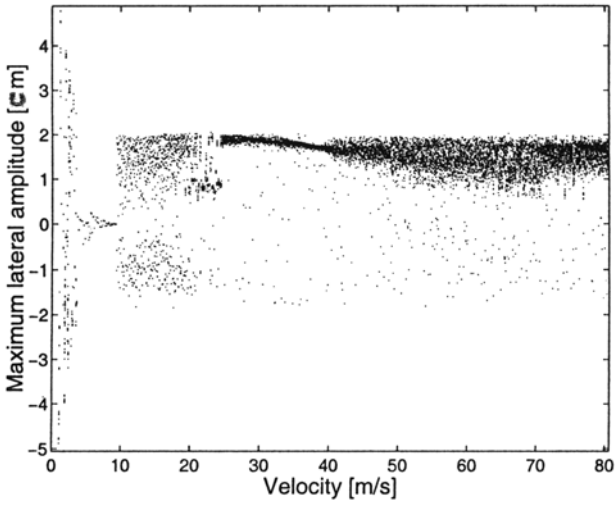

Figure 5. Bifurcation diagram showing the maximum amplitudes of the lateral oscillation versus the speed of the vehicle.

interval 25 m/s $<$ V $<$ 40 m/s the scatter of the chaotic amplitudes is small but the amplitudes are all close to the maximum value. Obviously the limitation of the yaw motion is very important in this speed interval. In the interval 40 m/s $<$ V $<$ 64 m/s the motion is strongly chaotic, but above V = 64 m/s the amplitudes of the chaos decrease.

We finally introduce a linear spring acting longitudinally between the axle box and the car body. We calculate its stiffness on the basis of the known data from the wellknown UIC standard link suspension (see Hanneforth and Fischer p.37 [Hanneforth and Fischer, 1986]). Our investigations show that the longitudinal spring has a very small stabilizing effect at low speeds. At higher speeds it has no effect at all. The longitudinal springs however always help guiding the wheelset through curves.

We shall now summarize the resulting dynamic behaviour in a single plot. We show the lateral displacement of the wheelset versus time, but the speed of the vehicle is increased instantaneously every twenty minutes. We display four basically different kinds of dynamic behaviour indicated by the letters A-D. Type 'A' is the motion that is controlled by the longitudinal springs. Type 'B' is the crawling motion at low speeds with impacts on the side bearings due to the yaw motion of the wheelset. Type 'C' is also a crawling motion but with an increase in the number of impacts. Type 'D' is the aperiodic (chaotic?) motion, which is dominated by the impacts in the longitudinal direction with the side bearings. This type of motion can be subdivided into four groups D1-D4 distinguished by the number of impacts per minute.

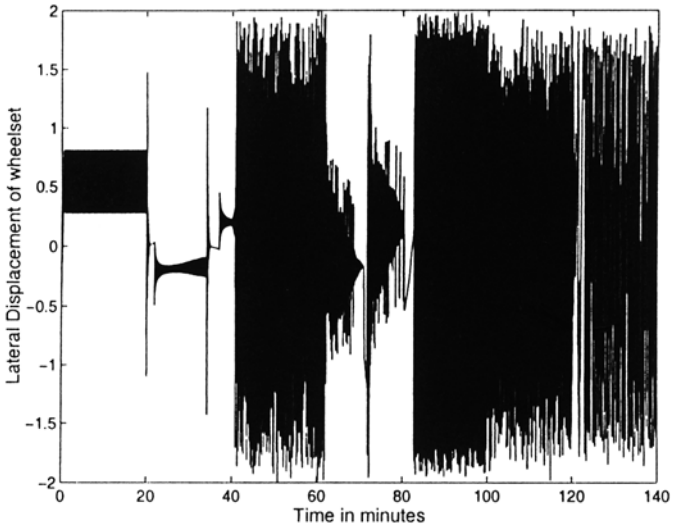

Figure 6. A simulation with a change of the speed every twenty minutes.

Time interval (*minutes*)	*Speed* (m/s)	*Type of motion*
0-20	5	A
20-40	9.5	B
40-60	15	D1
60-80	22	C
80-100	30	D2
100-120	55	D3
120-140	80	D4

The resulting dynamics is presented on figure 6. The different kinds of behaviour are seen clearly. It may look like the transitions happen instantaneously, when the speed jumps, but it is not the case. There is a small transition interval, when the motion changes type. The longest interval is found when we jump from the 'B' or 'C' type motion. The wheelset may get caught in a yaw oscillation until the series of impacts with the side bearings become so intense that the wheelset 'is knocked free'. This effect is better observed on a plot of the yaw oscillations verse time. On figure 7 we therefore show the lateral oscillations of the wheelset next to figure 8 showing the yaw versus time in the case of a type 'C' motion.

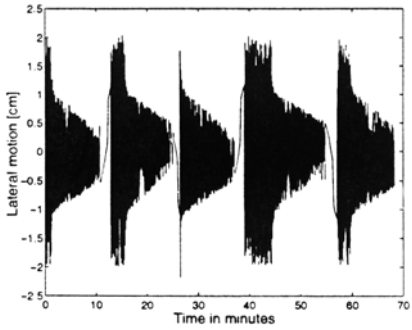

Figure 7. Lateral displacement at V = 20 m/s

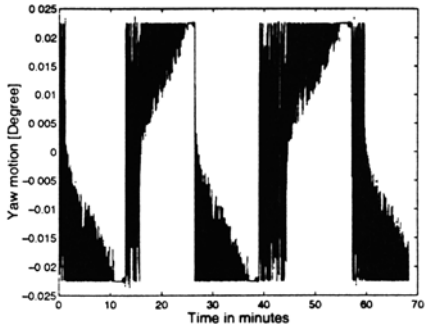

Figure 8. Yaw angle at V = 20 m/s

4. Conclusion

This work is a contribution to the analysis of the dynamics that may arise in railway vehicles due to dry friction in the suspensions. Without dry friction the model was investigated by Knudsen, Feldberg and True [Knudsen et al., 1992] and Knudsen, Slivsgaard, Rose, True and Feldberg [Knudsen et al., 1994]. Dry friction was introduced in the model by True and Asmund [True and Asmund, 2002], and it was found that the dynamics was so fundamentally altered that no features in common with the earlier results could be found. The danger of derailment existed at almost any speed, and it was concluded that this was due to the strong simplifications introduced in that model.

In this article we demonstrate that the realistic rail-wheel geometry improves the dynamics, but a large speed interval between 20 m/s and 40 m/s still exists in which the wheelset derails. Only a limitation of the maximum yaw angle of the wheelset will guarantee the safe run of the vehicle.

The dynamics is apparently chaotic in large speed intervals. The dry friction introduces a sensitive dependence of the motion on infinitesimal changes in the initial conditions. At speeds below 5 m/s the wheelset oscillates periodically around a neutral position with an offset that is determined by the initial conditions. At higher speeds (motion 'B') the motion alternates between stationary offset positions and apparently chaotic motion. At still higher speeds the motion becomes violently erratic (chaotic?) except in the speed interval 20 m/s$<$ V $<$24 m/s, where the lateral oscillations look like intervals of damped chaotic motion with decreasing amplitude divided by large amplitude jumps caused by the impacts of the axle boxes with the side bearings (type 'C').

Speed intervals exist where the oscillations are connected with violent impacts between the axle boxes and the side bearings. These oscillations may

create high stresses and large track forces that lead to fatigue and high wear of the rails.

The crawling motion we have found, has been observed in other mechanical systems where the motion is controlled by dry friction forces with stick-slip. The combination of dry friction damping with the nonlinear wheel-rail contact forces and the longitudinal linear spring in our model is the reason for the dynamics at very low speeds, where we observe a small amplitude oscillation around a neutral 'stick position'. That position depends on the initial conditions, and it can assume any arbitrary value in a large interval. At higher speeds the motion is in addition influenced by the impacts with the side bearings. Repeated impacts are known to create chaotic motion, and our results show some similarity with earlier investigations of a bouncing ball between a fixed and an oscillating wall. In our case, however, the energy necessary to maintain the motion comes from the nonlinear stress-strain relations in the wheel-rail contact surface.

References

[1] W. Hanneforth and W. Fischer, *Laufwerke*, Transpress, Berlin, DDR, 1986.

[2] C. Knudsen, R. Feldberg and H. True, "Bifurcations and chaos in a model of a rolling wheelset," *Phil. Trans. R. Soc. Lond.*, A 338:455–469, 1992.

[3] C. Knudsen, E. Slivsgaard, M. Rose, H. True and R. Feldberg "Dynamics of a model of a railway wheelset," *Nonlinear Dynamics*, 6:215–236, 1994.

[4] Z.Y. Shen, J.K. Hedrick and J.A. Elkins, "A comparison of alternative creep-force models for rail vehicle dynamical analysis," pages 591–605. *Proc. 8th IAVSD Symposium on Vehicle System Dynamics, The Dynamics of Vehicles on Roads and Tracks*, pp. 591–605, Swets & Zeitlinger, Lisse, 1984.

[5] H. True and R. Asmund, "The dynamics of a railway freight wagon wheelset with dry friction damping," *Vehicle System Dynamics*, 38:149–163, 2002.

III.

STRUCTURAL SYSTEMS

Bifurcation and chaos in *structural systems* are the focus of the second part of the Proceedings; these papers are compiled alphabetically, based on the last name of the first author. A number of papers deals with theoretical and/or experimental characterization of dynamic complexity in the response of infinite-dimensional systems, some of them also specifically addressing the formulation of proper reduced-order models, which is an issue of considerable interest also from the application viewpoint.

Benedettini and Alaggio show how experimental analysis allows one to characterize different classes of motion, transitions to nonregular motions, and the main characteristics of spatial flow, in the post-critical finite planar dynamics of a circular arch. They also give useful hints for the development of reliable minimal analytical models able to reproduce the experimental dynamics.

Georgiou directly addresses the construction of reduced order models for the dynamics of an exact nonlinear elastic rod by projecting its full order coupled equations of motion onto a set of proper orthogonal modes derived from a finite element analysis. Numerical study of the reduced models suggests that the subspace spanned by the POD modes represents an invariant subspace of the dynamics inside which a normal mode of vibration, whose shape is close to that of the dominant POD mode, resides.

Gonçalves and del Prado discuss the nonlinear oscillations and dynamic instabilities of thin-walled shells subjected to harmonic loads. A number of relevant issues are dealt with, including shell discretization processes, influence of modal coupling on nonlinear vibration modes, modal interaction between different nonlinear vibration modes, imperfection sensitivity, and fractal basin boundaries.

Lakrad and Belhaq present quasiperiodic and periodic bursters solutions of a two-mode model of a shallow arch subjected to a resonant external excitation and a very slow parametric excitation due to support motion.

G. Rega and F. Vestroni (eds.),
IUTAM Symposium on Chaotic Dynamics and Control of Systems and Processes in Mechanics, 169–170.

Behaviour charts and analytical approximations are obtained and comparison with numerical simulations are provided.

In a different context, Cusumano and Chelidze use the phase space warping concept from dynamical systems theory to develop a general framework for damage evolution tracking, diagnosis and prognosis. After summarizing the theory and its algorithmic implementation, they apply the method to a vibrating experimental beam with evolving material damage. Real-time estimates of the current damage state and accurate predictions in advance of the time to failure are obtained.

In the background of the increasing complexity of modern structures, which strongly reduces the possibility to use analytical methods in the study of structural dynamics, Galvanetto and Bornemann address the investigation of long-term behaviour and complex dynamics of realistic structures with the finite element method and suitable time integration schemes, discussing the performances of both fixed and adaptive time step techniques.

Two further papers deal with somehow specific nonlinear dynamic problems in structural mechanics. Ibrahim et al. study the nonlinear panel flutter with relaxation in the boundary conditions, based on a phenomenological model of joint preload relaxation. The analysis is restricted to two-mode interaction and includes the influence of boundary conditions relaxation on the panel modal frequencies and limit cycle amplitudes in time and frequency domains. Plaut et al. investigate the application of a buckled mechanism as a vibration isolator in structural and mechanical systems. They show the occurrence of nonlinear periodic and chaotic responses under the action of both parametric and external excitations.

POST-CRITICAL FINITE, PLANAR DYNAMICS OF A CIRCULAR ARCH: EXPERIMENTAL AND THEORETICAL CHARACTERIZATION OF TRANSITIONS TO NONREGULAR MOTIONS

F. Benedettini and R. Alaggio
Dipartimento di Ingegneria delle Strutture, delle Acque e del Terreno
Università degli Studi di L'Aquila, Monteluco di Roio, 67040 L'Aquila, Italy
ben@sgol.it

Abstract: The role of the experimental analysis in the formulation and validation of a reduced order analytical model of a planar arch under a vertical, sinusoidally varying, concentrated force on the tip, is analyzed in this work. One of the main dynamical phenomena exhibited by such systems is the loss of stability of the directly excited simple, 1-mode, symmetric, periodic solution and the evolution towards different regular and nonregular coupled motions where anti-symmetric components of the motion arise. The experimental analysis allows one to characterize the different classes of motion, bifurcation paths and main characteristics of the spatial flow and gives useful hints to be used in the analytical approximation. A minimal analytical model able to reproduce the actual dynamics of an experimental prototype is eventually proposed.

Key words: Experiments, nonlinear dynamics, non regular motions, reduced order models.

1. Introduction

The finite dynamics of elastic structures having initial curvature show a series of interesting phenomena due to the presence of symmetric and anti-symmetric nonlinearities. In the case of circular arches whose dynamics are confined to the initial configuration plane and are excited by an harmonic vertical load applied on the tip, the simple one-mode symmetric solution, stable for low excitation levels, loses stability around meaningful resonance conditions, and coupled symmetric anti-symmetric solutions appear. Possible internal resonance tunings furthermore enhances the nonlinear modal coupling. The problem already known for a long time [1] has been recently

G. Rega and F. Vestroni (eds.),
IUTAM Symposium on Chaotic Dynamics and Control of Systems and Processes in Mechanics, 171–181.

revisited and the bifurcation scenario towards coupled motions and the post-critical behavior has been described [3-7]. In this work, among different considered set-ups the case of an arch exibiting an internal resonance condition of 2:1 type between the first symmetric and first anti-symmetric modes is considered: the investigated phenomena are the dynamic instability of directly excited symmetric solution and the postcritical transition to non periodic motions. The analysis involves both an experimental and an analytical approach.

Aims of the work are: *i)* to characterize the postcritical response and the transition to nonregular dynamics exhibited by the experimental model and *ii)* to obtain an experimentally validated reduced order model able to reproduce regular and non regular dynamics, bifurcation scenario, routes to non regular motions.

The discussion proposed in the paper is based on the results of experimental tests conducted in the Nonlinear Dynamics Laboratory at the University of L'Aquila on a steel model of natural arch having a sag to span ratio of about 1:2. In particular, in par. 2.1 the modal properties of the experimental model are reported and discussed; a summary of the characteristics of the response in regular nonlinear regime is presented in par. 2.2 where the exhibited classes of motion and bifurcation limits are described; the main characteristics of nonregular dynamics are discussed in par. 2.3; in par. 3.1 an analytical model is introduced, a perturbation analysis is described and response, stability and bifurcations of amplitude and phase modulation equations (APMEs) are discussed; in par. 3.2 two scenarios involving homoclinic tangency and pertaining to two different regions in the frequency-amplitude excitation parameters plane, are presented; concluding remarks and future developments ends the paper.

2. Main Experimental Results

Two prototypes having different sag to span ratio have been constructed and tested. Different internal resonance conditions have been realized by varying the position of some tuning-masses located on the arch.

The external sinusoidal excitation has been applied using a small exciter, constituted by two counter rotating masses and moved by a step controlled electrical engine (fig.2).

The presented results refer, as previously discussed, to an arch with sag to span ratio 1:2 in the case of an internal resonance of 2:1 type between the first symmetric and first anti-symmetric modes (Fig. 1) and primary external resonance conditions with the first symmetric mode.

The first step of experimental characterization was devoted to the linear dynamics and so, at first, a modal identification procedure was performed using a frequency domain method.

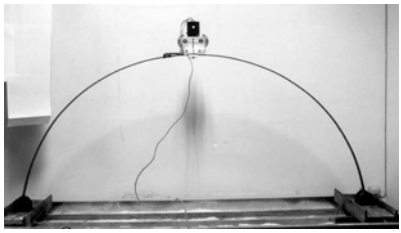

Figure 1. A steel model of the double hinged circular arch

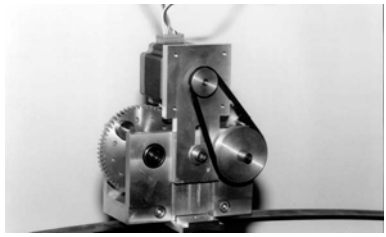

Figure 2. The exciter

2.1 Modal Testing

An output-only approach based on the Enanced Frequency Domain Decomposition tecnique has been adopted to identify the modal properties of the arch. In the following pictures a summary of the experimental set-up and the obtained results is reported. The accelerometers were located by using 2 different patches on 9 spatial points to measure both tangential and radial components of the acceleration field. (Fig. 3 a, b). The first 2 identified modal shapes are reported in fig. 3 c, d. The peak picking procedure and the validation of identified frequencies and dampings are reported in fig. 4. The obtained results are summarized in table 1.

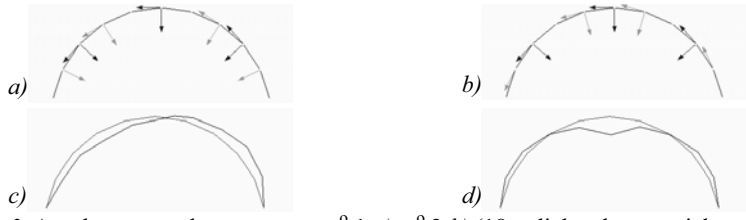

Figure 3. Accelerometers lay-out: setup n^{o} 1 *a)*, n^{o} 2 *b)* (18 radial and tangential positions); *c)*, *d)* identified modal shapes: 1st mode antisymmetric, 2nd mode symmetric.

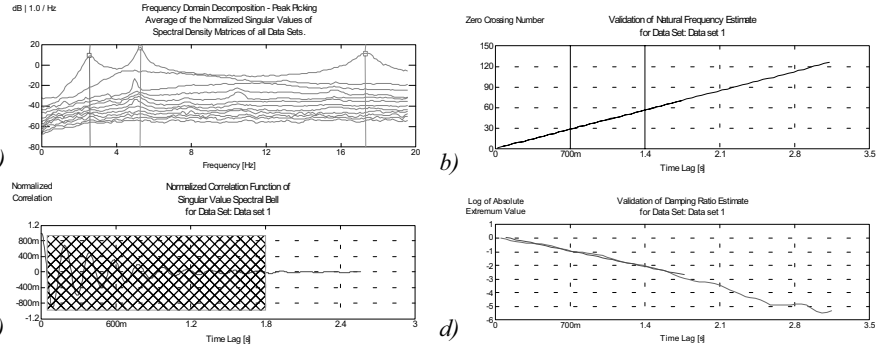

Figure 4. Singular values of spectral density matrices a), validation of natural frequenccy b); Damping estimate c), validation of damping ratio d).

Table 1. Results of frequency domain decomposition technique. Frequency ratio = 2.03.

Mode	Frequency [Hz]	Damping Ratio [%]
Mode 1 H1	2.578	6.366
Mode 2 V1	5.244	2.150

2.2 Response in Regular Regime

The experimental investigation shows a scenario characterized by a rich and varied regular and non regular dynamics. Systematic tests were performed varying the excitation parameters and recording the horizontal and vertical components of the displacement of the arch tip by means of an optical follower camera. The classes of motion and their stability regions were investigated processing the experimental time laws. The obtained results are presented and discussed by means of behavior charts and frequency-response curves (Fig. 6).

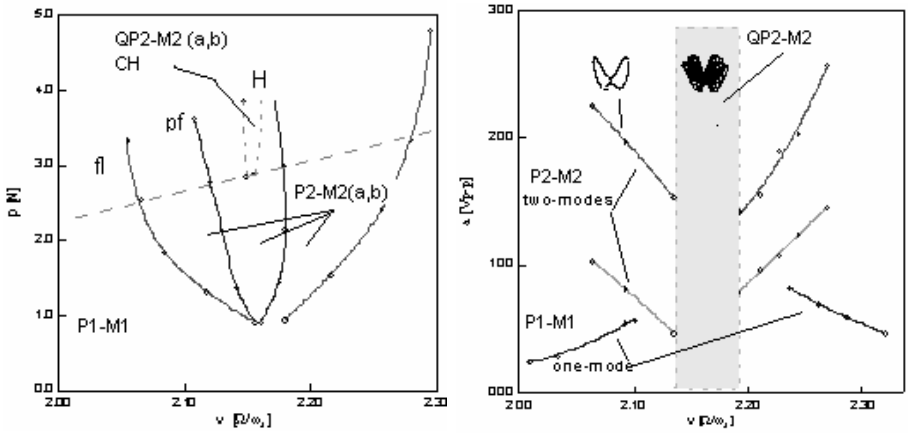

a) *b)*

Figure 6. Behavior chart *a)* and frequency-response curve *b)*.

Previous results [5] relevant to regular classes of motion, bifurcations and dimensionality can be summarized as follows: the period-1, 1-mode symmetric solution (P1-M1 in Fig. 6a) is limited by a pitchfork bifurcation on both sides of the instability region, it involves only the directly excited symmetric mode. Increasing the excitation frequency, after the pitchfork bifurcation, the response jumps on either one of a couple of coexisting and competing period-2 solutions (P2-M2 (a,b), Fig. 6a) symmetric in phase space. These periodic solutions are limited by Hopf bifurcations towards the inner part of the instability region and by fold bifurcations in the opposite direction generatig two coexisting solutions zones. After the fold bifurcation the system come back to the period-1, 1-mode symmetric solution (P1-M1).

2.3 Response in Nonregular Regime

Inside the region accessed by Hopf bifurcations (see Fig. 6) the response is very varied. At first, a quasiperiodic 2-modes solution arises (QP2-M2a,b) in a symmetric and competing couple (in phase space) evolving to chaotic response (CH). A second chaotic region CH2 located at higher frequencies and forcing amplitudes unaccessible with continuity conditions given during the experiments (and not reported in Fig. 6) is present as well.

A detailed characterization of postcritical response has been done evaluating the global invariants of the reconstructed attractors. In particular the correlation dimension, the maximum Lyapunov exponent and the underlyng structure of the spatial flow (Proper Orthogonal Decomposition (POD) of contemporaneous acquisitions) were used.

The main characteristics of the observed motion are: *i)* the dynamics of the continuous system, potentially infinite-dimensional, is low dimensional even in the nonregular regime; *ii)* there is evidence of non periodic bursting phenomena; *iii)* the complexity of the motion has been characterized by considering the dimensionality and stability of phase space invariants organizing the flow in nonregular regime.

Below, in the case of quasi-periodic and chaotic motions, the vertical and horizontal component of the arch-tip motion, the 2-D reconstruction of the phase space (delay-embedding procedure) and the Poincaré sections are reported to give a qualitative description of the system dynamics.

Figure 7 is relevant to the QP2-M2 class of motion, figure 8 and 9 to nonregular responses obtained for (CH) and (CH2) chaotic regions. In both the regions a non periodic bursting mechanism is evidenced. It is worth noticing how in CH zone, in between the bursting, the horizontal component goes to zero while the vertical is on its maximum permitting to classify the unstable fixed point approached between the bursts as P1-M1 (Fig. 8).

On the contrary, in figure 9, in the stages between the bursts, both the vertical and the horizontal components are present and the approached unstable fixed point is of (P2-M2)-type. In both figure 8 and 9 the relevant Poincaré sections show evidence of the presence of unstable fixed points, of an escape and reinjection structure in the phase space enlightening a seemingly homoclinic chaos scenario. To unfold the composition of the spatial flow the POD has been applied to the time series of eight equally-spaced points on the arch: even in non-regular regime the identified POMs near resemble the first symmetric and antisymmetric modes of the arch; moreover, the two POMs obtained in the whole range of excitation parameters newer go down the 97% of the total signal power.

This circumstance, together with the value of the embedding dimension corresponding to the saturation of attractor invariants allows to estimate low

dimensionality even in the nonregular regime and give hints towards the possibility to use a reduced order model (2 modes) able to reproduce the overall dynamics (Fig. 10).

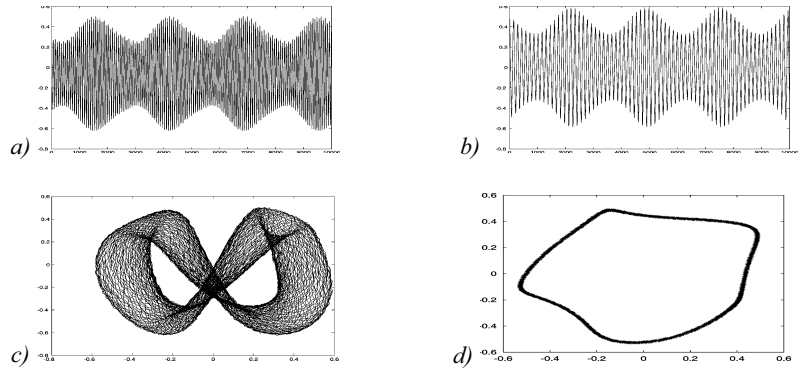

Figure 7. Experimental quasi periodic response QP2-M2: vertical *a)* and horizontal *b)* motion of the arch tip, plane projection of phase space *c)* and Poincaré section *d)* .

Accordingly, a Galerkin discretization of the PDEs of the motion is used to produce a 2 d.o.f. model involving the first anti-symmetric and the first symmetric planar modes. The experimental response furnishes even more information to be taken into account in the analytical modeling: *i)* the model equations have to posses (V,H)→ (V,-H) symmetry to reproduce the symmetry shown during the experiments by the various classes of motion; *ii)* the presence of non periodic bursting phenomenon suggests the involving of homoclinic tangencies to an unstable fixed point belonging either (CH) to a branch of an unstable periodic 1-mode solution P1-M1 or (CH2) to a branch of an unstable periodic 2-mode solution P2-M2.

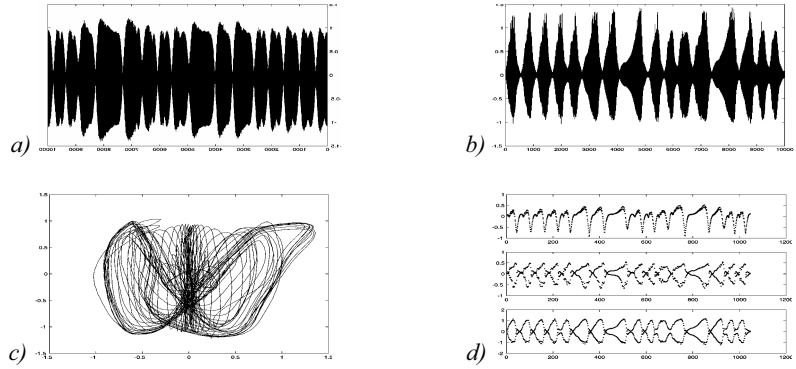

Figure 8. Experimental chaotic response: vertical *a)* and horizontal *b)* motion of the arch tip, plane projection of phase space *c)* time series of Poincaré section components *d)*

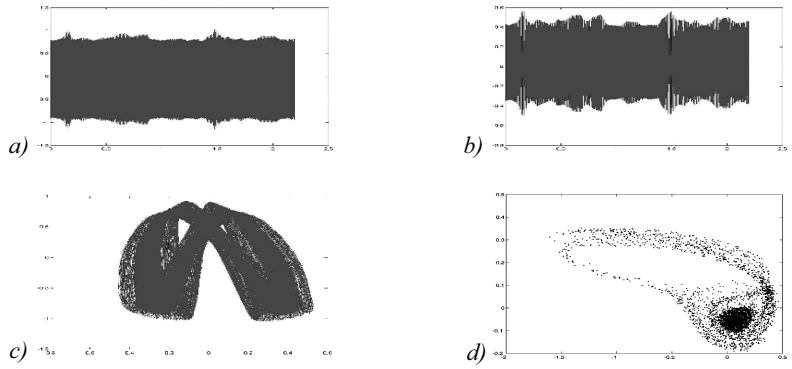

Figure 9. Experimental chaotic response: vertical *a)* and horizontal *b)* motion of the arch tip, plane projection of phase space *c)* plane projection of Poincaré section *d)* .

3 The Analytical Model

The equations of the motion were derived in [4] extending to finite deformations the model proposed in [2] assuming a kinematic description based on a negligible elongation (ε=0) and a nonlinear change of curvature of axis-fibers. The planar deformation of the arch is described by the two in-plane displacement components (tangential and radial [u(φ,t), v(φ,t)]).
An assumed mode expansion of the displacement field based on a truncated series of eigenfunctions fitting the 1st symmetric and 1st anti-symmetric experimental modes (presence of concentrated masses) and, alternatively, in the chaotic regions, the experimental POMs, was performed.
The obtained ODEs read:

$$\begin{aligned} &\ddot{q}_1 + \mu_1 \dot{q}_1 + c_{10} q_1 + c_{20} q_1^2 + c_{02} q_2^2 + c_{30} q_1^3 + c_{12} q_1 q_2^2 = P \sin(\Omega\tau) \\ &\ddot{q}_2 + \mu_2 \dot{q}_2 + q_2 + c_{11} q_1 q_2 + c_{02} q_2^2 + c_{03} q_2^3 + c_{21} q_1^2 q_2 = 0 \end{aligned} \tag{1}$$

By using the perturbational Multiple Time Scale Method (MTSM) the Amplitude and Phases Modulation Equations (APMEs) were obtained.

Eventually, a continuation procedure applied to APMEs have been used to evaluate response, stability and bifurcation scenario.

3.1 Response, Stability and Bifurcations of APMEs

The behavior chart in the frequency-amplitude excitation parameters plane identify classes of motion and bifurcations coherent with the experimental results.

Inside the left grey region (Fig. 11) due to an instability of the two-mode solution a non regular response arises (black region). At the excitation level evidenced in the figure and, for increasing frequencies, the following main

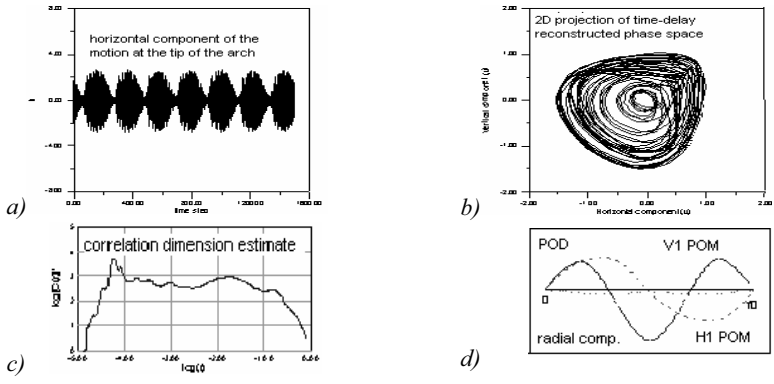

Figure 10. Experimental chaotic response: time-delay reconstructed time series *a)*, plane projection of phase space *b)*, correlation dimension estimate *c)* and POD of the flow *d)*.

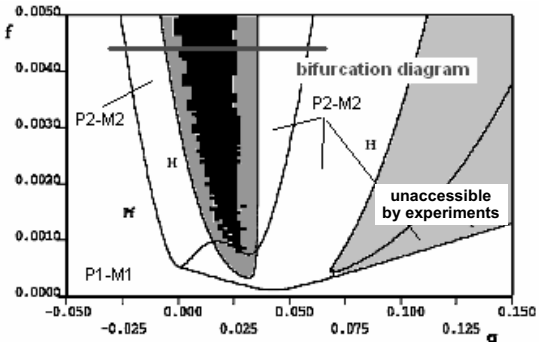

Figure 11. Behaviour chart obtained from APMEs continuation.

classes of motion and relevant bifurcation limits are identified: *i)* resonant 1-mode periodic solution P1-M1, ending by pitchfork; *ii)* resonant 2-mode periodic solutions P2-M2, symmetric couple in phase space ending by Hopf; *iii)*quasi-periodic solutions QP2-M2, QP4-M2, (left grey region); *iv)* chaotic solutions inside the quasi-periodic region (black region); An inaccessible region with continuity conditions given in the experiments (right grey) is reported as well. At the forcing level shown in Fig. 11, for increasing frequency the bifurcation diagram (Fig. 12a) shows the following classes of motion: P1-M1, P2-M2(a,b), QP2-M2 (a,b) and QP4-M2(a,b), chaotic. The Lyapunov spectrum (Fig. 12b) confirms the transition to nonregular dynamics in the inner part of the instability region.

3.2 Homoclinic Tangency and Transition to Chaos

Increasing the forcing frequency (Fig. 13a) the response curve shows a pitchfork bifurcation from P1-M1 to P2-M2(a,b). These solutions switches from stable to unstable due to an Hopf bifurcation in two different ranges (H1-H2 and H3-H4). Inside those intervals further involved phenomena are related to the presence of homoclinic tangencies to an unstable fixed point (Fig. 13c,d) and a chaotic response is exhibited. Following the branches of quasiperiodic response QP2-M2 emanating from the Hopf bifurcation point H1 (H2), an homoclinic tangency to a Saddle Focus (SF) is approached. This fixed point belongs to the upper (lower) unstable branch of the 1-mode solution P1-M1.

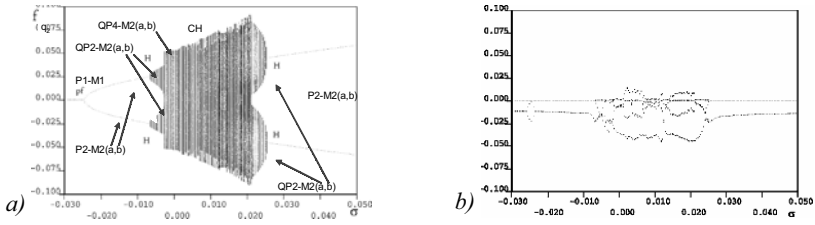

Figure 12. Bifurcation diagram *a)* and Lyapunov exponents *b).*

The dynamics are organized by: *i)* the unstable fixed point [4.7e-3, 7.e-4, 0., 0.] corresponding to the unstable 1-mode periodic solution P1-M1 (SF); *ii)* The stable 2-D manifold W_2^s corresponding to subspace spanned by the V1 mode (u,v in Fig. 13 e); *iii)* the unstable 1-D manifold W_1^u corresponding to a subspace spanned by the H1 mode (w,z) responsible for the ejection; *iv)* the homoclinic structure responsible for the reinjection of the trajectories in phase space towards the saddle focus SF. The presence of homoclinic orbits can produce non periodic bursting unfolding the corresponding experimental behavior.

On the same time, following the branches of quasi-periodic response emanating from the H3 (or H4) Hopf bifurcation point an homoclinic tangency to a Saddle Focus (SF) is approached. The SF is a fixed point corresponding to the unstable (lower) branch of the 2-mode periodic solution (P2-M2) having non zero coordinates both on V and H components.

However, the sub-critical Hopf bifurcation H3 generates a direct jump to the 1-mode P1-M1, non resonant, stable branch and no chaotic response is found (unfolding inaccessibility during the experiments of the left grey part of the behaviour chart, see Fig. 11 and 6a). On the contrary, the super-critical Hopf bifurcation H4 generates a 2-mode quasi-periodic solution eventually evolving to chaotic motions. Some of the torus doublings involved in the bifurcation path to homoclinic tangency (CH1) are reported in Fig. 14.

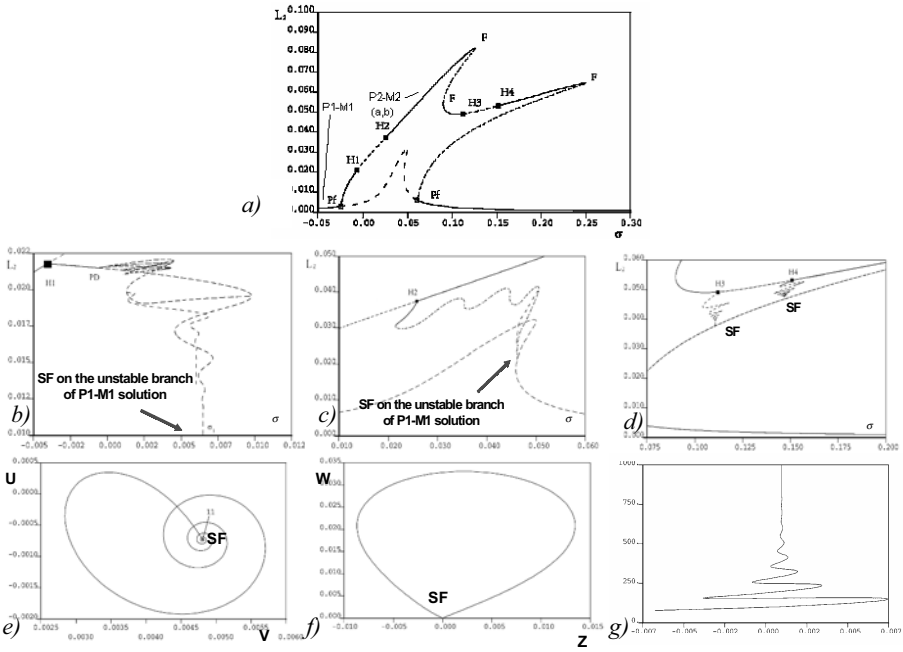

Figure 13. a),b),c),d) continuation of periodic solutions of APMEs; *e),f)* SF and homoclinic orbit; *g)*, period vs frequency parameter approaching homoclinic tangency.

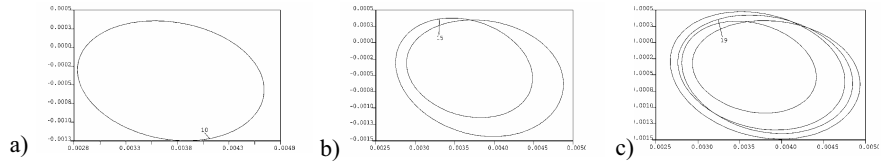

Figure 14. Torus doublings QP2-M2 -> QP4-M2 -> QP8-M2

4 Concluding Remarks

The dynamic instability of symmetric solutions under a symmetric excitation and the post critical behavior of a planar arch with internal 1:2 and primary external resonance conditions have been investigated. A reduced order model having 2 d.o.f. has been proposed and validated on the base of experimental tests. A good qualitative agreement between experiments and analytical results has been found concerning the bifurcation scenario, the post-critical behavior and the underlying structure of the phase space organizing the non-regular motion. The proposed analytical model, able to justify the global experimental behavior, can be used to focus the attention on local phenomena to be enlightened on the experimental model with a

more detailed investigations. This feedback process between analytical and experimental investigations represents an effective approach to go deep inside the observed phenomena.

References

[1] V.V. Bolotin, *The Dynamic Stability of Elastic Systems*, Holden-Day, San Francisco, 1964.

[2] J. Henrych, *The Dynamics of Arches and Frames* (Translated by R. Major), Amsterdam , Elsevier, 2002.

[3] J.J. Thomsen, "Chaotic vibrations of non-shallow arches," *Journal of Sound and Vibration*, 153(2), 239-258, 1992.

[4] F. Benedettini, "Planar finite forced dynamics of a double hinged circular arch: theory and experiments," *Proc. of the 1997 ASME DETC*, Sacramento, VIB-4092, 1-6, 1997.

[5] F. Benedettini, "Theoretical and experimental evidence of symmetric-response instability in the finite, planar dynamics of a circular arch," in *Recent development in Nonlinear Oscillations of Mechanical Systems* (Eds. E. Kreuzer, N. van Dao), 11-22, 2000.

[6] Win-Min Tien, N. Sri Namachchivaya, and A. Bajaj, "Non-Linear Dynamics of a Shallow Arch Under Periodic Excitation 1. 1:2 internal resonance", *Int. J. Non-Linear Mech.*, 29, 349-366, 1994.

[7] Win-Min Tien, N. Sri Namachchivaya, and A. Bajaj, "Non-Linear Dynamics of a Shallow Arch Under Periodic Excitation 2. 1:1 internal resonance," *Int. J. Non-Linear Mech.,* 29, 367-386, 1994.

PHASE SPACE WARPING

A Dynamical Systems Approach to Diagnostics and Prognostics

J. P. Cusumano
Department of Engineering Science & Mechanics
Penn State University
University Park, Pennsylvania 16801
jpc@crash.esm.psu.edu

D. Chelidze
Department of Mechanical Engineering & Applied Mechanics
University of Rhode Island
Kingston, Rhode Island 02881
chelidze@egr.uri.edu

Abstract: The concept of *phase space warping* is used to develop a general method for damage evolution tracking and failure prediction. After outlining the basic theory and describing its algorithmic implementation, a nonlinear vibrating beam experiment is described in which a crack propagates to complete fracture. Our method is shown to give real-time estimates of the current damage state, and remaining useful life is accurately predicted well in advance of actual failure.

Key words: Dynamical systems, diagnostics, prognostics, failure prediction, condition monitoring, phase space reconstruction.

1. Introduction

Most previous work done in the field of machinery condition monitoring has focused on the development of robust discriminators of *impending* failures. The work described here, however, aims to move past alarm-based diagnostics to the actual tracking of *incipient* damage, which is required for a true prognostic capability that gives continuously updated estimates of remaining

G. Rega and F. Vestroni (eds.),
IUTAM Symposium on Chaotic Dynamics and Control of Systems and Processes in Mechanics, 183–192.

life. We describe a new, general framework for damage evolution tracking, diagnosis, and prognosis, and apply the resulting method experimentally.

From the point of view taken here, damage evolution takes place in hierarchical dynamical system (Cusumano and Chatterjee, 2000) of the form:

$$\dot{\mathbf{x}} = \mathbf{f}(\mathbf{x}, \boldsymbol{\mu}(\phi), t)\,, \tag{1a}$$

$$\dot{\phi} = \epsilon\, \mathbf{g}(\mathbf{x}, \phi)\,, \tag{1b}$$

where: $\mathbf{x} \in U \subset \mathbb{R}^m$ is the fast dynamic variable (the directly observable state); $\phi \in V \subset \mathbb{R}^n$ is the slow dynamic variable (the "hidden" damage state); the parameter vector $\boldsymbol{\mu} \in \mathbb{R}^k$ is a function of ϕ; t is time; and the rate constant $0 < \epsilon \ll 1$ defines the time scale separation between the fast dynamics and slow "drift".

To study systems of the form of Eqs. (1) experimentally, the concept of *phase space warping* is introduced, which refers to the small distortions that occur in the fast subsystem's vector field as a result of the underlying slowly evolving damage process. After summarizing the basic theory and describing its implementation in an algorithm, we show the results of applying the method to a system with evolving material damage.

In (Chelidze et al., 2002; Cusumano et al., 2002), the method has been applied to the study of a system in which the potential energy is perturbed by a battery-powered electromagnet: "failure" of the system in that case corresponded to complete discharge of the battery. It was shown that the tracking metric output by the algorithm was related in a 1-1, approximately linear fashion to the scalar generalized damage variable, which in that case was the open circuit battery voltage. Here, we apply the method to a vibrating beam nonlinear oscillator in which a crack propagates to complete fracture. Again, the tracking metric is shown to provide a 1-1 relationship with an independent measurement of the damage.

Using empirical damage evolution models and recursive filtering, the tracking metric can be used to predict remaining useful life. This approach has been applied to the battery experiment in a forthcoming paper (Chelidze and Cusumano, 2003), and here we apply it to the fracture experiment. In both cases, one finds that accurate, real-time estimates of current damage state and time to failure can be made well in advance of actual failures.

2. Phase Space Warping

In Eqs. (1), we assume that U and V are compact subsets. The phase space of the entire system of Eqs. (1) is the Cartesian product $\mathcal{S} = U \times V \times T$, where T is the manifold of which t is an element. We also assume that T is itself a compact manifold such as, for example, a p-torus corresponding to the vector field $\mathbf{f}$ in Eq. (1a) being p-quasiperiodic in time. The key issue is that the

dynamics of Eq. (1) must take place in a region of the extended fast phase space $\mathcal{F} = U \times T$ that is diffeomorphic (via delay coordinate embedding) with a compact subset $W \subset \mathbb{R}^d$ where d is the embedding dimension.

Our goal is to use only experimental measurements of the fast variable $\mathbf{x}$ to track, and ultimately predict, the slow variable ϕ, which is not directly measurable. Letting the constant ϕ_R represent the "reference" or initial value of the damage variable (which occurred at time t_R), and defining the prediction time $t_p = t - t_0$, we refer to the solution $\mathbf{x} = \mathbf{X}(t_p, t_0, \mathbf{x}_0, \boldsymbol{\mu}(\phi_R); \epsilon)$ as the *reference model*. We then define the time t_p ahead *short-time reference model prediction error* (STRMP) starting at time t_0 as

$$\mathbf{e}_R(\phi_0; t_p, t_0, \mathbf{x}_0) = \mathbf{X}(t_p, t_0, \mathbf{x}_0, \boldsymbol{\mu}(\phi_0); \epsilon) - \mathbf{X}(t_p, t_0, \mathbf{x}_0, \boldsymbol{\mu}(\phi_R); \epsilon)\,, \quad (2)$$

in which the arguments for $\mathbf{e}_R$ indicate that we consider it to be a map $\mathbf{e}_R : V \to \mathbb{R}^m$ with parameters t_p, t_0, and $\mathbf{x}_0$. We would like to understand conditions under which $\mathbf{e}_R$ will provide a *tracking function*, that is, a smooth, injective mapping (preferably linear) from V into $\mathbb{R}^m$.[1]

Equation (2) can be related to the fast vector field $\mathbf{f}$, since taking the derivative with respect t_p gives

$$\dot{\mathbf{e}}_R = \mathbf{f}(t_0, \mathbf{x}_0, \boldsymbol{\mu}(\phi_0)) - \mathbf{f}(t_0, \mathbf{x}_0, \boldsymbol{\mu}(\phi_R))\,. \quad (3)$$

Thus, $\dot{\mathbf{e}}_R$ measures the rate at which distortions are occurring in the vector field $\mathbf{f}$ due to changes in the slow variable. We refer to such distortions as *phase space warping*. However, since it is difficult to measure vector fields directly in experiments, we use the flow form, Eq. (2), which gives the total amount of phase space warping at any given point $(\mathbf{x}_0, t_0) \in \mathcal{F}$.

For a fixed prediction time, we expect the solutions to be smooth both with respect to initial conditions and with respect to parameters. In addition, we require that the prediction time be "short", that is $t_p \ll 1/\epsilon$. Then for any given initial time t_0, the short prediction time allows the fast subsystem of Eq. (1a) to be treated as "quasistatic", i.e. as having an approximately constant damage variable ϕ_0. Thus, using regular perturbations we expand the terms in Eq. (2) in a power series about $\epsilon = 0$, as $\mathbf{X} = \mathbf{X}_0 + \epsilon\mathbf{X}_1 + \ldots \equiv \mathbf{X}(t_p, t_0, \mathbf{x}_0, \boldsymbol{\mu}(\phi_i); 0) + O(\epsilon t_p)$ where $\phi_i = \phi_0$ or ϕ_R. Substitution into Eq. (2) gives

$$\mathbf{e}_R = \mathbf{X}(t_p, t_0, \mathbf{x}_0, \boldsymbol{\mu}(\phi_0); 0) - \mathbf{X}(t_p, t_0, \mathbf{x}_0, \boldsymbol{\mu}(\phi_R); 0) + O(\epsilon t_p)\,. \quad (4)$$

We further expand the leading term in Eq. (4) in a Taylor series about $\phi = \phi_R$, which upon substitution into Eq. (2) gives the STRMP error as

$$\mathbf{e}_R = \frac{\partial \mathbf{X}}{\partial \boldsymbol{\mu}} \frac{\partial \boldsymbol{\mu}}{\partial \phi} \left(\phi_0 - \phi_R\right) + O\left(||\phi_0 - \phi_R||^2\right) + O(\epsilon t_p)\,, \quad (5)$$

[1] In other words, $\mathbf{e}_R$ is a tracking function if every point in its range corresponds to a unique point $\phi_0 \in V$.

in which we have suppressed the fact that the derivative matrices are evaluated at $(\epsilon, \phi) = (0, \phi_R)$.

Equation (5) shows that $\mathbf{e}_R$ is to leading order an affine transformation of the slowly drifting variable,

$$\mathbf{e}_R \approx \mathbf{C}(t_p, t_0, \mathbf{x}_0, \phi_R)\, \phi + \mathbf{c}(t_p, t_0, \mathbf{x}_0, \phi_R)\,, \tag{6}$$

where $\mathbf{C} = \frac{\partial \mathbf{x}}{\partial \boldsymbol{\mu}} \frac{\partial \boldsymbol{\mu}}{\partial \phi}$ is $m \times n$, and $\mathbf{c} = -\mathbf{C}\,\phi_R$ is $m \times 1$. We have dropped the zero subscript from ϕ_0 since the above discussion is true for *any* future value of the slow variable. However, the zero subscript is still required on t and $\mathbf{x}$ since the matrices of Eq. (6) will depend on the selected initial point in the extended fast-time phase space, $(\mathbf{x}_0, t_0) \in \mathcal{F}$, used to compute the STRMP error.

A necessary condition for the transformation of Eq. (6) to be a tracking function is that the matrix $\mathbf{C} : \mathbb{R}^n \to \mathbb{R}^m$ have maximal rank. We refer to this requirement on $\mathbf{C}$ as the condition for *linear observability* for the slow variable.[2] Thus, when $\mathbf{C}$ has maximal rank, for ϵ and $||\phi_0 - \phi_R||$ both sufficiently small, we can conclude that the STRMP error allows us to unambiguously track the changes in the slow variable ϕ using only measurements of the fast variable $\mathbf{x}$. Furthermore, we see that under ideal circumstances this tracking function can be expected to be approximately linear.

Given that the values of t_p, t_0, $\mathbf{x}_0$ and ϕ_R are fixed, we can take the time derivative of Eq. (6) to find that $\dot{\mathbf{e}}_R \approx \mathbf{C}\,\dot{\phi} = \epsilon\, \mathbf{C}\, \mathbf{g}(\mathbf{x}, \phi)$. In other words, the rate of change of the tracking function, which is the rate at which phase space warping is occurring, is to leading order determined by the slow vector field.

3. Algorithmic Implementation

In this brief paper it is only possible to outline the key ideas used in the current implementation of the algorithm: the reader is referred to previous work (Cusumano et al., 2002; Chelidze et al., 2002; Chelidze and Cusumano, 2003) for further details.

In experiments the tracking function provided by the STRMP error, Eq. (6), is difficult to apply directly because $\mathbf{C}$ and $\mathbf{c}$ depend on $\mathbf{x}_0$, t_0, and t_p, which can be thought of as parameters. Unfortunately, for most applications it is difficult or impossible to repeatedly start the fast subsystem Eq. (1a) from the same initial conditions $(\mathbf{x}_0, t_0)$. Thus one should use many values of $(\mathbf{x}_0, t_0) \in \mathcal{E} \subset \mathcal{F}$ from some ensemble $\mathcal{E}$ to deal with initial state repeatability problem as well as to increase the robustness of the method. Then for every fixed ϕ, the STRMP tracking function $\mathbf{e}_R$ can be thought of as a random variable determined by

[2] We remark in passing that even when linear observability fails, higher order observability may be possible.

random maps of the form of Eq. (6), with each map corresponding to a single element of $\mathcal{E}$.

Given such an ensemble of tracking functions, one can examine the multivariate statistics of the random vector $\mathbf{e}_R$ in order obtain information about the structure of the slow phase space. This general approach is the subject of current research by the authors. For example, in its simplest form this might mean replacing the map of Eq. (6) by $\langle \mathbf{e}_R \rangle = \langle \mathbf{C} \rangle \phi + \langle \mathbf{c} \rangle$, where the angled brackets indicate the (possibly weighted) average over $\mathcal{E}$.

If it is reasonable to assume, given the physics of the problem, that the slow variable is both *monotonic in time* and *scalar*, then an even simpler approach is to consider only the magnitude of $\mathbf{e}_R$, which gives to leading order

$$\langle \, ||\mathbf{e}_R|| \, \rangle \equiv e_R = C\phi + c \, , \tag{7}$$

where $C = \langle \, ||\mathbf{C}|| \, \rangle$ and $c = -C\phi_R$. This is the approach taken in the work presented here.

3.1 Damage Tracking

In practice, the existence of a tracking function is used experimentally *as a hypothesis*, since it is generally the case that measurements of the damage variable are unavailable (indeed, that is the entire motivation for the method). In general, then, under the assumptions presented above, the output of the tracking function will identify the damage state *to within an unknown, approximately affine transformation*. However, in cases where independent measurements of the damage variable are available the tracking function can, in effect, be calibrated, so that the exact transformation can be determined.

Some form of phase space reconstruction, for example using delay coordinate embedding (Takens, 1981; Sauer et al., 1991) for initially chaotic systems or stochastic interrogation (Cusumano and Kimble, 1995) for nonchaotic systems, can be used to generate $\mathcal{E}$. In the current implementation, we prepare our system to be chaotic in its reference condition, and data is collected in a sequence of time intervals of length $t_D \ll O(1/\epsilon)$. The required ensemble $\mathcal{E}$ is then obtained by using all of the data in a given interval, with a fixed prediction time $t_p < t_D \ll O(1/\epsilon)$. The delay time τ and embedding dimension d are determined using the first minimum of the average mutual information (Fraser and Swinney, 1986) and the method of false nearest neighbors (Kennel et al., 1992), respectively.

Since the form of the governing differential equations is assumed to be unknown, we instead consider a map

$$\mathbf{y}(r+1) = \mathbf{P}\left(\mathbf{y}(r), \phi\right) \, , \tag{8}$$

where $\mathbf{y}(r)$ is the reconstructed fast state at time step r. Then, the tracking function of Eq. (2) is

$$\mathbf{e}_R(\phi; k, r) = \mathbf{P}^k\left(\mathbf{y}(r), \phi\right) - \mathbf{P}^k\left(\mathbf{y}(r), \phi_R\right) , \tag{9}$$

where $\mathbf{P}^k$ is the k^{th} iterate of the map defined in Eq. (8).

The leading term on the right hand side of Eq. (9) is simply $\mathbf{y}(r+k)$, and is available from the data. There are various ways that one might estimate the reference model $\mathbf{P}(\,\cdot\,, \phi_R)$: in this work, we use locally linear models

$$\mathbf{y}(r+k) = \mathbf{A}(r)\mathbf{y}(r) + \mathbf{a}(r) , \tag{10}$$

where $\mathbf{A}(r)$ is a $d \times d$ matrix and $\mathbf{a}(r)$ is a $d \times 1$ vector. The parameters of the local linear models are determined using regression on the N nearest neighbors of $\mathbf{y}(r)$ and their future states *for data taken in the reference condition*. Then the damage tracking function Eq. (9) can be written as

$$\mathbf{e}_R = \mathbf{y}(r+k) - \mathbf{A}^k\mathbf{y}(r) - \mathbf{a}^k + \mathbf{E}^M(r) = \mathbf{E}_k(r, \phi) + \mathbf{E}^M(r) , \tag{11}$$

where, for simplicity, we have suppressed the dependency of $\mathbf{A}$ and $\mathbf{a}$ on r. In the above equation, $\mathbf{E}^M(r)$ represents the model error and

$$\mathbf{E}_k(r, \phi) = \mathbf{y}(r+k) - \mathbf{A}^k\mathbf{y}(r) - \mathbf{a}^k \tag{12}$$

is the *estimated tracking function* that can be determined experimentally.

We wish to use the ensemble-averaged scalar tracking function Eq. (7), which can be experimentally estimated as $e_R = \langle\, ||\mathbf{e}_R|| \,\rangle \approx \langle\, F\,(||\mathbf{E}_k||)\,\rangle$, where F is a suitable filter. The filter is needed because now there are two spurious fluctuations in e_R that occur as one moves from point to point in the reconstructed fast phase space, both of which occur because we must estimate $\mathbf{e}_R$ with $\mathbf{E}_k$. The first is due to changes in the accuracy of the linear map Eq. (10), even in the absence of noise. The second is caused by experimental noise.[3] The effect of both fluctuations can be significantly reduced (Chelidze and Cusumano, 2003) by taking F to be a simple Kalman filter. In the language of recursive filtering, the first of the above fluctuations can be treated as "process noise", whereas the second is "measurement noise".

3.2 Estimation of Remaining Life

Application of the ideas outlined in the previous section results in a *damage tracking time series* over the slow time scale. Given the form of the hierarchical system Eqs. (1), the dynamics of the slow variable will be closely

[3]Note that the "model fit error" $\mathbf{E}^M$ in Eq. (11) includes both of these sources of error.

approximated by the solution to the slow flow equation obtained by replacing the slow vector field g by its long time average (Cusumano and Chatterjee, 2000).[4] This means that one can consider candidate damage models of the form

$$\dot{\phi} = \epsilon\, \bar{g}\,(\phi)\ , \tag{13}$$

where $\bar{g}$ is the long-time average of $g(\mathbf{x}, \phi)$.[5] Note that we are *not* assuming that averaging can be applied analytically: rather, we use the concept of averaging only to justify the *autonomous* form of Eq. (13). A suitable model structure must be found from first principles or empirically from prior applications of the tracking algorithm.

Given the damage model Eq. (13), the time to failure can be estimated from the tracking function output. Again, recursive estimation is used, but in this case the "process" is typically nonlinear, and so a nonlinear method, such as an extended Kalman filter, or unscented filtering (Julier and Uhlmann, 1997), must be used. The difference equations used to define the estimator treat the damage tracking time series as a series of *observations* from which one wishes to estimate the actual damage state using the "sensor model" of Eq. (7). Thus, a side benefit of using the recursive filter with a specific damage model is that one is able to obtain an estimate of the actual damage state consistent with the model.

4. Experimental Application

For the experiments described here, we used a two-well magneto-elastic oscillator, modified as described in (Chelidze et al., 2002). In the system, a clamped-free beam is restricted to a single degree of freedom by stiffeners. Two rare-earth magnets near its free end provide a two-well potential. The beam displacement is measured by a strain gauge mounted close to the clamped end. A shallow notch is machined in the beam below the strain gauge and just above the stiffeners. The system is mounted on a shaker and is forced at 8 Hz. The damage in the beam accumulates slowly and the experiment is run until complete fracture of the beam. Strain gauge output is sampled at 160 Hz sampling frequency, digitized (16 bit A/D), and stored on a computer.

The experiment was stopped after approximately every 10 minutes of data acquisition to take a digital image of the beam profile near the notch. During the image acquisition, the beam was always positioned in the same potential well, so that the surface of the notch was in tension. After taking the image,

[4] Since ϕ is considered to be a scalar, so is g.

[5] It is worth noting that the effect of "load", i.e. the amplitude of $\mathbf{x}$, enters through its average effect on g.

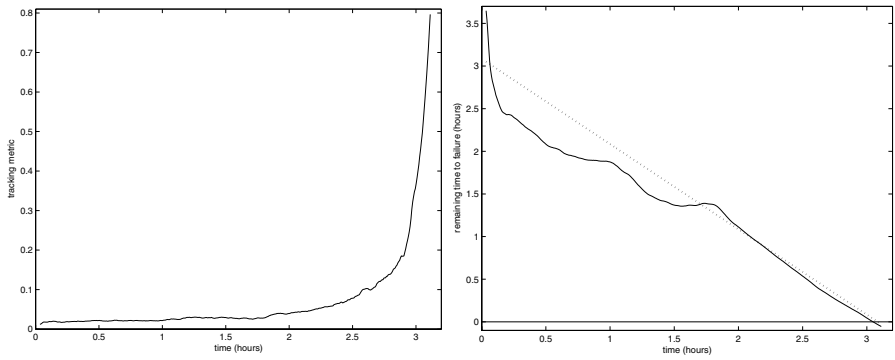

Figure 1. Damage tracking and failure prediction for a beam with growing crack: (*left*) plot of unscaled tracking metric vs. time showing simple power law behavior despite the complex dynamics of the beam; (*right*) estimated time to failure vs. time. Each black dot is the average one-step-prediction-error in a 4000 point record of fast time (160 Hz) strain gauge data. The gray line in the right figure is the actual time to failure, known *a posteriori*. The convergence to the actual time to failure occurs well before the actual failure.

forcing was restarted and collection resumed after letting initial transients die out. As the experiment progressed, there was a decrease in the beam stiffness at the notch caused by fatigue damage accumulation. As a measure of this damage, we estimated the change in the slope of the beam across the notch using the acquired digital images.

Delay time and embedding dimension were estimated to be $6t_s$ and 5, respectively. The first 2^{14} data points were used for the reference data set, and $N = 16$ nearest neighbors were used for the local linear model parameter estimation. After going through the embedding and modeling process, we split data into 456 non-overlapping records of $t_D = 4 \times 10^3 t_s$ size. The tracking function $\mathbf{e}_R$ was estimated by calculating the single sample step short-time prediction error $\mathbf{E}_1$ of the reference model for each record. The resulting damage tracking time series, in Fig. 1(left) shows smooth power law behavior, even though the actual load history at the notch is quite complex, consisting of many chaotic/periodic transitions.

For time-to-failure estimation we used a power law model, $g = \phi^\alpha$, with the final (failure) value of ϕ taken to be $\phi_F = 0.645$. Based on an examination of the tracking data, the values $\epsilon = 0.0061$ and $\alpha = 2$ were used in the recursive time-to-failure estimation procedure. The results for this process are show in Fig. 1.

Figure 1(right) demonstrates that the time-to-failure estimate converges to the true value (known *a posteriori*) over one hour before the total failure of the beam. The time required for convergence may be related to the difficulty of carrying out the required estimation when the tracking data is almost flat.

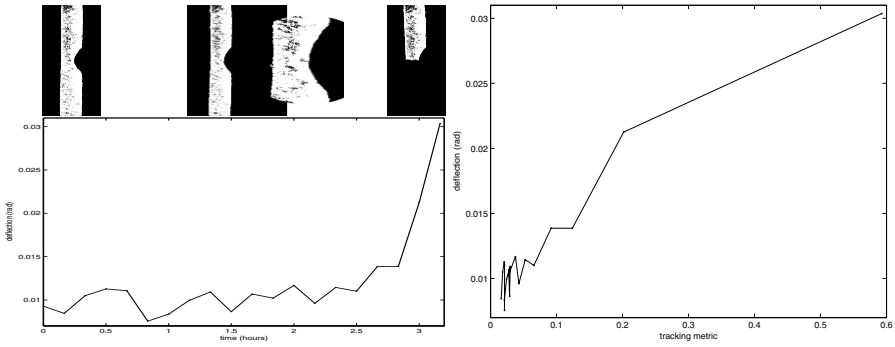

Figure 2. Calibration of tracking metric with independent measurement of damage state: (*left, top*) photos of the notch taken at 0, 3 and 3.17 hours, showing the first visible crack only 0.17 hours before the experiment's end. (*left, bottom*) Plot of angular deflection across notch during experiment, calculated from image; (*right*) plot of tracking metric vs. angular deflection. The approximately linear, 1-1 relationship is consistent with the assumptions of the phase space warping approach described in the text.

However, we also hypothesize that it indicates the difference between the crack nucleation phase, for which the simple power law model does not work, and the actual crack propagation phase, for which it does. The fact that the $\alpha = 2$ model, which is consistent with Paris' Law, works at all is remarkable given that the crack loading is decidedly not periodic.

In this case, we also have the independent measurement related to the beam damage, which is shown in Fig. 2. In Fig. 2(left, top) we sample images taken during the experiment at (from left to right) 0, 3 and 3.17 hours. The first visible crack occurred at the 3 hour mark, but actual prediction of time to failure converges about 1 hour before that point, and tracking even earlier, indicating the sensitivity of the tracking method. Figure 2(left, bottom) shows the static angular deflection across the notch computed from the images. It is seen to increase in a way that is qualitatively similar to the tracking function output. Finally, Fig. 2(right) presents a plot of the angular deflection data vs. the tracking metric. We see an approximately linear, 1-1 relationship: although this measurement is not a direct measurement of the damage variable, the result is consistent with the phase space warping theory presented in Section 1.

Acknowledgements

DC would like to acknowledge the support of this work by the NSF Career Award No. CMS-0237792. The work of JC is supported in part by the Air Force Research Laboratory, via UTC contract No. 03-S470-024-C1.

References

[1] D. Chelidze and J. Cusumano, "A dynamical systems approach to failure prognosis," *ASME Journal of Vibration and Acoustics*, 2003, in press.

[2] D. Chelidze, J. Cusumano and A. Chatterjee, "A dynamical systems approach to damage evolution tracking, part I: Description and experimental application," *ASME Journal of Vibration and Acoustics*, **124**:250–257, 2002.

[3] J. Cusumano, D. Chelidze and A. Chatterjee, "A dynamical systems approach to damage evolution tracking, part II: Model-based validation and physical interpretation," *ASME Journal of Vibration and Acoustics*, **124**:258–264, 2000.

[4] J.P. Cusumano and A. Chatterjee, "Steps towards a qualitative dynamics of damage evolution," *International Journal of Solids and Structures*, **37**(44):6397–6417, 2000.

[5] J.P. Cusumano and B. Kimble, "A stochastic interrogation method for experimental measurements of global dynamics and basin evolution: Application to a two-well oscillator," *Nonlinear Dynamics*, **8**:213–235, 1995.

[6] A.M. Fraser and H.L. Swinney, "Independent coordinates for strange attractors from mutual information," *Phys. Rev. A*, **33**(2):1134–1140, 1986.

[7] S.J. Julier and J.K. Uhlmann, "New extension of kalman filter to nonlinear systems," *In Signal Processing, Sensor Fusion, and Target Recognition VI*, volume 3068, pages 182–193, 1997.

[8] M.B. Kennel, R. Brown and H.D.I. Abarbanel, "Determining embedding dimension for phase-space reconstruction using a geometric construction," *Phys. Rev. A*, **45**(6):3403–3411, 1992.

[9] T. Sauer, J.A. Yorke and M. Casdagli, "Embedology," *J. Stat. Phys.*, **65**(3-4):579–616, 1991.

[10] F. Takens, "Detecting strange attractor in turbulence," In Rand, D. A. and Young, L. S., editors, *Dynamical Systems and Turbulence, Warwick*, pages 336–381. Springer Lecture Notes in Mathematics, Springer-Verlag, Berlin, 1981.

TIME INTEGRATION TECHNIQUES TO INVESTIGATE THE LONG-TERM BEHAVIOUR OF DISSIPATIVE STRUCTURAL SYSTEMS

Ugo Galvanetto and P. Burkhard Bornemann
Department of Aeronautics, Imperial College London, London SW7 2BY, United Kingdom
u.galvanetto@imperial.ac.uk

Abstract: The dynamics of a beam subjected to quasi-periodic excitation is simulated with a finite element model and an energy-conserving based time integration scheme. The numerical methods are capable of reproducing the dynamics of the system if a fixed time step size is applied, whereas the application of adaptive time step seems more problematic.

Key words: Numerical integration, structural dynamics, time-step adaptivity.

1. Introduction

Modern structures are making an increasing use of light flexible components; clear examples of such a tendency are given by light bridges, helicopter and windmill blades, telecom towers, satellite components, vibrating mechanical tools, pipes suspended on the sea bed ... In general non-linear effects cannot be neglected when studying the dynamics of such structures and they can constitute an insidious risk for the structural engineer, as the problems with the Millennium bridge in London have recently shown. Moreover the growing demand to reduce the maintenance costs, and the need not to diminish safety, require the capability to predict

G. Rega and F. Vestroni (eds.),
IUTAM Symposium on Chaotic Dynamics and Control of Systems and Processes in Mechanics, 193–201.

the behaviour of structural components subjected to variable loads for long periods of time.

The complexity of a large variety of modern structures reduces considerably the possibility of using analytical methods in the study of the structural dynamics. Therefore computational techniques seem to be the most appropriate tool to predict the long-term dynamic behaviour of complex structures. In the structural engineering research community the finite element method is the most popular technique to discretise the structure in space and it is usually coupled with finite difference techniques for the time integration.

The time integration algorithms to be applied must possess two important features: they must be robust and accurate in a global sense. Robustness refers to an algorithm that can handle problems with many degrees of freedom for a long time without incurring computational instabilities. With the words 'global accuracy' we mean that the time integration scheme (applied to a spatially discretised model) should be able to reproduce the 'global dynamic behaviour' of the system: steady states and bifurcations, chaotic dynamics.

Experimental results are necessary in order to assess the performance of different time integration schemes. In the last 25 years several experiments have been carried out and described in the scientific literature:

1) cantilever beam in a two-well magnetic field [1],
2) cantilever beam impacting a rigid stop [2, 3],
3) cantilever beam under frictional excitation [4, 5, 6],
4) clamped beam with quasi-periodic excitation [7, 8],
5) cantilever beam with elastic band [9].

All the above listed experiments present characteristics typical of non-linear systems: coexisting stable steady states, chaotic motions and bifurcations.

Study of those beam systems are often based on Global Galerkin methods with the eigenmodes as shape functions, which decompose the spatial-temporal differential equations.

More recently, finite element discretisations have been applied, based on a local Galerkin method, allowing potentially a more flexible representation. In particular, if the beam undergoes large deflections, a geometrically non-linear beam model is required and an accurate description of the dynamics by its eigenmodes associated to its linearisation may be questionable. Nonetheless a sophisticated beam model is not sufficient for an accurate quantitative prediction. Realistic simulations require a precise knowledge of the mechanical phenomena affecting the beam dynamics. A precise description of the forces due to magnetic fields (experiment 1), impacts (experiment 2), friction (experiment 3) and nonlinear response of the elastic band (experiment 4) would introduce too many uncertainties in the

numerical model; for that reason the experiment number 4 was selected as the most suitable to be simulated.

Yagasaki investigated in [7, 8] a simple clamped beam subjected to quasi-periodical excitation. The problem is modeled easily with planar Reissner beam elements and the numerical simulations presented in the remainder detected a non-linear behaviour similar to that found experimentally. The FEM discretisation presented in section 3 introduces 60 (or 30) degrees of freedom. Such a system has to be integrated for a long time (order of 10^3 seconds) and, therefore, an adaptive time step would seem an appropriate choice to reduce the computing time without reducing the accuracy of the computed solution. The application of different methods to adapt the time step length to the varying solution will be presented in the paper which is organized as follows: section 2 briefly describes the experiment, section 3 describes the beam element and the fixed time step integration method initially adopted, section 4 presents the different time step adaptivity techniques and section 5 contains results and conclusions.

2. Quasi-Periodically Excited Beam

The structure investigated in [7, 8] consists of a slightly pre-tensioned beam, clamped at both ends and subjected to a quasi-periodical excitation (Fig. 1):

$$y_e(t) = a_1 \sin(\omega_1 t) + a_2 \sin(\omega_2 t) \tag{1}$$

The beam is excited with frequencies $\omega_1 \cong \omega_2 \cong \Omega_1$, where Ω_1 is the lowest eigenfrequency. Without pre-tension a frequency $\Omega_0 < \Omega_1$ would characterize the first eigenmode. The forcing amplitudes a_1, a_2 are very small, of the same order of magnitude as the thickness h. The beam is homogeneous, slender and of constant cross section.

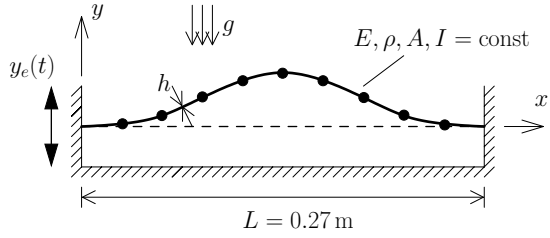

Figure 1

Yagasaki discretised the differential equation of motion with a modal decomposition, essentially a global Galerkin method, and then applied to the discretised system an averaging procedure. Yagasaki concluded that an

approximation for this weakly non-linear system is reasonable with only the first eigenform. Co-existing steady states, period-doubling and chaos could be anticipated analytically, found numerically and verified experimentally. As the reference [8] provides very accurate information about all important parameters involved in the experiment, the system seems a reliable basis for the evaluation of numerical results obtained with a finite element approach.

3. FEM and Time Integration

The beam is modeled with planar 2-noded Reissner beam elements, the model incorporates large translations and rotations with finite strains, see Figure (2). The energy-conserving based method (ECB) is applied as time marching integration method, [10, 9]. The algorithm consists of two parts, namely:

$$\frac{\boldsymbol{x}_{n+1}-\boldsymbol{x}_n}{\Delta t_n}=\frac{\boldsymbol{v}_{n+1}+\boldsymbol{v}_n}{2} \tag{2}$$

$$\boldsymbol{M}\frac{\boldsymbol{v}_{n+1}-\boldsymbol{v}_n}{\Delta t_n}=-\boldsymbol{D}\frac{\boldsymbol{v}_{n+1}+\boldsymbol{v}_n}{2}-\boldsymbol{q}_{i,m}+\boldsymbol{q}_e \tag{3}$$

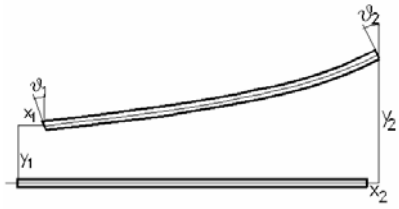

Figure 2

The vectors $\boldsymbol{x}_{n+j}$, j=0,1, contain the approximations for the six nodal degrees of freedom of one beam element at time t_{n+j}, for instance $\boldsymbol{x}_n$= [x_1, y_1, ϑ_1, x_2, y_2, ϑ_2]$_n$, and $\boldsymbol{v}_{n+j}$ is the vector of the relevant velocities. The consistent mass matrix $\boldsymbol{M}$ and the damping matrix $\boldsymbol{D}$=$c\boldsymbol{M}$, c>0, are symmetric and positive definite. The external force vector is constant, containing only the load due to gravity. Although Equation (2) resembles the trapezoidal rule, the second part of the ECB method, Equation (3), is different. The difference stems from the discretisation of the internal force vector $\boldsymbol{q}_{i,m}$ which is designed to recover exactly the change of internal energy V_i. The internal force vector is given as

$$(\boldsymbol{x}_{n+1}-\boldsymbol{x}_n)^T\boldsymbol{q}_{i,m}=V_{i,n+1}-V_{i,n} \tag{4}$$

Details can be found in [10]. The exact fulfillment of Equation (4) provides an inherently total energy-conserving algorithm, if applied to the beam problem without damping and external excitation. An interesting

consequence of the application of this energy-conserving algorithm to dissipative dynamics is the establishment of a 'discrete Lyapunov function'. Consider the change of total energy, H, consisting of kinetic energy, K, internal and external potential energies, V_{i} and V_{e}, in one time step:

$$\frac{H_{n+1}-H_n}{\Delta t_n}=\frac{K_{n+1}-K_n}{\Delta t_n}+\frac{V_{i,n+1}-V_{i,n}}{\Delta t_n}-\frac{V_{e,n+1}-V_{e,n}}{\Delta t_n}=-\left(\frac{\boldsymbol{v}_{n+1}+\boldsymbol{v}_n}{2}\right)^T\boldsymbol{D}\frac{\boldsymbol{v}_{n+1}+\boldsymbol{v}_n}{2}\le 0 \tag{5}$$

as $\boldsymbol{D}$ is positive definite. A global Lyapunov function guarantees stability of almost all trajectories: all motions converge to a static equilibrium position, e.g. [11, 12]. The above property makes the application of the ECB method desirable even in dissipative systems. However the introduction of an external force might introduce some additional difficulties.

4. Time-Step Adaptivity

Standard time-step adaptivity relies on a local error estimator, e.g. Hairer et al. [13]. The estimated error determines whether the step has to be repeated with a reduced size, if the error is too large, or accepted, and in this case the step size, Δt_{n+1} for the next step is also proposed. In essence the step size is changed to satisfy the following equation:

$$\left\|d_{n+1}\right\|\le tol \tag{6}$$

where d_{n+1} is the local discretisation error [13] and tol is a user-supplied tolerance. Inequality (6) can be used to express the 'optimal' step size ratio r^* and the new step size Δt_{new}:

$$r^*=\sqrt[p+1]{\frac{tol}{\left\|d_{n+1}\right\|}}\quad and\quad \Delta t_{new}=\Delta t_n\cdot min(\,r_{max},max(\,r_{min},sr^*\,)) \tag{7}$$

where p is the order of the scheme, 2 for the ECB method; moreover the new step size, Δt_{new} is restricted by maximum and minimum values of the ratio r, r_{max} and r_{min}, and decreased by a scalar $0<s<1$. These modifications reflect the limited reliability of the 'optimal value' r^*.

Local error estimators can be defined by comparison between the time marching scheme and an auxiliary scheme. Here two auxiliary schemes are presented: a linear multi-step method and single-step method. The marching scheme results are used to evaluate the auxiliary vectors to minimize the additional computational cost.

The linear multi-step method is the second order accurate member of the Adams-Bashforth methods (AB2) [13, chap. III]. It uses the positions and the velocities from the last converged step, $\boldsymbol{x}_n$ and $\boldsymbol{v}_n$, and the velocities from the penultimate converged step, $\boldsymbol{v}_{n-1}$, to extrapolate $\boldsymbol{x}_{n+1}$ with a parabola:

$$\boldsymbol{x}_{n+1}^{AB2} = \boldsymbol{x}_n - \frac{\Delta t_n^2}{2\Delta t_{n-1}}\boldsymbol{v}_{n-1} + \frac{2\Delta t_n \Delta t_{n-1} + \Delta t_n^2}{2\Delta t_{n-1}}\boldsymbol{v}_n \tag{8}$$

In Equation (8) and in the next Equations (9)-(13), the vectors $\boldsymbol{x}$, $\boldsymbol{v}$, $\boldsymbol{a}$, with no superscript indicate the values of the relevant quantities computed with the ECB method. The local error estimator is defined as:

$$\text{AB2: } \boldsymbol{d}_{n+1}^{AB2} \approx \frac{K^{ECB}(\boldsymbol{x}_{n+1} - \boldsymbol{x}_{n+1}^{AB2})}{K^{AB2} - K^{ECB}} \text{ where } K^{ECB} \approx -\frac{1}{12},\ K^{AB2} = \frac{2\Delta t_n + 3\Delta t_{n-1}}{12} \tag{9}$$

The constant K^{ECB} is only provided approximately, as the ECB method is not a linear integrator; the used value corresponds to its linearised form.

The single step method is the third order accurate member of Newmark's family (NM3) and was suggested by Zienkiewicz and Xie [14]:

$$\boldsymbol{x}_{n+1}^{NM3} = \boldsymbol{x}_n + \Delta t_n \boldsymbol{v}_n + \frac{\Delta t_n^2}{3}\boldsymbol{a}_n + \frac{\Delta t_n^2}{6}\boldsymbol{a}_{n+1} \tag{10}$$

In [14] $\boldsymbol{a}_n$ and $\boldsymbol{a}_{n+1}$ are known, but for the ECB method only 'mid-point' accelerations are needed in Equations (2). The acceleration could be obtained by inverting Equation (2):

$$\boldsymbol{a}_{n+1} = -\boldsymbol{a}_n + \frac{2}{\Delta t_n}(\boldsymbol{v}_{n+1} + \boldsymbol{v}_n) \tag{11}$$

A different determination was preferred:

$$\boldsymbol{a}_{n+1} = -\boldsymbol{M}^{-1}(\boldsymbol{D}\boldsymbol{v}_{n+1} + \boldsymbol{q}_i(\boldsymbol{x}_{n+1}) - \boldsymbol{q}_{e,n+1}) \tag{12}$$

The application of Equation (12) has a higher computational cost, but it reduces incremental error accumulation. The inverse of the mass matrix $\boldsymbol{M}$ is computed only once and then stored. Finally, the local error estimator is given by the following equation:

$$\text{ZX: } \boldsymbol{d}_{n+1}^{ZX} \approx \boldsymbol{x}_{n+1} - \boldsymbol{x}_{n+1}^{NM3} \tag{13}$$

5. Results and Conclusions

In all numerical simulations one component of the external excitation (1) was kept fixed as: a_1/h=0.05 and ω_1=1.167 Ω_1 with the relevant period $T_1=2\pi/\omega_1$. Amplitude and frequency of the second component were varied. Figure 3 shows a reasonably good agreement between the results obtained with the current finite element approach and those presented in [9]. The FEM numerical procedure correctly locates two bifurcations also presented in [9]: a subcritical period doubling bifurcation and a fold bifurcation of the period-2 orbit born at the period doubling point, see Figure 4. Figure 4 shows that a small number of elements is sufficient to capture the dynamics of the system since no appreciable difference can be noticed between the

results produced by two different models, with ten or twenty elements. Other bifurcations can be more sensitive to a change in the number of elements, such as the period doubling cascade shown in Figure 5 where two bifurcation diagrams are superimposed, one obtained with a 10 element mesh and the other with a 20 element mesh. A similar sensitivity can be noticed in Figure 6 with respect to the time step size.

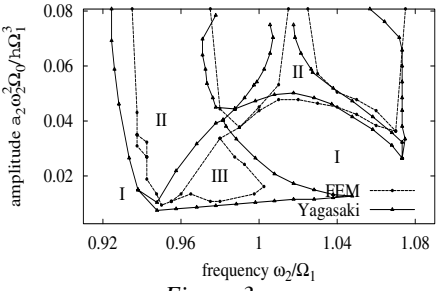

Figure 3

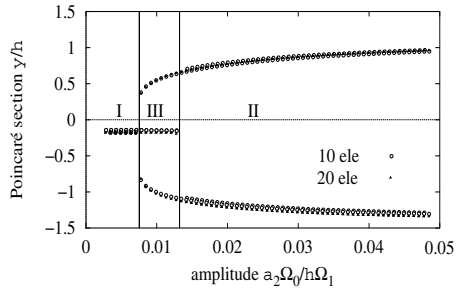

Figure 4

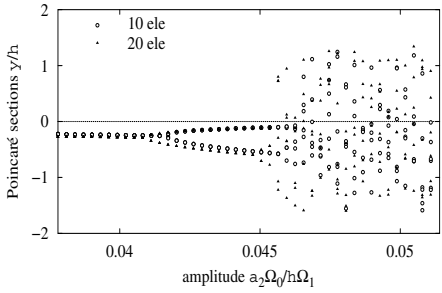

Figure 5

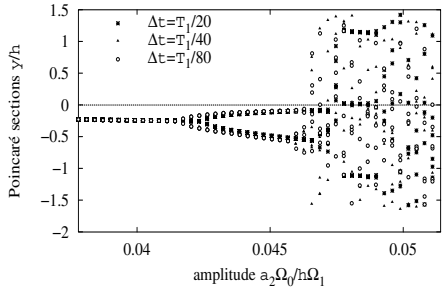

Figure 6

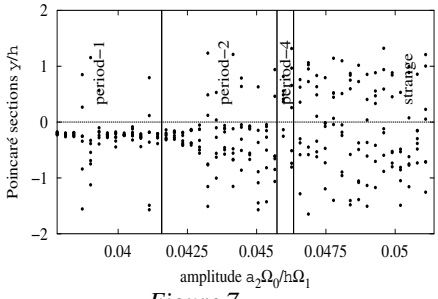

Figure 7

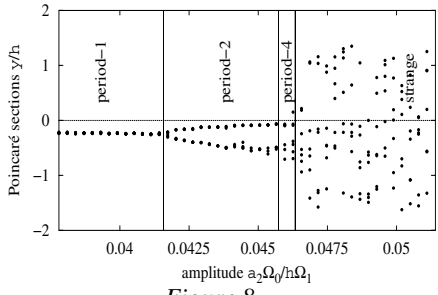

Figure 8

The production of simple bifurcation diagrams for a system with a large number of degrees of freedom (20 elements have 60 dof) may require a long time. Moreover, non-linear problems can be thought of as characterised by several frequencies. For these reasons it would seem reasonable to adapt the time step size to the current dynamics of the system in order to increase accuracy and reduce the computer time. Figures 7 and 8 show the bifurcation

diagrams obtained respectively with the adaptive time step strategies AB2 and ZX, previously defined. Even if both adaptive strategies use an average step size of $\Delta t=T_1/160$, they produce results that are worse than those obtained with a constant step size of $\Delta t=T_1/80$, as it is apparent from the comparison with Figure 5 or 6.

The paper shows that it is possible to investigate the complex dynamics of realistic structures with the finite element method and suitable time integration schemes. Intuition suggests that the investigation of the steady states of complex systems under the variation of one or more parameters would be an ideal field of application for time step adaptive techniques. Nonetheless the preliminary computations described in this paper seem to suggest a more prudent approach [15, chapter VIII].

Acknowledgements

This work was carried out thanks to the financial support of the Engineering and Physical Sciences Research Council of the UK. UG acknowledges also the support of the Royal Academy of Engineering.

References

[1] F. Moon and P. Holmes, "A magnetoelastic strange attractor," *J Sound Vib.,* **65** (2), 275-296, 1979.

[2] S.W. Shaw, "Forced vibrations of a beam with one-sided boundary constraint-Theory and experiment," *J. Sound Vib.,* **99** (2): 199-212, 1985.

[3] D.J. Wagg, G. Karpodinis, and S.R. Bishop, "An experimental study of the impulse response of a vibro-impacting cantilever beam," *J. Sound Vib.*, **228** (2): 243-264, 1999.

[4] K. Popp and P. Stelter, "Stick-slip vibrations and chaos," *Phil. T. Roy. Soc. A* **332** (1624): 89-105, 1990.

[5] M.F. Azeez and A.F. Vakakis, "Proper orthogonal decomposition (POD) of a class of vibroimpact oscillations," *J. Sound Vib*., **240** (5), 859-889, 2001.

[6] R.V. Kappagantu and B.F. Feeny, "Dynamical characterization of a frictionally excited beam," *Nonlin. Dyn*., **22**: 317-333, 2000.

[7] K. Yagasaki, "Chaotic dynamics of a quasi-periodically forced beam," *J. Appl. Mech.*, **59**:161-167, 1992.

[8] K. Yagasaki, "Bifurcations and chaos in a quasi-periodically forced beam: {Theory}, simulation and experiment," *J. Sound Vib*., **183** (1):1-31, 1995.

[9] P. B. Bornemann Ph.D. thesis in preparation, Department of Aeronautics, Imperial College London, 2003.

[10] N. Stander and E. Stein, "An energy-conserving planar finite beam element for dynamics of flexible mechanisms," *Engng. Comput.*, **13** (6):60-85, 1996.

[11] J. Guckeheimer and P. Holmes. *Nonlinear Oscillations, Dynamical Systems and Bifurcations of Vector Fields*, Springer Verlag, New York, 2002.

[12] P. B. Bornemann and U. Galvanetto, "Discrete dynamics of implicit time integration schemes for a dissipative system," to be published in *Comm. Num. Meth. Engng*., 2003.

[13] E. Hairer, S.P. Nørsett, and G. Wanner, *Solving Ordinary Differential Equations I, Nonstiff Problems*, volume 8 of Springer series in computational mathematics. Springer-Verlag, Berlin, 1987.

[14] O.C. Zienkiewicz and Y.M. Xie, "A simple error estimator and adaptive time-stepping procedure for dynamic analysis," *Earth. Eng. Struct.,***20**(9), 871-887, 1991.

[15] E. Hairer, C. Lubich, and G. Wanner. *Geometric Numerical Integrations*, volume 31 of Springer series in computational mathematics. Springer-Verlag, Berlin, 2002.

IDENTIFICATION AND CONSTRUCTION OF REDUCED ORDER MODELS FOR INFINITE-DIMENSIONAL SYSTEMS IN NONLINEAR ELASTODYNAMICS

Proper Orthogonal Decompositions

Ioannis T. Georgiou
National Technical University of Athens, Greece
georgiou@central.ntua.gr

Abstract: Reduced order models for the dynamics of an exact nonlinear elastic rod are derived by projecting its full order coupled equations of motion onto a set of Proper Orthogonal Modes. These optimal modes are identified by POD analysis of the finite element dynamics. Numerical study of the reduced models suggests that the subspace spanned by the POD modes represents an invariant subspace of the dynamics inside which a normal mode of vibration resides and whose shape is close to that of the dominant POD mode.

Key words: Infinite dynamical systems, proper orthogonal decomposition, reduced order models, nonlinear normal modes, invariant manifolds.

1. Introduction

One of the current important research issues concerning the dynamics of infinite-dimensional systems in nonlinear elasticity is to characterize the spatio-temporal complexity of dynamics, especially coupled vibrations. The dynamic response of these systems is expected to be quite complicated because the involved strongly and nonlinearly various coupled fields force the infinite-degrees-of-freedom to interact in various known and unknown ways. To capture the essentials of interactions among the various involved fields it is necessary to use models with high level of predictability. Such models are the so-called geometrically exact models for rods and shells. These models capture accurately the dynamics by taking into account

G. Rega and F. Vestroni (eds.),
IUTAM Symposium on Chaotic Dynamics and Control of Systems and Processes in Mechanics, 203–212.

exactly the nonlinear geometric coupling of the displacement of the middle curve (surface) and the rotation of the cross-section.

Long time dynamical processes of dissipative systems in elastodynamics usually involve only a small number of degrees-of-freedom, indicating indirectly the presence of an invariant subspace of low dimension [1]. Thus a way to characterize spatio-temporal complexity is to derive reduced order models by restricting such a system onto an invariant subspace. However, invariant subspaces for such dynamical systems (exact rods and shells) are not known a priory. In this work we extract (identify) information on the spatial structure of-not known a priory-invariant subspaces (manifolds) by processing high-resolution information on the trajectories of motions of an exact planar rod by the method of Proper Orthogonal Decomposition (POD) for coupled fields [2]. Reduced order models are derived by restricting the fully coupled nonlinear equations of motion onto the subspaces identified by the POD process. POD-based reduced order models provided effective means to characterize the spatio-temporal complexity of the dynamics of infinite coupled systems.

2. Pod Identification of Optimum Modes

We consider the equations of motion of a geometrically exact rod as a representative dynamical system for infinite nonlinear systems involving coupled multi-fields. In particular, the equations of motion of a planar exact rod are described by the following three coupled nonlinear PDEs:

$$\begin{aligned}
&\rho A u_{1,\mathrm{tt}}(s,t) + C u_{1,\mathrm{t}}(s,t) + AE u_{1,\mathrm{ss}}(s,t) \\
&\qquad + N_1\left\{u_1(s,t), u_2(s,t), \theta_3(s,t)\right\} = 0 \\
&\rho A u_{2,\mathrm{tt}}(s,t) + C u_{2,\mathrm{t}}(s,t) - GA\left[u_{2,\mathrm{ss}}(s,t) - \theta_{3,\mathrm{s}}(s,t)\right] \\
&\qquad + N_2\left\{u_1(s,t), u_2(s,t), \theta_3(s,t)\right\} = P\cos(\Omega t) \\
&\rho I \theta_{3,\mathrm{tt}}(s,t) + C\theta_{3,\mathrm{t}}(s,t) - EI\theta_{3,\mathrm{ss}}(s,t) + GA\left[\theta_3(s,t) - u_{2,\mathrm{s}}(s,t)\right] \\
&\qquad + N_3\left\{u_1(s,t), u_2(s,t), \theta_3(s,t)\right\} = 0.
\end{aligned} \tag{1}$$

The independent variables s,t denote space and time, respectively. The variables $u_1(s,t)$ and $u_2(s,t)$ denote respectively the longitudinal and transverse displacements of the neutral axis; whereas the variable $\theta_3(s,t)$ denotes rotational displacement of the cross-section. The constants L, A, I denote respectively the length, uniform rectangular cross-section, and second

moment of inertia I of the rod. The constants ρ, E, G, C denote respectively mass density, modulus of elasticity in extension and shearing, and coefficient of linear viscous damping. The material composing the rod is assumed to be linear elastic. The terms P and Ω denote respectively amplitude and frequency of the uniformly distributed transverse harmonic forcing. Moreover, the functions $N_m\{u_1(s,t), u_2(s,t), \theta_3(s,t)\}, m = 1,2,3$ denote nonlinearities, being very complicated mathematical expressions containing trigonometric terms, reflecting the fact that the geometric nonlinearity is modeled exactly.

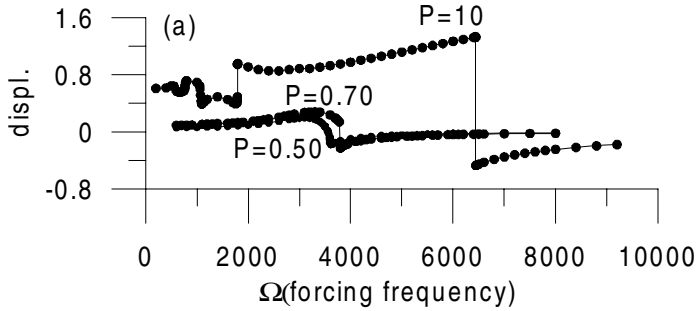

Figure 1. Typical frequency sweeps attractor diagrams for a harmonically excited planar rod. The vertical axis represents the Poincare map iterates for the transverse displacement of the middle point. All attractors are periodic motions (periodic coupled vibrations).

The equations of motion (1) constitute a dynamical system of infinite degrees-of-freedom which involves three strongly and exactly coupled fields. Depending on the level of excitation, we anticipate weak and strong interactions among these coupled fields. An analytic treatment of the equations of motion without simplifying the exact nonlinearity is not possible given the current state-of-art of nonlinear methods. However, the system can be solved as accurately as desired by an efficient algorithm based on the method of finite elements [3,4]. *The finite element model keeps intact the geometric nonlinearity*, *thus producing high-resolution information on the dynamics*. Figure 1 shows a picture of qualitative dynamics computed systematically by combining the methods of finite elements and Poincare sections.

Instead of following a classical way of analysis, which lowers the level of predictability of the model due to unavoidable approximations to the nonlinearies, we use the finite element dynamics as an information database on the dynamics to compute the Proper Orthogonal Decomposition [2,3] of the trajectory of a motion, that is,

$$\vec{\boldsymbol{V}}(s,t) = \sum_{m=1}^{\infty} A_m(t)\sqrt{\lambda_m}\vec{\boldsymbol{\Phi}}_m(s) = \sum_{m=1}^{\infty} A_m(t)\vec{\boldsymbol{\Psi}}_m(s) \tag{2}$$

The amplitudes $A_m(t)$ form a set of orthonormal functions over a specified time interval $[T_1, T_2]$. The companion vector-valued shape functions $\vec{\boldsymbol{\Psi}}_m(s)$ form a set of orthonormal functions over the space interval $[0, L]$ occupied by the rod. Such amplitude and its compaction shape form a Proper Orthogonal Decomposition (POD) mode. The constant λ_m determines the fraction of autocorrelation energy contained in this mode. We exploit the fact that the trajectory of a motion functions as a probe regarding the spatial structure of an invariant manifold possibly carrying it. The POD modes characterize (identify) optimally the spatial structure of invariant subspace (manifolds). Therefore, they can be used for optimal model reduction. We have the following result: For values of the excitation frequency in an interval containing only the first linear bending frequency and excitation amplitude ranging from very small to moderate levels, all attractors (periodic and chaotic) are characterized by three to five POD modes. In particular, almost all the autocorrelation energy, or signal energy, of the trajectory of a motion is contained in a single POD mode.

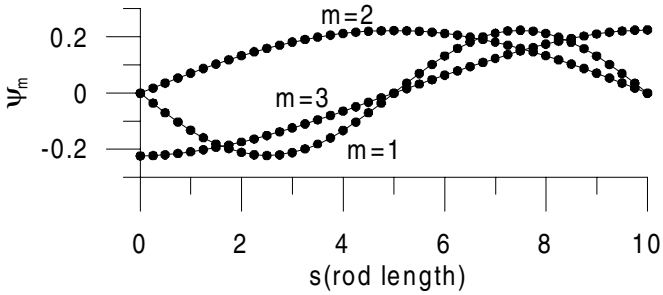

Figure 2. The identified normalized shapes of the axial (m=1), transverse (m=2), and rotatory (m=3) components of the dominant POD mode. The POD analysis of a motion furnishes the norms and the normalized shapes of the components of all POD modes.

Figure 2 shows the shapes of the components of the first (dominant) POD mode. The shapes and energy contents as well as the relative norms of the POD modes remain almost the same for a wide range of forcing amplitudes combined with low frequency harmonic excitation. The POD method furnishes a complete characterization of the POD modes that support a motion. Thus, if the motion resides on an invariant subspace, the POD modes characterize it uniquely and optimally. Clearly the POD process is a very effective tool to characterize the spatial structure of the coupling among the various fields, see Figure 2, of infinite coupled systems.

3. Model Reduction

Here we use the identified POD modes to derive low order reduced models for the dynamics of the exact planer rod, the representative infinite coupled system. Galerkin projection of the coupled equations of motion (1) onto the function space spanned by the first two POD modes yields the following 2-DOF system (amplitude equations),

$$\boldsymbol{M}\vec{\boldsymbol{A}}_{tt}(t) + \boldsymbol{D}\vec{\boldsymbol{A}}_{t}(t) + \boldsymbol{K}\vec{\boldsymbol{A}}(t) + \int_0^L \vec{\boldsymbol{N}}\left(\vec{\boldsymbol{A}}(t), \vec{\boldsymbol{\Psi}}_1(s), \vec{\boldsymbol{\Psi}}_2(s)\right) ds = \vec{\boldsymbol{F}}(t). \quad (3)$$

The 2×2 constant matrices $\boldsymbol{M}, \boldsymbol{D}, \boldsymbol{K}$ denote respectively mass, dissipation, and stiffness. The 2×1 vector

$$\int_0^L \vec{\boldsymbol{N}}\left(\vec{\boldsymbol{A}}(t), \vec{\boldsymbol{\Psi}}_1(s), \vec{\boldsymbol{\Psi}}_2(s)\right) ds$$

denotes a nonlinearity of *integral type*, reflecting the mathematical complexity of the geometric nonlinearities modeled exactly. Vector $\vec{\boldsymbol{A}}(t) \equiv \left(A_1(t), A_2(t)\right)^T$ denotes the amplitudes of the two POD modes. Since the motion is dominated by a single POD mode, we also derive a 1-DOF reduced system by restricting the full order system onto the dominant POD mode. The reduced order systems are integrated numerically to be compared to the full order system and predict its dynamics at low frequency excitation.

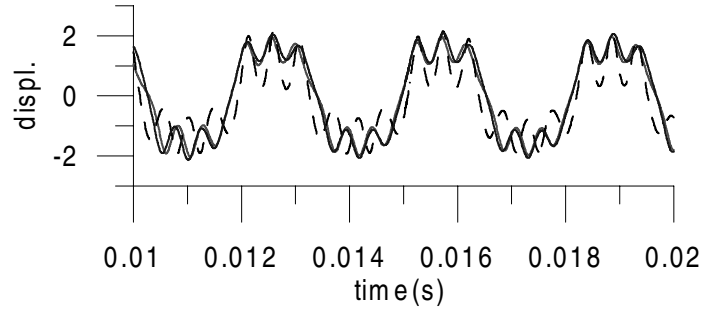

Figure 3. Comparison for the reduced (3) and full order (1) systems: 1-DOF system (dashed curve), 2-DOF system (solid line), equations of motion of the rod (solid line).

Figures 3, 4 reveal that the 2-DOF reduced system predicts exceptionally well the quantitative dynamics of the full order system (1). It was expected that the 1-DOF system would predict accurately the dynamics of the full order system since it is the restriction onto the single dominant POD mode. Figure 5, however, reveals that the 1-DOF and 2-DOF systems predict different qualitative dynamics *for small amplitude motions*. The reader is reminded that the second POD mode contains a tiny fraction of the

autocorrelation energy. It seems that the POD modes with small energy play an important role in determining the qualitative dynamics. Extensive numerical studies with the reduced and full order systems reveal that the discrepancy between the reduced systems is due to the interaction of nonlinearity and dissipation. This interaction is pronounced greatly at small levels of dissipation.

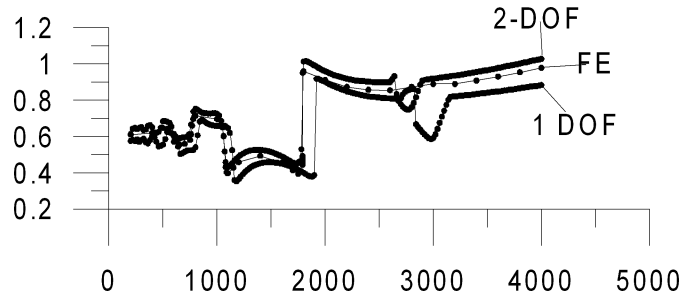

Figure 4. Comparison of attractor diagrams for the 1-DOD and 2-DOF reduced systems and the full order system (FE). The vertical axis records the Poincare map iterates of the transverse displacement at the middle of the rod. For frequency sweeps at low amplitude level, the reduced order systems predict exceptional well the dynamics of the full order system.

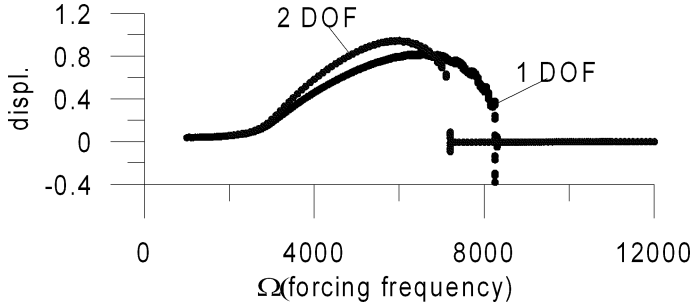

Figure 5. Typical frequency sweep bifurcation diagrams predicted by the 1-DOF and 2-DOF reduced systems at very small forcing amplitude (P=0.25). Notice a large difference in the value of the frequency at which a jump occurs.

4. Prediction of the Reduced Dynamics at Low Frequency Excitation

In this section we employ the 2-DOF reduced model to predict the dynamics of the full order system in the form of attractor and bifurcation diagrams. The system parameters are different than those used to identify the shapes of the POD modes used to derive the reduced order systems. Figure 6 compares the attractor diagrams predicted of the full order system (1) and the 2-DOF reduced system (2). Clearly the reduced system predicts very well the dynamics of the full-order system. We notice the excellent prediction of the frequencies at which jumps occur. We find that if the dissipation is increased the jumps become smooth. This indicates that these frequencies are characterized by amplitude amplification and phase shift. Thus, they must be resonant (sub-harmonic) frequencies.

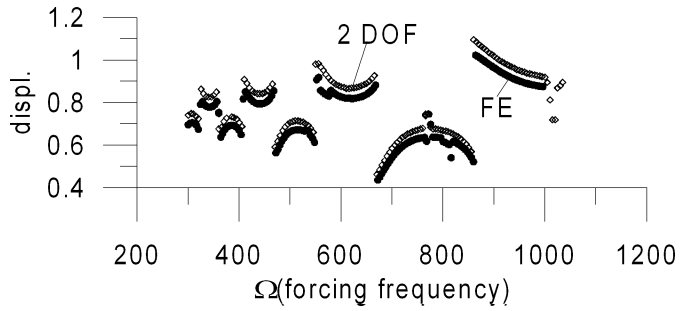

Figure 6. Attractor diagram for frequency response at amplitude P=15. The dissipation is about five times smaller than that used to derive the reduced order model. The 2-DOF system predicts exceptionally well the dynamics of the full order system (FE).

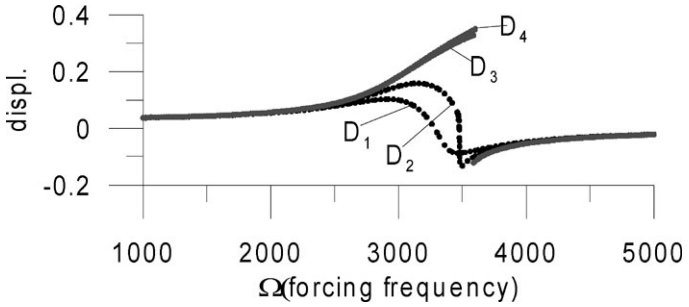

Figure 7. Frequency response at amplitude P=0.25 and four different dissipation levels. At large dissipation we detect a smooth resonant frequency zone. As the dissipation is decreased, the resonance zone shrinks and develops a jump.

The reduced order system is used to explore the interaction of nonlinearity and dissipation. Figure 7 shows several attractor diagrams for frequency sweeps at various levels of dissipation. The interaction of nonlinearity and dissipation is manifested in the form of discontinuities (jumps) in bifurcation diagrams. For large dissipation and sufficient small forcing amplitude nonlinearity effects are almost no existing. Figure 8 reveals a strong hyteresis effect in bifurcation diagrams for a frequency sweep at very low forcing amplitude. Bifurcation diagrams for amplitude sweep reveal the coexistence of multiple period and chaotic attractors and hysteresis. This is shown clearly in Figure 9.

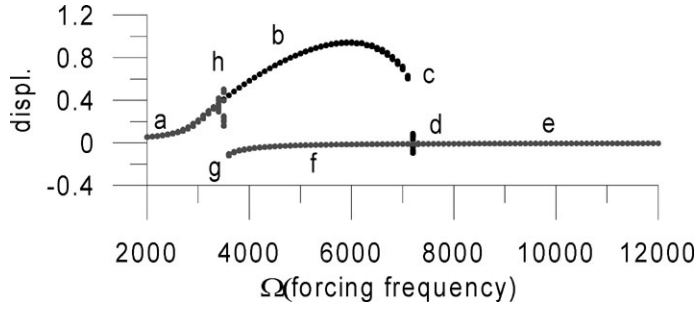

Figure 8. A typical frequency sweep bifurcation diagram at the small amplitude level (P=0.25) reveals hysteresis. Quasi-static sweep form left to right (abcde) and sweep from right to left (edfgha).

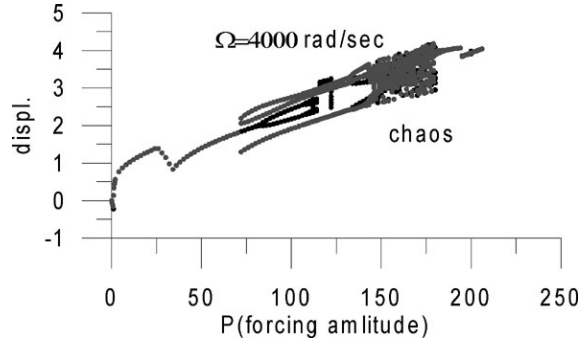

Figure 9. Frequency sweep bifurcation diagram predicted by the 2-DOF reduced system at a forcing frequency close to the first linear natural frequency of bending motion. We observe chaotic attractors, hysteresis, and multiple coexisting periodic attractors

The 2-DOF reduced system can be further analyzed as a Singular Perturbation Problem [2,5]. Indeed, this reduced system possesses a two-dimensional slow invariant manifold. The POD mode with smallest amount

of autocorrelation energy is slaved to the dominant one. As we have seen above, the POD mode with small energy content affects considerably not only the quantitative but also the qualitative dynamics predicted by the reduced model stemming from the dominant POD mode.

5. Conclusion

First and second order reduced models were derived for the dynamics of a nonlinear rod forced harmonically at low frequencies. We accomplished this by identifying the set of Proper Orthogonal Decomposition modes underlining the trajectory of a motion, computed numerically. The low frequency response is underlined by a single POD mode. The other participating POD modes contain tiny amounts of autocorrelation energy. The 1-DOF reduced model, the restriction of the full order system onto the dominant POD mode, does not predict satisfactorily the dynamics of the full order system at low dissipation levels, indicating the need to include more POD modes to refine it. Indeed, the 2-DOD system predicts exceptionally well the dynamics of the full order system. Therefore, we claim that the reduced order system describes the dynamics in an invariant subspace in the phase space of the full order system. Moreover, the 2-DOF reduced system possesses a slow invariant manifold, a fact implying that the dominant POD mode is close or identical to a two-dimensional invariant manifold representing a normal mode of oscillation.

Acknowledgement

This work was partially supported by an ARO contract to SAIC, McLean, Virginia. The author is a consulting scientist with SAIC.

References

[1] R. Temam, *Infinite-Dimensional Dynamical Systems in Mechanics and Physics,* Springer-Verlag, New York, 1988.

[2] I. Georgiou and I.B. Schwartz, "Dynamics of large scale coupled structural/mechanical systems: a singular perturbation/Proper Orthogonal Decomposition approach," *SIAM J. Appl. Math.*, 59, No. 4, pp. 1178-1207, 1999.

[3] I. Georgiou and J. Sansour, "Analyzing the Finite Element Dynamics of Nonlinear In-plane Rods by the Method of Proper Orthogonal Decomposition," *Computational Mechanics, New Trends and Applications*, S. Idelsohn, E. Onate and E. Dvorkin (Eds.), CIMNE, Barcelona, Spain, 1998.

[4] C. Sansour and H. Bednarczyk, "The Cosserat surface as a shell model, theory and finite element formulation," *Computer Methods in Applied Mechanics and Engineering*, 120, pp. 1-32, 1995.
[5] C. Jones, *Geometric Singular Perturbation Theory Dynamical in Systems* (Springer Lecture Notes Math. 1609), pp. 44-120, 1995.

THE NON-LINEAR DYNAMICS OF THIN WALLED SHELL STRUCTURES

Paulo B. Gonçalves and Zenón J. G. N. del Prado
Civil Engineering Department, Catholic University, PUC-Rio, 22453-900, Rio de Janeiro, Brazil.
paulo@civ.puc-rio.br

Abstract: This paper discusses the non-linear oscillations and dynamic instabilities of thin walled shells subjected to harmonic loads. Due to the presence of strong non-linearities and high sensitivity to small variations in control parameters, thin shells may display a complex dynamic behavior and, despite the recent advances in this field, there is still a lack of satisfactory solutions to this class of problems. There are several complicated issues relating to the dynamics of such structures. In this work some of these topics are addressed, namely shell discretization processes, influence of modal coupling on non-linear vibration modes, modal interaction between different non-linear vibration modes, imperfection sensitivity and fractal basin boundaries. To this end, the theory for quasi-shallow shells is used to study the non-linear vibrations and instabilities of thin cylindrical shells under axial load.

Key words: Thin walled shells, non-linear vibrations, dynamic buckling, modal interaction, modal coupling, imperfection sensitivity.

1. Introduction

1.1 Shell Structures

Man-made constructions and natural things exist in a great variety of forms. Shells stand out sharply against other structures built by man or nature and are found in a large variety of forms. Being essentially a thin walled curved structure, shells usually stand up well to various loads, in particular surface and edge loads, and look extremely attractive from a structural engineering point of view because of their relatively low weight. However, thin walled shells when subjected to distributed compressive

G. Rega and F. Vestroni (eds.),
IUTAM Symposium on Chaotic Dynamics and Control of Systems and Processes in Mechanics, 213–222

loads often exhibit a highly non-linear response and may be subjected to several types of instabilities which are a key feature to be considered in their structural analysis. Moreover, many of these structures will typically experience these loads in a dynamic environment. In order to be able to exploit the efficiency of these shell structures, their non-linear oscillations and buckling behavior need to be elucidated. In most practical shell problems instabilities or large amplitude vibrations may lead to permanent damage or even a catastrophic failure of the system, but there are some system where the non-linear shell behavior is a desirable feature [1]. In both cases the knowledge of shell non-linear behavior is essential for the establishment of proper design criteria.

However there are several difficulties in assessing this problem. The first problem is how to model correctly the continuous system as a low dimensional discrete system so that we can use most of the numerical tools of modern non-linear dynamics. This issue is closely related to other two key topics in non-linear shell analysis: modal coupling and modal interaction. These terms have been used in different ways in the literature. Here, the term modal coupling is related to the essential linear modes necessary to describe the non-linear behavior of the shell while modal interaction describes the interaction between different non-linear modes. Previous studies conducted by the authors on cylindrical and spherical shells [2,3] showed that the complex dynamics of thin walled shells is mainly due to the presence of strong quadratic and cubic non-linearities emerging, respectively, from the curved surface initial shape and from stretching of the middle plane and are responsible for a strong modal coupling and modal interaction. This coupling is responsible, for example, for the well known softening behavior exhibited by shells and a wealth of non-linear phenomena, some of them still coming to light. These topics are addressed in this paper and their importance on shell dynamics is clarified.

Among recent investigations on the dynamic instability of thin shell one should mention the works of Baumgarten et al. [4], Popov et al. [5,6], McRobie et al. [7], Teixeira et. al. [1], Gonçalves and Del Prado [2] and Soliman and Gonçalves [3]. These investigations using new numerical and analytical techniques related to low-dimensional models of complex dynamical systems have shed some light on the complex dynamics of thin shells.

The understanding of the instability phenomena is enhanced by the knowledge obtained from previous studies on the free and forced non-linear vibrations of thin shells. The pioneering studies on this subject were mainly concerned with the proper modal solution to obtaining meaningful low dimensional models and with the character (hardening or softening) and degree of non-linearity exhibited by thin shells. A discussion of these earlier studies was published by Amabili et. al. [8].

2. Theoretical Background

2.1 Shell Equations

By definition shell is a body bounded by two curved surfaces, the distance h between them being small in comparison with the other dimensions. This assumption has been used to reduce the three-dimensional problem to a two-dimensional one. The essence of shell theory is that the displacements of any point within the shell can be expressed in terms of the displacement components of a reference surface. This procedure is not unique and several shell theories are found in literature. But in the literature on buckling and large amplitude vibrations of shells, the theory for quasi-shallow shells is the most commonly used. Here this formulation is selected on the basis that it is the simplest approach that retains the essential non-linear features of the problem.

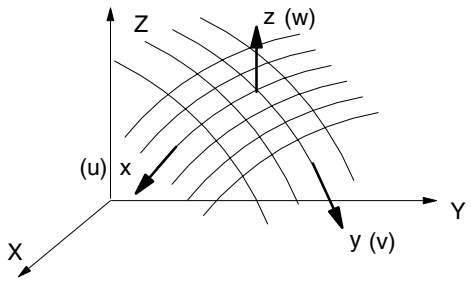

Figure 1. Shell co-ordinate system

Consider a thin walled shell of arbitrary shape made of an isotropic, homogeneous and elastic material. A general point P on the shell median surface is specified by two orthogonal curvilinear co-ordinates x and y, as shown in Figure 1. These directions are made to coincide with the directions of the principal curvatures, $1/R_x$ and $1/R_y$. Distances ds_x and ds_y along the co-ordinate lines are given by $ds_x = A\,dx$ and $ds_y = B\,dy$ where A and B are the Lamé coefficients (see, for example, Brush and Almroth, [9]).

Points outside the median surface are located by an additional co-ordinate z. The strains at a point x, y, z can be written in terms of the six median surface deformational quantities

$$\varepsilon_x^* = \varepsilon_x - z K_x \qquad \varepsilon_y^* = \varepsilon_y - z K_y \qquad \gamma_{xy}^* = \gamma_x - 2 z K_{xy} \tag{1}$$

where the median surface strains are given in terms of the displacement components u, v and w and the rotations β_x and β_y as

$$\varepsilon_x = \frac{u_{,x}}{A} + \frac{A_{,y}\, v}{AB} + \frac{w}{R_x} + \frac{1}{2}\beta_x^2 \quad \varepsilon_y = \frac{v_{,y}}{B} + \frac{B_{,x}\, u}{AB} + \frac{w}{R_y} + \frac{1}{2}\beta_y^2$$
$$\gamma_{xy} = \frac{v_{,x}}{A} + \frac{u_{,y}}{B} - \frac{B_{,x}\, v + A_{,y}\, u}{AB} + \beta_x \beta_y \tag{2}$$

with

$$\beta_x = -\frac{w_{,x}}{A} + \frac{u}{R_x} \qquad \beta_y = -\frac{w_{,y}}{B} + \frac{v}{R_y} \tag{3}$$

The changes of curvature are given by

$$K_{xx} = \frac{\beta_{x,x}}{A} + \frac{A_{,y}\, \beta_y}{AB} \qquad K_{yy} = \frac{\beta_{y,y}}{B} + \frac{B_{,x}\, \beta_x}{AB}$$
$$2K_{xy} = \frac{\beta_{y,x}}{A} + \frac{\beta_{x,y}}{B} - \frac{A_{,y}\, \beta_x + B_{,x}\, \beta_y}{AB} \tag{4}$$

Using these expressions, one arrives at the following equations of motion

$$(BN_x)_{,x} + (AN_{xy})_{,y} - B_{,x}\, N_y + A_{,y}\, N_{xy} = -ABp_x$$
$$(AN_y)_{,y} + (BN_{xy})_{,x} - A_{,y}\, N_x + B_{,x}\, N_{xy} = -ABp_y$$
$$M\ddot{w} + \beta_1 \dot{w} + \beta_2 \nabla^4 \dot{w} + \left[\frac{1}{A}(BM_x)_{,x}\right]_{,x} - \left(\frac{A_{,y}}{B} M_x\right)_{,y} + \left[\frac{1}{B}(AM_y)_{,y}\right]_{,y}$$
$$- \left(\frac{B_{,x}}{A} M_y\right)_{,x} + 2\left[M_{xy,xy} + \left(\frac{A_{,y}}{A} M_{xy}\right)_{,x} + \left(\frac{B_{,x}}{B} M_{xy}\right)_{,y}\right] - AB\left(\frac{N_x}{R_x} + \frac{N_y}{R_y}\right) -$$
$$\left[\left(BN_x\beta_x + BN_{xy}\beta_y\right)_{,x} + \left(AN_y\beta_y + AN_{xy}\beta_x\right)_{,y}\right] = -ABp_z \tag{5}$$

where N_x, N_y and N_{xy} are normal and shearing force intensities and M_x, M_y and M_{xy} are bending and twisting moment intensities. These non-linear equations have quadratic and cubic terms in the displacements and their derivatives. Applications of these equations to particular geometries show that the type and degree of non-linearity are very sensitive to the shell principal curvatures $1/R_x$ and $1/R_y$.

2.2 Shell Spatial Discretization

The usual approach when studying shells is to reduce the partial differential equations of the continuum system into an approximate system of finite dimension. Methods such as the FEM are useful for practical structural design, but it is certainly a time demanding and cumbersome approach to understand some fundamental problems of shell non-linear dynamics, where detailed parametric analyses must be performed to unveil the rich dynamics of the structure. In the non-linear dynamic analysis of shells Ritz or Galerkin methods have been traditionally used. For this the

displacement field must be described by a sum of approximate functions satisfying the necessary boundary conditions. Using separation of variables, these functions can be described as

$$u = \sum_i \sum_j U_{ij}(t) f_{1i}(x)\, g_{1j}(y); \quad v = \sum_i \sum_j V_{ij}(t) f_{2i}(x)\, g_{2j}(y);$$
$$w = \sum_i \sum_j W_{ij}(t)\, f_{3i}(x)\, g_{3j}(y) \tag{6}$$

A key point is this process is to know the minimum number of terms in each series, which must be used to capture the real system dynamics, at least qualitatively. From previous investigations on modal solutions for the non-linear analysis of shells it is observed that, in order to obtain a consistent modeling with a limited number of modes, the sum of shape functions for the displacements must express the non-linear coupling between the modes and describe consistently the type of non-linearity (hardening of softening) of the shell. Traditional perturbation methods may be used to identify these essential modes [10].

3. Numerical Results

3.1 Modal Coupling

Consider a perfect thin walled circular cylindrical shell of radius R, length L and thickness h. The shell is assumed to be made of an elastic, homogeneous and isotropic material with Young's modulus E, Poisson ratio ν and mass per unit area M. ($A=1$, $B=R_y=R$ and $1/R_x=0$ in equations (1) to (5)). The shell has: $h = 0{,}002$ m, $R = 0{,}2$ m, $L = 0{,}4$ m, $E = 2{,}1 \times 10^8$ kN/m^2, $\nu = 0{,}3$ and $M = 78{,}5$ kg/m^2, $C_1 = 1{,}6\%$ of the critical damping and $C_2 = \eta D$ with $\eta = 0{,}0001$. For such a shell, the transversal displacement can be written as [10]

$$w = \sum_{i=1,3,5} \sum_{j=1,3,5} W_{ij} \cos\left(i\, n \frac{y}{R}\right) \sin(j\, q\, x) +$$
$$\sum_{k=0,2,4} \sum_{\ell=0,2,4} W_{kl} \cos\left(k\, n \frac{y}{R}\right) \cos(\ell\, q\, x) \tag{7}$$

where n is the number of circumferential waves and $q = m\pi / L$, in which m is the number of axial half-waves in the linear problem and W_{ij} are time dependent generalized co-ordinates.

These modes represent both the symmetric and asymmetric components of the non-linear shell deflection pattern. Previous studies on buckling and non-linear oscillations of cylindrical shells have shown that the most important modes are [2]

$$w(x,y) = \xi_{11} \sin(qx) \cos(ny/R) + \xi_{02} \cos(2qx) \tag{8}$$

where $\xi_{ij} = W_{ij}/h$. Figure 2 illustrates the influence of modal coupling on the (a) post-buckling behavior and (b) frequency-amplitude relation of the shell. Equation (8) is the lowest order model capable to express, at least qualitatively, the correct non-linearity of this shell geometry.

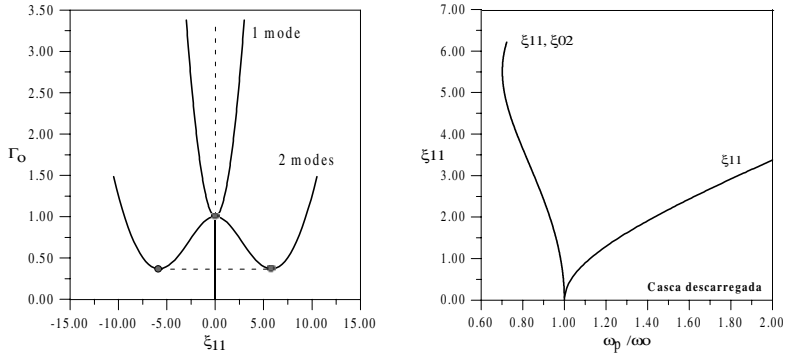

(a) (b)

Figure 2. Influence of modal coupling on the (a) post-buckling behavior of cylindrical shells under axial force and (b) its amplitude-frequency relation.

3.2 Modal Interaction

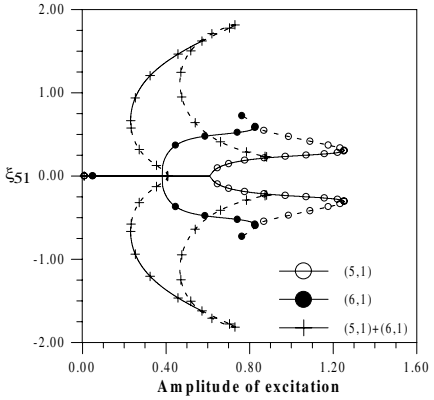

Figure 3. Bifurcation diagrams. Influence of modal interaction.

To illustrate the influence of modal interaction in shell dynamics, Figure 3 shows the bifurcation diagram for a parametrically loaded cylindrical shell subjected to a dynamic axial load of the type

$$\Gamma(t) = \Gamma_o + \Gamma_1 \cos(\omega t); \qquad \Gamma = P / P_{cr} \tag{9}$$

considering two modes with two nearly equal natural frequencies; modes *(n.m)= (5,1)* and *(6,1)* (the two lowest natural frequencies).

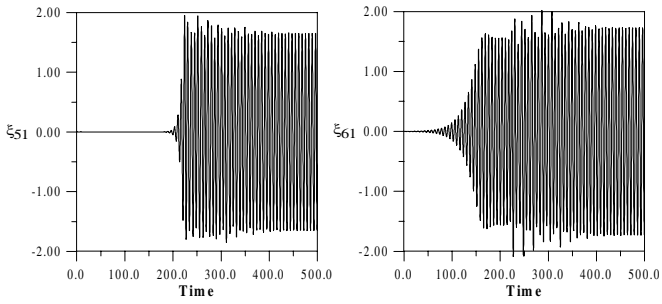

(a)– Parametric Instability. No escape. Both modes excited.

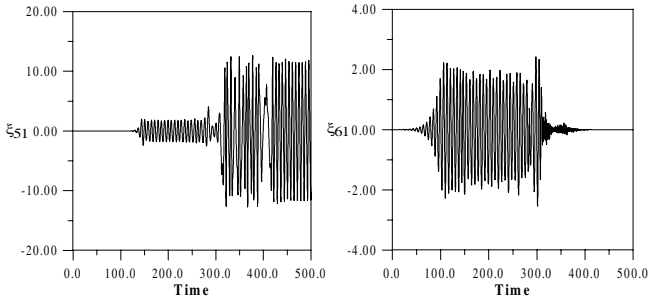

(b) – Energy exchange between modes. Long term behavior dominated by mode (5,1)

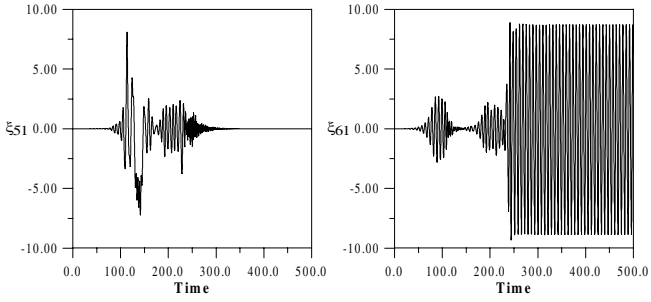

(c) - Energy exchange between modes. Long term behavior dominated by mode (6,1)

Figure 4. Influence of modal interaction on the long-term response of the shell. $\Omega=1.80$, $\Gamma_0=0.50$ and (a) $\Gamma_1=0.50$, (b) $\Gamma_1=0.58$, (c) $\Gamma_1=0.64$.

For the uncoupled vibration modes the multi-degree of freedom model associated with each non-linear mode gives a stable post-critical response (super-critical parametric bifurcation), while the response for the coupled model, (5,1)+(6,1), is unstable (sub-critical parametric bifurcation). It is interesting to notice that the dynamic behavior of the shell illustrated here is similar to the static behavior of the famous Augusti model, where the coupling of two stable responses leads to an unstable solution.

Figure 4 shows the influence of modal interaction on the transient and long-term behavior of the shell in a parameter region where modal interaction is dominant. As observed here, there is a noticeable energy transfer between the modes during the transient response and the long-term response is very sensitive to system parameters and may be controlled by one or two modes.

3.3 Imperfection Sensitivity and Fractal Basins Boundaries

Predicting the real non-linear static and dynamic responses of thin shells in numerical simulations is, despite the advent in recent year of extremely powerful computers and softwares, a difficult task because most models do not include some essential characteristics of the problem that initiate instabilities such as nonuniformities or imperfections in either the structure or loading. The influence of geometric imperfections on the non-linear response and load carrying capacity of thin shells has been one of the main issues of the theory of static stability [9]. However, this topic has been rarely treated in non-linear dynamics. In the present work, the influence of imperfections on bifurcations and basins of attraction are analyzed and their importance on shell design is evaluated.

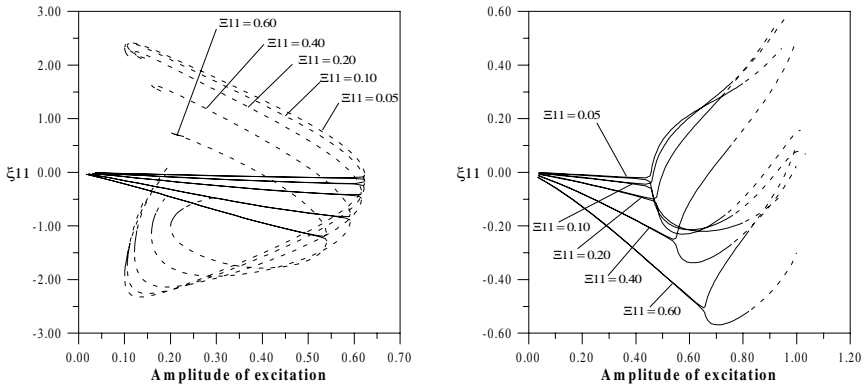

(a) $\Omega=\omega/\omega_n=1.00$ (b) $\Omega=\omega/\omega_n=1.70$

Figure 5. Influence of imperfections on shell dynamic bifurcations. (a) Decreasing critical load; (b) increasing critical load for increasing imperfection amplitude.

Consider a cylindrical shell with the following transversal imperfection field, based on the modal expansion (7)

$$w(x,y) = \Xi_{11} \sin(qx) \cos(ny/R) + \Xi_{02} \cos(2qx) \tag{10}$$

where Ξ_{ij} are the normalized imperfection amplitudes.

Figure 5 illustrates the influence of geometric imperfections on the bifurcation diagrams of the cylindrical shell under axial force. Depending on the relation between the excitation frequency ω and the lowest natural frequency ω_n, the critical load may increase or decrease with the imperfection, depending on the type of bifurcation of the perfect system.

Figure 6 shows cross-sections of the n-dimensional basin of attraction onto the ξ_{11}.vs. ξ_{02} plane for Γ_0 = 0.5 and two imperfection levels. The basin cross-section for the perfect system is symmetric with respect ξ_{11} and non-symmetric with respect ξ_{02} . This is explained by the symmetry breaking effect of the axi-symmetric term on the non-linear displacement field. As the imperfections increase the whole basin topology is distorted with a clear predominance of certain solutions. Also, the results show that the imperfections increase the velocity of the basin erosion and consequently the sensitivity of the system to initial conditions.

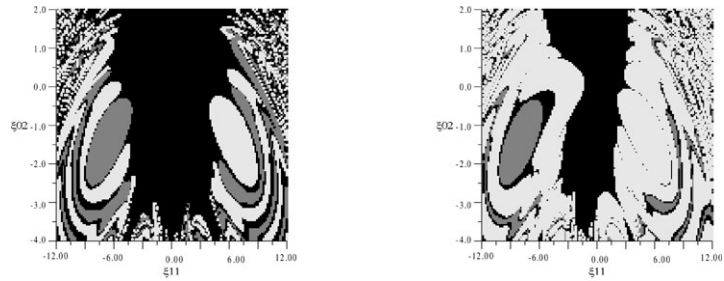

$\Xi_{11} = 0.05, \Xi_{02} = 0.0$ $\Xi_{11} = 0.60, \Xi_{02} = 0.0$

Figure 6. Influence of imperfections on the basin of attraction

Previous investigations on the non-linear dynamics of spherical and cylindrical shells [2,3] have also shown that stability boundaries in parameter space can become fractal. As in all dynamical systems there is uncertainty in the specification of the parameters values, the combined effects of imperfection sensitivity, sensitivity to initial conditions and system parameters makes it rather difficult to determine the response of a shell in the more sensitive parameter regions. This points out to the difficulties in obtaining reliable experimental results that can be used to check the accuracy and consistency of current mathematical models. Also, this leads to a difficulty in determine safe but non-conservative parameter values in design and this, together with the limited number of publications

on this subject, explains the lack of proper specifications for the design of thin shells under dynamic loads and the large knock-down factors still used in all engineering fields.

4. Final Remarks and Conclusions

The results of this research on shell dynamics highlight the influence of modal coupling and interaction and geometric imperfections on the non-linear oscillations and instabilities of shell structures. They also point out to the difficulties in modeling this class of problems and the steps still needed to arrive at conclusions that may help in the safe and yet non-conservative design of thin walled buckling sensitive shells under dynamic loads.

References

[1] P.B.C. Teixeira, P.B. Gonçalves, I.A. Cestari, A.A. Leirner, and D. Pamplona, "Mechanical behavior and stability of the internal membrane of the incor ventricular assist device," *Artificial Organs. International Society for Artificial Organs*, Blackwell Science, Inc., 25(11), 912-921, 2001.

[2] P.B. Gonçalves and Z.J.G.N. Del Prado, "Non-linear oscillations and stability of parametrically excited cylindrical shells," *Meccanica,* 37(6), 569-597, 2002.

[3] M. Soliman, and P.B. Gonçalves, "Chaotic behaviour resulting in transient and steady state instabilities of pressure loaded shallow spherical shells," *Journal of Sound and Vibration*, 259(3), 497-512, 2003.

[4] R. Baumgarten, E. Kreuzer, and A.A. Popov, "A bifurcation analysis of the dynamics of a simplified shell model," *Nonlinear Dyn.,*12, 307-317, 1997.

[5] A.A. Popov, J.M.T. Thompson, and J.G.A. Croll, "Bifurcation analyses in the parametrically excited vibrations of cylindrical panels," *Nonlinear Dynamics*, 17, 205-225, 1998.

[6] A.A. Popov, J.M.T. Thompson, and F.A. McRobie, "Low dimensional models of shell vibrations. Parametrically excited vibrations of cylinder shells," *Journal of Sound and Vibration*, 209, 163-186, 1998.

[7] F.A. McRobie, A.A. Popov, and J.M.T. Thompson, "Auto-parametric resonance in cylindrical shells using geometric averaging," *Journal of Sound and Vibration* 227(1), 65-84, 1999.

[8] M. Amabili, F. Pellicano, and M.P. Païdoussis, "Non-linear vibrations of simply supported, circular cylindrical shells, coupled to quiescent fluid," *Journal of Fluids and Structures*, 12, 883-918, 1998.

[9] D.O. Brush and B.O. Almroth, *Buckling of Bars, Plates and Shells*, McGraw-Hill Kogakusha, Tokyo, 1975.

[10] P.B. Gonçalves and R.C. Batista, "Non-linear vibration analysis of fluid-filled cylindrical shells," *Journal of Sound and Vibration* 127, 133-143, 1988.

INFLUENCE OF BOUNDARY CONDITIONS RELAXATION ON PANEL FLUTTER

R. A. Ibrahim, D. M. Beloiu
Wayne State University, Department of Mechanical Engineering, Detroit, MI 48202, USA
Raouf_Ibrahim@eng.wayne.edu

C. L. Pettit
Air Force Research Laboratory, AFRL/VASD, Wright-Patterson Air Force Base, OH 45433, USA

Abstract: The problem of nonlinear panel flutter with relaxation in the boundary conditions is studied based on a phenomenological model of joint preload relaxation. The conventional boundary value problem of the panel involves time-dependent boundary conditions that will be converted into autonomous ones using a special coordinate transformation. The resulting boundary conditions will be combined with the governing non-homogeneous, partial differential equation that will include the influence of the boundary conditions relaxation. The analysis will be restricted to two-mode interaction and includes the influence of boundary conditions relaxation on the panel modal frequencies and limit cycle amplitudes in the time and frequency domains. The relaxation and system nonlinearities are found to have opposite effects on the frequency evolution of the panel.

Key words: Panel flutter, boundary condition, nonlinear interaction.

1. Introduction

There are several factors affecting joint relaxation, which are well documented in references [1,3]. A fastener subjected to vibration will not lose all pre-loads immediately. First there will be a slow loss of pre-load caused by some of the relaxation mechanisms. Vibration will increase relaxation because wear and hammering will take place during vibration. Vibration-induced loosening and relaxation effects cause time-dependent boundary conditions and depend on the level of structural vibration. Under a stationary random

G. Rega and F. Vestroni (eds.),
IUTAM Symposium on Chaotic Dynamics and Control of Systems and Processes in Mechanics, 223–232.

excitation, the response of a nonlinear beam was analyzed by Qiao, et al. [8] and exhibited nonstationary behavior.

Panel flutter has been extensively studied under deterministic and stochastic air flow [6]. However, a limited number of studies considered the influence of uncertainties in aeroelastic structures. For example, Poiron [7] introduced uncertainties in analyzing the flutter characteristics of aircraft models and used a first-order perturbation method and Monte Carlo simulation to determine the flutter probability for different values of flow speeds and mass parameters. He found that the mean values of the mass parameter yield instability for a flow speed of 310 m/s, which is slightly greater than the critical speed. The effect of uncertainty in the boundary conditions combined with the variability of material properties on nonlinear panel aeroelastic response was studied by Lindsley, et al. [4,5]. Parametric uncertainty was examined by modeling variability in Young's modulus and the boundary conditions. The variability in the boundary conditions was restricted to a single value along the plate boundary edges for each realization. It was reported that for values of dynamic pressure in the deterministic limit cycle oscillation range, the variability in the boundary conditions affects the panel deflection in an essentially linear manner. However, for values in the neighborhood of a bifurcation point, the relationship is nonlinear. Variation in the boundary conditions results in a softening effect of the clamped panel, and thus induces an increase in the amplitude of plate oscillations.

These studies did not include the influence of boundary conditions relaxation on the flutter characteristics of aeroelastic structures. The present work is an extension of the work of Ibrahim, et al. [2] and Qiao, et al. [8] to examine the influence of relaxation of boundary conditions on the panel flutter characteristics such as modal natural frequencies and limit cycle amplitudes.

2. Analysis

Based on the quasi-steady state, supersonic theory, the deflection of a two-dimensional panel undergoing cylindrical bending is caused by the interaction of inertia, elastic, and aerodynamic forces. The governing equation of motion may be developed using Hamilton's principle. In order to estimate the work done by aerodynamic loading, the dynamic pressure is estimated using piston theory including quadratic nonlinearity. With reference to Figure 1, the governing equation of motion is

$$m_p \frac{\partial^2 w}{\partial t^2} + D\left(1 + c\frac{\partial}{\partial t}\right)\frac{\partial^4 w}{\partial x^4} - \left[N_{x0} + \frac{Eh}{2a}\int_0^a \left(\frac{\partial w}{\partial x}\right)^2 dx\right]\frac{\partial^2 w}{\partial x^2} + \frac{\rho_\infty U_\infty^2}{M}\left\{\begin{array}{c}\frac{\partial w}{\partial x} + \frac{1}{U_\infty}\frac{\partial w}{\partial t} + \frac{(\gamma+1)}{4}\times \\ \left[\frac{M}{U_\infty^2}\left(\frac{\partial w}{\partial t}\right)^2 + \frac{2M}{U_\infty}\frac{\partial w}{\partial t}\frac{\partial w}{\partial x} + M\left(\frac{\partial w}{\partial x}\right)^2\right]\end{array}\right\} = p_0 \tag{1}$$

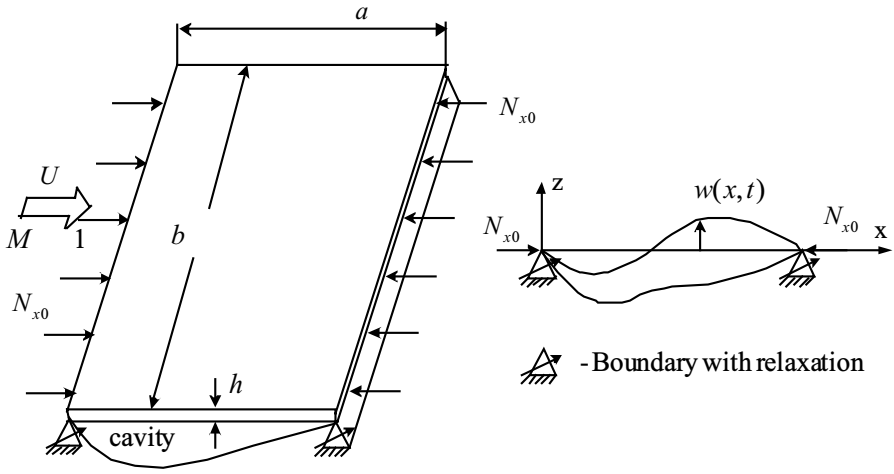

Figure 1. Schematic diagram of a panel in supersonic flow

where $w(x,t)$ is the panel deflection, m_p is the panel mass per unit area, a is the panel length, E is Young's modulus, h is the plate thickness, $D = \frac{Eh^3}{12(1-\nu^2)}$, ν is Poisson's ratio, p_0 is the static pressure across the panel, $a_\infty = \sqrt{\frac{\gamma p_\infty}{\rho_\infty}}$ is the speed of sound; p_∞ is the gas stream pressure, $M = U_\infty / a_\infty$ is the Mach number; $\gamma = C_p / C_v$ is the ratio of specific heat at constant pressure and volume, N_{x0} is the external in-plane load per unit span-wise length, and c is a linear viscous damping coefficient. Equation (1) is subject to the boundary conditions

$$D\frac{\partial^2 w(0,t)}{\partial x^2} - \alpha_1(t)\frac{\partial w(0,t)}{\partial x} = 0, \;\; w(0,t) = 0 \tag{2a,b}$$

$$D\frac{\partial^2 w(a,t)}{\partial x^2} + \alpha_2(t)\frac{\partial w(a,t)}{\partial x} = 0, \;\; w(a,t) = 0 \tag{2c,d}$$

where α_1 and $\alpha_2(t)$ measure the end slopes and represent torsional stiffness parameters such that for $\alpha_1(t) = \alpha_2(t) = \infty$ we have the case of a purely clamped-clamped panel. On the other hand, if we have simple supports, then $\alpha_1(t) = \alpha_2(t) = 0$. In real situations, both $\alpha_1(t)$ and $\alpha_2(t)$ do not assume these extreme cases and their values are very large for clamped supports, or very small for simple supports. In the dynamic case the boundary conditions (2a,c) are non-autonomous. In order to convert these conditions into an autonomous form, we introduce the following transformation of the response coordinate:

$$\begin{aligned} w(x,t) &= \left[\left(\frac{x}{a}\right)^2 + 2g_1(z_1,z_2)\frac{x}{a} + g_2(z_1,z_2)\right] u(x,t) \\ &= \varphi(x; z_1, z_2) u(x,t) \end{aligned} \tag{3}$$

where the dimensionless parameters $z_i(t) = D/(a\alpha_i(t))$, $i = 1, 2$, represent the ratio of the bending rigidity to the torsional stiffness of the joints. The functions $g_1(z_1, z_2)$ and $g_2(z_1, z_2)$ are chosen to render the boundary conditions autonomous for the new coordinate $u(x, t)$. Possible expressions of these functions are [8]

$$g_1(z_1, z_2) = -\frac{1 + 4z_2}{2(1 + 2z_1 + 2z_2)}; \quad g_2(z_1, z_2) = -\frac{2z_1(1 + 4z_2)}{1 + 2z_1 + 2z_2} \tag{4}$$

In this case, the boundary conditions (2) become

$$\frac{\partial^2 u(0, t)}{\partial x^2} = \frac{\partial^2 u(a, t)}{\partial x^2} = 0 \text{ and } u(0, t) = u(a, t) = 0. \tag{5}$$

Introducing the following nondimensional parameters

$$\tau = t\sqrt{\frac{D}{m_p a^4}}; \ \bar{w} = \frac{w}{h}; \ \bar{x} = \frac{x}{a}; \ \lambda = \frac{\rho_\infty U_\infty^2 a^3}{MD}; \ \mu = \frac{\rho_\infty a}{m_p};$$

$$\zeta = \frac{c}{a^2}\sqrt{\frac{D}{m_p}}; \ \bar{N}_{x0} = N_{x0}\frac{a^2}{D}; \quad \bar{p}_0 = p_0\frac{a^4}{Dh}; \ B_1 = 6(1 - \nu^2);$$

$$B_2 = \frac{\gamma + 1}{4}\frac{\rho h}{m_p}; \ B_3 = \frac{\gamma + 1}{2\sqrt{m_p D}}\rho_\infty U_\infty a h; \ B_3 = \frac{\gamma + 1}{2}\rho_\infty U_\infty^2\frac{a^2 h}{D}$$

$$\bar{u} = \frac{u}{h}; \ \bar{\varphi} = \left[\bar{x}^2 + 2g_1(z_1, z_2)\bar{x} + g_2(z_1, z_2)\right]; \ \hat{\zeta} = \sqrt{\frac{\mu}{M}}$$

equation (1) becomes

$$\frac{\partial^2(\bar{\varphi}\bar{u})}{\partial\tau^2} + \left(1 + \zeta\frac{\partial}{\partial\tau}\right)\frac{\partial^4(\bar{\varphi}\bar{u})}{\partial\bar{x}^4} - \left[\bar{N}_{x0} + B_1\int_0^1\left(\frac{\partial(\bar{\varphi}\bar{u})}{\partial\bar{x}}\right)^2 d\bar{x}\right]\frac{\partial^2(\bar{\varphi}\bar{u})}{\partial\bar{x}^2}$$
$$+\lambda\frac{\partial(\bar{\varphi}\bar{u})}{\partial\bar{x}} + \hat{\zeta}\sqrt{\lambda}\frac{\partial(\bar{\varphi}\bar{u})}{\partial\tau} + B_2\left(\frac{\partial(\bar{\varphi}\bar{u})}{\partial\tau}\right)^2 + B_3\frac{\partial(\bar{\varphi}\bar{u})}{\partial\tau}\frac{\partial(\bar{\varphi}\bar{u})}{\partial\bar{x}} +$$
$$B_4\left(\frac{\partial(\bar{\varphi}\bar{u})}{\partial\bar{x}}\right)^2 = \bar{p}_0 \tag{6}$$

Galerkin's method is applied to discretize equation (6) by assuming the general solution in the form:

$$\bar{u}(\bar{x}, \tau) = \sum_{n=1}^{N} q_n(\tau)\sin n\pi\bar{x} \tag{7}$$

where N is the total number of modes, $q_n(\tau)$ are the generalized coordinates. For the present study, we consider two-mode interaction, i.e., $N = 2$. Furthermore, it is assumed that $z_1 = z_2 = z/2$. The following two nonlinear ordinary differential equations are obtained:

$$q_1''(\tau) + (\zeta a_{11} + \hat{\zeta}\sqrt{\bar{\lambda}})q_1'(\tau) + (a_{12}\bar{N}_{x0} + a_{13})q_1(\tau) + (a_{14}\lambda + a_{15})q_2(\tau) + B_2 b_{11} q_1'(\tau)^2 + B_2 b_{12} q_2'(\tau)^2 + B_3 b_{13} q_1'(\tau) q_2(\tau) + B_3 b_{14} q_1(\tau) q_2'(\tau) + B_1 b_{15} q_1(\tau)^3 + B_1 b_{16} q_1(\tau) q_2(\tau)^2 + B_4 b_{17} q_1(\tau)^2 + B_4 b_{18} q_2^2 = \frac{2\bar{p}_0}{\pi} \tag{8a}$$

$$q_2''(\tau) + (\zeta a_{21} + \hat{\zeta}\sqrt{\bar{\lambda}})q_2'(\tau) + (a_{22}\bar{N}_{x0} + a_{23})q_2(\tau) + (a_{24}\lambda + a_{25})q_1(\tau) + B_2 b_{21} q_1'(\tau) q_2'(\tau) + B_3 b_{22} q_1'(\tau) q_1(\tau) + B_4 b_{42} q_1 q_2 + B_3 b_{23} q_2(\tau) q_2'(\tau) + B_1 b_{24} q_2(\tau)^3 + B_1 b_{25} q_1(\tau)^2 q_2(\tau) = 0 \tag{8b}$$

where the coefficients a_{ij} and b_{ij} are functions of the relaxation parameter z and are not listed here.

3. Modeling of the Relaxation Process

The preload relaxation process is phenomenologically modeled based on experimental results [1]. First, it is assumed that the torsional stiffness parameters are functions of the number of vibration cycles $n = n(t)$:

$$\bar{\alpha}_i(n) = \frac{a\alpha_i(n)}{D} = \frac{1}{z_i(n)} \tag{9}$$

where the over-bar denotes a dimensionless parameter. An explicit analytical expression for the parameters $\bar{\alpha}_i(n)$ can be obtained from experimental records [1]. These experimental measurements revealed the trend of the relaxation process as a slow drop between an original and an asymptotic value of the joint stiffness. An appropriate elementary function that emulates this behavior may be selected in the form

$$\bar{\alpha}(n) = A + B\tanh[-k(n - n_c)] \tag{10}$$

where the subscript i has been dropped, and n_c is a critical number of cycles, indicating the center location of the steepness with respect to the origin, $n = 0$. The parameter k is associated with the slope of the curve at point $n = n_c$.

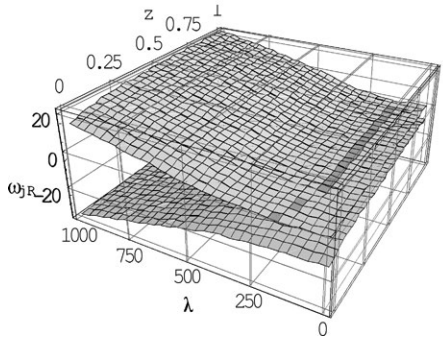

Figure 2(a) Real part

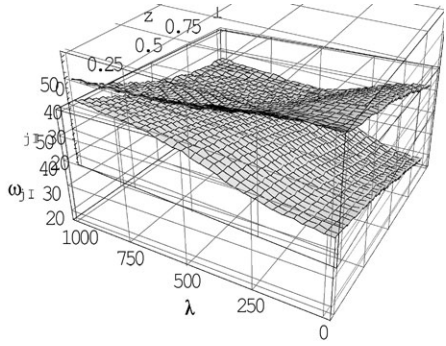

Figure 2(b) Imaginary part

The constants A and B are determined from the initial and final values of the stiffness parameter and evaluated by solving the two algebraic equations

$$\bar{\alpha}(0) = A + B\tanh[kn_c], \qquad \bar{\alpha}(\infty) = A + B \tag{11a,b}$$

Solving for A and B and substituting in relation (10) gives

$$\bar{\alpha}(n) = \bar{\alpha}(\infty) + [\bar{\alpha}(0) - \bar{\alpha}(\infty)]\left[\frac{1 + \tanh[-k(n - n_c)]}{1 + \tanh[kn_c]}\right] \tag{12}$$

The parameters $\bar{\alpha}(0)$ and $\bar{\alpha}(\infty)$ are obtained from the experimental curve. The slope parameter k can be found by taking the derivative of equation (12) with respect to n, i.e.,

$$k = \frac{\partial\bar{\alpha}(n)/\partial n|_{n_c}}{[\bar{\alpha}(\infty) - \bar{\alpha}(0)]}\,[1 + \tanh[kn_c]] \tag{13}$$

One can write an expression for $z(t)$ by using relations (9) and (12) in the form

$$z(\tau) = Z_0 Z_\infty \left[Z_0 - (Z_0 - Z_\infty)\frac{1 + \tanh(-\chi(\tau - \tau_c))}{1 + \tanh(\chi\tau_c)}\right]^{-1} \tag{14}$$

where $Z_0 = z(0)$; $Z_\infty = z(\infty)$; $\chi = \frac{<\varpi>}{2\pi k}$, where $<\bar{\omega}>$ is the mean value of the response frequency and can be taken as the center frequency. The phenomenological representation given by equation (14) can be used for any initial preload and will cause the panel to experience non-stationary behavior.

4. Discussion of the Results

The influence of boundary conditions relaxation on the panel eigenvalues can be examined by dropping the nonlinear terms and the non-homogeneous

term from the modal equations (8). The dependence of the real and imaginary parts of the modal eigenvalues on the dynamic pressure λ and relaxation parameter z is shown in Figures 2(a) and (b) by three-dimensional diagrams for damping parameter $\zeta = 0.01$, mass parameter $\hat{\zeta} = 0.1$, and static axial load parameter $\bar{N}_{xo}$=10. It is seen that the real parts are always negative up to a critical value of the dynamic pressure, depending on the value of the relaxation parameter z, above which one real part crosses to the positive zone indicating the occurrence of panel flutter. Note that the value $z = 0$ corresponds to a clamped-clamped panel and the corresponding critical dynamic pressure is greater than any case with $z \neq 0$. For equal modal viscous damping coefficients, the damping is known to stabilize the panel. However, as shown in [3], and cited references in [3], unequal modal damping coefficients result in a paradoxical effect.

The panel experiences flutter above those critical values of dynamic pressure and relaxation parameter. The inclusion of nonlinearities in equations (8) causes the flutter to achieve a limit cycle. However due to relaxation, shown in Figure 3(a), the panel response experiences nonstationary limit cycle oscillations as shown in Figures 3(b,c). The FFT shown in Figure 3(d) reveals that the frequency content of the first mode includes one spike at zero frequency, due to the static in-plane load, and another band limited response covering a frequency band ranging from mearly $5.8 \cdot 2\pi$ to $6.8 \cdot 2\pi$ (dimensionless frequency). This frequency band reflects the time variation of the panel frequency with time. This is demonstrated by using the spectrogram technique. The time evolution of the frequency content represented by the spectrogram in Figure 3(e) demonstrates the correlation between the variation of the frequency with the relaxation process given in Figure 3(a). It is seen that the response frequency increases as the joint passes through relaxation. On the one hand, the relaxation causes a decrease in the frequency. On the other hand, the nonlinearity of the panel is of a hard spring characteristic. It appears that the nonlinearity overcomes the softening effect of relaxation.

Figures 4(a) and (b) show the dependence of the limit cycle amplitudes on the dynamic pressure for different discrete values of the relaxation parameter z in the form of supercritical bifurcation. The two ideal cases of purely simple-simple and clamped-clamped boundary conditions are plotted by solid curves. Note that the relaxation results in moving the bifurcation point to lower values of dynamic pressure. Currently, the authors are studying the influence of boundary conditions relaxation on panel flutter under random aerodynamic loading.

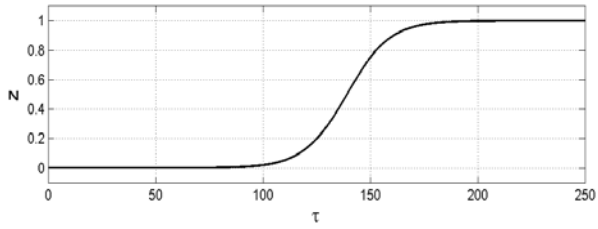

(a) Relaxation parameter z

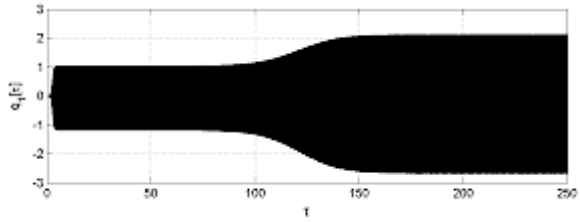

(b) First mode response

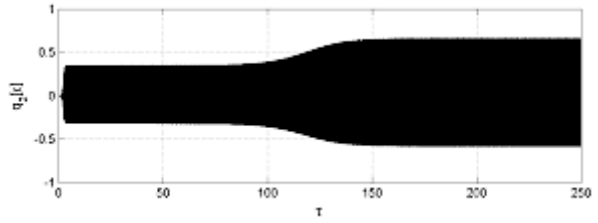

(c) Second mode response

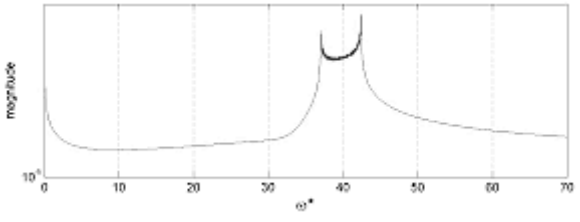

(d) First mode FFT

Figure 3. Relaxation, time history responses and FFT of the first mode

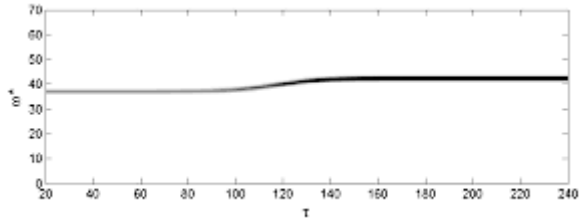

Figure 3(e) Spectrogram of the first mode

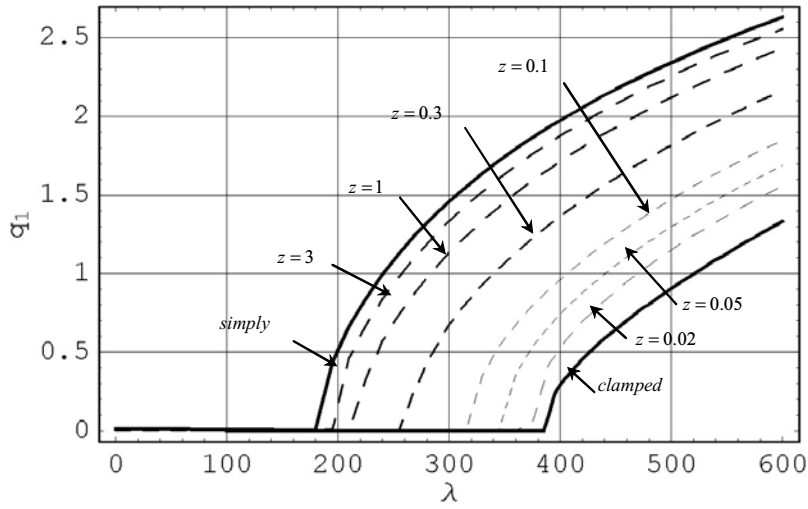

Figure 4(a) 1st mode bifurcation for different relaxation parameters

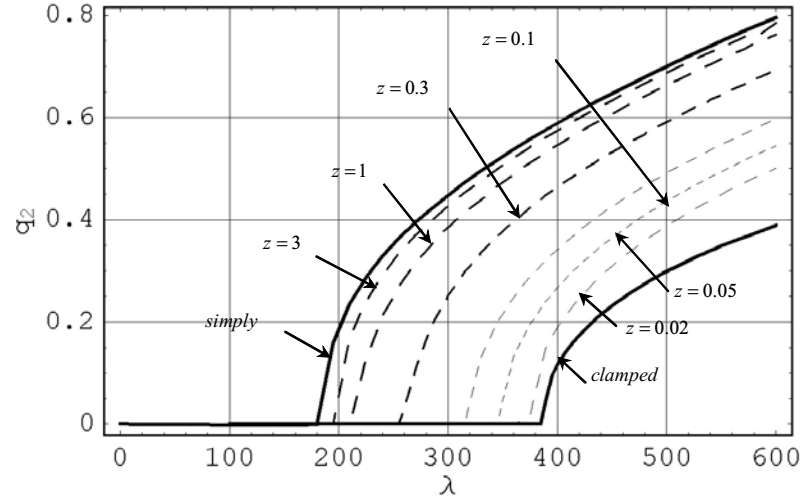

Figure 4(b) 2nd mode bifurcation for different relaxation parameters

Acknowledgements

This research is supported by grants from the Institute for Manufacturing Research and the Air Force Office of Scientific Research under grant F49620-03-1-0229. Dr. Dean Mook is the AFOSR Program Director.

References

[1] J.H. Bickford, *An Introduction to the Design and Behavior of Bolted Joints*, 2nd edition, Marcel Dekker, Inc., New York, 1990.

[2] R.A. Ibrahim and C.L. Pettit, "Uncertainties and dynamic problems of bolted joints and other fasteners," submitted to *Journal of Sound and Vibration*, 2003.

[3] R.A. Ibrahim, P.O. Orono and S.R. Madaboosi, "Stochastic flutter of a panel subjected to random-in-plane forces, Part I: Two mode interaction," *AIAA Journal*, **28**(4): 694-702, 1990.

[4] N.J. Lindsley, P.S. Beran and C.L. Pettit, "Effects of uncertainty on nonlinear plate response in supersonic flow," *9th AIAA Symp Multidisciplinary Analysis and Optimization*, Atlanta, GA, Paper 2002-5600, 2002.

[5] N.J. Lindsley, P.S. Beran and C.L. Pettit, "Effects of uncertainty on nonlinear plate aeroelastic response," *43rd AIAA/ASME/ASCE/ AHS/ASCE Struct Struct Dyn Mater Conf.*, Paper No. AIAA 2002-1271, 2002.

[6] C. Mei, K. Abdel-Mutagaly and R. Chen, "Review of nonlinear panel flutter at supersonic and hypersonic speeds," *ASME Appl Mech Rev*, **52**(10): 321-332, 1999.

[7] B. Poiron, "Impact of random uncertainties on aircraft aeroelastic stability," *Proc. Stochastic Structural Dynamics Conference*, San Juan, Puerto Rico, 1995.

[8] S. Qiao, V.N. Pilipichuk and R.A. Ibrahim, "Modeling and simulation of elastic structures with parameter uncertainties and relaxation of joints," *ASME J Vib Acoust*, **123**(1), 45-52, 2000.

SOLUTIONS OF A SHALLOW ARCH UNDER FAST AND SLOW EXCITATIONS

Faouzi Lakrad
Institute B of Mechanics, University of Stuttgart,
70550 Stuttgart, Germany
lakrad@recherche-maroc.org

Mohamed Belhaq
Laboratory of Mechanics, Faculty of Sciences Ain Chock,
BP 5366 Maarif, Casablanca, Morocco

Abstract: Quasi-Periodic (QP) and periodic burster solutions of a two degree of freedom shallow arch model, subjected to a very slow parametric excitation and a resonant external excitation, are investigated. A multiple-scales method is applied to have slowly modulated amplitudes and phases equations. Behavior charts and explicit analytical approximations to QP solutions are obtained and comparisons to numerical integration are provided.

Key words: Shallow arch, quasi-periodic solutions, slow manifold, bursters.

1. Introduction

Quasi-periodic (QP) excitations consisting of slow and fast periodic functions are very important sources of multiple scales phenomena. A wide range of these latter can be written as singularly perturbed systems or ODEs with slowly varying parameters. Several methods are available to analyze solutions of such systems. For instance, Bogoliubov and Mitropolskii [1] developed an averaging method considering the slowly varying parameters as constants during the averaging process. Belhaq and co-workers [2; 3] used the so-called double perturbation method to investigated non-linear QP Mathieu equations. For other techniques and applications see [4].
The main goal of the present work is to approximate analytically QP solutions and periodic bursters of a two mode double hinged shallow arch model. It is

G. Rega and F. Vestroni (eds.),
IUTAM Symposium on Chaotic Dynamics and Control of Systems and Processes in Mechanics, 233–240.

excited by two forcings, in the vicinity of a buckled symmetric state, under 1:2 internal resonance and the principal external resonance. The two excitations consist of a resonant external periodic excitation of the symmetric mode, and a very slow parametric periodic excitation of the two modes. This parametric excitation is due to the imposed motion of the arch support. Hence three time scales rule our system; the fast scale which is induced by the external excitation, the slow scale that is induced by the modulated amplitudes and phases, and the very slow scale caused by the parametric excitation.

This paper is organized as follows: in the first section we discuss the shallow arch model. Then, a Multiple scales Method (MSM) is applied to determine the slowly modulated amplitudes and phases equations. Finally, explicit conditions on the existence and stability of different dynamics are obtained. Analytical approximations of QP solutions are computed and comparisons to numerical simulations are provided.

2. Shallow Arch Model

A double-hinged shallow arch is assumed to be subjected to a lateral loading consisting on a static loading and a periodic excitation. It is also subject to an imposed slow periodic motion of its support. The non-dimensional equations of motion describing the evolution of the straightened amplitudes, of two sine functions taken as approximations of the two first modes of the shallow arch, can be written as

$$\begin{aligned} &\ddot{Q}_1 + \beta_1 \dot{Q}_1 + (1 + h\cos(\Omega\tau))Q_1 + Q_1(Q_1^2 - q_0^2 + 4Q_2^2) + q_0 - \lambda_0 \\ &\qquad + \rho\cos(\nu t) = 0 \\ &\ddot{Q}_2 + \beta_2 \dot{Q}_2 + 4(4 + h\cos(\Omega\tau))Q_2 + 4Q_2(Q_1^2 - q_0^2 + 4Q_2^2) = 0. \end{aligned} \tag{1}$$

Here t is time and τ is a very slow time scale defined as $\tau = \varepsilon^n t$ with the integer $n \geq 2$. The variables Q_1 and Q_2 are the amplitudes of the symmetric and the asymmetric modes respectively. The parametric excitation $h\cos(\Omega\tau)$ is due to the periodic motion of the end point of the arch. The parameters q_0 and λ_0 represents the non-dimensional initial rise and the static loading respectively. The details of this derivation and the definition of non-dimensional variables and parameters can be found in [5], in which the externally excited version of equations (0) was studied.

Under the action of the static loading λ_0 alone, increasing the initial rise q_0, a stable symmetric static solution bifurcates to three symmetric solutions. Two among them are stable. In what follows we will deal only with the two stable symmetric solutions. In all the numerical applications, $q_0 = 2.5$, $\lambda_0 = 6.95$ and the damping coefficients $\beta_i = 0.03$ $(i = 1, 2)$.

3. Perturbation Analysis

We perturb the variables (Q_1, Q_2) in equations (0) around one of the two stable buckled symmetric solutions $(\eta_0, 0)$

$$Q_1 = \eta_0 + \varepsilon q_1 \qquad\qquad Q_2 = \varepsilon q_2 \tag{2}$$

where ε is a small positive parameter. Let

$$\rho = \varepsilon^2 \tilde{\rho},\ h = \varepsilon \tilde{h},\ \text{and}\ \ \beta_i = \varepsilon \tilde{\beta}_i,\ i = 1, 2. \tag{3}$$

Inserting (1) and (2) into equations (0) leads to the following nonlinear variational equations up to $\mathcal{O}(\varepsilon^2)$

$$\begin{aligned} \ddot{q}_1 + \omega_1^2 q_1 &= -\tilde{h}\eta_0 \cos(\Omega\tau) + \varepsilon(-\tilde{\beta}_1 \dot{q}_1 - 3\eta_0 q_1^2 - 4\eta_0 q_2^2 - \tilde{\rho}\cos(\nu t) \\ &- \tilde{h}\cos(\Omega\tau) q_1), \\ \ddot{q}_2 + \omega_2^2 q_2 &= \varepsilon(-\tilde{\beta}_2 \dot{q}_2 - 8\eta_0 q_1 q_2 - 4\tilde{h}\cos(\Omega\tau) q_2), \end{aligned} \tag{4}$$

where $\omega_1^2 = 3\eta_0^2 + 1 - q_0^2$ and $\omega_2^2 = 16 - 4q_0^2 + 4\eta_0^2$ are the linearized frequencies corresponding to the first and second modes, respectively. We will restrict our analysis to $1:2$ internal resonance and to the principal external resonance

$$\omega_1 = 2\omega_2 + \varepsilon\sigma_1, \quad \nu = 2\omega_2 + \varepsilon\sigma_2, \tag{5}$$

where σ_1 and σ_2 are the detuning parameters. For an exhaustive review of the recent works on two-degree-of-freedom quadratic systems, under external or parametric excitations, we refer the reader to [6].

Reduced System

The MSM (see [7]) is applied to (3) to eliminate the fast time scale dependence. This process ultimately results in the following modulation equations of amplitudes a_1, a_2 and phases of the first and second modes respectively

$$\begin{aligned} a_1' &= -\frac{\tilde{\beta}_1}{2} a_1 - \frac{\tilde{\rho}}{2\omega_1}\sin(\gamma_1) - \frac{\eta_0}{\omega_1} a_2^2 \sin(\gamma_1 - 2\gamma_2) \\ a_1\gamma_1' &= (\sigma_2 - \sigma_1) a_1 - \frac{\eta_0}{\omega_1} a_2^2 \cos(\gamma_1 - 2\gamma_2) - \frac{\tilde{\rho}}{2\omega_1}\cos(\gamma_1) \\ &- \frac{\tilde{h}X}{2\omega_1} a_1 \cos(\Omega\tau) \\ a_2' &= -\frac{\tilde{\beta}_2}{2} a_2 + \frac{2\eta_0}{\omega_2} a_1 a_2 \sin(\gamma_1 - 2\gamma_2) \\ \gamma_2' &= \frac{\sigma_2}{2} - \frac{2\eta_0}{\omega_2} a_1 \cos(\gamma_1 - 2\gamma_2) - \frac{2\tilde{h}Y}{\omega_2}\cos(\Omega\tau), \end{aligned} \tag{6}$$

where $X=1-(6\eta_0^2/\omega_1^2)$ and $Y=1-(2\eta_0^2/\omega_1^2)$. The prime denotes the derivative with respect to εt. Here we have considered the slowly varying parametric excitation as constant during the averaging process.
The solutions of equations (3) are approximated up to $\mathcal{O}(\varepsilon)$ as follows

$$q_1(t) = a_1(\tau)\cos(\nu t - \gamma_1(\tau)) - \frac{\tilde{h}\eta_0}{\omega_1^2}\cos(\Omega\tau) + \mathcal{O}(\varepsilon), \quad (7)$$

$$q_2(t) = a_2(\tau)\cos(\frac{\nu}{2}t - \gamma_2(\tau)) + \mathcal{O}(\varepsilon). \quad (8)$$

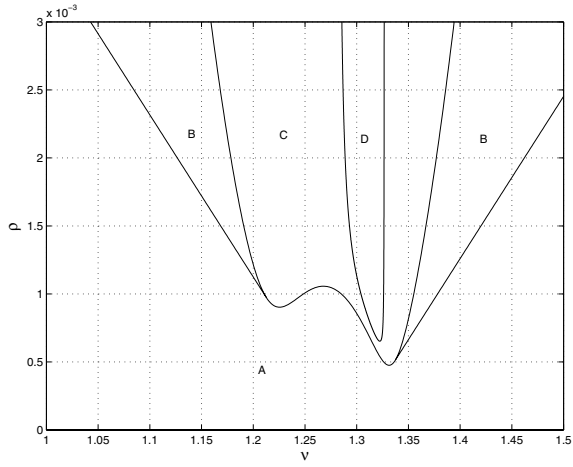

Figure 1. Boundaries of dynamic instability of the modulation equations (5) in the external excitation parameters plane (ν, ρ) for $h = 0$. Region A, only single symmetric mode exists and is stable. Region B, coexistence of coupled and single modes. Region C, only coupled mode is stable. Region D both modes are unstable.

In figure 1., we show the stability chart of system (5) in the absence of the parametric excitation i.e., $h = 0$. In region A, only the symmetric mode $(a_1, a_2 = 0)$ is excited and is stable. In region B, coexistence of the stable symmetric mode $(a_1, 0)$ and two coupled modes $(a_1, a_2 \neq 0)$, one of them is stable. In region C, coexistence of the destabilized single mode and the stable coupled mode. In region D, destabilization of the coupled mode through a Hopf bifurcation. For more results about this case see Tien *et. all* [8].

In figure 2, we consider a point in the region A with a static displacement of the support of the arch i.e., $\Omega = 0$ and $h \neq 0$. For low and high values of h only the stable semi-trivial solution exists and for $h \in [0.00118, 0.005]$ there is coupling between the existing modes.
One interesting contribution of the slow parametric excitation i.e., $h \neq 0$ and $\Omega \neq 0$ is that it enables the crossing of the borders between the different regions in figure 1 during one period of τ. This effect is the main cause for the occurrence of periodic bursters. See figure 3 for a burster solution $Q_2(t)$ of the original system (0). It consists of a heteroclinic cycle between a fixed point and a QP solution.

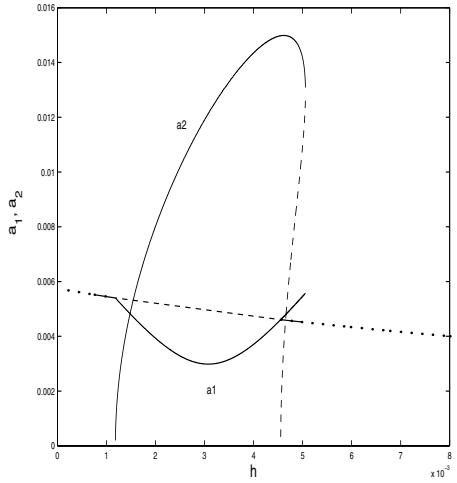

Figure 2. Stationary responses of (5) for $\rho = 0.0007$, $\nu = 1.29$, $\Omega = 0$. Continuous lines refer to stable solutions and dashed lines to unstable ones.

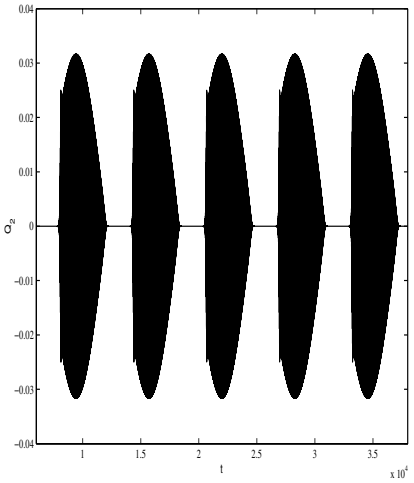

Figure 3. Periodic burster solution $Q_2(t)$ of the original equation (0) for $\rho = 0.002$, $\nu = 1.25$, $\Omega = 0.001$ and $h = 0.01$.

QP solutions and bursters

Equations of modulations (5) can be writen as a slow-fast system

$$\varepsilon \dot{\mathbf{z}} = f(\mathbf{z}, \tau), \qquad \dot{\tau} = \mathbf{1}, \tag{9}$$

where the vector $\mathbf{z} = (a_1, \gamma_1, a_2, \gamma_2)$ and the dot means the derivatives with respect to the very slow scale of time τ. In the limit $\varepsilon \to 0$ one can compute the *slow manifold* given by $\mathcal{M} = \{(\mathbf{z}, \tau) : f(\mathbf{z}, \tau) = \mathbf{0}\}$. It is composed of two types of solutions

- The semi-trivial solution

$$a_1(\tau) = \frac{\tilde{\rho}}{2\omega_1 \sqrt{[(\frac{\tilde{\beta}_1}{2})^2 + (\sigma_1 - \sigma_2 + \frac{\tilde{h}X}{2\omega_1}\cos(\Omega\tau))^2]}}, \tag{10}$$

$$a_2(\tau) = 0. \tag{11}$$

- The non-trivial solutions

$$a_1(\tau) = |\frac{\omega_2}{2\eta_0}| \sqrt{(\frac{\tilde{\beta}_2}{2})^2 + (\frac{\sigma_2}{2} - \frac{2\tilde{h}Y}{\omega_2}\cos(\Omega\tau))^2}. \tag{12}$$

The two nontrivial amplitudes of the anti-symmetric mode $a_2(\tau)$ are obtained by solving a fourth order algebraic equation.

It is known through the singular perturbation theory that when the slow manifold $\mathcal{M}$ is stable, there exists a solution of the frozen system (8) tracking $\mathcal{M}$ at a distance of order ε and admitting asymptotic series in ε. Near bifurcating equilibrium branches the center manifold theorem can be applied to reduce the dimension of the system to the number of bifurcating eigenvalues, see for instance Bajaj and co-workers [9] and Berglund [10]. In figure 4., we show the stability chart of system (5) for $h = 0.001$ in the plane of external excitation parameters. The stability behaviors of the solutions in the zones A, B, C and D are the same as in figure 1. However, instead of fixed points we deal now with periodic solutions. In the grey zones these periodic solutions are changing their nature or stability during one period of τ. These zones are the zones of existence of periodic bursters solutions.
Using equations (1), (6) and (7) we conclude that away from the boundaries of dynamic instability, i.e., in regions A, B and C, the stable solutions of the initial system (0) are mainly QP. The amplitude of the symmetric mode $Q_1(t)$ is a QP solution with basic frequencies ν and Ω. The amplitude of asymmetric mode $Q_2(t)$ is a trivial solution in the zones A and B. It is a QP solution in the zones B and C with basic frequencies $\nu/2$ and Ω. In region D, 3-period QP solution and non regular behaviors can be observed. In the grey zones, periodic bursters solutions exist and they alternate between the dynamics of zones delimiting them. As an example see figure 3.

In figure 5, we show for different values of parameters of the excitations, the comparisons between the results of MSM and the numerical simulations of equation (0). In every case, excellent agreements are shown. For the behavior of the solutions near the resonances boundaries (grey zones in figure 4.) and in the zone D, a more detailed investigation is in progress, and results will be reported elsewhere.

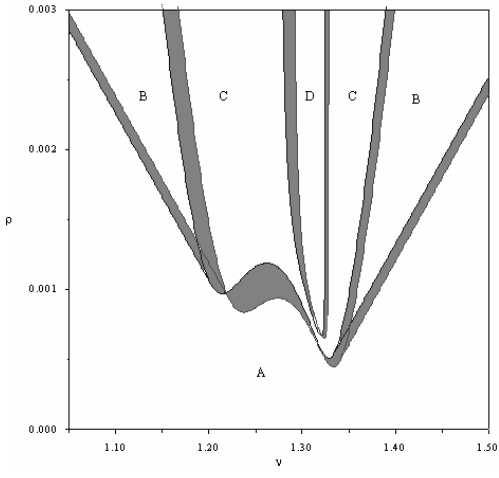

Figure 4. Behavior chart of equations (5) for $h = 0.001$. The grey areas correspond to zones of existence of bursters. The qualitative behaviors of the lettered zones are the same as in figure 1.

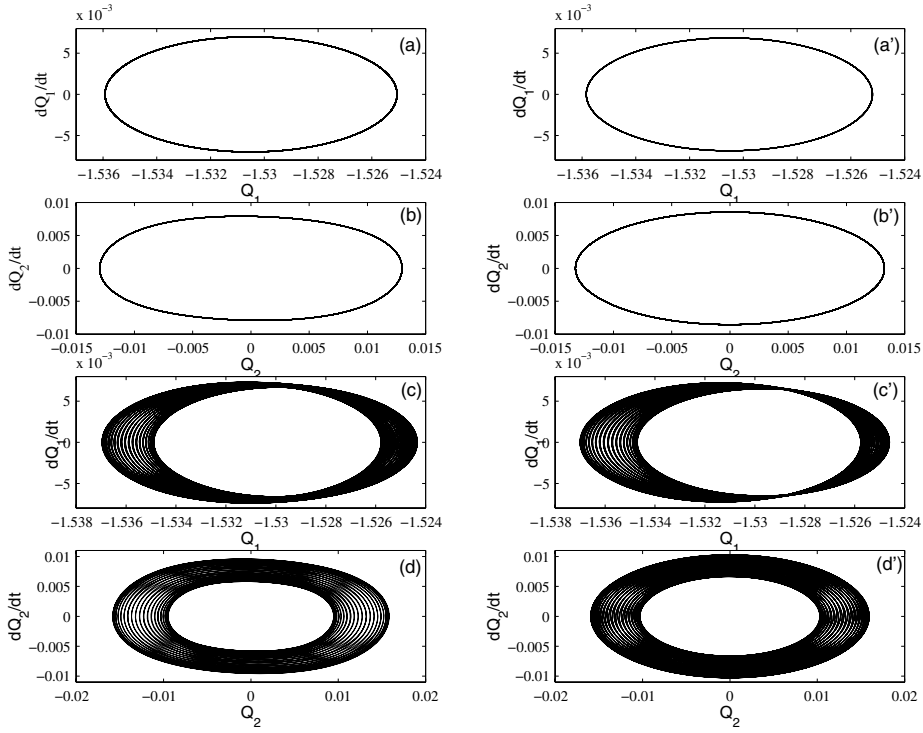

Figure 5. Comparisons of the approximated solutions and numerics of equation (0), for $\nu = 1.25$ and $\Omega = 0.06$. The right figures refer to the computer generated solutions and the left ones to the analytical solutions. The plots (a) (resp. (a')) and (c) (resp. (c')) correspond to a point in the zone A with $\rho = 0.00065$ and $h = 0$ and $h = 0.001$ respectively. The plots (b) (resp. (b')) and (d) (resp. (d')) correspond to a point in region C for $\rho = 0.0015$ and $h = 0$ and $h = 0.001$ respectively.

4. Summary

In this paper, we have investigated QP solutions and periodic bursters of a shallow arch subject to a very slow parametric excitation and a fast external excitation. The dynamic on the slow manifold is studied after a reduction through the MSM. Behavior charts and explicit analytical approximations of solutions are computed and comparisons to numerical integration are provided.

It is worth noting that for high amplitudes of the parametric excitation h the dynamics of the arch leaves the neighbourhood of the considered symmetric buckled position to oscillate around the other one. A global analysis is required to understand this jump.

Acknowledgments

The first author (F.L) would like to acknowledge that this research is financed by the Alexander von Humboldt Foundation. He also acknowledges the hospitality of Institut polytechnique privé de Casablanca.

References

[1] N.N. Bogoliubov and Y.A. Mitropolskii, *Asymptotic Methods in the Theory of Non-linear Oscillations*. Delhi: Hindustan Publ. Corp, 1961.

[2] K. Guennoun, M. Houssni and M. Belhaq, "Quasi-periodic solutions and stability for a weakly damped nonlinear quasi-periodic Mathieu equation," *Nonlinear Dynamics* **27**, 211-236, 2002.

[3] M. Belhaq, K. Guennoun and M. Houssni, "Asymptotic solutions for a damped non-linear quasi-periodic Mathieu equation," *Int. J. of Non-linear Mechanics* **37**, 445-460, 2002.

[4] J. Kevorkian and J.D. Cole, *Multiple Scale and Singular Perturbation Methods*. Berlin: Springer-Verlag, 1996.

[5] W.M. Tien, Chaotic and stochastic dynamics of nonlinear structural systems. Phd thesis in University of Illinois at Urbana-Champaign, 1993.

[6] A.H. Nayfeh, *Nonlinear Interactions*, Wiley, New York, 2000.

[7] A.H. Nayfeh, *Perturbation Methods*, Wiley, New York, 1973.

[8] W-M. Tien, N.S. Namachchivaya and A.K. Bajaj, "Nonlinear dynamics of a shallow arch under periodic excitation-I. 1:2 internal resonance," *Int. J. of Non-linear Mechanics* **29**(3), 349-366, 1994.

[9] A.K. Bajaj, B. Banerjee and P. Davies, "Nonstationary Responses in two degree-of-freedom nonlinear systems with 1-to-2 internal resonance," *Proceedings of IUTAM Symposium on New Applications of Nonlinear and Chaotic Dynamics in Mechanics*, 13-22, Kluwer Academic, 1999.

[10] N. Berglund, "Dynamic bifurcations: hysteresis, scaling laws and feedback control," *Proc. Theor. Phys. Suppl.* **139**, 325-336, 2000.

NONLINEAR OSCILLATIONS OF A BUCKLED MECHANISM USED AS A VIBRATION ISOLATOR

Raymond H. Plaut, Laurie A. Alloway
Charles E. Via, Jr. Department of Civil and Environmental Engineering
Virginia Polytechnic Institute and State University
Blacksburg, VA 24061-0105, USA.
rplaut@vt.edu

Lawrence N. Virgin
Department of Mechanical Engineering and Materials Science
Duke University, Durham, NC 27708-0300, USA.
l.virgin@duke.edu

Abstract: Various devices have been used to reduce the dynamic response of mechanical and structural systems connected to moving sources. A vibration isolator can be inserted between a system and source to absorb energy and reduce the system's motion. The application of a buckled mechanism as a vibration isolator is investigated here. Harmonic motion is applied to the base, and the response of the supported weight is examined. Both parametric and external (forcing) excitations are present. Small applied motions and responses are considered first, and the steady-state harmonic motion of the weight is plotted as a function of the applied frequency. Then large responses are investigated. The buckled mechanism may snap from one side to the other. After some initial transient response, period-one, period-two, period-four, and chaotic responses are observed for various applied frequencies and given values of the applied amplitude, supported weight, damping coefficient, and stiffness parameter.

Key words: Vibration isolation, buckling, nonlinear oscillations.

1. Introduction

A slightly-buckled structure, such as a mechanism, may have advantages over other types of isolators. It may exhibit less axial deformation than a

G. Rega and F. Vestroni (eds.),
IUTAM Symposium on Chaotic Dynamics and Control of Systems and Processes in Mechanics, 241–250.

helical spring, for example, and hence may be able to support a heavy system without large static deformation. Just beyond initial buckling, such a buckled isolator has a low fundamental frequency. If the basic frequency of the moving source is above this fundamental frequency, the transmissibility may be low, so that the amplitude of the system's motion may be significantly less than that of the source. [1–3] discussed isolators comprised of buckled struts with fixed ends. In this paper, a pinned mechanism containing two rigid bars, a rotational spring, and a rotational dashpot is analyzed.

Resonances are important in the effectiveness of an isolator [4–6]. The static postbuckling behavior of the isolator considered here is nonlinear. The equation of equilibrium and the equation of motion for vibrations about the equilibrium state are nonlinear. The latter equation contains both parametric and external (forcing) excitations. The transmissibility is computed under the assumption of small vibrations about the equilibrium state. For large responses, the equilibrium equation for the one-degree-of-freedom system is integrated numerically. Time histories, phase portraits, Poincaré plots, and bifurcation diagrams are presented for given parameter values, and various types of responses are demonstrated.

2. Formulation

Consider the single-degree-of-freedom mechanism shown in Fig. 1.

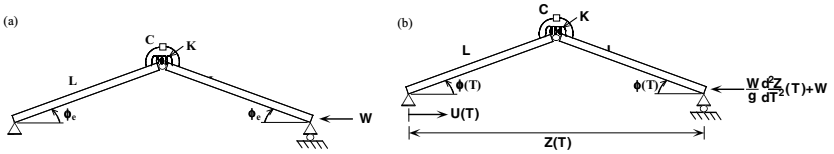

Figure 1. (a) Geometry of mechanism in equilibrium configuration, (b) geometry of mechanism in motion.

It is envisaged as a vertical structure supporting the weight W, but is drawn horizontally with the base at the left. The two bars have length L and are hinged together. Acting at the connecting hinge are a rotational spring with stiffness K and a rotational dashpot with damping coefficient C. The base (i.e., the left support) is subjected to an axial displacement $U(T)$, where T is time. The weight W is assumed to be greater than the critical load, so that the model attains a buckled configuration as depicted in Fig. 1(a). The coordinate $\phi(T)$ is shown in Fig. 1(b), along with the inertia force added to the weight at the top of the model (i.e., the right support), where $Z(T) = U(T) + 2L \cos\phi(T)$. The spring is unstrained when $\phi = 0$, and the equilibrium rotation is $\phi = \phi_e$. The objective is for the motion of the supported weight to be small.

The mass of each bar is M and the potential energy due to the weight of each bar is neglected. The axial coordinates of the centers of mass of the bars are $X_1 = U + (L/2)\cos\phi$ and $X_2 = U + (3L/2)\cos\phi$, respectively, and the transverse coordinates are $Y_1 = Y_2 = (L/2)\sin\phi$, while the moment of inertia of each bar about its center of mass is $I = ML^2/12$. The kinetic energy KE, potential energy PE, and dissipation function DF are given by

$$\begin{aligned} KE &= \frac{1}{2}M(\dot{X}_1^2 + \dot{Y}_1^2) + \frac{1}{2}I\dot{\phi}^2 + \frac{1}{2}M(\dot{X}_2^2 + \dot{Y}_2^2) + \frac{1}{2}I\dot{\phi}^2 + \frac{1}{2}\frac{W}{g}\dot{Z}^2, \\ PE &= \frac{1}{2}K(2\phi)^2 + WZ, \\ DF &= \frac{1}{2}C(2\dot{\phi})^2 \end{aligned} \tag{1}$$

Using Lagrange's equations, one obtains the following equation of motion:

$$\begin{aligned} &\left[\tfrac{1}{3}M + (M + 2\tfrac{W}{g})\sin^2\phi\right] L^2\ddot{\phi} + (M + 2\tfrac{W}{g})L^2\dot{\phi}^2 \sin\phi\cos\phi \\ &\quad -(M + \tfrac{W}{g})L\ddot{U}\sin\phi + 2C\dot{\phi} + 2K\phi - WL\sin\phi = 0 \end{aligned} \tag{2}$$

The analysis will be carried out in terms of the following nondimensional quantities:

$$\begin{aligned} &u = \tfrac{U}{L} \qquad z = \tfrac{Z}{L} \qquad p = \tfrac{WL}{K} \\ &r = \tfrac{K}{MgL} \quad c = \tfrac{C}{L\sqrt{KM}} \quad t = \tfrac{T}{L}\sqrt{\tfrac{K}{M}}, \end{aligned} \tag{3}$$

where p will be called the load and r will be called the stiffness parameter. Then the equation of motion in $\phi(t)$ is

$$\begin{aligned} &\left[\tfrac{1}{3} + (1 + 2rp)\sin^2\phi\right]\ddot{\phi} + (1 + 2rp)\dot{\phi}^2 \sin\phi\cos\phi \\ &\quad -(1 + rp)\ddot{u}\sin\phi + 2c\dot{\phi} + 2\phi - p\sin\phi = 0 \end{aligned} \tag{4}$$

If there is no base excitation $u(t)$, Eq. 4 provides the equilibrium equation

$$2\phi_e - p\sin\phi_e = 0 \tag{5}$$

for the equilibrium value ϕ_e of the rotation. The critical load is $p_{cr} = 2$, and it is assumed that $p > 2$. In the numerical examples to be considered, $p = 2.01$ and $\phi_e = 0.1729$. The system is assumed to be in its equilibrium state prior to base excitation, so that $\phi = \phi_e$ and $d\phi_e/dt = 0$ at $t = 0$. The base excitation is assumed to be harmonic with amplitude u_0 and frequency ω.

3. Transmissibility for Small Excitation and Motion

In this section, the base excitation is assumed to be small and the equation of motion is linearized. Let

$$u(t) = u_0 e^{i\omega t}, \quad \phi(t) = \phi_e + \phi_d e^{i\omega t} \tag{6}$$

Using Eq. 6 in Eq. 4, linearizing the result in the dynamic amplitude ϕ_d and excitation amplitude u_0, and making use of Eq. 5, one obtains

$$\begin{aligned}\left[\left(\tfrac{1}{3}+(1+2rp)\sin^2\phi_e\right)\omega^2-2ic\omega-2+p\cos\phi_e\right]\phi_d \\ =\left[(1+rp)\omega^2\sin\phi_e\right]u_0\end{aligned} \tag{7}$$

The axial motion $x_d(t)$ of the supported weight about its equilibrium position is

$$x_d(t)=u(t)+2\cos\phi(t)-2\cos\phi_e \tag{8}$$

With the use of Eq. 6, and assuming small motion, one can write

$$x_d(t)=(u_0-2\phi_d\sin\phi_e)e^{i\omega t} \tag{9}$$

The transmissibility *TR* is defined as the ratio of the amplitudes of the axial motions of the supported weight and the base excitation, i.e.,

$$TR=|x_d|/u_0 \tag{10}$$

where $u_0>0$.

The resonant frequency ω_n, defined here as the frequency at which *TR* approaches infinity when there is no damping ($c=0$), based on Eqs. 7, 9, and 10, is computed from

$$\omega_n^2=\frac{3(2-p\cos\phi_e)}{1+3(1+2rp)\sin^2\phi_e} \tag{11}$$

It has the values 0.204, 0.144, and 0.113, respectively, for $r=1$, 5, and 10. The transmissibility is plotted versus the excitation frequency ω in Figs. 2(a-c) for stiffness parameter values of $r=1,\ 5$, and 10, respectively.

Curves are plotted for damping coefficients $c=0, 0.001, 0.01,$ and 0.1. The peak values of the transmissibility for $r=1$ and $c=0.001$, 0.01, and 0.1, respectively, are 18.2, 2.20, and 1.05. For $r=5$, the corresponding values are 47.2, 4.87, and 1.16, and for $r=10$ they are 70.8, 7.18, and 1.29.

For small excitation and response, the model would be an effective isolator if the excitation frequency is sufficiently high so that the transmissibility would be low.

4. Nonlinear Response

The equation of motion (4) is now put into the form of two first-order differential equations and integrated numerically for base excitation $u(t)=u_0\sin\omega t$. The excitation involves both parametric and external (forcing) components acting on the motion about the equilibrium configuration [7–9]. The equation would have a trivial solution $\phi(t)=0$ if the initial conditions on ϕ and $d\phi/dt$

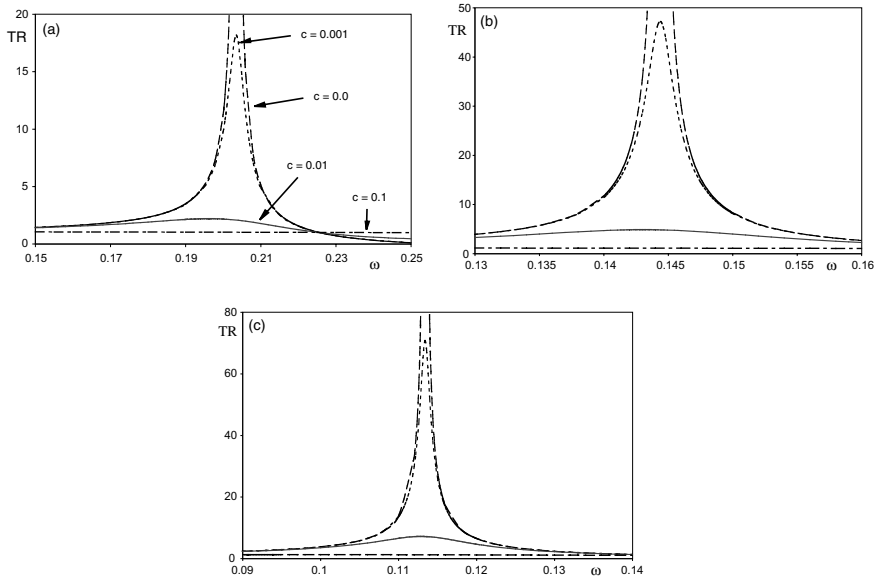

Figure 2. Transmissibility versus excitation frequency ω, (a) $r = 1$, (b) $r = 5$, (c) $r = 10$.

were trivial, but here the load is assumed to be greater than the critical load, i.e., $p = 2.01$, and the model has an initial buckled configuration with rotation $\phi(0) = 0.1729$ (and no initial velocity). Hence motion will occur.

Attention will be focused on long-term response following initial transient motion. Most results will involve the rotation $\phi(t)$, obtained by numerically solving Eq. 4, and the dynamic axial response $x_d(t)$ of the supported weight, computed from Eq. 8.

Consider the case of damping coefficient $c = 0.02$, stiffness parameter $r = 1$, and excitation amplitude $u_0 = 0.05$. The resonant frequency is $\omega_n = 0.204$.

For an excitation frequency of ω=0.1, the transient motion dies out quickly and the response is shown in Figs. 3(a) and (b) in terms of $\phi(t)$ and $x_d(t)$, respectively. After transient motion has died out, the phase plane projection, showing dx_d/dt versus x_d, is the closed loop plotted in Fig. 4, and the corresponding Poincaré plot is superimposed using data taken at time intervals $2\pi/\omega$: it consists of a single dot. Next, the excitation frequency $\omega = 0.2$ is considered, which is slightly below the resonant frequency. The rotational and axial responses are shown in Figs. 5(a) and (b), respectively.

The model exhibits a few cycles above the horizontal in Fig. 1 and then snaps below the horizontal and remains there. The response settles into a subharmonic period-two motion, i.e., its period is twice the period of the exci-

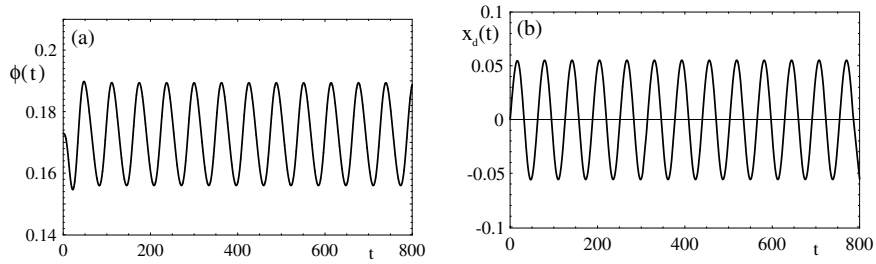

Figure 3. Time histories for the response when $\omega = 0.1$. (a) rotational, (b) axial.

tation. For the steady-state response, the (period-two) phase portrait is shown in Fig. 6. A period-four response occurs for $\omega = 0.39$.

Chaotic motions are exhibited at most of the frequency values that were considered between $\omega = 0.206$ and 0.39 (i.e., in the range between ω_n and $2\omega_n$). Phase projections for the axial motion $x_d(t)$ of the supported weight and the transverse motion $y(t)$ of the hinge are presented in Figs. 7(a) and (b), respectively, using data from the response for excitation frequency $\omega = 0.32$ in the range of time $4,700 < t < 5,000$. At equilibrium, $x_d = 0$ and $y = 0.1720$. The model moves erratically and snaps back and forth across the horizontal in Fig. 1(b).

Figure 8 presents Poincaré plots for chaotic motion. The case of $\omega = 0.32$ is shown in parts (a) and (b), corresponding to the phase portraits in Fig. 7, whereas $\omega = 0.209$ for part (c), just for the transverse motion.

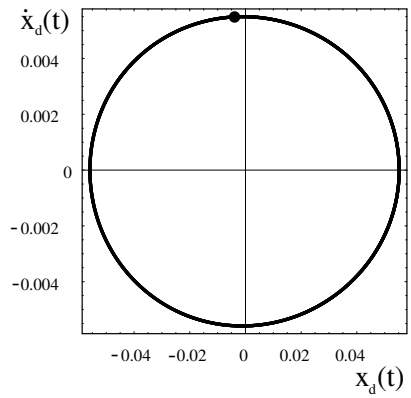

Figure 4. Phase projection and Poincaré section for axial response when $\omega = 0.1$.

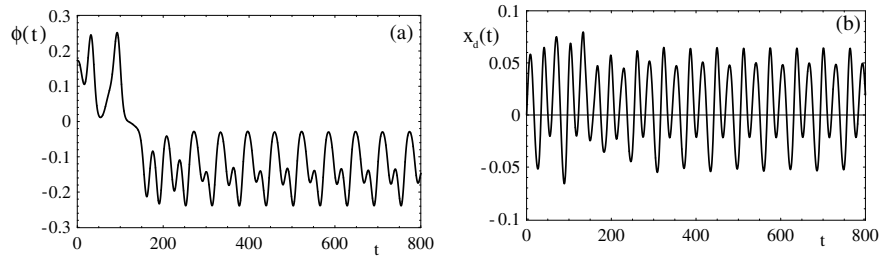

Figure 5. Time histories for the response when $\omega = 0.2$. (a) rotational, (b) axial.

Finally, Fig. 9 depicts bifurcation diagrams [10]. Data from Poincaré plots for the axial response x_d are plotted as dots at the given frequency. The diagram in Fig. 9(b) gives a more detailed picture of the results for the range $0.20 < \omega < 0.21$ than in Fig. 9(a). As ω is increased, period-one motion splits into period-two motion at $\omega \approx 0.19$, and chaotic motion begins at $\omega \approx 0.206$. A window with period-four response is seen at $\omega \approx 0.208$. With further increase in ω, the system returns to period-two motion at $\omega \approx 0.40$ and then returns to period-one motion at $\omega \approx 0.42$.

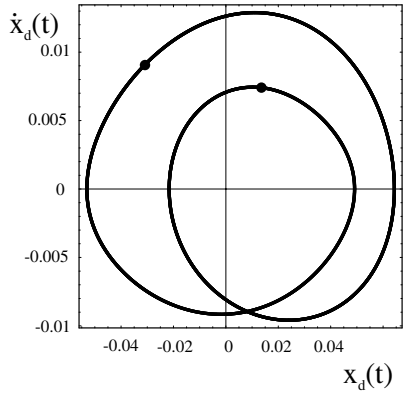

Figure 6. Phase projection when $\omega = 0.2$.

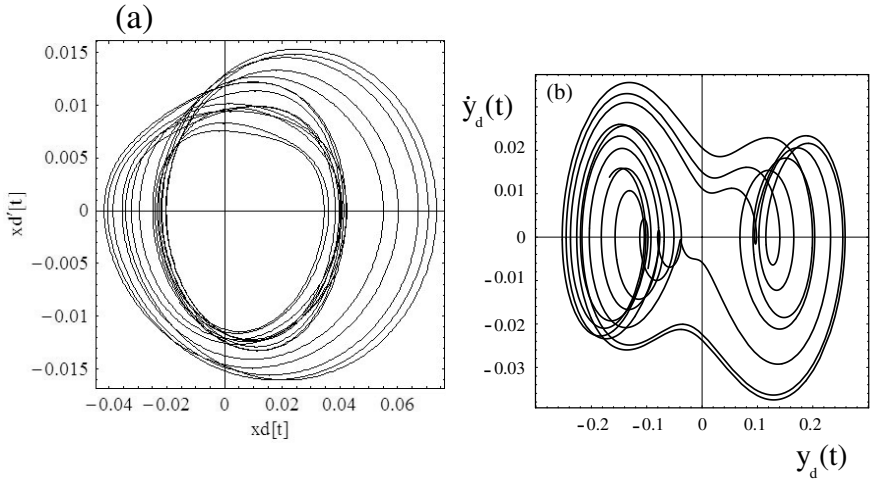

Figure 7. Phase projection when $\omega = 0.32$. (a) axial motion, (b) transverse motion.

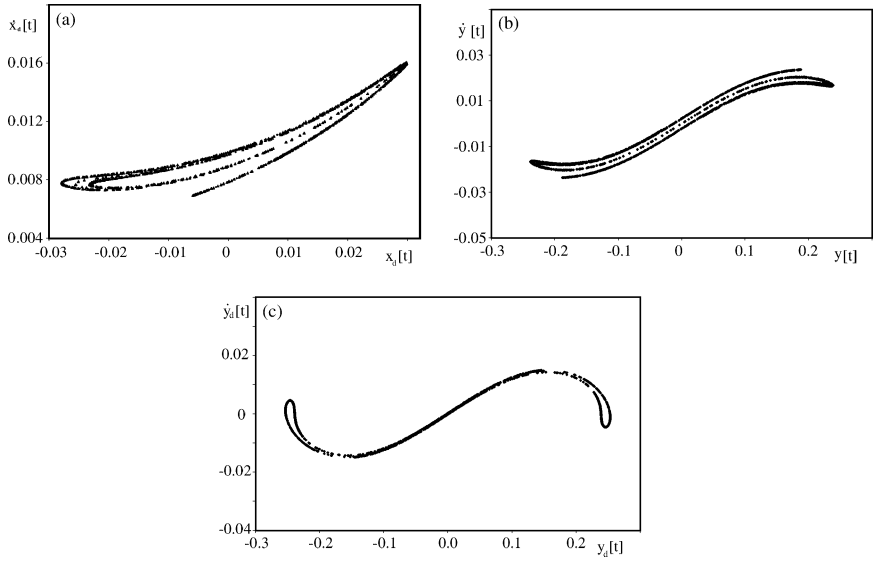

Figure 8. Chaotic Poincaré sections. (a) axial motion for $\omega = 0.32$, (b) transverse motion for $\omega = 0.32$, (c) transverse motion for $\omega = 0.209$.

5. Concluding Remarks

The equation of motion (4) for $\phi(t)$, or for the motion about the equilibrium rotation ϕ_e, does not have a stable trivial solution if the static load p is greater

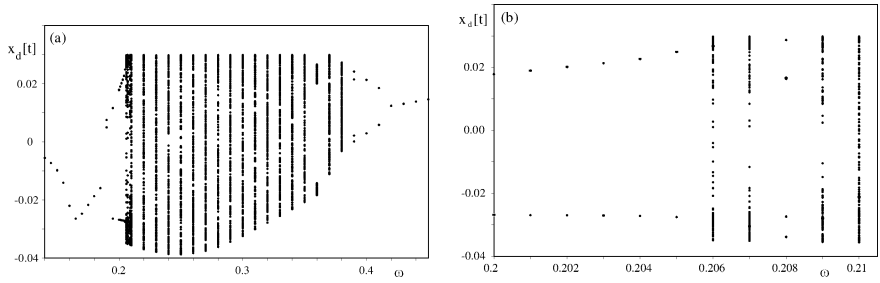

Figure 9. (a) Bifurcation diagram for the axial response, (b) magnification of the bifurcation diagram near the resonant frequency.

than the critical load $p_{cr} = 2$. Also, there is no rigid body motion in which the mechanism moves axially with the base motion $u(t)$ and with $\phi(t) = \phi_e$. The largest responses tend to occur when the excitation frequency is near the resonant frequency of the system, where the transmissibility would be infinite if no damping were present. In the bifurcation diagrams shown, chaotic motions occur for most of the frequencies considered in the range $\omega_n < \omega < 2\omega_n$ where ω_n is the resonant frequency and ω is the excitation frequency.

Experimental results were presented in [11] using two pinned struts in parallel as an isolator instead of the mechanism analyzed here. The weight supported by the struts was just enough to buckle them, and the base was subjected to vertical harmonic excitation. The variation of the transmissibility with applied frequency was qualitatively similar to the variation obtained here. For sufficiently high applied frequencies, the supported weight exhibited a very small response and then the pair of buckled struts was very effective as an isolator.

Acknowledgments

This research was funded by the National Science Foundation under Grant No. CMS-0301084 to Duke University and Virginia Tech.

References

[1] J. Winterflood, T. Barber and D.G. Blair, "Mathematical analysis of an Euler spring vibration isolator," *Physics Letters A*, 300:131–139, 2002.

[2] J. Winterflood, T. Barber and D.G. Blair, "Using Euler buckling springs for vibration isolation," *Classical and Quantum Gravity*, 19:1639–1645, 2002.

[3] J. Winterflood, T. Barber and B. Slagmolen, "High performance vibration isolation using spring in Euler column buckling mode," *Physics Letters A*, 300:122–130, 2002.
[4] F.C. Nelson, "Vibration isolation: A review, I. Sinusoidal and random excitations," *Shock and Vibration*, 3:485–493, 1994.
[5] R.H. Racca, *Characteristics of vibration isolators and isolation systems, in Shock and Vibration Handbook, 4th edition*, chapter 32. McGraw-Hill, New York, 1996.
[6] E.I. Rivin, *Passive Vibration Isolation*, ASME Press, New York, 2003.
[7] N. HaQuang, D.T. Mook and R.H. Plaut, "A non-linear analysis of the interactions between parametric and external excitations," *Journal of Sound and Vibration*, 118:425–439, 1987.
[8] R.H. Plaut and J.-C. Hsieh, "Chaos in a mechanism with time delays under parametric and external excitation," *Journal of Sound and Vibration*, 114:73–90, 1987.
[9] S.B. Yamgoué and T.C. Kofané, "Chaotic responses of a deformable system under parametric and external excitations," *Chaos, Solitons and Fractals*, 17:155–167, 2003.
[10] L.N. Virgin, *Introduction to Experimental Nonlinear Dynamics: A Case Study in Mechanical Vibration*, Cambridge University Press, Cambridge, UK, 2000.
[11] L.N. Virgin and R.B. Davis, "Vibration isolation using buckled structures," *Journal of Sound and Vibration*, 260:965–973, 2003.

IV.

NONSMOOTH DYNAMICS

One of the most common nonlinearities in mechanics is related to the characteristics of *system nonsmoothness*. The fourth part of the Proceedings collects a number of papers in the field which are compiled alphabetically, based on the last name of the first author. They deal with the effects of dry friction, clearances, impacts, intermittent contacts, as well as their combinations. Theoretical investigations and phenomenological observations of non-standard discontinuous bifurcations in maps and flows are presented. Overall, theoretical contributions and the analytical or experimental results obtained for different discontinuous systems may help in refining the bifurcation theory of nonsmooth systems, which is still an open matter.

A double-belt friction oscillator, to be considered as a simple representation of mechanical systems with multiple nonsmooth characteristics, is investigated by Casini and Vestroni. Its response exhibits nonclassical bifurcation scenarios as a consequence of multiple discontinuity boundaries. In the control parameter domain, several regions with different responses are detected and novel transitions are exhibited across the separating boundaries. Preliminary experimental results confirm the theoretical findings.

An overview of different bifurcations and their correct classification in nonsmooth mechanical systems is given by di Bernardo et al., with special attention paid to border collision and grazing. The classification focuses on events involving interactions with discontinuity boundaries of either fixed points or limit cycles of piecewise-smooth systems. The general ideas are discussed for a dry friction oscillator which exhibits sudden onset of chaotic stick-slip motion due to grazing-sliding of a periodic orbit with a switching manifold.

Griffin and Hogan show how the introduction of imperfection and noise in discontinuous systems can have a dramatic effect on the relevant behaviours. For a piecewise linear map and its associated ordinary differential equation, blurring of bifurcation boundaries, apparent loss of

G. Rega and F. Vestroni (eds.),
IUTAM Symposium on Chaotic Dynamics and Control of Systems and Processes in Mechanics, 251–252.

bistability, stochastic resonance, and an advance/delay of bifurcations do occur.

Measurements of the complicated behaviour of oilwell drillstring motion are simulated and explained by Leine and van Campen, as to the main aspects. A stick-slip whirl model that suitably simplifies the complex reality but includes lateral and torsional motions is shown to be able to capture the main nonlinear phenomena. Standard and non-standard bifurcations due to the system nonsmooth characteristics do occur, in particular the disappearance of stick-slip vibrations when whirl oscillations appear.

Luo makes use of the mapping dynamics approach to better understand the local and global dynamic behaviour of nonsmooth systems, and to analytically predict all possible periodic motions. The mapping structure and motion transition of periodic and chaotic solutions are examined for a three-piecewise linear system as a sample case of nonsmooth dynamical systems.

Pavlovskaia and Wiercigroch tackle the description of the behaviour of an impact oscillator with drift, which is a piecewise smooth system exhibiting complex dynamics. The analysis of the system can be simplified by separating the oscillatory part of the solution from the progressive motion by means of a suitable coordinate transformation. An implicitly defined map that allows reducing the dimension of state variables to two is used to study the system bifurcation scenarios.

Peterka presents new results on the dynamics of oscillators with soft impacts based on different models of the elastic and dissipative forces occurring during the contact. The approach allows him to describe the involved nonlinear dynamic regimes of mechanical systems whose contact stiffness between impacting bodies ranges from zero, which corresponds to impact-less motion, to infinity, which corresponds to motion with rigid impacts.

Finally, Wiercigroch et al. outline a general methodology for describing, analysing and solving nonsmooth dynamical systems, and illustrate it on a practical case study where the dynamics of a Jeffcott rotor with a snubber ring is examined by means of analytical, numerical, and experimental methods. Experiments confirm theoretical bifurcation diagrams, and highlight similar complex attractors.

NONSMOOTH DYNAMICS OF A DOUBLE-BELT FRICTION OSCILLATOR

P. Casini and F. Vestroni
Dipartimento di Ingegneria Strutturale e Geotecnica, Università di Roma "La Sapienza", 00184 Roma, Italia
paolo.casini@uniroma1.it

Abstract: The model of a double-belt friction oscillator is proposed, which exhibits multiple discontinuity boundaries in the phase space. The system consists of a visco-elastic oscillator dragged by two different rough supports moving with constant driving velocities. The evolution of steady-state attractors as the discontinuity parameters are varied is described. The presence of multiple discontinuity boundaries leads to nonsmooth responses which are studied here by means of analytical and numerical tools.

Key words: Stick-slip motions, nonstandard bifurcations, piecewise-smooth dynamical systems.

1. Introduction

Nonsmooth characteristics arise in many mechanical applications due to dry friction, impacts, clearances or a combination of these phenomena [1-13]. Smoothness in regions of phase space is lost as trajectories cross the boundaries between adjacent regions, where the vector field and its Jacobian can be discontinuous, or even discontinuous can be the vector state [6]. Depending on the properties of the *discontinuity boundaries*, piecewise smooth dynamical systems (PSS) can be divided into three classes: *continuous PSS* [8,13], *Filippov PSS* [1,3-5,7,12] and *hybrid PSS* [6,11]. In the first class the system vector field is the same in the adjacent regions

G. Rega and F. Vestroni (eds.),
IUTAM Symposium on Chaotic Dynamics and Control of Systems and Processes in Mechanics, 253–262.

separated by the boundary, whereas its Jacobian changes; in the second class the system vector field changes passing from a region to the adjacent; finally, in the third class the system vector state is discontinuous across a boundary.

To investigate the dynamics of these systems, a model of a visco-elastic oscillator (DBO) dragged by two different rough belts moving with constant velocities v_0 and v_1 is proposed. Two types of external excitation have been considered: *i)* energy is uniquely transferred from the moving supports to the mass via a velocity-dependent friction force discontinuous at zero relative velocity (autonomous PSS); *ii)* a harmonic driving force is also applied to the mass (non-autonomous PSS). The interactions between the mass and the belts lead to multiple discontinuity boundaries in the phase plane: aim of this study is to investigate how the number and positions of the discontinuity boundaries affect the dynamics of the system and the associated bifurcation scenarios.

With regard to belt locations, three particular configurations can be derived from the general model: *i)* the mass is always in contact only with belt 0 (*friction oscillator*); *ii)* the mass is always in contact with both belts (*uninterrupted double contact*); *iii)* the mass can only contact sequentially one belt at a time (*sequential contact*). Respectively one, two and three discontinuity boundaries characterizing a Filippov PSS arise in the phase plane. The first configuration has been extensively studied in the literature [1,5,7,8,12], the last two configurations, which still offer undisclosed aspects, are the subject of the present investigation.

2. Uninterrupted Double Contact

2.1 Equations of Motion

In this configuration, Fig. 1a, the mass is continuously in contact with both belts which are pushed onto the mass with a constant force F_n and possess the same friction characteristics. In the phase plane two discontinuity boundaries, governed by v_0 and v_1, are present: Σ_{F0} is defined by a zero relative velocity between mass and belt 0; Σ_{F1} is defined by a zero relative velocity between mass and belt 1. The discontinuity boundaries divide the phase plane into three smoothness regions, Fig. 1b: in region D_1 the kinetic friction forces on belt 0 and belt 1 are both positive, in region D_2 they are discordant, and in region D_3 they are both negative. No harmonic force is applied to the mass; regular motions are then governed by:

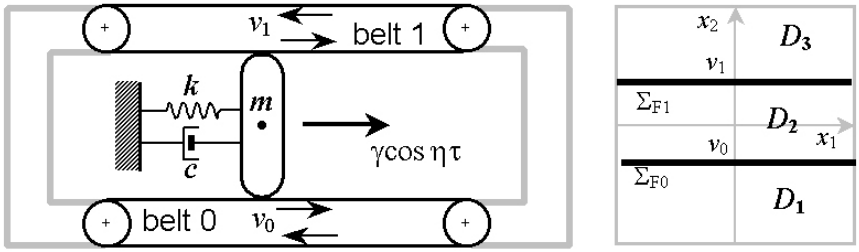

Figure 1. Double contact configuration (a); discontinuity boundaries in the phase plane (b)

$$\dot{\mathbf{x}} = \begin{cases} \mathbf{f}_1(\mathbf{x}), \ \mathbf{x} \in D_1 \\ \mathbf{f}_2(\mathbf{x}), \ \mathbf{x} \in D_2 \\ \mathbf{f}_3(\mathbf{x}), \ \mathbf{x} \in D_3 \end{cases} \tag{1}$$

where

$$\begin{aligned} \mathbf{f}_1(\mathbf{x}) &= \begin{cases} x_2 \\ -x_1 - \zeta x_2 + u_0 \mu_0 (v_0 - \omega x_2) + u_0 \mu_1 (v_1 - \omega x_2) \end{cases} \\ \mathbf{f}_2(\mathbf{x}) &= \begin{cases} x_2 \\ -x_1 - \zeta x_2 - u_0 \mu_0 (v_0 - \omega x_2) + u_0 \mu_1 (v_1 - \omega x_2) \end{cases} \\ \mathbf{f}_3(\mathbf{x}) &= \begin{cases} x_2 \\ -x_1 - \zeta x_2 - u_0 \mu_0 (v_0 - \omega x_2) - u_0 \mu_1 (v_1 - \omega x_2) \end{cases} \end{aligned} \tag{2}$$

Equations (2) have been derived by normalizing the equations of motion with respect to the stiffness and by introducing a non-dimensional time τ:

$$\tau = \omega t, \quad \omega = \sqrt{\frac{k}{m}}, \quad (\dot{\circ}) = \frac{d(\circ)}{d\tau} = \frac{d(\circ)}{dt}\frac{1}{\omega}, \quad u_0 = \frac{F_n}{k}, \quad \zeta = \frac{c}{\sqrt{km}} \tag{3}$$

The friction force, relevant to belt i, reads as follows [2,8]:

$$\mu_i(v_{Ri}) := \frac{\mu_{si} - p_{1i}}{1 + p_{3i} |v_{Ri}|} + p_{1i} + p_{2i} v_{Ri}^2, \qquad v_{Ri} := v_i - \omega x_2, \ i = 0,1 \tag{4}$$

where v_{Ri} is the relative velocity between the mass and belt i, μ_{si} is the static friction coefficient and p_{2i} is usually taken equal to zero: under this assumption, the friction coefficient hyperbolically decays to a residual value

of friction $p_{1i}<\mu_{si}$ whereas the coefficient $p_{3i}>1$ quantifies the descent steepness (negative slope) of the friction force.

Sliding motions on Σ_{F0} and Σ_{F1} are governed by the following equations:

$$\begin{cases} \dot{x}_1 = x_2 \\ \dot{x}_2 = 0 \end{cases}, \quad \left| -x_1 - \zeta x_2 + u_0 \mu_1(v_{R1}) \operatorname{sgn}(v_{R1}) \right| < u_0 \mu_{s0}$$
$$\begin{cases} \dot{x}_1 = x_2 \\ \dot{x}_2 = 0 \end{cases}, \quad \left| -x_1 - \zeta x_2 + u_0 \mu_0(v_{R0}) \operatorname{sgn}(v_{R0}) \right| < u_0 \mu_{s1} \tag{5}$$

Solutions have been constructed by 'gluing' standard motions on smoothness regions and sliding motions along the discontinuity boundaries. Switch methods and standard numerical tools have been adopted.

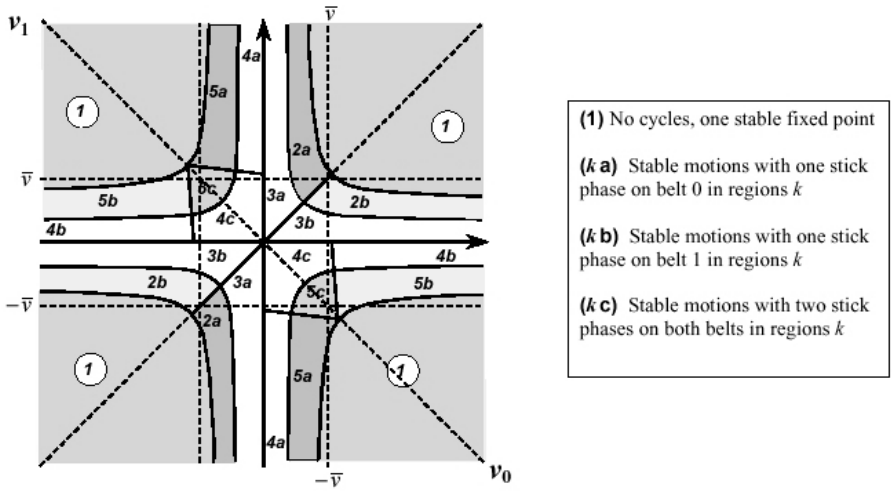

Figure 2. Regions of qualitatively different behaviours in the parameter plane

2.2 Dynamic Response

The influence of the discontinuity parameters v_0 and v_1 on the system dynamics has been investigated. Figure 2 shows a significant portion of the parameter plane (v_0, v_1) where regions of qualitatively different dynamic responses have been revealed. Due to the structure of the equations of motion and to the fact that the belts possess the same friction parameters, the domain evinces a polar symmetry. With the exception of regions 1, where only a stable fixed point exists, stable limit cycles exhibiting at least one

stick phase are present in all other regions: in the case of concordant belt velocities (first and third quadrants) the mass always sticks on the slower belt whereas stable motions with two distinct stick phases on both belts are possible in the case of discordant belt velocities (regions 4c and 5c).

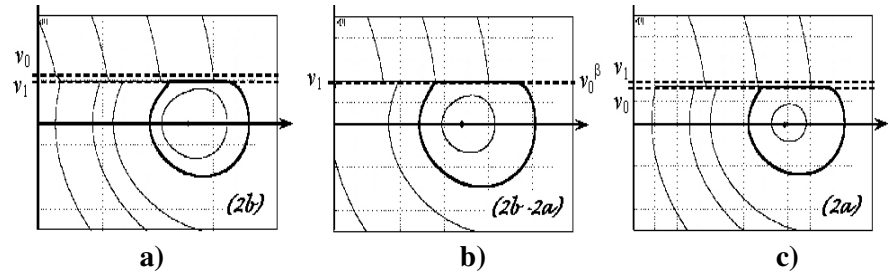

Figure 3. Phase portraits around the sliding-exchange bifurcation

Across the boundaries separating two adjacent regions in the parameter domain transitions in the system dynamics occur. In Fig. 3 a nonstandard transition is illustrated by decreasing v_0 with fixed v_1. The sliding motions in the stable cycle change: in fact, for values of v_0 larger than v_1 the stable cycle shows a sliding solution only in Σ_{F1}, i.e. the mass sticks on belt 1 (Fig. 3a); for values of v_0 smaller than v_1 the stable cycle shows a sliding solution only in Σ_{F0}, i.e. the mass sticks on belt 0 (Fig. 3c). Thus a transition occurs for $v_0=v_1=v_0^\beta$ since a sliding solution disappears in Σ_{F1} and appears in Σ_{F0} (Fig. 3b). This transition, strictly related to the presence of two different discontinuity boundaries, it will be called 'sliding-exchange' bifurcation. Another example of nonstandard transitions is illustrated in Fig. 4. At $v_0=0$ the fixed points of the system are located in Σ_{F0}: a segment of fixed points exist (thick line in Fig. 4b) which is an attracting set. The sliding motions in the stable cycle change: in fact, for positive values of v_0 the stable cycle shows a sliding solution only in Σ_{F0}, i.e. the mass sticks on belt 0 (Fig. 4a); for negative values of v_0 the stable cycle shows two different sliding motions in Σ_{F0} and Σ_{F1}, i.e. the mass sticks on both belts, Fig. 4c. Thus, at $v_0=v_0^\delta=0$ a transition occurs called 'sudden sliding appearance' bifurcation (Fig. 4b).

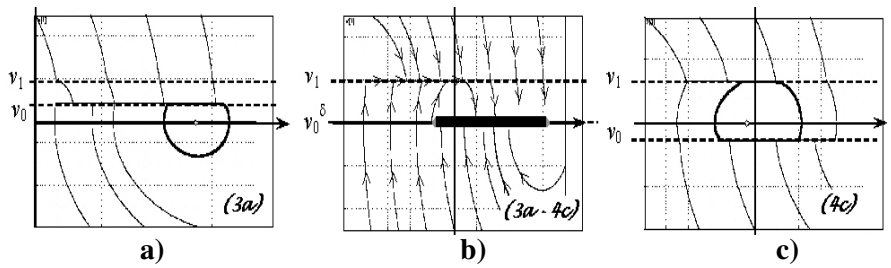

Figure 4. Phase portraits around the sudden sliding appearance bifurcation

3. Sequential Contact Configuration

3.1 Equations of Motion

In this configuration, the mass is in contact with one belt at a time, Fig. 5a. In the phase plane three discontinuity boundaries (Σ_{F0}, Σ_{F1}, Σ_σ) governed by v_0, v_1 and σ, are present, Fig. 5b. They divide the phase plane into four smoothness regions where the vector fields have the following expression:

$$\mathbf{f}_{1,2}(\mathbf{x}) = \begin{cases} x_2 \\ -x_1 - \zeta x_2 \pm u_0 \mu_0 (v_0 - \omega x_2) + \gamma \cos(\eta\tau) \end{cases}$$
$$\mathbf{f}_{3,4}(\mathbf{x}) = \begin{cases} x_2 \\ -x_1 - \zeta x_2 \mp u_0 \mu_1 (v_1 - \omega x_2) + \gamma \cos(\eta\tau) \end{cases} \tag{6}$$

Sliding motions on Σ_{F0} and Σ_{F1} are governed by the following equations:

$$\begin{cases} \dot{x}_1 = x_2 \\ \dot{x}_2 = 0 \end{cases}, \quad \left| -x_1 - \zeta x_2 + \gamma \cos(\eta\tau) \right| < u_0 \mu_{s0}$$
$$\begin{cases} \dot{x}_1 = x_2 \\ \dot{x}_2 = 0 \end{cases}, \quad \left| -x_1 - \zeta x_2 + \gamma \cos(\eta\tau) \right| < u_0 \mu_{s1} \tag{7}$$

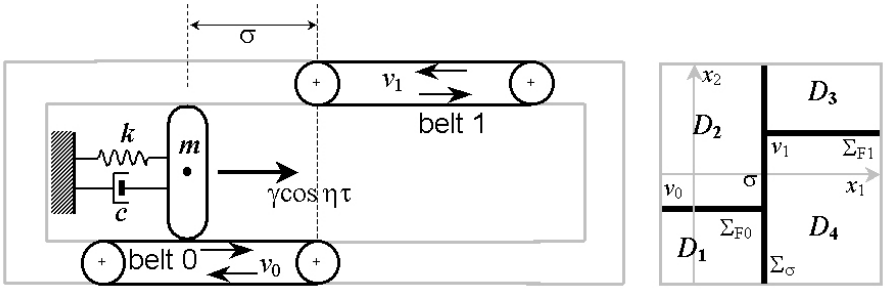

Figure 5. Sequential contact configuration (a); discontinuity boundaries in the phase plane (b)

3.2 Dynamic Response

The autonomous case, γ=0, has been first investigated. Figure 6 shows a section of the parameter space (v_0, v_1, σ) where regions characterized by a different number and/or type of cycles are reported. Unlike the case analysed in the previous subsection (Fig. 2) polar symmetry is no longer exhibited;

furthermore the path along the line $v_0=v_1$ reproduces the behaviour of the classical friction oscillator.

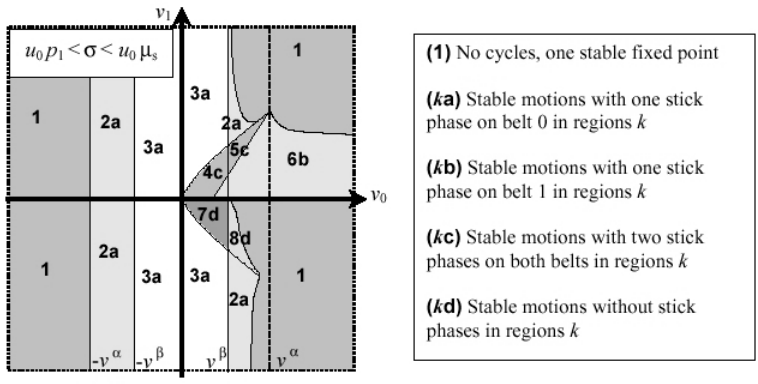

Figure 6. Regions of qualitatively different behaviours in the parameter space

In the sequential contact configuration, stable motions with two stick phases on both belts are possible in the case of concordant belt velocities; stable motions without stick phases are also possible for discordant belt velocities. An example of nonstandard transition occurring across a boundary is illustrated in Fig. 7 by increasing v_0 with fixed v_1. The sliding motions in the stable cycle changes: in fact, for values of v_0 smaller than v_0^{γ} the stable cycle shows one stick phase only on belt 0 (Fig. 7a); for values of v_0 larger than v_0^{γ} a sliding solution on Σ_{F1} is present and the mass sticks on both belts (Fig. 7c). Thus a transition occurs for $v_0=v_0^{\gamma}$ since, in the stable cycle, a sliding solution appears on Σ_{F1} (sequential sliding bifurcation, Fig. 7b).

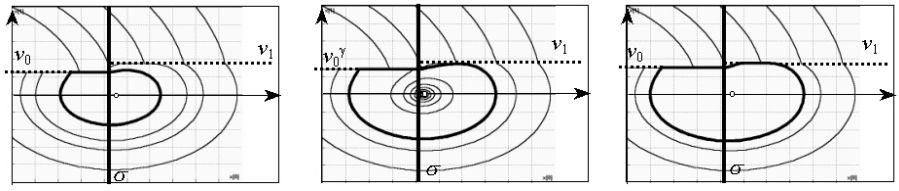

a) **b)** **c)**

Figure 7. Phase portraits around the sequential sliding bifurcation

In the non-autonomous case, for a driving force with given amplitude and frequency and for given initial conditions, the location of the discontinuity boundaries has been found to modify the dynamic response leading to one- and higher-periodic as well as quasi-periodic and chaotic solutions.

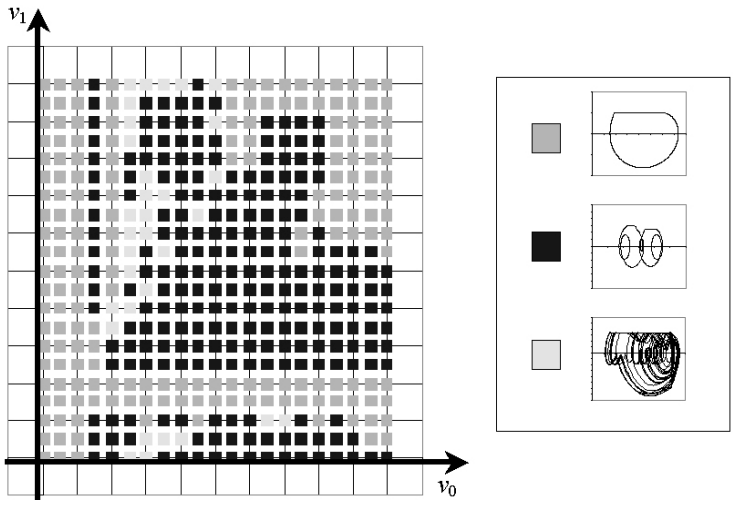

Figure 8. Influence of belt velocities on the forced responses (σ=0.68)

The diagram of Fig. 8, relevant to natural initial conditions and to a driving force with amplitude γ=1.0 and normalized frequency η=5.0, illustrates the occurrence of one-periodic, higher-periodic and chaotic steady state motions for varying v_0>0 and v_1>0.

An example of chaotic motion for discordant belt velocities is reported in Fig. 9 where the phase portrait (Fig. 9a) with the relevant Poincaré section (Fig. 9b) are illustrated. Figure 9c, which magnifies the region enclosed by the dotted rectangle in Fig. 9b, highlights the fractal structure of the attractor. The attractor has been reached through an intermittency route to chaos characterized by intervals of periodic motions interrupted by non-periodic bursts.

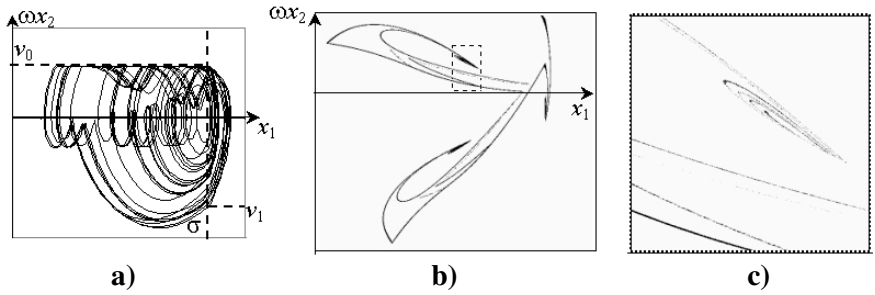

Figure 9. Chaotic attractor at σ=0.68, v_0=0.3495 and v_1=-0.60

4. Conclusions

The model of a double-belt friction oscillator has been proposed and investigated for two particular configurations: uninterrupted double contact with both belts and sequential contact. The dynamics of this system are of interest because it is a simple representation of mechanical systems with multiple nonsmooth characteristics and in the same time its response exhibits non-classical bifurcation scenarios as a consequence of the occurrence of multiple discontinuity boundaries caused by the belts.

In absence of driving forces, several regions in which the system exhibits qualitatively different responses have been detected and represented in the control parameter domain: the characteristic transitions exhibited by the system across the boundaries separating these regions have been subsequently analyzed for both configurations. Some novel transitions have been detected: in particular, sliding-exchange and sudden sliding appearance bifurcations have been found for the double contact oscillator. In the former case, a sliding solution disappears in the discontinuity boundary related to a belt and appears in the one related to the other belt; in the latter case, a sliding solution related to a belt abruptly occurs in addition to other sliding motions. For the sequential contact oscillator, sequential sliding bifurcations have been observed; they are characterized by the fact that a stick phase on a belt appears in sequence to a stick phase on the other belt.

The non-autonomous case is finally considered. For a driving force with given amplitude and frequency and for given initial conditions, the location of the discontinuity boundaries in the phase plane has been found to modify the dynamic response leading to one- and higher-periodic as well as quasi-periodic and chaotic solutions. A rich dynamic scenario has been disclosed: the evolution through stable closed orbits and period-doubling routes to chaos are studied in the parameter domains; strange attractors are revealed and their evolution illustrated.

Finally, a test set-up of the DBO model has been built in order to investigate whether the rich variety of the nonlinear phenomena predicted by the analytical model is observed in the physical prototype.

The analytical and experimental results obtained for these particular case studies could help to refine the bifurcation theory in nonsmooth systems which is still an open matter.

Acknowledgments

The work is partially supported by the Grant COFIN01 (2001/02) on “Dynamics of Flexible Structures” (www.disg.uniroma1.it/fendis)

References

[1] A.F. Filippov, *Differential Equations with Discontinuous Righthand Sides*. Kluwer Academic Publishers, 1988.

[2] S.J. Hogan, "Heteroclinic bifurcations in damped rigid block motions," *Proc. Roy. Soc. London A,* **439**, pp. 155-162, 1992.

[3] K. Popp, N. Hinrichs, and M. Oestreich, "Analysis of a self-excited friction oscillator with external excitation," in *Dynamics with Friction*, Guran A., Pfeiffer F., Popp K. (eds.), World Scientific, London, 1996.

[4] J. Awrejcewicz and M.M. Holicke, "Melnikov's method and stick-slip chaotic oscillations in very weakly forced mechanical systems," *International Journal of Bifurcations and Chaos*, **9**, pp. 505-518, 1999.

[5] R.I. Leine, D.H. van Campen, A. De Kraker, and L. van Den Steen, "Stick-slip vibration induced by alternate friction models," *Nonlinear Dynamics,* **16**, pp. 41-54, 1998.

[6] B. Brogliato, *Nonsmooth Impact Mechanics*. Springer-Verlag, London, 1999.

[7] U. Galvanetto, S.R. Bishop, "Dynamics of a simple damped oscillator undergoing stick-slip vibrations," *Meccanica*, **34**, pp. 337-347, 1999.

[8] R.I. Leine, *Bifurcations in Discontinuous Mechanical Systems of Filippov-type*. PhD Thesis, Technische Universiteit Eindhoven, 2000.

[9] M. Di Bernardo, C.J. Budd, and A.R. Champneys, "Unified framework for the analysis of grazing and border-collisions in piecewise-smooth systems," *Physical Review Letters*, **86**(12), pp. 2554-2556, 2001.

[10] F. Pfeiffer and C. Glocker, "Contacts in multibody systems", *Journal of Applied Mathematics and Mechanics,* **64**, pp. 773-782, 2001.

[11] P. Casini and F. Vestroni, Bifurcations in hybrid mechanical systems with discontinuity boundaries," *Int. Journal of Bifurcation and Chaos*, 2003, in press.

[12] P. Casini and F. Vestroni, "Nonstandard bifurcations in oscillators with multiple discontinuity boundaries," *Nonlinear Dynamics*, 2003, in press.

[13] F. Peterka, "Behaviour of impact oscillator with soft and preloaded stop," *Chaos, Solitons & Fractals*, **18**, pp. 79-88, 2003.

CORNER-COLLISION AND GRAZING-SLIDING

Practical examples of border-collision bifurcations

M di Bernardo, A.R. Champneys and P. Kowalczyk
Department of Engineering Mathematics
University of Bristol, Bristol, U.K.
{m.dibernardo,a.r.champneys,p.kowalczyk}@bristol.ac.uk

Abstract: This chapter gives an overview of the main types of nonsmooth transitions which can be observed in piecewise smooth dynamical systems. Particular attention is given to those events involving interactions with the discontinuity boundary of fixed points of piecewise-smooth maps and limit cycles of piecewise-smooth flows. Strategies to classify these phenomena are discussed. It is shown that only few cases lead to maps which are locally piecewise linear to leading order. A nonlinear friction oscillator is used as a representative example to illustrate the main ideas introduced in the chapter.

Key words: Bifurcations, piecewise-smooth systems, friction oscillators

1. Introduction

Vibro-impacting systems can exhibit a multitude of different nonsmooth bifurcation phenomena [1]. Recently, for example, self-excited vibrating systems with dry-friction were studied by [2]. A route to chaos is reported where a period-doubling cascade is abruptly terminated by an outburst of chaotic behaviour due to the transition from slip to stick-slip motion, that cannot be explained by smooth bifurcation theory. Often it is conjectured that these and similar observations in the literature can be explained by the theory of so-called border collision bifurcation, which applies to discrete-time maps which are to lowest-order piecewise linear [3]. In a few examples, border collisions have indeed been shown to organise the dynamics, e.g. in DC/DC converters in Power Electronics [4], but in general it is hard to analytically derive the border-collision maps direct from the nonsmooth ordinary differential equations.

G. Rega and F. Vestroni (eds.),
IUTAM Symposium on Chaotic Dynamics and Control of Systems and Processes in Mechanics, 263–273.

In fact, analytically there is a fundamental problem recently outlined in [5], [6]. Here, the theory of discontinuity mappings shows that periodic orbits hitting tangentially ("grazing") a discontinuity set in a nonsmooth continuous time system do *not* generically lead to maps which are locally piecewise linear. Instead the maps have either square-root or $O(3/2)$ singularities. It is now becoming clear that border-collision of piecewise linear maps therefore is not the whole story.

Nevertheless, in this chapter, we will present an overview of our recent work, showing two cases where border-collisions of piecewise linear maps *can* rigorously be derived and shown to organise the occurance of chaotic dynamics. These are so-called the corner-collision bifurcation and the grazing-sliding bifurcation, the former of which occurs when a switching boundary is itself nonsmooth, and the latter is one of the ways in which pure slip motion can transfrom into stick-slip. As a representative example, we will discuss in detail the latter bifurcation occuring in the friction oscillator studied in [2].

2. Bifurcations of Nonsmooth Systems

Piecewise smooth (PWS) dynamical systems can exhibit most of the standard bifurcations found in smooth systems, for instance fold or period-doublings. In addition to these, there are also some novel transitions which are unique to PWS systems, which were given the name C-bifurcations in the Russian literature [7]. A C-bifurcation in this sense is any transition which can be explained in terms of interactions between invariant sets and switching surfaces in phase space. Note that according to this definition a C-bifurcation does not necessarily imply the onset of a topologically non-equivalent phase portrait at the bifurcation point.

We focus on two types of C-bifurcations: (i) Border-Collisions of fixed points in maps; (ii) Grazing Bifurcations of limit cycles in flows. Both cases are characterised by the same phase space topology close to the bifurcation point. Namely, the map or flow exhibiting the bifurcation is defined over a region $D \subset R^n$ of phase space which is chosen so that, by an appropriate choice of local coordinates, the map or flow under investigation can be described as:

$$\Phi[x] = \begin{cases} g_1(x,\mu) & \text{if } H(x) < 0 \\ g_2(x,\mu) & \text{if } H(x) > 0 \end{cases} \tag{2.1}$$

where Φ is a differential or finite difference operator, $H(x)$=0 defines a smooth boundary Σ which separates D into two regions denoted by G_1 and G_2, i.e. $\Sigma := \{\mathbf{x} \in D \mid H(x) = 0\}, G_1 := \{x \in D \mid H(x) > 0\}, G_2 := \{x \in D \mid H(x) < 0\}$. We assume that $g_1(x,\mu) \in C^k$ if $x \in G_1$, $g_2(x,\mu) \in C^k$ if $x \in G_2$ and $g_1(x,\mu) = g_2(x,\mu)$ when $x \in \Sigma$, i.e. the map or flow is smooth to order k in each of the subregion G_1 and G_2 while is continuous but

nonsmooth on Σ. As discussed below particular care must be taken to define the system behaviour when $H(x) = 0$.

2.1 Border-Collision of Fixed Points

Let $\hat{\mathbf{x}}$ be a fixed point of a $g_1(x, \mu)$ which we assume depends continuously on the parameter $\mu \in (-\varepsilon, \varepsilon)$. We say that $\hat{\mathbf{x}}$ is a *border-crossing fixed point* if it approaches Σ, as μ is varied between $-\varepsilon$ and ε such that, if the dynamics in region G_2 close to the boundary were still generated by the map $g_1(x, \mu)$ then the crossing would be transversal. In other words (1) $\hat{\mathbf{x}} \in \Sigma$ for $\mu = 0$; (2) $\hat{\mathbf{x}} \in G_1$ for $-\varepsilon < \mu < 0$; (3) $\hat{\mathbf{x}} \in G_2$ for $0 < \mu < \varepsilon$.

We say that a fixed point $\hat{\mathbf{x}}$ undergoes a border-collision bifurcation for $\mu = 0$ if $\hat{x}^*$ is a border-crossing point.

Border-collisions can organise several types of transitions in a PWS system. Understanding the relationship between the properties of the map and the scenario observed is presented in Sec. 1.3.1 below. First, we continue our overview of the main types of bifurcations in nonsmooth systems.

2.2 Grazings of Limit Cycles

We now move to the case of C-bifurcations of limit cycles in flows. In this case, experiments, numerics and theoretical developments have clearly shown that complex transitions in PWS systems are often associated to tangential intersections (grazings) of a system periodic orbit (or parts of it) with the switching manifold.

We say that a periodic orbit $\hat{\mathbf{x}}=\hat{\mathbf{x}}(t)$ of 2.1 is a *grazing orbit* if for some time $t=t^*$, $\mathbf{x}(t)$ hits tangentially the switching manifold Σ (defined by $H(\mathbf{x}(t))=0$) at the point $\mathbf{x}^* = \mathbf{x}(t^*)$ which is termed the grazing point. We assume that no *sliding motion* can take place on Σ [8]. Such a solution can be seen heuristically as a motion taking place along the discontinuity surface in the limit of infinitely many switchings. A necessary condition to avoid sliding is that, under the flow of system (2.1) sufficiently close to the grazing point, the boundary $\{H = 0\}$ should never be simultaneously attracting (or repelling) from both sides G_1 and G_2; that is $\langle \nabla H, f_1 \rangle \langle \nabla H, f_2 \rangle > 0$ This assumption will be removed in Sec. 1.4 where grazings in systems with sliding are considered.

3. Classification of Nonsmooth Bifurcations

In applications it is important to possess a tool to predict and control the scenarios following a C-bifurcation event. In smooth systems normal forms allow the characterisation of bifurcations such as saddle-nodes, Hopf and period-doublings [9]. In the case of nonsmooth systems there is no such general strategy available. One methodology for border-collisions in maps, due to Feigin [7], [10], is to classify what happens to the simplest fixed points generated in the bifurcation, for general n-dimensional systems.

3.1 Feigin's Strategy for Border-Collisions

Feigin's strategy is based on a local analysis of the map under investigation in a sufficiently small neighborhood of the border-collision event. Classification is achieved by studying the eigenvalues of the map obtained by linearising the nonsmooth map about the border-collision point on both sides of the discontinuity boundary. Generically, this map will be obtained as the composition of the two submappings:

$$\Pi_1 : =\mathbf{x} \mapsto \mathbf{A_1 x} + \mathbf{B}\mu, \tag{3.2}$$

$$\Pi_2 : =\mathbf{x} \mapsto \mathbf{A_2 x} + \mathbf{B}\mu, \tag{3.3}$$

where A_1 and A_2 are the Jacobians of the nonsmooth map on both sides of the boundary.

To classify the possible scenarios following a border-collision, we look at the quantities σ_1^+, σ_2^+ defined as the number of real eigenvalues greater than 1 of A_1 and A_2 respectively together with the quantities σ_1^-, σ_2^-, i.e. the number of real eigenvalues less than -1. Similar quantities $\sigma_{11}^{\pm}$ and $\sigma_{12}^{\pm}$ are defined for fixed points of period two. These represent respectively the number of eigenvalues greater than 1 or less than -1 of the matrices A_1A_1 and A_1A_2 (see schematic representation of possible bifurcation scenarios depicted in Fig. 3.1).

Note that even when two-periodic point can be shown to exist, there are scenarios such as $A \to b, ab$ where no stable asymptotic solution is present after the border-collision. In these cases, other tools from nonlinear dynamics must be used to investigate the presence of other attractors, e.g. strange attractors or higher periodic points. A complete classification for border-collisions which include the proof of existence of higher-order periodic motion or chaos after a border-collision can be given only in one and two-dimensional PWS maps [10], [11].

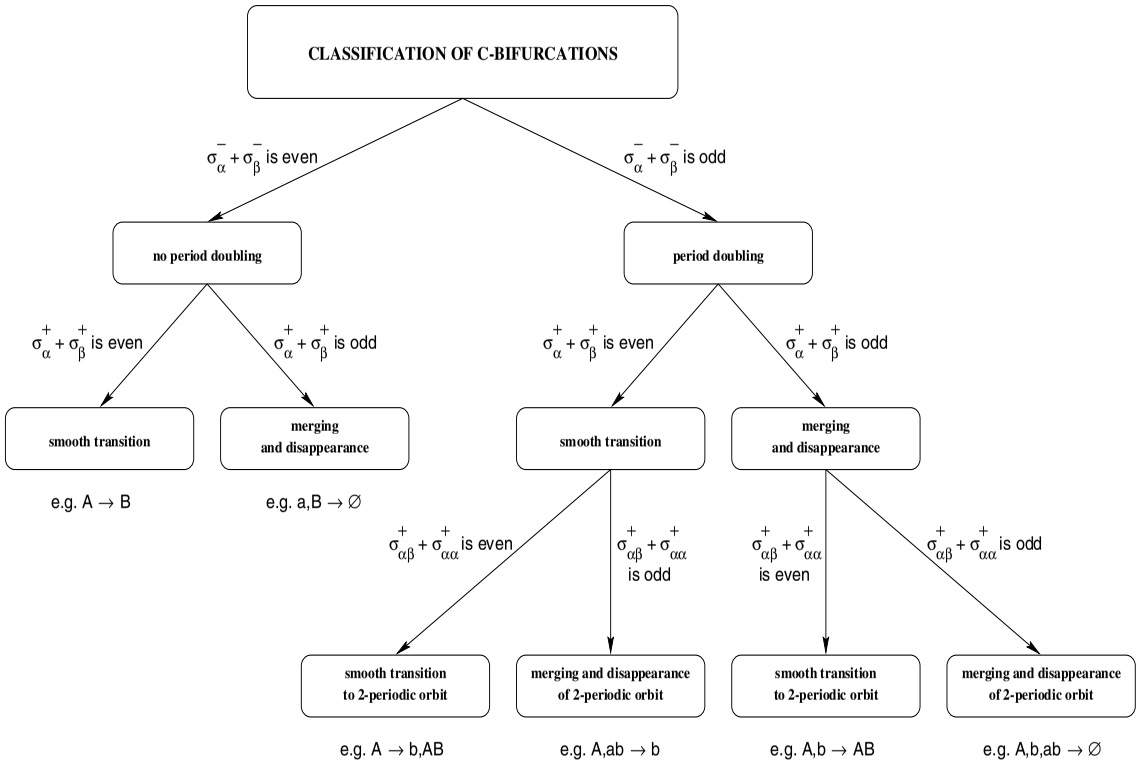

Figure 1. Schematic representation of C-bifurcation classification scheme.

3.2 Classification of Grazing Bifurcations

We now look at the problem of classifying grazing and sliding bifurcations of limit cycles in nonsmooth continuous-time systems. The starting point is to note that if we choose a Poincaré hyperplane Π transversal to the system flow, the grazing orbit is associated to a fixed point on Π. Under parameter variations, such fixed point can be shown to undergo a border-collision [12].

In order to carry out the classification we need therefore (1) a tool to derive analytically the PWS map associated to the grazing event; (2) a strategy to classify the bifurcations of the border-crossing fixed point of such a map. A solution to the former problem was recently presented by the authors in [5].

Using the concept of discontinuity mappings, due to Nordmark [13], it was shown that grazings are not associated, in general, to PWL maps but maps with a nonlinear power term whose exponent, γ, is either $1/2$, if the states are discontinuous at the bifurcation point, or $3/2$ if they are continuous but have discontinuos derivatives.

4. Corner-Collision and Grazing-Sliding

It was found that the nature of the local map associated to a grazing bifurcation can be changed by the presence of additional local properties of the system vector field or discontinuity set. We recently identified two cases where the presence of such extra properties renders the local map piecewise linear: (i) the switching manifold is discontinuous at the bifurcation point (corner-collision); (ii) the switching manifold is simultaneously attracting from both of its sides (grazing-sliding).

In both of these cases the presence of extra properties of the switching manifold at the bifurcation point causes the normal form map to change its order and exhibit a PWL structure.

4.1 Corner-Collision

We start with the bifurcation which was termed corner-collision in [14]. As shown in Fig. 2, we label corner-collision the interaction of a limit cycle with a nonsmooth switching manifold, i.e. a corner. It is assumed that sliding cannot occur. Such bifurcations were found to be associated to several nonsmooth transitions in electronic DC/DC power converters [4]. Local analysis of the vector field about the bifurcation point was carried out. It was found that the Poincaré map describing a corner-colliding orbit is piecewise linear and hence

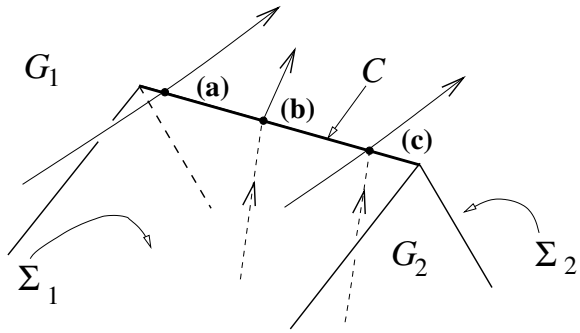

Figure 2. Three examples of corner-collision with a corner C in the switching manifold which is divided into two smooth regions Σ_1 and Σ_2. The unfolding of cases (a) and (b) lead to bifurcations governed by PWL maps to leading order. Case (c) is more complicated, becase sliding must result in the unfolding, and is not covered by PWL theory.

corner-collisions imply border-collisions that can lead to sharp corners in the bifurcation diagram [4] or the sudden onset of chaotic dynamics [15].

4.2 Grazing-Sliding

As shown in Fig. 3, in the grazing-sliding case the system trajectory is tangential to the switching manifold right on the boundary of the region where the system vector field is such that it points towards Σ from both subspaces G_1 and G_2. For this to be through, we assume that throughout this region the following condition holds: $\langle \nabla H, F_2 \rangle - \langle \nabla H, F_1 \rangle > 0$, where ∇H denotes a vector which is normal to Σ and $\langle \nabla H, F_i \rangle$ denotes the component of the vector field F_i along the normal to Σ. In the case presented in Fig. 3, a section of trajectory lying in region G_1 or G_2 grazes the boundary of the sliding region from below. Under parameter variations, this causes the formation of a section of sliding motion. To describe the system dynamics locally to the bifurcation point a normal form map of grazing-sliding can be derived as shown in [16].

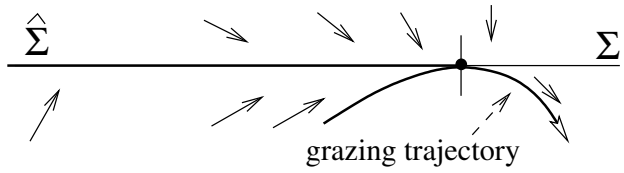

Figure 3. Schematic representation of a trajectory hitting tangentially the boundary of the sliding region (which is denoted by $\hat{\Sigma}$ in the figure)

It is worth mentioning here that grazing-sliding is one of four possible ways in which an orbit can interact with the sliding region in a nonsmooth system. The others, which are described in detail in [16] are termed as sliding-adding, sliding-crossing and sliding-switching bifurcations.

5. A Nonlinear Dry-Friction Oscillator

The stick phase of the dynamics of friction oscillators can be analysed as a segment of sliding motion [17]. This can be heuristically understood if we consider that the discontinuity in the dry-friction oscillators are encountered due to the transition from slip to stick mode of motion. The discontinuity set itself is defined by the system states such that no kinematic friction is exhibited in the system – stick phase. Therefore, as long as the system remains in the stick phase it evolves within the discontinuity set which in turn is the definition for sliding motion. Thus, the sliding bifurcation scenarios and in particular the grazing sliding scenario presented in the previous section are likely to occur in this important class of dynamical systems and can be used to explain the complex dynamics often reported in the literature.

An intriguing scenario is exhibited by the dry friction oscillator studied in [2], which is numerically shown to exhibit a route to chaos characterised by the abrupt transition from slip periodic motion to stick-slip chaotic behaviour. The bifurcation mechanism causing the onset of such aperiodic motion is left unexplained by the authors who conjecture that it must be due to some type of nonsmooth bifurcation without offering any analytical explanation.

Following [2], the dry friction oscillator under investigation in the dimensionless form can be expressed as:

$$\ddot{y} + y = f(1 - \dot{y}) + F\cos(\nu t), \tag{5.4}$$

where:

$$f(1 - \dot{y}) = \alpha_0 \mathbf{sgn}(1 - \dot{y}) - \alpha_1(1 - \dot{y}) + \alpha_2(1 - \dot{y})^3 \tag{5.5}$$

is a kinematic friction characteristic and $1-\dot{y}$ corresponds to a relative velocity between the driving belt and moving block of the dry-friction model. In the case when $1 - \dot{y} = 0$ the relative velocity is 0 and the kinematic friction is set valued i.e.: $-\alpha_0 < f(1 - \dot{y}) < \alpha_0$. The coefficients of the kinematic friction characteristic i.e.: α_0, α_1, α_2 are positive constants. F is an amplitude, ν a normalised angular velocity and T a period of the forcing term.

We focus, in particular, on the bifurcation scenario giving rise to the sudden emergence of chaotic stick-slip motion. Bifurcation diagram depicting one of the state space coordinates at stroboscopic $4T$ times versus bifurcation parameter ν is depicted in Fig. 4(a). The bifurcation was detected for parameter

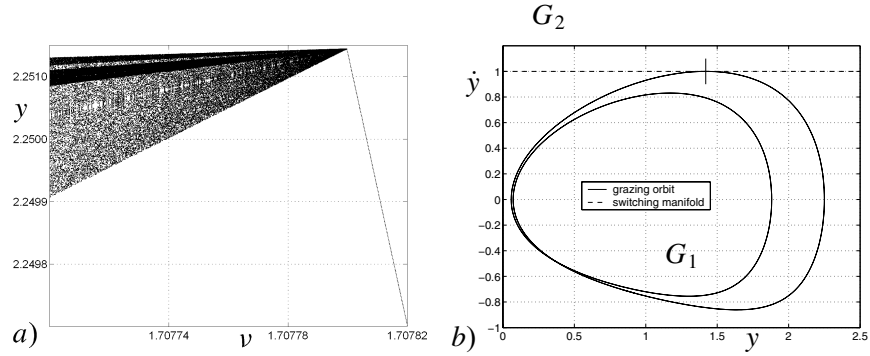

Figure 4. Bifurcation diagram obtained from the numerical integration of the system under consideration (a) (the stroboscopic section was first applied at $\dot{y} = 0$, $y \approx 2.25$) and (b) orbit of period $4T$ undergoing the grazing-sliding bifurcation for $\nu = 1.7077997$;

values $\alpha_0 = 1.5$, $\alpha_1 = 1.5$, $\alpha_2 = 0.45$, $F = 0.1$, under variation of the bifurcation parameter ν in a neighbourhood of $\nu = 1.7078$. As shown in Fig. 4(b), at the bifurcation point, a $4T$-periodic orbit grazes the switching manifold at the boundary of the sliding region (denoted in the figure by a short vertical line).

To confirm that the observed bifurcation scenario is indeed due to the grazing sliding event and to explain the dynamics triggered by the bifurcation we need:

- check if the set of analytical conditions determining the bifurcation is satisfied
- derive a map which captures the dynamics of the bifurcating cycle.

As was shown in [18] the set of analytical conditions which determine the grazing-sliding event is satisfied at the bifurcation point. The normal form map for the grazing sliding scenario yields PWL functional form [16]. The PWL character of this map remains qualitatively unchanged under the composition with some affine transformation needed to derive a mapping which captures the dynamics of the bifurcating cycle. Let us now concentrate our attention on the final form of the mapping.

Following [18] we can write an expression of a map capturing the dynamics of the bifurcating cycle as:

$$\tilde{\mathbf{x}}_{n+1} = \begin{cases} \begin{pmatrix} a_{11} & a_{12} \\ a_{21} & a_{22} \end{pmatrix} \tilde{\mathbf{x}}_n + \begin{pmatrix} b_1 \\ b_2 \end{pmatrix} \tilde{\nu} & \textbf{if} \quad \tilde{x}_{2n} < 0, \\ \begin{pmatrix} a_{11} & 0 \\ a_{21} & 0 \end{pmatrix} \tilde{\mathbf{x}}_n + \begin{pmatrix} b_1 \\ b_2 \end{pmatrix} \tilde{\nu} & \textbf{if} \quad \tilde{x}_{2n} \geq 0, \end{cases} \tag{5.6}$$

where $\tilde{x}_n = \begin{bmatrix} x_{1n} & x_{2n} \end{bmatrix}^T$ is a state vector (capturing values of the velocity and position coordinates at the stroboscopic times $4T$ with T being a period of the

forcing term) and a_{ij}, b_i (for i, $j=1, 2$) are some constant coefficients. It needs to be mentioned here that mapping (5.6) is such that the bifurcation values of the systems states and the bifurcation parameter ν^* are set at the origin.

For the $4T$ periodic orbit of interest computed earlier when $\nu^*=1.7077997$, we find that $a_{11} = -1.85$, $a_{12} = 4.396$, $a_{21} = -1.14$, $a_{22} = 2.704$.

To predict the dynamics following the bifurcation we can now use the classification strategy introduced earlier in Sec. 1.3.1. The eigenvalues of A_1 in (5.6) are $\lambda_{11} = 0.0107$, $\lambda_{12} = 0.8433$ while those of A_2 are $\lambda_{21} = 0$, $\lambda_{22} = -1.8500$. Hence, $\sigma_1^+ + \sigma_2^+ = 0$ is even while $\sigma_1^- + \sigma_2^- = 1$ is odd.

We can conclude that at the grazing-sliding, the bifurcating orbit will not persist. Namely, the transition will be observed from the stable $4T$-periodic solution (without any stick phase) to at least two coexisting unstable solutions: an unstable sliding orbit of period $4T$ and an unstable $8T$-periodic solutions. Our classification strategy does not provide any information on the possible existence of chaotic attractors accompanying the bifurcation. In the low dimensional cases (1 or 2 dimensional PWL maps) we can gather extra information either by using the classification of border-collisions in one or two-dimensional PWL maps (for instance classification recently presented in [11]) or by studying the dynamics of the map *a posteriori* for the parameter values for which some bifurcations have been observed. As the map (5.6) has the property that it is non-invertible in one of its regions of smoothness there does not exist any classification startegy which could be applied to further determine the dynamics. Nontheless, if we study the dynamics of the map (5.6) for the values at which the grazing sliding discussed occured it can be rigorously shown that under the variation of the bifurcation parameter μ the sudden onset of chaos will ensue in (5.6) (for further details see [19]).

Hence, the numerical results reported in [2] are explained analytically and the role of grazing-sliding in causing the transition from periodic non-sticking solutions to fully blown chaotic stick-slip motion is proved.

Acknowledgements

The authors gratefully acknowledge support from the U.K. Engineering and Physical Science Research Council (EPSRC - Grant no. GR/R72020) and the European Union (FP5 EU Project SICONOS IST-2001-37172).

References

[1] B. Brogliato, *Nonsmooth Mechanics*, Springer–Verlag, 1999.

[2] Y. Yoshitake and A. Sueoka, *Applied nonlinear dynamics and chaos of mechanical systems with discontinuities*, chapter Forced Self-Excited Vibration with Dry Friction, pages 237–259. World Scientific, 2000.

[3] H.E. Nusse and J.A. Yorke, "Border–collision bifurcations for piece-wise smooth one-dimensional maps," *International Journal of Bifurcation and Chaos*, 5:189–207, 1995.

[4] M. di Bernardo, A.R. Champneys and C.J. Budd, "Grazing, skipping and sliding: analysis of the nonsmooth dynamics of the DC/DC buck converter," *Nonlinearity*, 11:858–890, 1998.

[5] M. di Bernardo, C.J. Budd and A.R. Champneys, "Unified framework for the analysis of grazing and border-collisions in piecewise-smooth systems," *Physical Review Letters*, 86(12):2554–2556, 2001.

[6] H. Dankowicz and A.B. Nordmark, "On the origin and bifurcations of stick-slip oscillations," *Physica D*, 136:280–302, 1999.

[7] M.I. Feigin, "Doubling of the oscillation period with C-bifurcations in piecewise continuous systems," *Journal of Applied Mathematics and Mechanics (Prikladnaya Matematika i Mechanika)*, 34:861–869, 1970.

[8] A.F. Filippov, *Differential Equations with Discontinuous Right Hand Sides*, Kluwer, 3300 Dordrecht, The Netherlands, 1988.

[9] Y.A. Kuznetsov, *Elements of Applied Bifurcation Theory*, Springer-Verlag, 1995.

[10] M. di Bernardo, M.I. Feigin, S.J. Hogan and M.E. Homer, "Local analysis of C-bifurcations in n-dimensional piecewise smooth dynamical systems," *Chaos, Solitons and Fractals*, 10:1881–1908, 1999.

[11] S. Banerjee and C. Grebogi, "Border collision bifurcations in two-dimensional piecewise smooth maps," *Physical Review E*, 59:4052–4061, 1999.

[12] M. di Bernardo, C.J. Budd and A.R. Champneys, "Normal form maps for grazing bifurcations in n-dimensional piecewise-smooth dynamical systems," *Physica D*, 160:222–254, 2001.

[13] A.B. Nordmark, "Non-periodic motion caused by grazing incidence in impact oscillators," *Journal of Sound and Vibration*, 2:279–297, 1991.

[14] M. di Bernardo, C.J. Budd and A.R. Champneys, "Corner-collision implies border-collision bifurcation," *Physica D*, 154:171–194, 2001.

[15] G. Yuan, S. Banerjee, E. Ott and J.A. Yorke, "Border-collision bifurcations in the buck converter," *IEEE Transactions on Circuits and Systems–I*, 45:707–716, 1998.

[16] M. di Bernardo, P. Kowalczyk and A. Nordmark, "Bifurcations of dynamical systems with sliding: derivation of normal form mappings," *Physica D*, 170:175–205, 2002.

[17] S.W. Shaw, "On the dynamic response of a system with dry friction," *Journal of Sound and Vibration*, 108(2):305–325, 1986.

[18] M. di Bernardo, P. Kowalczyk and A. Nordmark, "Sliding bifurcations: a novel mechanism for the sudden onset of chaos in friction oscillators," Accepted for publication in *International Journal of Bifurcations and Chaos*, 2003.

[19] P. Kowalczyk, M.di Bernardo and A.R. Champneys, "Border-collision bifurcations and robust chaos in non-invertible piecewise linear planar maps," In preparation, 2003.

DYNAMICS OF DISCONTINUOUS SYSTEMS WITH IMPERFECTIONS AND NOISE

Tom Griffin
Applied Nonlinear Mathematics Group
University of Bristol, England
tom.griffin@bristol.ac.uk

S. John Hogan
Applied Nonlinear Mathematics Group
University of Bristol, England
s.j.hogan@bristol.ac.uk

Abstract: Many physical systems of engineering importance are discontinuous (examples include systems with impacts, freeplay, backlash, gears). The study of deterministic versions of these systems is now well established but these models tend to ignore any imperfections in the system or the effects of noise. In this paper we show how the introduction of imperfections and noise can have a dramatic effect on the systems behaviour. We focus our attention on a much studied simple generic model of discontinuous systems, namely that of the piecewise linear map and its associated ordinary differential equation.

Key words: Discontinuous systems, imperfections, noise.

1. A One-Dimensional Piecewise Smooth Map

1.1 Definition

We will study the following deterministic piecewise linear map.

$$x_{n+1} = S(x_n) = \begin{cases} \alpha x_n - \mu & : \quad x_n \geq 0 \\ \beta x_n - (\mu + \gamma) & : \quad x_n < 0 \end{cases} \tag{1}$$

where $x_n, \alpha, \beta, \gamma, \mu \in \Re$, γ representing an imperfection in the system. $\alpha > 0$, $\beta < 0$ and it suffices to only consider the cases when $\gamma = +1$, $\gamma = 0$ and $\gamma = -1$.

G. Rega and F. Vestroni (eds.),
IUTAM Symposium on Chaotic Dynamics and Control of Systems and Processes in Mechanics, 275–285.

To distinguish between fixed points, higher order periodic solutions and stability we define the following notation,

- A/a denotes *stable/unstable* **period-1 fixed point** with $x_n \geq 0$.
- B/b denotes *stable/unstable* **period-1 fixed point** with $x_n < 0$.
- $A^i B/a^i b$ denotes *stable/unstable* **period-(i+1) orbit** with one iterate on the negative side of the map and i iterates on the positive side of the map.
- $\leftrightarrow$ denotes the occurrence of a **C-bifurcation** as μ crosses a bifurcation point.

1.2 Simple Fixed Point Transitions

Stability and existence techniques can be used to find transitions between fixed points as one parameter is varied. These are shown graphically in Figures 1-3 for $\gamma = 0, +1$ and -1 respectively.

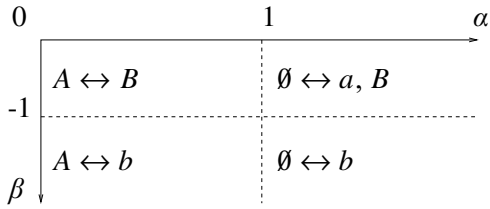

Figure 1. Bifurcations of fixed points in parameter space (for $\gamma = 0$). $\mu \in [-\infty, 0] \leftrightarrow \mu \in [0, \infty]$

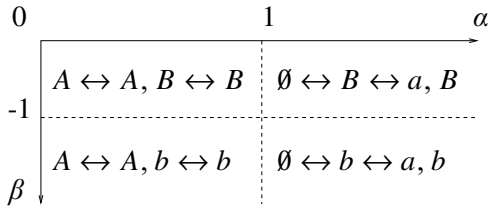

Figure 2. Bifurcations of fixed points in parameter space (for $\gamma = +1$). $\mu \in [-\infty, -1] \leftrightarrow \mu \in [-1, 0] \leftrightarrow \mu \in [0, \infty]$

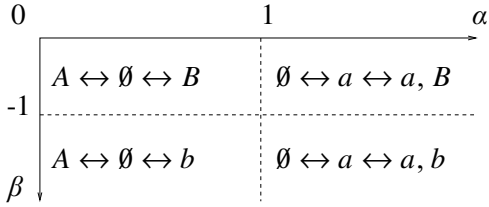

Figure 3. Bifurcations of fixed points in parameter space (for $\gamma = -1$). $\mu \in [-\infty, 0] \leftrightarrow \mu \in [0, 1] \leftrightarrow \mu \in [1, \infty]$

1.3 Higher Periodic Modes

It is possible to determine transitions between higher modes, examples are shown graphically in figures 4, 5 and 6 for $\gamma = 0, +1$ and -1 respectively. Figure 4 illustrates the bifurcations that occur as μ crosses the bifurcation point $\mu = 0$, whereas figures 5 and 6 show existence and stability curves for specific values of μ.

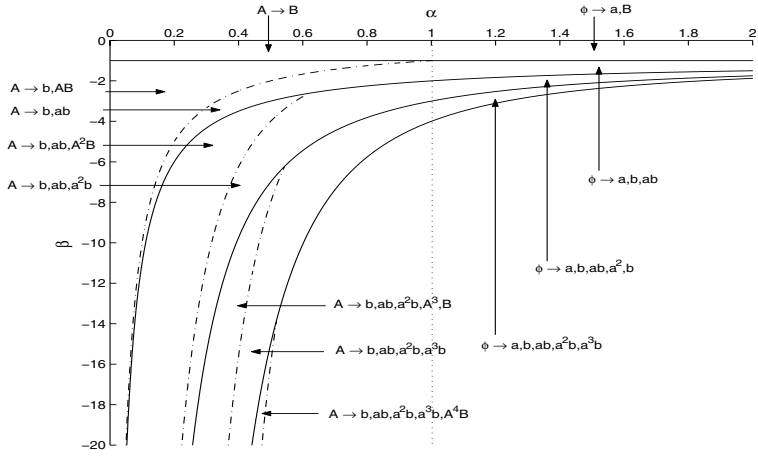

Figure 4. Simplest possible bifurcation structure in each region of parameter space for $\gamma = 0$. Solid lines represent existence boundaries and the dashed lines denote the stability boundaries, see [2]

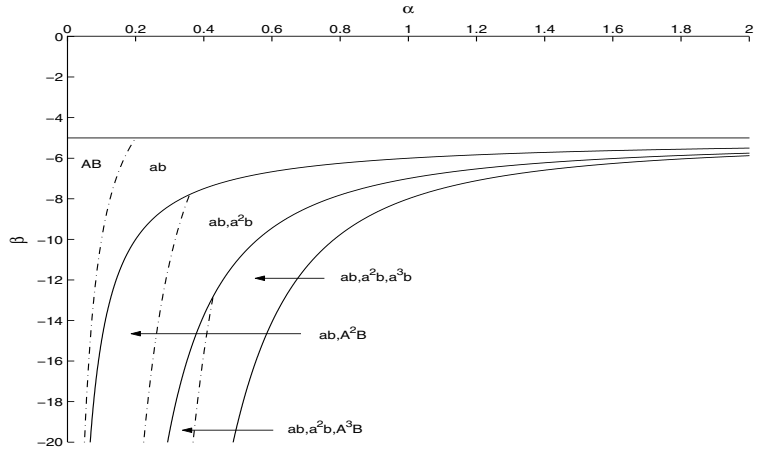

Figure 5. Existence and stability curves in parameter space for $\gamma = +1$ and $\mu = \frac{1}{4}$. Solid lines represent existence boundaries and the dashed lines denote the stability boundaries

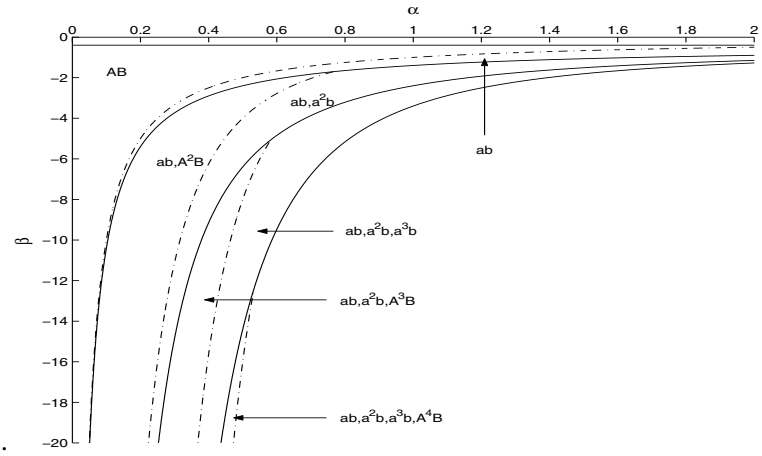

Figure 6. Existence and stability curves in parameter space for $\gamma = -1$ and $\mu = \frac{5}{3}$. Solid lines represent existence boundaries and the dashed lines denote the stability boundaries

2. The Addition of Noise

We now add noise to map (1),

$$x_{n+1} = S(x_n) + \xi_n = \begin{cases} \alpha x_n - \mu + \xi_n & : \quad x_n \geq 0 \\ \beta x_n - (\mu + \gamma) + \xi_n & : \quad x_n < 0 \end{cases} \tag{2}$$

where $\xi_0, ..., \xi_\infty$ are independent random variables each having the same Gaussian density $g(x)$ with variance σ^2 and mean 0.

In order to investigate this equation we will use the associated probability transfer operator for a map with additive noise

$$\bar{P}f(x) = \int_{\Re} f(y)g(x - S(y))dy \tag{3}$$

to evolve an initial distribution toward the invariant density function f^*.

2.1 Effect of Noise on the Map without a Discontinuity

Let us consider a simplified version of map (1) without the discontinuity

$$x_{n+1} = \alpha x_n - \mu \tag{4}$$

This map has a fixed point x^*, given by

$$x^* = \frac{\mu}{\alpha - 1} \tag{5}$$

We now define this map in the presence of additive noise,

$$x_{n+1} = \alpha x_n - \mu + \xi_n \tag{6}$$

where as before $\xi_0, ..., \xi_\infty$ are independent random variables each having the same Gaussian density $g(x)$ with variance σ^2 and mean 0.
The analytic solution of the associated probability transfer operator to map (6) is

$$f^*(x) = \frac{1}{2\sigma}\sqrt{\frac{2(1-\alpha^2)}{\pi}}e^{-\frac{1}{2}(1-\alpha^2)(\frac{x-\frac{\mu}{\alpha-1}}{\sigma})^2} \tag{7}$$

Note that the mean of the solution (7) is the fixed point given in (5). A typical invariant density is shown in Fig. 7.

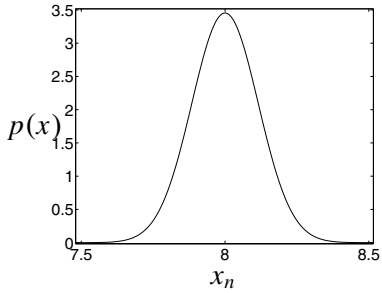

Figure 7. The invariant density of (6) with $\alpha = 0.5$, $\mu = -4$, and $\sigma^2 = 0.1$

2.2 Effect of Noise on the Bifurcation of the Stable Fixed Points

We now look at the effect of noise on some of the simple bifurcations that were introduced in section 1.2. This section is divided into 3 sections, $\gamma = 0, \pm 1$.

$\gamma = 0$. The noise free case is shown in the bifurcation diagram fig. 8(a), where the fixed point x^* is plotted against the bifurcation parameter μ. We have chosen $\alpha = 0.3$ and $\beta = -0.8$, the bifurcation point is at $\mu = 0$.

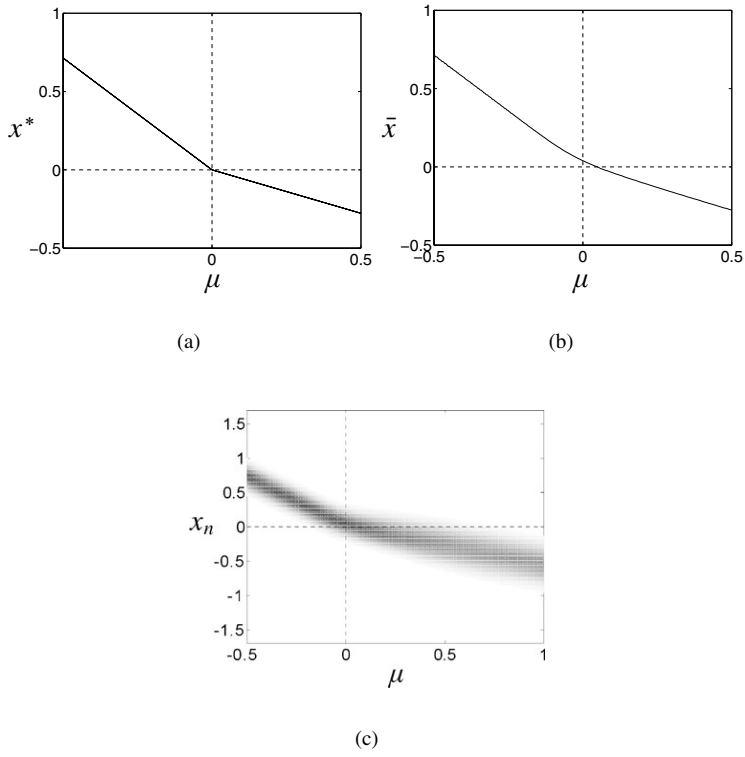

Figure 8. $\gamma = 0$: (a) The deterministic case from map (1); (b) The stochastic case from map (2) showing the mean $\bar{x}$ against the bifurcation parameter μ with $\sigma^2 = 0.01$; (c) The stochastic case from map (2) showing the invariant densities against the bifurcation parameter, μ with $\sigma^2 = 0.01$

We now compute the invariant density using operator (3) for μ=[−0.5, 0.5] with additive noise, and plot the mean values x^* against the bifurcation parameter μ, this is shown in Fig. 8(b). There is a smoothing of the bifurcation. Fig. 8(c) shows the invariant density for each value of μ, the probability of the invariant density is indicated by the relative shading in the figure.

γ = 1. Fig. 9(a) shows the bifurcation diagram for the deterministic case with $\alpha = 0.5$ and $\beta = -0.5$. To investigate the effect different noise intensities have on the bifurcation diagram, we alter the variance of the Gaussian density with which the noise is defined. The stochastic bifurcation diagrams Fig. 9(b) to Fig. 9(d) were calculated using operator 3 with an initial uniform density on $x = [-1, 2]$ so as to include both basins of attraction.

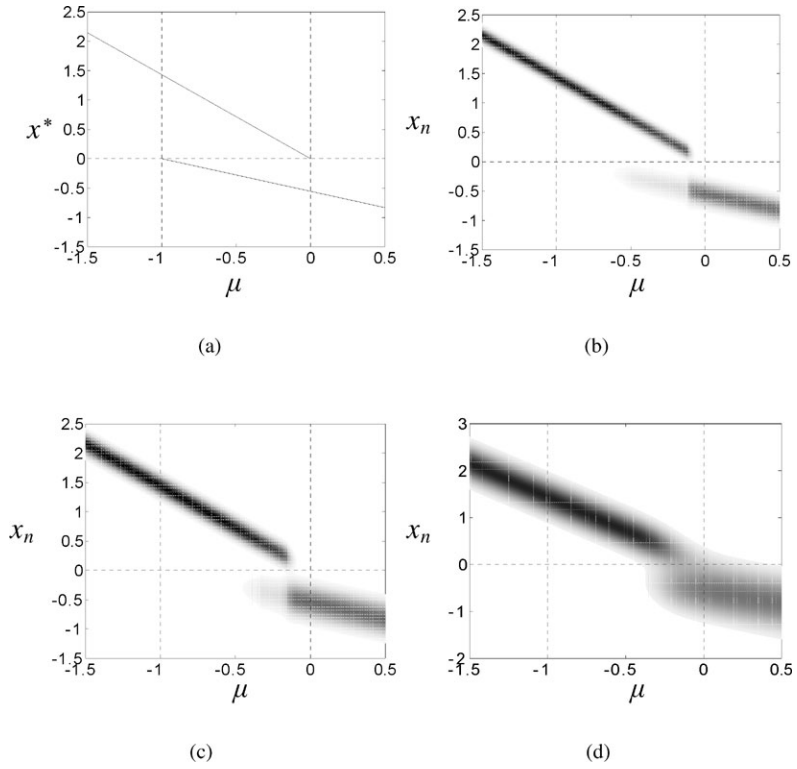

Figure 9. Bifurcation diagrams for $\gamma = 1$: (a) The deterministic case from map (1); (b)-(d) The stochastic case from map (2) showing the invariant densities against the bifurcation parameter, μ; (b) $\sigma^2 = 0.005$, (c) $\sigma^2 = 0.01$, (d) $\sigma^2 = 0.05$

The area of bistability has decreased from that of the deterministic case. The reason for this is found in the geometry of our map, the positive side of the maps fixed point basin of attraction is $[0, \infty]$ and $[-\infty, \frac{\mu+1}{\beta}]$, the negative side of the maps fixed point basin of attraction is $[\frac{\mu+1}{\beta}, 0]$. When a fixed point lies close to the seperatrix $x = 0$, noise with a small intensity is enough to push the solution onto the other attractor. This produces a leaking effect at both ends of the region of bistability of the deterministic case. As the intensity of the noise is increased the area of bistability is decreased. Noise with a large intensity produces an invariant density that is a combination of the two solutions from both the positive and negative parts of the map (see Fig. 10)

$\gamma = -1$. The bifurcations that occur are more complicated than those found previously. For $\mu > 0$ solutions of higher order exist in the deterministic case, an example is shown in Fig. 11(a). We will focus on the bifurcation that occurs at $\mu = 0$.

In the stochastic case the bifurcation happens at an earlier point (see Fig. 11(b)). An alternative way to demonstrate this behaviour is to change our bifurcation parameter from μ to σ^2. In doing this we are able to set our parameters so that they are located in the phase space that produces a single fixed point ($\mu < 0$, $\alpha < 1$ and $\beta > -1$) for the deterministic case. Fig. 12 shows four different solutions that exist in this part of phase space, each found by altering our new bifurcation parameter σ^2. When σ^2 is small a single peaked invariant density exists, with its mean equal to the fixed point of the deterministic map. As σ^2 is increased two smaller peaks are created due to the advance of the bifurcation. As the noise intensity is further increased the two smaller peaks are eventually engulfed by the larger.

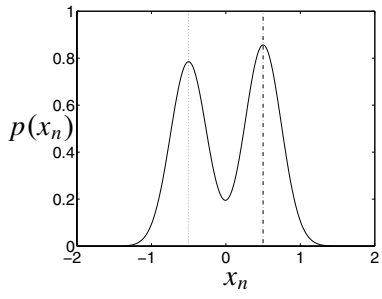

Figure 10. The invariant density with $\alpha = 0.5$, $\beta = -0.5$, $\mu = -0.25$, $\gamma = 1$ and $\sigma^2 = 0.05$

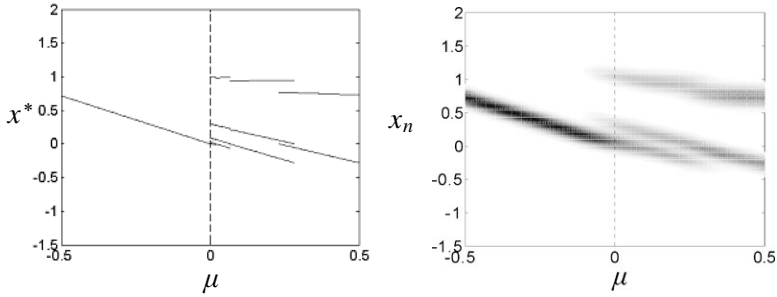

(a) (b)

Figure 11. Bifurcation diagrams for $\gamma = -1$, $\alpha = 0.3$, $\beta = -0.8$: (a) The deterministic case from map (1); (b) The stochastic case from map (2) showing the invariant densities against the bifurcation parameter, μ with $\sigma^2 = 0.005$

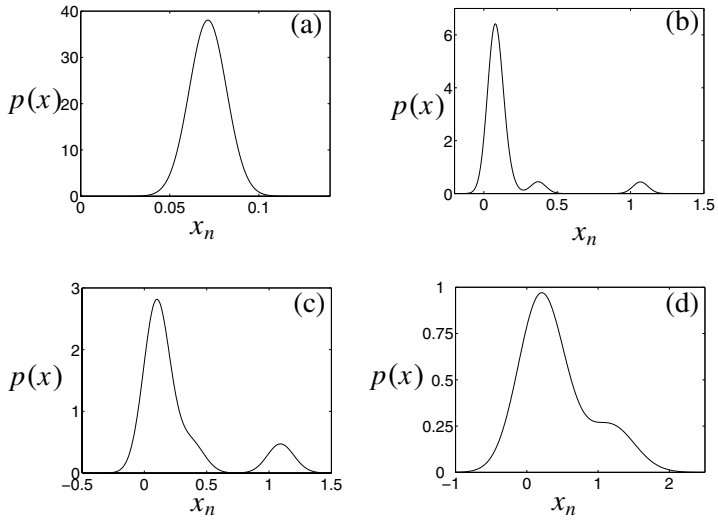

Figure 12. Invariant densities of the stochastic map (2) with $\alpha = 0.3$, $\beta = -0.8$, $\gamma = -1$ and $\mu = -0.05$: (a) $\sigma^2 = 0.0001$; (b) $\sigma^2 = 0.0025$; (c) $\sigma^2 = 0.01$; (d) $\sigma^2 = 0.1$.

3. A Piecewise Smooth Differential Equation

We define a set of first-order ordinary differential equations

$$\begin{aligned} \frac{dx}{dt} &= y \\ \frac{dy}{dt} &= 2p^{(j)}y - (1 + p^{(j)^2})x \end{aligned} \tag{8}$$

Where $p^{(j)}$ is a piecewise smooth function defined by

$$p^{(j)} = \begin{cases} \frac{1}{2\pi} log\left(\frac{3+\alpha(Y^{(j)}-3)+\mu}{Y^{(j)}}\right) & : \quad Y^{(j)} \leq 3 \\ \frac{1}{2\pi} log\left(\frac{3+\beta(Y^{(j)}-3)+(\mu+\gamma)}{Y^{(j)}}\right) & : \quad Y^{(j)} > 3 \end{cases} \tag{9}$$

where $Y^{(j)}$ is the y-coordinate of the jth intersection of the phase-plane trajectory with the half-line $x = 0$, $y > 0$.
It can be shown that the Poincare section along the half-axis $x = 0$, $y > 0$ produces a mapping identical to the map (1), see [1].

3.1 The Addition of Noise

The stochastic differential equation resulting from (8) with additive noise is

$$\begin{bmatrix} \dot{x} \\ \dot{y} \end{bmatrix} = \begin{bmatrix} 0 & 1 \\ -(1+p^{(j)^2}) & 2p^{(j)} \end{bmatrix} \begin{bmatrix} x \\ y \end{bmatrix} + \frac{\sigma}{\sqrt{2\pi}} \begin{bmatrix} \dot{w}_1 \\ \dot{w}_2 \end{bmatrix}, \tag{10}$$

where w_i is a Wiener process and $p^{(j)}$ is a piecewise smooth function defined by (9).

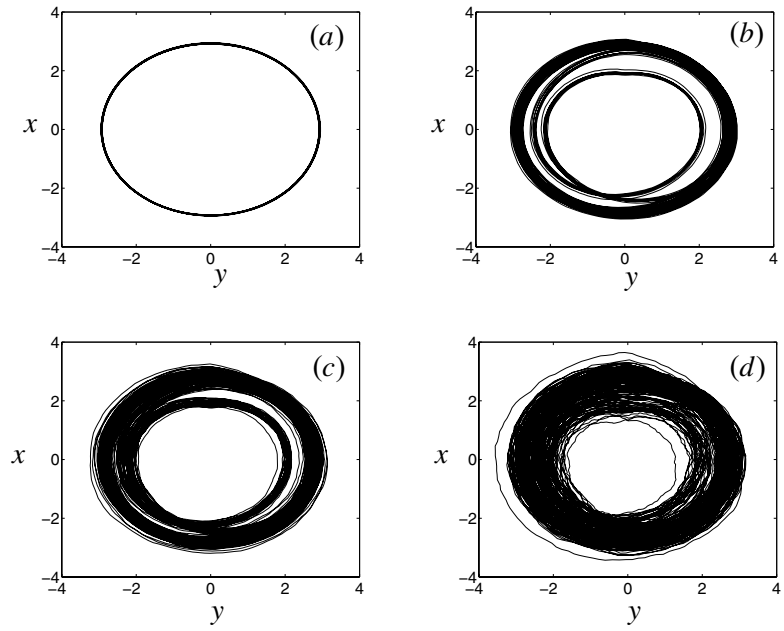

Figure 13. Trajectories of the stochastic differential equation (10) with $\alpha = 0.3$, $\beta = -0.8$, $\gamma = -1$ and $\mu = -0.05$: (a) $\sigma^2 = 0.0001$; (b) $\sigma^2 = 0.0025$; (c) $\sigma^2 = 0.01$; (d) $\sigma^2 = 0.1$.

Fig. 13 shows that the noise-induced bifurcations found for the map with $\gamma = -1$ (see Fig. 12) are identical to those found for the stochastic piecewise smooth differential equation (10).

4. Conclusion

In section 1.1 the simple piecewise linear map (1) is shown to have quite different behaviour in the cases $\gamma = 0, \pm 1$ in the absence of noise. Thus we can deduce that imperfections can significantly effect system dynamics. When noise is added to the system we see a blurring of bifurcation boundaries, apparent loss of bistability, stochastic resonance and an advance/delay of bifurcations. These results are verified in the ordinary differential equations that correspond to the map.

References

[1] M.I. Feigin, "Fundamental dynamic models and criteria of C-bifurcation structures for piecewise smooth systems," *Proceedings of the International Symposium on Analysis and Synthesis of Nonlinear Dynamical Systems*, 30-40, June, Riga, Latvia, 1996.

[2] M. Di Bernardo, M. Feigin, S. Hogan and M. Homer, "Local analysis of C-bifurcations in n-dimensional piecewise-smooth dynamical systems," *Chaos Solitons and Fractals*, Vol. 10, No. 11, pp. 1881-1908, 1999.

STICK-SLIP WHIRL INTERACTION IN DRILLSTRING DYNAMICS

R. I. Leine and D. H. van Campen
Department of Mechanical Engineering,
Eindhoven University of Technology,
P. O. Box 513, 5600 MB Eindhoven, The Netherlands
R.I.Leine@tue.nl
D.H.v.Campen@tue.nl

Abstract: A *Stick-slip Whirl Model* is presented which is a simplification of an oilwell drillstring confined in a borehole with drilling fluid. The disappearance of stick-slip vibration when whirl vibration appears is explained by bifurcation theory. The numerical results are compared with the experimental data from a full-scale drilling rig.

Key words: Drillstring vibrations, discontinuous bifurcations, stick-slip vibrations, whirl, non-smooth systems.

1. Introduction

This paper attempts to explain the complicated behaviour of oilwell drillstring motion when both torsional stick-slip and lateral whirl vibration are involved. It is demonstrated that the observed phenomena in experimental drillstring data could be due to the fluid forces of the drilling mud. A *Stick-slip Whirl Model* is presented which is a simplification of a drillstring confined in a borehole with drilling mud. The model is as simple as possible to expose only the basic phenomena but is discontinuous. Bifurcation diagrams of this discontinuous model for varying rotation speeds reveal discontinuous bifurcations. The disappearance of stick-slip vibration when whirl vibration appears is explained by bifurcation theory. The numerical results are compared with the experimental data from a full-scale drilling rig. A more detailed presentation of the results can be found in [1].

G. Rega and F. Vestroni (eds.),
IUTAM Symposium on Chaotic Dynamics and Control of Systems and Processes in Mechanics, 287–296.

2. Principles of Oilwell Drilling

For the exploration of oil and gas, wells are drilled, which connect the oil/gas reservoir to the surface. The cutting tool to drill those wells is called the drill bit. The bit is turned around with a very slender structure of pipes that are screwed together (see Figure 1). This structure is called the drillstring and can be a few thousand meters long.

To turn the bit, the whole drillstring is rotated from surface with the rotary table (a big flywheel). The lower part of the drillstring is called the Bottom Hole Assembly or BHA and consists of heavier thick-walled pipes, called drillcollars.

On the lower end, the drillstring is resting with the bit on the rock and at the upper end it is pulled upward with a hook at the rig. The slender drillpipe section of the drillstring is therefore constantly in tension while the thick-walled lower part is partly in compression.

Drilling mud, which is a kind of muddy fluid, is pumped through the hollow drillstring by a mudpump. The drilling mud flows through the drillstring, is pumped through nozzles in the bit, and returns to surface in the annulus

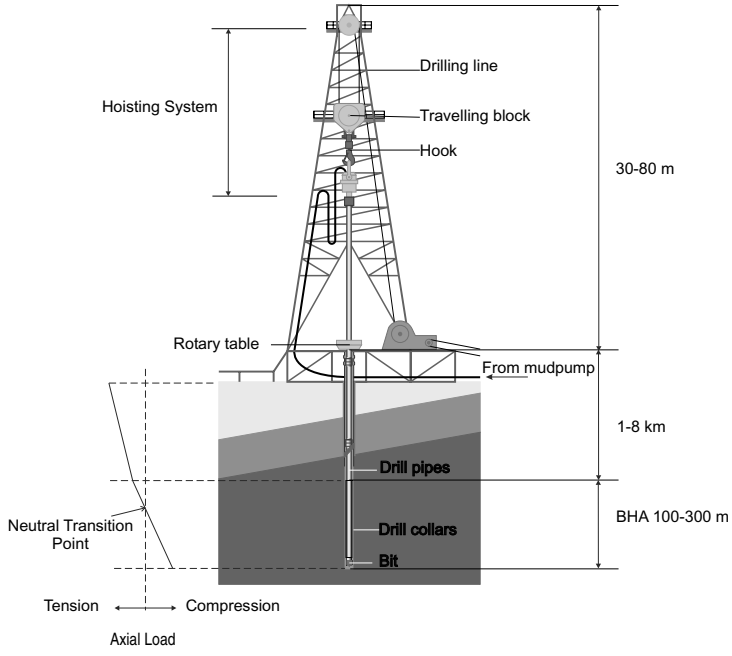

Figure 1. Drilling rig.

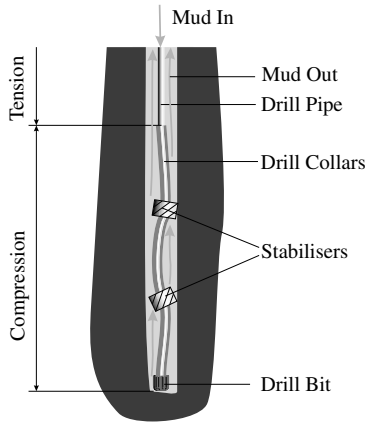

Figure 2. Bottom hole assembly.

between drillstring and borehole wall. The function of the mud is to transport the cuttings from the bit to the surface and to lubricate the drilling process.

The tension in the drillpipes avoids buckling of the drillpipe section. The torsional rigidity of the drillpipe section is however very small, due to its length and small wall thickness. The Bottom Hole Assembly is rigid in torsional direction as it is relatively short and thick-walled but experiences lateral deflection due to the compressive force. The drill collars in the BHA are kept in position by a number of stabilizers, which are short sections with nearly the same diameter as the bit. The friction forces on the bit and lower part of the drillstring induce a frictional torque that can cause torsional stick-slip vibrations due to the torsional flexibility of the drillpipes [2]. Similarly, whirl vibrations can exist in the drill collar section [3]. Both types of vibrations are detrimental to the drillstring and lower the rate of penetration.

3. Drilling Measurements

The measurements reported in this paper were recorded at a full-scale drilling rig [1]. The experiments were carried out with a measurement device which was screwed between the bit and the lowest drill collar.

A time history of the rotation speed of the torsionally rigid lower part of the drillstring is depicted in Figure 3. The drillstring is in a torsional stick-slip vibration for the first 30 seconds, during which the Bottom Hole Assembly acts like a torsional pendulum in which one can see the drillpipes as a torsional spring. After 30 seconds, the stick-slip vibration suddenly stops and the

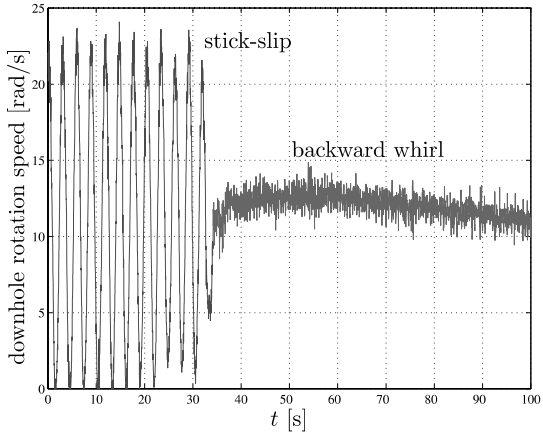

Figure 3. Measured downhole angular velocity versus time.

rotation speed of the Bottom Hole Assembly becomes constant. Whirl vibration is initiated, which is a lateral type of vibration.

The downhole measurement device also measured the bending moment which was exerted on it. The mean bending moment as a function of the downhole rotation speed is depicted in Figure 4. To some extent, the mean bending moment is a measure for the radial deflection of the drillstring. During whirl the mean bending moment is considerably larger than during stick-slip vibration. This indicates that the vibration denoted by 'whirl' in Figure 4 has a much larger lateral deflection and is indeed a whirl-type of vibration.

The frictional torque as a function of the rotational speed is depicted in Figure 5. The frictional torque is corrected for acceleration effects. A kind of friction curve is therefore obtained. During stick-slip vibration the friction curve clearly shows a Stribeck effect which explains the instability of steady rotation. Interestingly, during whirl the friction torque is higher. The additional torque is due to the lateral deflection during whirl. The larger lateral deflection will not only increase the contact between the Bottom Hole Assembly and the borehole wall, but will also increase fluid drag forces on the drillstring that give a kind a viscous friction torque. Therefore, the whirl phase is not only characterized by a higher level of the friction curve, but also by a positive slope of the friction curve due to the viscous friction induced by fluid forces. The fluid forces therefore annihilate the Stribeck effect and constant rotation becomes stable. The whirl vibration therefore excludes the stick-slip motion: the vibration is lateral whirl *or* torsional stick-slip. Stick-slip occurs for low angular velocities and whirl for high angular velocities (see Figure 4). There exists a hysteresis phenomenon in between, where the two types of vibration are co-existing stable attractors.

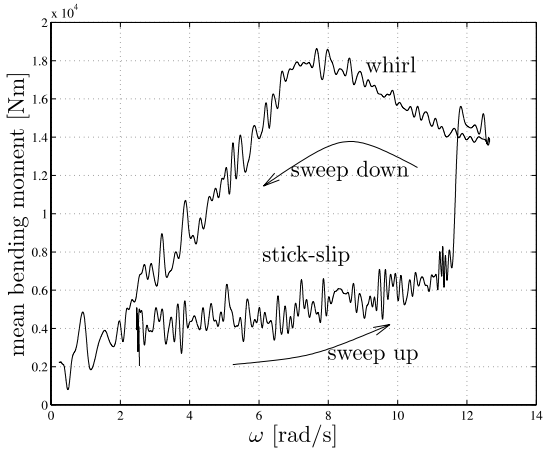

Figure 4. Measured downhole bending moment versus surface angular velocity; sweep-up followed by sweep-down.

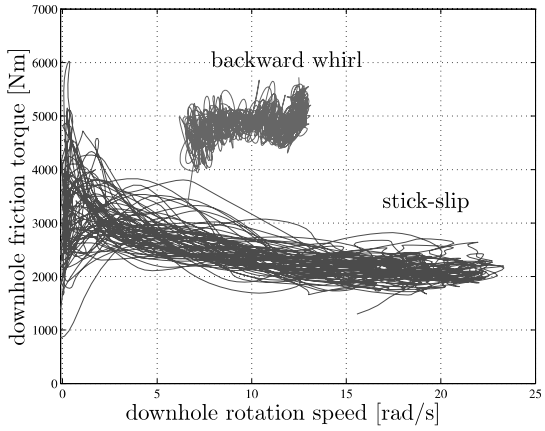

Figure 5. Measured downhole friction curve.

4. Modelling of Stick-slip Whirl Interaction

As a first step, the interaction phenomenon between stick-slip and whirl is modelled as simple as possible (see [1] for a detailed description of the model). The most simple model that can qualitatively describe the observations is a one-DOF model for the torsional vibration and a two-DOF model for the lateral vibration. The total model thus consists of 3 degrees of freedom: the twist and two lateral displacements (Figure 6).

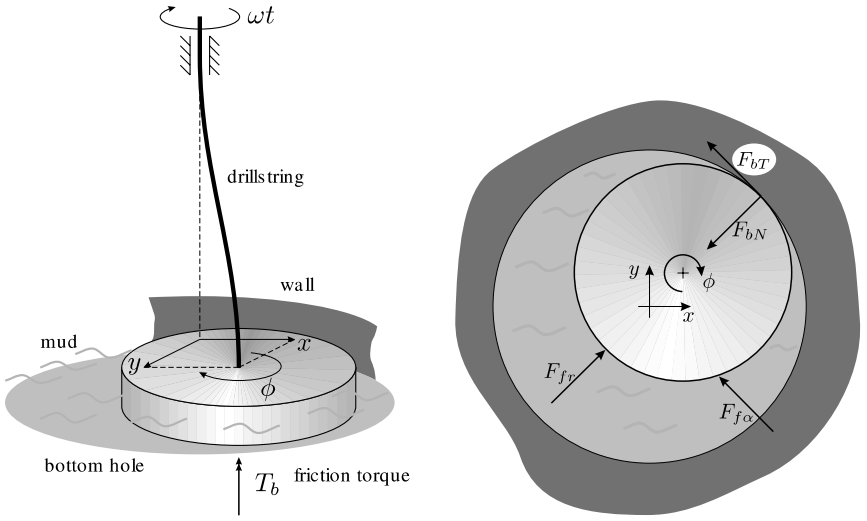

(a) Model. (b) Fluid forces.

Figure 6. Stick-slip Whirl Model.

A kind of interaction must exist between the torsional and the lateral model. Mass unbalance can explain the occurrence of whirl, but the whirl would then only be present for angular velocities near a resonance frequency. Instead, we observe that whirl takes place for angular velocities above a critical value. It is therefore assumed that fluid forces form the interaction mechanism between torsional motion and lateral motion.

The fluid forces are modelled as simple as possible by equations that are also used in the theory for full film bearings [4]

$$\begin{aligned} F_{fr} &= -m_f(\ddot{r} - \dot{\alpha}^2 r - \tfrac{\dot{\phi}^2}{4} r + \dot{\phi}\dot{\alpha} r) - (D + \psi_2(r))\dot{r} - \psi_1(r) r, \\ F_{f\alpha} &= -m_f(\ddot{\alpha} r + 2\dot{r}\dot{\alpha} - \dot{\phi}\dot{r}) - (\dot{\alpha} - \tfrac{\dot{\phi}}{2})(D + \psi_2(r)) r. \end{aligned} \tag{1}$$

The fluid motion results in a lift force F_{fr} in radial direction on the rotor and a drag force $F_{f\alpha}$ in the tangential direction (Figure 6b). The constant m_f is the added mass of the fluid and D is a damping parameter. The nonlinear functions $\psi_1(r)$ and $\psi_2(r)$ constitute the higher-order terms. The whirl speed is denoted by $\dot{\alpha}$ and the rotation speed of the disk by $\dot{\phi}$. The terms $m_f \dot{\alpha}^2 r$ and $m_f \frac{\dot{\phi}^2}{4} r$ are forces which push the drillstring to the wall. These terms are very important as they are the cause of an instability effect as will be explained in the sequel.

With numerical continuation methods, we are able to study the nonlinear dynamics of the Stick-Slip Whirl Model. First, only the Whirl Model is investigated.

4.1 Whirl Model

The Whirl Model contains only the 2 lateral degrees of freedom of the Stick-Slip Whirl Model. The bifurcation diagram of the Whirl Model is depicted in Figure 7, with the rotational speed as bifurcation parameter and the lateral deflection on the vertical axis.

For small rotational speeds the drillstring is in a trivial stable equilibrium position with no deflection. If the rotational speed is increased then the fluid forces increase and a pitchfork bifurcation occurs at point c. The trivial equilibrium branch is unstable for high rotational speeds because the destabilizing effect of the fluid forces is larger than the restoring elastic forces.

For rotational speeds just after point c the drillstring starts to whirl in forward direction. This whirl motion is a periodic solution in a frame fixed to the world, but is an equilibrium in a co-rotating frame of reference. All branches in the bifurcation diagram are therefore equilibria because a co-rotating frame was used for the Whirl Model.

The amplitude of the whirl motion rises until the borehole wall is hit. Bifurcation points d and f are discontinuous saddle-node bifurcations of the equilibrium branch $e_2 - e_3 - e_4$. Co-existing is a branch with stable backward whirling solutions. During backward whirl the drillstring is rolling over the borehole wall. An unstable branch connects the branch of stable forward whirl

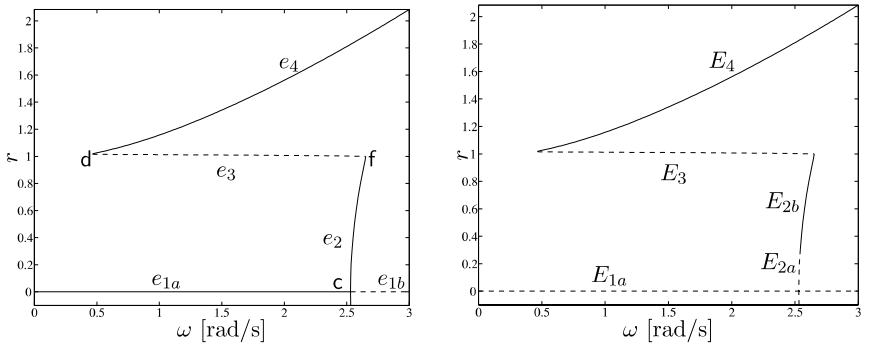

(a) Whirl Model.

(b) Stick-slip Whirl Model.

Figure 7. Equilibrium branches.

solutions with the branch of stable backward whirl solutions. Note that for very small rotational speeds the Whirl Model is in its trivial equilibrium position, whereas it is in backward whirl for very high rotational speeds. A kind of hysteresis phenomenon exists in between.

4.2 Stick-slip Whirl Model; Bifurcation Diagrams

We now study the same equilibrium branches, but for the full Stick-Slip Whirl Model which also includes the torsional degree of freedom. As the lateral and the torsional model are uncoupled to some extent, all equilibrium branches of the Whirl Model are also equilibria of the Stick-slip Whirl Model (something which is not true in general). The stability of the equilibrium branches, however, changes due to the torsional degree of freedom.

The disk in the Stick-Slip Whirl Model is a very simple model of the Bottom Hole Assembly and a dry friction torque T_b is assumed to act on it, which models the bit-rock interaction (as well as the stabilizer wall contact). The Stribeck effect in the friction curve destabilizes the trivial equilibrium (curve E_1) of the pure Whirl Model. Also a part of the forward whirl branch is unstable: branch E_2 contains a Hopf bifurcation.

The full bifurcation diagram of the Stick-Slip Whirl Model, showing the equilibrium branches in a co-rotating frame as well as the periodic branches, is depicted in Figure 8.

For small rotational speeds the full Stick-Slip Whirl Model undergoes a stable torsional stick-slip oscillation. If the rotational speed is increased, then the fluid forces destabilize the undeflected trivial position and the drillstring

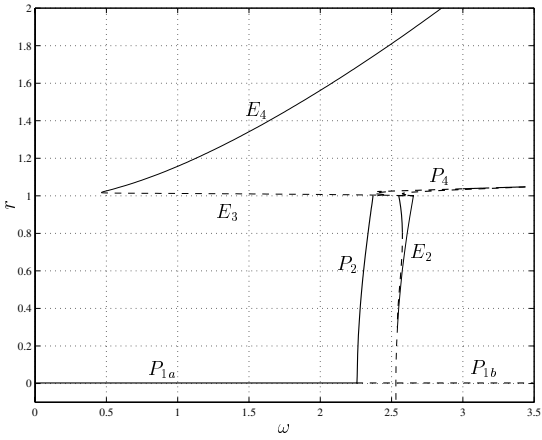

Figure 8. Stick-slip Whirl Model, periodic branches (bold).

will deflect in lateral direction. When the drillstring is laterally deflected the drillstring will act like a stirring spoon in a cup of tea. The torsional stick-slip vibration will therefore be damped due to the viscous fluid friction. The branch E_4 of stable backward whirling solution is unaffected by the torsional model.

For small rotational speeds the Stick-Slip Whirl Model is in torsional stick-slip oscillation, whereas it is in lateral backward whirl motion for high rotation speeds. A very complicated hysteresis region exists in between, where both types of motion can be present as well as many other mixed and period doubled types of oscillation. This region with very complicated dynamic behavior is, however, localized.

A zoom of the hysteresis region is depicted in Figure 9. Periodic branches are created at points where the equilibrium branches lose stability. From the Hopf bifurcation at the equilibrium branch E_2 emanates a periodic branch P_6. Branches P_2 to P_6 connect the solutions found from the Whirl Model with the solutions found from the pure Stick-Slip Model (see [1] for details). The bifurcation structure is apparently very complicated. Branch P_4 undergoes a number of period doubling bifurcations. The period doubled solutions have not been calculated. A number of bifurcation points are smooth, while other bifurcation points are non-smooth. These non-smooth bifurcation points behave sometimes like classical smooth bifurcation points, but can also show a behavior which is non-standard [5].

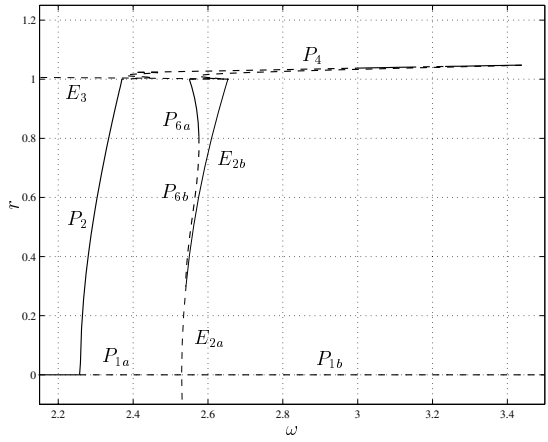

Figure 9. Stick-slip Whirl Model, zoom of Figure 8.

5. Conclusions

We concluded from the measurements on a real drillstring that torsional stick-slip and lateral whirl can be co-existing attractors in oilwell drilling. The presented Stick-slip Whirl Model is a highly simplified model of reality that describes the observed phenomena in its most simple form. A bifurcation analysis of the Stick-slip Whirl Model revealed non-standard bifurcations, which are due to the non-smoothness of the system.

Acknowledgments

This project was supported by the Dutch Technology Foundation, STW (grant EWT.4117). The experimental data in this paper were made available by Shell International Exploration and Production b.v. and were analyzed in cooperation with ir. J. Manie.

References

[1] R. I. Leine, D. H. Van Campen and W. J. G. Keultjes, "Stick-slip whirl interaction in drillstring dynamics," *ASME Journal of Vibration and Acoustics*, 124(2):209–220, 2002.

[2] L. Van den Steen, *Suppressing Stick-slip-induced Drillstring Oscillations: A Hyperstability Approach*, Ph.D. thesis, University of Twente, The Netherlands, 1997.

[3] J. D. Jansen, *Nonlinear Dynamics of Oilwell Drillstrings*, Ph.D. thesis, Delft University of Technology, The Netherlands, 1993.

[4] R. J. Fritz, "The effects of an annular fluid on the vibrations of a long rotor, part 1–theory," *Journal of Basic Engineering*, 92:923–929, 1970.

[5] R. I. Leine, *Bifurcations in Discontinuous Mechanical Systems of Filippov-Type*, Ph.D. thesis, Eindhoven University of Technology, The Netherlands, 2000.

THE MAPPING DYNAMICS OF A THREE-PIECEWISE LINEAR SYSTEM UNDER A PERIODIC EXCITATION

Albert C.J. Luo
Department of Mechanical and Industrial Engineering, Southern Illinois University Edwardsville, Edwardsville, IL 62026-1805, USA,
aluo@siue.edu

Abstract: The mapping dynamics of non-smooth dynamical systems is presented through a three-piecewise linear system with a periodic excitation. The mapping structures for periodic motions are developed and a transition from a periodic motion to another one is qualitatively discussed through the mapping structures. From such mapping structures, the stable and unstable periodic motions can be uniquely determined, and generic mapping series in chaotic motion can be certainly found. This methodology is extendable to any non-smooth dynamical system.

Key words: Piecewise linearity, mapping dynamics, grazing, non-smooth systems.

1. Introduction

Consider a periodically excited, piecewise linear system as

$$\ddot{x} + 2d\dot{x} + k(x) = a\cos\Omega t, \tag{1}$$

where $\dot{x} = dx/dt$. The restoring force is

$$k(x) = \begin{cases} cx - e, & \text{for} \quad x \geq E; \\ 0, & \text{for} \quad -E \leq x \leq E; \\ cx + e, & \text{for} \quad x \leq -E; \end{cases} \tag{2}$$

G. Rega and F. Vestroni (eds.),
IUTAM Symposium on Chaotic Dynamics and Control of Systems and Processes in Mechanics, 297–304.

with $E = e/c$. The parameters (Ω and a) are excitation frequency and amplitude, respectively. In the foregoing system, there are three linear regions of the restoring force (Region I: $x \geq E$, Region II: $-E \leq x \leq E$ and Region III: $x \leq -E$), and the solution for each region can be easily obtained.

The above piecewise linear dynamic system possesses very rich dynamic behaviors and it exists widely in mechanical and electrical engineering such as soft suspension systems in automobile industry. To understand such complicated behaviors, in recent decades, non-smooth dynamics appears in mechanics as a new field. In 1932, Hartog and Mikina [1] studied a piecewise linear system without damping and gave an analytical expression of periodic symmetric solution. In 1983, Shaw and Holmes [2] investigated a piecewise linear system with a single discontinuity through mapping and numerically predicted chaotic motion. In 1989 Natsiavas [3] identified the responses of a system with tri-linear springs. In 1992, Kleczka, et al [4] used the mapping approach to investigate periodic solutions and bifurcations of piecewise linear oscillator. Theodossiades and Natsiavas[5] modeled gear-pair vibrations as a piecewise linear problem in 2000. In 1999, Hogan and Homer [6] applied the graph theory to describe the piecewise smooth dynamical system. This qualitative description is very difficult to provide a quantitative analysis. In 2000, Lenci and Rega [7] investigated periodic solutions and bifurcation in an impact inverted pendulum under an impulsive excitation. In 1995, Han et al [8] initialized the mapping dynamics concept to develop the analytical solution of impact pairs with two amplitude constraints through mapping combinations. In 2002, Luo [9] analytically predicted the asymmetric period-1 motion by introduction of a time interval between two impacts, and the analytical prediction verified the numerical simulation of asymmetrical motion in Li et al [10]. In 2003, Monen and Luo [11] gave an analytical prediction of global periodic motion for such a system in Eq.(1).

For a better understanding of the local and global dynamic behaviors in non-smooth dynamical systems, in this paper, the mapping dynamics of non-smooth dynamical systems will be developed to obtain analytical predictions for all possible periodic responses. The mapping structure and motion transition for Eq.(1) will be investigated as a sampled problem.

2. Switching Sections and Mappings

For description of motion in Eq.(1), two switching sections (or sets) are:

$$\Sigma^{+} = \left\{ (t_i, x_i, y_i) \middle| x_i = E, \dot{x}_i = y_i \right\} \text{ and } \Sigma^{-} = \left\{ (t_i, x_i, y_i) \middle| x_i = -E, \dot{x}_i = y_i \right\}. \tag{3}$$

The two sets are decomposed as

$$\Sigma^{+} = \Sigma_{+}^{+} \cup \Sigma_{-}^{+} \cup \{t_i, E, 0\} \quad \text{and} \quad \Sigma^{-} = \Sigma_{+}^{-} \cup \Sigma_{-}^{-} \cup \{t_i, -E, 0\}. \tag{4}$$

where four subsets are defined as

$$\Sigma_{+}^{+} = \left\{ (t_i, x_{i,} y_i) \middle| x_i = E, \dot{x}_i = y_i > 0 \right\} \text{ and } \Sigma_{-}^{+} = \left\{ (t_i, x_{i,} y_i) \middle| x_i = E, \dot{x}_i = y_i < 0 \right\}; \tag{5}$$

$$\Sigma_{+}^{-} = \left\{ (t_i, x_{i,} y_i) \middle| x_i = -E, \dot{x}_i = y_i > 0 \right\} \text{and} \Sigma_{-}^{-} = \left\{ (t_i, x_{i,} y_i) \middle| x_i = -E, \dot{x}_i = y_i < 0 \right\}. \tag{6}$$

The points $\{t_i, E, 0\}$ and $\{t_i, -E, 0\}$ strongly dependent on the external force direction are singular. From four subsets, six basic mappings are:

$$\left.\begin{aligned} &P_1 : \Sigma_{+}^{+} \to \Sigma_{-}^{+}, \quad P_2 : \Sigma_{-}^{+} \to \Sigma_{-}^{-}, \quad P_3 : \Sigma_{-}^{-} \to \Sigma_{+}^{-}, \\ &P_4 : \Sigma_{+}^{-} \to \Sigma_{+}^{+}, \quad P_5 : \Sigma_{-}^{+} \to \Sigma_{+}^{+}, \quad P_6 : \Sigma_{+}^{-} \to \Sigma_{-}^{-}. \end{aligned}\right\} \tag{7}$$

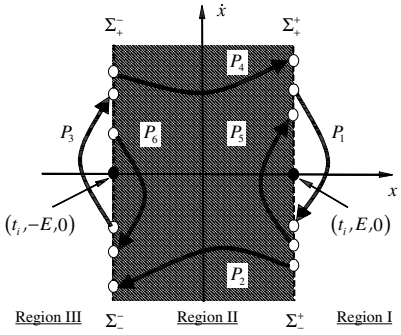

Figure 1. Switching sections and basic mappings in phase plane.

The mapping P_1 maps a state (t_i, x_i, y_i) with $y_i > 0$ into another state $(t_{i+1}, x_{i+1}, y_{i+1})$ with $y_{i+1} < 0$ at $x = E$ in Region I. The mapping P_3 similar to the mapping P_1 is also defined in Region III. The mappings P_1 and P_3 are two self-mappings. Two self-mappings and two transfer-mappings exist in Region II. The transfer-mappings P_2 and P_4 in Region II map the motion from Σ_{-}^{+} into Σ_{-}^{-} and from Σ_{+}^{-} into Σ_{+}^{+}, respectively. The self-mapping P_5 maps a state (t_i, x_i, y_i) with $y_i < 0$ into another state $(t_{i+1}, x_{i+1}, y_{i+1})$ with $y_{i+1} > 0$ at $x = E$ in Region II. The self-mapping P_6 maps a state (t_i, x_i, y_i) with $y_i > 0$ into another state $(t_{i+1}, x_{i+1}, y_{i+1})$ with $y_{i+1} < 0$ at $x = -E$ in Region

II. The expressions for all six mappings were given in [12]. The mappings P_2 and P_4 are termed the global mapping. The mappings P_1, P_3, P_5 and P_6 are termed the local mapping.

3. Mapping Structures

Before the mapping structure of periodic and chaotic motions in Eq.(1) are discussed, the following notation for mapping action is introduced as

$$P_{n_1 n_2 \cdots n_k} \equiv P_{n_1} \circ P_{n_2} \circ \cdots \circ P_{n_k}. \tag{8}$$

where $P_{n_i} \in \left\{ P_j \,\middle|\, j = 1,2,\cdots,6 \right\}$ and $n_i = \{1,2,\cdots,6\}$ with $i = \{1,2,\cdots,k\}$. Note that the clockwise and counter-clockwise rotation of the mappings in order gives the identical motion (i.e., $P_{n_1 n_2 \cdots n_k}, P_{n_2 \cdots n_k n_1}, \cdots, P_{n_k n_1 \cdots n_{k-1}}$), but the selected Poincare mapping sections are different. The period-m motion of the mapping $P_{n_1 n_2 \cdots n_k}$ is defined as

$$P^m_{n_1 n_2 \cdots n_k} \equiv \underbrace{\left(P_{n_1} \circ P_{n_2} \circ \cdots \circ P_{n_k}\right) \circ \cdots \circ \left(P_{n_1} \circ P_{n_2} \circ \cdots \circ P_{n_k}\right)}_{m\text{-sets}}. \tag{9}$$

To extend this concept to two local motions, define

$$P^m_{15} \equiv \underbrace{\left(P_1 \circ P_5\right) \circ \cdots \circ \left(P_1 \circ P_5\right)}_{m\text{-sets}} \text{ and } P^m_{36} \equiv \underbrace{\left(P_3 \circ P_6\right) \circ \cdots \circ \left(P_3 \circ P_6\right)}_{m\text{-sets}}. \tag{10}$$

For a special combination of global and local mappings, introduce a mapping structure

$$\begin{aligned} P_{n_1 n_2 \cdots (n_i n_l)^m \cdots n_k} &\equiv P_{n_1} \circ P_{n_2} \circ \cdots \circ P^m_{n_i n_l} \circ \cdots \circ P_{n_k} \\ &= P_{n_1} \circ P_{n_2} \circ \cdots \circ \underbrace{\left(P_{n_i} \circ P_{n_l}\right) \circ \cdots \circ \left(P_{n_i} \circ P_{n_l}\right)}_{m-\text{sets}} \circ \cdots \circ P_{n_k}. \end{aligned} \tag{11}$$

From the above definition, periodic and chaotic motions for Eq.(1) can be very easily labeled through mappings accordingly.

Consider one of global periodic motions with a Poincaré mapping $P : \Sigma^+_+ \to \Sigma^+_+$ with the following mapping structure as example.

$$P_{4(36)^{m_2}32(15)^{m_1}1} \equiv P_4 \circ P^{m_2}_{36} \circ P_3 \circ P_2 \circ P^{m_1}_{15} \circ P_1 \tag{12}$$

where m_1 and m_2 are arbitrary integers for an expected periodic motion. Consider an example for ($m_1 = 1,\ m_2 = 0$) and ($m_1 = 0,\ m_2 = 1$), the switching phase and velocity for periodic motion $P_{4(36)^{m_2}32(15)^{m_1}1}\mathbf{x}_i = \mathbf{x}_{i+6}$ where $\mathbf{x}_i = (t_i, y_i)^T$ at $x = \pm 1$ with the periodic condition $(t_{i+6}, y_{i+6}) = (t_i + 2\pi/\Omega, y_i)$ are illustrated as in Fig.2. The thin and dark solid curves represent two stable solutions of $P_{432(15)1}$ and $P_{4(36)321}$, respectively. The dashed and dash-dotted curves represent two unstable solutions of $P_{432(15)1}$ and $P_{4(36)321}$, respectively. For a periodic motion $P_{432(15)1}\mathbf{x}_i = \mathbf{x}_{i+6}$, we have $\{(t_i, y_i), (t_{i+2}, y_{i+2})\} \in \Sigma_+^+$, $\{(t_{i+1}, y_{i+1}), (t_{i+3}, y_{i+3})\} \in \Sigma_-^+$, $(t_{i+4}, y_{i+4}) \in \Sigma_-^-$ and $(t_{i+5}, y_{i+5}) \in \Sigma_+^-$. However, the periodic motion $P_{4(36)321}\mathbf{x}_i = \mathbf{x}_{i+6}$ gives the motion $(t_i, y_i) \in \Sigma_+^+$, $(t_{i+1}, y_{i+1}) \in \Sigma_-^+$, $\{(t_{i+2}, y_{i+2}), (t_{i+4}, y_{i+4})\} \in \Sigma_-^-$ and $\{(t_{i+3}, y_{i+3}), (t_{i+5}, y_{i+5})\} \in \Sigma_+^-$. The corresponding stability and bifurcation are determined as in [11,12]. From these mapping structures, any stable and unstable periodic motion can be determined analytically.

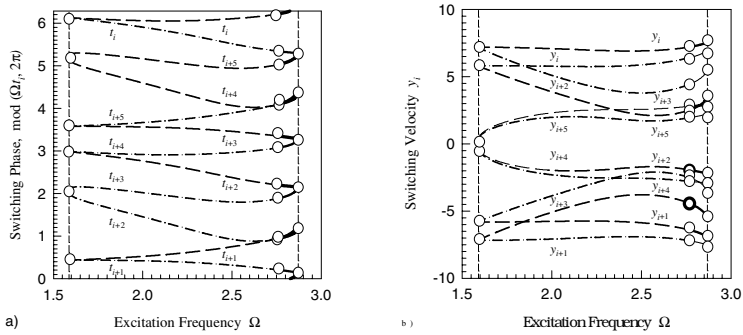

Figure 2. Analytical solutions of (a) switching phases and (b) switching velocities with system parameters ($d = 0.5, c = 100, E = 1.0, a = 20$). The circular symbols denote bifurcation points. (——— stable $P_{432(15)1}$, ▬▬ stable $P_{4(36)321}$, — — unstable $P_{4(36)321}$, — · — · unstable $P_{432(15)1}$).

4. Motion Transition

Consider a motion transition from a periodic motion of $P_{4(36)^m 32(15)^m 1}$ to an adjacent periodic motion of $P_{4(36)^{m+1}32(15)^{m+1}1}$. Since the motion of $P_{4(36)^m 32(15)^m 1}$ possesses two asymmetrical solutions, there are two transition routes, as shown in Fig.3. Once the motion of $P_{4(36)^m 32(15)^m 1}$ grazes at $x = E$, the motion of $P_{4(36)^m 32(15)^{m+1}1}$ appears. If the motion grazing of $P_{4(36)^m 32(15)^{m+1}1}$ occurs at $x = -E$, the motion of $P_{4(36)^{m+1}32(15)^{m+1}1}$ appears. For simplicity, four motion mappings are defined as

$$P_I \equiv P_{4(36)^m 32(15)^m 1},\ P_{II} \equiv P_{4(36)^m 32(15)^{m+1}1}, P_{III} \equiv P_{4(36)^{m+1}32(15)^m 1},\ P_{IV} \equiv P_{4(36)^{m+1}32(15)^{m+1}1}. \quad (13)$$

Using the above expressions, the motion transition routes are illustrated in Fig.4. Two possible routes represent the two motion transitions through grazing in Fig.4(a) and (b). For Route-1, with varying control parameter μ, the grazing of motion P_I at $x = E$ occurs for $\mu = \mu_{g1}^{I(+,s)}$ (i.e., the grazing bifurcation appears at Σ^+). After grazing, an asymmetric periodic motion of P_I starts to switch to a new motion relative to two mappings P_I and P_{II}. Suppose the motion transition from mapping P_I to P_{II} completed at $\mu = \mu_{g2}^{I(+,e)}$ without other grazing, the new motion is generated by mapping P_{II} only, and this motion is asymmetric. With further varying control parameter μ, if the motion grazing of P_{II} is relative to the switching plane Σ^-, the starting and ending grazing bifurcations are at $\mu = \mu_{g3}^{II(-,s)}$ and $\mu = \mu_{g4}^{II(-,e)}$, respectively. Once the motion of P_{II} disappears, the motion transition from P_I to P_{IV} is completed. Before the motion transition from P_I into P_{II} is completely done, the grazing of motion P_I at $x = -E$ occurs with $\mu = \mu_{g1}^{I(-,s)}$ and the motion of P_{III} appears. For $\mu = \mu_{g1}^{I(-,e)}$, the motion of P_I disappears completely. Similarly, the starting and ending grazing of motion P_{III} occur at $\mu = \mu_{g3}^{III(+,s)}$ and $\mu_{g4}^{III(+,e)}$, respectively.

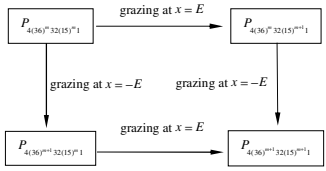

Figure 3. Two routes for the motion transition of $P_{4(36)^m32(15)^m1}$ to $P_{4(36)^{m+1}32(15)^{m+1}1}$.

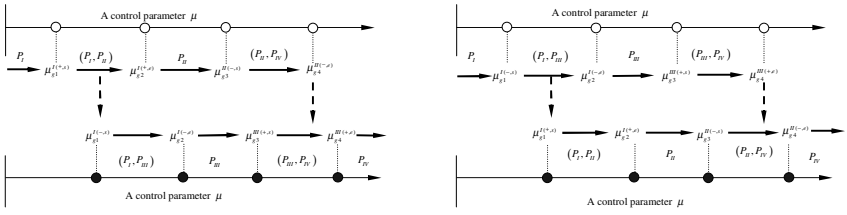

(a) Route-1 (b) Route-2

Figure 4. A control parameter chart for motion switching though grazing: (a) Route-1 and (b) Route-2.

From the above discussion, the motion of $\{P_I, P_{II}\}$ exists in the range of $\mu \in \left[\mu_{g1}^{I(+,s)}, \mu_{g1}^{I(-,s)}\right]$. For $\mu \in \left[\mu_{g1}^{I(-,s)}, \mu_{g2}^{I(+,e)}\right]$, the motion is relative to mappings $\{P_I, P_{II}, P_{III}\}$, and two asymmetrical motions of P_I are near the switching planes Σ^+ and Σ^-. For $\mu \in \left[\mu_{g2}^{I(+,e)}, \mu_{g2}^{I(-,e)}\right]$, the motion is still

associated with mappings $\{P_I, P_{II}, P_{III}\}$, and only the asymmetric trajectory of motion P_1 is near Σ^-. The motion relative to mappings $\{P_{II}, P_{III}\}$ lies in the range of $\mu \in \left[\mu_{g2}^{I(-,e)}, \mu_{g3}^{II(-,s)}\right]$. For $\mu \in \left[\mu_{g3}^{II(-,s)}, \mu_{g3}^{III(+,s)}\right]$, the motion includes mappings $\{P_{II}, P_{III}, P_{IV}\}$ and the asymmetric trajectory of P_{II} is near Σ^-. For $\mu \in \left[\mu_{g3}^{III(+,s)}, \mu_{g4}^{II(-,e)}\right]$, the motion includes $\{P_{II}, P_{III}, P_{IV}\}$, and the asymmetric trajectories of motions P_{II} and P_{III} are near Σ^- and Σ^+, respectively. For $\mu \in \left[\mu_{g4}^{II(-,e)}, \mu_{g4}^{III(+,e)}\right]$, the motion relative to $\{P_{III}, P_{IV}\}$ exists. For $\mu \in \left[\mu_{g4}^{III(+,e)}, \bullet\right]$, only the symmetrical and asymmetrical motions of mapping P_{IV} exist. In addition, for $\mu \in \left[\bullet, \mu_{g1}^{I(+,s)}\right]$, only the motion of mapping P_I appears. In a similar fashion, the motion in Route-2 can be discussed.

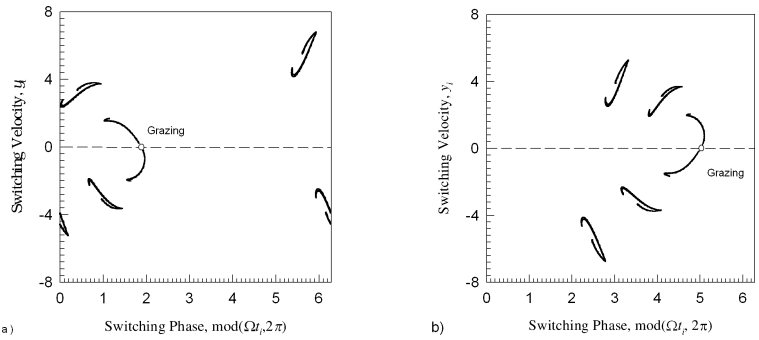

Figure 5. Poincaré mapping section of chaotic motion associated with mappings ($P_{4(36)^2 32(15)1}$, $P_{4(36)32(15)1}$, $P_{4(36)32(15)^2 1}$ and $P_{4(36)^2 32(15)^2 1}$) (a) Σ_+^+ and Σ_-^+ at $x = E$ and (b) Σ_+^- and Σ_-^- at $x = -E$. ($d = 0.5, c = 100, E = 1.0, a = 20$, $\Omega = 1.4$, $x_i = 1$, $\Omega t_i \approx 0.054427$ and $y_i \approx 2.433327$.)

The strange attractors of chaotic motions pertaining to mappings ($P_{4(36)^2 32(15)1}$, $P_{4(36)32(15)1}$, $P_{4(36)32(15)^2 1}$ and $P_{4(36)^2 32(15)^2 1}$) are presented herein. Choose excitation frequency $\Omega = 1.4$ with initial phase $\Omega t_i \approx 0.054427$ and velocity $y_i \approx 2.433327$ at $x_i = E$ for numerical simulation. The Poincaré mapping sections for four sub-switching planes are plotted. The location of grazing points is marked by a circular symbol and labeled by "Grazing". The Poincaré mapping sections in Fig.5 show three branches of the strange attractor in each subset of two switching planes, and the grazing points for two switching-planes $x_i = \pm E$ are with the switching phases $\Omega t_i \approx 1.98$ and 5.02 with velocity $y_i = 0$, respectively. In Fig.5(a), the subsets Σ_+^+ and Σ_-^+ of the strange attractor are illustrated on the upper and lower dashed-line. The subsets Σ_+^- and Σ_-^- separated by the dashed line are presented in Fig.5(b) for the strange attractor of chaotic motion. The generic mappings for this chaotic motion are ($P_{4(36)^2 32(15)1}$, $P_{4(36)32(15)1}$, $P_{4(36)32(15)^2 1}$ and $P_{4(36)^2 32(15)^2 1}$). The mapping codes (indices) series based on the generic mappings for such a chaotic motion varies with control parameters, which can be measured by the appearance probability of mapping. Further, by use of the appearance

probability, the fractal dimension can be obtained as well. Owing to page limitation, this article will not discuss about such an issue, and the grazing bifurcation will be discussed in sequel.

5. Conclusion

The mapping dynamics of non-smooth dynamical systems is presented for all possible periodic responses. The mapping structures and motion transition of the periodic and chaotic motions for the piecewise linear system are discussed. From such mapping structures, the stable and unstable periodic motions are uniquely determined, and generic mappings in chaotic motion are certainly determined. This methodology is extendable to any non-smooth dynamical system.

References

[1] J.P.D. Hartog and S.J. Mikina, "Forced vibrations with non-linear spring constants," ASME *Journal of Applied Mechanics*, 58, pp.157-164, 1932.

[2] S.W. Shaw and P.J. Holmes, "A periodically forced piecewise linear oscillator," *Journal of Sound and Vibration,* 90(1)*,* pp.121-155, 1983.

[3] M. Kleczka, E. Kreuzer, and W. Schiehlen, "Local and global stability of a piecewise linear oscillator," *Philosophical Transactions: Physical Sciences and Engineering, Nonlinear Dynamics of Engineering Systems*, 338 (1651), pp.533-546, 1992.

[4] S. Natsiavas, "Periodic response and stability of oscillators with symmetric trilinear restoring force," *Journal of Sound and Vibration,* 134(2), pp.315-331, 1989.

[5] S. Theodossiades and S. Natsiavas, "Non-linear dynamics of gear-pair systems with periodic stiffness and backlash," *Journal of Sound and Vibration*, 229(2), pp. 287-310, 2000.

[6] S.J. Hogan and M.E. Homer, "Graph theory and piecewise smooth dynamical systems of arbitrary dimension," *Chaos, Solitons and Fractals*, 10, pp.1869-1880, 1999.

[7] S. Lenci and G. Rega, "Periodic solutions and bifurcations in an impact inverted pendulum under impulsive excitation," *Chaos, Solitons and Fractals*, 11, pp. 2453-2472, 2000.

[8] R.P.S. Han, A.C.J. Luo, and W. Deng, "Chaotic motion of a horizontal impact pair," *Journal of Sound and Vibration*, 181, pp.231-250, 1995.

[9] A.C.J. Luo, "An unsymmetrical motion in a horizontal impact oscillator," *ASME Journal of Vibrations and Acoustics*, 124, pp. 420-426, 2002.

[10] G.X. Li, R.H. Rand, and F.C. Moon, "Bifurcation and Chaos in a forced zero-stiffness impact oscillator," *International Journal of Nonlinear Mechanics*, 25, pp.414-432, 1990.

[11] S. Menon and A.C.J. Luo, "An analytical prediction of the global period-1 motion in a periodically forced, piecewise linear system," *International Journal of Bifurcation and Chaos*, 2003, in press.

[12] A.C.J. Luo, and S. Monen, "Global chaos in a periodically forced, linear system with a dead-zone restoring force", *Chaos, Solitons and Fractals*, 19, pp.1189-1199, 2004.

TWO DIMENSIONAL MAP FOR IMPACT OSCILLATOR WITH DRIFT

Ekaterina E. Pavlovskaia and Marian Wiercigroch
Centre for Applied Dynamics Research, School of Engineering and Physical Sciences, Kings College University of Aberdeen, Scotland, UK
E.Pavlovskaia@eng.abdn.ac.uk

Abstract: An impact oscillator with a drift is considered. Using a simple co-ordinates transformation the bounded oscillations are separated from the drift. In general the dynamic state of the system is fully described by four variables: time, τ, relative displacement, p, and velocity, y, of the mass and relative displacement of the slider top, q. However, this number can be reduced by two if the beginning of the progression phase is monitored. In this paper a new two dimensional numerical map is developed and its dynamics is discussed.

Key words: Impact oscillator, drift, two dimensional map, bifurcations.

1. Introduction

Fundamental dynamic behaviour of impact oscillators has been studied vigorously in the past (e.g. [1] – [5]) showing great complexity and sensitivity to the system parameters and the initial conditions. In most cases it is assumed that the impacting system or its elements oscillate around their equilibrium positions. Only recently a combination of bounded oscillations and drifting motion has started to be considered [6]–[8]. Co-ordinate transformation proposed in [7] simplifies significantly the analysis of a drifting impact oscillator. It allows to study the bounded oscillations separately from the progressive motion and therefore standard nonlinear dynamic techniques can be used. In the current study, an implicitly defined map of reduced dimension, similar to those introduced in [9] – [10], is developed and studied.

The system considered in this work belongs to a class of piecewise smooth (PWS) systems, whose dynamics are known to exhibit complex bifurcation scenarios and chaos. These systems can undergo all types of bifurcations that smooth ones do, but apart from them there is whole class of bifurcations that

G. Rega and F. Vestroni (eds.),
IUTAM Symposium on Chaotic Dynamics and Control of Systems and Processes in Mechanics, 305–312.

are unique to PWS systems such as grazing [4, 11, 12], chattering [13] or sliding [14]. A good deal of work has been done to study these special bifurcations using normal form maps (see for example [14]). The general bifurcation scenarios in explicitly defined two dimensional PWS maps were also considered in [5]. However, it is difficult to apply the classical bifurcation theory to the map developed in the current study as it is not defined explicitly.

2. Impact Oscillator with Drift

We consider a simple two degree-of-freedom oscillator shown in Figure 1. A mass m is driven by an external force f containing static b and dynamic $a\cos(\omega\tau+\varphi)$ components. The weightless slider has a linear visco-elastic pair of stiffness k and damping ratio 2ξ. The mass and the stiffness are assumed to be equal to 1, which in effect, is equivalent to the nondimensionalization procedure. As reported in [6] the slider drifts in stick-slip phases where the relative oscillations between the mass and the slider are bounded and range from periodic to chaotic. The progressive motion of the mass occurs when the force acting on the slider exceeds the threshold of the dry friction force d. x, z, v represent the absolute displacements of the mass, slider top and slider bottom, respectively. It is assumed that the model operates in a horizontal plane, or the gravitational force is appropriately compensated. At the initial moment $\tau = 0$ there is a distance between the mass and the slider top called gap, g. For the simplicity of the further analysis the dimensionless friction threshold force, d is set to 1 and for all numerical examples $\varphi = \pi/2$, $g = 0.02$.

The considered system operates at the time in one of the following modes: *No contact*, *Contact without progression*, and *Contact with progression*. A detailed consideration of these modes and the dimensional form of equations of motion can be found in [6]. As it was reported in [7] by introducing a new system of co-ordinates (p, q, v) instead of (x, z, v):

$$\begin{aligned} p &= x - v, \\ q &= z - v, \end{aligned} \tag{1}$$

it is possible to separate the oscillatory motion of the system from the drift. In fact, in the new co-ordinates system p and q are displacements of the mass and the slider top relative to the current position of the slider bottom v. In this study we will consider the bounded oscillations and attempt to re-construct the progressive motion. For the purpose of clarity a brief summary outlining how all particular phases of the dynamic responses were defined is given below.

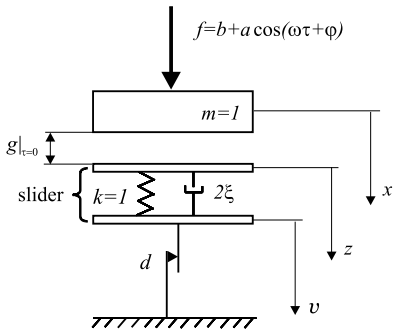

Figure 1. Physical model of impact system with drift.

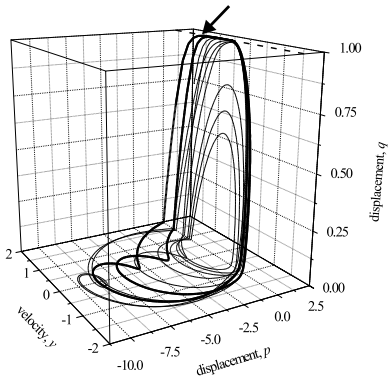

Figure 2. Trajectory of the system for period two motion (thick line, $b = 0.12$) and chaotic motion (thin line, $b = 0.1$) for $a = 0.3$, $\xi = 0.01$, $\omega = 0.1$.

No contact. If the distance between the mass and the slider top is greater than zero, $q + g - p > 0$, then the mass and the slider top move separately.

$$\begin{aligned} p' &= y \\ y' &= a\cos(\omega\tau + \varphi) + b, \qquad \text{for } p < q + g \\ q' &= -\frac{1}{2\xi}q \end{aligned} \tag{2}$$

Contact without progression. During this mode the distance between the mass and the slider top is equal to zero, i.e. $q + g - p = 0$, and the force acting on the mass from the slider is greater than zero but smaller than the threshold of the dry friction force.

$$\begin{aligned} p' &= y \\ y' &= -2\xi y - q + a\cos(\omega\tau + \varphi) + b, \text{ for } 0 < 2\xi y + q < 1 \\ q' &= y, \text{ and } p = q + g \end{aligned} \tag{3}$$

Contact with progression. During this mode the distance between the mass and the slider top remains equal to zero, $q + g - p = 0$, but the force acting on the mass is greater than the threshold of dry friction

force, the mass, the top and the bottom of the slider move together, and progression takes place.

$$\begin{aligned} p' &= -\frac{1}{2\xi}(q-1) \\ y' &= a\cos(\omega\tau+\varphi)+b-1, \text{ for } 2\xi y+q \geq 1 \\ q' &= -\frac{1}{2\xi}(q-1), \text{ and } p = q+g \end{aligned} \tag{4}$$

During *No contact* and *Contact without progression* phases the slider bottom remains stationary, $v'=0$, and during *Contact with progression* phase it moves with velocity $v' = y + \frac{1}{2\xi}(q-1)$.

The equations of motion are linear for each phase, therefore the global solution can be constructed by joining the local solutions at the points of discontinuities. The set of initial values $(\tau_0;\, p_0,\, y_0,\, q_0)$ defines in which phase the system will operate. If $p_0 < q_0+g$, it will be *No contact* phase. For $p_0=q_0+g$, it will be *Contact without progression* phase if $0 < 2\xi y_0 + q_0 < 1$ or *Contact with progression* phase if $2\xi y_0 + q_0 \geq 1$. When the conditions corresponding to the current phase fail, the next phase begins, and the final displacements and velocity for the preceding phase define the initial conditions for the next one. All details of the semi-analytical method allowing to calculate the responses of the system using this method are given in [7].

3. Two Dimensional Map

To study the dynamics of the considered system a new two dimensional (2D) numerical map has been developed [8], and these results are summarized below. In general the dynamic state of the system is fully described by four variables: time, τ, relative displacement, p, and velocity, y, of the mass and relative displacement of the slider top, q. However this number can be reduced to two and a 2D map can be constructed. This simplification is possible if the beginning of the *Contact with progression* phase is monitored. It is worth noting that there are certain regions of the system parameters where progression does not occur, and consequently the proposed 2D map can not be defined there.

The beginning of the progression phase is defined as a moment when the force acting on the slider has reached the critical value, i.e. the condition $2\xi y_* + q_* = 1$ is satisfied, which means that in this moment of time y_* and q_* are linearly dependent as $q_* = 1 - 2\xi y_*$. Also during the both types of contact phases (with and without progression) the relative displacements of the mass and the slider top remains linearly dependent $p_* = q_* + g = 1 - 2\xi y_* + g$. Thus the only two independent variables y_* and τ_* are needed to fully describe

the dynamic state of the system in the beginning of the progression phase. Instead of time τ_* one can use the angular displacement $\psi_* = \varphi + \omega\tau_*$, and a pair (y_*, ψ_*) can be used to construct a 2D map, which is the main motivation of this study.

Since the system dynamics can be monitored at the beginning of the progression phase, one can express the progression as a function of the previous one

$$\begin{aligned} y_{n+1} &= f_1(y_n, \psi_n), \\ \psi_{n+1} &= f_2(y_n, \psi_n). \end{aligned} \tag{5}$$

The map (5) can be determined from the solutions of the equations (2) – (4) which allows to avoid direct numerical integration and to reduce the problem to solving a set of nonlinear algebraic equations. Here (y_n, ψ_n) and (y_{n+1}, ψ_{n+1}) are current and consecutive positions of the system in the beginning of the progression phase.

To make the understanding of physical meaning of the proposed map (5) easier, let us consider a trajectory in three dimensions. In Figure 2 two time histories of period two and of chaotic motions are shown by thick an thin lines respectively. When system is in *No Contact* phase, the trajectory belongs to (p, y) plane. Once the mass hits the slider, the trajectory goes out of (p, y) plane as $q \neq 0$, and during most of the *Contact with progression* phase it belongs to the line $p \approx 1 + g$, $q \approx 1$, which is marked by a dash line. The map (5) allows evaluating only the beginning of the *Contact with progression* phase, which is marked by an arrow, and does not monitor to the dynamics between two consecutive *Contact with progression* phases. Also, it should be noted, that time between these two consecutive phases is not known *a priori*, and chaotic motion given by thin line in Figure 2 demonstrates that there could be quite a few *No Contact* and *Contact without progression* phases before the next progression will happen again.

4. Periodic and Chaotic Orbits

Some results from iterations of the 2D map are shown in Figure 3. As can be seen the motion of the system varies from chaotic to different types of periodic regimes. The durations of the periods for these regimes are not known *a priori*, because the points are taken at the beginning of *Contact with progression* phase, not once per period of external excitation as it is done in stroboscopic Poincaré maps. For example, period six motion shown in Figure 3(f) represents periodic response for which during the period *Contact with progression* phase occurs six times, and its period is $4\pi/\omega$, whereas for period two motion shown in Figure 3(e) *Contact with progression* phase occurs twice, and its period is equal to $2\pi/\omega$.

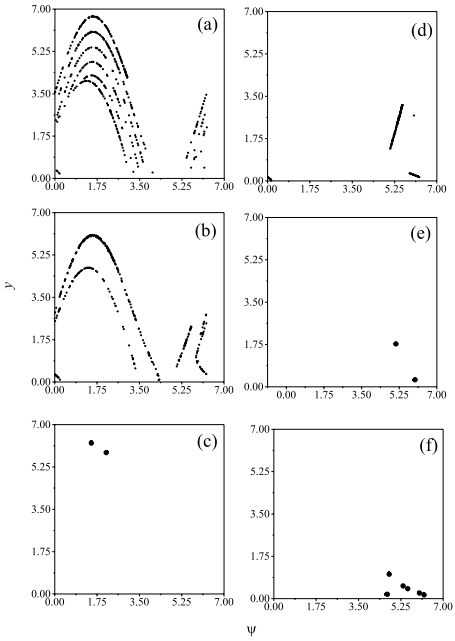

Figure 3. 2D maps computed for $a = 0.3$, $\xi = 0.01, \omega = 0.1$, and (a) $b = 0.02$,(b) $b = 0.05$, (c) $b = 0.11$, (d) $b = 0.24$, (e) $b = 0.27$, (f) $b = 0.29$.

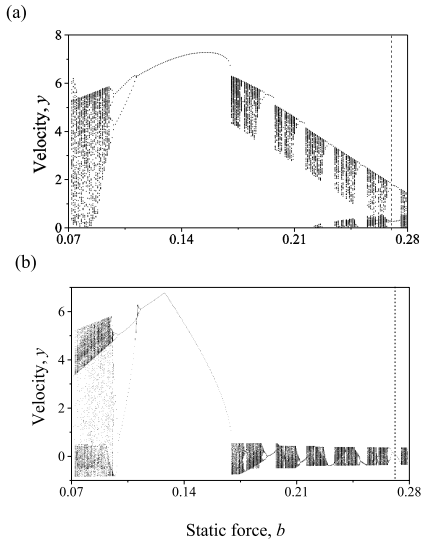

Figure 4. Bifurcation diagrams computed for $a = 0.3$, $\xi = 0.01, \omega = 0.1$ for (a) the developed 2D map (b) the original set of piecewise linear ordinary differential equations Eqs. (2)-(4).

A comparison of bifurcation diagrams calculated for the proposed 2D map and for the original set of piecewise linear ordinary differential equations Eqs. (2)-(4) is given in Figure 4. The diagram presented in Figure 4(a) is constructed by taking 300 points in the beginning of the progression phase after eliminating transient processes, while the diagram presented in Figure 4(b) is constructed by taking 300 points once per period of external excitation also after transient process has passed. As can be clearly seen from this figure for the most values of static force, b both diagrams indicate the same types of regimes. However there are several values where the bifurcation diagrams differ topologically. For example, for $b = 0.27$ (marked by dotted line) period two orbit shown in Figure 4(a) appears as period one orbit in Figure 4(b). This difference is caused by the ways how the points for bifurcation diagrams are collected. In particular, for $b = 0.27$, it means that the system responds periodically with the period of external excitation (period one regime in Figure 4(b)) where the progression phase occurs twice (period two regime in Figure 4(a)).

As it was mentioned earlier the proposed 2D map contains sufficient information to re-calculate all characteristics of the system dynamics, including the progression. For given a point (ψ_*, y_*) of (ψ_n, y_n) plane, the duration T of *Contact with progression* phase is found by solving nonlinear algebraic equation $2\xi y(\tau_* + T) + q(\tau_* + T) = 1$, where $\tau_* = (\psi_* - \varphi)/\omega$, and $y(\tau)$ and $q(\tau)$ are determined from Eqs. (4). Once this equation is solved, T is substituted into $v(\tau)$ found from $v' = y + \frac{1}{2\xi}(q - 1)$, and the progression, v_* during this phase can be expressed as

$$\begin{aligned} v_* &= -2\xi y_* - 2\xi y_* \exp\left(-\frac{T}{2\xi}\right) + y_* T + \frac{b-1}{2} T^2 \\ &- \frac{a}{\omega^2}\left[\cos(\omega T + \psi_*) - \cos(\psi_*) + \omega T \sin(\psi_*)\right]. \end{aligned} \tag{6}$$

For example, the period two motion shown in Figure 3(c) for $b = 0.11$ has two *Contact with progression* phases. First of them is described by $\psi_{*1} = 2.14221$, $y_{*1} = 5.88428$, and according to Eq.(5) it has the progression $v_{*1} = 15.7256$. Second *Contact with progression* phase is described by $\psi_{*2} = 1.50147$, $y_{*2} = 6.27903$ has the progression $v_{*2} = 20.9695$. Thus the total progression per period for this motion is $v_{*1} + v_{*2} = 36.6951$. For the period two motion shown in Figure 3(e) for $b = 0.27$, we have $\psi_{*1} = 5.9506$, $y_{*1} = 0.27231$, $v_{*1} = 0.0779602$ and $\psi_{*2} = 5.07541$, $y_{*2} = 1.77533$, $v_{*2} = 2.60751$, and the total progression per period is 3.66048. Thus taking into account the difference in the periods for these regimes we can deduce that during the same time the progression for $b = 0.11$ will be approximately 5 times larger than for $b = 0.27$.

Equation (6) allows to calculate the progression as functions of initial angular displacement ψ_* and velocity y_*. Thus a surface $v(\psi_*, y_*)$ shows the level of progression for the given set of system parameters and should be useful to develop appropriate control strategies.

5. Conclusions

In this paper, an impact oscillator with a drift was considered. To study the bounded dynamics of this system a new two dimensional numerical map was developed.

The results of numerical iterations of this two-dimensional map show that the system responses range from periodic to chaotic motion. In contrast to a classical Poincaré map where a trajectory is sampled once per period of external excitation, in the introduced two dimensional map the points are taken at the beginning of the progression phase. As a result the duration and the shape of periodic orbit are not known *a priori*. For this reason, it appeared that period two motion on the bifurcation diagram calculated for this map looks as period one motion on the bifurcation diagrams calculated for the original

system. Calculating progression by iterating the developed 2D map should prove to be useful in devising control strategies for vibro-impact systems.

Acknowledgments

This research was supported by EPSRC under the grant GR/R85556/01.

References

[1] J.M.T. Thompson and R. Ghaffari, Phys. Rev. A 27, 1741-1743, 1983.
[2] S.W. Shaw and P.J. Holmes, "A periodically forced piecewise linear oscillator," *J. Sound Vib*. 90, 129-155, 1983.
[3] S. Foale and S.R. Bishop, "Dynamic complexities of forced impacting systems," *Philos. Trans. R. Soc. London A* 338, 547-556, 1992.
[4] W. Chin, E. Ott, H.E. Nusse and C. Grebogi, *Phys. Rev. E* 50, 4427-4444, 1994.
[5] S. Banerjee and C. Grebogi, *Phys. Rev. E* 59, 4052-4061, 1999.
[6] E. Pavlovskaia, M. Wiercigroch and C. Grebogi, "Modeling of an impact system with a drift," *Phys. Rev. E* 64, 056224, 2001.
[7] E. Pavlovskaia and M. Wiercigroch, "Analytical drift reconstruction for impact oscillator with drift," *Chaos, Solitons and Fractals* 19, 151-161, 2004.
[8] E. Pavlovskaia and M. Wiercigroch, "Two dimensional map for impact oscillator with drift," submitted in 2003.
[9] M. Oestreich, N. Hinrichs and K. Popp, "Bifurcation and stability analysis for a non-smooth frictional oscillator," *Arch. Appl. Mech*. 66, 301-314, 1996.
[10] U. Galvanetto, "Numerical computation of Lyapunov exponents in discontinous maps implicitly defined," *Computer Physics Communications* 131, 1-9, 2000.
[11] A.B. Nordmark, "Non-periodic motion caused by grazing incidence in an impact oscillator," *J. Sound Vib*. 145, 279-297, 1991.
[12] M.di Bernardo, M.I. Feigin, S.J. Hogan and M.E. Holmer, "Local analysis of C-bifurcations in n-dimensional piecewise smooth dynamical system," *Chaos, Solitons and Fractals* 10(11), 1881-1908, 1999.
[13] C. Budd and F. Dux, "Chattering and related behaviour in impact oscillators," *Philos. Trans. R. Soc. London A* 347, 365-389, 1994.
[14] M.di Bernardo, P. Kowalczyk and A. Nordmark, "Bifurcations of dynamical systems with sliding: derivation of normal-form mapping," *Physica D* 170, 175-205, 2002.

DYNAMICS OF MECHANICAL SYSTEMS WITH SOFT IMPACTS

František Peterka†
Institute of Thermomechanics, Academy of Sciences of the Czech Republic
182 00 Prague 8, Czech Republic
peterka@it.cas.cz
†*Deceased*

Abstract: Rigid impacts are described by the Newton elementary theory with coefficient of restitution. Different models of elastic and dissipative forces during the contact of impacting bodies should be assumed in the investigation of the motion of the oscillators with soft impacts, when impact duration cannot be neglected. This approach allows also understand the dynamics of mechanical systems, when the contact stiffness of impacting bodies changes from zero, corresponding to the impact-less motion, to infinity, which corresponds to the motion with rigid impacts.

Key words: Piecewise-linear motion, impact interaction, numerical simulation, periodic and chaotic motions, regions of existence and stability, bifurcation diagrams.

1. Introduction

The work naturally continues on the article [1] on dynamics of the impact oscillator shown in Fig. 1. The development of non-linear phenomena, when stiffness k_2 of the stop changes from zero to infinity, was explained there in more detail. In the meantime was analytically proved the continuous and stable transition cross grazing bifurcation boundary [2] and the oscillator motion with different model of soft impacts was investigated [3-6]. Fundamental problems of the dynamics of the simplest impact oscillator were resolved and their main features are summarized here.

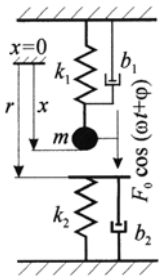

Figure 1.

G. Rega and F. Vestroni (eds.),
IUTAM Symposium on Chaotic Dynamics and Control of Systems and Processes in Mechanics, 313–322.

2. Mathematical Models of Oscillators

The oscillator motion is described gradually by one of two dimensionless differential equations (the Kelvin-Voigt model of the soft impact):

$$X'' + 2\beta_1 X' + X = \cos(\eta\tau + \varphi), \quad \text{for } X < \rho, \tag{1}$$

$$X'' + 2(\beta_1 + \beta_2)X' + X + \frac{k_2}{k_1}(X - \rho) = \cos(\eta\tau + \varphi), \quad \text{for } X > \rho, \tag{2}$$

where $\tau = \Omega t$, $\Omega = \sqrt{k_1/m}$, $\eta = \omega/\Omega$, $\beta_1 = b_1/2\sqrt{k_1 m}$, $\beta_2 = b_2/2\sqrt{k_1 m}$, $\rho = r/x_{st}$, $X' = dX/d\tau$, $X'' = d^2X/d\tau^2$, $X = x/x_{st}$, $x_{st} = F_0/k_1$, x_{st} - static displacement, dimensionless parameters: τ - time, η - excitation frequency, β - viscous damping, ρ - static clearance. It is assumed that $b_1 = b_2$.

The piecewise-linear (triangle) model of soft impact will be also assumed in this paper. Its scheme is included into Fig. 10 and Eq. (2) will change into

$$X'' + 2\beta_1 X' + X + (X - \rho)(k_2 + k_3 \text{ sign } X')/k_1 = \cos(\eta\tau + \varphi). \tag{3}$$

This model corresponds, for example, to contact interactions of leaf springs with dry friction or piercing forces in a forming machine.

The analytical solution of a special set of periodic impact motions and their stability [2] is more difficult in the comparison with the oscillator with rigid impacts [7]. There exist nevertheless many more complex periodic and chaotic impact motions. Numerical integration of motion equations of the impact oscillator (motion simulation) is the most effective tool, which shows the factual dynamics of the system. All results obtained in this work were therefore obtained using this method.

3. Subharmonic Impact Motions

It was ascertained in [1], that the series of subharmonic impact motions exist outside the region of the necessary onset of the impact motion bounded by grazing bifurcation boundary $\rho_0 = 1/|1 - \eta^2|$ shown in Fig. 2 (for $\beta_1 = 0$). Regions of subharmonic impact motions of order $z = p/n$ ($p = 2$ and $n = 2, 3, 4, 5, 6$) are also over boundary ρ_0, where impactless ($z = 0$) motion exists. Quantity z classifies periodic impact motion regime, where p is number of impacts in n is number of excitation periods T in one period of the impact motion. Regions of subharmonic impact motions $z = 2/5, 2/6$ exist only over boundary ρ_0. Such regimes of impact motion were excited by adventitious way and it was not sure that all possible stable motions were found. The special program for the evaluation of basins of attraction was therefore prepared [8] and new regions of impact motions $z = (2/5), 2/7, 2/8, 2/9, 2/10$ were ascertained (Figs. 2, 3).

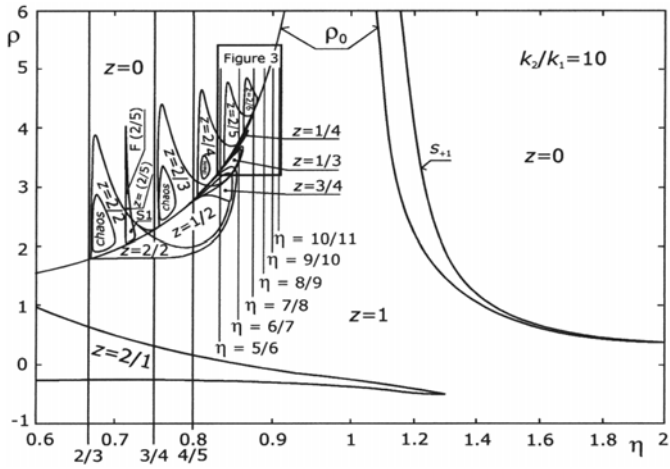

Figure 2. Regions of existence and stability of impact motions.

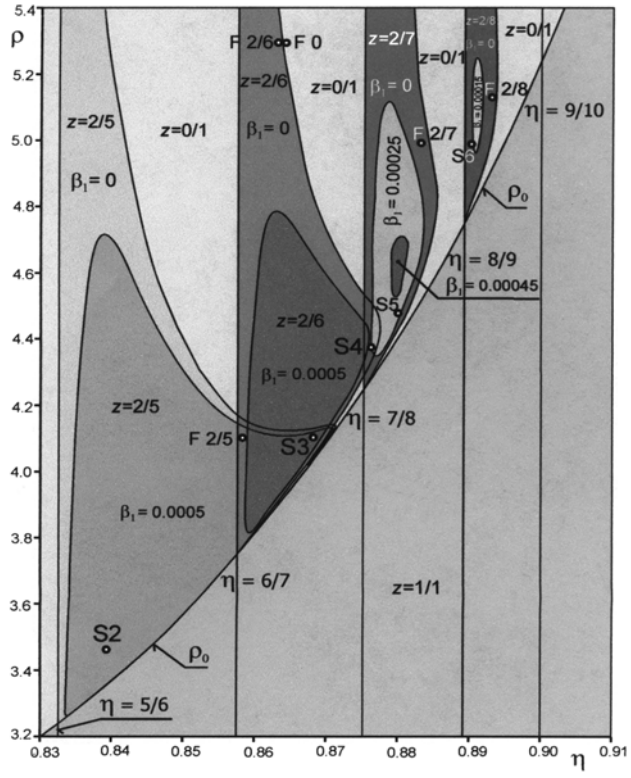

Figure 3. Enlarged subregion of Figure 2.

Motion initial conditions $X(0)$, $X'(0)$ and initial phase φ of the excitation force at $\tau = 0$ determine the resulting stationary regime for certain combination of system parameters. Section of space $\{X(0), X'(0), \varphi\}$ for $\varphi = 0$ shows then basins of attraction in plane $\{X(0), X'(0)\}$. Variable parameters η, ρ were chosen closely over the grazing boundary ρ_0. Examples of basins of attraction at points S2, S3 in Fig. 3 are shown in Fig. 5. Both points correspond to triple possible system response. Similar basins of attraction were evaluated for subharmonic motions $z = 2/9$ and $z = 2/10$, while motion $z = 2/11$ was no longer ascertained.

Stability boundaries in plane η, ρ of every impact response can be obtained by quasistationary changes of η, ρ starting from arbitrary point of basin of attraction. Existence and stability regions of different subharmonic impact motions are represented by grey areas in Fig. 3 and motion trajectories in points F(2/5), F2/5, F2/6, F2/7, F2/8, F0 are shown in Fig. 4. Motions $z = 2/n$ are characterized by two impacts, which occur in two succeeding excitation periods T, while remaining $(n-2)T$ periods in motion period nT are impactless. Motion $z = (2/5)$, which exists in narrow region shown in Fig. 2, differs from motion $z = 2/5$ by one impactless period T included between impacts (compare trajectories F(2/5) and F2/5 in Fig. 4).

Regions in Fig. 3 were evaluated for different values of damping $\beta_1 = \beta_2$. The extent of regions decreases with increasing damping and order n of subharmonic motion $z = 2/n$. Regions of subharmonic motions with $\beta_1 = 0$ enlarge to high clearances (theoretically they exist along lines $\eta = n/(n+1)$ to infinite value ρ, as was proved by theoretical analysis of the motion with rigid impacts in [7]). Right hand stability boundaries of subharmonic impact motions correspond to saddle-node stability boundary, where impacts vanish and quasiperiodic impactless motion remains as is shown on the grey area of phase trajectories F0 in Fig. 5. Amplitudes of impactless motion after the loss of stability equal corresponding clearance ρ, because the part of free vibration in system motion increases amplitude ρ_0 of the excited vibration. Amplitudes of impactless quasiperiodic motion decrease on value ρ_0 (see ellipse in Fig. 4, F0), when very small damping β_1 is supplemented.

4. Hysteresis Phenomena

The development of non-linear phenomena of the oscillator with increasing dimensionless stiffness $\kappa = k_2/k_1$ will be explained by the appearance and development of hysteretic effects of fundamental $z = 1/1$ impact motion. Figure 6 shows one example of the difference between impact motion regions of the oscillator with rigid and soft impacts. Grazing bifurcation boundary ρ_0 divides plane η, ρ on region of impactless motion $z = 0/1$ ($\rho > \rho_0$) and region

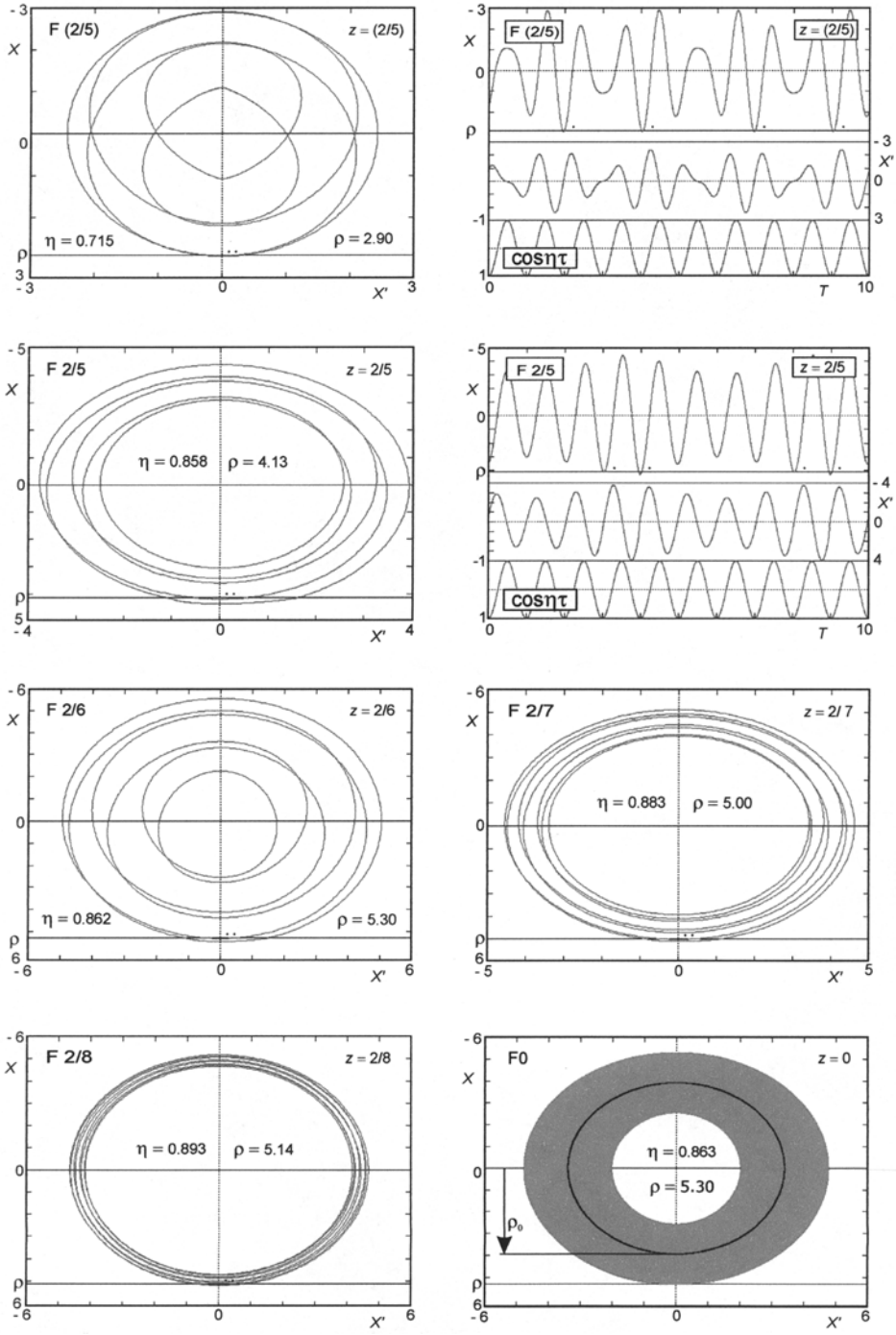
F (2/5)
z = (2/5)
η = 0.715
ρ = 2.90
F 2/5
z = 2/5
η = 0.858
ρ = 4.13
F 2/6
z = 2/6
η = 0.862
ρ = 5.30
F 2/7
z = 2/ 7
η = 0.883
ρ = 5.00
F 2/8
z = 2/8
η = 0.893
ρ = 5.14
F0
z = 0
η = 0.863
ρ = 5.30
ρ0
cosητ
X
X'
ρ
T

Figure 4.

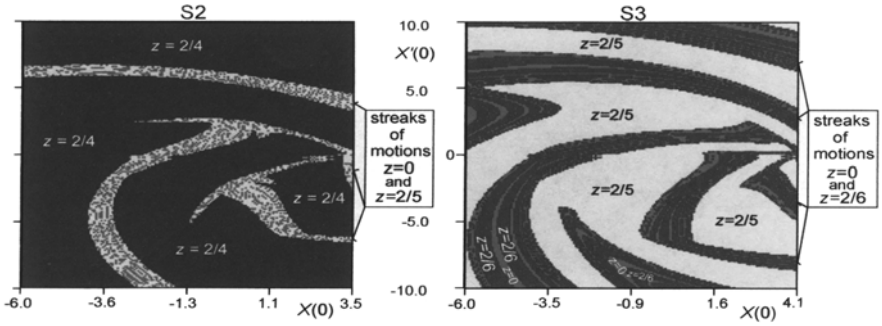

Figure 5. Basins of attraction corresponding to points S2, S3 in Figure 3.

of the necessary onset of impact motion ($\rho < \rho_0$). The transition from impactless motion cross grazing boundary ρ_0 is never stable for the oscillator with rigid impacts [7]. The $z = 1/1$ motion is stable under stability boundaries SN_∞ and PD_∞, which link each other in points X of grazing boundary ρ_0 (see dash and dot-and-dash lines in Fig. 6). There exist two different transition regions between regions of $z = 0$ and $z = 1$ motions:

a) hysteresis regions between boundaries ρ_0 and SN_∞, where the system response is ambiguous ($z = 0$ or $z = 1$) and

b) beat motion regions between boundaries ρ_0 and PD_∞, where exist subharmonic and chaotic impact motions.

Similar regions exist also for oscillator with soft impacts, but they birth inside the region $\rho < \rho_0$ and increase with increasing κ up to mentioned transition regions of motion with rigid impacts ($\kappa = \infty$). Hysteresis region for $\kappa = 7$ exists between points B_1 and B_2 and is bounded by boundaries $SN_{7\mathrm{w}}$ and $SN_{7\mathrm{s}}$. Beat motion region is represented by regions of motions $z = 1/2$ and $z = 2/2$.

The process of the development of hysteresis regions will be explained using bifurcation diagrams (Fig. 7) along the line $a(\rho = 0.9)$ in Fig. 6. Motion amplitudes $X_\mathrm{m}(\eta)$ of linear (impactless) motion are identical with grazing boundary ρ_0. Amplitudes $X_\mathrm{m}(\eta)$ for increasing κ are labeled in Fig. 6 by corresponding value κ. With decreasing η from the region of impactless motion the oscillator begins touch the stop in point G on grazing boundary ρ_0. The transition into impact motion is continuous, stable and reversible. It means that motion with zero before-impact velocity is stable in point G. This velocity continuously increases with decreasing η for $\kappa < 5.8$. Bifurcation diagram $X_\mathrm{m}(\eta)$ for $\kappa = 5.8$ has inflexion point and a fold begins to appear. Motion $z = 1_\mathrm{w}$ with weak impacts losses the stability and jumps into regime $z = 1_\mathrm{s}$ with stronger impact for $\kappa > 5.8$. This motion losses again the stability, when η increases and it jumps back into regime $z = 1_\mathrm{w}$ (see curves $\kappa \geq 6$ with

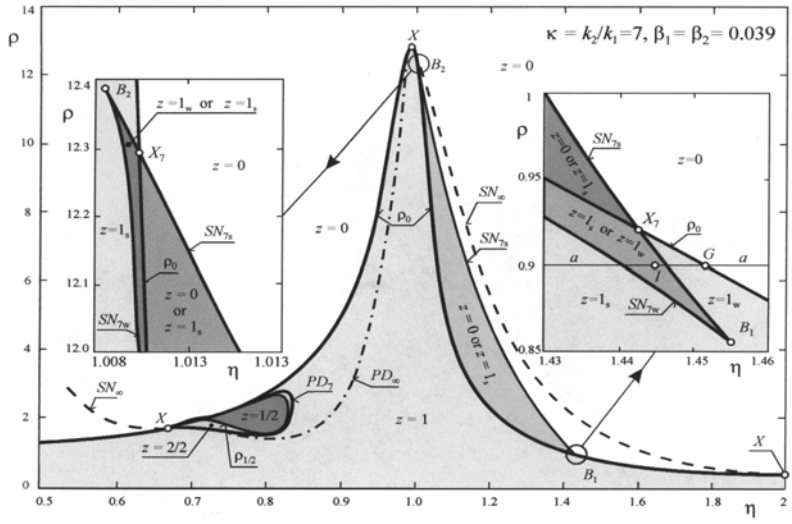

Figure 6. Difference between impact motion regions for rigid and soft impacts.

saddle-node jumps $SN_{\kappa w}$ and $SN_{\kappa s}$ in Fig. 7). Weak and strong regimes of $z = 1$ motion are introduced in Figs. 8 (a) and (b) and they correspond to points I_w and I_s on curves $\kappa = 8$ in Fig. 7. The general scheme of hysteresis is introduced in Fig. 9(a). Similar, but more complex scheme exist for beat motion regions (Fig. 9(b)). The transition cross grazing boundary ρ_0 is also continuous and reversible but inside the region $\rho < \rho_0$ arises the instability of the period doubling type on stability boundary $PD_{1/1}$ and subharmonic motion $z = 2/2$ stabilises. This process is also reversible. Motion $z = 2/2$ losses one impact on grazing boundary $\rho_{1/2}$ and subharmonic motion $z = 1/2$ appears. The transition of the system motion cross grazing boundaries is generally reversible for motion with soft impacts.

The instability of the saddle-node type appears inside region $z = 1/2$ between points B_3 and B_4 (Fig. 9(b)) and motion $z = (1/2)_w$ jumps into regime $z=(1/2)_s$ with stronger impact. Stronger versions of motion $z=1/2$ and $z=2/2$ can exhibit hysteresis into the region of impactless motion $z = 0$. Mentioned

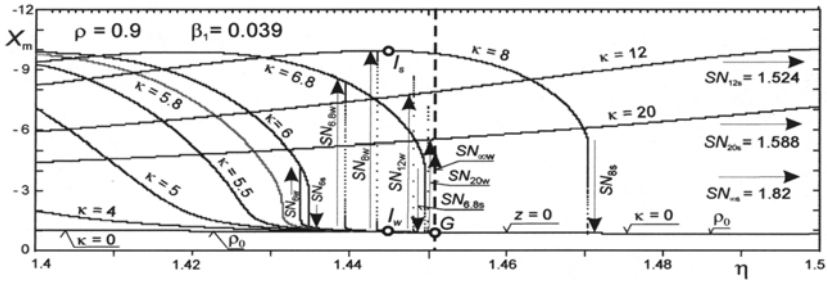

Figure 7. Bifurcation diagrams along line a in Fig. 6 for increasing stiffness $\kappa = k_2/k_1$.

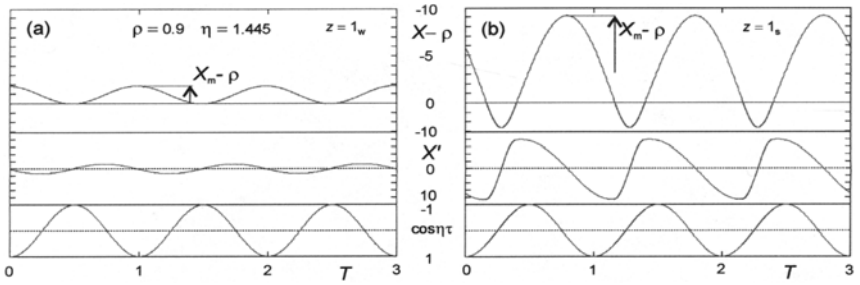

Figure 8. Times series of two regimes of $z = 1/1$ motion with weak (a) and strong impacts (b).

scheme explains the possibility of hysteresis phenomena for subharmonic motions with soft impacts.

5. System Behaviour with Decreasing Clearance

The system behaviour was so far explained for positive values of clearance ρ. Negative values ρ correspond to static prestress force between body m and the stop. It was shown in [7] for the oscillator with rigid stop that number z increases with decreasing clearance ρ. Regimes with sliding impacts appear and lastly the body remains at the rest on the rigid stop. The situation in the case of motion with soft impact will be explained on the impact oscillator with piecewise-linear model of soft impact shown in Fig. 10 (see also Eq. 3). Regions of different periodic and chaotic impact motion regimes in plane η, ρ are shown in Fig. 10. Phase trajectories of selected motions are shown in Fig. 11 for parameters marked by points F in Fig. 10.

The transition between impactless motion without the contact of mass m with the stop (linear motion $z = 0/1_h$, see Fig. 11, $F0_h$) and impactless motion with continuous connection of oscillating mass with the stop (non-linear motion $z = 0/1_d$ see Fig. 11, $F0_d$) is realized by decreasing of static clearance

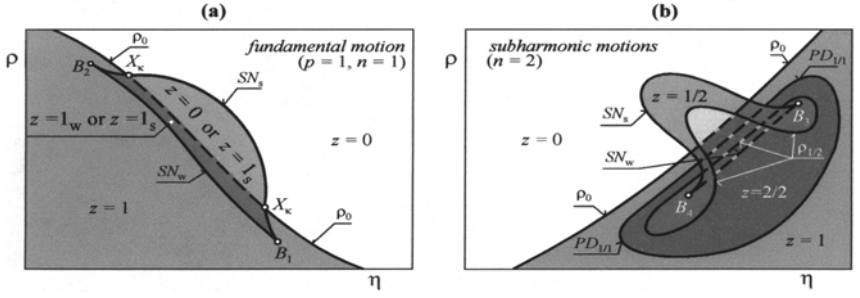

Figure 9. Schematic structure of hysteresis regions of oscillator with soft impacts.

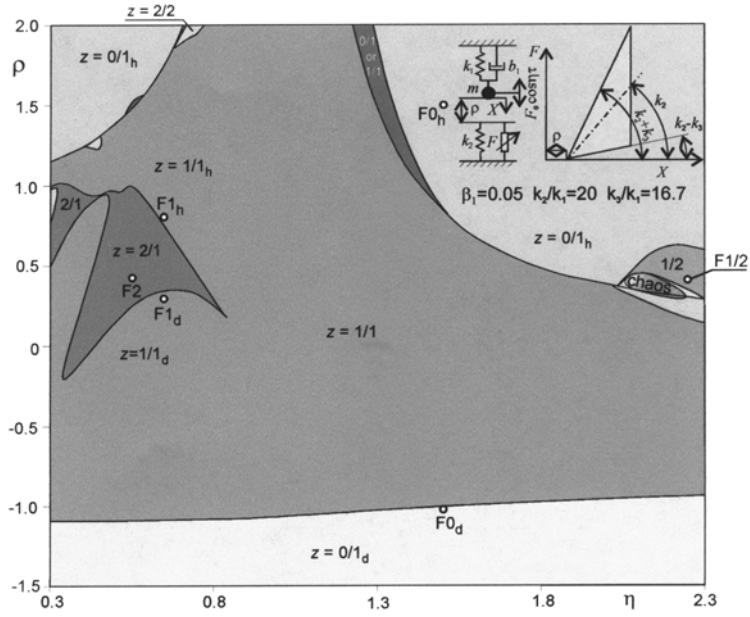

Figure 10. Regions of motions for oscillator with triangle model of soft impacts.

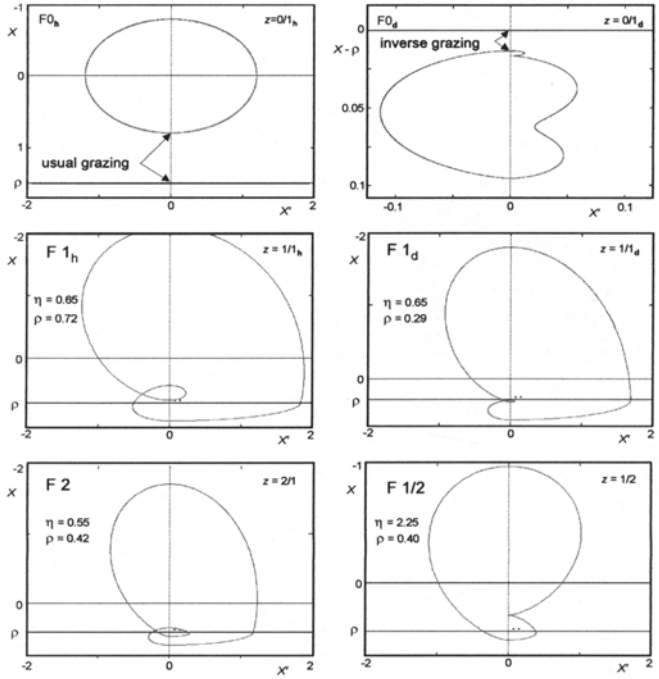

Figure 11. Phase trajectories of motions in points F in Figure 10.

ρ from positive values to negative values. It was necessary to introduce, on the difference with usual grazing bifurcation (Fig. 11, $F0_{\mathrm{h}}$), the conception of the *inverse grazing bifurcation* (Fig. 11, $F0_{\mathrm{d}}$) for the phenomenon of the emergence of the impact motion after impactless motion with the stop.

6. Conclusion

This paper presents new results of the investigation of the oscillator with soft impact. Transition between two types of impactless motion is explained. Inverse grazing bifurcation is defined and the development of non-linear phenomena during the transition from linear to strongly non-linear oscillator motion is shown.

Acknowledgements

This work was considerably supported by the Grant Agency of the Czech Republic, projects 101/97/0670, 101/00/0007 and the Institute of Thermomechanics AS CR under the research purpose No. AVOZ 2076919.

References

[1] F. Peterka and O. Szőllős, "Influence of the stop stiffness on impact oscillator dynamics," *Proc. IUTAM Symposium on Unilateral Multibody Contacts*, Kluwer Academic Publisher, pp.127–135, 1999.

[2] L. Kocanda, "Application of two appropriate analytical approaches to the piecewise-linear system stability analysis of periodic motion based on eigenvalue and small difference methods," *Proc. Colloquium Dynamics of Machines*, Institute of Thermomechanics AS CR, Prague, pp.69–76, 2002.

[3] L. Půst and F. Peterka, "Impact oscillators with Hertz's model of contact," *Meccanica* 38, pp.99–114, 2003.

[4] F. Peterka, "Behaviour of impact oscillator with soft and preloaded stop," *Chaos, Solitons and Fractals* 18, pp.79–88, 2003.

[5] F. Petereka and S. Čipera, "Regions of subharmonic motions of the oscillator with Hertz's model of impact," *Proc. Colloquium Dynamics of Machines*, Institute of Thermomechanics AS CR, Prague, pp.145–152, 2002.

[6] L. Půst and F. Peterka, "Response curves of vibroimpact system," *Proc. Colloq. Dynamics of Machines*, Institute of Thermomechanics AS CR, Prague, pp.159–166, 2002.

[7] F. Peterka, *Introduction to Vibration of Mechanical Systems with Internal Impacts*, ACADEMIA, Prague, 1981 (in Czech).

[8] F. Peterka and S. Čipera, "Ambiguousness and basins of attraction of the oscillator with soft impacts," *Institute of Thermomechanics AS CR*, Prague, pp.155–162, 2003.

NONLINEAR DYNAMICS OF NON-SMOOTH MECHANICAL SYSTEMS: THEORETICAL AND EXPERIMENTAL STUDIES

Marian Wiercigroch, Ekaterina E. Pavlovskaia and Evgueni V. Karpenko
Centre for Applied Dynamics Research, School of Engineering and Physical Sciences, Kings College, University of Aberdeen, Scotland, UK
M.Wiercigroch@eng.abdn.ac.uk

Abstract: In this paper a brief account on the methodology of describing and solving non-smooth dynamical system is given. This is illustrated by a case of study from rotordynamics, where a combination of analytical, numerical and experimental methods are employed to investigate nonlinear dynamic interactions between a rotor system and a snubber ring.

Key words: Non-smooth system, bifurcations, rotordynamics.

1. Introduction

Most of real systems are nonlinear and their nonlinearities can be manifested in many different forms. One of the most common in mechanics is the non-smooth characteristics. One may think of the noise of a squeaking chalk on a blackboard, or more pleasantly of a violin concert. Mechanical engineering examples include noise generation in railway brakes, impact print hammers, percussion drilling machines or chattering of machine tools. These effects are due to the non-smooth characteristics such clearances, impacts, intermittent contacts, dry friction, or combinations of these effects.

Non-smooth dynamical systems have been extensively studied for nearly three decades showing a huge complexity of dynamical responses even for a simple impact oscillator or Chua's circuit. The theory of discontinuous and non-smooth dynamical systems has been rapidly developing and now we are in much better position to understand those complexities occurring in the non-smooth vector fields and caused by generally discontinuous bifurcations. There are numerous practical applications, where the theoretical findings on

G. Rega and F. Vestroni (eds.),
IUTAM Symposium on Chaotic Dynamics and Control of Systems and Processes in Mechanics, 323–332.

nonlinear dynamics of non-smooth systems have been applied to verify the theory and optimize the engineering performance. However from mathematical point of view, problems with non-smooth characteristics are not easy to handle as the resulting models are dynamical systems whose right-hand side, are discontinuous [1], and therefore they require a special mathematical treatment and robust numerical algorithms to produce reliable solutions [2].

Practically, a combination of numerical, analytical and semi-analytical methods is used to solve and analyse such systems and this particular aspect will be explored here. The main aim of the paper is to outline a general methodology for describing, solving and analysing of non-smooth dynamical systems. As these systems may produce irregular responses, it is necessary to look at the chaotic properties of the system behaviour and study their stability. The developed methodology will be illustrated on a practical case study, where the dynamics of a Jeffcott rotor with a snubber ring will be examined by a suite of numerical, analytical and experimental methods.

2. General Methodology

General methodology of describing and solving non-smooth dynamical system presented here will be an extension of the work undertaken by Wiercigroch [3]. First this approach considers a dynamical system, which is continuous in global hyperspace $\mathbf{\Omega}$, and can be described by the following first order differential equation

$$\dot{\mathbf{x}} = \mathbf{f}(t; \mathbf{x}, \mathbf{p}) \tag{1}$$

where $\mathbf{x} = [x_1, x_2, \ldots, x_n]^T$ is the state space vector, $\mathbf{p} = [p_1, p_2, \ldots, p_m]^T$ is a vector of the system parameters, and $\mathbf{f}() = [f_1, f_2, \ldots, f_n]^T$ is the vector function which is dependent upon the process being modelled. Then assume that the dynamical system (1) is continuous only in N defined subspaces $\mathbf{X}_i$ of the global hyperspace $\mathbf{\Omega}$ (see Figure 1), therefore, the right hand side of equation (1) may be written as follows

$$\forall_{t\in[t_1,t_2]}\forall_{\mathbf{x}\in\mathbf{X}_i}\mathbf{f}_i(t; \mathbf{x}, \mathbf{p}), \quad i = 1, ..N. \tag{2}$$

The global solution is obtained by "stitching" local solutions on the hypersurfaces $\Pi\mathbf{X}_{i,i+1}$ (where $i \in N$). As the dynamic system goes through different subspaces, as shown in Figure 1, a typical path of a periodic motion can be drawn. If a response of the investigated system is periodic, its trajectories repeat themselves in the state space, and their paths will form closed loops. Otherwise chaotic, unstable or quasiperiodic motion can occur. When a hypersurface $\Pi\mathbf{X}_{i+1,i+2}$ is intersected by a trajectory emanating from the subspace $\mathbf{X}_{i+2}$ towards $\mathbf{X}_{i+1}$ for the k-th discontinuity crossing, the mapping

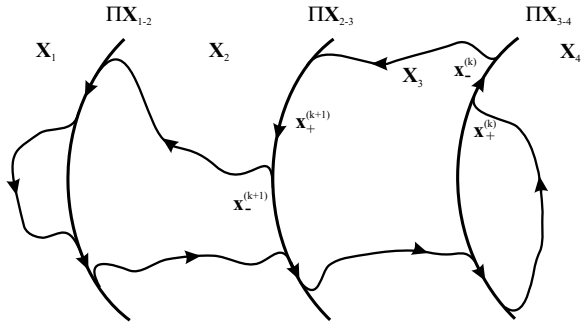

Figure 1. A conceptual model of a dynamical system with motion dependent discontinuities or in other words non-smooth dynamical system.

$\mathbf{x}_{(+)}^{(k)} \longrightarrow \mathbf{x}_{(-)}^{(k)}$ takes place. In order to solve the system (2) with piecewise continuous or discontinuous forcing functions, a thorough mathematical justification of such treatment is given in [1], the precise value of the crossing time $t^{(k)}$ has to be evaluated since the response can be very sensitive to any inaccuracy of the computed solution on the above-mentioned hypersurface. Consequently, a suitable switch function for the discontinuity location has to be formulated, and a precise value of time determined when the discontinuity occurs. Such determined procedure has to be repeated for each time when discontinuities are detected.

After transforming ordinary differential equations (ODEs) into the algebraic form, in principle, any numerical integration solver can be used, however a special attention must be paid to the solution error. An appropriately short integration time step or its on-line adjustment has to be used in order to estimate a local truncation error locating discontinuities sufficiently precisely. In practical terms, a satisfactory solution for non-smooth nonlinear system can be obtained using the classical fourth-order Runge-Kutta method supplemented by two extra steps, (i) the discontinuity detection, and (ii) the calculation of the precise time value when the discontinuity occurs.

3. Jeffcott Rotor with Preloaded Snubber Ring

A two-degrees-of-freedom model of the rotor system with a preloaded snubber ring is shown in Figure 2a. The excitation is provided by an out-of-balance rotating mass $m\rho$. During operation the rotor of mass M makes intermittent contact with the snubber ring. It is assumed that contact is non-impulsive and that the friction between the snubber ring and the rotor is

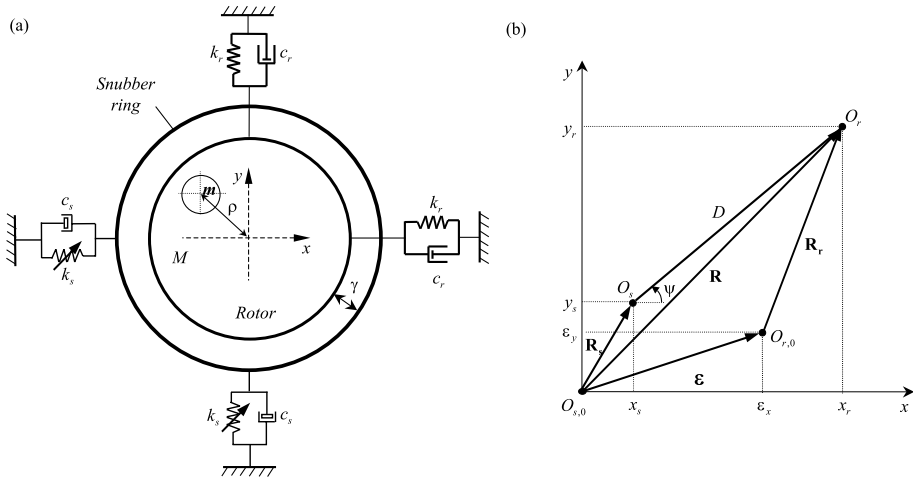

Figure 2. (a) Physical model of the Jeffcott rotor with snubber ring and (b) adopted co-ordinate system.

neglected. Since the mass ratio between the snubber ring and the mass of the rotor is small (for existing experimental rig it is equal to $\sim 1/19$) and the ratio between the stiffnesses of the snubber ring and the rotor is large, it is assumed that the snubber ring itself is massless. The stiffness and the viscous damping of the snubber ring are equal to k_s ($k_{sx}=k_{sy}=k_s$) and c_s. The stiffness and the damping of the rotor are respectively k_r and c_r. The springs supporting the snubber ring are preloaded by Δ_x in horizontal and Δ_y in vertical directions respectively. There is a gap γ between the rotor and the snubber ring. Also in the initial position, the centre of the rotor is displaced from the centre of the snubber ring by the eccentricity vector ε. The system can operate in one of two following regimes: (a) no contact and (b) contact between the rotor and the snubber ring. In the latter case, existence of the preloading makes the dynamics of the system more complicated as the force acting from the snubber ring on the rotor depends on whether the displacement of the snubber ring exceeds the preloadings (in one or both directions) or not. Thus the following unique regimes of the system motion can be distinguished:

I No contact between rotor and snubber ring.

II Contact between the rotor and the snubber ring, where the both displacements of the snubber ring are smaller than the preloadings, i.e. $|x_s| \leq \Delta_x$ and $|y_s| \leq \Delta_y$.

III Contact between the rotor and the snubber ring, where the displacement of the snubber ring in the horizontal direction is larger than the preloading, $|x_s| > \Delta_x$, and in the vertical direction is smaller than preloading, $|y_s| \leq \Delta_y$.

IV Contact between the rotor and the snubber ring, where the displacement of the snubber ring in the horizontal direction is smaller than the preloading, $|x_s| \leq \Delta_x$, and in the vertical direction is larger than preloading, $|y_s| > \Delta_y$.

V Contact between the rotor and the snubber ring, where the displacements of the snubber ring are larger than the preloadings, i.e. $|x_s| > \Delta_x$ and $|y_s| > \Delta_y$.

3.1 Equations of Motion

The co-ordinate system adopted in this study is presented in Figure 2b. The initial position of the rotor $O_{r,0}$ differs from the initial position of the snubber ring $O_{s,0}$ by the eccentricity vector ε. The vectors $\mathbf{R}_r = (x_r, y_r)$ and $\mathbf{R}_s = (x_s, y_s)$ show the current positions of the rotor and the snubber ring, and $D = \sqrt{(x_r - x_s)^2 + (y_r - y_s)^2}$ is the distance between the centres of the rotor and the snubber ring at any given time. $R = \sqrt{x_r^2 + y_r^2}$ is the radial displacement of the rotor. For no contact situation the distance between the centres of the rotor and the snubber ring is smaller than the gap, γ, that is $D \leq \gamma$. Therefore equations of motion for the rotor and the snubber ring are

$$\begin{aligned} &M\ddot{x}_r + c_r\dot{x}_r + k_r(x_r - \varepsilon_x) = m\rho\Omega^2\cos(\varphi_0 + \Omega t),\\ &M\ddot{y}_r + c_r\dot{y}_r + k_r(y_r - \varepsilon_y) = m\rho\Omega^2\sin(\varphi_0 + \Omega t),\\ &c_s\dot{x}_s + k_s x_s = 0,\\ &c_s\dot{y}_s + k_s y_s = 0, \end{aligned} \tag{3}$$

where φ_0 is the initial phase shift and Ω is shaft angular velocity.

Once $D = \gamma$, the rotor hits the snubber ring and one or more of the contact regimes may occur, for which the equations of motion can be written as

$$\begin{aligned} &M\ddot{x}_r + c_r\dot{x}_r + k_r(x_r - \varepsilon_x) + F_{s_x} = m\rho\Omega^2\cos(\varphi_0 + \Omega t),\\ &M\ddot{y}_r + c_r\dot{y}_r + k_r(y_r - \varepsilon_y) + F_{s_y} = m\rho\Omega^2\sin(\varphi_0 + \Omega t),\\ &x_s = x_s(x_r, y_r),\\ &y_s = y_s(x_r, y_r). \end{aligned} \tag{4}$$

Here the force in the snubber ring $\mathbf{F}_s = (F_{s_x}, F_{s_y})$ varies for different contact regimes. The unknown $x_s(x_r, y_r)$ and $y_s(x_r, y_r)$ give the current location of the snubber ring as a function of the current location of the rotor.

3.2 Location of the Snubber Ring

When the rotor and the snubber ring are in contact, the distance between their centres remains constant and equal to the gap, so $(x_r - x_s)^2 + (y_r - y_s)^2 = \gamma^2$. In order to find the location of the snubber ring centre when it moves being in contact with the rotor, the following approach has been adopted.

The problem of finding the current location of the snubber ring can be reduced to finding the minimum of the energy E with the constraint condition $D = \gamma$. This can be done using the Lagrange multipliers method by constructing the Lagrange function $L = E + \lambda\delta$, where λ is Lagrange multiplier, E is the elastic energy of the snubber ring, δ is the constraint function $\delta = (x_r - x_s)^2 + (y_r - y_s)^2 - \gamma^2$. As E and δ are the continuous and differentiable functions, the current position of the snubber ring (x_s and y_s) as a function of the of the current rotor position (x_r and y_r) can be determined from the conditions of the existence of extremum:

$$\frac{\partial L}{\partial x_s} = 0, \quad \frac{\partial L}{\partial y_s} = 0, \quad \frac{\partial L}{\partial \lambda} = \delta = 0, \tag{5}$$

where $L = E + \lambda\left((x_r - x_s)^2 + (y_r - y_s)^2 - \gamma^2\right)$.

Minimising the energy E with the constraint $(x_r - x_s)^2 + (y_r - y_s)^2 = \gamma^2$, the functions $x_s(x_r, y_r)$ and $y_s(x_r, y_r)$ can be obtained [4], which allow to analytically describe the geometrical location of the snubber ring (see Figure 3) and the borders between different regimes of operation as shown in Figure 4.

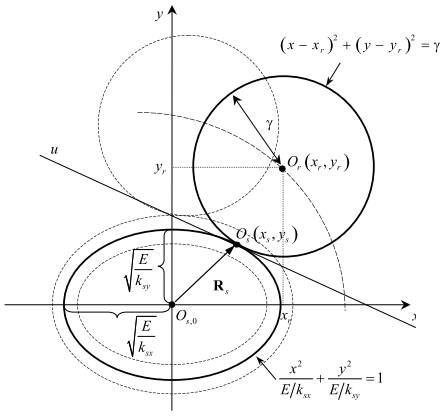

Figure 3. Geometrical interpretation of the location of the snubber ring position for different stiffnesses of the snubber ring in the x- and y-directions.

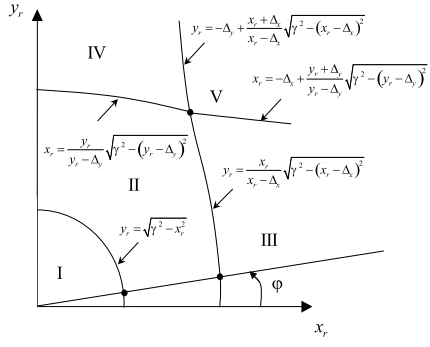

Figure 4. Regions of operation and their boundaries for the first quadrant of (x_r, y_r) plane.

3.3 Nonlinear Dynamic Analysis

An extensive nonlinear dynamics analysis has been carried out by a combination of direct numerical integration of Eqs. 3 and 4 and solving nolinear algebraic equations (x_s, y_s in Eq. 4). Bifurcation diagrams shown in Figure 5 were constructed for the displacement of the rotor under varying the frequency ratio for the unpreloaded (Figure 5a) and preloaded (Figure 5b) cases. As can be clearly seen from this Figure the preloading significantly changes the bifurcation structure. First of all it shifts the existing bifurcation points; dash lines point out such behaviour. For instance the period one observed in the beginning of the diagram bifurcates at $\eta = 2.165$ for unpreloaded and at $\eta = 2.213$ for preloaded case. The point of bifurcation of period four motion into period two motion moves from $\eta = 2.717$ to $\eta = 2.824$, and the period two bifurcates into period four at $\eta = 3.803$ and $\eta = 3.893$ for unpreloaded and preloaded cases respectively. Secondly, the introduction of the preloading changes the character of bifurcations. For example, the period one motion marked the leftmost dash line, roughly speaking bifurcates into period three motion for unpreloaded case and into quasi-periodic motion for preloaded case. Finally and most importantly the preloading introduces new bifurcations and new regimes. For example, an additional bifurcation of the period two motion into quasi-periodic motion appears at $\eta \approx 3.107$ for the preloaded case. Also a large window of new regimes containing periodic, quasi-periodic and chaotic

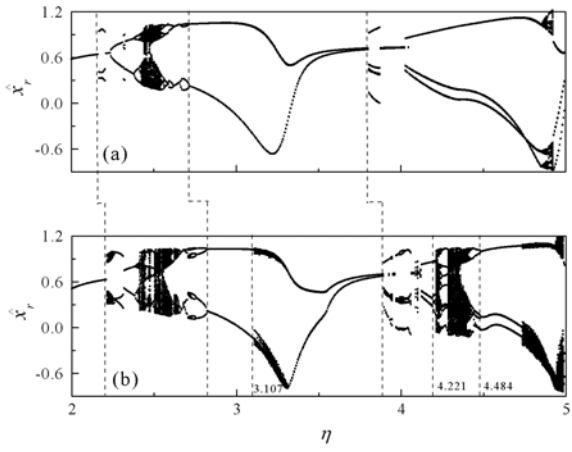

Figure 5. Bifurcation diagrams $\hat{x}_r(\eta)$ calculated for (a) $\hat{\Delta}_x = \hat{\Delta}_y = 0$, (b) $\hat{\Delta}_x = \hat{\Delta}_y = 0.1$, and $\nu_1 = 0.125$, $\nu_2 = 0.02$, $\hat{K} = 30$, $\eta_m = 0.0017$, $\hat{\rho} = 70$, $\hat{\varepsilon}_x = 0.9$ and $\hat{\varepsilon}_y = 0$.

motions arises between $\eta \approx 4.221$ and $\eta \approx 4.484$ where for unpreloaded case the only period three motion is observed.

3.4 Experimental Verification

Figure 6 shows the experimental rig which comprises essentially two main parts, a rigid rotor (1), which is visco-elastically supported by four flexural rods (2), and excited by the out-of-balance mass (3), and a snubber ring (4), which is also elastically supporting using four compression springs. The rotor assembly consists of a mild steel rotor, running in two angular bearings. Holes (5) are drilled and tapped in both inner sleeves for the addition of imbalance weights. A pair of dampers (6) is attached to the rotor, one in each direction, to provide the system with heavier damping. The damping is assumed to be viscous type. Four flexural rods (2) are symmetrically clamped at one end to the outer bearing housing and at the other to a large support block. The support block (7) is in turn bolted to a large cast iron bed. The discontinuous stiffness is provided by a ring to which four compression springs (8), of much greater stiffness than that of the flexural rods, are symmetrically secured. The other ends of the springs are fixed to a large frame, clamped to the bed. The rotor runs inside the ring, with a radial clearance between the ring (4) and the outer bearing housing (1).

The response of the rotor system was monitored by noncontacting eddy probes. Two probes were used for the rotor and another two for the snubber ring. Subsequently, the displacement and forcing frequency signals were collected by a data acquisition system LabView, with a purpose-written program controlling rate of sampling, number of samples, calibration and computation of the rotational frequency. The relative velocities of the rotor and the snubber

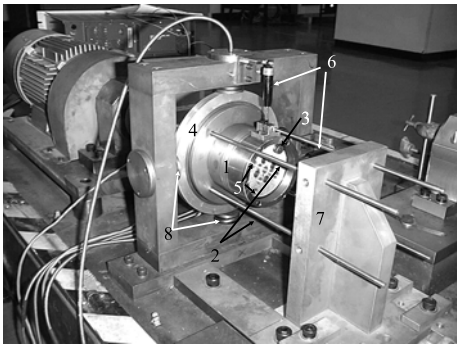

Figure 6. Experimental rig of the investigated rotor system.

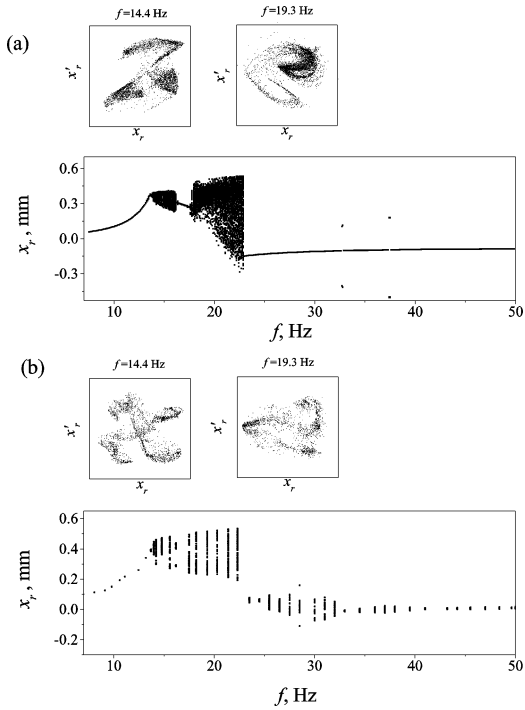

Figure 7. A comparison between (a) theoretical and (b) experimental bifurcation diagrams constructed for varying frequency keeping viscous damping of the snubber ring at $c_s = 3.5\ kg/sec$.

ring $\dot{x}_r$, $\dot{y}_r$, $\dot{x}_s$ and $\dot{y}_s$ were calculated using the LabView digital differentiation facility applied to the output signals from eddy current probes. The data was collated on the computer, where it was scaled, plotted and analysed in the form of Poincaré maps and bifurcation diagrams.

In experiments the rotor mass was $M = 9.7\ kg$. The mass of the out-of-balance was equal to $m = 0.028\ kg$. The combined stiffness of the rods supporting the rotor was $k_{r_x} = k_{r_y} = 79\ kN/m$ and this yields a natural frequency 14.4 Hz. Snubber ring stiffness was $k_s = 2354\ kN/m$. Damping from the rods and the dampers with the fix damping in the horizontal and vertical directions was the same equal to $c_{r_x} = c_{r_y} = 105\ kg/sec$. The out-of-balance radius was $\rho = 35\ mm$.

For the bifurcation diagrams for the forcing frequency the shaft speed was varied from 7 up to 30 Hz. The system responses were investigated by collecting data at intervals around 0.6-1 Hz, each step starting with the final initial conditions for the previous regime and discarding about 400 cycles, in order to exclude transients.

A comparison between theoretical and experimental bifurcation diagrams depicted in Figure 7 shows a number of similarities. In both figures for the low magnitude of the forcing frequency period one motion is observed both at $f \in (7, 13.6)$ Hz and at $f \in (16.2, 17.7)$ Hz followed by chaotic regimes at $f \in (13.6, 16.2)$ Hz and $f \in (17.7, 22.8)$ Hz respectively. In the theoretical and experimental diagrams the width of both periodic and chaotic regimes are the same. After the flip bifurcation at f=22.8 Hz the theoretical rotor response becomes periodic up to the end of the diagram. In experimental bifurcation diagram in Figure 7(b) at $f \in (25.6, 32)$ Hz some kind of quasi-periodic regime was obtained. In both diagrams two cross sections were examined by Poincaré maps. Here chaotic attractors were obtained for: $f = 14.4$ Hz, and $f = 19.3$ Hz keeping the other parameters $\gamma = 0.5\ mm$, $\varepsilon_x = 0.025\ mm$, $\varepsilon_y = 0.2\ mm$ and $\Delta_x = \Delta_y = 0.04\ mm$ constant. The simulated maps show folding and stretching. It is also seen that theoretical and experimental attractors are similar in shape.

Acknowledgments

The financial support provided by EPSRC, Rolls-Royce plc and ORS Award Scheme is gratefully acknowledged.

References

[1] A. F. Filippov, "Differential equations with discontinuous right-hand side," *American Mathematical Society Translations* 42(2), 199-231, 1978.

[2] M. Wiercigroch and B. de Kraker, eds., *Applied Nonlinear Dynamics and Chaos of Mechanical Systems with Discontinuities*. Nonlinear Science Series A Vol. 28. Singapore: World Scientific, 2000.

[3] M. Wiercigroch, "On modelling discontinuities in mechanical systems," *Machine Vibration* 5, 112-119, 1996.

[4] E. E. Pavlovskaia, E. V. Karpenko and M. Wiercigroch, "Nonlinear dynamic interactions of a Jeffcott rotor with a preloaded snubber ring," *Journal of Sound and Vibration*, 2003, in press.

V.

DELAY AND RANDOM SYSTEMS

Problems with *delay* and *random* phenomena play an increasing role in many nonlinear engineering systems and processes,. A few relevant papers in the field are compiled alphabetically in the fifth part of the Proceedings, based on the last name of the first author.

Hu investigates the rich behaviour of a damped Duffing oscillator with negative feedback of delayed velocity, which exhibits abundant dynamic features such as stability switches, an infinite number of Hopf bifurcations, and associated periodic motions. They ensue from the infinite dimensional nature of the system owing to the time delay, and explain why a flexible structure under negative velocity feedback exhibits various self-excited vibrations when the feedback gain is large. Sri Namachchivaya et al. aim at clarifying the mechanism of suppression of regenerative chatter by spindle speed variation, and study nonlinear differential equations with periodic delays which model machine tool chatter with continuously modulated spindle speed. They use the center manifold reduction and the method of normal forms to determine periodic solutions, and analyse the tool motion, and highlight the importance of explicit formulae in the design of real-time control.

Kovaleva determines stochastic resonance and locking conditions for noise-induced interwell jumps in a bistable system. She demonstrates that the phenomena of stochastic resonance and synchronization are not contradictory and can be interpreted as the limiting cases of hopping dynamics modulated by a weak signal. A boundary between the relevant domains of occurrence is obtained as a function of system parameters. Wedig investigates the critical speeds of cars riding on rough road surfaces by analysing quarter car models with bilinear damping characteristics under stochastic and harmonic base excitations. It is shown that there are critical parameter values of the wheel suspension where stationary car vibrations bifurcate into chaos and exponential growth behaviour.

G. Rega and F. Vestroni (eds.),
IUTAM Symposium on Chaotic Dynamics and Control of Systems and Processes in Mechanics, 333.

GLOBAL DYNAMICS OF A DUFFING SYSTEM WITH DELAYED VELOCITY FEEDBACK

Haiyan Hu
Key Lab of Smart Materials and Structures,
Nanjing University of Aeronautics and Astronautics, 210016, Nanjing, China
csve@mail.nuaa.edu.cn

Abstract: The paper presents the rich dynamics of a damped Duffing oscillator with negative feedback of delayed velocity. When the absolute value of feedback gain is less than the damping coefficient, the equilibrium of system is delay-independent stable. Otherwise, it undergoes a number of stability switches with an increase of time delay, and becomes unstable at last. At each stability switch, a Hopf bifurcation occurs. The amplitude and frequency of the bifurcated periodic motion depend on the time delay. When the time delay is long enough, any perturbed motion from the unstable equilibrium may become chaotic though the oscillator of single degree of freedom is autonomous. All these features come from the infinite dimensions of system owing the time delay. They explain why a flexible structure under negative velocity feedback exhibits various self-excited vibrations when the feedback gain is large.

Key words: Delay control, stability switch, Hopf bifurcation, basin of attraction.

1. Introduction

Recent years have witnessed a rapid development of active control of various mechanical systems. With increasingly strict requirements for control speed and system performance, the unavoidable time delays, albeit very short, in controllers and actuators have become a critical problem in the active control of vibration. These time delays often deteriorate the control performance or even cause the instability of the system. On the other hand, delayed control can be utilized to improve the performance of dynamic systems. For instance, the delayed feedback has found its applications to controlling chaos and to semi-active vibration absorption [1,2].

G. Rega and F. Vestroni (eds.),
IUTAM Symposium on Chaotic Dynamics and Control of Systems and Processes in Mechanics, 335–344.

Most engineering systems having time delays can be modeled as a set of ordinary differential equations with time delays. Even though the number of unknowns in the ordinary differential equations is finite, the time delay implies that the change of any system state depends on the previous history of system. Hence, the initial state space and the solution space of a delayed dynamic system are of infinite dimensions. The exact analysis of such a system falls into the theory of functional differential equations [3], and few methods and results are available for engineering systems [4,5].

The objective of this study is to reveal the global dynamics of a damped Duffing oscillator with delayed velocity feedback as following

$$\begin{cases} \ddot{x}(t)+c\dot{x}(t)+x(t)+\mu x^3(t)=v\dot{x}(t-\tau), \quad t>0, \\ x(t)=\varphi(t), \quad t\in[-\tau,0]; \end{cases} \tag{1}$$

where the system parameters yield $c\geq 0$, $\mu>0$, $c-v>0$ such that the system is asymptotically stable when $\tau=0$. This simple system serves as a single-mode model for many practical systems, such as the slender beams equipped with velocity feedback as artificial damping.

2. Stability Switches of Equilibrium

The system of concern has a unique equilibrium $x\equiv 0$. Any perturbed motion $\Delta x(t)$ near $x\equiv 0$ yields a linearized delay differential equation with the following characteristic equation in λ

$$D(\lambda,\tau)\equiv\lambda^2+c\lambda+\omega_0^2-\lambda v\mathrm{e}^{-\lambda\tau}=0. \tag{2}$$

Equation (2) has no zero roots since $\omega_0>0$. When Equation (2) has any pure imaginary root $\lambda=\mathrm{i}\omega$ with $\omega>0$, its real and imaginary parts yield

$$\begin{cases} \mathrm{Re}[D(\mathrm{i}\omega,\tau)]\equiv(\omega_0^2-\omega^2)-v\omega\sin(\omega\tau)=0, \\ \mathrm{Im}[D(\mathrm{i}\omega,\tau)]\equiv c\omega-v\omega\cos(\omega\tau)=0. \end{cases} \tag{3}$$

The imaginary part in Equation (3), together with $c-v>0$, requires that $v<-c$. If this condition does not hold, there must be $|v|<c$ such that Equation (3) has no real root ω and the equilibrium $x\equiv 0$ is delay-independent stable. Otherwise, one has

$$\sin(\omega\tau)=\frac{\omega_0^2-\omega^2}{v\omega}=\frac{\omega^2-\omega_0^2}{|v|\omega}, \quad \cos(\omega\tau)=\frac{c}{v}=-\frac{c}{|v|}. \tag{4}$$

Eliminating the harmonic terms in Equation (4) yields

$$F(\omega)\equiv(\omega_0^2-\omega^2)^2+(c\omega)^2-(v\omega)^2=\omega^4+p\omega^2+q=0, \tag{5}$$

where $p\equiv c^2-v^2-2\omega_0^2$ and $q\equiv\omega_0^4$. Equation (5) has two positive roots

$$\omega_{1,2}=\sqrt{\frac{1}{2}(-p\pm\sqrt{p^2-4q})}\,, \tag{6}$$

such that $\omega_1^2>\omega_0^2$ and $\omega_2^2<\omega_0^2$ hold since $p<0$ and $p^2-4q\geq 0$. At these roots, one has

$$\left.\frac{\mathrm{d}F}{\mathrm{d}\omega}\right|_{\omega=\omega_{1,2}}=\pm 2\omega_{1,2}\sqrt{p^2-4q}>0\ \ (<0)\,. \tag{7}$$

For each of these two roots, hence, Equation (4) gives a series of critical time delays

$$\tau_{1,k}=\frac{1}{\omega_1}[\arccos(-\frac{c}{|v|})+2k\pi],\quad k=0,1,... \tag{8a}$$

$$\tau_{2,k}=\frac{1}{\omega_2}[2\pi-\arccos(-\frac{c}{|v|})+2k\pi],\quad k=0,1,... \tag{8b}$$

As shown in [4], a pair of roots of $D(\lambda,\tau)$ is crossing the imaginary axis from the left to the right when $\tau=\tau_{1,k}$, and from the right to the left when $\tau=\tau_{2,k}$. With an increase of time delay τ from zero to infinity, the number of roots with positive real parts varies and gives rise to stability switches.

Here is an example for $\omega_0=1$, $c=0$, $v=-0.5$ to illustrate the stability switches, similar to those reported in [6], of the oscillator. Obviously, Equations (6) and (8) give $\omega_{1,2}=(\sqrt{17}\pm 1)/4$ and the corresponding critical time delays

$$\tau_{1,k}=\frac{4}{\sqrt{17}+1}(\frac{\pi}{2}+2k\pi)=1.226,\ 6.132,\ 11.04,\ 15.94,\ \ldots \tag{9a}$$

$$\tau_{2,k}=\frac{4}{\sqrt{17}-1}(\frac{3\pi}{2}+2k\pi)=6.035,\ 14.08,\ 22.13,\ 30.17,\ \ldots \tag{9b}$$

These time delays can be ranked as

$$0<\tau_{1,0}<\tau_{2,0}<\underline{\tau_{1,1}<\tau_{1,2}}<\tau_{2,1}<\tau_{1,3}<\cdots. \tag{10}$$

As analyzed in [4], this sequence of critical time delays indicates that the equilibrium is asymptotically stable for $\tau\in[0,\tau_{1,0})$ and $\tau\in(\tau_{2,0},\tau_{1,1})$, but unstable for $\tau\in(\tau_{1,0},\tau_{2,0})$ and $\tau\in(\tau_{1,1},+\infty)$. Thus, the equilibrium undergoes 3 stability switches with an increase of time delay.

3. Hopf Bifurcations

To avoid the tedious analysis [3] of Hopf bifurcation for $x \equiv 0$, the method of multiple scales is used to determine the periodic motions as done in [4,7]. Now, the study is confined to the case of small damping, weak nonlinearity and weak feedback. That is, $c = 2\varepsilon\zeta$, $v = 2\varepsilon\hat{v}$, $\mu = \varepsilon\hat{\mu}$, where $0 < \varepsilon << 1$, $\zeta = O(1)$, $\hat{v} = O(1)$, $\hat{\mu} = O(1)$. Equation (1) is an autonomous system, the period ω of a periodic motion, hence, is an unknown, which can be written as $\omega^2 = \omega_0^2 + \varepsilon\sigma$, where $\sigma = O(1)$ is the detuning frequency. Upon these assumptions, applying the method of multiple scales to Equation (1) gives the first order approximation of periodic motion

$$x(t) = \alpha(\varepsilon t)\cos[\omega t + \beta(\varepsilon t)] + o(\varepsilon), \tag{11}$$

where $\alpha(\varepsilon t)$ and $\beta(\varepsilon t)$ yield a set of autonomous differential equations

$$D_1\alpha = [-\zeta + \hat{v}\cos(\omega\tau)]\alpha, \quad \omega\alpha D_1\beta = -[\frac{\sigma}{2} + \hat{v}\omega\sin(\omega\tau)]\alpha + \frac{3\hat{\mu}}{8}\alpha^3. \tag{12}$$

Imposing $D_1\alpha = 0$ and $D_1\beta = 0$ on Equation (12) leads to the equation of steady state motion. Because the behavior of equilibrium is clear, attention is hereafter paid to the case when $\alpha \neq 0$. That is,

$$-\zeta + \hat{v}\cos(\omega\tau) = 0, \quad \frac{\sigma}{2} + \hat{v}\omega\sin(\omega\tau) - \frac{3\hat{\mu}}{8}\alpha^2 = 0. \tag{13}$$

Solving these two triangle equations, one arrives at the amplitude-frequency relations and the corresponding frequency-delay relations

$$\alpha_{12,k} = \sqrt{\frac{4}{3\mu}(\omega_{12,k}^2 - \omega_0^2 \mp \omega_{12,k}\sqrt{v^2 - c^2})}, \tag{14a}$$

$$\omega_{12,k} = \begin{cases} \dfrac{1}{\tau}[\arccos(-\dfrac{c}{|v|}) + 2k\pi], & \text{for } \alpha_{1,k}, \\ \dfrac{1}{\tau}[2\pi - \arccos(-\dfrac{c}{|v|}) + 2k\pi], & \text{for } \alpha_{2,k}, \end{cases} \tag{14b}$$

where $k = 0, 1, 2, \cdots$ implies an infinite number of periodic motions. As $\omega^2 = \omega_0^2 + \varepsilon\sigma$ is assumed, Equation (14) is reliable only when $k = 0$.

Now, a special case when $c = 0$, $\omega_0 = 1$, $\mu = 0.1, v = -0.5$ is studied to demonstrate the above results. Substituting the system parameters into Equations (14) gives the first two branches of those infinite periodic motions

$$\alpha_{1,0} = \sqrt{\frac{4}{0.3}[(\frac{\pi}{2\tau})^2 - 0.5(\frac{\pi}{2\tau}) - 1]}, \quad \alpha_{2,0} = \sqrt{\frac{4}{0.3}[(\frac{3\pi}{2\tau})^2 + 0.5(\frac{3\pi}{2\tau}) - 1]}, \tag{15}$$

where $\tau \in (0,\ \tau_{2,0}) = (0,\ 6.035)$ is for the stable branch $\alpha_{2,0}$ and $\tau \in (0,\ \tau_{1,0}) = (0,\ 1.226)$ for the unstable branch $\alpha_{1,0}$. Figure 1 shows the amplitude of periodic motion versus the time delay given by Equation (15), together with the numerical results obtained by using the Runge-Kutta approach. In the terminology of bifurcation, the equilibrium undergoes the Hopf bifurcation twice at $\tau_{1,0} = 1.266$ and $\tau_{2,0} = 6.035$ respectively with an increase of time delay.

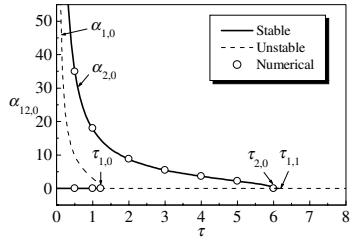

Figure 1. Relation of vibration amplitude and time delay

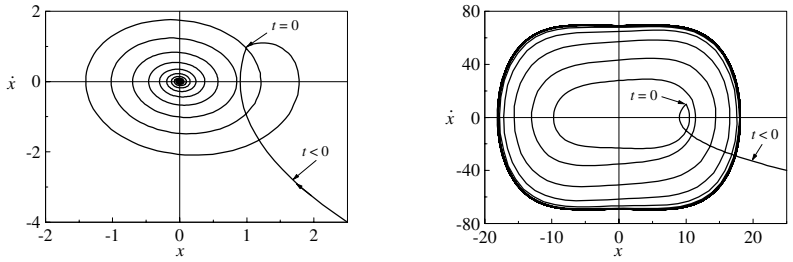

a. A trajectory approaching equilibrium *b.* A trajectory approaching limit circle

Figure 2. Two phase trajectories of system when $\tau = 1$

Figure 2 presents two typical phase trajectories of the system with negative velocity feedback delay $\tau = 1$. The phase trajectory initiating from $\varphi(t) = 1 + t + 2.5t^2,\ t \in [-\tau, 0]$ approaches the asymptotically stable equilibrium, while that initiating from $\varphi(t) = 10 + 10t + 25t^2,\ t \in [-\tau, 0]$ approaches a periodic motion with fundamental frequency $\omega = 4.713$, rapidly. This numerical result coincides very well with the approximate solution given by Equation (15), where $\alpha \to 17.73$ and $\omega \to 3\pi/2 \approx 4.713$ with an increase of time.

4. Global Dynamics

To check the infinite number of periodic motions, the initial value problem (1) are studied for different $\varphi(t) \in C$, where $C \equiv C([-\tau, 0], R^1)$ is

the space of continuous functions on the interval $[-\tau, 0]$. This is undoubtedly a very tough problem. If the time delay τ is very short, however, it is possible to select a few of scale functions on $[-\tau, 0]$ as the base functions to approximate $\varphi(t)$, For instance, the second-order Taylor approximation of $\varphi(t)$ reads

$$\varphi(t)=\varphi_0+t\dot{\varphi}_0+\frac{1}{2}t^2\ddot{\varphi}_0, \tag{16}$$

where $\varphi_0 \equiv \varphi(0) \in R^1$, $\dot{\varphi}_0 \equiv \dot{\varphi}(0) \in R^1$, $\ddot{\varphi}_0 \equiv \ddot{\varphi}(0) \in R^1$. The oscillatory property of the system reminds that the Fourier expansion is also applicable to $\varphi(t)$. For example, the approximation of fundamental harmonics reads

$$\varphi(t)=a_0+a_1\cos(\omega t)+b_1\sin(\omega t), \quad \omega=2\pi/\tau \tag{17}$$

where $a_0=\varphi_0+\ddot{\varphi}_0/\omega^2$, $a_1=-\ddot{\varphi}_0/\omega^2$, $b_1=\dot{\varphi}_0/\omega$. If three base functions on $[-\tau, 0]$, with $[\varphi_0, \dot{\varphi}_0, \ddot{\varphi}_0]^{\mathrm{T}} \in R^3$, are used, the function space C can be mapped onto the Euclidean space R^3, where the global dynamics can be examined by using the conventional methods such as the Poincarè mapping.

Now, the Poincarè section is defined on the phase plane $(x, \dot{x})$ as

$$\Sigma \equiv \{(x, \dot{x}) \,|\, \dot{x}=0, x \geq 0\}, \tag{18}$$

and the intersections $x_{p1}, x_{p2}, \cdots$ of a phase trajectory with the Poincarè section are used to describe the system dynamics. For a very large integer n, the different points in the limit set $x_p \equiv \{x_{pn}\}$ characterize the long-term dynamics. For instance, the zero in x_p corresponds to the equilibrium, while a finite number of points in x_p correspond to a periodic motion.

Given a region $\Omega \subset R^3$ and an arbitrary $(\varphi_0, \dot{\varphi}_0, \ddot{\varphi}_0) \in \Omega$, either the second-order Taylor approximation or the Fourier approximation of fundamental harmonics can be used to approximate $\varphi(t) \in [-\tau, 0]$. Then, a trajectory $x(t)$ of Equation (1) for $t>0$ can be computed by using the Runge-Kutta algorithm and the limit set $\{x_p\}$ can be recorded when $x(t)$ intersects the Poincarè section. This way, the limit sets $\{x_{pk}\}$, $k=1, 2, \cdots$ corresponding to $(\varphi_{0k}, \dot{\varphi}_{0k}, \ddot{\varphi}_{0k}) \in \Omega$, $k=1, 2, \cdots$ are determined. For simplicity, the maximal value in each $\{x_{pk}\}$ is used to represent $\{x_{pk}\}$ and denoted by x_{pk}, $k=1, 2, \cdots$. Thus, it is possible to describe the basins of attraction in $\Omega \subset R^3$ through x_{pk}, $k=1, 2, \cdots$ for the equilibriums, periodic motions and other complicated motions.

4.1 A System with a Relatively Short Time Delay

Consider the case when $c=0$, $\omega_0=1$, $\mu=0.1$, $v=-0.5$, $\tau=1$. As analyzed in Section 3, the equilibrium $x \equiv 0$ is asymptotically stable, and

there co-exist an infinite number of asymptotically stable periodic motions bifurcated from the Hopf bifurcations. The corresponding amplitudes and frequencies of periodic motions determined in Equation (14) read

$$\omega_{2,k} = \frac{3\pi}{2} + 2k\pi = \frac{3\pi}{2}, \frac{7\pi}{2}, \frac{11\pi}{2}, \frac{15\pi}{2}, \cdots \tag{19a}$$

$$\alpha_{2,k} = \sqrt{\frac{4}{0.3}(\omega_{2,k}^2 + 0.5\omega_{2,k} - 1)} = 17.72,\ 40.89,\ 63.90,\ 86.87,\ \ldots \tag{19b}$$

The basins of attraction of those periodic motions were computed in $\Omega \equiv [-50,\ 50] \times [-50,\ 50] \times [-50,\ 50]$ with help of Equation (16). Figure 3 shows the correspondence between $x_{pk}, k = 1, 2, \cdots$ and $(\varphi_{0k}, \dot{\varphi}_{0k})$, $k = 1, 2, \cdots$ on section $\ddot{\varphi}_0 = 0$ in Ω. That is, $\varphi(t)$ was assumed to be a linear function in time t. In Figure 3, the basin of attraction for the equilibrium $x_{p0} = 0$ corresponds to the white elliptic region around the origin of the $(\varphi_0, \dot{\varphi}_0)$ plane. The basin of attraction for the periodic motion of amplitude $x_{p1} \approx 18$ is the gray region surrounding the basin of attraction for the equilibrium on the $(\varphi_0, \dot{\varphi}_0)$ plane. The dark regions represent two parts of the basin of attraction for the periodic motion of amplitude $x_{p2} \approx 41$, whereas the basins of attraction corresponding to $x_{p3} \approx 64$, $x_{p4} \approx 87, \ldots$ were computed, but not shown here. This figure fully coincides with the theoretical prediction.

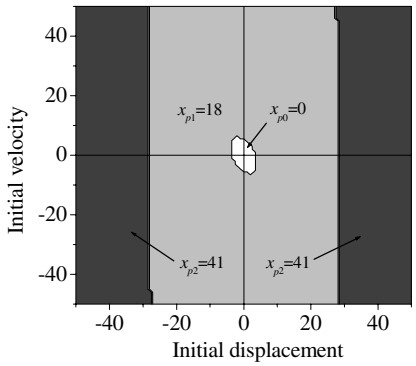

Figure 3. Basins of attraction on $\ddot{\varphi}_0 = 0$

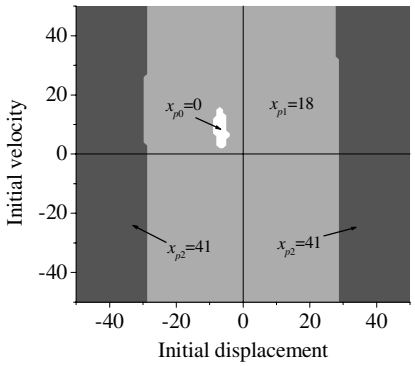

Figure 4. Basins of attraction on $\ddot{\varphi}_0 = -50$

Figures 4 and 5 show the basins of attraction on sections $\ddot{\varphi}_0 = -50$ and $\ddot{\varphi}_0 = 50$ respectively in Ω for the periodic motions. Now, $\varphi(t)$ includes the effect of non-zero acceleration $\ddot{\varphi}_0$ when $t = 0$. On these two sections, the basin of attraction for the equilibrium shrinks and moves from the origin of the $(\varphi_0, \dot{\varphi}_0)$ plane. One may be surprised that the basin of attraction for the equilibrium does not include the equilibrium itself. In fact, what Figures 4 and 5 show are two sections of three-dimensional basins of attraction

parallel to the $(\varphi_0, \dot{\varphi}_0)$ plane. As for the basin of attraction for the periodic motion of amplitude $x_{p1} \approx 18$, it looks almost unchanged in Figures 4 and 5. So, this periodic motion is likely to happen.

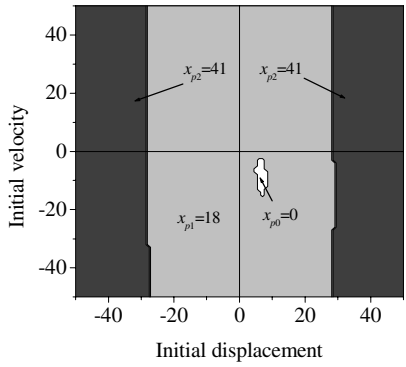

Figure 5. Basins of attraction on $\ddot{\varphi}_0 = 50$

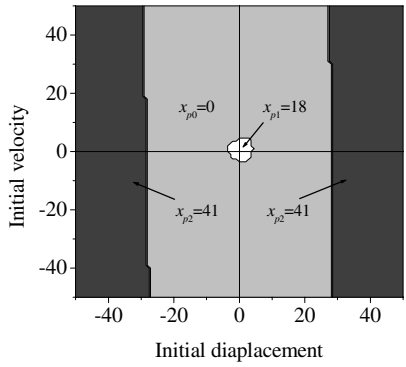

Figure 6. Basins of attraction on $\ddot{\varphi}_0 = 50$

To check the effect of $\varphi(t)$ on the system dynamics further, the displacement approximated by the fundamental harmonics was also used to compute the system dynamics. Figure 6 shows the basins of attraction on $\ddot{\varphi}_0 = 50$ in Ω. Now, the non-zero initial acceleration $\ddot{\varphi}_0$ does not move the basin of attraction for the equilibrium position. This implies again that only the initial displacement and velocity (and even initial acceleration) at the moment $t = 0$ are not able to determine the subsequent dynamics of a delayed dynamic system.

4.2 A System with a Relatively Long Time Delay

The system parameters in this case are $c = 0$, $\mu = 0.1$, $v = -0.5$, $\tau = 4$. Now, the equilibrium $x \equiv 0$ is unstable, and the frequencies and the amplitudes of bifurcated periodic motions yield

$$\omega_{2,k} = \frac{1}{4}\left(\frac{3\pi}{2} + 2k\pi\right) = \frac{3\pi}{8}, \frac{7\pi}{8}, \frac{11\pi}{8}, \frac{15\pi}{8}, \cdots \tag{19a}$$

$$\alpha_{2,k} = \sqrt{\frac{4}{0.3}(\omega_{2,k}^2 + 0.5\omega_{2,k} - 1)} = 3.61,\ 10.28,\ 16.26,\ 22.10,\ \ldots \tag{19b}$$

Given $\Omega \equiv [-20,\ 20] \times [-20,\ 20] \times [-20,\ 20]$, the basins of attraction of various steady-state motions were computed for different approximations of $\varphi(t)$. Figure 7 shows the basins of attraction on $\ddot{\varphi}_0 = 0$ in Ω. Now, the white elliptic region is the basin of attraction for the periodic motion of amplitude of $x_{p1} \approx 3.7$, while the surrounding region is the basin of

attraction of a steady-state motion with the maximal amplitude $x_{p2} \approx 12.5$. As shown in Figure 8, the phase trajectory of this motion intersects itself and involves many harmonics in the Fourier spectrum, where the frequency of dominant harmonic component coincides with the frequency $f_2 = \omega_2/2\pi = 0.4375$ of the periodic motion predicted by the method of multiple scales. Meanwhile, the attractor on the Poincarè section looks quite chaotic. The motion starting from the dark regions looks chaotic, and the corresponding phase trajectory, the Fourier spectrum and the attractor on the Poincarè section are shown in Figure 9. This evidence indicates that it is almost impossible to realize the periodic motions predicted by using the method of multiple scales when the time delay is relatively long.

Geometrically speaking, the asymptotically periodic motion determined by the method of multiple scales appears on a two dimensional central manifold of the equilibrium when a pair of characteristic roots is crossing the imaginary axis. The basin of its attraction, however, occupies so small space in the infinite dimensional state space that such a motion can not always observed, especially when the unstable manifold of equilibrium is of high dimensions.

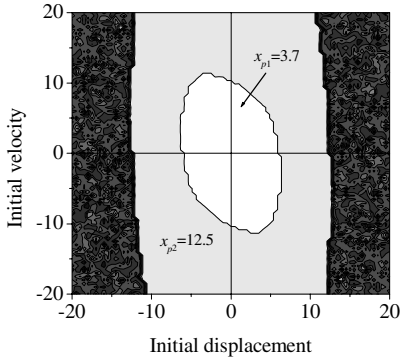

Figure 7. Basins of attraction on $\ddot{\varphi}_0 = 0$

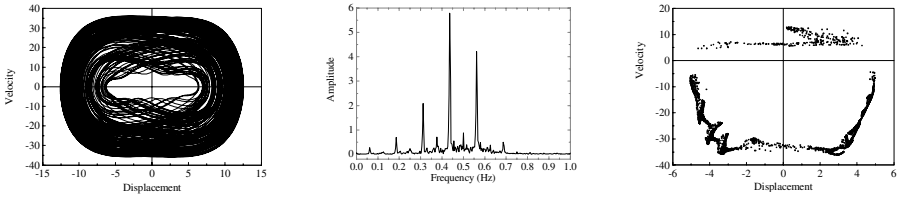

a. Phase portrait *b.* Fourier Spectrum *c.* Poincarè section

Figure 8. Motion starting from $\varphi(t) = 10, t \in [-4, 0]$

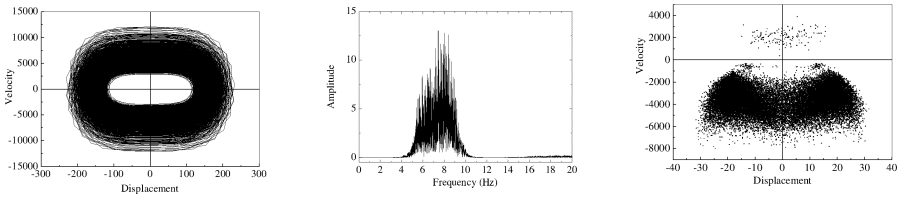

a. Phase portrait *b.* Fourier Spectrum *c.* Poincarè section

Figure 9. Motion starting from $\varphi(t)=13, t\in[-4,0]$

5. Concluding Remarks

As an infinite dimensional dynamic system, the damped Duffing oscillator with delayed velocity feedback exhibits abundant dynamic features such as the stability switches, an infinite number of Hopf bifurcations and associated periodic motions. The corresponding basins of attraction are surrounded one by one on the plane of $(\varphi_0, \dot{\varphi}_0)$ when $\ddot{\varphi}_0$ is fixed. For a large $|\ddot{\varphi}_0|$, the equilibrium $(0, 0)$ may go out of the basin of attraction for the equilibrium on the plane of $(\varphi_0, \dot{\varphi}_0)$ because the initial displacement space C is infinite dimensional. These results well explain why a slender beam with strong negative velocity feedback often exhibits various self-excited vibrations of high frequency all of a sudden if the feedback gain is excessively large. In addition, the numerical studies support the applicability of method of multiple scales to the Duffing oscillators with a relatively short time delay in velocity feedback.

References

[1] K. Pyragas and A. Tamasevicius, "Experimental control of chaos by delayed self-controlling feedback," *Physics Letters A,* **180**, 99-102, 1993.

[2] N. Olgac and B. Holm-Hansen, "Tunable active vibration absorber: the delayed resonator," *Journal of Dynamic Systems, Measurement and Control,***117**, 513-519, 1995.

[3] J.K. Hale and S.M.V. Lunel, *Introduction to Functional Differential Equations*, New York: Springer-Verlag, 1993.

[4] H.Y. Hu and Z.H. Wang, *Dynamics of Controlled Mechanical Systems with Delayed Feedback*, Berlin: Springer-Verlag, 2002.

[5] G. Stépán, *Retarded Dynamical Systems: Stability and Characteristic Functions*, Essex: Longman Scientific and Technical, 1989.

[6] G. Stépán, "Great delay in a predator-prey model," *Nonlinear Analysis TMA,* **10**, 913-929, 1986.

[7] A.H. Nayfeh, C.M. Chin, and J. Pratt, "Perturbation methods in nonlinear dynamics: applications to machining dynamics," *Journal of Manufacture Science and Technology* **119**: 485-493, 1997.

NOISE-INDUCED SYNCHRONIZATION AND STOCHASTIC RESONANCE IN A BISTABLE SYSTEM

Agnessa Kovaleva
Russian Academy of Sciences, Space Research Institute, Moscow 117997, Russia
a.kovaleva@ru.net

Abstract: We determine stochastic resonance and locking conditions for noise-induced interwell jumps in a bistable system. We demonstrate that the phenomena of stochastic resonance and synchronization are not contradictory and can be interpreted as the limit cases of hopping dynamics modulated by a weak signal. The boundary between the domains of synchronization and stochastic resonance is found as a function of the system parameters.

Key words: Stochastic systems, synchronization, stochastic resonance.

1. Introduction

We study hopping between stable states in the bistable system

$$\ddot{x} + \varepsilon\beta\dot{x} + U'(x) = \varepsilon\sigma W(t) + \varepsilon\gamma\sin\omega t \tag{1}$$

where $U(x)$ is a double-well potential with the maximum $U(0) = 0$ and the minima $U(+a) = U(-a) < 0$, ε is a small parameter. Noise $W(t)$ is a zero-mean mixing process, harmonic signal is assumed to be a slow process compared to the unperturbed system time scales.

We suppose that the low frequency signal alone is unable to induce transitions across the potential barrier $U(0) = 0$, whereas the weak noise helps to bring about such transitions, i.e., it induces jumps between wells.

G. Rega and F. Vestroni (eds.),
IUTAM Symposium on Chaotic Dynamics and Control of Systems and Processes in Mechanics, 345–353.

In the absence of noise, as well as in the presence of very weak noise, motion evolves in a single well. In this case any increase in the input noise would result in a decrease in the output signal to noise ratio (SNR). As the input noise increases, the hopping dynamics is becoming dominant. Nonlinear interaction between signal and noise can under certain conditions result in an improvement of the output SNR as the input noise increases. A further increase of the input noise suppresses the signal effect on the system, and the output SNR decreases. Hence, SNR may pass through a maximum at an optimal value of the noise intensity. The optimally tuned system with the maximum SNR is then said to be in *stochastic resonance* (SR).

In a mathematically rigorous sense, this notion is still poorly understood. A simple hypothesis has been proposed in [1]. The system dynamics has been taken to be discrete: a particle at the bottom of the potential well exhibits instant random Poisson switching between the wells, with some degree of coherence with the signal. For an overview a wide range of applications of this hypothesis see [2], [3].

A rigorous mathematical investigation of transition between different stable states is heavily based on large deviation theory [4]. In particular, it has been proved that, if the difference between the wells depths is of $O(1)$, and the wells switch periodically, then the interwell jumps occur periodically with the period of switching [5], [6], [7]. Rudiments of these arguments can be found in [1]. However, synchronization of hopping and signal is not implicit in SR theory [1], [2], [3]. Following this theory, the output spectrum is a sum of a flat wide-band spectrum of the Lorentzian type and a discrete spectrum with a peak at the signal frequency; no coherence between the switching rate and the signal frequency is implicit in this result.

In this report we show that these two concepts are not contradictory. We will demonstrate that the SR and synchronization effects can be interpreted as limiting case of the hopping dynamics for a relatively small and relatively high level of signal against noise. Some experimental data and simulation results [8], [9] have supported this assumption. A boundary between the domains of occurrence of stochastic resonance and synchronization is found as a function of the system and excitations parameters.

We note that the reduced inertia-less model ($\ddot{x} = 0$) is commonly used in the SR theory [1], [2], [3]. This model is in a rather poor agreement with a real dynamics. We derive an asymptotic formula for the escape rate in the second-order model. Comparison with the reduced model demonstrates that the second-order model is more sensitive to noise.

2. Mean Escape Rate

We recall the main results of large deviation theory [4] needed for our purposes. Let an unperturbed system have an asymptotically stable fixed point. Then a weakly perturbed system rests in a small vicinity of the stable point over an exponentially large time interval until the burst-like escape through the potential barrier. The hopping dynamics in a bistable system is reduced to a simple discrete model. In this model, a particle may be either at $+a$, or at $-a$, the burst-like passages between the wells are not taken into consideration. The central feature of the theory is calculation of the mean escape time T_0.

Mean escape rate for a non-modulated system ($\gamma = 0$). At the first stage, we estimate the mean escape time for the non-modulated noisy system

$$\ddot{x} + \varepsilon\beta\dot{x} + U'(x) = \varepsilon\sigma W(t) \tag{2}$$

We suppose that the stable states $x = \pm a$ of the unperturbed systems ($\sigma = 0$) are exponentially asymptotically stable. Let $Q_{\pm}$ be the symmetric domains of attraction of the points $x = \pm a$, respectively. In the phase plane each domain corresponds to a region inside the loop of the unperturbed separatrix. Then the mean escape time T_0 can be interpreted as the mean time to reach the separatrix from the stable point.

In order to calculate T_0, we make use of the machinery of stochastic averaging. Introduce the new variables, the slow energy evolution h and the associated fast angle-variable ϕ [10]

$$h = p^2/2 + U(x), \quad \phi = \Omega(h)\int^{x} p^{-1}(h, z)\mathrm{d}z \tag{3}$$

where $\Omega(h)$ is the associated angular frequency [10]. The change of variables (3) brings equation (2) to the standard form with slow and fast variables

$$\dot{h} = -\varepsilon\beta P^2(h,\phi) + \varepsilon P(h,\phi)\sigma W(t) \tag{4}$$

$$\dot{\phi} = \Omega(h) + \varepsilon F(h,\phi)P(h,\phi)[-\beta P(h,\phi) + \sigma W(t)]$$

in which $P(h,\phi) = p(h, x(h,\phi)) = \pm [2(h - U(x)]^{1/2}$, $F(h,\phi) = \partial\phi/\partial h$. The right hand sides of (4) are 2π-periodic in the angle-variable ϕ,

The right hand sides of (4) are assumed to satisfy the requisite conditions, for the stochastic averaging assumptions hold [11], [12], [13], [14]. Under

these assumptions, the process $h(t,\varepsilon)$ converges weakly as $\varepsilon \to 0$ to a slow diffusion process $\eta(t)$ with the generator [11]

$$L = \varepsilon b(\eta)\frac{\partial}{\partial \eta} + \varepsilon^2 \frac{\partial}{\partial \eta} a(\eta)\frac{\partial}{\partial \eta} \tag{5}$$

The drift and diffusion coefficients are calculated as

$$b(\eta) = \beta <P^2(\eta,\phi)>,\ a(\eta) = \sigma^2 \int_0^\infty R(s)<P(\eta,\phi)P(\eta,\phi + \Omega(e)s)>\mathrm{d}s \tag{6}$$

where $R(s)$ is the autocorrelation function of the process $W(t)$, $<.>$ represents averaging over a period in ϕ. Let the process $\eta(t)$ satisfy the assumption of the exponential stochastic stability [12]. This implies the weak convergence $h(t,\varepsilon) \to \eta(t)$ for all $t > 0$ and allows consideration of escape on the exponentially large time interval [12], [13].

To make the results transparent, we consider $W(t)$ as white noise with autocorrelation function $R(s) = \delta(s)$, where $\delta(s)$ is the Dirac δ –function. In this case we derive from (6)

$$<P^2(\eta,\phi)> = I(\eta),\ \beta(\eta) = \beta\Omega(\eta)I(\eta),\ \ a(\eta) = \sigma^2\Omega(\eta)I(\eta)/2 \tag{7}$$

where $I(\eta)$ is action [10]. Let η_s and η_a be the energy levels corresponding to the separatrix and the attracting focus, respectively. The asymptotic estimate of the mean time required to reach the separatrix from an arbitrary point η is

$$T_0 = \lim_{\varepsilon \to 0} u(\eta_s, \varepsilon) = u_0(\eta_s)$$

where $u(\eta,\varepsilon)$ is a solution of the boundary problem

$$-\varepsilon\beta\Omega(\eta)I(\eta)u' + \frac{1}{2}\varepsilon^2\sigma^2\omega(\eta)[I(\eta)u']' = -1$$

$$u(\eta_s,\varepsilon) = 0,\ u'(\eta_a, \varepsilon) = 0 \tag{8}$$

As a result of transformation [4], we find the limit solution

$$T_0 = \frac{1}{K}\exp\left[\frac{2b(\Delta U)}{D^2}\right],\ \lambda_0 = K\exp\left[-\frac{2b(\Delta U)}{D^2}\right],\ K = \frac{2b^2\Omega_0 I_s}{D^2} \tag{9}$$

where $b = \varepsilon\beta$, $D = \varepsilon\sigma$, $\Omega_0 = [U''(\pm a)]^{1/2}$ is the natural frequency of linear oscillation in a small vicinity of the stable points $\pm a$. I_s is action calculated over the separatrix, $\Delta U = |\eta_a - \eta_s| = |U(\pm a)|$ is the depth of the well. Approximation (9) is valid if $\Delta U >> D^2/2b$.

Finally, we compare λ_0 with the Kramers rate α_0 calculated for the simplified first-order model. For α_0 we have [1] – [3]

$$\alpha_0 = \kappa \exp\left[-\frac{2b(\Delta U)}{D^2}\right], \ \kappa = \varepsilon\frac{\Omega_o S}{2\pi b}, \ S = [U''(0)] \tag{10}$$

Since the coefficient κ is independent of σ, the rate λ_0 is more sensitive to the noise intensity but decreases slower as $\varepsilon \to 0$ than α_0.

Mean escape rate for a weakly modulated system. Introduce a slowly varying potential

$$V(\tau, x) = U(x) - \varepsilon\gamma x\sin\tau, \quad \tau = \omega t \tag{11}$$

Consider the slow dimensionless time $\tau = \omega t$ as a "frozen" parameter. By repeating previous transformations for the potential $V(\tau, x)$ and taking into account the assumptions $\Delta U >> ag$, $\Delta U >> D^2/2b$, we obtain the escape rates from the right and left wells as

$$\lambda(\tau) = \lambda_0 \exp(\mp \nu\sin\tau), \ \nu = 2bag/D^2 \tag{12}$$

where λ_0 is found in (9), $g = \varepsilon\gamma$, the indices $\pm$ correspond to the right and left wells with the minima at $\pm a$, respectively. The Fourier decomposition of the periodic escape rate (12) has the form

$$\lambda^{\pm}(\tau) = \lambda_0[I_0(\nu) + 2\sum_{n=1}^{\infty} (-1)^n I_n(\pm\nu)\sin n\tau] \tag{13}$$

where $I_n(\nu)$ is the modified Bessel function of order n.

3. Characteristics of Motion

Synchronization in a weakly perturbed system. We analyse the escape rates for $\nu > 1$ or $\nu < 1$. The asymptotic representation of the modified Bessel functions for $\nu > 1$ is

$$I_n(\nu) \sim (2\pi\nu)^{-1/2} e^{\nu}[1 + O(\nu^{-1})] \quad \text{for all } n \geq 0 \tag{14}$$

This implies that the escape rates can be written as

$$\lambda^{+}(\tau) \approx \alpha_0(\nu)[1+2\sum_{n=1}^{\infty}(-1)^n \sin n\tau\,], \quad \lambda^{-}(\tau) \approx \alpha_0(\nu)[1 + 2\sum_{n=1}^{\infty}\sin n\tau\,] \tag{15}$$

where $\alpha_0(\nu) = \lambda_0 I_0(\nu)$. Series (15) can be summed in the sense of distribution

$$\lambda^{+}(\tau) \approx \alpha_0(\nu)\sum_{n=1}^{\infty}\delta[\tau - (2k-1)\pi], \quad \lambda^{-}(\tau) \approx \alpha_0(\nu)\sum_{n=1}^{\infty}\delta(\tau - 2k\pi) \tag{16}$$

where $\delta(\tau)$ is the Dirac δ-function. From (15), (16) we deduce that, with probability close to 1, a particle rests at the bottom of the deepest well until the wells switch and the bottom of the well takes up the highest position. The moments of escape for the right (+) and left (−) wells are

$$t_k^{+} = (2k-1)\pi/\omega, \quad t_k^{-} = 2k\pi/\omega, \quad k = 1, 2,.. \tag{17}$$

It follows from (15), (16), (17) that hopping can be interpreted as a series of $2\pi/\omega$-periodic interwell jumps. The system dynamics can be described as

$$x(t) = -a, \ (2k-1)\pi < \omega t < 2k\pi, \ x(t) = a, 2k\pi < \omega t < (2k+1)\pi \tag{18}$$

We thus obtain a synchronization-like effect. Interwell jumps are induced by noise, but the motion becomes "captured" and sustained by a relatively strong signal, and the hopping rate coincides with the signal frequency.

In fact, we present an idealized depiction of the hopping dynamics. Noise induces an eventual excursion from a deeper well to a higher well, or escapes from a higher well at the moments different from t_k. Due to these random walks, the spectrum of hopping is continuous, with sharp peaks at the signal's harmonics.

Stochastic resonance in a weakly modulated system. In case $\nu < 1$, $\omega < \lambda_0$, the model corresponds to SR assumptions. The approaches of SR theory are used in order to calculate SNR as a function of the mean escape rate and the system parameters, details can be found in [1], [2], [3] and references therein. The task is to compare the optimum values of the noise intensity for the first-order and second-order models

In case $\nu << 1$, the mean escape rate (12) can be presented as

$$\lambda^{\pm}(\tau) \approx \lambda_0[1 \mp \nu \sin\tau],\ \nu < 1 \tag{19}$$

By repeating the transformations [1], we find the averaged power spectrum $S(k)$ of the hopping process and define *signal-to-noise ratio* (SNR) at the signal frequency $\omega << 2\lambda_0$

$$S(k) = \frac{4a^2\lambda_0}{4\lambda_0^2 + k^2} + 2\pi(a\nu)^2[\delta(k-\omega) + \delta(k+\omega)] = S_N(k) + 2\pi(a\nu)^2 S_\delta(k)$$

$$SNR = \frac{2\pi(a\nu)^2}{S_N(\omega)} \tag{20}$$

where $S_N(k)$ is the flat Lorentzian portion of the spectrum generated only by noise, $S_\delta(k)$ is the discrete part of the spectrum. By letting $\omega << 2\lambda_0$ and taking into account (9), (20), we find

$$SNR = \eta(D) = 2\pi\nu^2\lambda_0 = 8\pi\frac{(b^2ga)^2 I_s \Omega_0}{D^6}\exp\left[-\frac{2b(\Delta U)}{D^2}\right] \tag{21}$$

A similar ratio for the first order model takes the form [1]

$$SNR = \eta^*(D) = 2\pi\nu^2\alpha_0 = \frac{2}{\pi}\frac{\varepsilon^2 b(ga)^2 S\Omega_0}{D^4}\exp\left[-\frac{2b(\Delta U)}{D^2}\right] \tag{22}$$

As seen from equations (21), (22) the functions $\eta(D)$ and $\eta^*(D)$ are similar and have a maximum at an optimal value of the noise intensity D. The optimum is found from the equation $d\eta/dD = 0$ and takes the value $D = [2b(\Delta U)/3]^{1/2}$ for function (21). A similar calculation for the first-order model (22) gives $D^* = [b(\Delta U]^{1/2}$. The difference is about 20 %.

Note that ratio (21) are obtained under the assumption $\nu = 2ba/D^2 < 1$, as a similar ratio (22) for the first-order model. This makes it impossible to extrapolate the SR curve to small $D \to 0$ [1], [2], [3]. As $D \to 0$ and, therefore, $\lambda_0 \to 0$, a particle remains at the initial position, and calculation of the signal enhancement becomes meaningless.

4. Summary

This paper has investigated the phenomena of stochastic resonance and synchronization in a bistable system subject to weak periodic and random forcing. We have shown that SR it not directly correlated with the matching of the signal frequency and the switching rate. Stochastic resonance can be interpreted as a nonlinear effect arising due to the passage from oscillatory to noise-induced hopping motion. The mean switching rate has been derived and the signal-to-noise ratio has been calculated for the second-order model of a bistable system.

The boundary between the domains of stochastic resonance and synchronization has been defined as a function of the parameters. If signal is weak compared to noise, the hopping dynamic is random, with a weak periodic component, and stochastic resonance can appear. While the relative signal intensity increases, the wide band portion of the spectrum decreases, and, in the limit, a nearly periodic hopping motion occurs. If noise is weak compared to signal the escape rates exhibit sharp peaks at the extrema of the cycles, and the intervals between interwell jumps correspond to the signal period. The occurrence of periodic motion induced by noise but locked to a periodic signal can be interpreted as synchronization.

Acknowledgements

Useful exchanges with Dr. Emil Simiu from National Institute of Standards and Technology (NIST), Gaithersburg, USA, and support provided by NIST for this study are acknowledged with thanks. Partial financial support from the Russian Foundation for Basic Research (grant 02-01-00011) is appreciated.

References

[1] B. McNamara and K. Wiesenfeld, "Theory of stochastic resonance," *Phys. Rev.* **A 39**, 4854-4869, 1989.

[2] D.S. Broomhead, E.A. Luchinskaya, P.V.E. McClintock, and T. Mullin, eds., *Stochastic and Chaotic Dynamics in the Lakes*, American Institute of Physics, Melville, N.Y., 2000.

[3] L. Gammaitoni, P. Hanggi, P. Jung, and F. Marchezoni, "Stochastic resonance," *Reviews of Modern Physics,* **70**, 223-287, 1998.

[4] M. Freidlin and A. Wentzell, *Random Perturbations of Dynamical Systems,* 2nd ed. Springer-Verlag, Berlin., 1998.

[5] M. Freidlin, "Quasi-deterministic approximation metastability and stochastic resonance," *Physica* **D 137,** 313 – 332, 2000.

[6] P. Imkeller, "Energy balance models - viewed from stochastic dynamics," in: *Stochastic Climate Models* (P. Imkeller, and J. von Storch (Eds)), 1-27. Birkhauser-Verlag AG, Switzerland, 2000.

[7] P. Imkeller and I. Pavljukevich, "Stochastic resonance in two-state Markov chains," *Archiv der Mathematik,* **77**, 107-115, 2001

[8] B. Shulgin, A. Neiman and V. Anishchenko, "Mean switching frequency locking in stochastic bistable systems driven by a periodic force," *Phys. Rev. Letters,* **75**, 4157-4160, 1995.

[9] M. Tretyakov, *Numerical Studies of Stochastic Resonance,* preprint nr 302, Weierstrass-Institute fur Angewandte Analysis and Stochastic, Berlin, 1997.

[10] J. Guckenheimer and P. Holmes, *Nonlinear Oscillations, Dynamical Systems, and Bifurcations of Vector Fields*. New York: Springer-Verlag, 1986.

[11] R. Knapp, G.,Papanicolaou and B. White, "Nonlinearity and localization in one-dimensional random media," in: *Disorder and Nonlinearity* (A.R. Bishop, ed.), 2-26. Springer-Verlag, Berlin, 1989.

[12] H.J. Kushner, *Approximation and Weak Convergence Methods for Random Processes, with Applications to Stochastic Systems Theory*. Cambridge: The MIT Press, 1984.

[13] G. Blankenship, and G.Papanicolaou, "Stability and control of stochastic systems with wide band perturbations," *SIAM J. Appl. Math.* **34,** 437-476, 1978.

[14] A. Kovaleva, "Higher orders approximations of the perturbation method for systems with random coefficients," *J. Appl. Math. Mech*., **55**, 612-619, 1991.

DELAY EQUATIONS WITH FLUCTUATING DELAY: APPLICATION TO VARIABLE SPEED MACHINING

N. Sri Namachchivaya,[1] R. Beddini,[1,3] H. J. Van Roessel,[2] and Sarah Wustrack[1]

[1] *Department of Aerospace Engineering*
University of Illinois at Urbana–Champaign
Urbana, Illinois 61801, USA
sri@nsgsun.aae.uiuc.edu

[2] *Department of Mathematical and Statistical Sciences*
University of Alberta
Edmonton, Alberta T6G-2G1, Canada

[3] *Deceased*

Abstract: The suppression of regenerative chatter by spindle speed variation is attracting increasing attention. In this paper, we study nonlinear delay differential equations with periodic delays which model the machine tool chatter with continuously modulated spindle speed. We make use of the center manifold reduction and the method of normal forms to determine the periodic solutions and analyze the tool motion. Analytical results are very close to those obtained experimentally.

Key words: Delay equations, machine tool chatter, center manifold, normal forms.

1. Introduction

Functional Differential Equations (**FDE**) have a number of applications in a variety of research areas ranging from population dynamics to physiology. Since **FDE** are more realistic than ordinary differential equations in some important applications, they are generating increasing interest from engineers and scientists in recent years. Delay Differential Equations (**DDE**) also referred to as Retarded Functional Differential Equations, where the time derivative can depend on both past and present values of the variable, are of interest in this paper. This work is motivated by an important problem in

G. Rega and F. Vestroni (eds.),
IUTAM Symposium on Chaotic Dynamics and Control of Systems and Processes in Mechanics, 355–369.

manufacturing called regenerative chatter, the self-excited relative vibration between workpiece and cutting tool that grows to prohibitive proportions. Its adverse effects include noise, poor surface finish, reduced dimensional accuracy and shortened machine tool life. In models that take into consideration the regenerative effect, the forces acting on the cutting tool depend not only on the current state, but also on the past state one revolution earlier (the surface generated by the tool on one pass becomes the upper surface of the chip on the subsequent pass). Therefore, the equations governing the tool motion are differential equations with time-delay terms– **DDE**.

A method of chatter suppression or elimination, applicable irrespective of machine cutter class and physical configuration, would clearly be beneficial. The purpose of this paper is to clarify the mechanism of suppression of regenerative chatter through modulating the spindle speed continuously. We achieve this by center-manifold and normal form methods and evaluate the effects of the system parameters such as amplitude and frequency of the spindle speed variation on the chatter suppression. In addition to recovering the previous results [1, 2] we also provide some new results pertaining to suppression of chatter. Moreover, the approach employed in these proceedings, based on the paper [3], is superior in that it provides a more transparent derivation of the chatter suppression results. Analytical results will serve as an effective guide for rapidly locating stability boundaries, predicting post-critical behavior and suppressing chatter. Explicit formulae are very useful in the development and design of real-time control.

2. Hanna-Tobias Model and Spindle Speed Variation

In regenerative chatter nonlinear differential equations with time delay serve as convenient models. A widely accepted one degree of freedom model to describe regenerative cutting-tool chatter in turning or milling was developed by Hanna and Tobias [4],

$$\begin{aligned}
&\ddot{x}(t) + 2\zeta p\dot{x}(t) + p^2\left[x(t) + \beta_2 x^2(t) + \beta_3 x^3(t)\right] \\
&= -\kappa p^2\{x(t) - x(t-\tau) + \hat{\beta}_2\left(x(t) - x(t-\tau)\right)^2 + \hat{\beta}_3\left(x(t)\right. \\
&\quad \left. -x(t-\tau)\right)^3\} \qquad (1)\\
&p^2 = \frac{k_0}{m}, \quad \zeta = \frac{\Delta}{2}\frac{p}{\hat{\omega}}, \quad \Delta = \frac{h}{k_0}, \quad \kappa = \frac{k_1}{k_0}, \quad \tau = \frac{1}{N} \quad \text{and} \quad N = \mathbf{z}\Omega
\end{aligned}$$

where $x(t)$ is the displacement normal to the machined surface at time t, m is the equivalent mass of the tool, k_0 is the linear stiffness, p is the natural frequency of the system, $h = \hat{\omega}d$ is the hysteretic damping coefficient, $\hat{\omega}$ is the chatter frequency which *depends on system parameters*, d represents damping, and k_1 is the width-of-cut parameter. The regenerative effect enters the

equation of motion through chip thickness where Ω is the spindle speed and $\mathbf{z}$ is the number of cutter blades. Coefficients β_2 and β_3 are two constants describing the nonlinear stiffness of the machine tool, and $\hat{\beta}_2$ and $\hat{\beta}_3$ are constant coefficients of the nonlinear cutting force function which depends on chip thickness. These parameters are often evaluated empirically and representative values are given in [4].

For $\tau = 0$, linear part has two roots with negative real parts. As soon as $\tau > 0$, the characteristic equation is transcendental and has infinitely many solutions for $\hat{\rho}(\kappa, \tau) = \hat{\delta}(\kappa, \tau) + i\hat{\omega}(\kappa, \tau)$, expressed in terms of the *width-of-cut* κ, and *time delay* τ, which are the natural control parameters in the machine cutting process. These new roots may cross the imaginary axis as τ or κ is further increased. Assuming that at $\kappa = \kappa_c$, and $\tau = \tau_c$ we have such a crossing, with the critical chatter frequency $\hat{\omega}_c$, we find the critical value of the width-of-cut as

$$\kappa_c = \frac{\hat{\omega}_c^2 - p^2}{2p^2} + \frac{\Delta^2 p^2}{2(\hat{\omega}_c^2 - p^2)} \tag{2}$$

In addition, we have

$$\tau_c = \frac{2(\arctan(\frac{p^2 - \hat{\omega}_c^2}{\Delta p^2}) + k\pi)}{\hat{\omega}_c} \qquad k = 1, 2, 3, \cdots \tag{3}$$

Equations (2) and (3), which are solved parametrically in terms of critical chatter frequency, $\hat{\omega}_c$, yield the conventional stability chart [4].

As mentioned in the introduction that greater widths of cut could be achieved without chatter by modulating the spindle speed continuously. To this end, we let

$$\tau \to \tau_0 + \varepsilon\hat{\sigma}(t) \quad \text{where} \quad \hat{\sigma}(t) \stackrel{\text{def}}{=} \hat{\mu}_1 e^{i\hat{\nu}t} + \bar{\hat{\mu}}_1 e^{-i\hat{\nu}t} \tag{4}$$

as in Inamura and Sata [5] and Sexton *et al.* [6], $\varepsilon << 1$. The mean value of the period of spindle rotation, τ_0, and complex constant, $\hat{\mu}_n$, are related to mean cutting speed, N, and the amplitude of spindle speed variation, $\pm\delta N$.

Rescaling time $t \to \frac{t}{\hat{\omega}_c}$ with $r_0 = \hat{\omega}_c \tau_0$ and defining the new variables

$$u(t) \stackrel{\text{def}}{=} x(\frac{\tau_0}{r_0}t) \quad \text{and} \quad \sigma(t) \stackrel{\text{def}}{=} \frac{r_0}{\tau_0}\hat{\sigma}(\frac{\tau_0}{r_0}t)$$

and by augmenting the system, the explicit time-dependent delay terms may be replaced by state dependent delay terms. Periodic modulation of the delay can easily be generated by an oscillator with the correct frequency, that is $\ddot{\sigma}(t) + \nu^2\sigma(t) = 0$ and appropriate initial conditions. Letting $x = (x_1, x_2, x_3, x_4)$ where $x_1(t) = u(t)$, $x_2(t) = \dot{u}(t)$ in the original equation (1) , and $\nu x_3(t) = -\dot{\sigma}(t)$ and $x_4(t) = \sigma(t)$ for the fluctuation, and after simplification, we can replace the

original equation (1) by the following augmented set of autonomous first order equations

$$\dot{x}(t)=E(\alpha)x(t)+D(\alpha)x(t-r_0-\varepsilon\sigma(t))+\hat{F}(x(t),x(t-r_0-\varepsilon\sigma(t)),\alpha), \quad (5)$$

where

$$E(\alpha)\stackrel{\text{def}}{=}\begin{pmatrix}0 & 1 & 0 & 0\\ -B(\alpha) & -A(\alpha) & 0 & 0\\ 0 & 0 & 0 & \nu\\ 0 & 0 & -\nu & 0\end{pmatrix}, \quad D(\alpha)\stackrel{\text{def}}{=}\begin{pmatrix}0 & 0 & 0 & 0\\ -C(\alpha) & 0 & 0 & 0\\ 0 & 0 & 0 & 0\\ 0 & 0 & 0 & 0\end{pmatrix}$$

and $\hat{F}=(0,\hat{f}(x(t),x(t-r_0-\varepsilon\sigma(t)),\alpha),0,0)$ with

$$\begin{aligned}&\hat{f}(x(t),x(t-r_0),\alpha)=c_{20}(\alpha)x_1^2(t)+c_{11}(\alpha)x_1(t)x_1(t-r_0-\epsilon x_4(t))\\&+c_{02}(\alpha)x_1^2(t-r_0-\epsilon x_4(t))+c_{30}(\alpha)x_1^3(t)\\&+c_{21}(\alpha)x_1^2(t)x_1(t-r_0-\epsilon\sigma(t))\\&+c_{12}(\alpha)x_1(t)x_1^2(t-r_0-\epsilon x_4(t))+c_{03}(\alpha)x_1^3(t-r_0-\epsilon x_4(t))\end{aligned}$$

and the linear and nonlinear coefficients are given explicitly as

$$A(\alpha)=A_0+A_1\alpha, \quad B(\alpha)=B_0+B_1\alpha, \quad C(\alpha)=C_0+C_1\alpha.$$

In the case of fixed spindle speed, with varying *width-of-cut*, we choose κ as the bifurcation parameter while r_0 is fixed. The coefficients, in terms of machine tool parameters, are given as

$$\begin{aligned}&A_0=2\zeta_c\omega_p=\Delta\omega_p^2, \quad B_0=\omega_p^2(1+\kappa_c), \quad C_0=-\kappa_c\omega_p^2,\\&A_1=2\zeta_c'\omega_p=-\Delta\omega_p^2\,\omega_c', \quad B_1=\omega_p^2, \quad C_1=-\omega_p^2\\&c_{20}(0)=-\omega_p^2(\beta_2+\kappa_c\hat{\beta}_2),\ c_{11}(0)=2\kappa_c\omega_p^2\,\hat{\beta}_2,\ c_{02}(0)=-\kappa_c\omega_p^2\,\hat{\beta}_2\\&c_{30}(0)=-\omega_p^2(\beta_3+\kappa_c\hat{\beta}_3),\ c_{03}(0)=\kappa_c\omega_p^2\,\hat{\beta}_3,\ -c_{12}(0)=c_{21}(0)=3c_{03}(0).\end{aligned} \quad (6)$$

The machine tool parameters are evaluated empirically through experiments and are given below:

$$\begin{cases} h &= 78250\ lb\ rad/in \qquad k_0=1.87\ 10^6\ lb\ rad/in\\ p &= 173.25\ c/sec \qquad z=24\ HSS\ blades\\ \beta_2 &= 479.3\ 1/in \qquad \beta_3=264500\ 1/in^2\\ \hat{\beta}_2 &= 5.668\ 1/in \qquad \hat{\beta}_3=-3715.2\ 1/in^2\end{cases} \quad (7)$$

To our knowledge, there are no known Hopf bifurcation theorems for such state-dependent delay equations. Hence, the natural question here is, how do we apply or extend the results from general Hopf bifurcation theories for constant delay equations to the state dependent delay system (5) knowing that the fluctuations in the delay are small.

Since the fluctuations are small, $|\epsilon| << 1$, bounded, and independent of the tool motion $x_1(t)$, one of the strategies for attacking this is to use Taylor expansions and expand in powers of $|\epsilon|$ about a *finite mean delay* r_0 as

$$\begin{aligned} x_1(t - r_0 - \epsilon x_4(t)) &= x_1(t - r_0 - \epsilon\sigma(t)) \\ &= x_1(t - r_0) - \epsilon x_2(t - r_0)\sigma(t) + \tfrac{\epsilon^2}{2}\dot{x}_2(t - r_0)\sigma^2(t) + h.o.t. \end{aligned} \tag{8}$$

Since the original **DDE** is second order, it is obvious that $\dot{x}_2(t-r_0) = \ddot{x}_1(t-r_0)$ is bounded. The problem would be with the higher orders derivatives of the solution $x_1(t - r_0)$ which may not exist at points kr_0. In bifurcation studies such as the one that is presented in this paper, we are interested in the asymptotic or long time behavior. Using the method of steps, it is easily shown that solutions for nonlinear **DDE**s with continuously varying delay become smoother with increasing values of time, provided the nonlinear functions are sufficiently smooth. The nonlinear function in (5) is C^∞, being a polynomial in $x(t)$ and $x(t - r(t))$, and so the existence of higher order derivatives of the solution is ensured for sufficiently large time t. Though we do not rigorously justify the existence of derivatives beyond second order, due to this smoothing property, we shall assume that sufficient higher derivatives exist while analyzing its asymptotic behavior.

Now we follow the procedure of order reduction that is often used in the evaluation of the higher time-derivative terms in (8). This procedure uses repeated substitution of the equations of motion to yield a second order equation. Hence, by adding a time lag in the equation of the motion, we replace $\dot{x}_2(t-r_0)$ on the right hand side of the above approximation by

$$\dot{x}_2(t - r_0) \sim -B(\alpha)x_1(t - r_0) - A(\alpha)x_2(t - r_0) - C(\alpha)x_1(t - 2r_0)$$

Now that we have given an heuristic justification for the Taylor expansion of the term $x_1(t - r_0 - \epsilon\sigma(t))$ about a finite mean delay r_0, we shall drop ϵ and consider the truncated system neglecting the higher order terms. Hence, the state dependent delay equations (5) can be written as autonomous constant delay equations

$$\dot{x}(t) = E(\alpha)\,x(t) + D(\alpha)\,x(t - r_0) + F(x(t), x(t - r_0), \alpha), \tag{9}$$

where, again, the relevant expressions can be found in Appendix-I of [2].
The corresponding linear system is decoupled

$$\begin{aligned} &\ddot{x}_1(t) + A(\alpha)\,\dot{x}_1(t) + B(\alpha)\,x_1(t) + C(\alpha)x_1(t - r_0) = 0, \\ &\ddot{x}_4(t) + \nu^2\,x_4(t) = 0, \end{aligned} \tag{10}$$

with the characteristic equations

$$\rho^2 + A(\alpha)\,\rho + B(\alpha) + C(\alpha)\,e^{-\rho r_0} = 0 \quad \text{and} \quad \rho^2 + \nu^2 = 0.$$

It is obvious that the eigenvalues of the augmented oscillator is $\rho = \pm i\nu$. The transcendental equation, at $\alpha = 0$, has a pair of pure imaginary roots, which we normalize to one, that is $\rho = \pm i$. This normalization of chatter frequency gives the following relations between the mean delay and the linear critical coefficients

$$C_0 \cos r_0 = 1 - B_0, \quad C_0 \sin r_0 \ = A_0 \tag{11}$$

where $A_0 \stackrel{\text{def}}{=} A(0)$, $B_0 \stackrel{\text{def}}{=} B(0)$, $C_0 \stackrel{\text{def}}{=} C(0)$. We shall use the relations (11) to simplify some of the expressions in the subsequent sections.

ASSUMPTION 1 (NON-RESONANCE) *In the absence of the periodic perturbation, $\sigma(t)=0$, the* **DDE** (9) *exhibits a Hopf bifurcation at $\alpha=\alpha_c=0$ (a critical value of some system parameter), with a simple pair of pure imaginary eigenvalues $\pm i$ and all the other roots of the characteristic equation have negative real parts. We furthermore assume that in the presence of periodic perturbation, we have two non-resonant pairs of simple eigenvalues $\pm i$ and $\pm\nu i$ on the imaginary axis, with $0 < \nu << 1$, such that there is no rational number $\frac{k_1}{k_2}$ with small $|k|$ ($|k| < 5$) satisfying $1 = \frac{k_1}{k_2}\nu$, that is, there are no* primary resonances *due to the low value of ν. However, there are infinitely many* weaker resonances *(with a larger norm $|k|$) which can be neglected due to the presence of dissipation.*

In the subsequent sections we examine the effects of periodic variation in delay ($\sigma(t) \neq 0$) on the asymptotic stability of the trivial solution of (0) and the associated bifurcations close to the critical parameter, $\alpha = 0$. We hope that stabilization or further destabilization of the trivial solution for $\alpha > 0$ may explain the mechanism of SSV in chatter suppression.

3. Problem Formulation as FDE

The theory of **FDE** [7] has been developed to a point of high sophistication and provides successful description of the evolution of **DDE**. Suppose $r_0 \geq 0$ is a given number. We denote the Banach space of continuous functions from the interval $[-r_0, 0]$ to $\mathbb{R}^4$ by $\mathscr{C} \stackrel{\text{def}}{=} C([-r_0, 0], \mathbb{R}^4)$ endowed with sup norm. If $x \in C([-r_0, \infty), \mathbb{R}^4)$, then for any $t \in [0, \infty)$, we let $x_t \in \mathscr{C}$ be defined by

$$x_t(\theta) \stackrel{\text{def}}{=} x(t + \theta), \quad -r_0 \leq \theta \leq 0$$

to denote a segment of the solution. For each different t, we get a new continuous function x_t on this Banach space. Hence the delay differential equation (9) is defined as in [7]

$$\dot{x}(t) = L(\alpha)x_t + F(x_t, \alpha), \qquad x_0 = \phi \in \mathscr{C} \tag{12}$$

where $L(\cdot)$ is a bounded linear operator from $\mathscr{C} \times \mathbb{R}$ to $\mathbb{R}^4$ which by the Riesz theorem has an unambiguous representation given by the following Stieltjes integral

$$L(\alpha)x_t = \int_{-r_0}^{0} [d\eta(\theta, \alpha)]x_t(\theta) \tag{13}$$

and $F : \mathscr{C} \times \mathbb{R} \to \mathbb{R}^4$ is a smooth nonlinear vector functional. For discrete delays the measure $[d\eta(\theta, \alpha)]$ which defines the linear operator on $\mathscr{C}$ is just a combination of *Dirac delta* functions, that is

$$d\eta(\theta, \alpha) \stackrel{\text{def}}{=} E(\alpha)\delta(\theta)d\theta + D(\alpha)\delta(\theta + r_0)d\theta \tag{14}$$

The characteristic matrix of $L(\alpha)$ is given as

$$\triangle(s, \alpha) \stackrel{\text{def}}{=} sI - \int_{-r_0}^{0} e^{s\theta}[d\eta(\theta, \alpha)] \tag{15}$$

Setting the determinant of the characteristic matrix equal to zero gives us a transcendental equation which has infinitely many solutions; hence we have an infinite dimensional dynamical system.

For any initial condition $\phi \in \mathscr{C}$, the solution of the **DDE** is a continuously differentiable function x_t that satisfies equation (12) for every $t \geq 0$ and $x_0(\theta) = \phi(\theta)$ for every $\theta \in [-r_0, 0]$. An orbit of a solution is traced out by the family of functions x_t for $t \in [0, \infty)$ (for details, see, Hale and Verduyn-Lunel [7]). It is well known [7] that the translation along the solution of the linear equation

$$\dot{x}(t) = L(\alpha)x_t, \qquad x_0 = \phi \in \mathscr{C} \tag{16}$$

induces a strongly continuous semigroup $T(t) : \mathscr{C} \to \mathscr{C}$ defined by the relation

$$T(t)\phi \stackrel{\text{def}}{=} x_t(.; \phi). \tag{17}$$

The infinitesimal generator $\mathscr{A} : \mathscr{D}(\mathscr{A}) \to \mathscr{C}$ for the strongly continuous semigroup $T(t)$ is given by

$$\begin{aligned} \mathscr{A}\phi &\stackrel{\text{def}}{=} \frac{d\phi(\theta)}{d\theta} \\ \mathscr{D}(\mathscr{A}) &\stackrel{\text{def}}{=} \left\{ \phi \in \mathscr{C} : \frac{d\phi}{d\theta} \in \mathscr{C}, \ \frac{d\phi(0)}{d\theta} = L\phi \stackrel{\text{def}}{=} \int_{-r_0}^{0} [d\eta(\theta, \alpha)]\phi(\theta) \right\} \end{aligned} \tag{18}$$

which has only a point spectrum

$$\sigma(\mathscr{A}(\alpha)) = \sigma_P(\mathscr{A}(\alpha)) \stackrel{\text{def}}{=} \{\lambda : \det(\triangle(\lambda, \alpha)) = 0\} \tag{19}$$

At $\alpha = 0$, based on assumption 1, equation (16) has two eigenvalues on the imaginary axis and all other eigenvalues have negative real parts. Suppose that

$$\Lambda \stackrel{\text{def}}{=} \{\lambda \in \sigma(\mathscr{A}(0)) : \Re(\lambda) = 0\} = \{\pm i,\ \pm i\nu\} \tag{20}$$

and let P be the generalized eigenspace associated with the eigenvalues of Λ with the bases given by $\Phi \stackrel{\text{def}}{=} \Phi(\theta)$. Let $\Psi \stackrel{\text{def}}{=} \Psi(\tau)$ be the bases for the generalized eigenspace (dual space P^*) of the transposed equation associated with Λ and Ψ is normalized by the condition $\langle \Psi, \Phi \rangle = I$. The bilinear form $\langle \cdot, \cdot \rangle$ is given by

$$\langle \psi, \phi \rangle = (\psi(0), \phi(0)) - \int_{-r}^{0} \int_{0}^{\theta} \psi(\xi - \theta)[d\eta(\theta, \alpha)]\phi(\xi) d\xi \tag{21}$$

and $(\cdot, \cdot)$ stands for Hermite inner product. Then $\mathscr{C}$ can be decomposed by Λ as

$$\mathscr{C} = P \oplus Q, \quad \text{where} \quad Q \stackrel{\text{def}}{=} \{\phi \in \mathscr{C} : \langle \Psi, \phi \rangle = 0\} \tag{22}$$

and any element $x_t \in \mathscr{C}$ can be written as $x_t = x_t^P + x_t^Q$ where $x_t^P \in P$ with

$$x_t^P = \Phi \langle \Psi, x_t \rangle \quad \text{and} \quad x_t^Q \in Q$$

3.1 Nonlinear Problem

Making use of $T(t)$, in the integrated form, equation (12) with initial data ϕ becomes

$$x_t = T(t)\phi + \int_0^t T(t-s) X_0 F(x_s, \alpha) ds, \quad \text{where} \quad X_0(\theta) = \begin{cases} 0, & -r \le \theta < 0, \\ I, & \theta = 0. \end{cases} \tag{23}$$

Equation (23) on differentiation with respect to time yields a formal expression

$$\frac{dx_t}{dt} = \mathscr{A}(\alpha) x_t + X_0 F(x_t, \alpha), \qquad x_0 = \phi \in \mathscr{C}. \tag{24}$$

The nonlinear equation (24) has jump discontinuities at $\theta = 0$. Hence, the appropriate solution space for (24) is

$$\begin{aligned} \mathscr{BC} &\stackrel{\text{def}}{=} \mathscr{C} \oplus < X_0 > \\ &= \big\{\phi : [-r_0, 0] \to \mathbb{R}^4;\ \phi \text{ is continuous on } [-\mathrm{r}_0, 0) \text{ with jump} \\ &\qquad \text{discontinuities at } 0\} \end{aligned}$$

Then any solution of (9) for $t \geq 0$, satisfies the abstract ODE in $\mathscr{BC}$

$$\frac{dx_t}{dt} = \widehat{\mathscr{A}}(\alpha)x_t + X_0 F(x_t, \alpha), \qquad x_0 = \phi \in \mathscr{C}. \tag{25}$$

where

$$\widehat{\mathscr{A}}\phi \stackrel{\text{def}}{=} \phi' + X_0 \left\{ L\phi - \phi'(0) \right\} \tag{26}$$

This procedure of treating the equation in $\mathscr{BC}$ was used effectively by Faria and Magalhães [8] in their development of normal form theory for **FDE**. Let the projection $\hat{\phi}^P$ of any $\hat{\phi} \in \mathscr{BC}$ onto P be defined as

$$\pi : \mathscr{BC} \to P, \qquad \pi\,(\phi + X_0\beta) \stackrel{\text{def}}{=} \Phi\,[\langle \Psi, \phi \rangle + \Psi(0)\beta] \tag{27}$$

It can be shown [8] that the projection π commutes with $\widehat{\mathscr{A}}$ in $\mathscr{C}^1$, that is, $\widehat{\mathscr{A}}\pi = \pi\widehat{\mathscr{A}}$ for elements in $\mathscr{C}^1$. Making use of this commutative property of π and the decomposition of $\mathscr{C} = P \oplus Q$ it can be easily shown that $\mathscr{BC}$ has a direct sum decomposition, that is

$$\mathscr{BC} = P \oplus \ker(\pi).$$

Then, for $x_t \in \mathscr{C}^1$, we write

$$x_t = \Phi z(t) + y_t, \quad \text{where} \quad z \in \mathbb{R}^4, \quad \text{and} \quad y_t \in Q \cap \mathscr{C}^1 \tag{28}$$

Making use of the domain decomposition (28), the relation $\mathscr{A}\Phi = \Phi B$ with $B = \text{diag}\{i, -i, iv, -iv\}$ and the fact that $\langle \Psi, y_t \rangle = 0$, in the abstract ODE (25) yields

$$\begin{aligned} \Phi\dot{z}(t) + \frac{dy_t}{dt} &= \Phi B z(t) + (I - \pi)\widehat{\mathscr{A}} y_t \\ &\quad + \Phi\Psi(0)F\left(\Phi z(t) + y_t, \alpha\right) + (I - \pi)X_0 F\left(\Phi z(t) + y_t, \alpha\right). \end{aligned} \tag{29}$$

Now projecting (29) onto P and its complement in $\mathscr{BC}$ yields

$$\begin{aligned} \dot{z}(t) &= Bz(t) + \Psi(0)F\left(\Phi z(t) + y_t, \alpha\right) \\ \frac{dy_t}{dt} &= (I - \pi)\widehat{\mathscr{A}} y_t + (I - \pi)X_0 F\left(\Phi z(t) + y_t, \alpha\right) \end{aligned} \tag{30}$$

where we have once again used the fact that $\langle \Psi, y_t \rangle = 0$. The abstract ODE (25) in $\mathscr{BC}$ is equivalent to (30). It is very important to realize that these *almost decoupled equations* are the *starting point* for the rest of our analysis. The second equation in (30) is interpreted as an equality for each $\theta \in [-r_0, 0]$, but we may informally think of it as an equation in $Q \cap \mathscr{C}^1$. The complete decomposition of (30) into a *four-dimensional equation* and an infinite-dimensional equation is the main goal of the subsequent section.

4. Center Manifold Reduction and Normal Forms

The existence of such a manifold for **FDE** was first proved by Chafee [9] and is given by

$$W^c_{loc}(0) = \{\phi \in \mathscr{C} : \phi = \Phi z + h(z),\ z \in V\} \tag{31}$$

where V is a neighborhood of zero in $\mathbb{R}^4$. The center manifold theorem assures that the four-dimensional invariant manifold is tangent to the center subspace P, that is $h(0) = 0$ and $D_z h(0) = 0$, and $h : V \to Q \cap \mathscr{C}^1$ is C^k-smooth. Furthermore, the long term behavior of solutions of the original **DDE** (12) is described by the solutions of the four-dimensional ODE

$$\dot{z}(t) = Bz(t) + \Psi(0) F\left(\Phi z(t) + h\left(z(t)\right), 0\right) \tag{32}$$

In equation (32), B is the 4×4 diagonal matrix of eigenvalues with zero real parts, $\Psi(0)$ are the bases evaluated at $\theta = 0$ for the invariant dual subspace P^*, and Φ are the bases for the invariant subspace P. The stability on the center manifold determines the stability of the original equation. This is the framework in which we shall construct the center manifold and then the normal forms to study the bifurcations of the trivial equilibrium in (12).

Construction of center manifolds for **FDE** is still a computationally intensive exercise, unlike their construction for **ODE**'s. Taking the solution of the center manifold as $x_t(\theta) = \Phi(\theta) z(t) + h\left(z(t); \theta\right)$ in (12) or equivalently, substituting for y_t the expression $h\left(z(t); \theta\right)$ in (30) yields

$$\begin{aligned} D_z h\left(z(t); \theta\right) \dot{z}(t) &= \mathscr{A} h\left(z(t); \theta\right) - \Phi(\theta)\Psi(0) F\left(\Phi(\theta) z(t)\right. \\ &\left. + h\left(z(t); \theta\right), 0\right) + X_0 \left[L h\left(z(t); \theta\right) - h'\left(z(t); 0\right) F\left(\Phi(\theta) z(t)\right.\right. \\ &\left.\left. + h\left(z(t); \theta\right), 0\right)\right] \end{aligned} \tag{33}$$

where $\dot{z}(t)$ is given by the four-dimensional ODE (32). On substitution in the left hand side of equation (33) yields a system of partial differential equations for $h\left(z; \theta\right)$, viz.

$$\begin{aligned} &D_z h\left(z; \theta\right) Bz + D_z h\left(z; \theta\right) \Psi(0) F(\Phi(\theta) z + h\left(z; \theta\right), 0) \\ &\quad = \mathscr{A} h\left(z; \theta\right) - \Phi(\theta)\Psi(0) F(\Phi(\theta) z + h\left(z; \theta\right), 0) \qquad -r_0 \le \theta < 0 \\ &D_z h\left(z; 0\right) Bz + D_z h\left(z; 0\right) \Psi(0) F(\Phi(0) z + h\left(z; 0\right), 0) \\ &= \int_{-r_0}^{0} [d\eta(\tau, 0)] h\left(z; \tau\right) + \left(I - \Phi(0)\Psi(0)\right) F(\Phi(0) z \\ &\quad + h\left(z; 0\right), 0)\theta = 0. \end{aligned} \tag{34}$$

We can approximate $h\left(z; \theta\right)$, using the standard approach in center manifold theory, as a polynomial or power series in z. Construction of center manifolds

and numerical calculation (approximation) of Hopf bifurcation for **FDE** was given by Hassard *et al.* [10] for the first time. Since only terms up and including $|z|^3$ are needed in the normal forms for non-degenerate Hopf bifurcations, it is sufficient to construct, as shown in [3], an approximation to the center manifold up and including $|z|^2$.

4.1 Computation of Normal Forms

Based on assumption 1, the two pairs of pure imaginary eigenvalues, at $\alpha = 0$, are such that there are no rational numbers $\frac{k_1}{k_2}$ with small $|k|$ satisfying $1 = \frac{k_1}{k_2}\nu$, that is, there are no *primary resonances* due to the low value of ν. Identifying $z_2 = \bar{z}_1$, $z_4 = \bar{z}_3$, the amplitude of the spindle speed modulation as $\mu = \sqrt{|z_3 z_4|}$ (a constant which depends on the initial conditions of the augmented ODE), and introducing the linear unfolding term given by $\lambda' \stackrel{\text{def}}{=} \frac{d\lambda}{d\alpha}|_{\alpha=0}$ yields the necessary differential equation in normal form for the unknown amplitude $z \stackrel{\text{def}}{=} z_1$, i.e.,

$$\dot{z}(t) - iz(t) - \alpha\lambda' z(t) - |\mu|^2 S(r_0, \nu)z(t) - \Lambda(r_0)|z(t)|^2 z(t) = 0, \tag{35}$$

where

$$\begin{aligned}
\Lambda(r_0) = &\left(c_{12} + \frac{c_{11}(2c_{02} + c_{11})}{B_0 + C_0} + \frac{2c_{11}c_{02} + c_{11}c_{20} + 2c_{20}c_{02}}{2i\,A_0 - 4 + B_0 + C_0 e^{-2ir_0}}\right)\frac{e^{-2ir_0}}{N} \\
&+ \left(c_{21} + \frac{c_{11}(c_{11} + 2c_{20})}{B_0 + C_0} + \frac{c_{11}c_{20}}{2i\,A_0 - 4 + B_0 + C_0 e^{-2ir_0}}\right)\frac{e^{ir_0}}{N} \\
&+ \left(3c_{03} + 2c_{21} + \frac{4{c_{02}}^2 + {c_{11}}^2 + 4c_{20}c_{02} + 4c_{11}c_{20} + 2c_{11}c_{02}}{B_0 + C_0}\right. \\
&\left.+ \frac{2c_{20}c_{02} + 2c_{11}c_{20} + c_{11}c_{02}}{2i\,A_0 - 4 + B_0 + C_0 e^{-2ir_0}}\right)\frac{e^{-ir_0}}{N} \\
&+ \frac{3c_{30} + 2c_{12}}{N} + \frac{4c_{20}c_{02} + {c_{11}}^2 + 4{c_{20}}^2 + 2c_{11}c_{20} + 4c_{11}c_{02}}{N(B_0 + C_0)} \\
&+ \frac{2{c_{02}}^2 e^{-3ir_0} + {c_{11}}^2 e^{-3ir_0} + c_{11}c_{02}e^{-4ir_0} + 2{c_{20}}^2 + {c_{11}}^2}{N\left(2i\,A_0 - 4 + B_0 + C_0 e^{-2ir_0}\right)}
\end{aligned}$$

$$\lambda' = -\frac{1}{N}\left(C_1 e^{-ir_0} + i\,A_1 + B_1\right), \quad N = A_0 + 2i - r_0 C_0 \exp(-ir_0),$$

$$S(r_0, \nu) = \frac{C_0 e^{-ir_0}}{N} \sum_{n\in\{-1,1\}} \left(\frac{1}{2} - \frac{C_0(1 + n\nu)\,e^{-i(1+n\nu)r_0}}{B_0 - (1 + n\nu)^2 + C_0 e^{-i(1+n\nu)r_0} + i\,(1 + n\nu)\,A_0}\right)$$

and the coefficients in terms of machine tool parameters are defined in (6) and (6). The main objective of this paper can now be answered by studying the reduced nonlinear equation (35), which represents the "normal form" of the original system (1) with periodic time delay.

5. Stability and Bifurcation Analysis

First, we clarify the mechanism for the suppression of regenerative chatter by examining the stability of the trivial solution, which is governed by equation (35) in polar coordinates

$$\dot{r}(t) = \left[\alpha\delta_c' + \mathcal{R}(r_0, \nu)\ |\mu|^2 + \Lambda^{Re}(r_0) r^2(t)\right] r(t) \tag{36}$$

where δ_c' is the crossing condition, stability index $\mathcal{R}(r_0, \nu)$ is the real part of $S(r_0, \nu)$, and $\Lambda^{Re}(r_0)$ is the real part of the nonlinear coefficient $\Lambda(r_0)$ all given in Appendix-II of [3]. When μ=0, it is obvious that the machine tool system is unstable for $\alpha > 0$, which is the chatter instability for constant spindle speed, as discussed in Section 2. Hence, stabilization is possible only if the real part of $S(r_0, \nu)$ is negative, i.e.,

$$\mathcal{R}(r_0, \nu) = \sum_{n\in\{-1,1\}} \frac{\mathcal{A}_n^c \cos(n\nu r_0) + \mathcal{A}_n^s \sin(n\nu r_0) + \mathcal{A}_n^0}{\mathcal{B}_n^c \cos(n\nu r_0) + \mathcal{B}_n^s \sin(n\nu r_0) + \mathcal{B}_n^0} < 0 \tag{37}$$

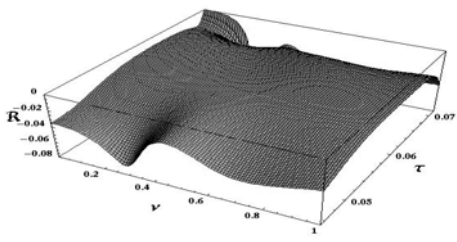

Figure 1. Variation of stability index $\mathcal{R}$

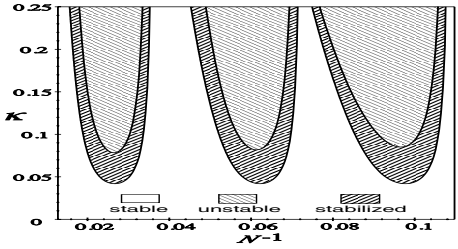

Figure 2. Stability chart with ν= 0.30

where the coefficients $\mathscr{A}_n$'s and $\mathscr{B}_n$'s are given in Appendix-III of [2, 3]. It is obvious from the above expression (37) that $\mathcal{R}(r_0, \nu)$ fluctuates with ν. It is important to determine the optimal value of ν for which $\mathcal{R}(r_0, \nu)$ has an infimum. Since the coefficients $\mathscr{A}_n$'s and $\mathscr{B}_n$'s are long and contains various powers of ν, tedious computations are involved to determine this optimal value of ν explicitly. Instead, by plotting the variation of $\mathcal{R}(r_0, \nu)$ and its derivative with ν, we identify the optimal frequency of the spindle speed variation. They are obtained in each lobe and the variation for the second lobe is shown in Figure 1.

As expected, the stability of the system improved with increasing **SSV**-frequency ν and the value of the optimal **SSV**-frequency varies form region to region.

From (37), we derive a new stability boundary which depends on the SSV-amplitude μ and SSV-frequency ν and the bifurcation parameter α. The new stability boundary, in terms of the width of cut, is given as

$$\alpha_{cr}^{ssv} = -|\mu|^2 \, \mathcal{R}(r_0, \nu)/\delta_c'. \tag{38}$$

Positive values of α_{cr}^{ssv} imply stabilization and greater widths of cut that could be achieved without chatter, while negative values of α_{cr}^{ssv} imply further destabilization. Finally, we show in Figure 2 a modest level of increase of stability, and the curves have similar parabolic lobes as the constant stability curves. The actual value of the improved width of cut can be easily calculated by multiplying the value from Figure 2 by the factor $|\mu|^2$, which denotes the square of the amplitude of the spindle speed modulation.
From (36), we have

$$r_1 = 0, \quad r_2 = \{-[\alpha\delta' + \mathcal{R}(r_0, \nu) \, |\mu|^2]/\Lambda^{Re}(r_0)\}^{1/2} \tag{39}$$

as the stationary solutions. The nontrivial solution indicates a delayed Hopf bifurcation and the sign of $\Lambda^{Re}(r_0)$ governs the qualitative behavior close to the new bifurcation point α_{cr}^{ssv}. The bifurcation is supercritical when $\Lambda^{Re}(r_0) < 0$, and subcritical when $\Lambda^{Re}(r_0) > 0$. In both cases the trivial solution becomes unstable for widths of cut larger than α_{cr}^{ssv}. However in subcritical bifurcations the increase of oscillation amplitude is sudden and sometimes very dangerous, a well known result in classical bifurcation theory.

6. Results and Conclusions

The mechanism of the SSV has been made clear through the development of a systematic analytic method, therefore obtaining the parameters crucial for SSV chatter control. An explicit formula (38) for the stability boundaries was obtained in terms of modulation amplitude, μ, and frequency, ν. This was achieved by developing an algebraic construction of four-dimensional center manifolds and the subsequent calculations of Hopf bifurcation for the **FDE** (12). Since these results are explicit, making use of the expression (37), we have showed how an optimal frequency ν can be determined to achieve greater widths of cut. We have also emphasized several key points that shed light on the underlying mathematical structure and the stabilization mechanism that exist in such infinite dimensional systems with one critical mode. It was shown in [2, 3] that the theoretical value of the optimal frequency ν was very close to that obtained experimentally in [11]. Finally, we predicted analytically the nonlinear behavior beyond the *new threshold of chatter* using three possible combinations of the nonlinear stiffness and cutting force coefficients. The delayed subcritical bifurcation behavior corresponding to the problem with only

cutting force characteristics, agrees with the results of Kalmár-Nagy *et al.* [12] and Liang [13].

In this and previous work [1–3], the *first author* and his co-workers were able to demonstrate analytically the potential effectiveness of **SSV** to eliminate cutting-tool chatter in turning based on a *one degree of freedom* model developed by Hanna and Tobias [4]. While these preliminary analytical studies were successful, there are many important questions that are left unanswered. For example, if the delayed bifurcation is subcritical, the stabilization due to SSV will not be significant due to the fact that any small disturbance can cause the oscillations to jump from small to large amplitudes. Hence, for a robust **SSV** design it is imperative to include random perturbations due to surface roughness, material inhomogeneity, environmental fluctuations, temperature variations and other unknown effects that are inherent in any cutting process. Random excitations can, over a long time interval, have significant interplay with the dynamics of nonlinear systems with periodic delay [14]; this effect can have direct impact upon material removal processes. There are no significant results reported on chatter dynamics which provide the effect of such random fluctuations on chatter characteristics. Therefore, the influence of these random excitations must be considered for an effective analysis. Future work should aim to address these issues using a combination of analytical and numerical efforts, bridging the gap from the one-degree of freedom turning model to realistic multi-degree of freedom models, specifically, for *high-speed milling* processes. These results are not presented due to the page limitation of these proceedings.

Acknowledgments

The first author and Ms. Sarah Wustrack would like to acknowledge the support of the National Science Foundation under grant numbers CMS 03-01412 and CMS 00-84944 (REU), respectively. Any opinions, findings, and conclusions or recommendations expressed in this paper are those of the authors and do not necessarily reflect the views of the National Science Foundation.

References

[1] Ali Demir, N. Sri Namachchivaya and W. F. Langford, "Nonlinear Delay Equations with Fluctuating Delay: Application to Regenerative Chatter," IMECE2002-32389, *American Society of Mechanical Engineers*; New York, NY, 12 pages, CD-ROM 2002.

[2] N. Sri Namachchivaya and R. Beddini, "Spindle Speed Variation for the Suppression of Regenerative Chatter," *Journal of Nonlinear Science*; 13:265-288, 2003.

[3] N. Sri Namachchivaya and H. J. Van Roessel, "A Center Manifold Analysis of Variable Speed Machining," *Dynamical Systems*; 18:245-270, 2003.

[4] N. A. Hanna and S. A. Tobias, "A Theory of Nonlinear Regenerative Chatter," *Journal of Engineering for Industry*, Transactions of the ASME; 35:247-255, 1974.

[5] T. Inamura and T. Sata, "Stability Analysis of Cutting Under Varying Spindle Speed," *Journal of The Faculty of Engineering, University of Tokyo-B*; 23:13-29, 1975.

[6] J. S. Sexton, R. D. Miline and B. J. Stone, "The Stability of Machining with Continuously Varying Spindle Speed," *App. Math. Modeling*; 1:311-318, 1977.

[7] J. K. Hale and S. J. Verduyn-Lunel, *Introduction to Functional Differential Equations*, Springer-Verlag; New York, 1993.

[8] T. Faria and L. T. Magalhães, "Normal Forms for Retarted Functional Differential Equations and Applications to Bogdanov-Takens Singularity," *Journal of Differential Equations*; 122:201-224, 1995.

[9] N. Chafee, "A Bifurcation Problem for a Functional Differential Equation of Finitely Retarded Type," *Journal of Mathematical Analysis and Applications*; 5:312-348, 1973.

[10] B. D. Hassard, N. D. Kazarinoff and Y. -H. Wan, "Theory and Applications of Hopf Bifurcation," *London Mathematical Society Lecture Note Series*. 41 Cambridge University Press, 1983.

[11] T. C. Tsao, M. W. McCarthy and S. G. Kapoor, "A New Approach to Stability Analysis of Variable Speed Machining Systems," *International Journal of Machine Tools and Manufacture*; 33:791-808, 1993.

[12] T. Kalmár-Nagy, G. Stépán and F. C. Moon, "Subcritical Hopf bifurcation in the delay equation model for machine tool vibrations," *Nonlinear Dynamics*; 26:121-142, 2001.

[13] Yan Liang, *Nonlinear Dynamics in Manufacturing Process*. Master's Thesis, University of Illinois, 2000.

[14] N. Sri Namachchivaya and R. Sowers, "Unified Approach for Noisy Nonlinear Mathieu-Type Systems," *Stochastics & Dynamics*; 1:405-450, 2001.

VERTICAL DYNAMICS OF RIDING CARS UNDER STOCHASTIC AND HARMONIC BASE EXCITATIONS

Walter V. Wedig
Institut für Technische Mechanik
Universität Karlsruhe (TH), Germany
wedig@itm.uni-karlsruhe.de

Abstract: Cars riding on rough road surfaces possess critical speeds for which the vertical car vibrations become resonant. The paper investigates these effects in case of harmonic and stochastic base excitations. The investigations are extended to nonlinear dynamics to calculate Lyapunov exponents and rotation numbers for quarter car models with bilinear damping characteristics. In the nonlinear case there are critical parameter values of the wheel suspension where stationary car vibrations bifurcate into chaos and exponential growth behavior.

Key words: Vertical car dynamics, resonant car speeds, bilinear damping, Lyapunov exponents, chaos and exponential growth.

1. Introduction

To investigate critical speeds v=const. of cars riding on rough road surfaces, quarter car models under stochastic and harmonic base excitations are considered. Figure 1 shows a car model with one degree of freedom consisting on a mass m, a linear spring with the elasticity constant c and a dashpot b with a bilinear damping characteristic depending on the vertical relative vibration velocity. If $z(t)$ denotes the given base excitation in dependence on the time t and $y(t)$ is the response of the car mass, the equation of motion is given by

$$\ddot{y} + 2D\omega_1(\dot{y} - \dot{z} + \gamma\,|\dot{y} - \dot{z}|) + \omega_1^2(y - z) = 0. \tag{1}$$

Herein, dots on $y(t)$ denote derivatives with respect to the time t. The parameters $\omega_1^2 = c/m$ and $D = b/(2\omega_1 m)$ are the squared natural frequency of the linear

G. Rega and F. Vestroni (eds.),
IUTAM Symposium on Chaotic Dynamics and Control of Systems and Processes in Mechanics, 371–381.

system and its dimensionless damping measure, respectively. Introducing the relative coordinate $x = y - z$ the equation of motion takes the form

$$\ddot{x} + 2D\omega_1(\dot{x} + \gamma\,|\dot{x}|) + \omega_1^2 x = -\ddot{z}, \qquad (x = y - z). \tag{2}$$

In both equations (1) and (2), the parameter γ quantifies the nonlinearity intensity of the bilinear damping mechanism.

According to [1], the bilinear damping characteristic can be realized e.g. by two different hydraulic bypasses for the up and down of the wheels, respectively by means of two different piston valves in the hydraulic damping cylinder. Moving up the first valve is closed and the second one is opened. Moving down both valves are operating vice versa. If the cross sections of the two valves are different, the bilinear damping characteristic, shown in figure 1, is evident. Note that the nonlinearity parameter is bounded by $|\gamma| < 1$ provided that the bilinear damping characteristic has to be realized by passive elements of dissipation. Bilinear damping characteristics with $|\gamma| \geq 1$ can only be realized by active elements of control. In extension to [2], both cases of nonlinearities are investigated particularly with respect to the stability of stationary vibrations. Main goal is to answer the question whether there are critical parameter values of the wheel suspension or which the stationary vibrations bifurcate into chaotic attractors.

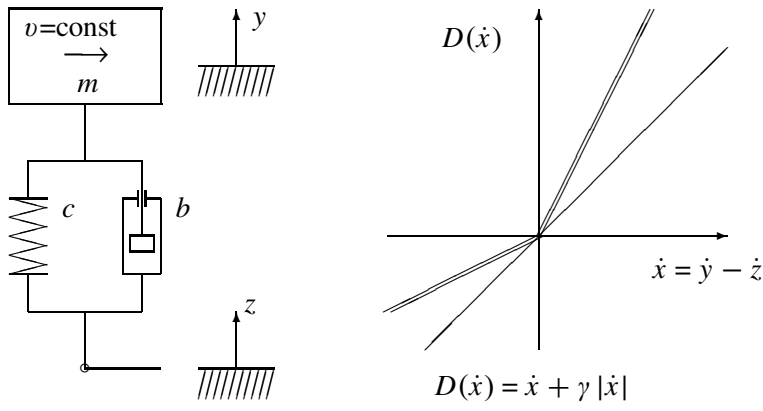

Figure 1. Quarter car model with bilinear damping characteristics

2. Resonances of Linear Car Vibrations

Base excitations of cars riding on roads are generated by rough surfaces of ways and roads. In a first investigation, the equation of motion (1) may be linear for a vanishing nonlinearity ($\gamma = 0$) and the road surface $z(s)$ is assumed to be harmonic of the form

$$z(s) = Z \cos \Omega s, \qquad \Omega = 2\pi / L. \tag{3}$$

Herein, Z denotes the amplitude of the harmonic surface function $z(s)$, s is the road coordinate and Ω is the road frequency defined by the wave length L of the road, as noted in (3). For constant car velocities, the road coordinate s is transformed into the time domain by $s = vt$. Accordingly, the stationary response of the vertical car vibrations is calculated by the set-up

$$y(t) = Y \cos(\Omega v t - \varepsilon), \qquad s = vt. \tag{4}$$

Herein, Y and ε are amplitude and phase, respectively. Introducing (4) into the equation (1) leads to the amplitude ratio

$$\frac{Y}{Z} = \sqrt{\frac{1 + (2D\nu)^2}{(1 - \nu^2)^2 + (2D\nu)^2}}, \qquad \nu = \Omega \frac{v}{\omega_1}. \tag{5}$$

This is a well-known result of the linear vibration theory completely determined by the two parameters D and ν, where ν is the related frequency speed given by the road frequency Ω times the car velocity v related to the natural frequency ω_1 of the vertical car vibrations. Figure 2 shows typical amplitude frequency diagrams for the damping values $D = 0.11, 0.2, 0.3$ and $D = 0.5$. Note that the scaling of the relative frequency speed in figure 2 is linear with $\nu = n$ in the first range $0 \leq n \leq 1$ and hyperbolic with $\nu = 1/(2 - n)$ in the second range $1 \leq n < 2$.

Following [3], more realistic road surfaces are random functions appropriately generated from broad-banded processes by means of filter equations. For this purpose, the following first order filter equation is applied:

$$dZ_s = -\Omega Z_s ds + \sigma dW_s, \qquad E(dW_s^2) = ds. \tag{6}$$

Herein, Z_s is the filter process in dependence on the way coordinate s and W_s denotes the Wiener process with stationary increments dW_s normally distributed with zero mean and normalized mean square, as noted in (6). The parameter σ denotes the intensity of dW_s and Ω is a way frequency with dimension $1/m$ determining the bandwidth of Z_s in the way domain. The stationary solution of the filter equation (6) has a zero mean, the mean square σ_z^2 and the power spectrum $S_z(\bar{\omega})$, as follows:

$$S_z(\bar{\omega}) = \frac{\sigma^2}{\bar{\omega}^2 + \Omega^2}, \qquad \sigma_z^2 = E(Z_s^2) = \frac{\sigma^2}{2\Omega}. \tag{7}$$

According to [3], the transformation of the filter equation into the time domain is performed by means of the momentary car velocity v, as follows:

$$dW_s = \sqrt{v}\,dW_t, \qquad E(dW_t^2) = dt \tag{8}$$

$$dZ_t = -\Omega v Z_t dt + \sigma\sqrt{v}\,dW_t, \qquad ds = v\,dt. \tag{9}$$

In the time domain, the filter equation (8) possesses stationary solutions which have the following power spectrum and mean square value:

$$S_z(\omega) = \frac{\sigma^2 v}{\omega^2 + \Omega^2 v^2}, \qquad \sigma_z^2 = E(Z_s^2) = \frac{\sigma^2}{2\Omega}. \tag{10}$$

Same results can be derived by a direct transforming of the power spectra from road frequencies to time frequencies [4]. Some more details are given in [5].

Applied to the equation of motion (1) the spectral method leads for vanishing nonlinearity ($\gamma = 0$) to the power spectrum $S_y(\omega)$ of the entire road-vehicle system

$$S_y(\omega) = \frac{\sigma^2 v[\omega_1^4 + (2D\omega_1\omega)^2]}{[(\omega_1^2 - \omega^2)^2 + (2D\omega_1\omega)^2](\omega^2 + \Omega^2 v^2)}. \tag{11}$$

It is integrated over the entire frequency range to obtain the root-mean-square

$$\frac{\sigma_y}{\sigma_z} = \sqrt{\frac{2D + (1 + 4D^2)\nu}{2D[1 + (\nu + 2D)\nu]}}, \qquad \nu = \Omega\frac{v}{\omega_1}. \tag{12}$$

It gives a measure for the amplitudes of the vertical car vibrations. Figure 2 shows numerical evaluations of the related σ_y over the related frequency

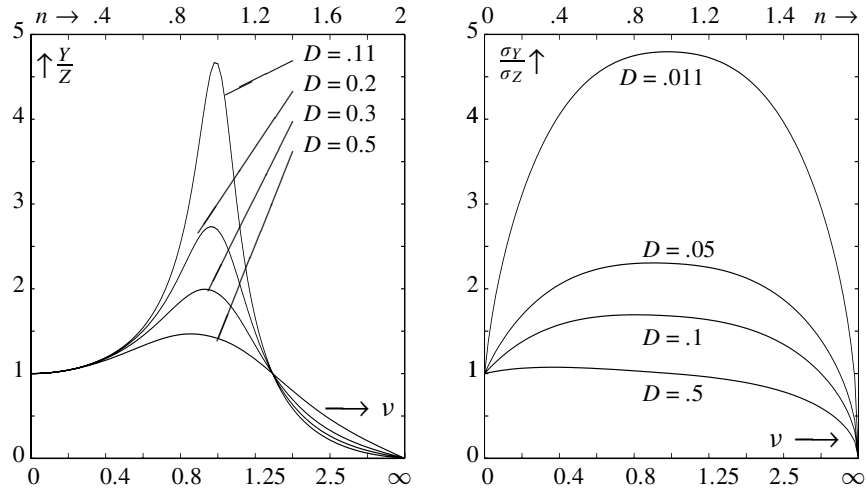

Figure 2. Resonances in case of harmonic and stochastic excitations

speeds ν. Comparing both resonance diagrams in figure 2 shows clearly that both excitations, the harmonic and stochastic base excitation, lead to similar resonance effects when the dimensionless car speeds are near one. The only difference between both is that the resonance peaks become broader when the narrow banded harmonic excitation is replaced by a broad band excitation in the stochastic case.

3. Main Effects of Bilinear Damping

To derive main effects of bilinear damping mechanisms, it is sufficient to replace the base excitation of the filter process Z_t by white noise $-\sigma \dot{W}_t$ of intensity σ. For this purpose, the equation of motion is applied in its relative form (2), where $X_t = Y_t - Z_t$. Introducing the state process $V_t = \dot{X}_t$ of the vertical vibration velocity, the equation (2) takes the first order form

$$\dot{X}_t = V_t, \qquad V_t = -2D\omega_1(V_t + \gamma\,|V_t|) - \omega_1^2 X_t + \sigma \dot{W}_t\,. \tag{13}$$

This modelling by white noise reduces the number of parameters. However, it possesses the disadvantage that only relative motions of the vertical car vibrations can be investigated and there is no influence of the car velocities.

Introducing the dimensionless time $\tau = \omega_1 t$ and the related processes

$$X_t = \bar{X}_t\sqrt{E(X_t^2)}, \qquad E(X_t^2) = \sigma^2/(2D\omega_1^3), \tag{14}$$

$$V_t = \bar{V}_t\sqrt{E(V_t^2)}, \qquad E(V_t^2) = \sigma^2/(2D\omega_1), \tag{15}$$

the first order equations (13) take the dimensionless increment form

$$d\bar{X}_\tau = \bar{V}_\tau d\tau, \qquad d\bar{V}_\tau = -[2D(\bar{V}_\tau + \gamma\,|\bar{V}_\tau|) + \bar{X}_\tau]d\tau + 2\sqrt{D}\,dW_\tau\,, \tag{16}$$

wherein the time increment and corresponding noise terms are given by

$$d\tau = \omega_1 dt, \qquad dW_\tau = \sqrt{\omega_1}\,dW_t\,. \tag{17}$$

Note that in the linear case ($\gamma = 0$), the dimensionless equations (16) have the stationary solutions $E(\bar{X}_\tau^2) = E(\bar{X}_\tau^2) = 1$. For $|\gamma| > 0$, the 4 parameters in equation (13) are reduced to D and γ, meanwhile the other two parameters σ and ω_1 are eliminated. They have no influence in the following analysis.

Figure 3 shows a typical density distribution of the stationary state processes $\bar{X}_\tau$ and $\bar{V}_\tau$. The right side of figure 3 gives a three dimensional picture of the density $p(x, v)$. Associated contour lines are shown in the left side o figure 3. Both pictures are taken for the parameters $D = 0.25$ and $\gamma = 3.0$. In comparison with the elliptic, perfectly symmetric contour lines of a normal distribution obtained in the linear case for $\gamma = 0$, the nonlinear density distribution, shown in figure 3, is highly nonsymmetric. The top point of the density

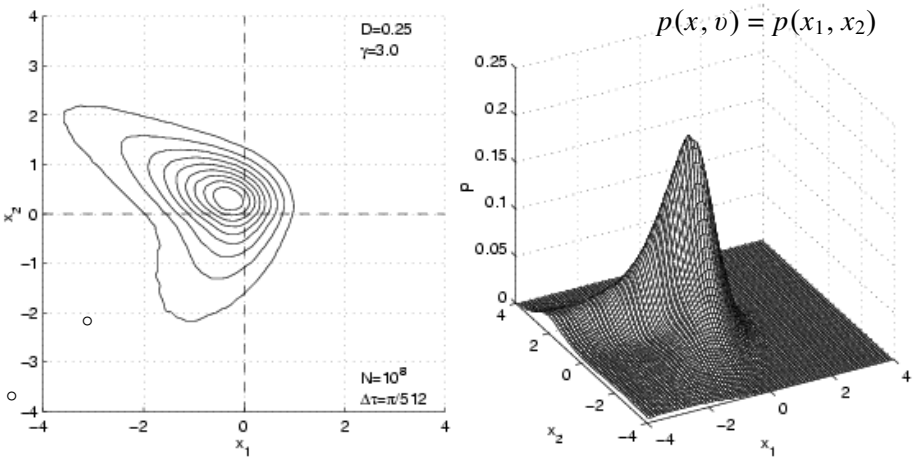

Figure 3. Stationary distribution density of the state space processes

is shifted to the upper left quarter of the state space and the distribution is obviously clockwise rotated out of the symmetry axis indicating that both state processes are correlated in the nonlinear case. To obtain the two-dimensional density in figure 3, the system equations (16) are approximated by means of the Euler forward difference scheme

$$\bar{X}_{n+1} = \bar{X}_n + \bar{V}_n \Delta\tau, \qquad \Delta W_n = R_n \sqrt{\Delta\tau}, \tag{18}$$

$$\bar{V}_{n+1} = \bar{V}_n - [2D(\bar{V}_n + \gamma\,|\bar{V}_n|) + \bar{X}_n]\Delta\tau + 2\sqrt{D}\,\Delta W_n\,. \tag{19}$$

Herein, R_n denotes a sequence of random numbers normally distributed with zero mean and the normalized mean square $E(R_n^2) = 1$. The scan rate selected for the Monte-Carlo simulation in figure 3, was $\Delta\tau = \pi/512$ applied for $n = 0, 1, 2, \ldots$ up to $N = 10^8$ sample points.

The same simulation data are applied to obtain the mean values of both related state processes $\bar{X}_\tau$ and $\bar{V}_\tau$ and their stationary root-mean-square values in dependence on the nonlinearity parameter γ for the fixed damping value $D = 0.5$. The results, given in figure 4, show the main effect of the bilinear damping mechanism. For increasing nonlinearity parameter $\gamma > 0$, the mean values are proportionally shifted to the negative range meanwhile the root-mean-square values remain approximately unchanged. Therewith, the danger that the bouncing wheel sets hit their upper limits is reduced without any loss of comfort. Furthermore, the driving safety is increased since lowering the mean values leads to higher contact forces between wheel and road.

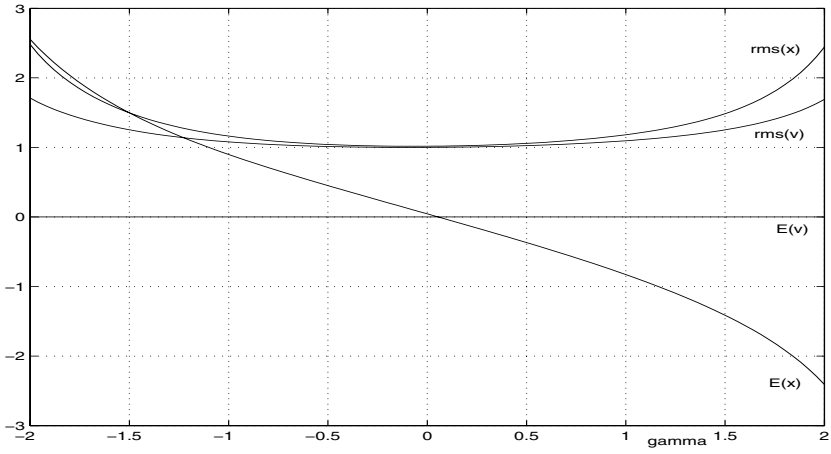

Figure 4. Mean- and rms-values of the stationary state processes

4. Stability, Chaos and Exponential Growth

The above statement on driving stability of cars is only true provided that the stationary car vibrations remain asymptotically stable with increasing nonlinearity. Therefore, it is necessary to investigate the stability reserve by means of the Lyapunov exponents of the stationary car vibrations. For this purpose, the stationary car vibrations X_{st} and V_{st} are perturbed so that perturbations ΔX_τ and ΔV_τ are generated which are investigated by

$$\bar{X}_\tau = X_{st} + \Delta X_\tau, \qquad \bar{V}_\tau = V_{st} + \Delta V_\tau. \tag{20}$$

Introducing (20) into the equation system (13) leads to two dynamic systems: the first one for the stationary car vibrations which satisfy the original equation of motion

$$dX_{st} = V_{st}d\tau, \quad dV_{st} = -[2D(V_{st} + \gamma\ |V_{st}|) + X_{st}]d\tau + 2\sqrt{D}dW_\tau \tag{21}$$

and the second one for the perturbations which is derived to

$$d\Delta X_\tau = \Delta V_\tau d\tau, \quad d\Delta V_\tau = -[2D\Delta V_\tau(1 + \gamma\,\mathrm{sign}V_{st}) + \Delta X_\tau]d\tau. \tag{22}$$

Note that the sign-function in (22) follows from the limiting procedure

$$\lim_{\Delta V_\tau \to \infty} \frac{1}{\Delta V_\tau}(|V_{st} + \Delta V_\tau| - |V_{st}|) = \mathrm{sign}V_{st} \tag{23}$$

provided that the perturbations are infinitesimally small. Correspondingly, the variational equations (22) are linear. They decide the exponential time behavior of the perturbations and therewith the asymptotic stability of the stationary car vibrations.

According to [6], the polar coordinate processes defined by

$$A_\tau = \sqrt{\Delta X_\tau^2 + \Delta V_\tau^2}, \qquad \Psi_\tau = \arctan \frac{\Delta V_\tau}{\Delta X_\tau}\ , \tag{24}$$

are introduced into the variational equations (22). They lead to transformed equations of the following form:

$$d\Psi_\tau = -[1 + D(1 + \gamma\ \mathrm{sign} V_{st}) \sin 2\Psi_\tau] d\tau, \tag{25}$$

$$d \ln A_\tau = -2D(1 + \gamma\ \mathrm{sign} V_{st}) \sin^2 \Psi_\tau d\tau\ . \tag{26}$$

Both increment equations can formally be integrated and related to the time in order to obtain the corresponding mean value in the time domain. The first time average (26) denotes the rotation number ϱ_1

$$\varrho_1 = -1 - D \lim_{t\to\infty} \frac{1}{t} \int_0^t (1 + \gamma\ \mathrm{sign} V_{st}) \sin 2\Psi_\tau d\tau \tag{27}$$

$$\lambda_1 = -2D \lim_{t\to\infty} \frac{1}{t} \int_0^t (1 + \gamma\ \mathrm{sign} V_{st}) \sin^2 \Psi_\tau d\tau \tag{28}$$

and the second time average (27) represents the top Lyapunov exponent λ_1. According to the multiplicative ergodic theorem of Osceledec, it determines the exponential time behavior of the perturbations ΔX_τ and ΔV_τ and therewith the asymptotic stability of the stationary vibration X_τ and V_τ.

The variational equations (22) possess the linear vector form

$$\dot{\vec{x}} = A(t)\vec{x}, \qquad \lambda_n \le \ldots \le \lambda_2 \le \lambda_1, \tag{29}$$

where $A(t)$ is a n×n matrix of the system and $\vec{x}$ is a n-dimensional state vector whose exponential growth behavior is determined by the Lyapunov exponents, noted in (29). Associated to the above vector equation, there is an adjoint system of the form

$$\dot{\vec{y}} = -A^T(t)\vec{y}, \qquad \mu_n \le \ldots \le \mu_2 \le \mu_1. \tag{30}$$

The Lyapunov exponents λ_i and μ_i of both systems satisfy the relation [7]

$$\lambda_i + \mu_i = 0 \qquad \text{for all} \quad i = 1, 2, \ldots, n. \tag{31}$$

Therewith, the smallest Lyapunov exponent λ_n of the original system can easily be calculated by the top Lyapunov exponent of the adjoint system. According to the theorem of Liouville, the sum of all Lyapunov exponents is given by

$$\Lambda = \sum_{i=1}^n \lambda_i = \lim_{t\to\infty} \frac{1}{t} \int_0^t \sum_{i=1}^n a_{ii}(t) dt, \tag{32}$$

where $a_{ii}(t)$ are the diagonal terms of the system matrix $A(t)$. Figure 5 shows numerical evaluations of the three Lyapunov exponents λ_1, λ_2 and Λ=$E(divf)$ for the damping measure $D = 0.5$ in dependence on the nonlinearity parameter γ. Obviously, the top Lyapunov exponent changes the sign shortly before $\gamma = 2.75$ denoting the boundary between stability and chaos, where the stable stationary vibrations bifurcate into a stochastic attractor. At $\gamma = 3.0$, all Lyapunov exponents jump to positive values where the stochastic attractor bifurcates into hyper-chaos. Probably, the jumps of all Lyapunov exponents are due to the bilinear damping mechanism and can be avoided when the damping characteristic is smoothed out. The last figure represents a stability map over the parameter space of damping D and nonlinearity γ. Solid lines give zero values of both Lyapunov exponents λ_1 and λ_2. Dot-dashed lines belong to vanishing Lyapunov exponents Λ of the phase volume behavior. Note that between stability and exponential growth behavior there is only a small chaos region.

5. Summary and Conclusions

Bilinear damping characteristics of quarter car models lead to the effect, that the stationary response of cars riding on rough road surfaces possesses highly nonsymmetric distribution densities with the consequence, that the stationary mean of the vertical car vibrations is shifted to negative values meanwhile all other mean values and the response variances remain unchanged,

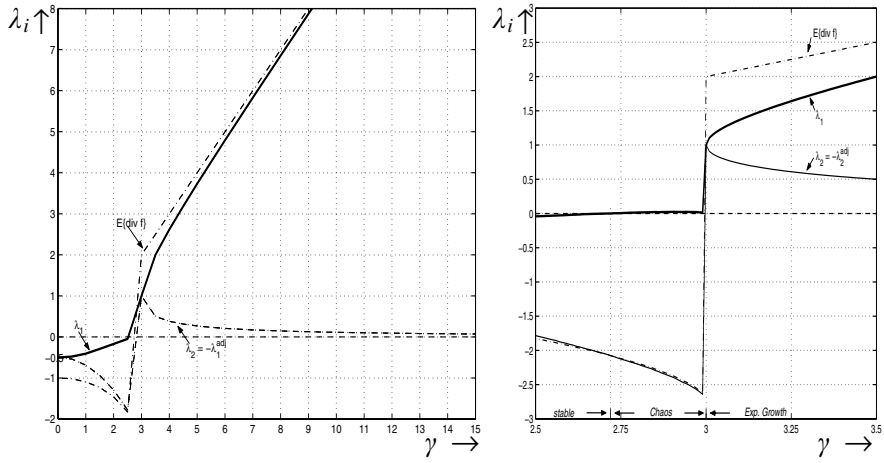

Figure 5. Lyapunov exponents versus nonlinearity parameter γ [8]

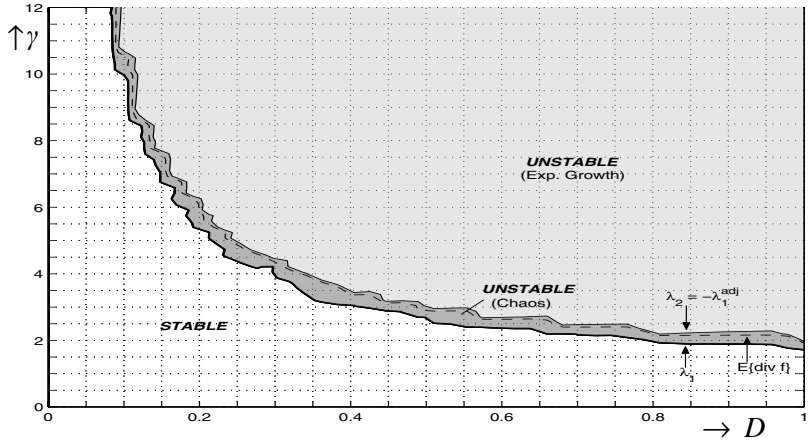

Figure 6. Stability, chaos and exponential growth in the parameter space [8]

approximately. Lowering mean values of the vertical vibrations effect higher contact forces between wheel and road leading to more safety and driving stability.

The paper investigates the stability of the vertical car vibrations for increasing nonlinearity parameter γ. For this purpose, the stationary solution is perturbed in order to determine the top Lyapunov exponent of the perturbed solution by means of the multiplicative ergodic theorem. For negative Lyapunov exponents the stationary solution is asymptotically stable. If the top Lyapunov exponent becomes positive for increasing nonlinearity parameter γ, the perturbed solution will become unstable leading to stochastic attractors.

References

[1] D. Ammon, *Modellbildung und Systementwicklung in der Fahrzeugdynamik*, B.G. Teubner, Stuttgart, 1997.

[2] W. V. Wedig and U. von Wagner, "Stochastic car vibrations with strong nonlinearities," *ASME 2001 Design Engineering Technical Conferences*, September 9-12, Pittsburgh, PA, VIB-21605, pp. 1-7, 2001.

[3] W. Wedig, "Dynamics of cars driving on stochastic roads," (Proceedings of the fourth International Conference on Computational Stochastic Mechanics, Corfu, Greece, June 2002). In: *Computational Stochastic Mechanics* ed. by P.D. Spanos & G. Deodatis, Millpress, Rotterdam, pp. 647-654, 2003.

[4] K. Popp and W. Schiehlen, *Fahrdynamik*, B.G. Teubner, Stuttgart, 1993.

[5] J.D. Robson and C.J. Dodds, "Stochastic Road Inputs and Vehicle Response," *Vehicle System Dynamics* 5, pp.1-13, 1975/76.

[6] W. Wedig, "Characteristic Numbers — Vertical Dynamics of Cars Riding on Roads," *6eme Congres de Mecanique, Mecanique des Solides*, Tome I, Tanger, Maroc. Universite Abdelmalek Essaadi, Societe Marocaine des Sciences Mecanique, pp. 44-45, Avril 2003.

[7] W. Hahn, *Stability of Motion*, Springer-Verlag, Berlin, 1967.

[8] H. Hetzler, *Stabilität eines nichtlinearen Schwingungssystems unter harmonischer und stochastischer Anregung*. Diplomarbeit am Institut für Technische Mechanik der Universität Karlsruhe, Februar 2003.

VI.

CONTROL OF SYSTEMS AND PROCESSES

Control of nonlinear dynamic *systems* and *processes* is at the center of many engineering applications. Several relevant techniques and phenomena are the focus of the sixth part of the Proceedings, which opens with the Key Lecture of the Symposium given by Ali Nayfeh of the Virginia Polytechnic Institute and State University, USA. The rest of the papers are compiled alphabetically, based on the last name of the first author.

Ali Nayfeh *et al* report on the design and implementation of a nonlinear controller, based on delayed-position feedback, that suppresses cargo pendulation on cranes in the presence of noise, initial sway, and wind disturbances. The effectiveness of the controller is demonstrated through nonlinear numerical simulations and scaled models of ship-mounted, rotary, and container cranes. As a result of pendulation reduction, both the rate of cargo-transfer operation and the range of operating sea conditions can be greatly improved.

A few papers are related to applications in biomechanics of locomotion, robotics, and manipulation. Chernousko investigates multibody systems moving along a plane in the presence of dry friction. Control forces created by actuators installed at the joints of the mechanism show to be effective in ensuring periodic motions of different configurations of multibody systems, as well as a maximum average speed of the relevant motions.

Schiehlen and Guse address the problem of realizing periodic motions by a passive limit cycle of a nonlinear conservative system and some additional low energy control. They show how, by adding control to conservative systems, asymptotic stable, weakly dissipative limit cycle oscillations can be obtained and adapted to prescribed motions in manufacturing processes, by significantly reducing the energy consumption.

Yabuno et al. propose a method for motion control of an underactuated manipulator, in which information on the free link is not required. The concept is based on the appropriate actuation of the perturbation of pitchfork

G. Rega and F. Vestroni (eds.),
IUTAM Symposium on Chaotic Dynamics and Control of Systems and Processes in Mechanics, 383–384.

bifurcations produced in the free link under high-frequency excitation, and is validated through experiments on a simple apparatus.

The nonlinear coupling between flexural and torsional oscillations in long slender drillstrings is investigated by Kreuzer and Struck. Vibrations generated during the drilling process for the exploration of oil and gas resources are dangerous, and reduce the overall efficiency. A theoretical and experimental study is performed to model the phenomenon and implement a control strategy. Since the bending vibrations depend on torsion, just the torsional vibrations are actively damped through an effective control procedure in which the measured signals are reduced by a recursive use of proper orthogonal decomposition.

Steindl et al. address the optimal control of the retrieval of a tethered subsatellite to a space ship, which is an important and complicated operation during a tethered satellite system mission. Uncontrolled retrieval results in strong oscillatory motion of the tether. The proposed optimal control strategy is a first successful step to achieve a force controlled retrieval of the subsatellite from the radial relative equilibrium position far away from the space ship to the corresponding position close to the space ship.

Finally, two papers investigate mechanisms of passive vibration control, based on attaching a proper subsystem to the main system. Popp and Rudolph give an insight in basic excitation mechanisms of friction-induced vibrations, which are unwanted phenomena in technical applications, and show possible ways of avoidance. Investigating in detail a dynamic vibration absorber, they show numerically and experimentally that stick-slip vibration can be avoided or reduced by an additional spring-mass-damper system attached to the main oscillator. Vakakis et al. deal with the energy pumping phenomenon, which denotes a passive, one-way, irreversible transfer of energy from a linear structure to a nonlinear attachment. Theoretically and experimentally observed multifrequency energy pumping cascades are particularly interesting from a practical point of view, since they indicate that nonlinear attachments can be designed to resonate and extract energy from an a priori specified set of modes of a linear structure, consistent with design objectives.

A DELAYED-POSITION FEEDBACK CONTROLLER FOR CRANES

Ali H. Nayfeh, Ziyad N. Masoud, and Nader A. Nayfeh
Department of Engineering Science and Mechanics, MC 0219,
Virginia Polytechnic Institute and State University, Blacksburg, VA 24061
anayfeh@vt.edu/zmasoud@vt.edu

Abstract: We have designed and implemented a nonlinear controller, based on delayed-position feedback, that suppresses cargo pendulation on most common military and commercial cranes in the presence of noise, initial sway, and wind disturbances. The controller is designed to operate transparently to the crane operator, thereby eliminating any special training requirements for crane operators and furnishing smoother and faster transport operations. The system can be operated in both the automated and manual modes and is capable of handling an operator stop command at any random time. Neither the trajectory nor the end point of the transport maneuver needs to be predefined. The controller is insensitive to the system parameters and can handle base excitations, initial sways, and noise. Such a control can be achieved with the heavy equipment that is already part of existing cranes so that retrofitting them would require a small effort. Most large-scale mechanical drivers have inherent time delays. Instead of compensating for these time delays, the proposed feedback controller makes use of these time delays. The effectiveness of the controller has been demonstrated using fully nonlinear numerical simulations as well as on scaled models of ship-mounted, rotary, and container cranes. The numerical and experimental results demonstrate that pendulations can be significantly reduced, and therefore the rate of operation can be greatly increased and the range of sea conditions in which cargo-transfer operations can take place can be greatly expanded. Moreover, because the controller eliminates pendulations of the load, the power needed in the controlled case is guaranteed to be less than the power needed in the uncontrolled case.

Key words: Delay controller, boom crane, rotary crane, container crane, ship-mounted crane, pendulation, pendulum

G. Rega and F. Vestroni (eds.),
IUTAM Symposium on Chaotic Dynamics and Control of Systems and Processes in Mechanics, 385–395.

1. Introduction

Ship-mounted cranes, such as those shown in Figure 1, are used to transfer cargo at sea from large container ships to smaller ships. During the transfer operation, wave-induced ship motions can produce large pendulations of cargo being hoisted and cause operations to be suspended. Vaughers [1] and Vaughers and Mardiros [2] reported that, in Joint Logistic over the Shore (JLOTS), JLOTS II, and JLOTS III operations, once seas built to a low sea state 3 (as defined by the Pierson-Moskowitz Sea Spectrum with significant wave heights in the range of 1.0 - 1.6 m), crane payload pendulations on The Auxiliary Crane Ships (T-ACS ships) became dangerously large and the operations had to be suspended. Since much time and money can be wasted waiting for acceptable sea conditions, it is important to develop ship-mounted cranes capable of cargo transfer in sea state 3 and higher.

Also, cranes are increasingly used in transportation and construction. During operations using rotary cranes, inertial forces due to operator commands lead to an increase in payload pendulations. In addition to posing hazardous work conditions, these pendulations slow down the rate of operation and increase the operational cost. Moreover, cranes are getting larger, faster, and higher, necessitating efficient controllers to guarantee fast turn-over time and

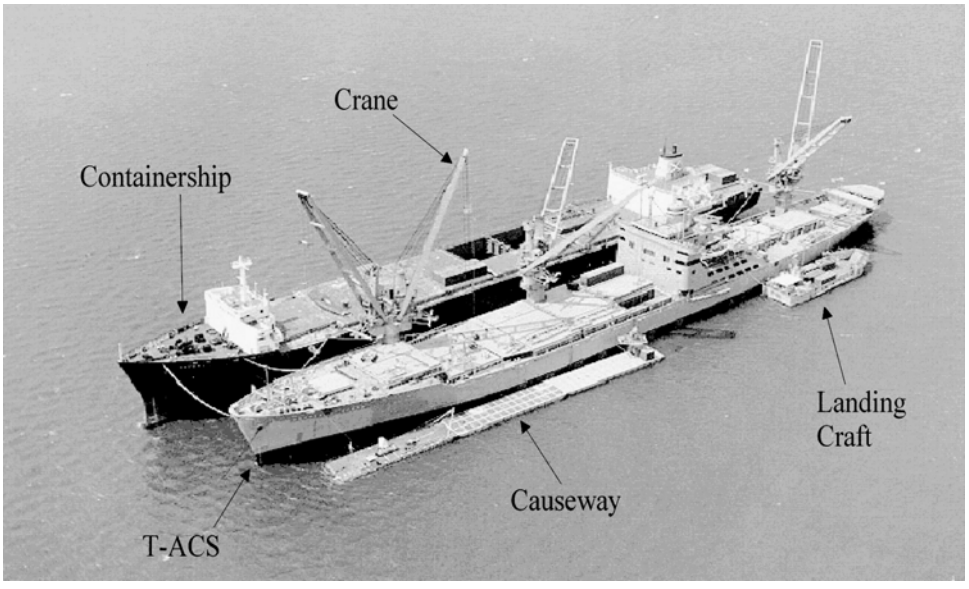

Figure 1. Typical T-ACS cargo transfer scenario.

to meet safety requirements. Consequently, the last 40 years have seen mounting interest in research on the modeling and control of cranes [3].

One of the common recent strategies of controlling payload pendulations without including the operator in the control loop is "Input Shaping" [3-5]. For a predefined endpoint of transport, the input shaping controller adjusts the length of the hoist cable and drives the suspension point of the payload along predefined (shaped) trajectories that avoid exciting payload pendulations. This approach requires time optimal trajectories of the crane system. Also, in controllers based on LQR, the crane maneuvers had to be pre-defined [6]. Another approach is an input shaping strategy in which the controller accelerates in steps of constant acceleration and then kills the acceleration when the load reaches zero-pendulation angle. The same approach is used in the deceleration stage [7-12]. Filtering out unwanted frequencies in the input commands of the crane operator, Parker et al. [13,14] and Lewis et al. [15] used a three-dimensional linear model of a boom crane to include the crane operator commands in the control loop of rotary and boom cranes. Experimental results showed a significant reduction in the cargo pendulations. However, the filtering process imposed significant delays between the operator-commanded input and the filtered input to the crane.

Optimal control techniques and input shaping techniques are limited by the fact that they are extremely sensitive to variations in the parameter values about the nominal values and to changes in the initial conditions and external disturbances and that they require "highly accurate values of the system parameters" to achieve satisfactory system response [16-18]. While a good design can minimize the controller's sensitivity to changes in the payload mass, it is much harder to alleviate the controller's sensitivity to changes in the cable length. In fact, Singhose et al. [19] showed that input shaping techniques are sensitive to the pendulation natural frequency. As a result, they suffer significant degradation in crane maneuvers that involve hoisting. Furthermore, input shaping and optimal control techniques require a predetermined endpoint of the transport process. This makes them less practical because most crane operations are coordinated visually by the crane operator. Linear controllers and static feedback linearization control techniques have very poor performance and usually fail due to the highly nonlinear nature of the payload oscillations [20]. Moreover, these control strategies are of limited use when excitations are introduced through the base of the crane, as in ship-mounted cranes. Imazeki et al. [21] used a 35-ton active mass-damper system to control the pendulations in one plane of a barge-mounted crane. The system reduced the payload pendulations by 67%.

We have developed a strategy [22-26] by which cargo pendulations of a crane payload are significantly suppressed by forcing the suspension point of the payload hoisting cable to track inertial reference coordinates, which

consist of a percentage of the delayed motion of the payload in the inertial horizontal plane relative to the suspension point superimposed on the operator commanded motion. The in-plane and out-of-plane pendulations in boom and tower cranes are controlled by simply actuating the luff and slew angles of the boom. These degrees of freedom already exist in ship-mounted cranes, and therefore modification to the hardware of current cranes would be limited to the addition of a few sensors and electronics to execute the control algorithm. The control strategy is based on time-delayed position feedback of the payload cable angles. This control algorithm is superimposed transparently on the input of the crane operator, which eliminates any special training requirements for crane operators and furnishes smoother and faster transport operations.

The effectiveness of the control strategy has been demonstrated using numerical simulations of computer models of ship-mounted (the T-ACS crane), rotary, and container cranes. Furthermore, the control strategy has been applied to, and tested on, experimental scaled models of rotary cranes operating in both rotary and gantry modes of operation and the T-ACS crane excited by the motion of a platform with three degrees of freedom, which correspond to the heave, pitch, and roll of a ship. These results are summarized next.

2. Ship-Mounted Cranes

A number of numerical simulations was carried out for the full-scale T-ACS crane. At the beginning of one set, the crane was oriented so that the boom was extended over the side of the ship perpendicular to its axis. The boom luff angle was set equal to 45°. The controller was turned off, and the crane operator executed a sinusoidal slewing action through 90° and back in every 40 seconds. The same simulation was then repeated with the controller turned on. The results of the controlled and uncontrolled in-plane and out-of-plane angles of the hoisting cable are shown Figure 2. The payload pendulation in the uncontrolled simulation grew rapidly to approximately 85° in-plane and 80° out-of-plane; while in the controlled simulation the in-plane and out-of-plane pendulation angles remained within 8°.

To validate the theory and the computer simulations, we built an experimental setup. A $1/24$ scale model of a T-ACS crane was mounted on the moving platform of a Carpal wrist mechanism, as shown in Figure 3. A rotary platform with a 1:45 gear ratio was used to give the crane its slewing degree of freedom.

The platform used is capable of producing arbitrary independent roll, pitch, and heave motions. A desktop computer supplies the roll, pitch, and heave commands to the platform motors. The platform was driven to simulate the motion of the crane ship. A $1/24$ scale model of an 8 ft by 8 ft by 20 ft

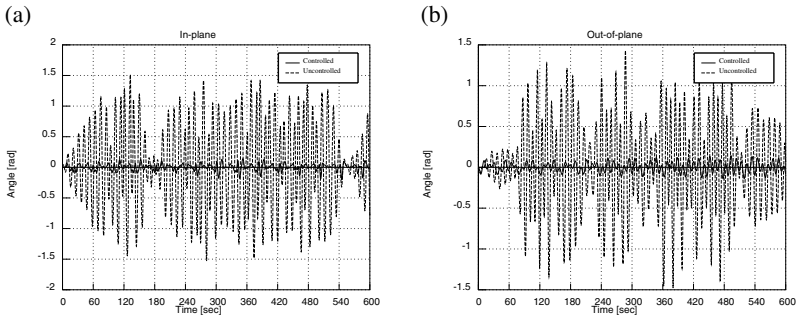

Figure 2. Computer simulations: (a) in-plane and (b) out-of-plane angles of the payload cable as functions of time. The ship was excited sinusoidally in roll and pitch at the natural frequency of the payload pendulation and sinusoidally in heave at twice the natural frequency of the payload pendulation and the crane was performing a slewing action through 90° and back every 40 seconds.

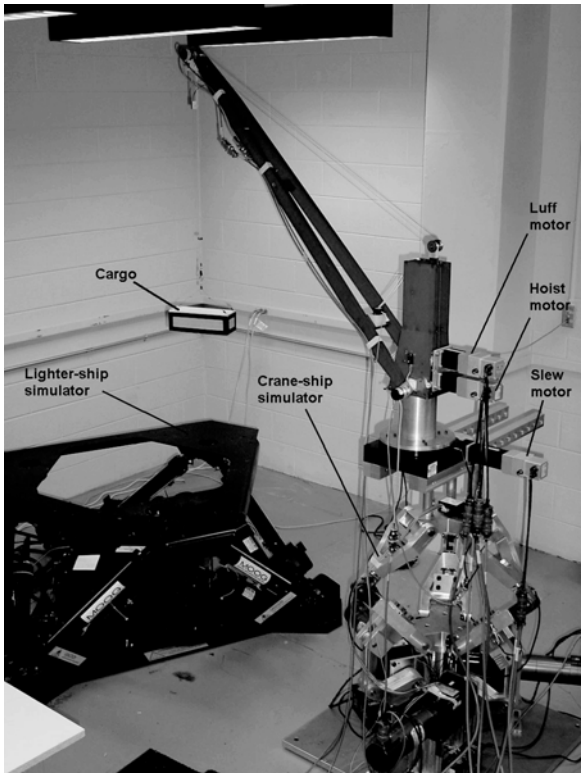

Figure 3. A 1/24 scale model of the T-ACS crane mounted on the three-degrees-of-freedom Carpal wrist platform used to simulate ship motions.

container weighing 20 *tons* was used as a payload. The center of gravity of the payload was located 1 *m* below the boom tip. This length yields a pendulation frequency of 0.498 Hz. The delayed-position feedback controller algorithm was designed in a way that it could be turned on and off at any time during the experiment.

Again, a number of experiments were carried out. In one set, the crane model was initially extended over the side of the modeled ship and perpendicular to its axis. The boom luff angle was set equal to 45°. The crane operator performed a sinusoidal slewing action from 0° to 90° in every 8 seconds. In the uncontrolled case, as shown in Figure 4, the excitation together with the slewing action caused the amplitude of the pendulation angles to grow rapidly, and the experiment had to be stopped after 10 seconds when the in-plane pendulation angle reached approximately 70°. The same experiment was then repeated with the controller being turned on. The maximum amplitude of the in-plane and out-of-plane pendulation angles remained less than 6°.

3. Container Cranes

A number of full-scale simulations were carried out for the container crane shown in Figure 5. The operation requirement is to move the container from a ship to a waiting truck 50 m away in 21.5 seconds while the crane performs a variety of hoisting maneuvers. At the end of the transfer maneuvers, the payload sway should settle to less than 50 mm within 5 seconds.

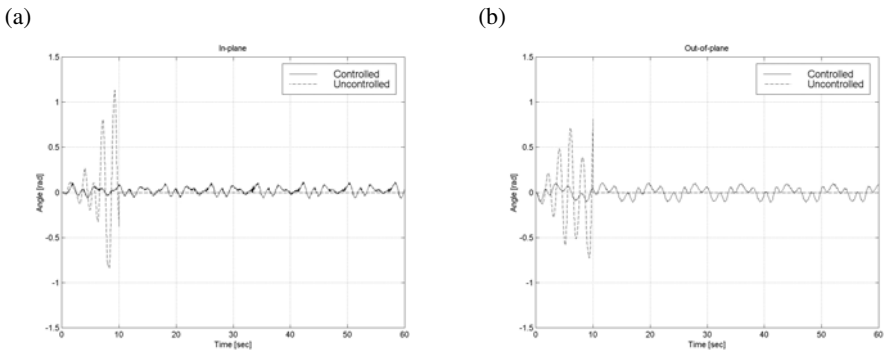

Figure 4. Experimental results: (a) in-plane and (b) out-of-plane angles of the payload cable as functions of time. The platform was excited sinusoidally in roll and pitch at the pendulation frequency of the payload and sinusoidally in heave at twice the pendulation frequency of the payload and the crane model was performing a slewing action through 90° and back every 8 seconds.

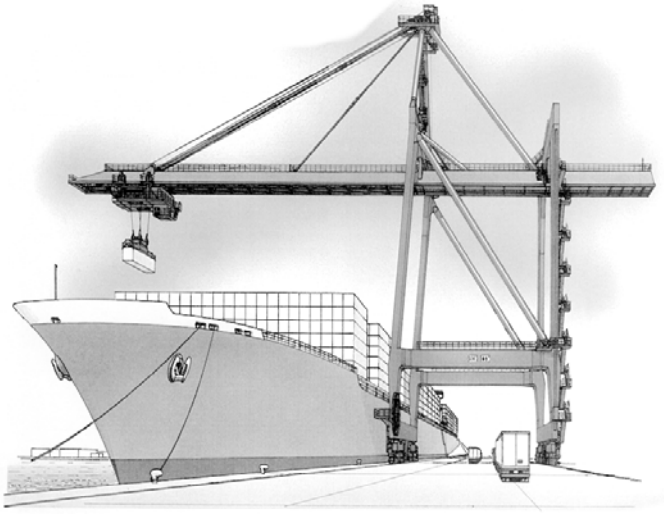

Figure 5. Typical container crane.

We present numerical simulations obtained with a fully nonlinear computer model of a 65-ton container crane with its actual hoisting assembly, including a 15-ton spreader bar. At the beginning of the transfer maneuver, the container is raised from 35 m below the trolley to 20 m and lowered 15 m to a waiting truck. The operator inputs are step functions.

In the mathematical model, we used the actual configuration of the hoisting mechanism because it is significantly different from a simple pendulum with a lumped mass. The hoisting mechanism consists typically of a four hoisting cable arrangement. The cables are hoisted from four different points on the trolley and are attached on the payload side to four points on a spreader bar used to lift containers. The mathematical model is linearized to obtain the gain and delay required by the controller. Then, using the controller with these delay and gain, we numerically solved the full nonlinear equations and obtained the results shown in Figure 6. Clearly, the container settles to less than 50 *mm* in 4 seconds after the end of the transfer although the lowering maneuver ended at 28.5 seconds.

We used an experimental 1/10 scale model, Figure 7, of the 65-ton container crane to test the performance of the controller. The crane model was built by Ishikawajima-Harima Heavy Industries (IHI) and is located at their Yokohama Research Facility. The model has a 4.8 m track, a 15 kg spreader bar, and a 65 kg payload. The payload consists of four 250 by 250 mm steel slabs mounted to the bottom of the spreader bar. The trolley is driven with a pulley-cable system. Four cables are used as a hoisting mechanism. The

(a) (b)

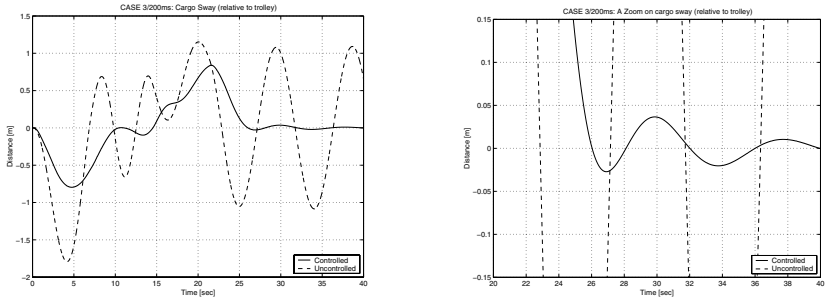

Figure 6. Controlled and uncontrolled cargo sway motions for a container crane.

distance separating the front and rear hoisting cables at the trolley is 282 mm. The four cables are then attached to the spreader bar. The distance between the front and rear hoisting cables is 141 mm. A heavy set of cables supported on one side of the spreader bar, shown in Figure 7, are used to transmit signals from and to a number of sensors and actuators on the spreader bar. These sensors and actuators are used for experiments conducted by IHI. DC brushless rotary motors are used to drive the trolley and the hoisting mechanism. Each

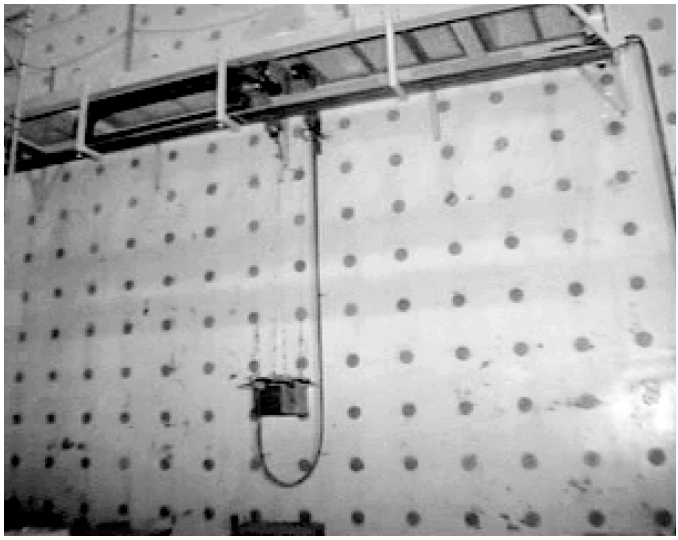

Figure 7. IHI's 1/10 experimental model of a 65-ton container crane.

motor is equipped with an optical encoder to track its motion. Amplifiers with internal PI velocity tracking controllers are used to drive the crane motors. An optical encoder attached to one of the hoisting cables is used to measure the payload sway.

To test the performance of the controller, we also developed a 1/10 scale computer model of the experimental container crane. The commanded acceleration and the controlled simulation and experimental accelerations are shown in Figure 8a. The simulation and experimental results are in excellent agreement and the payload sway was within the 5 mm requirement at 8.2 seconds, Figure 8b.

4. Concluding Remarks

We have designed and implemented a controller based on delayed position feedback that is applicable to most commercial and military cranes: ship-mounted, rotary, and container cranes. Significant reductions in the pendulation angles can be achieved with relatively small control inputs. The system can be operated in both the automated and manual modes. Neither the trajectory nor the end point of the transport maneuver need be predefined. The controller is insensitive to the system parameters and can handle base excitations, initial sways, and noise. The controller is nonlinear and hence it can handle large pendulations. Most large-scale mechanical drivers have inherent time delays. Instead of compensating for these time delays, the controller makes use of these time delays. The effectiveness of the controller has been demonstrated using fully nonlinear numerical simulations as well as on scaled models of ship-mounted, rotary, and container cranes. Dramatic reductions in the pendulation angles of the payload in the controlled system have been achieved in the simulations as well as in the experiments. The controller

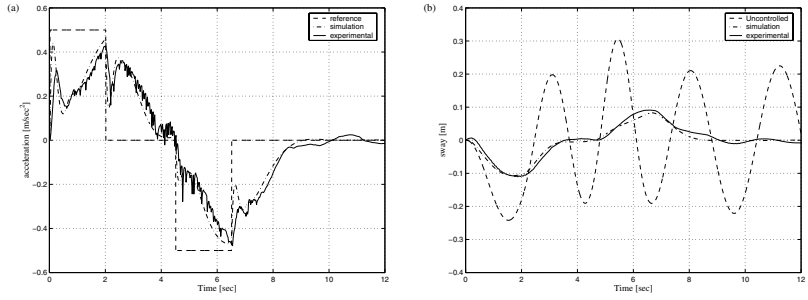

Figure 8. (a) Reference and controlled trolley accelerations and (b) controlled and uncontrolled payload sway.

has been demonstrated to be effective in absorbing these pendulations at high speeds during and at the end of the commanded motions. The controller is effective in handling and rapidly absorbing pendulations due to inertial forces resulting from operator commands as well base-induced motions.

The cost effectiveness of the delayed position-feedback controller is another advantage. The controller does not require any modifications to crane structures. Modifications are usually very expensive, time consuming, and, in some instances, impractical to make. A few sensors and a personal computer or a programmable control board are all that it takes to apply the controller. Moreover, the operator commands are channeled through the control board to the crane actuators, and hence the controller functions transparently. Furthermore, the controller can respond to any operator input. In the manual phase of the demonstration conducted on a scaled model of a container crane at IHI, many people operated the crane randomly, yet the controller was able to eliminate the pendulation at the end of each operation.

References

[1] T. Vaughers "Joint logistics over the shore operations," *Naval Engineers Journal* 106(3), 256-263, 1994.

[2] T. Vaughers and M. Mardiros, "Joint logistics over the shore operation in rough seas," *Naval Engineers Journal*, May, 385-393, 1997.

[3] E. M. Abdel-Rahman, A. H. Nayfeh and Z. N. Masoud, "Dynamics and control of cranes: A review," *Journal of Vibration and Control* 9(7), 863-908, 2003.

[4] G. Parker, B. Petterson, C. Dohrmann and R. Robinett, "Command shaping for residual vibration free crane maneuvers," in *Proceedings of the American Control Conference*, pp. 934-938, 1995.

[5] A. Golafshani and J. Aplevich, "Computation of time-optimal trajectories for tower cranes," in *Proceedings of the IEEE Conference on Control Applications*, pp. 1134-1139, 1995.

[6] Y. Sakawa and A. Nakazumi, "Modeling and control of a rotary crane," *ASME Journal of Dynamic Systems, Measurement, and Control*, 107, 200-206, 1985.

[7] C.F. Alsop, G.A. Forster and F.R. Holmes, "Ore unloader automation - a feasibility study," in *Proceedings of IFAC on Systems Engineering for Control Systems*, Tokyo, Japan, pp. 295-305, 1965.

[8] L. Carbon, "Automation of grab cranes," *Siemens Review XLIII* 2, 80-85, 1976.

[9] J.F. Jones and B.J. Petterson, "Oscillation damped movement of suspended objects," in *Proceedings of the IEEE International Conference on Robotics and Automation,* Philadelphia, PA, Vol. 2, pp. 956–962, 1988.

[10] M.W. Noakes, B.J. Petterson and J.C. Werner, "An application of oscillation damped motion for suspended payloads to the advanced integrated maintenance system," in *Proceedings of the 38th Conference on Remote Systems Technology,* San Francisco, CA, Vol. 1, pp. 63-68, 1990.

[11] M.W. Noakes and J.F. Jansen, "Shaping inputs to reduce vibration for suspended payloads," in *Proceedings of the 4th ANS Topical Meeting on Robotics and Remote Systems,* Albuquerque, NM, pp. 141-150, 1990.

[12] M.W. Noakes and J.F. Jansen, "Generalized inputs for damped-vibration control of suspended payloads," *Robotics and Autonomous Systems* 10(2), 199-205, 1992.

[13] G. Parker, K. Groom, J. Hurtado, J. Feddema, R. Robinett and F. Leban, "Experimental verification of a command shaping boom crane control system," in *Proceedings of the American Control Conference*, pp. 86-90, 1999.

[14] G. Parker, R. Robinett, B. Driessen and C. Dohrmann, "Operator-in-the-loop control of rotary crane," in *Proceedings of the SPIE Confrence*, Vol. 2721, pp. 364-372, 1996.

[15] D. Lewis, G.G. Parker, B. Driessen and R.D. Robinett, "Command shaping control of an operator-in-the-loop boom crane," in *Proceedings of the American Control Conference*, pp. 2643-2647, 1998.

[16] A.S.I. Zinober and A.T. Fuller, "The sensitivity of nominally time-optimal control of systems to parameter variation," *International Journal of Control* 17, 673-703, 1973.

[17] J. Virkkunen and A. Marttinen, "Computer control of a loading bridge," in *Proceedings of the IEE International Conference: Control'88,* Oxford, UK, pp. 484-488, 1988.

[18] J.S. Yoon, B.S. Park, J.S. Lee and H.S. Park, "Various control schemes for implementation of the anti-swing crane," in *Proceedings of the ANS 6th Topical Meeting on Robotics and Remote Systems,* Monterey, CA, pp. 472-479, 1995.

[19] W.E. Singhose, L.J. Porter and W.P. Seering, "Input shaped control of a planar crane with hoisting," in *Proceedings of the American Control Conference,* Albuquerque, NM, pp. 97-100, 1997.

[20] B. d'Andrea-Novel and J. Levine, "Modeling and nonlinear control of an overhead crane," in *Proceedings of the International Symposium MTNS-89*, Vol. 2, pp. 523-529, 1989.

[21] M. Imazeki, M. Mutaguchi, I. Iwasaki and K. Tanida, "Active mass damper for stabilizing the load suspended on a floating crane," *IHI Engineering Review* 31(2), 61-69, 1998.

[22] R.J. Henry, Z.N. Masoud, A.H. Nayfeh and D.T. Mook, "Cargo pendulation reduction on ship-mounted cranes via boom-luff angle actuation," *Journal of Vibration and Control*, 7(8), pp. 1253-1264, 2001.

[23] Z.N. Masoud, A.H. Nayfeh and A. Al-Mousa, "Delayed position-feedback controller for the reduction of payload pendulations of rotary cranes," *Journal of Vibration and Control* 9, 257-277, 2003.

[24] Z.N. Masoud and A.H. Nayfeh, "Sway reduction on container cranes using delayed feedback controller," submitted for publication, *Nonlinear Dynamics*.

[25] Z.N. Masoud, A.H. Nayfeh and D.T. Mook, "Cargo pendulation reduction of ship-mounted cranes," accepted for publication, *Nonlinear Dynamics*.

CONTROLLED MOTIONS OF MULTIBODY SYSTEMS ALONG A PLANE

F.L. Chernousko
Institute for Problems in Mechanics of the Russian Academy of Sciences,
Moscow 119526, Russia
chern@ipmnet.ru

Abstract: Motions of multibody systems along a horizontal plane are investigated in the presence of dry friction forces acting between the system and the plane. The dry friction forces obey Coulomb's law. The motions are controlled by actuators installed at the joints of the system. Various configurations of multibody systems are analyzed in which the bodies are connected by prismatic or revolute joints. Periodic motions of the systems along the plane are constructed. Optimal parameters corresponding to the maximum average speed are evaluated. The obtained results are related to applications in robotics and biomechanics of locomotions.

Key words: Multibody system, control, dry friction, snake-like locomotion.

1. Introduction

The motion of multilink systems along a plane are of interest with respect to locomotions of snakes and other animals [1]. Snake-like robots consisting of separate links equipped with passive wheels are described in [2], see also [3, 4].

In the paper, we consider multibody systems moving along a plane in the presence of dry friction. Control forces (torques) are created by actuators installed at the prismatic (revolute) joints of the mechanism. Note that the dry friction plays an important role here: the motion is impossible in the absence of friction, and at the same time the friction is directed against the velocity of the moving point. Therefore, one must apply the internal control forces and torques in such way as to ensure the desired motion. For different configurations of multibody systems, we show that they can perform periodic motions along the plane and find the maximum average speed of the motions.

G. Rega and F. Vestroni (eds.),
IUTAM Symposium on Chaotic Dynamics and Control of Systems and Processes in Mechanics, 397–406.

2. Linear Motion

First, consider a system of N identical rigid bodies if mass m on a horizontal plane (Fig. 1). Dry friction forces, obeying Coulomb's law, act between each body and the plane; the coefficient of friction is denoted by k. Adjacent bodies may interact with one another via control forces F. Let us describe a simple mode of motion of the system along the x-axis. At the initial instant, all the masses are the rest. First, mass 1 moves along the x-axis for a certain distance Δx and then stops, while all other masses stay at rest. During this motion, mass 1 first accelerates ($F > mgk$) and then decelerates ($F < mgk$). Here, g is the gravity acceleration. Next, mass 2 moves along the x-axis in a way similar to mass 1 at the previous stage, while all other masses stay at rest. Continuing the process for masses 3, 4, ..., N, we displace the whole system by the distance Δx. Repeating this procedure, we obtain a periodic motion of the multibody system along the x-axis. It is easily shown that this motion is possible if and only if the force F lies within the limits: $mgk < |F| \leq (N-1)mgk$. Thus, the described simple motion is possible only if $N \geq 3$. Therefore, it is of interest to investigate possible motions of a two-mass system ($N = 2$).

Consider a system of two interacting rigid bodies of masses m_1 and m_2 which can move along the horizontal x-axis in the presence of dry friction (Fig. 2). The coefficients of friction for masses m_1 and m_2 are k_1 and k_2, respectively. The force that mass m_2 exerts on mass m_1 is denoted by F; then mass m_1 exerts a force $-F$ on mass m_2. Suppose the distance L between the masses may vary within the interval $L_0 - \eta \leq L \leq L_0$, where L_0 is the initial distance and $\eta \leq L_0$ is the admissible range of the relative displacement.

Let x_i be the displacement of the mass m_i from the initial position, and v_i its velocity, $i = 1, 2$. The distance between the masses is $L_0 + x_2 - x_1$. The eqations of motion of the masses m_1 and m_2 are

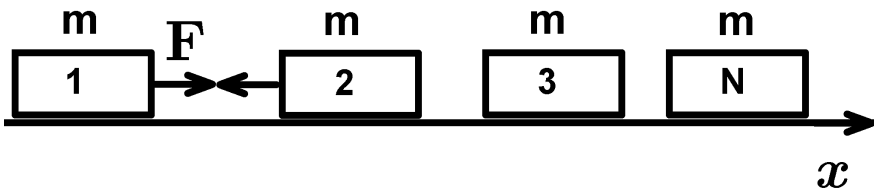

Figure 1. System of N masses.

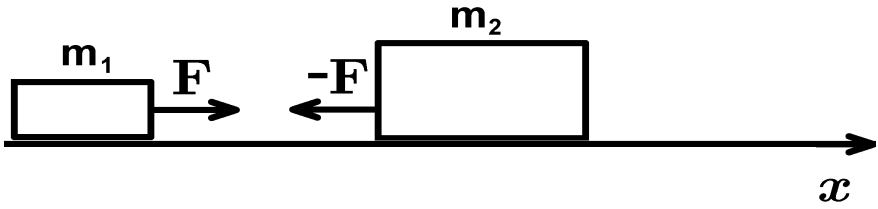

Figure 2. Two-mass system.

$$
\begin{aligned}
&m_1\dot{v}_1 = F - m_1 g k_1 \operatorname{sign} v_1 \quad \text{for} \quad v_1 \neq 0 \\
&m_2\dot{v}_2 = -F - m_2 g k_2 \operatorname{sign} v_2 \quad \text{for} \quad v_2 \neq 0 \\
&|F| \leq m_i g k_i \quad \text{for} \quad v_i = 0, \qquad \dot{x}_i = v_i, \qquad i = 1, 2.
\end{aligned} \tag{1}
$$

Suppose at the initial time instant $t = 0$ both masses are at rest and at the maximal admissible distance L_0 from one another.

We will construct a piecewise-constant law for the control force $F(t)$, under which both masses move by the same distance ξ in a time T and come to rest at the end of motion. Throughout, the distance between the masses must stay within the limits $0 \leq x_1(t) - x_2(t) \leq \eta$, $t \in [0, T]$, where $\eta > 0$ is given. The required motion consists of four steps.

1) Forward accelerated motion of mass m_1, mass m_2 stays at rest.

2) Forward decelerated motion of mass m_1, forward accelerated motion of mass m_2.

3) Reverse accelerated motion of mass m_1, forward accelerated motion of mass m_2.

4) Reverse decelerated motion of mass m_1, forward decelerated motion of mass m_2.

Let us explain the meaning of these steps. We assune that mass m_2 is the main body, and m_1 is an auxilary one, $m_1 < m_2$. At the first step, mass m_1 approaches m_2 in such a way as not to produce reverse motion of m_2. During the second and third steps, mass m_2 moves forward due to the strong repulsion of masses. In the fourth step, both masses slow down and halt simultaneously at the same distance from one another as initially.

We denote by τ_i the durations of the steps and by F_i the constant values of the control force at these steps, $i = 1, 2, 3, 4$. To simplify matters, we assume that $F_2 = F_3$. The following inequalities ensure that the motion satisfy the imposed properties:

$$
m_1 g k_1 < F_1 < m_2 g k_2, \qquad F_2 < -m_2 g k_2, \qquad F_4 > -m_1 g k_1. \tag{2}
$$

The introduced parameters τ_i, F_i must also satisfy certain relations which follow from equations (1) and imposed conditions. These relations are deduced in [5]. Here, we restrict ourselves with a case where explicit formulas can be presented.

Suppose the force F_2 is big enough: $|F_2| \gg m_1 g k_1$, so that steps 2 and 3 can be treated as an impulse motion of zero duration. Denote

$$\begin{aligned} &\mu = m_1 m_2^{-1} < 1, \qquad \nu = m_2 k_2 (m_1 k_1)^{-1}, \\ &f_i = F_i (m_1 g k_1)^{-1}, \quad i = 1, 4, \quad T = \tau_1 + \tau_2 + \tau_3 + \tau_4. \end{aligned} \tag{3}$$

Here, T is the duration of the motion, f_i are the dimensionless forces, μ and ν are dimensionless parameters. Calculations [5] show that in our case we have

$$\begin{aligned} &\tau_1 = \frac{(\nu - 1)T}{f_1 + \nu - 2}, \qquad \tau_2 \to 0, \qquad \tau_3 \to 0, \qquad \tau_4 = \frac{(f_1 - 1)T}{f_1 + \nu - 2}, \\ &f_4 = \frac{(\nu - 1)^2 - (f_1 - 1)(1 + \mu\nu)}{(f_1 - 1)(1 + \mu)}, \qquad F_2 \to \infty, \\ &F_2(\tau_2 + \tau_3) \to q = m_1 g k_1 (f_1 - 1)(f_4 + \nu)(\nu - 1)^{-1} \\ &\xi = \frac{g k_1 \tau_1^2 \mu (f_1 - 1)(f_1 + \nu - 2)}{2(\nu - 1)(1 + \mu)}, \qquad \eta = \frac{g k_1 \tau_1^2 (f_1 - 1)}{2}. \end{aligned} \tag{4}$$

Here, q is the value of the impulse, ξ is the total displacement during the time T, and η is a given admissible range for the relative distance. Eliminating τ_1 from the last two equations (4), we evaluate the average speed of the periodic motion of our system

$$v = \frac{\xi}{T} = \left[\frac{g k_1 \eta (f_1 - 1)}{2}\right]^{1/2} \frac{\mu}{1 + \mu}.$$

The parameter f_1 can be chosen within the limits $1 < f_1 < \nu$ which follow from (2) and (3). Choosing f_1 so that to maximize v, we obtain:

$$\begin{aligned} &f_1 \to \nu, \qquad \tau_1 = \tau_4 = \frac{T}{2} = \left[\frac{2\eta}{g k_1 (\nu - 1)}\right]^{1/2}, \qquad \xi = \frac{2\eta\mu}{1 + \mu}, \\ &v_{\max} = \left[\frac{g k_1 \eta (\nu - 1)}{2}\right]^{1/2} \frac{\mu}{1 + \mu}. \end{aligned} \tag{5}$$

Let us analyze the influence of the coefficients of friction and the mass ratio on the maximal speed. If the coefficients of friction lie within the limits $k_i \in [k^-, k^+]$, $i = 1, 2$, the maximum velocity is reached when $k_1 = k^-$, $k_2 = k^+$. For fixed k_1 and k_2, the maximum value of $v_{\max}$ with respect to μ is reached when $\mu = k_2 (2k_1 + k_2)^{-1}$ and is equal to

$$v_{\max}^* = (g\eta)^{1/2} k_2 [8(k_1 + k_2)]^{-1/2} \tag{6}$$

In the special case $k_1 = k_2 = k$ we obtain

$$\mu = m_1/m_2 = 1/3,\ T = 2\eta^{1/2}(gk)^{-1/2},\ \xi = \eta/2,\ v^*_{\max} = (g\eta k)^{1/2}/4.$$

Thus, we have explicit relations for the optimal motion. The two-mass system considered above is a simple mechanical model capable of moving along a plane in the presence of dry friction under the influence of internal control forces.

3. Snake-Like Locomotions

Multilink mechanisms represent a more complicated case of systems which can move along a plane in the presence of dry friction. These mechanisms imitate, to some extent, locomotions of snakes [1, 2]. Control torques are applied at the revolute joints of the mechanisms.

We have considered mechanisms with two [6], three [7, 8], and many [9] links, and constructed periodic motions of these systems. For two-link and three-link mechanisms shown in Figs. 3 and 4, respectively, the periodic motions consist of slow and fast phases. In slow phases, only the tail of the two-link mechanism (respectively, the end links of the three-link mechanism) moves, whereas the "main" link (respectively, the central link of the three-link mechanism) stays at rest. In fast phases, all links move with a sufficiently high

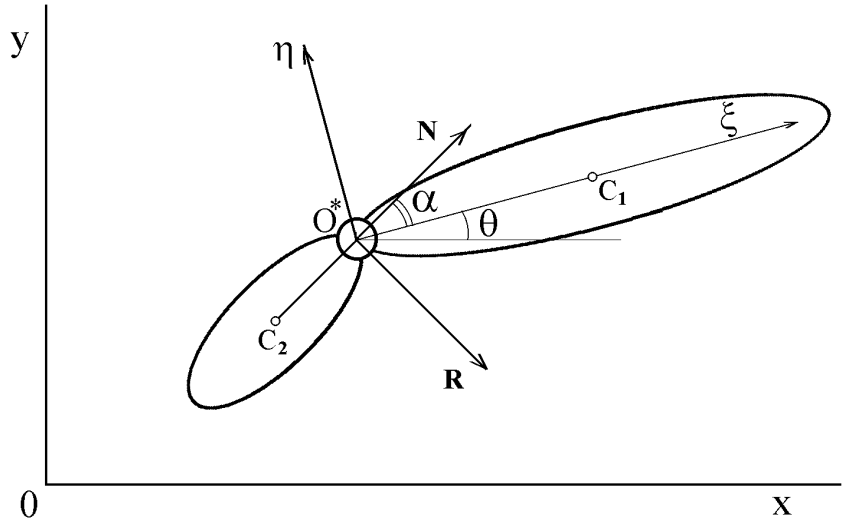

Figure 3. Two-link mechanism.

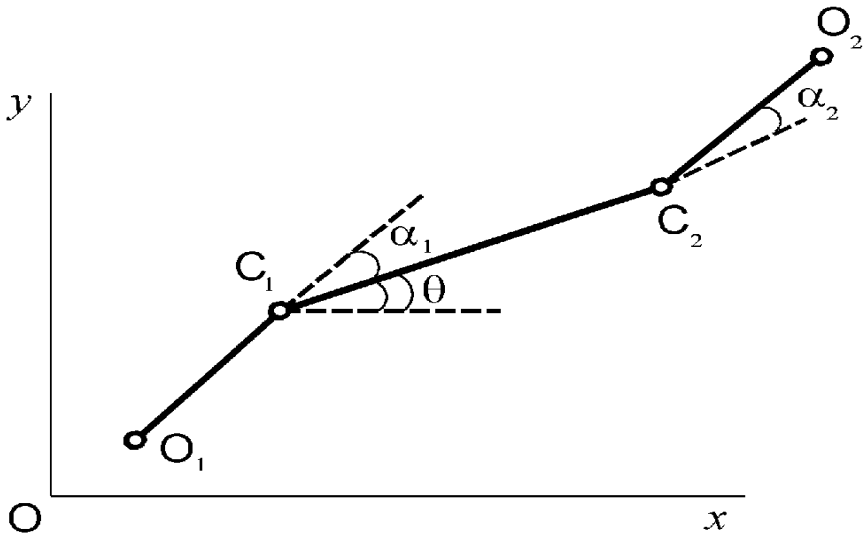

Figure 4. Three-link mechanism.

speed, so that the influence of the dry friction is negligible. Thus, the slow and fast phases resemble the steps of the linear motion described in Section 2.

For the longitudinal motion of the two-link mechanism, the phases of the periodic motion are shown in Fig. 5. For the three-link mechanism, the phases of different motions are shown in Figs. 6-8. In Figs. 5-8, even (odd) numbers correspond to slow (fast) phases.

Let us consider the three-link mechanism (Fig. 4) in more detail. Suppose the mass of the linkage is concentrated at the joints and end points which have the masses m_1 and m_0, respectively. The total mass of the mechanism is $m = 2(m_0 + m_1)$. Denote by l the length of the end links, by $2a$ the length of the central link, and by k_0 and k_1 the coefficients of friction for the end masses and joints, respectively. The proposed periodic motions are realizable, if $m_0 k_0 (a + l) < m_1 k_1 a$ [8]. The average speed of the longitudinal motion [8] is given by:

$$v = 8 m_0 m^{-1} l T^{-1} \sin^2(\gamma/2), \tag{7}$$

where T is the duration of the cycle of Fig. 6 and γ is the angle of rotation of the end links.

Similar formulas are obtained for other types of motion of the three-link mechanism [7, 8] and also for the two-link mechanism [6]. It is shown that these mechanisms can reach any prescribed position and configuration in the plane. The magnitude of the required torques produced by the actuators of two-link and three-link mechanisms is about $M \sim 10 mgLk$, where m is the

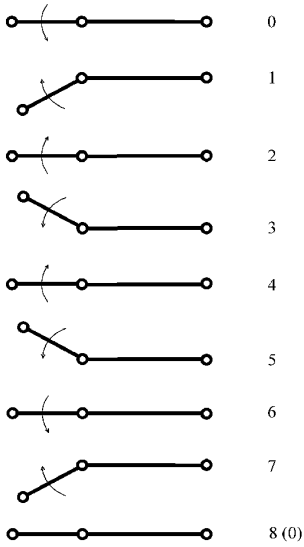

Figure 5. Motion of two-link mechanism.

mass of the system, L is the length of the link, and k is the maximal value of the friction coefficients.

Since the average speed of motion depends significantly on the geometrical and mechanical parameters of mechanisms, it is natural to find the optimal values of parameters corresponding to the maximum average speed.

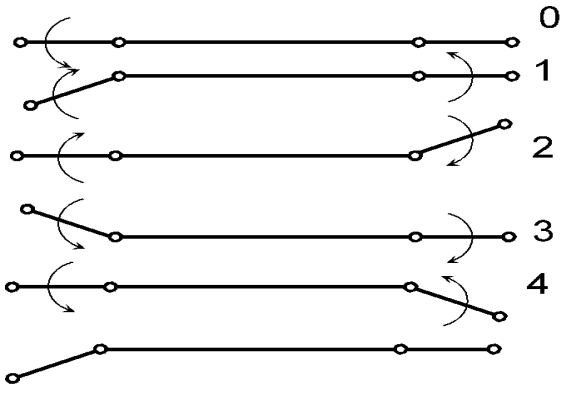

Figure 6. Longitudinal motion of three-link system.

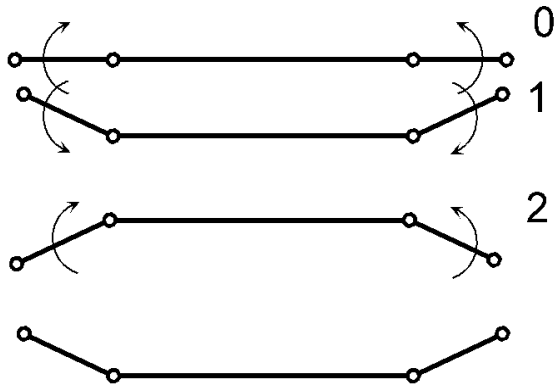

Figure 7. Laterial motion of three-link system.

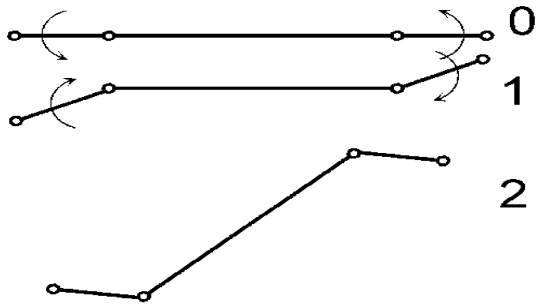

Figure 8. Rotation.

Let us consider the optimization of the longitudinal motion for the three-member linkage shown in Fig. 4. We use the same notation as in equation (7). Suppose the mass m_1 of the joints, the length $2a$ of the central link, and the angle of rotation γ are fixed. The mass m_0, the length l of the end links, the duration T, and the coefficients of friction k_0 and k_1 satisfying the inequalities $k^- \le k_0 \le k^+$, $k^- \le k_1 \le k^+$ are to be chosen in order to maximize the average velocity v of the periodic motion given by (7). Also, certain constraints ensuring the possibility of the described periodic longitudinal motion should be taken into account. It is shown [10] that the desired maximum of v is reached when $k_0 = k^-$, $k_1 = k^+$. The maximum dimensionless speed $V = v(gak^+)^{-1/2}$ as a function of the angle γ is shown in Fig. 9. Here, γ is measured in radians, and χ is the ratio of the minimal and maximal coefficients of friction: $\chi = k^-/k^+$. One can see that the maximum speed V depends significantly on the angle γ and increase with γ. The saturation occurs as $\gamma \sim 2.5$. Also,

V decreases with χ. The detailed results of the parametric optimization are presented in [10].

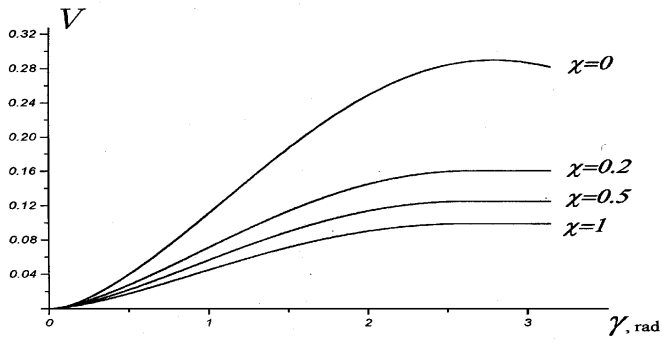

Figure 9. Maximum speed.

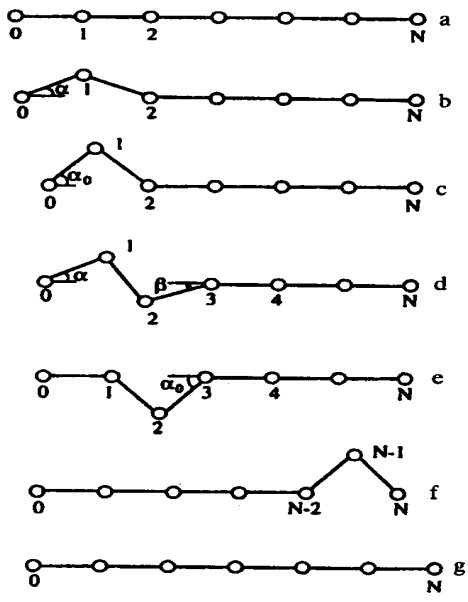

Figure 10. Wavelike motion with three moving links.

As a rough estimate, the maximum longitudinal speed of the three-link mechanism can be evaluated as $v \sim 0.1(glk^{+})^{1/2}$.

The maximum lateral speed of this mechanism is several times higher. Since the two-link mechanism is controlled by only one actuator, its maximum speed is several times smaller than that of the three-link mechanism.

For multilink mechanisms with more than four links, wavelike modes of motion are possible. In these motions, a wave of twisting travels along the mechanism which, as a result, moves forward. One type of wavelike motions is presented in Fig. 10. Here, only slow phases of motions are involved, and the magnitude of the required control torques is smaller than that for the mechanisms with two or three links: $M \leq 2mgLk$.

Results of computer simulation as well as experimental data confirm the obtained theoretical results.

The principle of motion and the structure of mechanisms considered here are simple and can be of interest for mobile robots, especially for small ones.

Acknowledgments

The work was supported by the Russian Foundation for Basic Research, Project 02-01-00201, and by Grant of the President of RF for leading scientific schools N 1627.2003.1.

References

[1] James Gray, *Animal Locomotion*, London: Weidenfeld & Nicolson, 1968.

[2] S. Hirose, *Biologically Inspired Robots: Snake-like Locomotors and Manipulators.* Oxford: Oxford University Press, 1993.

[3] J. Ostrowski and J. Burdick, "Gait kinematics for a serpentine robot," *Proceedings of the IEEE International Conference on Robotics and Automation* 2, Minneapolis, 1996.

[4] Z.Y. Bayraktaroglu and P. Blazevic, "Snake-like locomotion with a minimal mechanism," *Proceedings of the Third International Conference on Climbing and Walking Robots* CLAWAR 2000, Madrid, 2000.

[5] F.L. Chernousko, "The optimum rectilinear motion of a two-mass system," *J. Applied Mathematics and Mechanics* 66 (1):1-7, 2002.

[6] F.L. Chernousko, "Controllable motions of a two-link mechanism along a horizontal plane," *J. Applied Mathematics and Mechanics* 65 (4):565-577, 2001.

[7] F.L. Chernousko, "The motion of a multilink system along a horizontal plane," *J. Applied Mathematics and Mechanics* 64 (4):497-508, 2000.

[8] F.L. Chernousko, "On the motion of a three-member linkage along a plane," *J. Applied Mathematics and Mechanics* 65 (1):13-18, 2001.

[9] F.L. Chernousko, "The wavelike motion of a multi-link mechanisms," *J. Applied Mathematics and Mechanics* 64 (4):497-508, 2000.

[10] F.L. Chernousko, "Snake-like locomotions of multilink mechanisms," *J. Vibration and Control* 9:235-256, 2003.

ACTIVE DAMPING OF SPATIO–TEMPORAL DYNAMICS OF DRILL–STRINGS

Edwin Kreuzer and Henning Struck
Mechanics and Ocean Engineering; Technical University Hamburg–Harburg;
Eissendorfer Strasse 42; 21071 Hamburg; Germany
kreuzer@tu-harburg.de
h.struck@tu-harburg.de

Abstract: In the drilling process for the exploration of oil and gas resources a variety of vibration phenomena occur. Here, just self–excited torsional vibrations and forced flexural vibrations of the drill–string are considered. An experimental setup which models a real drill–string was designed and constructed. The aim is to actively damp these vibrations. The string of the setup was modeled as a one–dimensional continuum. The resulting equations of motion were approximated using Galerkin's method. Reducing the system's order by applying the proper orthogonal decomposition results in only one coordinate which is fed back in order to actively damp the system.

Key words: Modelling, stick–slip vibrations, optimisation, nonlinear control.

1. Introduction

In long slender drill–strings different vibration phenomena occur during the operation. Moreover, a coupling of torsional vibrations with bending and axial vibrations is often observed. These spatio–temporal vibrations reduce the quality and efficiency of the drilling process and may even cause a complete failure of the drill–string, which is very costly in offshore industry. Therefore, various passive and active damping methods have been suggested in recent years. Field measurements are rare and field test are rather impossible. In order to overcome this drawback and to investigate these vibrations as well as to evaluate control strategies an experimental setup was designed and constructed at the Technical University Hamburg–Harburg.

The outline of the paper is as follows. In section 2 the experimental setup is introduced. The modelling of the drill–string and the control strategy are

G. Rega and F. Vestroni (eds.),
IUTAM Symposium on Chaotic Dynamics and Control of Systems and Processes in Mechanics, 407–417.

described in sections 3 and 4. In section 5 the implementation and the results from measurements are presented.

2. Experimental Setup

The experimental investigations are intended to allow for both, a thorough study of all kinds of vibration phenomena occurring in slender drill–strings as well as the implementation of controllers for the active damping of vibrations. The mechanical parts of the experimental setup are presented in Figure 1. Two motors are attached at both ends of a vertical brass string (length $\ell = 10m$, diameter $2R = 5mm$).

The upper motor imitates the rotary table of a drilling–rig and drives the string with a prescribed angular speed. This motor can neither be displaced nor be inclined in any direction. The lower motor simulates the friction between the bit and the ground. It applies a torsional moment M_e according to a prescribed characteristic. A roller bearing allows the motor to move only vertically. The weight of the motor produces an external tension force on the string. Five angular sensors are attached to the string, one to each motor and three equally spaced between them. Bearings protect the sensors from lateral loads. These bearings just enable rotations and displacements about the vertical axis. The bearings and the sensors form units which are fixed to their

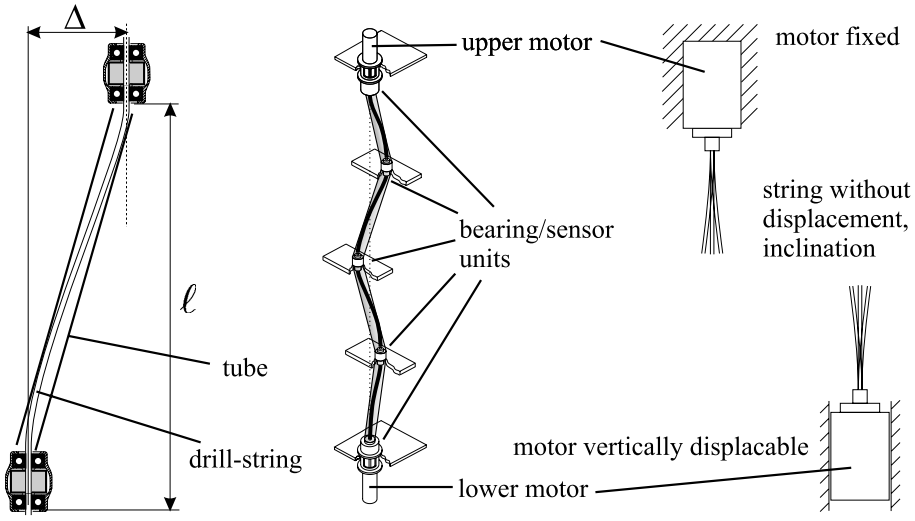

Figure 1. Sketch of experimental setup and boundary conditions at both ends

position during the operation but can be displaced horizontally during off–state. The units subdivide the string into four sections of same length. The parallel offset (up to $\Delta = 0.3\,m$) of the units cause a slight curvature of the string. The string resides in a tube (inner diameter $D = 35\,mm$) which constrains unilaterally the motion of the string. The tube can be filled with a fluid. This fluid is intended to model the fluid–structure interaction of a real drill–string and fluid.

The friction characteristic is derived from field data [1]. The applied moment M_e depends on the angular speed ω_{bit} at the bit:

$$M_e = M_d \frac{\omega_{\text{bit}}}{\omega_{\text{bit}}^2 + c_d^2} + M_s \tanh\left(\frac{\omega_{\text{bit}}}{c_s}\right). \tag{1}$$

The diagram given in Figure 2 was obtained using the following parameters: $M_s = 0.136\,Nm$, $M_d = 1.087\,Nm$, $c_s = 1.0\,rad/sec$, and $c_d = 2.0\,rad/sec$. The mass of the lower motor is $m_M = 16\,kg$, hence, the tensional force applied on the string is approximately $S_e = 160\,N$.

On a transputer five parallel processes are implemented: the first evaluates the sensor signals and provides the other processes with the measured data, the second and third one control the motors by means of prescribed characteristics for M_e and Ω_{des}, the fourth and the fifth one carry out the identification and the feedback control for the active damping. A personal computer is used for the evaluation of the measured data as well as the programming of the transputer.

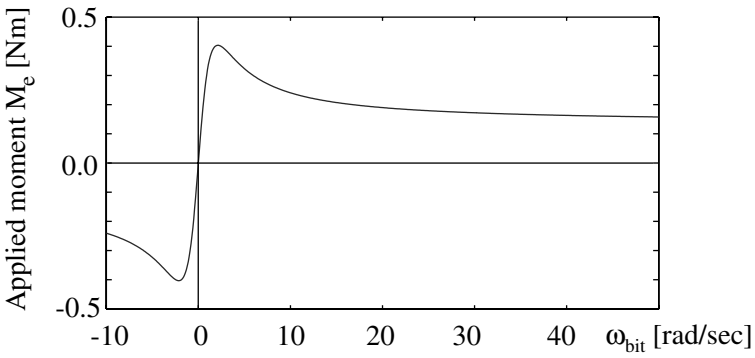

Figure 2. Friction characteristic.

3. Modelling of the Drill–String

The dynamics of the string can be described in a compact form using Hamilton's Principle. At first, the external loads are assumed to be constant. Then, the Lagrangian is analysed. Finally, the equations of motion are derived.

3.1 Kinematic Relations

The string is assumed to be stiff in axial direction. Furthermore, according to the Euler–Bernoulli beam theory, cross sections remain plain and perpendicular with respect to the axis of the string under any deformation. The deformation is assumed to be so small, hence, Hooke's law is valid and only linear terms contribute to the strain. Plain stress is presumed.

The theorem of Pythagoras yields an expression for the vertical displacement w in terms of u and v (compare the orientation of the coordinate frames according to Figure 3):

$$\begin{aligned} dz^2 &= (u'dz)^2 + (v'dz)^2 + (dz + w'dz)^2 \\ \Rightarrow \quad w' &= -1 + \sqrt{1 - (u'^2 + v'^2)}, \end{aligned} \tag{2}$$

where $(\bullet)'$ denotes the partial derivative of $(\bullet)$ with respect to z. The analysis in the forthcoming section yields that w can be neglected. The vertical displacement w is approximated by

$$\begin{aligned} w &= \int_0^{4\ell} \left[-1 + \sqrt{1 - (u'^2 + v'^2)}\right] dz \\ &\approx \int_0^{4\ell} \left[-1 + \left(1 - \left(u'^2 + v'^2\right)/2\right)\right] dz \approx -2\ell \left(u'^2 + v'^2\right). \end{aligned} \tag{3}$$

Figure 3 presents two sets of coordinates. On the right hand side, the deformation is described by Cardan angles α, β, and γ. The base vectors are transformed according to three consecutive rotations: the first rotation α is about the x–axis, the second β about the new y–axis resulting the base vectors $\underline{e}_i^*$. In the figure only the third rotation γ about $\underline{e}_z^*$ is shown. On the left hand side of the same figure the displacements u, v and w are defined. In order to express α and β in terms of u, v and γ, the tangent vector of the deformed string is expressed in two different ways.

In the undeformed configuration a local frame fixed to an arbitrary cross section has the same orientation as the inertial frame, i.e. the z–axis points down vertically, the x– and the y– axis span a horizontal plane. Under any deformation the base remains perpendicular. Hence, the base vectors $\overset{0}{\underline{e}}_i$ in the

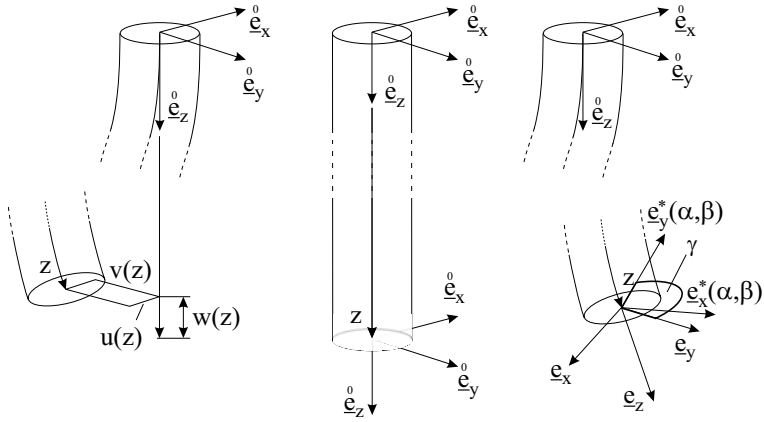

Figure 3. Two ways to describe the deformation: displacement and rotation

undeformed configuration can be transformed with a rotation matrix $\underline{\underline{R}}$ to the deformed configuration:

$$\underline{e}_i = \underline{\underline{R}} \cdot \overset{0}{\underline{e}}_i \ . \tag{4}$$

Now, $\underline{\underline{R}}$ is expressed using Cardan angles and equation (4) is evaluated for the vector $\underline{e}_z$ which is tangential to the centre line of the string:

$$\underline{e}_z = \sin(\beta)\ \overset{0}{\underline{e}}_x - \sin(\alpha)\cos(\beta)\ \overset{0}{\underline{e}}_y + \cos(\alpha)\cos(\beta)\ \overset{0}{\underline{e}}_z \ . \tag{5}$$

Any material point of the string in the undeformed configuration is denoted with $\overset{0}{\underline{r}}$ and the displacement from this configuration with $\underline{u} = [u, v, w]$, where u, v, and w refer to the inertial frame. The position vector of a material point in the deformed configuration is

$$\underline{r} = \overset{0}{\underline{r}} + \underline{u} = (x + u(z))\ \overset{0}{e}_x + (y + v(z))\ \overset{0}{e}_y + (z + w(z))\ \overset{0}{e}_z \ . \tag{6}$$

By using Frenet's formula (see [6]) the vector $\underline{e}_z$ is expressed in terms of u and v:

$$\underline{e}_z = \frac{d}{dz}\underline{r} = u'\ \overset{0}{e}_x + v'\ \overset{0}{e}_y + \sqrt{1 - u'^2 - v'^2}\ \overset{0}{e}_z \ . \tag{7}$$

Comparing the coefficients of eq. (5) with those of eq. (7) yields

$$\sin(\beta) = \frac{\partial u}{\partial z}, \tag{8}$$

$$\tan(\alpha) = -\frac{\partial v}{\partial z} / \sqrt{1 - u'^2 - v'^2}. \tag{9}$$

The angle γ_e describes the rotation of the string projected onto the z–axis in the undeformed configuration. The partial derivative of γ_e with respect to z is:

$$\gamma_e' = \cos(\alpha)\cos(\beta)\gamma' + \sin(\alpha)\beta' - \cos(\alpha)\sin(\beta)\alpha'. \tag{10}$$

The vector of angular velocity in terms of Cardan angles is

$$\underline{\omega} = \begin{bmatrix} \dot{\alpha}\cos(\beta)\cos(\gamma) + \dot{\beta}\sin(\gamma) \\ -\dot{\alpha}\cos(\beta)\sin(\gamma+) + \dot{\beta}\cos(\gamma) \\ \dot{\gamma} + \dot{\alpha}\sin(\beta) \end{bmatrix}. \tag{11}$$

3.2 Hamilton's Principle

Nonconservative systems cannot be handled with a variational principle like Hamilton's principle but in a generalized form, see [2]:

$$\delta \int_{t_1}^{t_2} L(\dot{u}, \dot{v}, u'', v'', \dot{\gamma}, \gamma')dt + \int_{t_1}^{t_2} \delta W(u', v', u'', v'', \gamma')dt = 0. \tag{12}$$

Here, the virtual work of the external loads δW is not the variation of a functional W as long as these loads are not conservative. It is much more simple to analyse the Lagrangian than the equations of motion. Generally, a nonconservative system cannot be described by a Lagrangian. Hence, all applied loads are approximated using constant values. The order of magnitude of the terms of the Lagrangian are compared and the smaller ones are neglected. The equations of motion are derived using the simplified Lagrangian. In the equations of motion the constant terms for M_e, q_x, and q_y are replaced by state dependent terms.

The Lagrangian consists of three parts: the kinetic energy, the strain energy, and the energy of the external loads. The kinetic energy is given by (note, that $(\bullet)\cdot(\bullet)$ denotes a single–dot product of two tensors, see [3]):

$$\begin{aligned} T &= \tfrac{1}{2}\int_0^{4\ell} \left[\underline{\omega}\cdot\underline{\underline{I}}\cdot\underline{\omega} + \rho R^2\pi\left(\dot{u}^2 + \dot{v}^2 + 2\ell\left(\dot{u}' + \dot{v}'\right)^2\right)\right] dz \\ &= \rho R^2\pi\left[\tfrac{R^2}{8}\left(\dot{\alpha}^2[1+\sin^2(\beta)] + \dot{\beta}^2 + 2\dot{\gamma}^2\right) + \dot{u}^2 + \dot{v}^2\right]. \end{aligned} \tag{13}$$

The strain energy due to bending and torsion can be expressed as:

$$U = \frac{1}{2}\int_0^{4\ell} \left[EI_b\left(\alpha'^2 + \beta'^2\right) + GI_p\gamma'^2\right] dz, \tag{14}$$

where EI_b denotes the bending stiffness and GI_p the torsional stiffness. The virtual work done by the constant external loads is:

$$W = \int_0^{4\ell}\left[q_x u + q_y v\right] dz + S_e w(4\ell) + M_e\gamma_e(4\ell), \tag{15}$$

$$= \int_0^{4\ell} \left[q_x u + q_y v + S_e w' + M_e \gamma_e' \right] dz. \tag{16}$$

Here, q_x and q_y are distributed forces acting along the string.

3.3 Reduction of the Equations of Motion

The terms of equation (12) are known and can be expressed in terms of u, v, and γ, respectively, and the derivatives of these quantities. By means of a Taylor series expansion, the Lagrangian $L = T - U + W$ is approximated using a third order polynom, which corresponds to equations of motion of second order. The parallel offset Δ acts in the x–direction only. Hence, displacement u is subdivided into a static and a dynamic part $u = u_s + u_d$, whereas v only consists of a dynamic part. Both displacements are related to Δ. The angle γ is also subdivided into a static and a dynamic part. The variables t and z are normalized:

$$\begin{aligned} z &= \ell\xi, \quad & u &= \Delta\,(\tilde{u}_s + \tilde{u}_d)\,, \qquad & v &= \Delta\tilde{v}, \\ t &= \tfrac{1}{\omega_0}\tau \quad & \gamma &= \quad \gamma_s + \gamma_d = \theta\,(4\ell + \ell\tilde{\gamma})\,. \end{aligned} \tag{17}$$

The tilde indicates that the according quantity is dimensionless. The orders of magnitude are $O(\tilde{u}_s)$=1, $O(\tilde{u}_d)$=$(\tilde{v}_d)$=0.1 since the string resides in a tube and, therefore, the displacement is bounded. The order of magnitude of $\tilde{\gamma}_d = 0.1$ was taken from measurements at the straight string. By means of the kinetic energy related to the coordinate z the comparison of the terms is presented:

$$\begin{aligned} \frac{\partial T}{\partial z} = R^2\rho\pi\omega_0^2 \Bigg[& \tfrac{R^2\Delta^2}{4\ell^2}\left[\tilde{u}_{d,\tau\xi}^2 + \tilde{v}_{d,\tau\xi}^2\right] + R^2\Delta^2\theta/\ell\,\tilde{\gamma}_{,\tau}\,\tilde{v}_{,\xi\tau}\left(\tilde{u}_{s,\xi} + \tilde{u}_{d,\xi}\right) \\ & + \frac{R^2}{2\theta^2\ell^2}\Delta^2\left[\tilde{u}_{d,\tau}^2 + \tilde{v}_{d,\tau}^2 + 2\ell^2\theta^2/2\tilde{\gamma}^2{}_{,\tau}\right] \Bigg]. \end{aligned} \tag{18}$$

Here, $(\bullet)_{,\eta}$ abbreviates the derivation with respect to a dimensionless variable $\eta \in (\xi, \tau)$. The geometrical quantities as well as values for the Young's modulus ($E = 8 \cdot 10^{10}\, N/m^2$) and the shear modulus ($G = 3 \cdot 10^{10}\, N/m^2$) are taken into consideration. Experiments on the straight string show a power spectrum with a maximum at $3\,Hz$, hence, ω_0 is set to $\omega_0 = 20\,rad/s$. The terms indicated in gray in (17) are small compared to the remaining ones and can be neglected. By means of Euler's equation the equations of motion are obtained:

$$\begin{aligned} 0 = \int_0^{4\ell} \Bigg[& \left[\left(\rho I_p + \delta(z-4\ell)\Theta_M\right)\ddot{\gamma} - GI_p\gamma'' - M_e\delta(z-4\ell)\right]\delta\gamma \\ & + \left[\mu\ddot{u} + EI_b u^{iv} - S_e\left(u_s'' + u''\right) + M_e v''' - q_x\right]\delta u \\ & + \left[\mu\ddot{v} + EI_b v^{iv} - S_e v'' - M_e u''' - q_y\right]\delta v \Bigg] dz. \end{aligned} \tag{19}$$

Equation (19) even holds for nonconservative loads M_e, q_x, and q_y and can directly be applied to approximate the motion using Galerkin's method. Note, that $\delta\gamma$, δu, and δv are arbitrary and independent of each other. Hence, the expressions in the brackets are equal to zero. The resulting equations superimpose different elementary effects: statical and dynamical behaviour of chords, beams and strings, compare [4]. The simulation of equation (18) as well as experiments reveal self excited torsional vibrations due to the friction characteristics (1).

4. Control–Strategy

Equation (18) shows that the torsional vibration is independent from bending vibration. On the other hand, the bending vibration depends on the external moment M_e, which depends on the torsional vibration. Therefore, just the torsional vibrations are actively damped. The dynamics of the system is reduced due to the Proper–Orthogonal–Decomposition (POD) decomposing the signal in so–called *characteristic functions* which optimally approximate the signal with respect to the kinetic energy.

4.1 The Recursive Proper–Orthogonal–Decomposition

The control of the drill–string using the POD was already examined in [1]. The characteristic functions change after closing the control loop. Thus, the technique is improved and the characteristic functions are calculated recursively.

The angular velocities of the five sensors are measured at discrete time instances t_i $(i = 1, 2, \cdots)$. The deviation of the five measured values from the mean is put in the column matrix $\underline{u}(t_i)$. A matrix $\underline{\underline{C}}(t_i)$ is recursively calculated such that

$$\begin{aligned} &x_i = 1 + \lambda x_{i-1}, && x_0 = 0; \\ &\underline{\underline{C}}(t_i) = \tfrac{1}{x_i}\underline{u}(t_i) \cdot \underline{u}^T(t_i) + \lambda \underline{\underline{C}}(t_{i-1}), && \underline{\underline{C}}(t_0) = \underline{\underline{0}}. \end{aligned} \tag{20}$$

Here, λ denotes a value which describes the decrease of the influence of previous measurements. For $\lambda = 1$ all values are considered equally, for $\lambda = 0$ only the actual value is considered. Here, the influence of previous data is supposed to decay, but at the same time, sufficient information is needed for an accurate calculation of the characteristic functions. A good compromise between these contradicting demands is $\lambda = 0.975$. The orthogonal eigenvectors ϕ_i of the eigenvalue problem $(\underline{\underline{C}}(t_i) - \mu \underline{\underline{E}})\underline{\phi}$ are the characteristic functions, the eigenvalues μ denote the content of kinetic energy contained in the corresponding characteristic function. For the drill–string the first characteristic function

contains about 98% of the total kinetic energy. The motion is approximated by:

$$\underline{u}(t_i) \approx a(t_i)\underline{\phi}, \quad \text{with:} \quad a(t_i) = \underline{u}^T(t_i) \cdot \underline{\phi}. \tag{21}$$

The driving speed is controlled using this signal and a feedback PD–controller:

$$\Omega_c(t_i) = \Omega_{des} + k_p a(t_{i-1}) + k_d \dot{a}(t_{i-1}). \tag{22}$$

The parameters k_p and k_d have to be adjusted experimentally.

4.2 Nonlinear Optimisation

The simplex algorithm of Nelder and Mead [5] is a useful tool for minimizing a cost functional J_c, e.g. for minimizing the least square sum

$$J_c = \int_{t_1}^{t_2} (\omega_{bit} - \Omega_{des})^2 \, dt \approx \sum_{t_a}^{t_b} \Big(\omega_{bit}(t_i) - \Omega_{des}\Big)^2. \tag{23}$$

The idea of the simplex algorithm is shown in Figure 4. The two optimal parameters form a point in a two dimensional plane corresponding k_p and k_d, respectively. The algorithm works as follows: At first, three arbitrary points which construct a triangle are chosen and the cost functional is evaluated for these points. The worst point is replaced by a new point which is symmetric about the *centre of mass* of the remaining points, i.e. the position of the triangle is changed. The cost functional is evaluated for the new point. Depending on the value of the new point in comparison with the others, different rules can apply: the triangle can change its position and its size. Figure 4 only shows

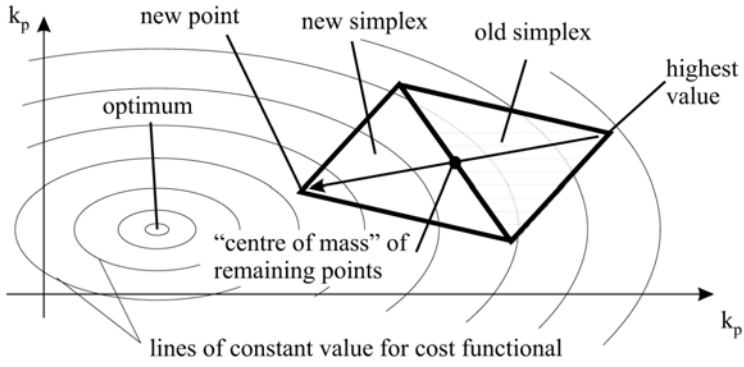

Figure 4. Simplex algorithm - mirroring of a simplex

the case of mirroring. After each iteration the simplex approaches the optimum. When the size of the simplex falls below a certain bound, the iteration is stopped and the optimal values of k_p and k_d are reached.

5. Implementation

The POD was implemented in the transputer using a dialect of the language basic which does not provide special functions for eigenvalue calculation. Since only the biggest eigenvalue is needed, this value is calculated by vector iteration:

$$\underline{\phi}_k = \frac{\underline{\underline{C}}(t_i) \cdot \underline{\phi}_{k-1}}{||\underline{\underline{C}}(t_i) \cdot \underline{\phi}_{k-1}||}. \tag{24}$$

After few iterations (3 to 5) the eigenvector is approximated sufficiently well. The cost functional (22) is evaluated from experimental data, the value varies statistically. Thus, multiple measurements are taken and the sum of the mean and the variance is used.

Using this approach for the active damping results in the speed of the drill–string presented in Figure 5. The angular velocities at the top and the bottom of the string are shown. The vibrations of the speed at the bit are actively damped after the control is started.

6. Summary

A detailed modelling process yields linear equations of motion which describe torsional and flexural vibrations. The torsional vibrations are self–excited vibrations caused by the characteristics of the applied moment. This

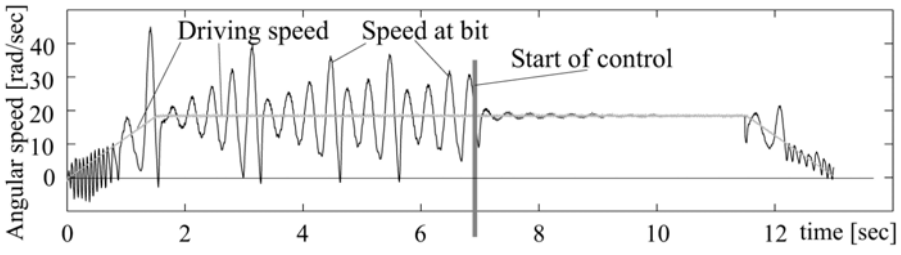

Figure 5. Angular speed at bit - uncontrolled and controlled

moment depends on the angular velocity at the bit and varies as long as torsional vibrations occur. The state dependent applied external moment excites flexural vibrations. In order to minimize the torsional and the flexural vibrations only the torsional vibrations are actively damped. The angular speed is measured at five locations and the signal is reduced applying a recursive POD. The recursive algorithm guarantees a fast calculation and decaying influence of previously measured data. The resulting signal is used for the feedback control. The controller parameters are optimized with respect to a cost functional using a simplex method. This approach was implemented in an experimental setup and the torsional vibrations were successfully actively damped.

References

[1] O. Kust. *Selbsterregte Drehschwingungen in schlanken Torsionssträngen. Nichtlineare Dynamik und Regelung*. Fortschr.-Ber. VDI, Reihe 11, Nr. 270. VDI Verlag, Düsseldorf, 1998.

[2] A. I. Lurie, *Analytical Mechanics*, Berlin, Springer, 2002.

[3] L. E. Malvern, *Introduction to the Mechanics of a Continuous Medium*, Prendice–Hall, London, 1969.

[4] L. Meirovitch, *Analytical Methods in Vibrations*, The Macmillan Company, New York, 1967.

[5] R. Nelder and J.A. Mead, "A simplex method for function minimization," *Computer Journal*, 7:308–313, 1965.

[6] R. Walter, *Differentialgeometrie*, BI-Wissenschaftsverlag, Mannheim, Wien, Zürich, 2. edition, 1989.

DYNAMIC VIBRATION ABSORBER FOR FRICTION INDUCED OSCILLATIONS

Combined Dynamics to Settle Vibrations

Karl Popp and Martin Rudolph
Institute of Mechanics, University of Hannover, Germany
popp@ifm.uni-hannover.de

Abstract: Friction induced vibrations in technical applications are usually unwanted, as they create noise, diminish accuracy and increase wear. By this article the authors intend to give an insight in basic excitation mechanisms of friction induced vibrations and to show possible ways of avoidance. A dynamic vibration absorber is investigated in detail. Numerical and experimental results show that stick-slip vibrations can be avoided or at least reduced considerably by an additional spring-mass-damper system attached to the main oscillator.

Key words: Vibration absorber, stick-slip, nonlinear dynamics.

1. Introduction

Friction is an everyday phenomenon which everybody is familiar with. From an engineering point of view two different phenomena can be distinguished. First, the resistance against the start of a relative motion of bodies (sticktion) which is caused by the contact between these bodies. Secondly, the resistance against an existing relative motion (sliding) of two contacting bodies. An intermittant change of sticktion and sliding is called a stick-slip motion, it belongs to friction induced oscillations.

In the following sections a mechanism to generate self-excited friction induced vibrations will be shown and explained by means of a simple mechanical model. If this mechanism has been understood countermeasures can be taken. Thus, subsequently some measures to avoid friction induced vibration will be summarized and a dynamic vibration absorber will be presented.

G. Rega and F. Vestroni (eds.),
IUTAM Symposium on Chaotic Dynamics and Control of Systems and Processes in Mechanics, 419–427.

2. Excitation Mechanisms

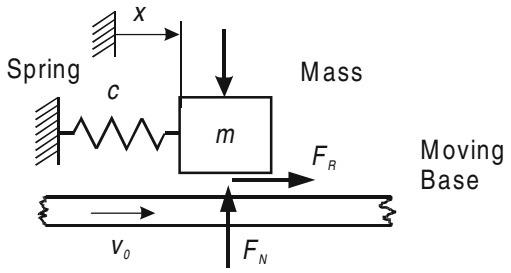

Figure 1. Model of a simple friction oscillator.

As an example we investigate the simple friction oscillator shown in Fig. 1. This oscillator with one degree of freedom DOF represents a classical self-excited system, cp. [5].

The energy source is a moving base with constant speed v_0 driving the mass m of the discrete spring-mass oscillator. The friction force F_R usually depends on the relative velocity $v_{rel} = v_0 - \dot{x}$ between base and mass. Different friction characteristics $F_R = F_R(v_{rel})$ are shown in Fig. 2.

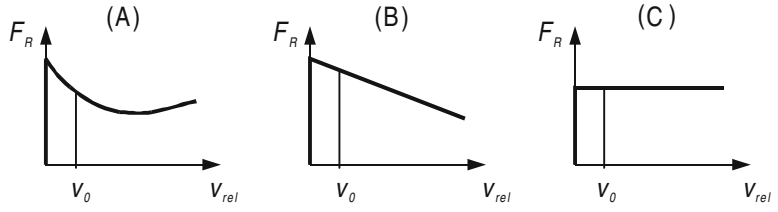

Figure 2. Friction characteristics : (A) generally decreasing, (B) linearly decreasing, (C) constant.

In the characteristics (A) and (B) the limit value of the static friction force $F_R(v_{rel} \to 0)$ is greater than the kinetic friction force $F_R(v_{rel} \neq 0)$, thus, the friction force characteristic is decreasing for small values of v_{rel}.

This effect has been observed experimentally many times, cp. [1], [3], [4]. If the base velocity is adjusted so that the friction force shows a negative slope at the equilibrium state $x = x_S$, $\dot{x} = 0$, then this state becomes unstable if no damping is present. Hence, the amplitudes grow and the trajetory in the $x, \dot{x}$-phase plane reaches a limit cycle.

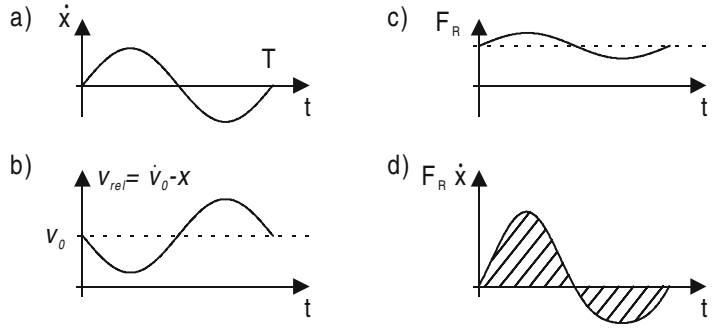

Figure 3. Mechanical power input at the mass.

The physical reason for the instability is an energy transfer from the base to the mass. This is quantitatively shown in Fig. 3 by a sequence of time histories of one period duration. Assuming a small mass motion around the equilibrium position with a sinusodial velocity, Fig. 3a, results in a sinusoidal fluctuation of the relative velocity around the mean value v_0, Fig. 3b. Due to the force characteristic the corresponding friction force is larger for small values of v_{rel} than for large values of v_{rel} , Fig. 3c. Thus, the product $F_R\dot{x}$ that denotes the mechanical power input at the mass shows larger positive than negative values, Fig. 5d. Hence, a positive input of mechanical energy,

$$\Delta E_{in} = \int_0^{T_S} F_R \dot{x}\, dt > 0\,, \tag{1}$$

results during each period T_S , which in turn leads to increasing vibration amplitudes until the limit cycle is reached. However, the decreasing friction characteristic is not the only mechanism that can lead to an increase of mechanical energy due to eq. (1). Even for a constant kinetic friction coefficient according to characteristic (C) a positive energy input is possible if we assume fluctuating normal forces F_N. This can also be shown by the same sequence of diagrams in Fig. 3, only the interpretation of Fig. 3c has to be changed. Suppose the normal force F_N consists of a constant part and a superimposed sinusoidally fluctuating part,

$$F_N(t) = F_0 + \hat{F}_N \sin(2\pi t / T_S)\,. \tag{2}$$

Then it follows that the friction force $F_R(t) = \mu F_N(t)$, $\mu = \text{const.}$, fluctuates as shown in Fig. 3c. The consequence is a positive input of mechanical energy, compare eq. (1). Important for this excitation mechanism is, that the sinusoid of $\dot{x}$, Fig. 3a, and that of F_R, Fig. 3c, are in phase. If they would be in antiphase, the energy input would turn out to be negative

resulting in damping. The last mentioned mechanism can be used to reduce the vibration amplitudes and to stabilize the equilibrium position. This mechanism is the basic idea behind the vibration control by the dynamic vibration absorber which will be described later in this paper.

3. Measures to Avoid Friction Induced Vibrations

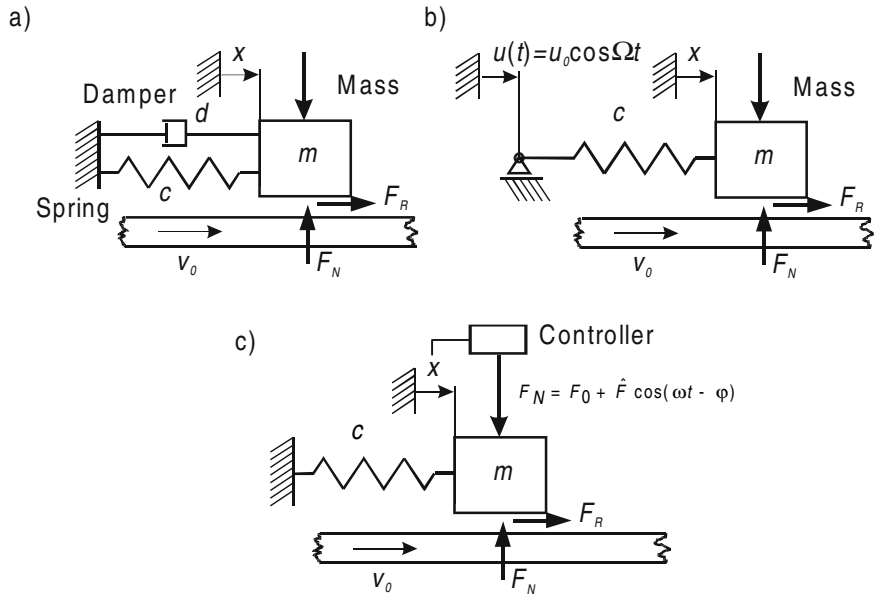

Figure 4. Measures to avoid stick-slip motion: a) additional external damping, b) additional external excitation, c) fluctuating normal forces.

In this section different measures shall be summarized that allow to avoid self-excited friction induced vibration. We start with a review of the 1 DOF-systems depicted in Fig. 4.

Firstly, an increase of external damping can compensate the negative damping induced by a decreasing friction characteristic, see Fig. 4a.

Secondly, an additional external excitation can be applied, either as a harmonic base excitation, cp. Fig. 4b, or as a harmonic force excitation of the mass. This excitation can break up the robust stick-slip limit cycle, however, it usually leads to chaotic motions showing a rich bifurcational behaviour. This case has extensively been studied in [5], [7], [8], [10], and shall not be discussed here. However, for high excitation frequencies a stabilisation is possible, see e.g. [12].

Thirdly, vibration control can be used to provide fluctuating normal forces that can result in a negative energy input as has been shown in the above chapters.

In the following it will be shown that it is possible to neutralize the self-excitation mechanism of the falling friction characteristic by fluctuating normal forces.

Considering a block sliding on a moving base, cp. Fig. 4c, we assume a harmonic motion

$$x(t) = \hat{x}\cos\omega t, \quad \omega = \frac{2\pi}{T_S} \quad , \tag{3}$$

of the block and a harmonic normal force

$$F_N(t) = F_0 + \hat{F}\cos(\omega t - \varphi) \, , \tag{4}$$

where there is a phase shift φ between normal force and motion.

Further on, calculations are done with friction characteristic (B), but assuming that always $v_{rel} > 0$ holds, i. e. no sticking occurs. Then the energy transferred into the system by the friction force during one period T_S of vibration can be determined by

$$\Delta E_{in} = \int_0^{T_S} F_R(t)\,\dot{x}(t)\,dt = -(\mu_0 - \delta v_0)\pi\sin\varphi\,\hat{F}\hat{x} + \delta\pi\omega F_0\hat{x}^2 = E^- + E^+ . \tag{5}$$

Expression E^+ gives the energy growth due to negative damping created by the friction characteristic. The dynamical part of F_N leads to E^-, which is a dissipated energy if $\sin\varphi > 0$. So, this inequality is a necessary condition for a damping effect by fluctuating normal forces.

A sufficient condition for the wanted effect is

$$\Delta E_{in} < 0 \Rightarrow \sin\varphi > \frac{\delta\omega F_0\hat{x}}{(\mu_0 - \delta v_0)\hat{F}} \, . \tag{6}$$

Optimal damping is given if ΔE_{in} becomes a minimum,

$$\Delta E_{in} \to \text{Min} \quad \Rightarrow \quad \varphi = \varphi^* = \frac{\pi}{2} \, . \tag{7}$$

In this case, the optimal dissipated energy reads

$$\Delta E_{in}^* = \Delta E_{in}(\varphi = \varphi^*) = -(\mu_0 - \delta v_0)\pi\hat{F}\hat{x} + \delta\pi\omega F_0\hat{x}^2 \, . \tag{8}$$

The optimal force amplitude $\hat{F}$ is given for $\hat{F} = F_0$. For amplitudes $\hat{F} > F_0$ the mass would lift off from the moving base.

The effect of fluctuating normal forces can be realized by active vibration control, cp. Fig. 5c. Measuring the stick-slip displacement $x(t)$ or the stick-slip acceleration $\ddot{x}(t)$ results in a control to get the optimal phase shift

$\varphi = \varphi^* = \pi/2$ for the optimal normal force $F_N(t)$. The phase shift can be provided by using either the displacement measurement at a shifted time,

$$F_N(t) = F_0 + \hat{F}\cos(\omega t - \frac{\pi}{2}) = F_0 + \frac{\hat{F}}{\hat{x}}x(t - \frac{T_S}{4}), \qquad (9)$$

or to take the acceleration measured at a shifted time ,

$$F_N(t) = F_0 + \hat{F}\cos(\omega t - \frac{\pi}{2}) = F_0 - \frac{\hat{F}}{\hat{\ddot{x}}}\ddot{x}(t - \frac{T_S}{4}). \qquad (10)$$

Also other control regimes are possible e.g. using delayed feedback, cp. [2]. Active control, however, requires additional energy. Thus, a passive control regime would be desirable that adds damping and provides fluctuating normal forces. The idea behind passive vibration control is to introduce an additional degree of freedom normal to the motion of the body and to couple both degrees of freedom. This can be done by a coupling with a tilted spring or by an inertia coupling, see Fig.5 and the following section about dynamic vibration absorber.

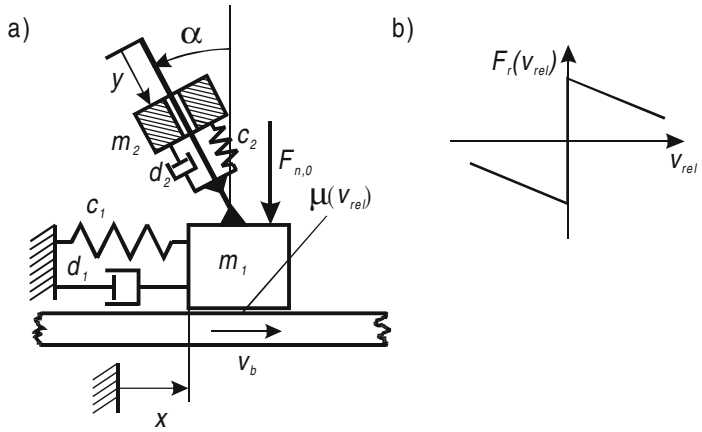

Figure 5. a) Extended friction oscillator, b) Friction characteristic

4. Dynamic Vibration Absorber

The basic friction oscillator is extended by an additional oscillator (absorber) which is tilted against the normal direction of the friction contact, like in Fig. 5a. In the case of sliding the equations of motion for this system are given by

$$\sin\alpha\, x'' + y'' + 2D_2 b y' + b^2 y = 0\,, \qquad (11)$$

$$(1+a)x'' + a\sin\alpha\, y'' + 2D_1 x' + x = F_r(v_{rel})\,, \qquad (12)$$

where

$$(\,)' = \frac{d}{d\tau},\ \tau = \omega_1 t,\ \omega_{1,2} = \sqrt{\frac{c_{1,2}}{m_{1,2}}},\ D_{1,2} = \frac{d_{1,2}}{2m_{1,2}\omega_{1,2}}$$

$$a = \frac{m_2}{m_1}, b = \frac{\omega_2}{\omega_1}, F_r(v_{rel}) = \mu(v_{rel})F_n^*.$$

The right hand side of eq. (12) is composed by the friction characteristic

$$\mu(v_{rel}) = \mathrm{sgn}(v_{rel})(\mu_0 - k|v_{rel}|),\ v_{rel} = v_b - \dot{x}. \tag{13}$$

which is depicted in Fig. 5b, and the normal force

$$F_n^* = \frac{1}{c_1}(F_{n0} + F_{n\,dyn}) = F_{n0}^* - a\cos\alpha\, y''. \tag{14}$$

If the mass m_1 sticks to the base, the friction force $F_r(v_{rel} = 0)$ becomes a reaction force and eq. (12) changes to

$$x'' = 0 \ \text{ with } x' = \frac{v_b}{\omega_1} \equiv \tilde{v}_b. \tag{15}$$

while eq. (11) stays the same.

The condition for the transition from sliding to sticking is

$$x' = \tilde{v}_b \ \text{ and } \left| a\sin\alpha\, y'' + 2D_1 x' + x \right| \le \mu_0 F_n^* \tag{16}$$

while the transition from sticking to sliding takes place if

$$\left| a\sin\alpha\, y'' + 2D_1 x' + x \right| > \mu_0 F_n^*. \tag{17}$$

5. Experimental Results

The theoretical results were checked by experiments. Therefore an existing test rig for stick-slip vibrations has been equipped by an additional oscillator. The mechanical parameters of this setup have been identified to

$$\begin{aligned} &a = 0.56, b = 0.924, D_1 = 0.01, N_0^* = 2.638\cdot 10^{-3}\,\mathrm{m}, \\ &\tilde{v}_b = 1.74\cdot 10^{-3}\,\mathrm{m}, \mu_0 = 0.37, k_w = 27.82(\mathrm{ms})^{-1}. \end{aligned} \tag{18}$$

As it can be seen in Fig. 6, theoretical and experimental results agree quite well bearing in mind the known complexity of frictional processes. An unsymmetry of the stick-slip region has been found which indicates the effect of fluctuating normal forces. As the time histories show, the system behavior is unequal for negative and positive values of α. Deviations from the theoretical results are due to variations in the friction characteristic.

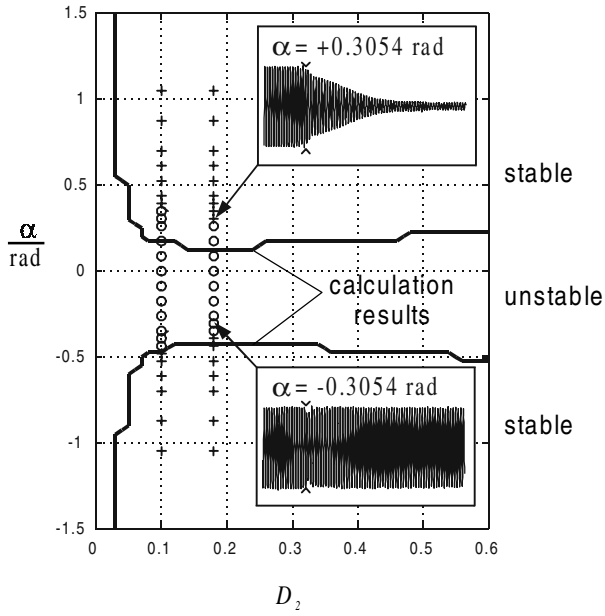

Figure 6. Calculated stability bounderies (solid lines) and experimental results (crosses indicate decaying vibrations and circles stand for limit cycles). time series showing the system's behavior for two different values of α, which are equal in the absolute value but have opposite sign.

6. Concluding Remarks

Knowing and understanding the mechanisms to generate self-excited friction induced vibrations can help to avoid these unwanted motions. To this aim the following measures have been shown and described shortly: (a) adding proportional damping, (b) applying a harmonic external base excitation or force excitation, (c) implementing active or passive vibration control. The vibration control is based on the mechanism of fluctuating normal forces. This effect results in an energy flow into the system as mentioned above. However, choosing the proper phase relation this effect can be used to take energy out of the system and, thus, achieve damping.

Numerical and experimental investigations show that stick-slip vibrations can be avoided or at least reduced by this dynamic vibration absorber. Two effects are responsible for this.: (i) The absorber contributes linear damping to the system. (ii) Fluctuating normal forces neutralize the excitation due to a decreasing friction characteristic. Experiments show that the theoretically

predicted stable operation regions do exist and that the absorber works efficiently.

References

[1] E. Brommundt, "Ein reibschwinger mit selbserregung ohne fallende kennlinie," *ZAMM*, **75**, 11, pp. 811-820, 1995.

[2] F.J. Elmer, "Controlling friction," *Phys. Rev. E*, 57, 5, pp. 4903-4906, 1998.

[3] J. Franke, "Über die abhängigkeit der gleitenden reibung von der geschwindigkeit," *Civil Ing.* , 1882.

[4] I. Galton, "The action of brakes. On the effect of brakes upon railway trains," *Engng.,* 25, pp. 469-472, 1878.

[5] N. Hinrichs, M. Oestreich, and K. Popp, "On the modelling of friction oscillators," *J. Sound Vib.*, **216**, pp. 435-459, 1998.

[6] A. Luongo, A. Di Egidio, and A. Paolone, "Multiple scale bifurcation analysis for finite-dimensional autonomous systems," *Recent Res. Devel. Sound & Vibration*, 1, pp. 161-201, Transworld Research Network Publ., Kerala, India, 2002.

[7] K. Magnus and K. Popp, *Schwingungen*, 6th edition, Teubner, Stuttgart, 2002.

[8] M. Oestreich, N. Hinrichs, and K. Popp, "Bifurcation and stability analysis for a non-smooth friction oscillator," *Arch. Appl. Mech*., **66**, 5, pp. 301-314,1996.

[9] K. Popp (editor), *Detection, Utilization and Avoidance of Nonlinear Dynamical Effects in Engineering Applications*, Shaker, Aachen, 2001.

[10] K. Popp and P. Stelter, "Stick-slip vibrations and chaos," *Phil. Trans. R. Soc. Lond.*, **332**, pp. 89-105, 1990.

[11] R. Schroth, W. Rumold, N. Hoffmann, and M. Fischer, "Development of an elastic multibody system approach for friction induced oscillations," Short Comm. at *GAMM Conf. 2001*, Zürich, 2001.

[12] J.J. Thomsen, *Using Fast Vibrations to Quench Friction Induced Oscillations*, Report No 613, TU Denmark, 1999.

CONTROL OF LIMIT CYCLE OSCILLATIONS

Werner Schiehlen and Nils Guse
Institute B of Mechanics
University of Stuttgart
70550 Stuttgart, Germany
wos@mechb.uni-stuttgart.de

Abstract: Limit cycles are defined as periodic motions in mechanical systems. Self excited systems like Van der Pol oscillators are characterized by asymptotically stable limit cycles due to steady energy dissipation. On the other hand, conservative systems show marginally stable limit cycles without energy dissipation. However, such motions are very sensitive to disturbances and, therefore, less helpful in engineering. By adding control to conservative systems asymptotic stable, weakly dissipative limit cycles can be found. It is shown how limit cycle oscillations can be adapted to prescribed motions in manufacturing processes reducing energy consumption. For this purpose the shooting method is employed, harmonic and arbitrary prescribed motions are considered.

Key words: Control, limit cycle, energy consumption, shooting method.

1. Introduction

Manufacturing processes require periodic motions which may be realized by active robot control with high energy demand or by a passive limit cycle of a nonlinear conservative system and some additional low energy control.

A well established robot control principle is inverse dynamics which is used to overcome high nonlinearities typical for mechanical systems undergoing large displacement motion. Based on an accurate model of the system under consideration, all the nonlinearities are compensated first by control action and, then, the remaining double integrator is controlled by linear feedback. This approach is very attractive to control engineers since a broad variety of design tools can be applied successfully. However, this principle results in high energy demand, see e.g. WALDRON.

In this paper, the application of nonlinear conservative oscillators is proposed to generate the required motion coarsely without energy dissipation and

G. Rega and F. Vestroni (eds.),
IUTAM Symposium on Chaotic Dynamics and Control of Systems and Processes in Mechanics, 429–439.

to adjust the motion finely by linear control with strongly reduced energy consumption. Thus, periodic trajectories are adapted as closely as possible to the limit cycle of the underlying mechanical system. A similar approach was chosen by BABITSKY et. al. for resonant vibration machines. Here, we will additionally specify the period and desired trajectory of the system. The fundamentals of energy consumption and energy storage of mechanical systems with rheonomic constraints have been analyzed for a linear harmonic oscillator, see SCHIEHLEN. it is shown how spring characteristics can be chosen to reduce the energy consumption for arbitrary periodic trajectories of a robot arm.

The power aspects of inverse dynamics control systems or rheonomic constraints, respectively, will be reported for an actively controlled oscillators with one degree of freedom. Then, these principles will be applied to a robot arm which shows very good results featuring the control of limit cycles.

2. Power Aspects of an Actively Controlled Oscillator

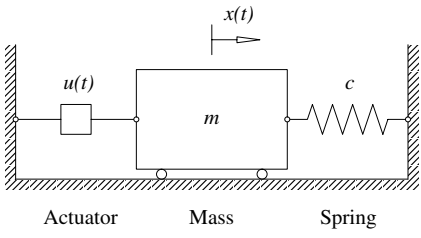

Figure 1. Actively controlled oscillator.

It is very well known that a harmonic oscillator is a conservative system with a periodic exchange of kinetic and potential energy. The resulting motion is characterized by a fixed frequency which can not be adjusted during operation. In technological processes, however, motions with an adjustable frequency are often required demanding active control. Due to the necessary power supply a controlled oscillator, shown in Figure 1, is no longer conservative. The equation of motion reads simply $m\,\ddot{x}(t) + c\,x(t) = u(t)$ where m is the mass, c is the spring coefficient and $u(t)$ is the actuator force. For a harmonic prescribed motion $r(t) = -A\,\cos\omega t$ the actuator force follows from the principle of inverse dynamics as $u_p(t) = A\,(m\omega^2 - c)\cos\omega t$, see also FALB et. al. and CRAIG.

The energy consumed in the first quarter of a cycle is $W(t = \pi/2\omega) = \frac{1}{2}A^2(m\omega^2 - c)$. Thus, for the spring coefficient $c = m\omega^2$ the actively controlled system remains conservative. By adding a velocity feedback $u(t) = u_p(t) - D(\dot{x}(t) - \dot{x}_p(t))$ with some positive coefficient $D > 0$ an asymptotically stable limit cycle is obtained. The resulting control system including the energy supervision is shown in figure 2. A limit cycle is presented in figure 3.

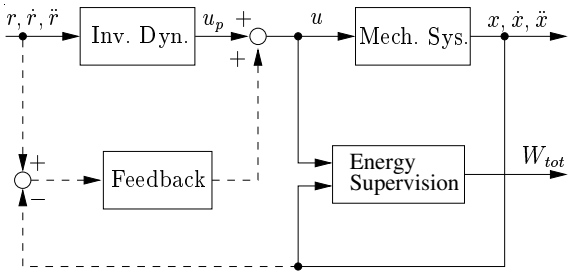

Figure 2. Control loop of the system.

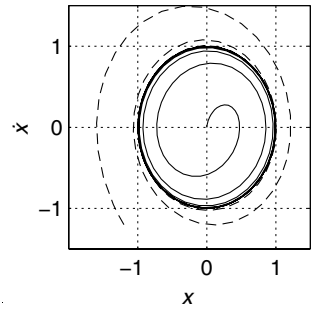

Figure 3. Limit cycle.

For prescribed motions with piecewise constant accelerations often found in technological processes nonlinear springs with a characteristic $n(x)$ may be used. Typical characteristics read as

$$n(x) = \begin{cases} \alpha\, x(t) - \beta\, x^3(t) & \text{cubic degressive} \\ x(t) & \text{linear} \\ \delta\, x(t) + \varepsilon\, x^3(t) & \text{cubic progressive} \end{cases} \tag{1}$$

It has been shown that nonlinear springs offer a saving up to 61% for a prescribed motion with piecewise constant acceleration, see SCHIEHLEN.

3. Control Based on Limit Cycles

The spring mass oscillator shows that the storage property of springs exploited in a controlled system offers energy savings of easily more than 50%. For more complex systems, the problem is to design these springs such that still energy can be saved. For systems which undergo periodic motions, it is promising, to adjust the control system such that its limit cycle is very close to the desired trajectory.

The desired trajectory of the system defines the boundary conditions for the state of the motion as well. These conditions are the position and the velocity at the beginning and at the end of the motion, respectively. Thus, for a periodic motion, the state has to be the same after a full cycle. The goal is to adjust the mechanical system to meet the boundary conditions by adjusting its parameters, like spring fastening and stiffness. Therefore, the standard shooting method which is a helpful tool to solve boundary value problems is modified to get these parameters.

4. Shooting Method with Robot Application

With the standard shooting method as described e.g. in STOER a differential equation

$$\ddot{y} = f(t, y, \dot{y}) \tag{2}$$

with be boundary conditions $y(t_1) = A$ and $y(t_2) = B$ is solved by setting up the function

$$F(s) = y(t_2, s) - B = 0 \tag{3}$$

where $s = \dot{y}(t_1)$ is the variational value to be found. In other words: the end point $y(t_2)$ is a function of the initial slope s and has to meet B at time t_2. When $F(s)$ is solved for s, the starting slope s is found such that the differential equation meets the boundary conditions. For nonlinear systems it is rather difficult to solve equation (2) explicitly for s. Therefore, numerical solvers like the Newton-Raphson iteration are used to find the roots of equation (3).

Now, the shooting method is modified, so that system parameters instead of the initial slope can be found to meet the bounding conditions. As already said, the boundary conditions for this case are the position and the velocity.

For simplicity, an assembly robot is modeled as a double pendulum moving in a horizontal plane within a manufacturing process, as shown in figure 4.

The model consists of two particles m_1 and m_2 connected by two bars of length l_1 and l_2. The rotational springs (spring stiffness c_1 and c_2) can be mounted differently. In the zero position of the springs denoted by the constant

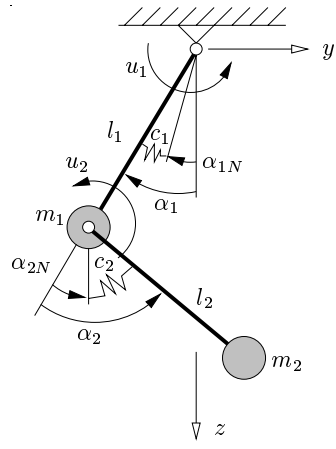

Figure 4. Model of a simplified assembly robot.

angles α_{1N} and α_{2N} the spring torque is vanishing. Two drive motors generate the torque u_1 and u_2 at the joints of the robot. The equations of motion read as

$$\begin{bmatrix} 2m_2 l_1 l_2 \cos\alpha_2 + (m_1+m_2)l_1^2 + m_2 l_2^2 + J_1 + J_2 & sym. \\ m_2(l_1 l_2 \cos\alpha_2 + l_2^2) + J_2 & m_2 l_2^2 + J_2 \end{bmatrix} \begin{bmatrix} \ddot{\alpha}_1 \\ \ddot{\alpha}_2 \end{bmatrix} + \begin{bmatrix} -m_2 l_1 l_2 \sin\alpha_2 (\dot{\alpha}_2^2 + 2\dot{\alpha}_1\dot{\alpha}_2) \\ m_2 l_1 l_2 \dot{\alpha}_1^2 \sin\alpha_2 \end{bmatrix} = \begin{bmatrix} c_1(\alpha_{1N} - \alpha_1) + u_1 \\ c_2(\alpha_{2N} - \alpha_2) + u_2 \end{bmatrix}.$$

For vanishing drive torques, the shooting method is applied to calculate the parameters for the system featuring a limit cycle close to the desired trajectory: starting with the given initial conditions, the position and velocity after the desired cycle period are calculated by integration. Estimated values for the design parameters c_1, c_2, α_{1N} and α_{2N} are used as initial values for the shooting process.

Now, equation (3) results in four boundary conditions written as

$$\begin{aligned} F_1(\boldsymbol{s}) &= \alpha_1(t_{end}, \boldsymbol{s}) - \alpha_{10} = 0 \\ F_2(\boldsymbol{s}) &= \alpha_2(t_{end}, \boldsymbol{s}) - \alpha_{20} = 0 \\ F_3(\boldsymbol{s}) &= \dot{\alpha}_1(t_{end}, \boldsymbol{s}) - \dot{\alpha}_{10} = 0 \\ F_4(\boldsymbol{s}) &= \dot{\alpha}_2(t_{end}, \boldsymbol{s}) - \dot{\alpha}_{20} = 0 \end{aligned}$$

composing the error vector

$$\boldsymbol{F} = \begin{bmatrix} F_1 & F_2 & F_2 & F_4 \end{bmatrix}^T \tag{4}$$

and the parameter vector

$$\boldsymbol{s} = \begin{bmatrix} c_1 & c_2 & \alpha_{1N} & \alpha_{2N} \end{bmatrix}^T . \tag{5}$$

The roots of $\boldsymbol{F}$ can be calculated using the Newton-Raphson iteration with

$$\left.\frac{\partial \boldsymbol{F}}{\partial \boldsymbol{s}}\right|_{\boldsymbol{s}^i} \Delta \boldsymbol{s}^i = -\boldsymbol{F}(\boldsymbol{s}^i) \tag{6}$$

and

$$\boldsymbol{s}^{i+1} = \boldsymbol{s}^i + \Delta \boldsymbol{s}^i \ . \tag{7}$$

where the Jacobian $\frac{\partial \boldsymbol{F}}{\partial \boldsymbol{s}}$ is numerically computed using finite differences. The result is a set of parameters $\boldsymbol{s}$ for the robot model such that the boundary conditions of the integration for a cycle are met.

Four limit cycle trajectories of the robot are treated, see also REBER. Firstly, a harmonic constraint motion in $z-$ and $y-$direction, then the same two trajectories with an arbitrarily prescribed motion.

5. Actively Controlled Harmonic Motion

Firstly, the motion of the second particle is prescribed as a harmonic oscillation in $z-$direction as

$$y = 0\,, \tag{8}$$

$$z = B + A\sin\omega t\,. \tag{9}$$

Figure 5 shows the corresponding trajectory. The parameters (spring stiffness and spring mounting) of the system have been calculated using the shooting method as described above. In figure 6 the resulting trajectory of the system without control is shown for some starting parameters (dashed line) and for the parameters computed by the shooting method resulting in a limit cycle (solid line). A difference between the desired trajectory in figure 5 and the limit cycle can hardly be noticed but there is a very small deviation to the right. Figure 7 shows the angles α_1 and α_2 as well for the desired trajectory as for the limit cycle motion. No difference is visible.

Figure 8 shows the total work W_{tot} that is required by the drive motors when the system is controlled by inverse dynamics control for one cycle of the periodic motion. The values are normalized using the maximum amount of work. The solid line shows the work consumed without springs in the system. The dashed line shows the amount of work that is needed when the springs are added resulting in a limit cycle very close to the desired trajectory. Now, much less energy is required to force the system onto the desired trajectory. In this case saving of 94% is obtained.

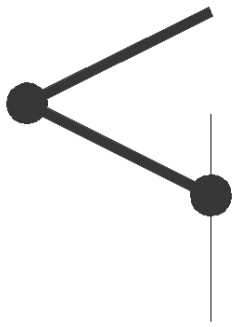

Figure 5. Desired trajectory of motion in $z-$direction.

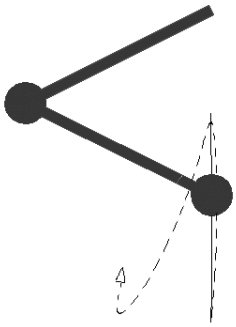

Figure 6. Trajectory of the system using starting parameters (dashed line) and the limit cycle computed by the shooting method (solid line).

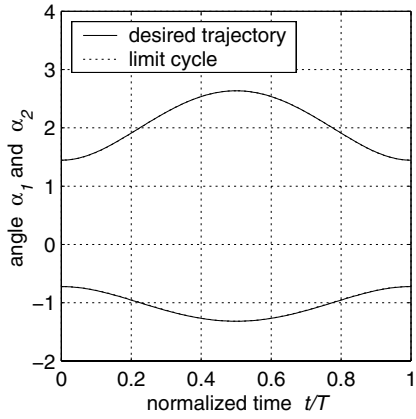

Figure 7. Angles α_1 and α_2 for the desired trajectory and the limit cycle of the motion in $z-$direction.

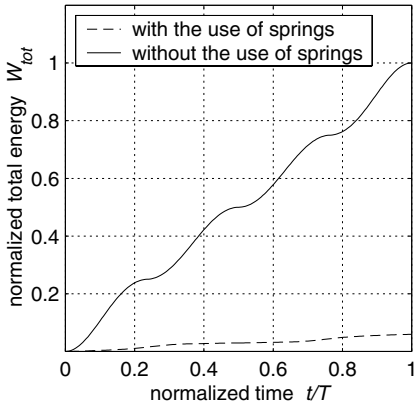

Figure 8. Energy consumed by the drives for the motion in $z-$direction.

Secondly, the motion in $y-$direction is investigated, see figure 9, which is prescribed to

$$y = A \sin \omega t \ , \tag{10}$$

$$z = B \ . \tag{11}$$

Due to the strongly nonlinear behavior of the system, it is more difficult to find a limit cycle that is close to the desired trajectory. In Figure 10 the dashed

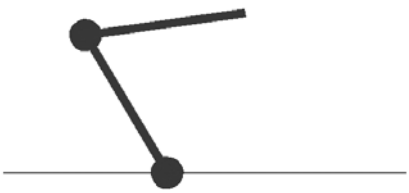

Figure 9. Desired trajectory of motion in $y-$direction.

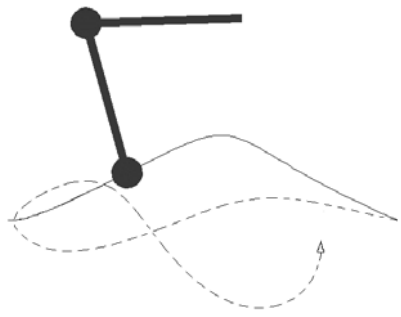

Figure 10. Trajectory of the system using starting parameters (dashed line) and the limit cycle computed by the shooting method (solid line).

line shows the trajectory using estimated starting parameter, the solid line represents the trajectory after the computation of the parameters by the shooting method. The limit cycle is not really close to the desired motion. This is due to the characteristic of the system, a straight motion can not be achieved by the two rotational springs. However, the shooting method leads to the closest possible limit cycle.

Here, the dashed line shows again the trajectory using estimated starting parameter, the solid line represents the trajectory after the computation of the parameters by the shooting method.

As shown in figure 11 the difference between the desired trajectory and the limit cycle is visible for both angles. Obviously, more torque has to be applied by the drive motors to force the system onto the desired trajectory. Therefore, the savings of the system with springs compared to the system without springs are less than for the motion in , $z-$direction see figure 12. But still, 52% of energy can be saved.

6. Arbitrarily Prescribed Motion and Nonlinear Springs

It has already been shown by SCHIEHLEN that for technological processes that require a prescribed motion, e.g, with piecewise constant acceleration nonlinear springs offer additional savings. Therefore, the motions in $y-$ and

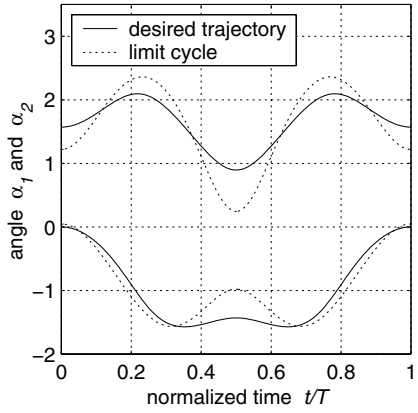

Figure 11. Angles α_1 and α_2 for the desired trajectory and the limit cycle of the motion in $y-$direction.

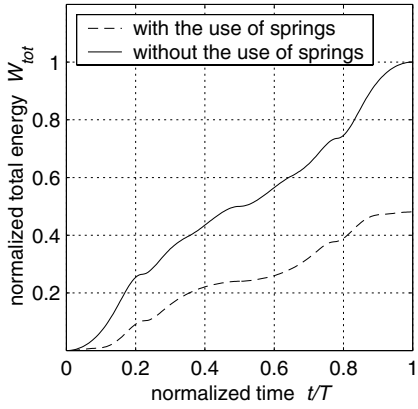

Figure 12. Energy consumed by the drives for the motion in $y-$direction.

in $z-$direction now are investigated for a rheonomic constraint of intervals of constant acceleration

$$y = 0 , \tag{12}$$

$$z = B + \frac{1}{2}At^2 \tag{13}$$

as shown in figure 13. The trajectory is geometrically the same as before, see figure 5, only the time history is different.

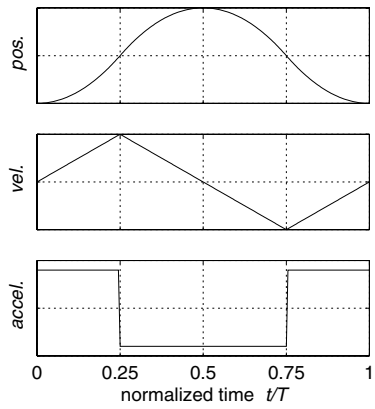

Figure 13. Position, velocity and acceleration of a prescribed motion.

Again, the modified shooting method is used to find a combination of parameters such that the system limit cycle is close to the desired trajectory. For the motion in $z-$direction, very good parameters can be found. The work consumed by the drive motors is reduced by almost 58%, see the dotted line in figure 16. Moreover, according to the findings for the mass-spring oscillator, cubic degressive nonlinear spring with two additional parameters α and β are used, which offer another 11% saving.

For the motion in $y-$direction, shown in figure 14, the parameters are calculated as described above. A limit cycle is found, see figure 15, which is slightly better than for the harmonic motion. Here, also the amount of consumed energy can be reduced by 33% when linear springs are used. It is reduced by another 5% when cubic degressive nonlinear springs are used, see figure 17.

7. Summary

It has been shown that adapting the limit cycle of a system to a prescribed periodic trajectory offers significant amounts of power savings. Firstly an actively controlled mass spring oscillator was considered to show the basic concept using nonlinear springs for systems with rheonomic constraints, too. These findings were extended to a more complex system, a two degree of freedom robot arm.

A shooting method was applied to adjust the system to the boundary conditions of a limit cycle close to the desired trajectory. Then, a low energy control is sufficient to force the system onto the desired trajectory.

An assembly robot model is supposed to operate on perpendicular straight trajectories with harmonic time history, and a time history with constant

Figure 14. Desired trajectory of motion in $y-$direction.

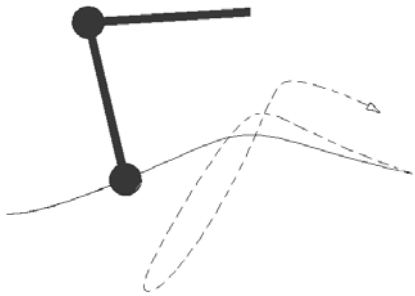

Figure 15. Trajectory of the system with *nonlinear* springs using starting parameters (dashed line) and the limit cycle computed by the shooting method (solid line).

accelerations. For the harmonic motion in $z-$direction, the limit cycle of the system could be adjusted very precisely by proper spring coefficients and mounting positions of the springs resulting in 94% energy saving. For the harmonic motion in $y-$direction, the limit cycle could be adjusted only coarsely reducing the energy consumption nevertheless by 52%. In the nonharmonic case also significant savings could be achieved. Here, nonlinear springs were investigated, too. The design parameters for the nonharmonic motion were

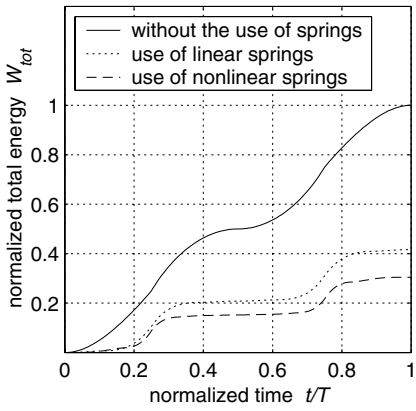

Figure 16. Energy consumed by the drives for the arbitrarily prescribed motion in $z-$direction.

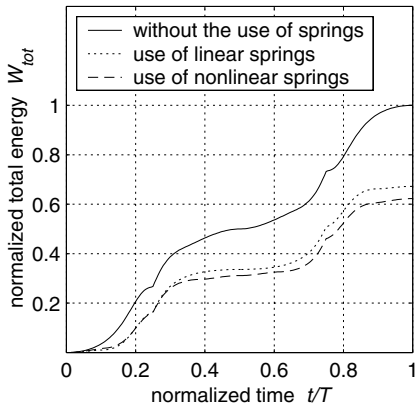

Figure 17. Energy consumed by the drives for the the arbitrarily prescribed motion in $y-$direction.

stiffness coefficients, spring mountings and the characteristics of nonlinearity. Nonlinear springs are recommended for all nonharmonic motions.

References

[1] K. J. Waldron, "Some Thoughts on the Design of Power Systems for Legged Vehicles," *Advances in Multibody Systems and Mechatronics*, Gerhard-Mercator-Universität, Duisburg, pp. 389–394, 1999.

[2] V. Babitsky, A. Kovaleva and A. Shipilov, "Relieved control in cyclic systems," *Arch. Appl. Mech.* 65:488-495, 1995.

[3] W. O. Schiehlen, "Power Demand of Actively Controlled Multibody Systems," *ASME Proceedings of DETC2001*, ASME Design Engineering Conference, DETC2001/VIB-21343, Pittsburgh, Pennsylvania, USA, 2001.

[4] P. L. Falb and W. A. Wolovich, "Decoupling in the Design and Synthesis of Multivariable Control Systems," *IEEE Transactions on Automatic Control* 12(6):651–655, 1967.

[5] J. J. Craig, *Introduction to Robotics: Mechanics and Control*, Reading, Massachusetts, Addison-Wesley, 1986.

[6] J. Stoer, *Einführung in die Numerische Mathematik*, Berlin, Heidelberg, New York: Springer, 1978.

[7] V. Reber, Energieuntersuchungen an einem nichtlinearen Mehrkörpersystem mit Grenzzykel, Studienarbeit STUD-210. Stuttgart: Universität, Institut B für Mechanik, 2003.

OPTIMAL CONTROL OF RETRIEVAL OF A TETHERED SUBSATELLITE

Alois Steindl[1], Wolfgang Steiner[2], Hans Troger[1]
[1] *Institute for Mechanics, Vienna University of Technology*
[2] *Wels College of Engineering*
Hans.Troger@tuwien.ac.ut

Abstract: The most important and complicated operations during a tethered satellite system mission are deployment and retrieval of a subsatellite from or to a space ship. The deployment process has been treated in [15]. In this paper retrieval is considered. We restrict to the practically important case that the system is moving on a circular Keplerian orbit around the Earth. The main problem during retrieval is that it results in an unstable motion concerning the radial relative equilibrium which is stable for a tether of constant length. The uncontrolled retrieval results in a strong oscillatory motion. Hence for the practically useful retrieval of a subsatellite this process must be controlled. We propose an optimal control strategy using the Maximum Principle to achieve a force controlled retrieval of the tethered subsatellite from the radial relative equilibrium position far away from the space ship to the radial relative equilibrium position close to the space ship.

Key words: Time optimal control, maximum principle, Pontrijagin, space pendulum

1. Introduction

The optimal control of deployment of a tethered subsatellite from a main satellite has been treated in [15]. We consider in this paper, supplementing the investigation in [15], the retrieval process. Although the optimal control strategy is similar, some additional aspects have to be taken into account, as it is immediately understandable, if one looks at the simpler but analogous problem of the motion of a string pendulum with fixed pivot point in the constant gravitational field. It is well known that the vertical stable rest position for constant string length remains stable for increasing the length of the string (deployment) but becomes unstable if the string is shortened (retrieval) as a function of time. In fact by analytic methods or by

G. Rega and F. Vestroni (eds.),
IUTAM Symposium on Chaotic Dynamics and Control of Systems and Processes in Mechanics, 441–450.

numerical simulation it can be shown that in this latter case symmetric oscillations about the vertical position are excited. These have the interesting property that the transversal amplitude defined by the initial condition remains constant whereas, the angular deflection increases strongly if the string length of the pendulum is continuously decreased. This behaviour will be characteristic for the out of plane behaviour of the tethered satellite in deployment or retrieval, respectively.

The concept of TSS (Fig. 1), that is, two or more satellites in orbit connected by thin and long cables – a length of 100 km is not unusual – has now been well established in astrodynamics. There exist various ideas of this concept for future space applications ([4, 5, 7, 8, 12]). Some flights (SEDS- and TSS1-projects) in orbit around the Earth were already performed by NASA during the last decade of the 20th century ([12]). The fundamental property

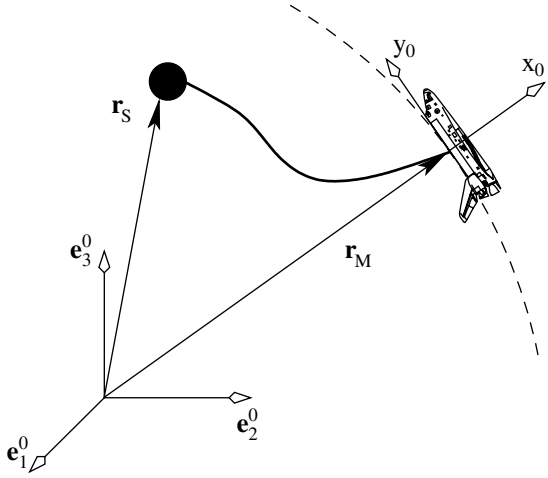

Figure 1. Tethered satellite system, consisting of two satellites connected by a massive tether, in orbit around a planet.

of a TSS, important for its practical applications ([5]), is that a system of two satellites connected by a tether with constant length moving on a circular Keplerian orbit around the Earth possesses a stable radial relative equilibrium, provided the length of the tether is not too long, that is, if it is not of the order of the radius of the orbit ([5], [10]). In this radial relative equilibrium the tether is under tension due to the action of the centripetal acceleration and the nonlinear gravitational field.

We investigate in this paper retrieval of a subsatellite to a space ship (see also [11], [6]), which moves on a Keplerian circular orbit. We want to retrieve the subsatellite from its initial configuration, which is the stable radial relative equilibrium, in which the subsatellite is far away from the space ship, to a radial relative equilibrium position, in which the subsatellite is close to the space ship.

That the process of retrieval will lead also to motion strongly deviating from the local vertical position which is rotating with orbital angular velocity in the orbital plane is due to the action of the Coriolis force. This has been shown already for the deployment process treated in [15], where a strong deviation from the local vertical relative equilibrium position in the plane of orbit occurs. For retrieval strong oscillatons set in as numerical simulations show ([16]). Even if the main control problem both of retrieval or deployment takes place in the orbital plane at least one has to be aware of the fact that these two operations are distict concerning perturbations out of the plane of orbit. However, from a practical point of view the planar problem can be treated since comparisons with the string pendulum and numerical simulations of the TSS show, that for retrieval the transversal motions out of the plane of orbit remain bounded.

It is important to mention a peculiarity of TSS, namely, how the control action is applied to the system. Of course, the control action to suppress undesired oscillations could be realized by thrusters acting on the subsatellite. However it is much simpler but still very effective to act on the motion of the system only by changing the tension force in the cable, which in the literature is called "tension control". We adopt this strategy and want, only by means of varying the tension force, to steer the subsatellite as fast as possible from its stable initially radial relative equilibrium position far away from the main satellite to its final position, which for constant tether length again is the stable radial relative equilibrium but now very close to the main satellite.

Making use of the Maximum Principle allows us to introduce constraints which are important from the practical point of view. We will consider in this paper two different constraints: (A) The motion of the retrieving tether should be monotonically decreasing. From a practical point of view this might be relevant, since it is only possible to pull the tether and it is impossible to push it. (B) The tension force during steered retrieval must always be positive and its maximum value must be bounded. In [15] also the constraint was considered that the deviation of the deploying subsatellite from the local vertical should remain small. Due to lack of space we do not include it here.

The paper is organized as follows: Since a straight forward application of the mathematical methods of optimal control theory can be easily formulated only for a finite dimensional system we consider a simplified system model, where the tether is assumed to be massless. The corresponding equations of motion to the three-dimensional motion are derived in [2] and presented in the next section. We also give a simple explanation for the out of plane instability during retrieval for an exponential law of reduction of the length of the string.

Since the basic application of the Maximum principle to such a process is described in detail in [15] for deployment and we only consider the planar problem, the difference between deployment and retrieval in the formulation

is marginal and we immediately present the corresponding results obtained for the simple massless model.

Finally, we shortly discuss the implementation of the obtained control strategy into a simulation package developed for a system of two satellites connected by a massive tether ([16]), which is described by a coupled system of nonlinear partial and ordinary differential equations. A comparison of these results for the more accurate model with those of the simplified model and their interpretation is given. Finally we comment whether applying tension control a three-dimensional analysis might be possible.

2. Simple Mechanical Model and Equations of Motion

We assume that the two satellites are modelled as point masses and are connected by a straight massless inextensible string. For such a system in its orbital motion around the Earth the equations of motion are derived in [2]. In dimensionless variables they are

$$\begin{aligned}
&\xi'' - \xi\left[\vartheta'^2 + \left((\varphi'-1)^2 + 3\cos^2\varphi\right)\cos^2\vartheta - 1\right] = \frac{Q_l}{m\omega^2 l_0} = -u \\
&\varphi'' + \frac{3}{2}\sin 2\varphi - 2(\varphi'-1)\vartheta'\tan\vartheta + 2\frac{\xi'}{\xi}(\varphi'-1) = 0 \\
&\vartheta'' + \frac{1}{2}\left((\varphi'-1)^2 + 3\cos^2\varphi\right)\sin 2\vartheta + 2\frac{\xi'}{\xi}\vartheta' = 0\,.
\end{aligned} \tag{1}$$

Here $\xi = l/l_0$, where l_0 is the length of the cable at the begining of the retrieval process. u denotes the dimensionless tether force. $(\quad)'$ designates the derivative with respect to a dimensionless time $\tau = \omega t$, where ω is the angular velocity of the Keplerian motion of the main satellite.

From the equations of motion (0) follows that for constant tether length the radial relative equilibrium position $\vartheta = 0, \varphi = 0, l = l_0$ (or. $\xi = 1$) is a solution resulting into the static tether tension $Q_l^{\text{stat}} = -3m\omega^2 l_0$ or $u_S = 3$.

For the special retrieval law

$$\ell(t) = \ell_0 e^{\nu\tau} \tag{2}$$

the equations of motion (0) become autonomous because

$$\xi'/\xi = \nu, \quad \xi''/\xi = \nu^2.$$

The first equation of (0) yields the necessary retrieval force and the two other equations yield the equilibrium angles

$$\vartheta = \vartheta_0 = 0 \quad \text{and} \quad \sin 2\varphi_0 = 4\nu/3.$$

By linearization of equations (0) about this equilibrium we see that the equation for the out of plane angle $\vartheta(t)$ completely decouples and takes the following form (we use again $\vartheta(t)$ as variable for the small displacement)

$$\vartheta'' + 2\nu\vartheta' + \left(1 + 3\cos^2\varphi_0\right)\vartheta = 0. \tag{3}$$

Since for retrieval according to (2) ν is negative, there appears in (3) a damping term with negative coefficient resulting in an unstable out of plane angular motion.

For the formulation of the control problem we make additional simplifying assumptions: (1) As drawn in Fig. 2 the main satellite (M) is supposed to move on a circular Keplerian orbit around the Earth. (2) The subsatellite m is connected to M by a massless straight string, on which the control force Q_ℓ acts. (3) We further neglect the influence of the motion of m on the dynamics of M. This is a practically reasonable assumption, since the mass ratio between M and m is of the order of 10^2, if, for example, M is the space shuttle and m is a satellite as it is used in the TSS1 experiment. (4) As in ([5]) we approximate the local gravity gradient by the so-called "near-field dynamics", that is by a locally linearly varying gravitational field. (5) The subsatellite (m) moves only in the orbit plane of M.

The control variable u, which is proportional to the tension force Q_ℓ, is allowed to vary in the interval $[u_{\min}, u_{\max}]$, where $u_{\min} \geq 0$, because the tether cannot transmit compressive forces. The upper bound $u_{\max}$ is chosen larger than the static force $u_S = 3$, which is necessary to sustain the equilibrium configuration at the beginning of the retrieval process. We choose $u_{\max} = 1.05\, u_S$ for our calculations. Instead of using the tension force u one could also think

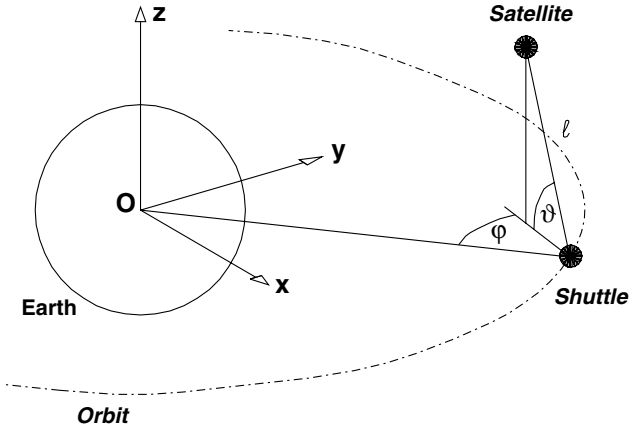

Figure 2. System geometry showing the shuttle with mass M on a prescribed circular orbit, the in-plane angle φ and out-of-plane angle ϑ of the straight tether of length l connecting the satellite (m) to M

of using the length change rate $\dot{\xi}$ as control variable. Since the tether is modelled as a string we are not able to apply a compressive force, i.e. to push the tether. Hence we could not satisfy the constraints for u.

Our main goal is to search for a time optimal solution.

3. Optimal Control Problem

The formulation of the optimal control problem is completely analogous to the one given in [15]. Only the constraint equation

$$\dot{\xi} \leq 0 \tag{4}$$

and the boundary conditions, where we assume that the subsatellite is steered from its relative equilibrium far away from the main satellite (tether length ξ_0) into a new relative equilibrium with tether length $\xi_T < \xi_0$:

$$\begin{array}{llllllll} \vartheta(0) & = 0, & \dot{\vartheta}(0) & = 0, & \vartheta(T) & = 0, & \dot{\vartheta}(T) & = 0, \\ \xi(0) & = \xi_0 = 1, & \dot{\xi}(0) & = 0, & \xi(T) & = \xi_T, & \dot{\xi}(T) & = 0. \end{array} \tag{5}$$

have to be changed.

The numerical solution of the boundary value problem by a homotopy strategy is also described in detail in [15].

For a tether length ratio $\xi_0/\xi_T = 100$ this procedure results in a time optimal solution (no monotonicity constraint (4)) with 5 switching points, which are obtained from the zeros of the switching function λ_4 as depicted in Fig. 3. The corresponding control function is depicted in Fig. 4 showing the "bang-bang" character of the control switching between $u_{\min} = 0$ and $u_{\max} = 3.15$. In

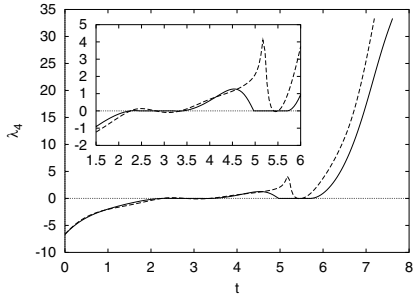

Figure 3. Switching function $\lambda_4(t)$ of the time optimal solution with (full line) and without (dotted line) the constraint $\dot{\xi} \leq 0$. Five (resp. seven) switching points are obtained for the length ratio $\xi_0/\xi_T = 100$.

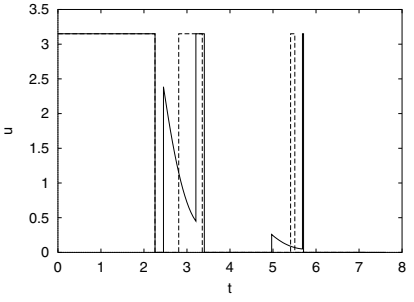

Figure 4. Bang-bang shaped control function $u(t)$ corresponding to the switching function of Fig. 3. Full lines with and dotted lines without constraint.

both figures the full lines designate the control taking the constraint (4) into account. If the switching function vanishes on an interval, so called boundary control is necessary, where the length is kept constant ([15]). The dotted lines in Fig. 3 and Fig. 4 are the switching function λ_4 and the control u, without taking into account of the constraint (4), hence resulting in the time optimal solution. The corresponding time dependence of the retrieving tether length and the variation of the in plane angle are shown in Fig. 8, where it is clearly visible that the constraint (4) is taken into account because of the occurence of sections where the tether length is kept constant.

The time optimal orbits in the orbital frame are depicted in Fig. 5 in the unconstrained case and in Fig. 6 taking the constraint (4) into account. The five switching points are marked by changing the drawn line of the orbit.

Those branches of the trajectory in Fig. 6, where $\dot{\xi}=0$, start at cusps and are denoted by u_{bnd}. They are circular arcs about the suspension points because the length is kept constant. The difference in retrieval time between the two solutions shown in Fig. 5 and in Fig. 6, which are distinguished by taking into account or neglecting the constraint (4), is about 4%.

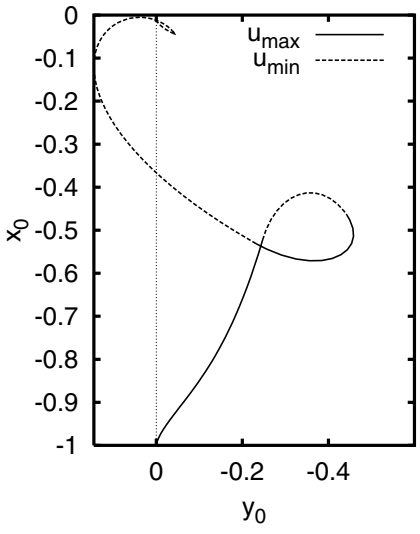

Figure 5. Time optimal flight paths of the subsatellite in the orbital coordinate frame (x_0, y_0) of Fig. 1 for unrestricted deviation without constraint (4).

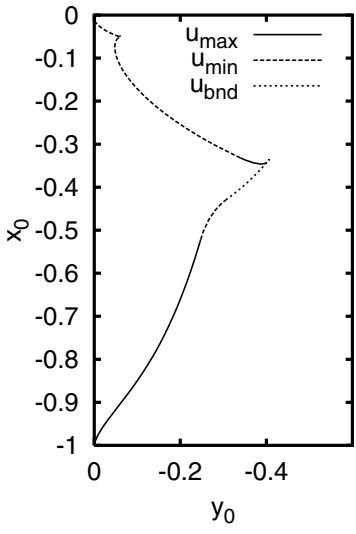

Figure 6. As in Fig. 5 but taking the constraint (4) into account.The dashed curves denote boundary arcs (ξ= const.)

4. Application of the Optimal Strategy to a Massive Tether System

The optimal control strategy works fine for the simplified model of the tethered satellite system. Since for a real system a flexible massive tether joins the two satellites we now want to show whether the strategy developed for the massles tether model can be of practical use for the system with massive tether. For this purpose we implement the optimal control strategy into the computer code developed in [16] which is based on the finite element discretization for a massive tether model.

We consider the case of the time optimal solution obtained for the system (0) with massless tether and without taking into account the constraint (4), that is $\dot{\xi} \leq 0$. We recall that for $\xi_0/\xi_T = 100$ in the time optimal case, 5 switching points are obtained, as is shown in Fig. 5. For a length ratio $\xi_0/\xi_T = 20$ we apply this result to the massive system and obtain Fig. 7.

We note that as in Fig. 5, neglecting the constraint (4) results in a loop in the motion of the subsatellite due to the fact that now the tether also partly is deployed during the time optimal retrieval process. The switching intervals

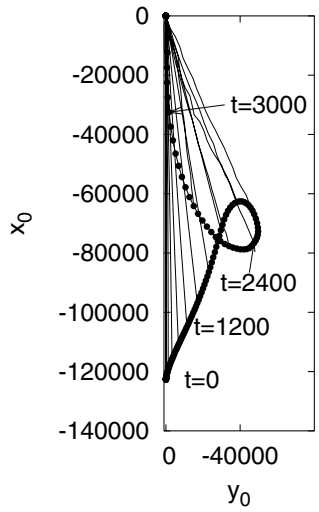

Figure 7. Trajectory of the subsatellite for the time optimal solution without the constraint $\dot{\xi} \leq 0$ for the massive tether model in the orbital frame. Three switching points are applied for the length ratio $\xi_0/\xi_T = 20$.

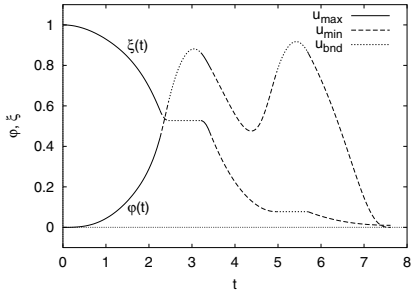

Figure 8. Retrieving tether length ξ and in-plane angle φ for the massless tether model corresponding to the control shown in Fig. 4 with active constraint (4).

obtained for the massless tether system are taken as inputs for the simulation of the continuous massive tether system. For the free flight phase we additionally used $u_{\min} = 0.005 u_S$. The flight path of the subsatellite with the massive tether shown in Fig. 7 follows the trajectory of the simpler optimal control model quite closely, but fails to meet the final boundary conditions precisely, because the dynamics of the simplified model used in the optimal control model and the model used in the FE simulation differ sligthly. By slightly adjusting the location of the switching points this small deviation could be corrected. See also the comments made in ([15]).

That the controlled motion of the continuous system, which is governed by a set of partial differential equations, is so close to the optimally controlled motion of the simple finite dimensional system is surprising at the first glance. But a plausible explanation is that the control action on the system by tension control is practically the same for both systems and is effective for the system with massive tether only if the tether is streched. This, however, is exactly the situation stipulated for the simplified model.

5. Conclusions

The main result of this paper is the extension of the optimally controlled deployment process of a tethered satellite presented in [15] to the process of retrieval.

Although the optimal control processes for deployment and retrieval in the orbital plane and their analyses are quite similar it still has to be remarked that for the retrieval process also the motion out of the orbital plane must, at least, be addressed. Here the question arises if assuming, as we did, that only tension control is applied, whether the three-dimensional problem of retrieval of a subsatellite from the radial relative equilibrium position far away from the main satellite to the radial relative equilibrium position close to the main satellite is controlable. Looking at the simpler problem of the motion of the string pendulum mentioned above might indicate that this is not the case, because for the string pendulum only planar oscillations can be extinguished by length manipulations and not three dimensional motions.

Hence our investigation performed in the orbital plane is a first step to be done in the full three dimensional control problem of retrieval of a subsatellite to a main satellite which still requires further investigations.

Acknowledgments

Financial support of this work was given by the Austrian Science Foundation (FWF) in the frame of project P15825-N05.

References

[1] E.M. Abdel-Rahman and A.H. Nayfeh, 'Pendulation reduction in boom cranes using cable length manipulation', *Nonlinear Dynamics*, 27, 255–269, 2002.

[2] P. Bainum and V.K. Kumar, 'Optimal control of the shuttle-tethered-subsatellite system', *Acta Astronautica*, 7, 1333–1348, 1980.

[3] B. Barkow, A. Steindl, H. Troger and G. Wiedermann, 'Some methods of controlling the deployment of a tethered satellite', *Int. J. Vibration and Control,* 9, 187–208, 2003.

[4] T. Beardsley, 'The way to go in Space', *Scientific American*, pp. 40-77 February 1999.

[5] V.V. Beletsky and E.M. Levin, 'Dynamics of space tether systems', *Advances of the Astronautical Sciences*, 83, 1993.

[6] F.L. Chernousko, 'Dynamics of retrieval of a space tethered system', *J. Appl. Maths. Mechs*, 59, 165-173, 1995.

[7] R.P. Hoyt, R.L. Forward, G.D. Nordley and C.W. Uphoff, 'Rapid interplanetary tether transport systems', IAF-99-A.5.10, *50th IAF Congress Amsterdam*, 31 pages, 1999.

[8] M. Krupa, A. Kuhn, W. Poth, M. Schagerl, A. Steindl, W. Steiner, H. Troger and G. Wiedermann, 'Tethered satellite systems: A new concept of space flight', *Eur. J. Mech. A/Solids* 19, S145-S164, 2000.

[9] M. Krupa, M. Schagerl, A. Steindl and H. Troger, 'Stability of relative equilibria. Part I: Comparison of four methods', *Meccanica* 35, 325–351, 2001.

[10] M. Krupa, A. Steindl and H. Troger, 'Stability of relative equilibria. Part II: Dumbell satellites', *Meccanica* 35, 353–371, 2001.

[11] A.K. Misra and V.J. Modi, 'Deployment and retrieval of shuttle supported tethered satellites', *J. Guidance and Control*, 5, 278–285, 1982.

[12] 'Proceedings of the fourth international conference on tethers in space', Science and Technology Corporation, Hampton, VA, 1995.

[13] W. Steiner, A. Steindl and H. Troger, 'Dynamics of a space tethered satellite system with two rigid endbodies', in [12], 1367–1379, 1995.

[14] W. Steiner, A. Steindl and H. Troger, 'Center manifold approach to the control of a tethered satellite system,' *Applied Mathematics and Computation*, 70, 315-327, 1995.

[15] A. Steindl and H. Troger, 'Optimal control of deployment of a tethered subsatellite', *Nonlinear Dynamics*, 31, 257-274, 2003.

[16] G. Wiedermann, M. Schagerl, A. Steindl and H. Troger, 'Computation of force controlled deployment and retrieval of a tethered satellite system by the finite element method', in *Proceedings of ECCM'99*, W.Wunderlich (ed.), pp. 410–429, 1999.

PASSIVE VIBRATION CONTROL BY NONLINEAR ENERGY PUMPING

Theoretical and Experimental Results

Alexander F. Vakakis[1], D. Michael McFarland[2], Lawrence Bergman[2], Leonid Manevitch[3] and Oleg Gendelman[3]

[1]*Division of Mechanics, National Technical University of Athens, and Dept. of Mechanical and Industrial Engineering (adjunct), University of Illinois at Urbana-Champaign*

[2]*Dept. of Aeronautical and Astronautical Engineering,University of Illinois at Urbana-Champaign*

[3]*Institute of Chemical Physics, Russian Academy of Sciences*

vakakis@central.ntua.gr

Abstract: We analyze energy pumping phenomena in a linear periodic substructure, weakly coupled to an essentially nonlinear attachment. By energy pumping we denote passive, one-way, irreversible transfer of energy from the linear substructure to the nonlinear attachment. As a specific application the dynamics of a system of linear coupled oscillators with a nonlinear end attachment is examined. Both theoretical and experimental results are discussed, including resonance capture cascades, i.e., a series of energy pumping phenomena occurring at different frequencies, with sudden lower frequency transitions between sequential events. The observed multi-frequency energy pumping cascades are particularly interesting from a practical point of view, since they indicate that nonlinear attachments can be designed to resonate and extract energy from an *a priori* specified set of modes of a linear structure, in compatibility with the design objectives.

Key words: Nonlinear energy pumping, vibration control.

1. Introduction

It was shown recently [1-3] that under certain conditions essentially nonlinear attachments can passively absorb energy from linear nonconservative (damped) structures, acting, in essence, as nonlinear energy sink. Then, *energy pumping* from the linear structure to the attachment

G. Rega and F. Vestroni (eds.),
IUTAM Symposium on Chaotic Dynamics and Control of Systems and Processes in Mechanics, 451–458.

occurs, namely, a one-way, irreversible transfer of energy. This is due to *resonance capture* [2-7], e.g., temporary transient capture of the dynamical flow on a resonance manifold of the system. In this paper we summarize the main theoretical results related to nonlinear energy pumping, and provide some preliminary experimental verification. In addition, we show that there exists even the possibility of *resonance capture cascades* whereby, the attachment resonates sequentially with a number of modal oscillators, extracting energy from each at a different frequency range.

2. Theoretical Results

Consider the system of Figure 1, composed of a linear substructure with (N+1) degrees-of-freedom (DOF) that is weakly coupled to a local essentially nonlinear attachment at point O – termed nonlinear energy sink (NES). The attachment consists of a nonlinearizable stiffness nonlinearity of the third order in parallel with a viscous dashpot that models energy dissipation; throughout this work the mass of the NES will be taken m=1. The coupling stiffness between the linear and nonlinear parts is assumed to be linear and weak, of order ε, $0 < \varepsilon << 1$. In addition, the connection between the two systems is assumed to be one-dimensional.

Introducing modal coordinates $a_m(t), m = 0,...,N$ for the linear substructure, its response $y_0(t)$ at the point of attachment O is expressed in the following modal form,

$$y_0(t) = \sum_{k=0}^{N} \phi_0^{(k)} a_k(t) \tag{1}$$

where $\phi_0^{(k)}$ denotes the element at position O of the k-th mass normalized eigenvector; in general, $\phi_j^{(i)}$ denotes the element at position j of the mass-normalized eigenvector $\bar{\phi}^{(i)}$ of the uncoupled linear substructure with $\varepsilon = 0$. In (1) it is assumed that the uncoupled linear substructure possesses (N+1) mass-normalized eigenvectors $\bar{\phi}^{(i)}$ corresponding to (N+1) distinct eigenfrequencies ω_i, i=0,1,…,N. Taking into account (1), the (N+1) equations of motion of the combined system are expressed in the following form,

$$\ddot{v}(t) + C v^3(t) + \varepsilon\lambda\dot{v}(t) + \varepsilon\left(v - \sum_{k=0}^{N} \phi_0^{(k)} a_k(t) \right) = 0$$

$$\ddot{a}_m(t) + \omega_m^2 a_m(t) + \varepsilon\lambda\dot{a}_m(t) + \varepsilon\left(\sum_{k=0}^{N} \phi_0^{(k)}\phi_0^{(m)} a_k(t) - \phi_0^{(m)} v(t) \right) = 0, \quad m = 0,1,...,N \tag{2}$$

where the viscous damping forces are also weak and ordered by the small parameter ε. In (2) the equations of motion are expressed in terms of the (N+1) modal oscillators of the uncoupled linear substructure.

Of interest is to study resonance interactions between the nonlinear attachment and individual modes of the linear substructure. As shown in [1-3] such resonance interactions can lead to interesting *resonance capture* [5] and *energy pumping* phenomena, whereby externally imparted energy in the linear system gets transferred (pumped) to the nonlinear attachment in a one way irreversible fashion. In that case *the nonlinear attachment acts, in essence, as a nonlinear energy sink*.

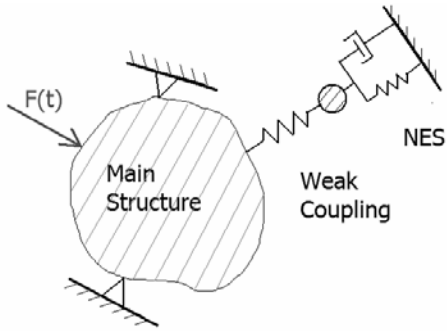

Figure 1. Linear (main) substructure with a weakly connected local nonlinear attachment.

For the simulations the system depicted in Figure 2 was considered with N=9 (that is, a ten DOF linear chain with an end nonlinear attachment), with each oscillator (including the nonlinear attachment) possessing a grounded weak viscous damper with constant equal to $\varepsilon\lambda$. The parameters of the system are chosen as, $\omega_0^2 = 0.4$, $d = 3.5$, $C = 5.0$, $\lambda = 0.5$, and $\varepsilon = 0.1$, with initial conditions, $v(0) = \dot{v}(0) = 0$, $y_m(0) = 0$, $m = 0,1,...,N$, and $\dot{y}_m(0) = 0$, $m = 0,1,3,...,N$, $\dot{y}_2(0) = 10$; these correspond to an impulsive excitation of magnitude Y applied to the third from the right end particle of the chain. In Figure 3 the responses $v(t)$, $y_0(t)$ and $y_9(t)$ are depicted, together with the variation of the instantaneous frequency of oscillation of the nonlinear attachment, $\Omega(t)$, versus time. This instantaneous frequency was estimated elsewhere [2]. Note, that this frequency differs from the frequencies of oscillation of the particles of the chain during the damped motion of the system, since the *transient dynamics* is considered.

Judging from the instantaneous frequency of the nonlinear attachment, one notes that there occurs a cascade of resonance captures involving the lowest three linearized modes of the chain. Referring to Figure (3b), at the initial stage of the motion when the energy is relatively high, the attachment resonates with linearized mode 2 and energy pumping from the chain to the

attachment takes place at frequencies near ω_2. As energy decreases due to damping there occurs a sudden lower frequency transition (jump) into a regime where the attachment resonates with linearized mode 1; this results in energy pumping at frequencies near ω_1. With further decrease of the energy, there occurs a second lower frequency transition in the neighborhood of ω_0; at this third stage pumping is realized at frequencies near the lowest eigenfrequency of the linear chain. One concludes that *for sufficiently strong excitations energy pumping from the chain to the attachment occurs at different frequency regimes that are reached through sudden transitions (jumps) from higher to lower frequencies; these regimes of energy pumping and resonance in the system represent resonance capture cascades.*

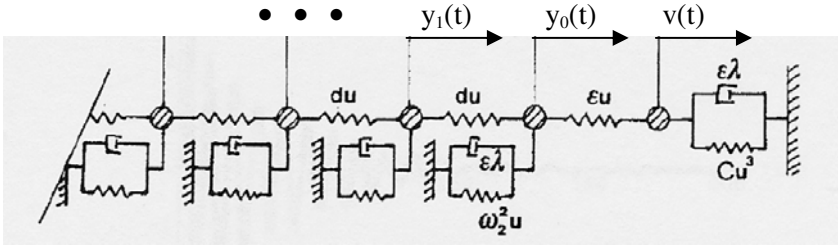

Figure 2. The (N+1) DOF linear periodic chain with a nonlinear end attachment

In an additional illustrative example of energy pumping, consider the 10 DOF damped linear chain with the nonlinear end attachment considered previously, with the same parameters, and initial conditions,

$$v(0) = \dot{v}(0) = 0,\ y_m(0) = 0,\ m = 0,1,...,N,$$
$$\dot{y}_m(0) = 0,\ m = 0,1,2,...,8,\ \dot{y}_9(0) = 70$$

Hence, an impulsive excitation is applied to the most distant from the attachment particle of the chain. In Figure 4 the response of the attachment $v(t)$ is depicted, together with the variation of the instantaneous frequency of oscillation of the nonlinear attachment versus time. Note the vigorous resonance capture cascading involving as many as six of the linearized modes of the chain (including both the highest and lowest linearized modes in the frequency domain).

2.1 Experimental Results

The experimental fixture built [9] to examine the nonlinear energy pumping phenomenon is depicted in Figure 5. It consists of two single-degree-of-freedom oscillators (the 'subsystems') connected by means of a linear coupling stiffness. The left oscillator (the linear subsystem) is grounded by means of a linear spring, whereas the right one (the nonlinear energy sink) is grounded by means of a nonlinear spring with essential cubic

nonlinearity. To dissipate the pumped energy, a grounded viscous damper exists in the NES. Transient (shock) excitation of the system is provided by means of a rod that impacts elastically with the left mass. Assuming that an impulsive (broadband) excitation of finite duration is acting on the linear oscillator, it is of interest to study the transient (damped and essentially nonlinear) dynamics. Hence, the aim of the experimental work is to show that broadband energy initially imparted to the linear subsystem is passively 'pumped' to the NES where it is confined and dissipates without 'spreading' back to the linear subsystem. More details of the experimental fixture and the experimental protocol can be found in [9].

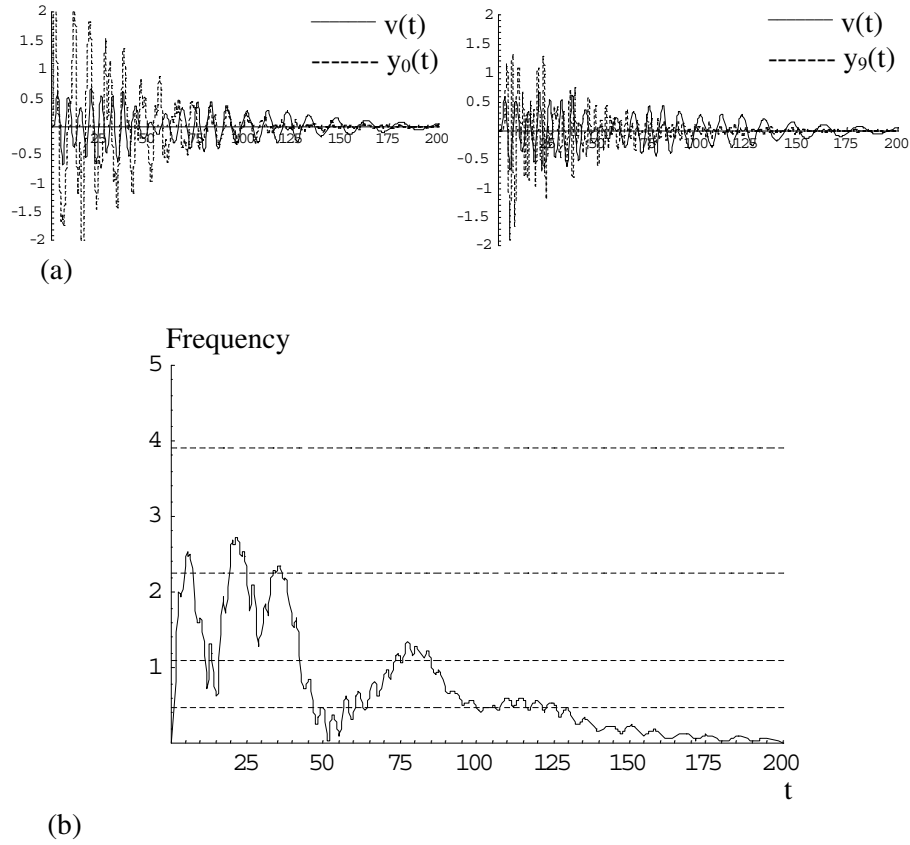

Figure 3. Resonance capture cascades leading to energy pumping for the strongly forced system: (a) Transient (solid line corresponds to the attachment); (b) Instantaneous frequency of the attachment versus time (dashed lines indicate the linearized eigenfrequencies).

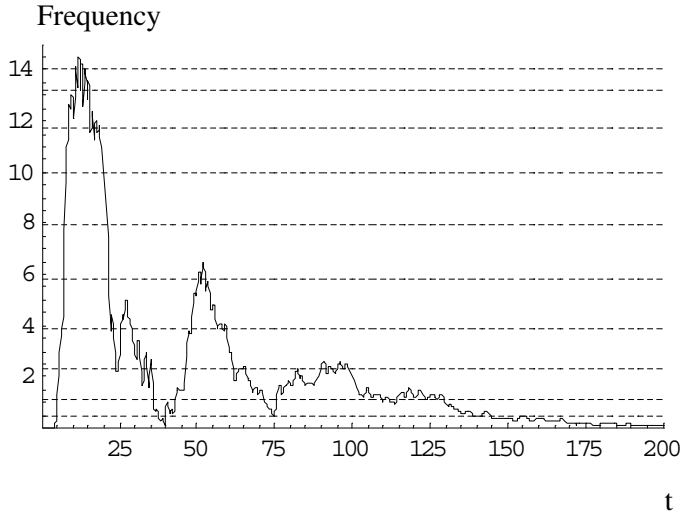

Figure 4. Resonance capture cascades leading to energy pumping for the strongly forced system: Instantaneous frequency of the attachment versus time (dashed lines indicate the linearized eigenfrequencies).

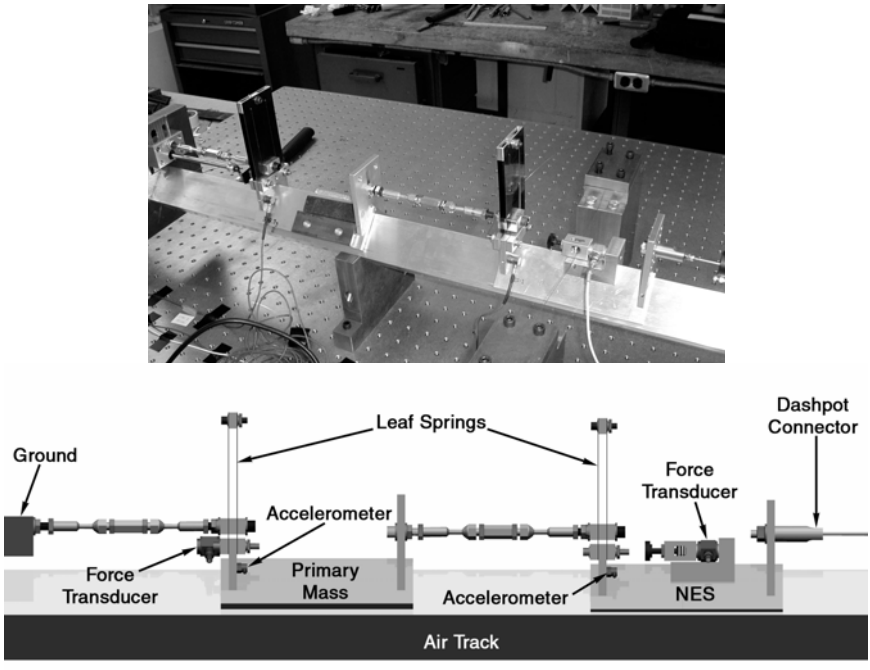

Figure 5. Experimental fixture for nonlinear energy pumping.

In Figure 6 a case of experimental energy pumping is presented, together with a comparison between the experimental and theoretical acceleration time series of the two subsystems. Good agreement between theory and experiment is noted. Such agreement is typical of what was observed for all experimental trials [9]. Nonlinear energy pumping is noted, especially at early times of the response (in the period 0 – 4 sec) when the energy of the system is relatively high and the nonlinear effects are more profound.

By studying the experimental time series one notes that, in the energy pumping regime 0 – 4 sec, the NES oscillates with a dominant 'fast' frequency, which is approximately equal to the eigenfrequency of the linear subsystem. As mentioned earlier, this is a manifestation of resonance capture of the dynamics in the neighborhood of a 1:1 resonance manifold of the system. In the reported experiment eventually 88.5% of the total input energy is absorbed and dissipated at the NES.

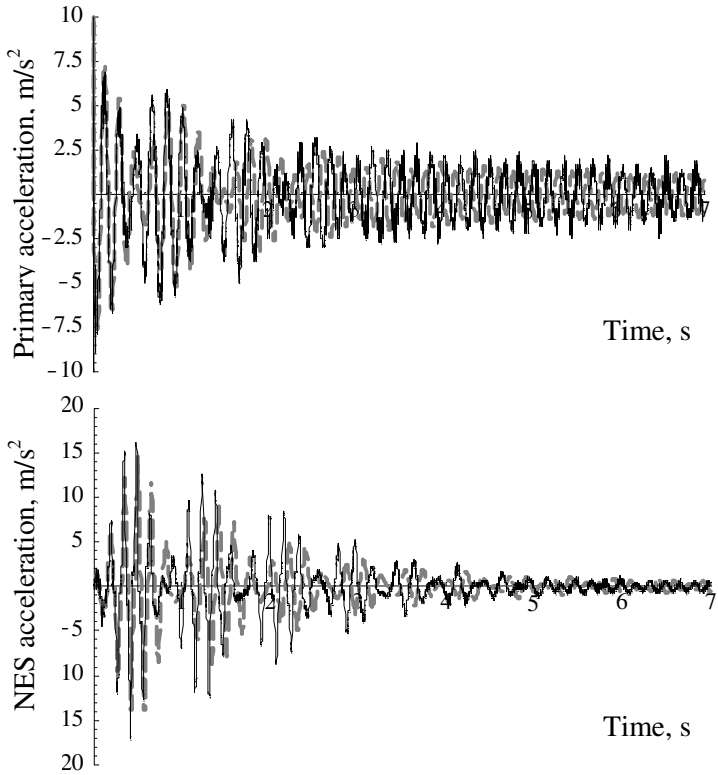

Figure 6. Case of energy pumping: Experimental ——— and numerical — — — acceleration time series of (a) the linear (directly excited) subsystem and (b) the NES.

Acknowledgements

This work was supported in part by AFOSR Contract 00-AF-B/V-0813, by Grant 01-03-11322 from the Russian Federation for Basic Research, and by Grant No. 123 from the Commission for Support of Young Scientists.

References

[1] O. Gendelman, "Transition of energy to a nonlinear localized mode in a highly asymmetric system of two oscillators," *Nonlinear Dynamics,* **25**, 237-253, 2001.

[2] A.F. Vakakis and O. Gendelman, "Energy pumping in nonlinear mechanical oscillators II: Resonance capture," *Journal of Applied Mechanics,* **68**(1), 42-48, 2001.

[3] A.F. Vakakis, "Inducing passive nonlinear energy sinks in linear vibrating systems," *Journal of Vibration and Acoustics,* **123**(3), 324-332, 2001.

[4] A.I. Neishtadt, "Passage through a separatrix in a resonance problem with a slowly-varying parameter," *Prikl. Mat. Meck. (PMM),* **39** (4), 621-632, 1975.

[5] V.I. Arnold (ed.), *Encyclopedia of Mathematical Sciences, Dynamical Systems III*, Berlin and New York: Springer Verlag, 1988.

[6] P. Lochak and C. Meunier, *Multiphase Averaging for Classical Systems*, Berlin and New York: Springer Verlag, 1988.

[7] D. Quinn and R.H. Rand, "The dynamics of resonance capture," *Nonlinear Dynamics,* **8**, 1-20, 1995.

[8] A.F. Vakakis, L.I. Manevitch, Y.V. Mikhlin, V.N. Pilipchuk and A.A. Zevin, *Normal Modes and Localization in Nonlinear Systems*, New York: Wiley Interscience, 1996.

[9] D.M. McFarland, L.A. Bergman and A.F. Vakakis, "Experimental study of nonlinear energy pumping occurring at a single frequency," *Journal of Applied Mechanics*, 2003*,* (submitted, under review).

MOTION CONTROL OF AN UNDERACTUATED MANIPULATOR BY USING HIGH-FREQUENCY EXCITATION

Hiroshi Yabuno
University of Tsukuba
Institute of Engineering Mechanics and Systems, Tsukuba, 305-8573, Japan
yabuno@esys.tsukuba.ac.jp

Kazukuni Goto
Fuji Heavy Industry LTD,
Ohizumi, Gunnma, Japan

Nobuharu Aoshima
University of Tsukuba
Institute of Engineering Mechanics and Systems, Tsukuba, 305-8573, Japan
aoshima@esys.tsukuba.ac.jp

Abstract: A technique without state feedback is proposed for swing-up and stabilization at the upright position of the free link in a two-link underactuated manipulator (the first and second links are active and passive, respectively). The objectives are accomplished by actuating the perturbation of bifurcations produced in the second link under high-frequency excitation for the first link. Experimental results confirm the validity of the proposed method for the underactuated manipulator.

Key words: Underactuated manipulator, high-frequency excitation, pitchfork bifurcation, perturbation of bifurcation, bifurcation control.

1. Introduction

Manipulators with free joints (links) are called underactuated manipulators and in these systems, the number of generalized coordinates is larger than the number of control inputs (the number of actuators). The equations of motion

G. Rega and F. Vestroni (eds.),
IUTAM Symposium on Chaotic Dynamics and Control of Systems and Processes in Mechanics, 459–466.

for the free links are regarded as nonholonomic constraints because they are nonintegrable.

There have been many studies on the control of underactuated manipulators (comprehensive references can be found in [1]). In all previous methods, the control of the free joint is carried out by actuating the active joint based on the motion of the free link. On the other hand, the method presented in this study does not require any information on the motion of the free link. Namely, from the practical point of view, while the application of the past methods is for overcoming actuator failure due to unexpected accident, the proposed method can also be regarded as a control strategy for the case when not only the actuator but also the sensor breaks down. The control objective is for the two link underactuated manipulator (Fig. 1) to swing up the second (free) link, which hangs down in the direction of gravity in the initial state, to the state where the second (free) link points in the direction opposite the gravity effect and also to stabilize the free link. The control is based on the actuation of the perturbation of bifurcations in the free link produced by changing the configuration of the high-frequency excited active link. Finally, the efficiency of the proposed control method is experimentally validated.

2. Bifurcations Produced under High-Frequency Excitation and Their Perturbations

Before proposing our control method, we briefly consider the behavior of a pendulum under high-frequency excitation from a general point of view. The equation of motion of a pendulum subjected to sinusoidal excitation at the supporting point is expressed in dimensionless form as

$$\ddot{\theta} + \mu\dot{\theta} + \sigma^2 \sin\theta + a\cos t^* \sin(\theta - \gamma) = 0, \tag{1}$$

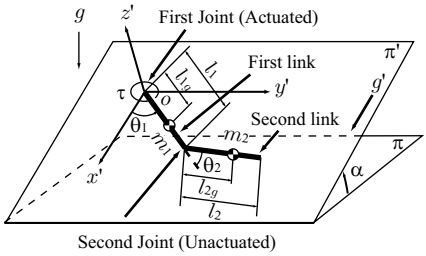

Figure 1. Two-link underactuated manipulator.

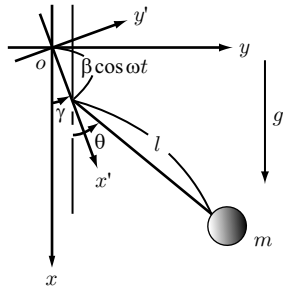

Figure 2. Pendulum periodically excited in any direction.

where $a = \beta/l$ and $\sigma^2 = (g/l)/\omega^2$. $\dot{()}$ denotes the derivative with respect to dimensionless time, $t^* = t \cdot \omega$, and the viscous damping effect $\mu\dot{\theta}$ is considered. In particular, in the cases where the excitation direction is nearly lateral ($\gamma = \pi/2 + \Delta\gamma$) and nearly vertical ($\gamma = 0 + \Delta\gamma$), the above equation is rewritten as follows:

$$Lateral: \quad \ddot{\theta} + \mu\dot{\theta} + \sigma^2 \sin\theta - a\cos t^* \cos(\theta - \Delta\gamma) = 0 \tag{2}$$

$$Vertical: \quad \ddot{\phi} + \mu\dot{\phi} - \sigma^2 \sin\phi - a\cos t^* \sin(\phi - \Delta\gamma) = 0, \tag{3}$$

where $\phi = \theta - \pi$. After linearization, Eq. (3) corresponds to the well-known Mathieu equation [2].

We set the magnitude of the excitation frequency ω to be a large value compared with the linear natural frequency of the pendulum $\sqrt{g/l}$, and then the dimensionless parameter σ is very small. We also set a small value for the dimensionless excitation amplitude a. Now, by using a small parameter ϵ ($|\epsilon| \ll 1$) as a bookkeeping device, we quantitatively set the magnitudes of the parameters as

$$\sigma = \epsilon^2\hat{\sigma},\ a = \epsilon\hat{a},\ \mu = \epsilon\hat{\mu} \quad (\hat{\sigma} = \hat{a}_{\theta 1} = \hat{\mu} \equiv O(1)), \tag{4}$$

where $\hat{}$ denotes "of the order $O(1)$." Then the dimensionless equation (3) is written as follows:

$$\ddot{\phi} + \epsilon\hat{\mu}\dot{\phi} - \epsilon^2\hat{\sigma}\sin\phi - \epsilon\hat{a}\sin(\phi - \Delta\gamma)\cos t = 0. \tag{5}$$

We analyze Eq. (5) using the multiple time scales as $t_0 = t^*,\ t_1 = \epsilon t^*,\ t_2 = \epsilon^2 t^*$. We seek an approximate solution in the form [3]

$$\phi = \phi_0 + \epsilon\phi_1 + \epsilon^2\phi_2 \cdots. \tag{6}$$

Substituting Eq. (6) into Eq. (5) and equating the coefficients of like powers of ϵ yield the following equations for the orders:

$$O(\epsilon^0): \quad D_0^2\phi_0 = 0 \tag{7}$$

$$O(\epsilon^1): \quad D_0^2\phi_1 = -2D_0D_1\phi_0 - \hat{\mu}D_0\phi_0 + \hat{a}\sin(\phi_0 - \gamma)\cos t_0 \tag{8}$$

$$O(\epsilon^2): \quad D_0^2\phi_2 = -2D_0D_1\phi_1 - 2D_0D_2\phi_0 - D_1^2\phi_0 - \hat{\mu}(D_0\phi_1 + D_1\phi_0) + \hat{\sigma}\sin\phi_0 + \hat{a}\cos(\phi_0 - \gamma)\phi_1\cos t_0, \tag{9}$$

where $D_i \equiv \partial/\partial t_i$. From conditions under which the secular term in each order is not produced, we obtain the following autonomous equation:

$$D_1^2\phi_0 + \hat{\mu}D_1\phi_0 - \hat{\sigma}\sin\phi_0 + \frac{1}{4}\hat{a}^2\sin 2(\phi_0 - \Delta\gamma) = 0. \tag{10}$$

Furthermore, the above equation can be rewritten in neglecting the error of $O(\epsilon)$ as follows:

$$\ddot{\phi} + \mu\dot{\phi} - \sigma\sin\phi + \frac{1}{4}a^2\sin 2(\phi - \Delta\gamma) = 0. \tag{11}$$

Analogously, we obtain the autonomous equation governing the motion of a pendulum excited nearly in the lateral direction as follows:

$$\ddot{\theta} + \mu\dot{\theta} + \sigma \sin\theta - \frac{1}{4}a^2 \sin 2(\theta - \Delta\gamma) = 0. \tag{12}$$

Because Eqs. (11) and (12) are autonomous, it is very easy to perform bifurcation analysis.

Equations (11) and (12) with $d/dt^{*2} = d/dt^* = 0$ lead to the following bifurcation equations with the accuracy of $O(3)$ as follows:

$$Vertical : -(\sigma - \frac{a^2}{2})\phi - (\frac{a^2}{3} - \frac{\sigma}{6})\phi^3 + \frac{a^2}{2}\Delta\gamma = 0 \tag{13}$$

$$Lateral : (\sigma - \frac{a^2}{2})\theta + (\frac{a^2}{3} - \frac{\sigma}{6})\theta^3 + \frac{a^2}{2}\Delta\gamma = 0. \tag{14}$$

Therefore, in the case of $\Delta\gamma = 0$, it follows that the bifurcations for vertical and lateral excitations are complete subcritical and supercritical pitchfork bifurcations, as shown in Figs. 3(a) and (b), respectively. On the other hand, the tilt ($\Delta\gamma \neq 0$) perturbs these complete bifurcations as shown in Figs. 3(c) and (d), respectively.

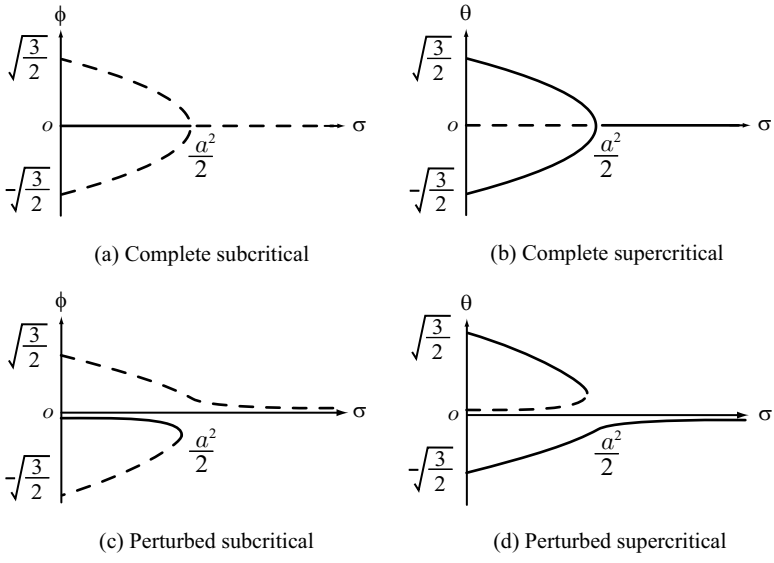

Figure 3. Bifurcation diagram in the pendulum under high-frequency excitation (solid line: stable, dashed line: unstable): (a) vertical excitation ($\gamma = 0$); (b) lateral excitation ($\gamma = \pi/2$); (c) tilted vertical excitation ($\gamma = 0 + \Delta\gamma$); (d) tilted lateral excitation ($\gamma = \pi/2 + \Delta\gamma$).

3. Motion Control of Underactuated Manipulator by Actuating the Perturbation of the Pitchfork Bifurcations

We consider the analytical model shown in Fig. 1. The manipulator experiences the gravity effect $g'(=g\sin\alpha)[\mathrm{m/s^2}]$ in the positive direction of the x' axis. Here we can set the position of the first link as follows:

$$\theta_1 = a_{\theta_1}\cos\omega t + \theta_{1off}, \tag{15}$$

where the first term is for applying high-frequency excitation to the second link (the frequency ω is called excitation frequency). The second term expresses the configuration of the first link with respect to the direction of the gravity effect (θ_{1off} is called the offset of excitation). Then the equation governing the motion of the second link is expressed in dimensionless form as

$$\begin{aligned}&\ddot{\theta}_2 + \mu\dot{\theta}_2 - a_{\theta 1}(1 + c\cos\theta_2)\cos t^* \\ &\quad + ca_{\theta 1}^2\sin\theta_2\sin^2 t^* + \sigma\,\sin(a_{\theta 1}\cos t^* + \theta_{1off} + \theta_2) = 0,\end{aligned} \tag{16}$$

where $(\dot{})$ denotes the derivative with respect to dimensionless time, $t^* = t\cdot\omega$, and the dimensionless parameter values corresponding to the subsequent experiment are $c = 0.635$, $\sigma = 4.08/\omega^2$, and $\mu = 0.524/\omega$, where the excitation frequency of the first link ω is variable. By applying the method of multiple scales, as described in section 2, Eq. (16) can be transformed into the autonomous differential equation:

$$\ddot{\theta}_2 + \mu\dot{\theta}_2 + \sigma\,\sin(\theta_{1off} + \theta_2) - \frac{c^2a_{\theta 1}^2}{2}\sin\theta_2\cos\theta_2 = 0. \tag{17}$$

From Eq. (17) we can show the bifurcation diagrams as function of the offset of the excitation θ_{1off}. Figure 4(a) is the bifurcation diagram for the case of $\theta_{1off} = 0$ which includes the supercritical pitchfork bifurcation for Fig. 3 (b), because $\theta_{1off} = 0$ corresponds to the lateral excitation of the pendulum: $\gamma = \pi/2$. Figure 4(c) is the bifurcation diagram for the case of $\theta_{1off} = \pi/2$ which includes the subcritical pitchfork bifurcation in Fig. 3 (a), because $\theta_{1off} = \pi/2$ corresponds to the vertical excitation of the pendulum: $\gamma = 0$. Furthermore, Fig. 4(b) is the bifurcation diagram for the case of $\theta_{1off} = \pi/4$ which includes both the perturbed subcritical and supercritical pitchfork bifurcations in Figs. 3 (c) and (d), because the excitation in the case of $\theta_{1off} = \pi/4$ simultaneously possesses the characteristics of both tilted vertical and lateral excitations. The three branches of (1) in Figs. 4(a) and (2) in Fig. 4(b) and (c) are smoothly connected by a continuous change of the value of θ_{1off} from 0 to $\pi/2$ [4]. Therefore, the high-frequency excitation indicated by point a in Fig. 4, i.e., $\sigma < c^2\theta_{1a}/4$, carries out the swing-up of the second link and can change the absolute angle of the second link, $\theta_{2abs} = \theta_1 + \theta_2 \approx \theta_{1off} + \theta_2$, from 0 to π.

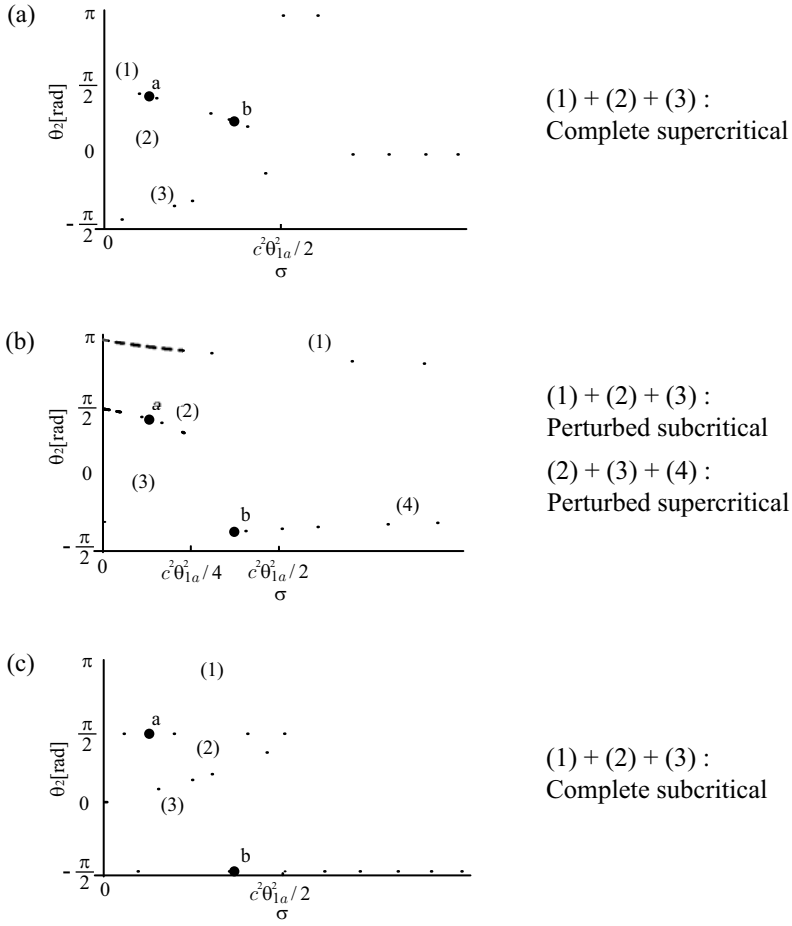

Figure 4. Strategy of motion control for the underactuated manipulator: swing-up and stabilization by actuating the perturbation of pitchfork bifurcations (solid line: stable, dashed line: unstable) ((a) $\theta_{1off} = 0$, (b) $\theta_{1off} = \pi/4$, (c) $\theta_{1off} = \pi/2$) .

Also, when the free link reaches the upright position, this state is stable because the subcritical pitchfork bifurcation is produced, as shown in Fig. 4(c). On the other hand, in the case of the low excitation frequency, as indicated by point b in Fig. 4, i.e., $\sigma > c^2\theta_{1a}/4$, the swing-up cannot be realized.

4. Experiment

We experimentally investigate the validity of the theoretically proposed control method using the experimental apparatus shown in Fig. 5. Figure 6(a) shows the time histories of the first and second links for sufficiently

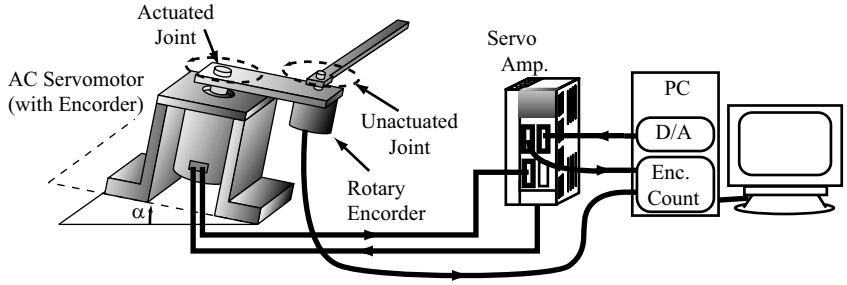

Figure 5. Experimental apparatus (the values of the parameters of the experimental setup corresponding to those in Fig. 1 are as follows: $m_1 = 1.50 \times 10^{-1}$kg, $m_2 = 7.18 \times 10^{-2}$kg, $l_1 = 1.23 \times 10^{-1}$m, $l_2 = 0.19$m, $l_{1g} = 0.70 \times 10^{-1}$m, $l_{2g} = 0.55 \times 10^{-1}$m, $I_1 = 8.71 \times 10^{-4}$kg $\cdot$ m^2, $I_2 = 5.49 \times 10^{-4}$kg $\cdot$ m^2, $g' = 7.92 \times 10^{-1}$m/s^2($\alpha = 8.10 \times 10^{-2}$rad)).

high-frequency excitation. It is experimentally clarified that the second link is swung up to the upright position and is stabilized at this position. In Fig. 6(b), the swing-up cannot be realized because of insufficiently high frequency excitation.

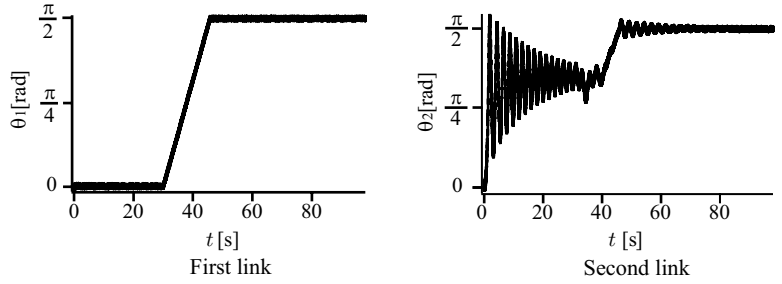

(a) Time history ($\omega/2\pi = 35$Hz, $\theta_{1a} = 0.03$rad)

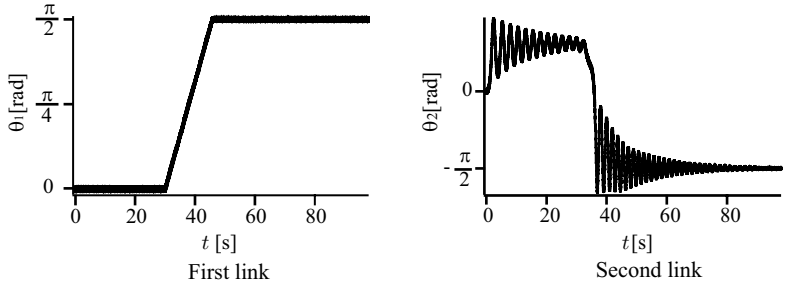

(b) Time history ($\omega/2\pi = 30$Hz, $\theta_{1a} = 0.03$rad)

Figure 6. Swing-up and stabilization of the underactuated manipulator

5. Summary

We proposed a method for motion control of an underactuated manipulator, in which information on the free link is not required. The concept is based on the appropriate actuation of the perturbation of supercritical and subcritical pitchfork bifurcations produced in the free link under high-frequency excitation. The experiments performed using a simple apparatus confirmed the validity of the proposed control method.

Acknowledgments

The authors wish to thank Mr. T. Matsuda, graduate student at the University of Tsukuba, for his assistance. This work is supported by Grants-in-Aid for Scientific Research of Japanese Ministry of Education, Culture, Sports, Science and Technology, Nos. 13650243 and 15360222.

References

[1] H. Arai, K. Tanie and N. Shiroma, "Nonholonomic control of a three-DOF planar underactuated manipulator," *IEEE Trans. Robot. Auto.*, Vol. 14, pp. 681-695, Oct. 1998.

[2] A. H. Nayfeh and D. T. Mook, *Nonlinear Oscillations*, New York: Wiley, 1979.

[3] H. Yabuno, M. Miura and N. Aoshima, "Bifurcation in an inverted pendulum with tilted high-frequency excitation," *Journal of Sound and Vibration*, 2004, in press.

[4] H. Yabuno, K. Goto and N. Aoshima, "Swing-up and stabilization of an underactuated manipulator without state feedback of free joint," *IEEE Trans of Robotics and Automation*, 2004, in press.

VII.

CHAOS CONTROL AND SYNCHRONIZATION

Reminding us that *control* and *synchronization* of *chaos* are topics of great interest in a large number of disciplines that go beyond mechanics, the lead paper of the last part of the Proceedings is the Key Lecture of the Symposium given by Tito Arecchi of the University of Florence, Italy.

Tito Arecchi discusses how homoclinic chaos appears as the easiest way to encode information in time by a code consisting of trains of equal spikes occurring at erratic times, and deals with the relevant implications for neurodynamics. Based on recent investigations of how homoclinic chaotic systems mutually synchronize by weak coupling, a novel conjecture on the dynamics of the single neuron is formulated. The central issue of cognitive science, namely how a large collection of coupled neurons combines external data with internal memories into new coherent patterns of meaning, is investigated, and a laboratory model of brain behaviour as an array of a large number of homoclinic chaotic nodes into a synchronized network is proposed.

Two further papers appear in this area. Fradkov and Andrievsky briefly survey the state of the art in the field of control of chaotic systems, which has registered a tremendous amount of research in the last few years. They discuss several major methods (feedforward control, OGY method, delayed feedback, conventional engineering techniques, adaptive and intelligent control), as well as applications in mechanics (control of pendulums, beams, and plates; of stick-slip friction; of vibroformers; of microcantilevers). Also, they show the efficiency of the energy-based speed-gradient control strategy in suppressing chaotic motions of a spinning spacecraft.

In turn, Stefanski et al. address the problem of estimating the largest Lyapunov exponent of dynamical systems with time delay, for which the classical robust algorithms allowing an easy estimation of the entire spectrum of exponents for continuous and differentiable ODEs do not work. They propose a procedure, applicable also to nonsmooth systems, based on the easily detectable phenomenon of synchronization of coupled identical systems, which is shown to work satisfactorily.

G. Rega and F. Vestroni (eds.),
IUTAM Symposium on Chaotic Dynamics and Control of Systems and Processes in Mechanics, 467.

CONTROL AND SYNCHRONIZATION OF HOMOCLINIC CHAOS:

Implications for Neurodynamics

F. Tito Arecchi
Department of Physics, University of Firenze, Italy
arecchi@ino.it

Abstract: Homoclinic chaos implies the recurrent return of the dynamical trajectory to a saddle focus, in whose neighbourhood the system susceptibility (response to an external perturbation) is very high and hence it is very easy to lock to an external stimulus. Thus homoclinic chaos appears as the easiest way to encode information in time by a code consisting of trains of equal spikes occurring at erratic times.Based on recent laboratory investigations of homoclinic chaotic systems, and how they mutually synchronize by weak coupling, a novel conjecture on the dynamics of the single neuron is formulated. The central issue of cognitive science is how a large collection of coupled neurons combines external data with internal memories into new coherent patterns of meaning. Such a process is called "feature binding", insofar as the coherent patterns combine together features which are extracted separately by specialized cells, but which do not make sense as isolated items. A powerful conjecture ,with experimental confirmation, is that feature binding in perceptual tasks implies the mutual synchronization of axonal spike trains in neurons which can be far away and yet contribute to a well defined perception by sharing the same sequence. Thus we use our expertise in arraying a large number of homoclinic chaotic nodes into a synchronized network as a laboratory model of the brain behavior.

Key words: Homoclinic chaos, array synchronization.

1. Synchronization of Homoclinic Chaos

A wide class of sensory neurons demonstrates homoclinic chaotic spiking activity [Izhkievich].

G. Rega and F. Vestroni (eds.),
IUTAM Symposium on Chaotic Dynamics and Control of Systems and Processes in Mechanics, 469–480.

Precisely, a saddle focus instability separates in parameter space an *excitable* region, where axons are silent (Fig.4b), from a *periodic* region, where the spike train is periodic (equal interspike intervals (Fig.4a)). If a control parameter is tuned at the saddle focus , the corresponding dynamical behavior (homoclinic chaos) consists of a frequent return to the instability [Allaria]. This manifests as a train of geometrically identical spikes, which however occur at erratic times (chaotic interspike intervals). Around the saddle focus the system displays a large susceptibility to an external stimulus, hence it is easily adjustable and prone to respond to an input, provided this is at sufficiently low frequencies; this means that such a system is robust against high frequency noise as discussed later.

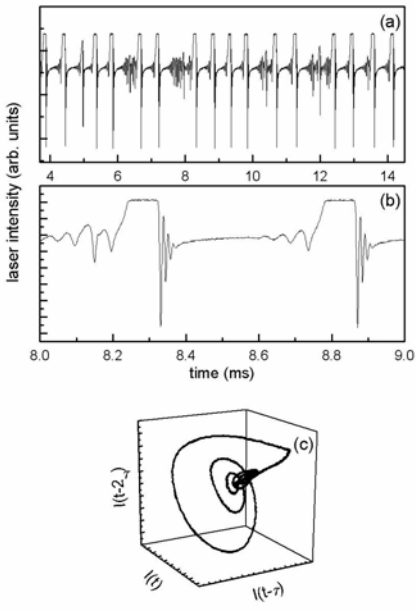

Figure 1. (a) Experimental time series of the laser intensity for a CO2 laser with feedback in the regime of homoclinic chaos. (b) Time expansion of a single orbit. (c) Phase space trajectory built by an embedding technique with appropriate delays [from Allaria et al.].

Such a type of dynamics has been recently dealt with in a series of reports that here I recapitulate as the following chain of linked facts.

A single spike in a 3D dynamics corresponds to a quasi-homoclinic trajectory around a saddle focus SF; the trajectory leaves the saddle and returns to it (Fig.1,2).We say "quasi-homoclinic" because, in order to stabilize the trajectory away from SF, a second fixed point, namely a saddle node SN, is necessary to assure a heteroclinic connection.

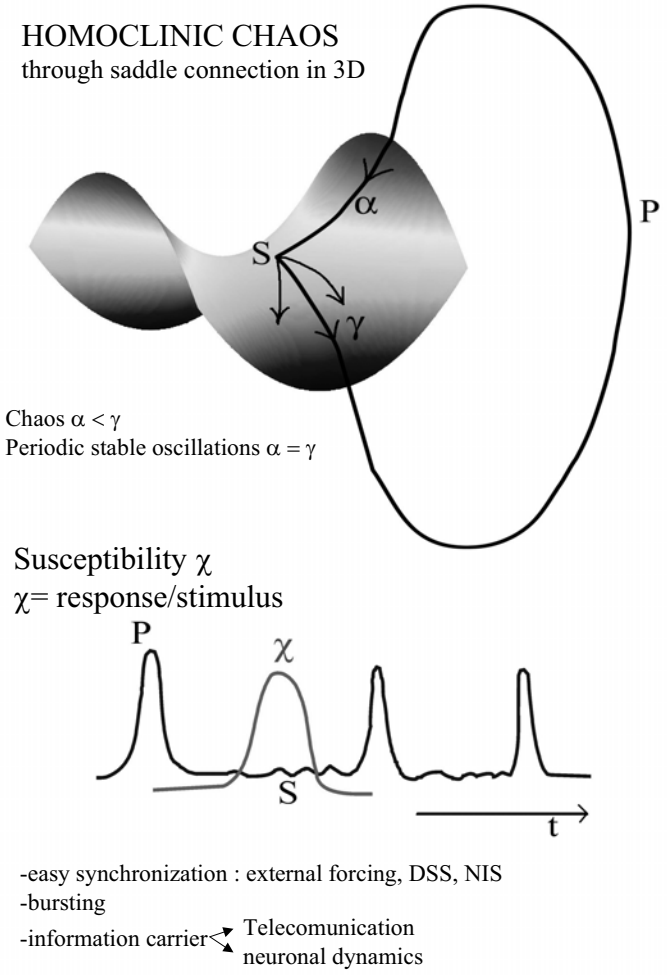

Figure 2. Schematic view of the phase space trajectory approaching the saddle S and escaping from it. Chaos is due to the shorter or longer permanence around S; from a geometrical point of view most of the orbit P provides a regular spike.

The homoclinic chaos (HC) reported in Fig.1 and Fig.2 has a localized chaotic tangle surrounded by an island of stability (Fig.3 –left). This provides a sensitivity region corresponding to the chaotic tangle and an active region corresponding to the identical spikes. Such a behavior is crucial to couple large arrays of HC systems, as it occurs in the neuron coupling in the brain [Arecchi2003]. On the contrary, standard chaos as Lorenz where the chaotic behavior fills the whole attractor is inconvenient for synchronization purposes (Fig.3 – right).

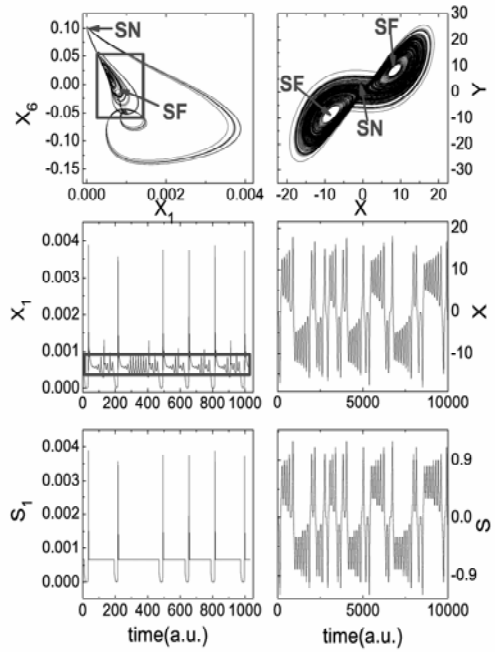

Figure 3. Comparison between HC(homoclinic chaos) (left column) and Lorenz chaos (right column). The top row is a phase space projection over two dynamical variables; SF denotes the saddle focus and SN the saddle node, on the left the two SF map one onto the other after an inversion (x → - x, y→ - y) around the origin. The intermediate row shows the time series for variables x1 of HC (it represents the laser intensity in the case of the CO2 laser) and x of Lorenz; in the former case, a suitable threshold cuts off the chaotic background; in the latter case, no convenient region for thresholding can be isolated. Bottom row, left : after threshold, the new variable S(t) alternates spikes with flat regions where the systems has a high sensitivity and short refractive windows where the intensity S(t) goes to zero.

A train of spikes corresponds to the sequential return to, and escape from, the SF. A control parameter can be fixed at a value B_C for which this return is erratic (chaotic interspike interval) even though there is a finite average frequency. As the control parameter is set above or below B_C, the system moves from *excitable* (single spike triggered by an input signal) to *periodic* (yielding a regular sequence of spikes without need for an input), with a frequency monotonically increasing with the separation ΔB from B_C (Fig.4) .A low frequency modulation of B around B_C provides alternation of silent intervals with periodic bursts. Such bursting behavior, peculiar of neuron on CPG (Central Pattern Generators) as the cardio-respiratory system, has been modeled by a laser experiment [Meucci].

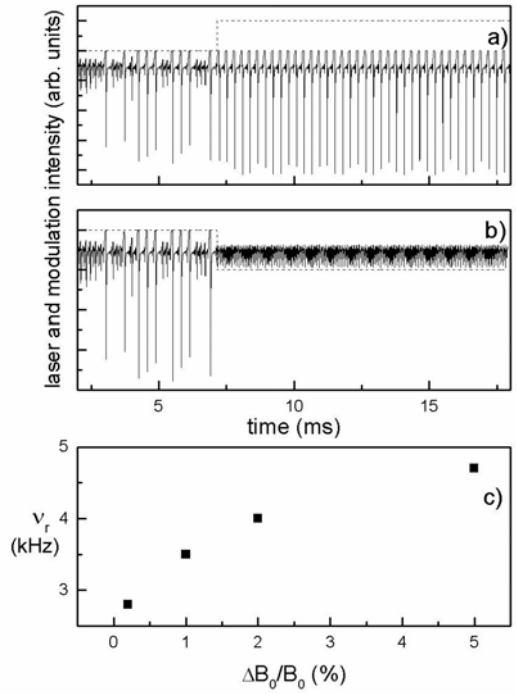

Figure 4. Stepwise increase a) and decrease b) of control parameter B0 by +/- 1% brings the system from homoclinic to periodic or excitable behavior. c) In case a) the frequency ν_r of the spikes increases monotonically with ΔB_0 [from Meucci et al.].

Around SF , any tiny disturbance provides a large response. Thus the homoclinic spike trains can be synchronized by a periodic sequence of small

disturbances (Fig. 5). However each disturbance has to be applied for a minimal time, below which it is no longer effective; this means that the system is insensitive to broadband noise, which is a random collection of fast positive and negative signals[Zhou et al].

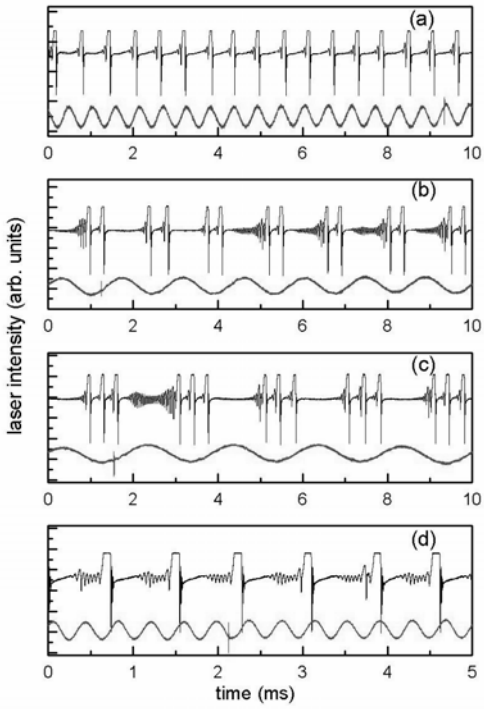

Figure 5. Experimental time series for different synchronization induced by periodic changes of the control parameter. (a) 1:1 locking, (b) 1:2, (c) 1:3, (d) 2:1 [from Allaria et al.].

The above considerations lay the floor for the use of mutual synchronization as the most convenient way to let different neurons respond coherently to the same stimulus, organizing as a space pattern. In the case of a single dynamical system, it can be fed back by its own delayed signal (DSS = delayed self synchronization). As the delay is long enough the system is decorrelated with itself and this is equivalent to feeding an independent system. This process allows to store meaningful sequences of spikes as necessary for a short term memory [Arecchi et al.2002].

A dynamical sketch of a single neuron is presented in Fig.6 and its HC behavior is discussed e.g in [Izkhievich]. The feature binding conjecture, based on synchronization of different neurons exposed to the same image, is shown in Fig.7 [Singer] and the role of threshold resetting due to past memories (ART= Adaptive Resonance Theory [Grossberg]) is illustrated in Fig.8.

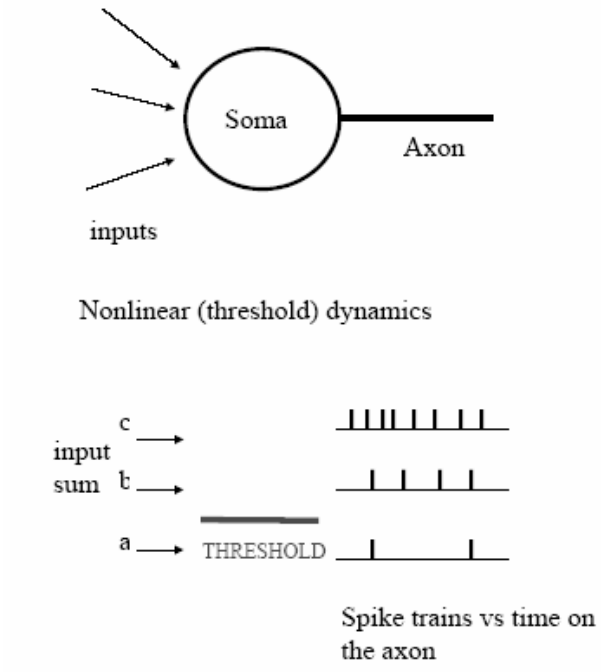

Figure 6. Dynamical behavior of a single neuron. The sum of the inputs compares with a threshold level; if it is below (a) only a few noisy spikes occur as electrical activity on the axon; if it is just above (b) we have a periodic spike train, whose frequency increases as the input goes high above threshold (c).

In presence of localized stimuli over a few neurons, the corresponding disturbances propagate by inter-neuron coupling (either excitatory or inhibitory); a synchronized pattern is uniquely associated with each stimulus; different patterns compete and we conjecture that the resulting sensory response, which then triggers motor actions, corresponds by a majority rule to that pattern which has extended over the largest cortical domain. An example is discussed for two inputs to a one-dimensional array of coupled HC systems [Leyva et al.].

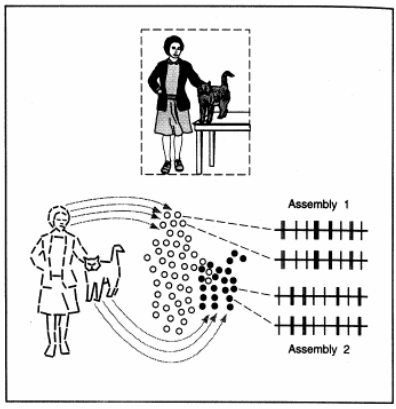

Figure 7. Feature binding: the lady and the cat are respectively represented by the mosaic of empty and filled circles, each one representing the receptive field of a neuron group in the visual cortex. Within each circle the processing refers to a specific detail (e.g. contour orientation). The relations between details are coded by the temporal correlation among neurons, as shown by the same sequences of electrical pulses for two filled circles or two empty circles. Neurons referring to the same individual (e.g. the cat) have synchronous discharges, whereas their spikes are uncorrelated with those referring to another individual (the lady) [from Singer].

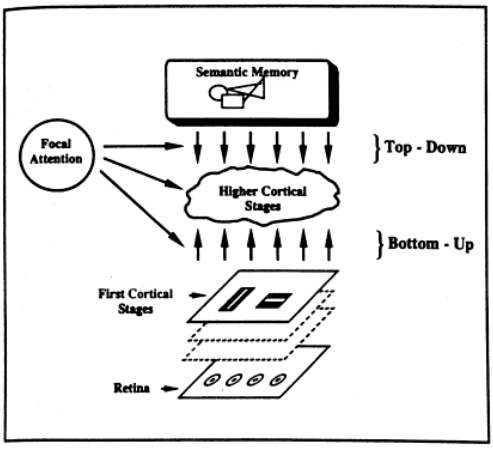

Figure 8. ART = Adaptive Resonance Theory. Role of bottom-up stimuli from the early visual stages an top-down signals due to expectations formulated by the semantic memory. The focal attention assures the matching (resonance) between the two streams [from Julesz].

These facts have been established experimentally and confirmed by a convenient model in the case of a class B laser[1] with a feedback loop which readjusts the amount of losses depending on the value of the light intensity output[Arecchi 1987 b].

The above listed facts hold in general for any dynamical system which has a 3-dimensional sub-manifold separating a region of excitability from a region of periodic oscillations: indeed, this separatrix has to be a saddle focus. If a dynamical system has N>3 dimensions, then a local stability analysis shows that around a saddle focus the systems behaves locally as 3D, since N-3 variation rates are largely negative.

In particular all biological clocks are of HC type in order to have an adaptive period which can be re-adjusted whenever necessary (think e.g. of the cardiac pace-maker).

2. Perceptions and Feature Binding

Let us consider the visual system; the role of elementary feature detectors has been extensively studied in the past decades [Hubel]. By now we know that some neurons are specialized in detecting exclusively vertical or horizontal bars, or a specific luminance contrast, etc. However the problem arises: how elementary detectors contribute to a holistic (Gestalt) perception? A hint is provided by [Singer]. Suppose we are exposed to a visual field containing two separate objects. Both objects are made of the same visual elements, horizontal and vertical contour bars, different degrees of luminance, etc. What are then the neural correlates of the identification of the two objects? We have one million fibers connecting the retina to the visual cortex. Each fiber results from the merging of approximately 100 retinal detectors (rods and cones) and as a result it has its own receptive field. Each receptive field isolates a specific detail of an object (e.g. a vertical bar). We thus split an image into a mosaic of adjacent receptive fields.

Now the "feature binding" hypothesis consists of assuming that all the cortical neurons whose receptive fields are pointing to a specific object synchronize the corresponding spikes, and as a consequence the visual

[1] I recall the classification widely accepted in laser physics. Class A lasers are ruled by a single order parameter, the amplitude of the laser field, which obeys a closed dynamical equation; all the other variables having much faster decay rate, thus adjusting almost instantly to the local field value. Class B lasers are ruled by two order parameters, the laser field and the material energy storage providing gain; the two degrees of freedom having comparable characteristic times and behaving as activator and inhibitor in chemical dynamics [Arecchi 1987a]

cortex organizes into separate neuron groups oscillating on two distinct spike trains for the two objects.

Direct experimental evidence of this synchronization is obtained by insertion of microelectrodes in the cortical tissue of animals just sensing the single neuron (Fig.7)[Singer]. Indirect evidence of synchronization has been reached for human beings as well, by processing the EEG (electro-encephalo-gram) data [Rodriguez et al.].

The advantage of such a temporal coding scheme, as compared to traditional rate based codes, which are sensitive to the average pulse rate over a time interval and which have been exploited in communication engineering, has been discussed in a recent paper [Softky].

Based on the neurodynamical facts reported above, we can understand how this occurs [Grossberg]. The higher cortical stages where synchronization takes place have two inputs. One (bottom-up) comes from the sensory detectors via the early stages which classify elementary features. This single input is insufficient, because it would provide the same signal for e.g. horizontal bars belonging indifferently to either one of the two objects. However, as we said already, each neuron is a nonlinear system passing close to a saddle point, and the application of a suitable perturbation can stretch or shrink the interval of time spent around the saddle, and thus lengthen or shorten the interspike interval. The perturbation consists of top-down signals corresponding to conjectures made by the semantic memory (Fig.8).

In other words, the perception process is not like the passive imprinting of a camera film, but it is an active process whereby the external stimuli are interpreted in terms of past memories. A focal attention mechanism assures that a matching is eventually reached. This matching consists of resonant or coherent behavior between bottom-up and top-down signals. If matching does not occur, different memories are tried, until the matching is realized. In presence of a fully new image without memorized correlates, then the brain has to accept the fact that it is exposed to a new experience.

Notice the advantage of this time dependent use of neurons, which become available to be active in different perceptions at different times, as compared to the computer paradigm of fixed memory elements which store a specific object and are not available for others (the so called “grandmother neuron” hypothesis).

We have above presented qualitative reasons why the degree of synchronization represents the perceptual salience of an object. Synchronization of neurons located even far away from each other yields a space pattern on the sensory cortex, which can be as wide as a few square millimeters, involving millions of neurons. The winning pattern is

determined by dynamic competition (the so-called “winner takes all” dynamics).

This model has an early formulation in ART and has been later substantiated by the synchronization mechanisms. Perceptual knowledge appears as a complex self-organizing process.

3. From the Single HC Node to a Synchronized Network

When passing from a single system to an array, a relevant problem emerges related to the ability of the array to respond to external periodic perturbations localized at one end site, yielding synchronized patterns. The issue we are addressing is relevant for biological or artificial communication networks.

We first study the emergence of synchronization in the absence of external stimuli, as the coupling strength ε increases. Due to the coupling, a spike on one site induces the onset of a spike in the neighbor sites.

The transition to phase synchronization is anticipated by regimes where clusters of oscillators spike quasi-simultaneously. Clusters are delimited by "phase slips" or defects, easily seen as holes in the space time fabric. A defect appears as a 2π "phase slip" in the difference between the phases of two adjacent sites. Full phase synchronization is reached when the defect density falls below one defect per site.

Next we address the question of how two different frequencies applied at the far ends of the chain compete in generating two separate spatial patterns of synchronization [Leyva].

We explore the problem of spatial competition between synchronization regions, which is preliminary to controlling the dynamics of an extended system as well as to studying the response of neural assemblies to competing external perturbations.

To answer this question, we apply to the first (i=1) and last (i=N) site periodic perturbations with different frequencies.

We find that, when two simultaneous forcings are applied at different points of the array, a rich phenomenology of stable competitive states is observed. The features and stability of these states depend on the intrinsic dynamics of the system independently of the chain size.

References

[1] E. Allaria, F.T. Arecchi, A. Di Garbo, and R. Meucci, "Synchronization of homoclinic chaos," *Phys. Rev. Lett.*, 86, 791, 2001.

[2] F.T. Arecchi, "Instabilities & chaos in single mode homogeneous line lasers," in: *Instabilities and Chaos in Quantum Optics*, (eds. F.T. Arecchi & R.G. Harrison), Springer Series Synergetics, vol. 34 ,pp. 9-48, 1987a.

[3] F.T. Arecchi, R. Meucci, and W. Gadomski, "Laser dynamics with competing instabilities," *Phys. Rev. Lett*., 58, 2205, 1987b.

[4] F.T. Arecchi, "Complexity and adaptation: a strategy common to scientific modeling and perception," *Cognitive Processing*, 1, 23, 2000.

[5] F.T. Arecchi, R. Meucci, E. Allaria, A. Di Garbo, and L.S. Tsimring, "Delayed self-synchronization in homoclinic chaos," *Phys. Rev. E*, 65, 046237, 2002.

[6] F.T. Arecchi, E. Allaria, I. Leyva, "A propensity criterion for networking in an array of coupled chaotic systems," *Phys Rev Lett*, 2003, to be published.

[7] S. Grossberg, "The attentive brain," *The American Scientist*, 83, 439, 1995.

[8] D.H. Hubel, "Eye, brain and vision", *Scientific American Library*, n. 22, W.H. Freeman, New York, 1995.

[9] E.M. Izhikevich, "Neural excitability, spiking, and bursting," *Int. J. of Bifurcation and Chaos,* 10, 1171, 2000.

[10] B. Julesz, "Early vision and focal attention," *Reviews of Modern Physics*, 63, 735-772, 1991.

[11] I. Leyva, E. Allaria, S. Boccaletti and F.T. Arecchi, "Competition of synchronization patterns in arrays of homoclinic chaotic systems," *Phys Rev E,* 2003 to be published.(e-print:nlin.PS/0302008).

[12] E. Rodriguez, N. George, J.P. Lachaux, J. Martinerie, B. Renault and F. Varela, "Perception's shadow: Long-distance synchronization in the human brain," *Nature* 397:340-343, 1999.

[13] W. Singer and C.M. E Gray, "Visual feature integration and the temporal correlation hypothesis," *Annu.Rev.Neurosci.* 18, 555, 1995.

[14] W. Softky, "Simple codes versus efficient codes," *Current Opinions in Neurobiology*, 5, 239, 1995.

[15] C. Von der Malsburg, "The correlation theory of brain function," reprinted in E. Domani, J.L. Van Hemmen and K. Schulten (Eds.), *Models of Neural Networks II*, Springer, Berlin, 1981.

[16] C.S. Zhou, E. Allaria, S. Boccaletti, R. Meucci, J. Kurths, and.F.T. Arecchi, "Noise induced synchronization and coherence resonance of homoclinic chaos," *Phys. Rev. E* 67, 015205, 2003.

METHODS AND EXAMPLES OF CONTROLLING CHAOS IN MECHANICAL SYSTEMS

Alexander Fradkov and Boris Andrievsky
Institute for Problems of Mechanical Engineering of Russian Academy of Sciences, Saint Petersburg, 199178, Russia.
{alf,andr}@control.ipme.ru*

Abstract: State-of-the-art of the field related to control of chaotic systems is surveyed. Several major branches of research are discussed: feedforward ("nonfeedback") control, "OGY method", "Pyragas method", traditional for control engineering methods of nonlinear and adaptive control. A new solution to the problem of angular velocity stabilization for the spinning spacecraft is suggested. Numerical simulation results are presented showing efficiency and robustness of the speed-gradient control strategy for suppression of possible chaotic motion of the spacecraft.

Key words: Nonlinear control, chaotic behavior.

1. Introduction

The idea of controlling chaos in dynamical systems has come under detailed investigation during last decade, see [1]. Starting with a few papers in 1990, the number of publications in peer reviewed journals exceeded 2700 in 2000, with more than half published in 1997–2000. According to the Science Citation Index, in 1997-2002 about 400 papers per year related to control of chaos were published in peer reviewed journals, see bibliography [2] and surveys [3, 4]. Authors of numerous papers have developed new methods for control of nonlinear systems and demonstrated advantages of their usage both for analysis of system dynamics and for significant change of system behavior by small forcing.

*Partial funding provided by the Russian Foundation for Basic Research, project 02-01-00765 and by the Presidium of Russian Academy of Sciences (Program 19, project 1.4.).

G. Rega and F. Vestroni (eds.),
IUTAM Symposium on Chaotic Dynamics and Control of Systems and Processes in Mechanics, 481–491.

State-of-the-art of the field related to control of chaotic systems is surveyed in the paper. Several major branches of research are discussed: feedforward ("nonfeedback") control (based on periodic excitation of the system), "OGY method" (based on linearization of Poincare map), "Pyragas method" (based on a time-delayed feedback), traditional for control engineering methods of nonlinear and adaptive control. Most attention is paid to the control of continuous-time chaotic systems.

A number of application examples in mechanics and mechanical engineering are discussed, including control of pendulum systems, beams, plates, control of stick-slip friction motion, control of vibroformers, control of microcantelivers.

As an example, a new solution to the problem of angular velocity stabilization for the spinning spacecraft is suggested. The energy-based speed-gradient (SG) control law is proposed and numerical examination of the closed-loop system is provided. Numerical simulation results are presented showing efficiency of the SG control strategy for suppression of possible chaotic motion of the spacecraft.

2. Methods of Chaos Control

Consider a continuous-time system with lumped parameters described in the state space by differential equations

$$\dot{x} = F(x, u), \tag{1}$$

where x is an n-dimensional vector of state variables; $\dot{x} = d/dt$; u is an m-dimensional vector of inputs (control variables). A typical goal of controlling a chaotic system is full or partial stabilization of an unstable trajectory (orbit) $x_*(t)$ of the unforced ($u = 0$) system. The trajectory $x_*(t)$ may be either periodic or chaotic (nonperiodic). An important requirement is the restriction of the control intensity: only small controls are of interest.

A specific feature of this problem is the possibility of achieving the goal by means of an arbitrarily small control action. Other control goals like synchronization (concordance or concurrent change of the states of two or more systems) and chaotization (generation of a chaotic motion by means of control) can also be achieved by small control in many cases.

More subtle objectives can also be specified and achieved by control, for example, to modify a chaotic attractor of the free system in the sense of changing some of its characteristics (Lyapunov exponents, entropy, fractal dimension), or delay its occurrence, or change its locations, etc.

Feedforward control by periodic signal. Historically the first method to transform a chaotic trajectory into aperiodic one was based on applying a "nonfeedback" control, e.g. a harmonic one: $u(t) = Asin(\omega t)$. Excitation

can reflect influence of some physical actions. In these cases, the value $u(t)$ depends only on time and does not depend on the current measurements of the system variables. Such an approach is attractive because of its simplicity: no measurements or executions are needed for state information.

The possibility of transforming a periodic motion into a chaotic one, or vice versa, by means of periodic excitation of a medium level was demonstrated in [5, 6]. These results were based on computer simulations. In [7, 8] suppression of chaos in one degree-of-freedom nonlinear oscillators is studied analytically, via the Melnikov method.

Linearization of Poincaré map (OGY method). The real burst of interest in the control of chaotic systems was triggered by a paper [9], before which there was a common perception that chaos was not controllable. In this seminal paper two key ideas were introduced:

– to use the discrete system model based on linearization of the Poincaré map for controller design;

– to use the recurrence property of chaotic motions and apply control action only at an instant when the motion returns to the neighborhood of a desired state of the orbit.

Introduction of the switching off threshold ("outer" deadzone) has the effect of bounding control action and allows to respect the small control restriction, pertaining only to the special recurrence feature of chaotic motions.

Numerous extensions and interpretations have been proposed in subsequent years, and the method is commonly referred to as the "OGY method." Efficiency of this approach has been confirmed by numerous simulations as well as physical experiments. However, the convergence rate may be low, which is the price for achieving nonlocal stabilization of a nonlinear system by small control.

To overcome uncertainty of the linearized plant model, the authors of [9] and their followers suggest estimation of parameters in state-space form. The problem is of course well known in identification theory and is not straightforward, because identification in closed loop under "good" control may prevent "good" estimation.

In [1, 25] a justification of the above method was given for the special case when $y_{k,i} = y_{k-i}$, $i = 1, \ldots, n$. In this case the outputs are measured and control action is changed only at the instants of crossing the surface. For controller design an input-output model was used containing fewer coefficients than the state-space one. For estimation, the method of recursive goal inequalities due to Yakubovich was used, introducing an additional inner deadzone to resolve the problem of estimation in closed loop. An inner deadzone combined with the outer deadzone of the OGY method, provides robustness of the identification-based control with respect to both model errors and measurements errors.

Delayed feedback (Pyragas method). The method of time-delayed feedback was proposed in [26]. It suggests to find and stabilize a τ-periodic orbit of the nonlinear system (1) in the simple form of

$$u(t) = K[x(t) - x(t-\tau)] \tag{2}$$

in which K is the feedback gain and τ is the constant time delay.

If τ is equal to the period of an existing periodic solution $\bar{x}(t)$ of system (1) with $u = 0$, and if the solution $x(t)$ to the closed-loop system (1), (2) starts from $\Gamma = \{\bar{x}(t)\}$, then it will remain in Γ for all $t \geq 0$. However, it has been noticed that $x(t)$ may converge to Γ even if $x(0) \bar{\in} \Gamma$.

The control law (2) applies also to stabilization of forced periodic motions in system (1) with a T-periodic right-hand side. Then, τ should be chosen equal to T. A number of modifications of the method were proposed lately.

This method is subjected to the so-called "odd number limitation" meaning that if the Jacobian of system (1) at the target UPO has an odd number of real eigenvalues that are unstable, then the UPO cannot be stabilized by the controller (2) no matter what constant gain K is used. Some extended versions of the algorithm (2) where constant gain K is replaced by a dynamical system (filter) may overcome the "odd number limitation" [10].

Linear and nonlinear control. Many conventional engineering control techniques are effective for controlling chaos. In some cases, even the simple proportional feedback controller works quite well.

More sophisticated methods of nonlinear control can also be applied: geometric methods (feedback linearization, center manifold approach); goal-oriented techniques (Lyapunov design, speed-gradient method, passivity based feedback design, sliding mode control), frequency-domain methods (harmonic balance), iterative design methods (backstepping), etc.

A number of methods are based on continual reduction of some goal (objective) function $Q(x(t), t)$. The current value $Q(x(t), t)$ may reflect the distance between the current state $x(t)$ and the current point of the goal trajectory $x_*(t)$, such as $Q(x, t) = |x - x_*(t)|^2$, or the distance between the current state and the goal surface $h(x) = 0$, such as $Q(x) = |h(x)|^2$. For continuous-time systems the value $Q(x)$ does not depend directly on the control u and decreasing the value of the speed $\dot{Q}(x) = \partial Q / \partial x F(x, u)$ can be posed as an immediate control goal instead of decreasing $Q(x)$. This is the basic idea of the *speed-gradient* (SG) method [11], where a change in the control u occurs along the gradient in u of the speed $\dot{Q}(x)$. This approach was first used for control of chaotic systems in [27]. Systematic exposition and further references can be found in [1]. The general SG algorithm has the form

$$u = -\Psi[\nabla_u \dot{Q}(x, u)], \tag{3}$$

where $\Psi(z)$ is vector-function forming an acute angle with its argument z. For affine controlled systems $\dot{x} = f(x) + g(x)u$ the algorithm (3) simplifies to $u = -\Psi[g(x)^{\mathrm{T}} \nabla Q(x)]$.

Note that directly using the well-developed machinery of modern linear and nonlinear control theories often implies "brute force control" and does not take into account the special features of chaotic motions. This means that the "small control" requirement is ignored or violated; therefore, this simple-minded application of conventional control theory works, but not in a way as efficient and effective as expected when chaos is available for control utilization.

Adaptive and intelligent control. Because of complex nonlinear behaviors of chaotic systems and uncertainty of parameters in many physical systems, adaptive and intelligent control techniques can be quite desirable. Among numerous methods of intelligent control, those using neural network and fuzzy systems are the most popular ones. Various control algorithms can be applied to create a fuzzy control system. The most convenient one for control design and applications is the so-called Takagi–Sugeno fuzzy models.

3. Examples of Controlling Chaos in Mechanics

As it was mentioned in [12], chaos occurs widely in applied mechanical systems. A few recent examples are mentioned below.

Control of pendulums, beams, plates. A number of studies have been devoted to the control of chaos in systems of one or more pendulums. Due to interesting and readily observable behavior, pendulum systems have been used for numerical and experimental demonstration of most existing methods of chaos control [13–15]. Chaos suppression and creation has been studied in standard mechanical structures like beams [16], plates [17], impact systems [13, 18], externally forced array of oscillators with nearest-neighbor viscoelastic coupling [19].

Control of friction. It is known that a low velocity regime of mechanical systems is characterized by chaotic stick-slip motion caused by the interplay between static and kinetic friction forces. From a practical point of view one may wish to control the system in such a way that the overall friction is reduced or enchanced, the chaotic mode is eliminated and smooth sliding is achieved. Such a control is of high technological importance for micromechanical devices e.g. in computer disk drives, where the early stages of motion and the stopping process, which exhibit chaotic stick slip, pose a real problem. Controlling frictional forces has been traditionally approached by chemical means, namely, using lubricating liquids. A different approach, proposed in [20, 21] is based on controlling the system mechanically. The

goal is twofold: a) to achieve smooth sliding at low driving velocities, which otherwise correspond to the stick-slip regime; b) to decrease the frictional forces. The disadvantage of the method of [21] is the necessity of reconstructing the dynamics. This may be more or less difficult depending on the details of the dynamics of the internal degrees of freedom at the friction interface.

Besides achieving the goals mentioned in the beginning, controlling friction provides a better understanding of friction by measuring velocity-weakening friction forces.

Control of vibroformers. As it is known, the vibration-compaction of the heated mixed paste in the manufacturing of anodes for reduction cells is much more effective than monotone compression. The vibration-compaction helps a good mixing of the material, produces well compacted anode blocks and, above all, tends to eliminate air bubbles decreasing strength of the anodes. In the paper [22] a method for vibroformer control is proposed. The vibroformer is considered as an impact oscillator and is described by a version of the bouncing ball model. The frequency of the vibroformer exciter rotation is used as a control variable. To speed up changing the regime of the unit, targeting methods of [23] are applied.

Control of microcantilevers. The dynamics and control of a microcantilever system are studied in [24]. The cantilever is vibrated by a sinusoidal input, and its deflection is detected optically.

4. Stabilization of the Spinning Spacecraft

In a number of applications irregular vibrations of mechanical units arise from rotation of unbalanced rotors, vibrations in appendages, etc. The control goal is then suppression of these undesirable vibrations. Problems of this kind are often solved by the methods of linear control. In some cases nonlinear approaches are reported to be successful, e.g. [28] designed a stabilization algorithm for a spinning spacecraft using system energy as a Lyapunov (goal) function.

4.1 Model of the System Dynamics and Uncontrolled Motion Analysis

For the sake of simplicity, the 1-DOF model of the satellite angular motion is used below. The degrees of freedom of the system describe the damper mass displacement and rotation of the satellite. The damper is centered on the body fixed X-axis and has a point mass m. That mass moves along an axis

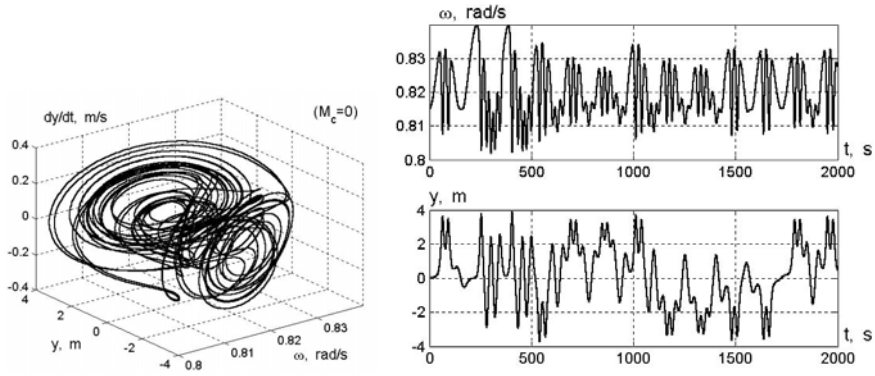

Figure 1. Chaotic oscillations for the case of uncontrollabe motion

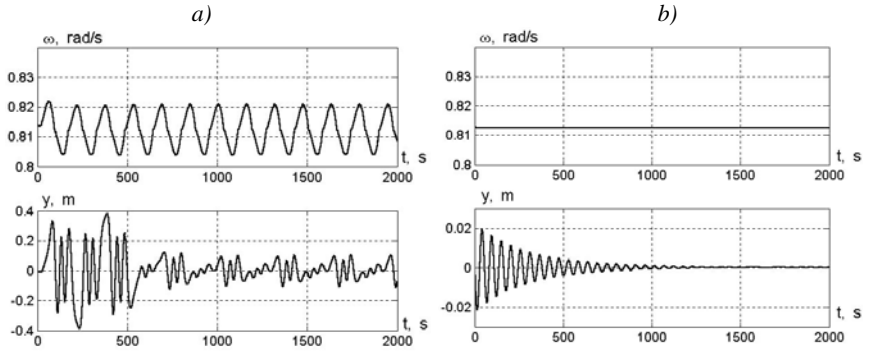

Figure 2. Active damping via control algorithm (7)

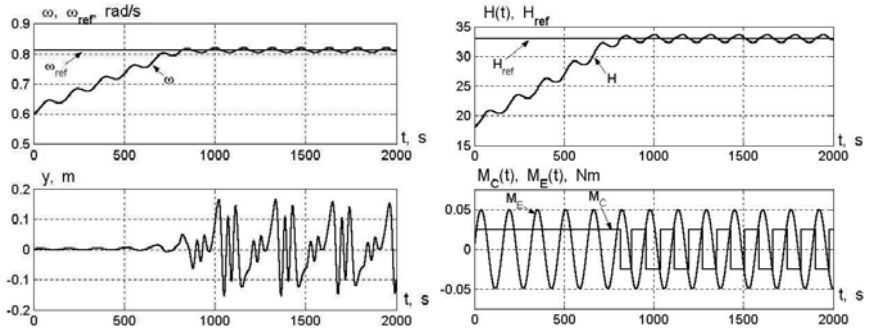

Figure 3. Satellite speeding-up via the control law (7), $\bar{M} = 0.5\bar{M}_E$

perpendicular to X-axis at the some distance of the principal axis Z. Under these assumptions the system satellite-damper model can be written as follows [28]:

$$\begin{cases} (I + m(1-\mu)y^2)\dot{\omega} + 2m(1-\mu)y\dot{y}\omega - mb\ddot{y} = M(t), \\ m(1-\mu)\ddot{y} + c\dot{y} + \big(k - (1-\mu)\omega^2\big)y - b\dot{\omega} = 0, \end{cases} \tag{4}$$

where ω, y denote satellite angular velocity and damper mass displacement; I, m, k, c stand for the satellite moment of inertia about Z-axis, damper mass, spring constant and viscous resistance gain; $\mu = m/m_T$, where m_T denotes a total mass of the considered system. The external torque $M(t)$ is a sum of the excitational torque and the control torque, i.e. $M(t) = M_E(t) + M_C(t)$. It is assumed that $M_C(t) \le \bar{M}$, where $\bar{M}$ represents restriction on the control torque.

The system (4) examinations show that if $M(t) \equiv 0$ and initial conditions belong to some region, the system is dissipative and is attracted to the equilibrium state of constant angular velocity ω^* and no damper mass deflection. If these conditions are violated, the amplitude of $y(t)$ becomes inadmissible large and the system can perform chaotic jumps between two stable equilibrium points [28]. To improve the system performance let us use, in addition, the active damping by means of the resistojets torque M_C.

4.2 Control Law Design

The control aim is to stabilize the desired state $[y, \dot{y}, \omega]^{\mathrm{T}} = [0, 0, \omega_{ref}]^{\mathrm{T}}$. This aim corresponds to the desired constant rotation rate $\omega(t) \equiv \omega_{ref}$ and zero displacement of the damper mass $y(t) \equiv 0$. Following [29–31] let us use an energy-based approach and apply the SG-method [1, 32] for control law design.

The total energy H of the system (4) may be derived as

$$H(y, \dot{y}, \omega) = 0.5\big((m(1-\mu)+k)y^2 + I\big)\omega^2 - mb\dot{y}\omega - 0.5m(1-\mu)\dot{y}^2. \tag{5}$$

Substitution of $y = \dot{y} = 0$, $\omega = \omega_{ref}$ to (5) gives the desired energy H_{ref} as $H_{ref} = 0.5I\omega_{ref}^2$. Let us introduce the *goal function* $Q = (H - H_{ref})^2$ and derive the SG control laws in the finite form ([32]). It gives the "proportional" and relay algorithms as follows:

$$M_C = \gamma\,\big(H_{ref} - H(y, \dot{y}, \omega)\big) \cdot \big(\omega + \dot{\tilde{y}}(\tilde{I} + \tilde{y}^2 - 1)^{-1}\big), \tag{6}$$

$$M_C = \gamma\ \mathrm{sign}\,\big(H_{ref} - H(y, \dot{y}, \omega)\big) \cdot \mathrm{sign}\,\big(\omega + \dot{\tilde{y}}(\tilde{I} + \tilde{y}^2 - 1)^{-1}\big), \tag{7}$$

where $\tilde{y} = (1-\mu)b^{-1}y$, $\tilde{I} = (1-\mu)m^{-1}b^{-2}I$ are introduced. The control law (7) can be directly implemented by means of the on-off operating resistojets.

In such a case the gain γ gives the control torque amplitude: $\bar{M} = \gamma$. The pulse-width modulation can be used for implementation of the "proportional" control law (6) by means of the on-off thrusters.

4.3 Simulation Results

For numerical examination the parameters of the spinning spacecraft with circumferential nutational damper were chosen to be similar to that of *Intelsat-II* being $m = 0.3$ kg, $b = 1$ m, $k = 0.2$ N/m, $\mu = 0.01$, $I = 100$ kgm^2, $c = 0.002$ Ns/m, [28]. The harmonic disturbance torque M_E is taken: $M_E(t) = \bar{M}_E \sin \Omega t$. The excitation frequency Ω=0.04 s^{-1} and the amplitude $\bar{M}_E$=0.05 Nm. Following initial conditions are picked up for the simulations: $\omega(0) = 0.815$ s^{-1}, $y(0) = 0$, $\dot{y}(0) = 0$. Two cases of the control torque amplitude $\bar{M}$ are studied: *a*) $\bar{M}$=0.0225 Nm, $\bar{M} < \bar{M}_E$, and *b*) $\bar{M}$=0.055 Nm, $\bar{M}$=1.1$\bar{M}_E > \bar{M}_E$ (for example, the SSTL's water resistojets producing the thrust in the order $0.01 \div 0.10$ N would be meant).

Some simulation results are shown in Figs. 1–3.

The simulation results for the case of active damping absence $M_C \equiv 0$ are plotted in Fig. 1. One sees that the chaotic motion with a large magnitude of $y(t)$ appears. (Note that in practice $y(t)$ is restricted due to travel limits, but it is seen that the damper can not be effective in that case.) The effect of the feedback control via relay SG-law (7) is demonstrated in Fig. 2. It is taken $H_{ref} = 33$ kgm^{2}s^{-2}, which corresponds to $\omega_{ref} = 8.124$ rad/s. It is seen that even in the case when the amplitude of control torque is less that one of the disturbance, $\bar{M} = 0.5\bar{M}_E$ (see Fig. 2*a*), the system behaviour is improved in a great extent in comparison with the uncontrollable case. Perfect supression of oscillations is obtained for the case $\bar{M} = 1.1\bar{M}_E$ (Fig. 2*b*). Note that in [28] the ratio $\bar{M}/\bar{M}_E$ is about 15. Therefore the proposed method is characterized as a low level control.

Speeding-up the satellite rotation from $\omega(0) = 0.6$ rad s^{-1} to given velocity ω_{ref} is demonstrated in Fig. 3 for the case $\bar{M} = 0.5\bar{M}_E$. In the case $\bar{M} = 1.1\bar{M}_E$ the finite-time convergence of $\omega(t)$ to ω_{ref} takes place. The transient time is about 360 s. The sliding motion with exact holding the desired state arises after the transient is finished. (The similar processes are pictured in Fig. 2*b*.) The control algorithm with a dead-zone or a pulse-width modulation control can be used to reduce propellent consumption and working fluid discharge.

The simulations demonstrate effeciency of the SG control strategy in eliminating chaotic instabilities in a spinning spacecraft and robustness properties with respect to excitation torque amplitude.

5. Conclusions

State-of-the art of the field related to control of chaotic systems is briefly surveyed and some examples for control of chaos in mechanical systems are presented. The authors do not insist that chaos should be used in realistic applications: the point of the paper is to show a variety of methods capable either to increase chaos, or to eliminate it. These methods often achieve the goal with smaller control power compared with traditional control engineering approaches, as it is demonstrated in the problem of supression chaotic behaviour of the spinning satellite.

References

[1] A.L. Fradkov and A.Yu. Pogromsky. *Introduction to Control of Oscillations and Chaos.* World Scientific, 1998.

[2] A.L. Fradkov. Chaos Control Bibliography (1997 – 2000). In *Russian Systems and Control Archive* (RUSYCON), www.rusycon.ru/chaos-control.html, 2001.

[3] A.L. Fradkov and R.J. Evans. Control of Chaos: Survey 1997–2000. *Preprints of 15th IFAC World Congress on Automatic Control. Plenary papers, Survey papers, Milestones.* Barcelona. 143–154, 2002.

[4] B.R. Andrievskii and A.L. Fradkov. "Control of chaos: Methods and applications. Part I: Methods," *Automation and Remote Control*, 64 (5):673–713, 2003.

[5] K. Matsumoto and I. Tsyda, "Noise induced order," *J. Stat. Phys.* 31: 87–106, 1983.

[6] V.V. Alekseev and A.Yu. Loskutov, "Destochastization of a system with a strange attractor by parametric interaction," *Moscow Univ. Phys. Bull.*, 40 (3):46–49, 1985.

[7] R. Lima and M. Pettini, "Parametric resonant control of chaos," *Int. J. Bifurc. and Chaos*, 8:1675–1684, 1998.

[8] R. Chacon, "Maintenance and suppression of chaos by weak harmonic perturbations: A unified view," *Phys. Rev. Lett.* 86: 1737–1740, 2001.

[9] E. Ott, C. Grebogi and J. Yorke, "Controlling chaos," *Phys. Rev. Lett.* 64 (11):1196–1199, 1990.

[10] M. Basso, R. Genesio and A. Tesi, "Stabilizing periodic orbits of forced systems via generalized Pyragas controllers," *IEEE Trans. Circ. Syst.–I.* 44:1023–1027, 1997.

[11] A.L. Fradkov, "Speed-gradient scheme in adaptive control," *Autom. Remote Control*, 40 (9):1333–1342, 1979.

[12] T. Kapitaniak, J. Brindley and K. Czolczynski, "Chaos in mechanical systems and its control," In *Controlling Chaos and Bifurcations in Engin. Systems*, Ed. G. Chen. CRC Press. 71–88, 1999.

[13] S. Lenci and G. Rega, "Controlling nonlinear dynamics in a two-well impact system I. Attractors and bifurcation scenario under symmetric excitations," *Int. J. Bifurcation and Chaos*. 8:2387–2407. "II. Attractors and bifurcation scenario under unsymmetric optimal excitation," *Int. J. Bifurcation and Chaos*, 8:2409–2424, 1998.

[14] S. Kaart, J.C. Schouten and C.M. van den Bleek. "Synchronizing chaos in an experimental chaotic pendulum using methods from linear control theory," *Phys. Rev. E.* 59:5303–5312, 1998.

[15] K.I. Thomas and G. Ambika, "Suppression of Smale horseshoe structure via secondary perturbations in pendulum systems," *Pramana – J. of Physics*, 52:375–387, 1999.

[16] S.R. Bishop and D. Xu, "The use of control to eliminate subharmonic and chaotic impacting motions of a driven beam," *J. Sound and Vibration*, 205:223–234, 1997.

[17] L.Q. Chen and C.J. Cheng, "Controlling chaotic oscillations of viscoelastic plates by the linearization via output feedback," *Applied Mathematics and Mechanics – English Edition*, 20:1324–1330, 1999.

[18] T.L. Vincent and A.I. Mees. "Controlling a bouncing ball," *Int. J. Bifurcation and Chaos.* 10:579–592, 2000.

[19] C. Barratt. "On the control of chaos in extended structures," *J. of Vibration and Acoustics – Trans. ASME*, 119:551–556, 1997.

[20] F.J. Elmer. "Controlling friction," *Phys. Rev. E*, 57:R4903–R4906, 1998.

[21] M.G. Rozman, M. Urbakh and J. Klafter. "Controlling chaotic frictional forces," *Phys. Rev. E*. 57:7340–7343, 1998.

[22] Paskota, M. "On modelling and the control of vibroformers in aluminium production," *Chaos Solitons & Fractals*, 9:323–335.

[23] M. Paskota and H.W.J. Lee. "Targeting moving targets in chaotic dynamical systems," *Chaos Solitons & Fractals,* 8:1533–1544, 1997.

[24] M. Ashhab, M.V. Salapaka, M. Dahleh and I. Mezic. "Dynamical analysis and control of microcantilevers," *Automatica*, 35:1663–1670, 1999.

[25] A.L. Fradkov and P.Yu. Guzenko. "Adaptive control of oscillatory and chaotic systems based on linearization of Poincaré map," In *Proc. 4th Europ. Contr. Conf.* Brussels, 1997.

[26] K. Pyragas. "Continuous control of chaos by self-controlling feedback," *Phys. Lett. A.* 170:421–428, 1992.

[27] A.L. Fradkov. "Nonlinear adaptive control: regulation–tracking–oscillations," In *Proc. of 1st IFAC Workshop "New Trends in Design of Control Systems,"* 426–431, 1994.

[28] P.A. Meehan and S.F. Asokanthan. "Control of chaotic instabilities in a spinning spacecraft with dissipation using Lyapunov's method," *Chaos Solitons Fractals*, 13 (9):1857–1869, 2002.

[29] A.L. Fradkov. "Swinging control of nonlinear oscillations," *Intern. J. Control,* 64 (6):1189–1202, 1996.

[30] A.S. Shiriaev, O. Egeland, H. Ludvigsen and A.L. Fradkov. "VSS-version of energy-based control for swinging up a pendulum," *Syst., Control Let.* 44 (1):45–56, 2001.

[31] A.L. Fradkov and B.R. Andrievsky. "Damping the spinning spacecraft via low level control," In *Proc. 10th Int.Conf. "Integrated Navigation and Control Systems."* St.Petersburg, 106–108, 2003.

[32] A.L. Fradkov, I.V. Miroshnik and V.O. Nikiforov. *Nonlinear and adaptive control of complex systems*. Kluwer Academic Publishers, 1999.

THE LARGEST LYAPUNOV EXPONENT OF DYNAMICAL SYSTEMS WITH TIME DELAY

Andrzej Stefański, Tomasz Kapitaniak and Artur Dąbrowski
Division of Dynamics, Technical University of Lodz, 90-924 Lodz, Poland
tomaszka@ck-sg.p.lodz.pl

Abstract: We show that the largest Lyapunov exponent of the dynamical system with time delay can be estimated by the procedure based on the phenomenon of chaos synchronization. Our approach can be applied both for flow and discrete maps.

Key words: Lyapunov exponents, chaos synchronization, systems with delay.

1. Introduction

Lyapunov exponents are numbers which describe exponential convergence or divergence of trajectories that start close to each other. The existence of such numbers has been proved by Oseledec theorem [1]. The number of Lyapunov exponents, which characterize the behavior of dynamical system, is equal to the dimension of this system. If the sum of all Lyapunov exponents is negative then the system has an attractor. For practical applications it is most important to know the largest Lyapunov exponent. If the largest value in the spectrum of Lyapunov exponents is positive, it means that the system is chaotic. The largest value equal to zero indicates periodic or quasi-periodic dynamics. If all Lyapunov exponents are negative then the stable critical point is an attractor.

Currently there exist robust algorithms for calculating Lyapunov exponents for the system given by a continuous and differentiable ordinary differential equation (for example [2-6]). These algorithms allow an easy estimation of entire spectrum of Lyapunov exponents but they do not work for the system with discontinuities or time delay and in the case when the equations of

G. Rega and F. Vestroni (eds.),
IUTAM Symposium on Chaotic Dynamics and Control of Systems and Processes in Mechanics, 493–500.

motion describing dynamics of the system are unknown. In such a case the estimation of Lyapunov exponents is not straightforward [7-10].

Our method is based on the phenomenon of synchronization of coupled identical systems [11]. Previously it has been successfully used for dynamical systems with discontinuities [12-14].

2. Estimation Procedure

Consider two identical dynamical systems $\dot{\mathbf{x}} = \mathbf{f}(\mathbf{x})$ and $\dot{\mathbf{y}} = \mathbf{f}(\mathbf{y})$, which are unidirectionally coupled by the negative feedback mechanism

$$\dot{\mathbf{x}} = \mathbf{f}(\mathbf{x}) + \mathbf{D}(\mathbf{y} - \mathbf{x}), \tag{1a}$$

$$\dot{\mathbf{y}} = \mathbf{f}(\mathbf{y}), \tag{1b}$$

where $\mathbf{x}, \mathbf{y} \in \mathbb{R}^k$, $\mathbf{D}=\text{diag}[d, d, \ldots, d] \in \mathbb{R}^k$ is the diagonal coupling matrix and $d \in \mathbb{R}$ represents a coupling coefficient. Now, we introduce a new variable $\mathbf{z}$ representing the *trajectory separation* between both subsystems during the time evolution. This variable is defined by the expression:

$$\dot{\mathbf{z}} = \mathbf{x} - \mathbf{y}, \tag{2}$$

After substituting equations (1a) and (1b) into equation (2) we obtain:

$$\dot{\mathbf{z}} = \mathbf{f}(\mathbf{x}) - \mathbf{f}(\mathbf{y}) - \mathbf{D}\mathbf{z}. \tag{3}$$

In the first part of our considerations, let us assume that for $d=0$ (lack of coupling) each of the subsystems given by equations (1a) and (1b) evolves on the asymptotically stable chaotic attractor $\boldsymbol{A}$. In this case the equation (3) is simplified to the following form:

$$\dot{\mathbf{z}} = \mathbf{f}(\mathbf{x}) - \mathbf{f}(\mathbf{y}). \tag{4}$$

Since these both systems are identical, it can be assumed that the solutions to both equations (1a) and (1b), starting from different initial points of the same basin of attraction, represent two uncorrelated trajectories evolving on the same attractor $\boldsymbol{A}$ (after a period of the transient motion).

For sufficiently small *trajectory separation* vector, that is to say, $\|\mathbf{z}\| \ll |\boldsymbol{A}|$, where $|\boldsymbol{A}| \in \mathbb{R} \geq 0$ is the attractor's size, i.e. the maximum distance between two points on the attractor in the phase space, we can assume that an average distance between trajectories of the subsystems under

consideration is given by the linearized solution resulting from the definition of the Lyapunov exponent

$$\mathbf{z}(t) = \mathbf{E}(t)\mathbf{z}(0)\,, \tag{5}$$

where $\mathbf{E}(t)$=diag[exp($\lambda_1 t$), exp($\lambda_2 t$), ... , exp($\lambda_k t$)] and λ_i (i=1, 2, … , k) are Lyapunov exponents. Equation (5) describes the time evolution of the sphere with infinitely small initial radius $z(0)$ in the phase space. The first time derivative of equation (5) is given by the relation

$$\dot{\mathbf{z}} = \mathbf{\Lambda}\mathbf{E}(t)\mathbf{z}(0)\,, \tag{6}$$

where $\mathbf{\Lambda}$=diag[λ_1, λ_2, ... , λ_k] is diagonal matrix of Lyapunov exponents. Substituting equation (5) into equation (6) and comparing with equation (4) we obtain

$$\mathbf{f}(\mathbf{x}) - \mathbf{f}(\mathbf{y}) = \mathbf{\Lambda}\mathbf{z}\,. \tag{7}$$

Next, we can put the above equality (equation (7)) into equation (3). Hence, taking into consideration diagonal coupling ($\mathbf{D}=d\mathbf{I}$), for small *trajectory separation* equation (3) takes the following form:

$$\dot{\mathbf{z}} = (\mathbf{\Lambda} - d\mathbf{I})\mathbf{z}\,. \tag{8}$$

Matrix $\mathbf{\Lambda}-d\mathbf{I}$ with eigenvalues $s_i=\lambda_i-d$ (i=1, 2, … , k) determines stability of ideal synchronization (i.e. $\lim_{t\to\infty}\|\mathbf{z}(t)\|=0$ [15]) between both subsystems (equations (1a) and (1b)). Synchronuous regime is stable if the largest eigenvalue of stability matrix is negative:

$$s_1 = \lambda_1 - d < 0\,. \tag{9}$$

Thus, the following condition of ideal synchronization for the system under consideration (equations (1a) and (1b)) results from equation (9):

$$d > \lambda_1\,, \tag{10}$$

where λ_1 is the largest Lyapunov exponent.

Inequality (10) allows us to propose a novel method of estimation of the largest Lyapunov exponent for dynamical systems. In fact, it follows from inequality (10) that the smallest value of the coupling coefficient d for which synchronization takes place is equal to the maximum Lyapunov exponent λ_1.

To apply our method for any dynamical system $\dot{\mathbf{x}} = \mathbf{f}(\mathbf{x})$ it is necessary to build an augmented system according to equations (1a) and (1b). The next action is numerical search for the smallest synchronization parameter d for such a system, which approximates to the largest Lyapunov exponent of the investigated system. The numerical procedure of estimation process is described in details in [12-14]. Since the synchronization is easily detectable, the presented method has significant practical advantage over more traditional algorithmic methods, especially in dealing with non-smooth systems or systems with time delay.

In this paper we describe the method which allows the estimation of the largest Lyapunov exponent for the systems with time delay described by the retarded differential equation

$$\dot{\mathbf{x}} = \mathbf{f}\big(\mathbf{x}(t), \mathbf{x}(t-\tau)\big), \tag{11}$$

where $\mathbf{x} \in \mathbb{R}^k$, $\tau \in \mathbb{R}$ denote the delay. Equation (11) can be easily integrated numerically but due to the retarded arguments in $\mathbf{x}(t-\tau)$, Lyapunov exponents cannot be calculated using algorithms based on the Oseledec theorem [1-6]. In the case of equation (11) one can develop argument $\mathbf{x}(t-\tau)$ into the Taylor's series in the neighbourhood of τ

$$\mathbf{x}(t-\tau) = \mathbf{x}(t) + \frac{1}{i!}\sum\nolimits_i (-\tau)^i \frac{d^i \mathbf{x}(t)}{dt^i}. \tag{12}$$

(where $i \in \mathbb{N}$). After substitution of equation (12) into equation (11) the retarded differential equation (11) becomes ordinary differential equation with delay τ as one of the constant parameters. Then we can apply the classical algorithms for calculation of Lyapunov exponents. This transformation gives some approximation of the dynamics governed by equation (11) only in the case of small time delay τ for which it is sufficient to consider only a few first components of power series (equation (12)). However, it should be noted here that the dynamics governed by equation (11) is very sensitive to the changes of the delay τ, particularly in the case of chaotic behavior, so the approximation given by equation (12) rarely gives good results.

In practice, our synchronization based method of the estimation of the largest Lyapunov exponent for the systems with time delay can be implemented by substitution of equation (11) into equations (1a) and (1b).

3. Numerical Example

As a numerical example we consider nonlinear Van der Pol oscillator with external harmonic excitation and time delay [16]

$$\ddot{y} - \alpha(1 - y^2)\dot{y} + \beta y^3 = \kappa y(t - \tau) - p\cos(\eta t)\,. \tag{13}$$

where $\alpha, \beta, p, \eta, \kappa$ and time delay τ are constant.

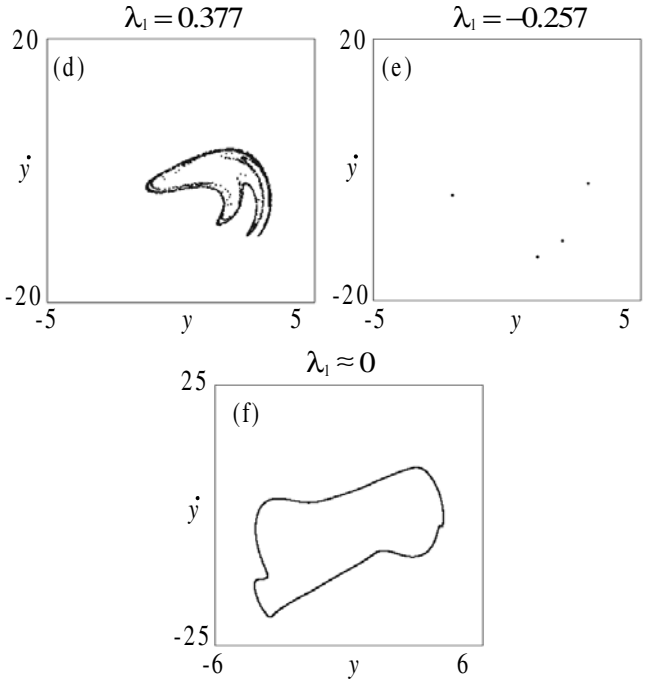

Figure 1. The Poincaré maps of the delayed Van der Pol oscillator (equation (13)) together with estimated values of the largest Lyapunov exponent (on the top); α=0.20, β=1.00, τ=2.00, η=4.00, p=17.00: (a) chaotic attractor – κ=0.80, (b) periodic attractor – κ=2.20, (c) quasi-periodic attractor – κ=6.00.

After the change of variables (x=x_1, $\dot{x} = x_2$) and substitution of equation (13) into equations (1a) and (1b) we obtain the augmented system

$$\begin{aligned}
\dot{x}_1 &= x_2 + d(y_1 - x_1),\\
\dot{x}_2 &= \kappa x_1(t - \tau) - p\cos(\eta\, t) + \alpha(1 - x_1^2)x_2 - \beta x_1^3 + d(y_2 - x_2),\\
\dot{y}_1 &= y_2,\\
\dot{y}_2 &= \kappa y_1(t - \tau) - p\cos(\eta\, t) + \alpha(1 - y_1^2)y_2 - \beta y_1^3,
\end{aligned} \tag{14}$$

which is numerically integrated.

In the numerical simulation we took α=0.20, β=1.00, τ=2.00, η=4.00, p=17.00 and assumed κ as a control parameter. The assumed large value of delay excludes the application of equation (12) in practice. The examples of Poincaré maps of the system (13) and the estimated values of the largest Lyapunov exponent λ_1 are shown in Figures 1a, 1b, and 1c. In Figures 2a and 2b the comparison of the bifurcation diagram of the system (equation (13)) with the bifurcation diagram of the largest Lyapunov exponent obtained by means of proposed method is shown. In both Figures good agreement between the values of the largest Lyapunov exponent and character of motion is observed.

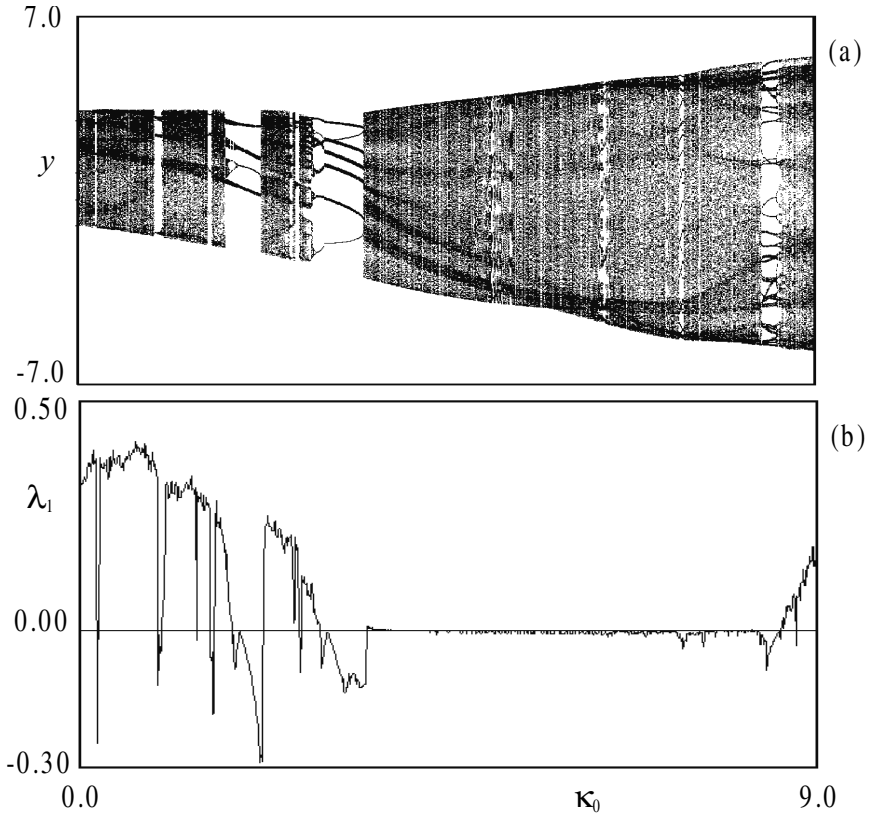

Figure 2. Bifurcation diagram of the Van der Pol oscillator with time delay (equation(13)) – (a) and corresponding the largest Lyapunov exponent (b) estimated by means of the proposed method; α=0.20, β=1.00, τ=2.00, η=4.00, p=17.00.

4. Conclusions

In summary, we conclude that the proposed method allows the estimation of the largest Lyapunov exponent for the dynamical systems with time delay. Our numerical examples showed that the synchronization based approach can be applied for such systems no matter how large the delay is. The novelty of the method lies in its use of the synchronization phenomenon (readily recognized). Since the synchronization is easily detectable, the method has significant practical advantage over more traditional algorithmic methods, especially in dealing with systems with delay and also in dealing with non-smooth systems.

Acknowledgment

This study has been supported by the Polish Committee for Scientific Research (KBN) under project No.5 T07A 014 23.

References

[1] V.I. Oseledec, "A multiplicative ergodic theorem: Lyapunov characteristic numbers for dynamical systems," *Trans Moscow Math Soc*, 19, 197-231, 1968.

[2] G. Benettin, L. Galgani, J.M. Strelcyn, "Kolmogorov entropy and numerical experiment," *Physical Review A*, 14, 2338-2345, 1976.

[3] G. Benettin, L. Galgani, A. Giorgilli, J.M. Strelcyn, "Lyapunov exponents for smooth dynamical systems and Hamiltonian systems; a method for computing all of them, Part I: Theory," *Meccanica*, 15, 9-20, 1980.

[4] G. Benettin, L. Galgani, A. Giorgilli, J.M. Strelcyn, "Lyapunov exponents for smooth dynamical systems and Hamiltonian systems; a method for computing all of them, Part II: Numerical application," *Meccanica,* 15, 21-30, 1980.

[5] I. Shimada and T. Nagashima, "A numerical approach to ergodic problem of dissipative dynamical systems," *Progress of Theoretical Physics*, 61(6), 1605-1616, 1979.

[6] A. Wolf, "Quantifying chaos with Lyapunov exponents," *Chaos* (V. Holden eds), Manchester University Press, Manchester, 273-290, 1986.

[7] J.P. Eckmann, S.O. Kamphorst, D. Ruelle, S. Ciliberto, "Lyapunov exponents from a time series," *Physical Review Letters,* 34(9), 4971-4979, 1986.

[8] N. Hinrichs, M. Oestreich, K. Popp, "Dynamics of oscillators with impact and friction," *Chaos, Solitons & Fractals*, 4(8), 535-558, 1997.

[9] P. Müller, "Calculation of Lyapunov exponents for dynamical systems with discontinuities", *Chaos, Solitons & Fractals,* 5(9), 1671-1681, 1995.

[10] A. Wolf, J.B. Swift, H.L. Swinney, J.A. Vastano,"Determining Lyapunov exponents from a time series," *Physica D*, 16, 285-317, 1985.

[11] H. Fujisaka, T. Yamada, "Stability theory of synchronized motion in coupled-oscillator systems," *Progress of Theoretical Physics*, 69(1), 32-47, 1983.

[12] A. Stefański, T. Kapitaniak, "Using chaos synchronization to estimate the largest Lyapunov exponent of non-smooth systems," *Discrete Dynamics in Nature & Society*, 4, 207-215, 2000.
[13] A. Stefański, "Estimation of the largest Lyapunov exponent in systems with impacts," *Chaos, Solitons & Fractals,* 11(15), 2443-2451, 2000.
[14] A. Stefański, T. Kapitaniak, "Estimation of the dominant Lyapunov exponent of non-smooth systems on the basis of maps synchronization," *Chaos, Solitons & Fractals,* 15, 233-244, 2003.
[15] L.M. Pecora, T.L. Carroll, "Synchronization of chaos," *Physical Review Letters,* 64, 221-224, 1990.
[16] J. Awrejcewicz, J. Wojewoda, "Observation of chaos in a nonlinear oscillator with delay: Numerical study," *KSME Journal*, 3(1), 15-24, 1989.

INDEX OF CONTRIBUTORS

G. Rega and F. Vestroni (eds.),
IUTAM Symposium on Chaotic Dynamics and Control of Systems and Processes in Mechanics, 501–502.

INDEX OF KEYWORDS

G. Rega and F. Vestroni (eds.),
IUTAM Symposium on Chaotic Dynamics and Control of Systems and Processes in Mechanics, 503–504.

Mechanics

SOLID MECHANICS AND ITS APPLICATIONS

Series Editor: G.M.L. Gladwell

Aims and Scope of the Series

The fundamental questions arising in mechanics are: *Why?*, *How?*, and *How much?* The aim of this series is to provide lucid accounts written by authoritative researchers giving vision and insight in answering these questions on the subject of mechanics as it relates to solids. The scope of the series covers the entire spectrum of solid mechanics. Thus it includes the foundation of mechanics; variational formulations; computational mechanics; statics, kinematics and dynamics of rigid and elastic bodies; vibrations of solids and structures; dynamical systems and chaos; the theories of elasticity, plasticity and viscoelasticity; composite materials; rods, beams, shells and membranes; structural control and stability; soils, rocks and geomechanics; fracture; tribology; experimental mechanics; biomechanics and machine design.

1. R.T. Haftka, Z. Gürdal and M.P. Kamat: *Elements of Structural Optimization*. 2nd rev.ed., 1990 ISBN 0-7923-0608-2
2. J.J. Kalker: *Three-Dimensional Elastic Bodies in Rolling Contact.* 1990 ISBN 0-7923-0712-7
3. P. Karasudhi: *Foundations of Solid Mechanics.* 1991 ISBN 0-7923-0772-0
4. *Not published*
5. *Not published.*
6. J.F. Doyle: *Static and Dynamic Analysis of Structures.* With an Emphasis on Mechanics and Computer Matrix Methods. 1991 ISBN 0-7923-1124-8; Pb 0-7923-1208-2
7. O.O. Ochoa and J.N. Reddy: *Finite Element Analysis of Composite Laminates.* ISBN 0-7923-1125-6
8. M.H. Aliabadi and D.P. Rooke: *Numerical Fracture Mechanics.* ISBN 0-7923-1175-2
9. J. Angeles and C.S. López-Cajún: *Optimization of Cam Mechanisms.* 1991 ISBN 0-7923-1355-0
10. D.E. Grierson, A. Franchi and P. Riva (eds.): *Progress in Structural Engineering.* 1991 ISBN 0-7923-1396-8
11. R.T. Haftka and Z. Gürdal: *Elements of Structural Optimization.* 3rd rev. and exp. ed. 1992 ISBN 0-7923-1504-9; Pb 0-7923-1505-7
12. J.R. Barber: *Elasticity*. 1992 ISBN 0-7923-1609-6; Pb 0-7923-1610-X
13. H.S. Tzou and G.L. Anderson (eds.): *Intelligent Structural Systems.* 1992 ISBN 0-7923-1920-6
14. E.E. Gdoutos: *Fracture Mechanics.* An Introduction. 1993 ISBN 0-7923-1932-X
15. J.P. Ward: *Solid Mechanics*. An Introduction. 1992 ISBN 0-7923-1949-4
16. M. Farshad: *Design and Analysis of Shell Structures*. 1992 ISBN 0-7923-1950-8
17. H.S. Tzou and T. Fukuda (eds.): *Precision Sensors, Actuators and Systems*. 1992 ISBN 0-7923-2015-8
18. J.R. Vinson: *The Behavior of Shells Composed of Isotropic and Composite Materials*. 1993 ISBN 0-7923-2113-8
19. H.S. Tzou: *Piezoelectric Shells*. Distributed Sensing and Control of Continua. 1993 ISBN 0-7923-2186-3
20. W. Schiehlen (ed.): *Advanced Multibody System Dynamics*. Simulation and Software Tools. 1993 ISBN 0-7923-2192-8
21. C.-W. Lee: *Vibration Analysis of Rotors.* 1993 ISBN 0-7923-2300-9
22. D.R. Smith: *An Introduction to Continuum Mechanics.* 1993 ISBN 0-7923-2454-4
23. G.M.L. Gladwell: *Inverse Problems in Scattering*. An Introduction. 1993 ISBN 0-7923-2478-1

Mechanics

SOLID MECHANICS AND ITS APPLICATIONS

Series Editor: G.M.L. Gladwell

24. G. Prathap: *The Finite Element Method in Structural Mechanics*. 1993 ISBN 0-7923-2492-7
25. J. Herskovits (ed.): *Advances in Structural Optimization.* 1995 ISBN 0-7923-2510-9
26. M.A. González-Palacios and J. Angeles: *Cam Synthesis.* 1993 ISBN 0-7923-2536-2
27. W.S. Hall: *The Boundary Element Method.* 1993 ISBN 0-7923-2580-X
28. J. Angeles, G. Hommel and P. Kovács (eds.): *Computational Kinematics.* 1993 ISBN 0-7923-2585-0
29. A. Curnier: *Computational Methods in Solid Mechanics*. 1994 ISBN 0-7923-2761-6
30. D.A. Hills and D. Nowell: *Mechanics of Fretting Fatigue*. 1994 ISBN 0-7923-2866-3
31. B. Tabarrok and F.P.J. Rimrott: *Variational Methods and Complementary Formulations in Dynamics.* 1994 ISBN 0-7923-2923-6
32. E.H. Dowell (ed.), E.F. Crawley, H.C. Curtiss Jr., D.A. Peters, R. H. Scanlan and F. Sisto: *A Modern Course in Aeroelasticity*. Third Revised and Enlarged Edition. 1995 ISBN 0-7923-2788-8; Pb: 0-7923-2789-6
33. A. Preumont: *Random Vibration and Spectral Analysis.* 1994 ISBN 0-7923-3036-6
34. J.N. Reddy (ed.): *Mechanics of Composite Materials*. Selected works of Nicholas J. Pagano. 1994 ISBN 0-7923-3041-2
35. A.P.S. Selvadurai (ed.): *Mechanics of Poroelastic Media*. 1996 ISBN 0-7923-3329-2
36. Z. Mróz, D. Weichert, S. Dorosz (eds.): *Inelastic Behaviour of Structures under Variable Loads*. 1995 ISBN 0-7923-3397-7
37. R. Pyrz (ed.): *IUTAM Symposium on Microstructure-Property Interactions in Composite Materials.* Proceedings of the IUTAM Symposium held in Aalborg, Denmark. 1995 ISBN 0-7923-3427-2
38. M.I. Friswell and J.E. Mottershead: *Finite Element Model Updating in Structural Dynamics*. 1995 ISBN 0-7923-3431-0
39. D.F. Parker and A.H. England (eds.): *IUTAM Symposium on Anisotropy, Inhomogeneity and Nonlinearity in Solid Mechanics.* Proceedings of the IUTAM Symposium held in Nottingham, U.K. 1995 ISBN 0-7923-3594-5
40. J.-P. Merlet and B. Ravani (eds.): *Computational Kinematics '95*. 1995 ISBN 0-7923-3673-9
41. L.P. Lebedev, I.I. Vorovich and G.M.L. Gladwell: *Functional Analysis.* Applications in Mechanics and Inverse Problems. 1996 ISBN 0-7923-3849-9
42. J. Menčik: *Mechanics of Components with Treated or Coated Surfaces.* 1996 ISBN 0-7923-3700-X
43. D. Bestle and W. Schiehlen (eds.): *IUTAM Symposium on Optimization of Mechanical Systems.* Proceedings of the IUTAM Symposium held in Stuttgart, Germany. 1996 ISBN 0-7923-3830-8
44. D.A. Hills, P.A. Kelly, D.N. Dai and A.M. Korsunsky: *Solution of Crack Problems*. The Distributed Dislocation Technique. 1996 ISBN 0-7923-3848-0
45. V.A. Squire, R.J. Hosking, A.D. Kerr and P.J. Langhorne: *Moving Loads on Ice Plates*. 1996 ISBN 0-7923-3953-3
46. A. Pineau and A. Zaoui (eds.): *IUTAM Symposium on Micromechanics of Plasticity and Damage of Multiphase Materials*. Proceedings of the IUTAM Symposium held in Sèvres, Paris, France. 1996 ISBN 0-7923-4188-0
47. A. Naess and S. Krenk (eds.): *IUTAM Symposium on Advances in Nonlinear Stochastic Mechanics*. Proceedings of the IUTAM Symposium held in Trondheim, Norway. 1996 ISBN 0-7923-4193-7
48. D. Ieşan and A. Scalia: *Thermoelastic Deformations.* 1996 ISBN 0-7923-4230-5

Mechanics

SOLID MECHANICS AND ITS APPLICATIONS

Series Editor: G.M.L. Gladwell

49. J.R. Willis (ed.): *IUTAM Symposium on Nonlinear Analysis of Fracture*. Proceedings of the IUTAM Symposium held in Cambridge, U.K. 1997 ISBN 0-7923-4378-6
50. A. Preumont: *Vibration Control of Active Structures*. An Introduction. 1997 ISBN 0-7923-4392-1
51. G.P. Cherepanov: *Methods of Fracture Mechanics: Solid Matter Physics*. 1997 ISBN 0-7923-4408-1
52. D.H. van Campen (ed.): *IUTAM Symposium on Interaction between Dynamics and Control in Advanced Mechanical Systems.* Proceedings of the IUTAM Symposium held in Eindhoven, The Netherlands. 1997 ISBN 0-7923-4429-4
53. N.A. Fleck and A.C.F. Cocks (eds.): *IUTAM Symposium on Mechanics of Granular and Porous Materials.* Proceedings of the IUTAM Symposium held in Cambridge, U.K. 1997 ISBN 0-7923-4553-3
54. J. Roorda and N.K. Srivastava (eds.): *Trends in Structural Mechanics*. Theory, Practice, Education. 1997 ISBN 0-7923-4603-3
55. Yu.A. Mitropolskii and N. Van Dao: *Applied Asymptotic Methods in Nonlinear Oscillations*. 1997 ISBN 0-7923-4605-X
56. C. Guedes Soares (ed.): *Probabilistic Methods for Structural Design.* 1997 ISBN 0-7923-4670-X
57. D. François, A. Pineau and A. Zaoui: *Mechanical Behaviour of Materials.* Volume I: Elasticity and Plasticity. 1998 ISBN 0-7923-4894-X
58. D. François, A. Pineau and A. Zaoui: *Mechanical Behaviour of Materials.* Volume II: Viscoplasticity, Damage, Fracture and Contact Mechanics. 1998 ISBN 0-7923-4895-8
59. L.T. Tenek and J. Argyris: *Finite Element Analysis for Composite Structures.* 1998 ISBN 0-7923-4899-0
60. Y.A. Bahei-El-Din and G.J. Dvorak (eds.): *IUTAM Symposium on Transformation Problems in Composite and Active Materials*. Proceedings of the IUTAM Symposium held in Cairo, Egypt. 1998 ISBN 0-7923-5122-3
61. I.G. Goryacheva: *Contact Mechanics in Tribology*. 1998 ISBN 0-7923-5257-2
62. O.T. Bruhns and E. Stein (eds.): *IUTAM Symposium on Micro- and Macrostructural Aspects of Thermoplasticity*. Proceedings of the IUTAM Symposium held in Bochum, Germany. 1999 ISBN 0-7923-5265-3
63. F.C. Moon: *IUTAM Symposium on New Applications of Nonlinear and Chaotic Dynamics in Mechanics*. Proceedings of the IUTAM Symposium held in Ithaca, NY, USA. 1998 ISBN 0-7923-5276-9
64. R. Wang: *IUTAM Symposium on Rheology of Bodies with Defects*. Proceedings of the IUTAM Symposium held in Beijing, China. 1999 ISBN 0-7923-5297-1
65. Yu.I. Dimitrienko: *Thermomechanics of Composites under High Temperatures*. 1999 ISBN 0-7923-4899-0
66. P. Argoul, M. Frémond and Q.S. Nguyen (eds.): *IUTAM Symposium on Variations of Domains and Free-Boundary Problems in Solid Mechanics*. Proceedings of the IUTAM Symposium held in Paris, France. 1999 ISBN 0-7923-5450-8
67. F.J. Fahy and W.G. Price (eds.): *IUTAM Symposium on Statistical Energy Analysis*. Proceedings of the IUTAM Symposium held in Southampton, U.K. 1999 ISBN 0-7923-5457-5
68. H.A. Mang and F.G. Rammerstorfer (eds.): *IUTAM Symposium on Discretization Methods in Structural Mechanics.* Proceedings of the IUTAM Symposium held in Vienna, Austria. 1999 ISBN 0-7923-5591-1

Mechanics

SOLID MECHANICS AND ITS APPLICATIONS

Series Editor: G.M.L. Gladwell

69. P. Pedersen and M.P. Bendsøe (eds.): *IUTAM Symposium on Synthesis in Bio Solid Mechanics*. Proceedings of the IUTAM Symposium held in Copenhagen, Denmark. 1999 ISBN 0-7923-5615-2
70. S.K. Agrawal and B.C. Fabien: *Optimization of Dynamic Systems*. 1999 ISBN 0-7923-5681-0
71. A. Carpinteri: *Nonlinear Crack Models for Nonmetallic Materials*. 1999 ISBN 0-7923-5750-7
72. F. Pfeifer (ed.): *IUTAM Symposium on Unilateral Multibody Contacts*. Proceedings of the IUTAM Symposium held in Munich, Germany. 1999 ISBN 0-7923-6030-3
73. E. Lavendelis and M. Zakrzhevsky (eds.): *IUTAM/IFToMM Symposium on Synthesis of Nonlinear Dynamical Systems*. Proceedings of the IUTAM/IFToMM Symposium held in Riga, Latvia. 2000 ISBN 0-7923-6106-7
74. J.-P. Merlet: *Parallel Robots*. 2000 ISBN 0-7923-6308-6
75. J.T. Pindera: *Techniques of Tomographic Isodyne Stress Analysis.* 2000 ISBN 0-7923-6388-4
76. G.A. Maugin, R. Drouot and F. Sidoroff (eds.): *Continuum Thermomechanics.* The Art and Science of Modelling Material Behaviour. 2000 ISBN 0-7923-6407-4
77. N. Van Dao and E.J. Kreuzer (eds.): *IUTAM Symposium on Recent Developments in Non-linear Oscillations of Mechanical Systems*. 2000 ISBN 0-7923-6470-8
78. S.D. Akbarov and A.N. Guz: *Mechanics of Curved Composites*. 2000 ISBN 0-7923-6477-5
79. M.B. Rubin: *Cosserat Theories: Shells, Rods and Points*. 2000 ISBN 0-7923-6489-9
80. S. Pellegrino and S.D. Guest (eds.): *IUTAM-IASS Symposium on Deployable Structures: Theory and Applications.* Proceedings of the IUTAM-IASS Symposium held in Cambridge, U.K., 6–9 September 1998. 2000 ISBN 0-7923-6516-X
81. A.D. Rosato and D.L. Blackmore (eds.): *IUTAM Symposium on Segregation in Granular Flows.* Proceedings of the IUTAM Symposium held in Cape May, NJ, U.S.A., June 5–10, 1999. 2000 ISBN 0-7923-6547-X
82. A. Lagarde (ed.): *IUTAM Symposium on Advanced Optical Methods and Applications in Solid Mechanics*. Proceedings of the IUTAM Symposium held in Futuroscope, Poitiers, France, August 31–September 4, 1998. 2000 ISBN 0-7923-6604-2
83. D. Weichert and G. Maier (eds.): *Inelastic Analysis of Structures under Variable Loads*. Theory and Engineering Applications. 2000 ISBN 0-7923-6645-X
84. T.-J. Chuang and J.W. Rudnicki (eds.): *Multiscale Deformation and Fracture in Materials and Structures*. The James R. Rice 60th Anniversary Volume. 2001 ISBN 0-7923-6718-9
85. S. Narayanan and R.N. Iyengar (eds.): *IUTAM Symposium on Nonlinearity and Stochastic Structural Dynamics.* Proceedings of the IUTAM Symposium held in Madras, Chennai, India, 4–8 January 1999 ISBN 0-7923-6733-2
86. S. Murakami and N. Ohno (eds.): *IUTAM Symposium on Creep in Structures*. Proceedings of the IUTAM Symposium held in Nagoya, Japan, 3-7 April 2000. 2001 ISBN 0-7923-6737-5
87. W. Ehlers (ed.): *IUTAM Symposium on Theoretical and Numerical Methods in Continuum Mechanics of Porous Materials.* Proceedings of the IUTAM Symposium held at the University of Stuttgart, Germany, September 5-10, 1999. 2001 ISBN 0-7923-6766-9
88. D. Durban, D. Givoli and J.G. Simmonds (eds.): *Advances in the Mechanis of Plates and Shells The Avinoam Libai Anniversary Volume*. 2001 ISBN 0-7923-6785-5
89. U. Gabbert and H.-S. Tzou (eds.): *IUTAM Symposium on Smart Structures and Structonic Systems*. Proceedings of the IUTAM Symposium held in Magdeburg, Germany, 26–29 September 2000. 2001 ISBN 0-7923-6968-8

Mechanics

SOLID MECHANICS AND ITS APPLICATIONS

Series Editor: G.M.L. Gladwell

90. Y. Ivanov, V. Cheshkov and M. Natova: *Polymer Composite Materials – Interface Phenomena & Processes*. 2001 ISBN 0-7923-7008-2
91. R.C. McPhedran, L.C. Botten and N.A. Nicorovici (eds.): *IUTAM Symposium on Mechanical and Electromagnetic Waves in Structured Media*. Proceedings of the IUTAM Symposium held in Sydney, NSW, Australia, 18-22 Januari 1999. 2001 ISBN 0-7923-7038-4
92. D.A. Sotiropoulos (ed.): *IUTAM Symposium on Mechanical Waves for Composite Structures Characterization*. Proceedings of the IUTAM Symposium held in Chania, Crete, Greece, June 14-17, 2000. 2001 ISBN 0-7923-7164-X
93. V.M. Alexandrov and D.A. Pozharskii: *Three-Dimensional Contact Problems*. 2001 ISBN 0-7923-7165-8
94. J.P. Dempsey and H.H. Shen (eds.): *IUTAM Symposium on Scaling Laws in Ice Mechanics and Ice Dynamics*. Proceedings of the IUTAM Symposium held in Fairbanks, Alaska, U.S.A., 13-16 June 2000. 2001 ISBN 1-4020-0171-1
95. U. Kirsch: *Design-Oriented Analysis of Structures*. A Unified Approach. 2002 ISBN 1-4020-0443-5
96. A. Preumont: *Vibration Control of Active Structures*. An Introduction (2^{nd} Edition). 2002 ISBN 1-4020-0496-6
97. B.L. Karihaloo (ed.): *IUTAM Symposium on Analytical and Computational Fracture Mechanics of Non-Homogeneous Materials.* Proceedings of the IUTAM Symposium held in Cardiff, U.K., 18-22 June 2001. 2002 ISBN 1-4020-0510-5
98. S.M. Han and H. Benaroya: *Nonlinear and Stochastic Dynamics of Compliant Offshore Structures*. 2002 ISBN 1-4020-0573-3
99. A.M. Linkov: *Boundary Integral Equations in Elasticity Theory*. 2002 ISBN 1-4020-0574-1
100. L.P. Lebedev, I.I. Vorovich and G.M.L. Gladwell: *Functional Analysis.* Applications in Mechanics and Inverse Problems (2^{nd} Edition). 2002 ISBN 1-4020-0667-5; Pb: 1-4020-0756-6
101. Q.P. Sun (ed.): *IUTAM Symposium on Mechanics of Martensitic Phase Transformation in Solids*. Proceedings of the IUTAM Symposium held in Hong Kong, China, 11-15 June 2001. 2002 ISBN 1-4020-0741-8
102. M.L. Munjal (ed.): *IUTAM Symposium on Designing for Quietness*. Proceedings of the IUTAM Symposium held in Bangkok, India, 12-14 December 2000. 2002 ISBN 1-4020-0765-5
103. J.A.C. Martins and M.D.P. Monteiro Marques (eds.): *Contact Mechanics*. Proceedings of the 3^{rd} Contact Mechanics International Symposium, Praia da Consolação, Peniche, Portugal, 17-21 June 2001. 2002 ISBN 1-4020-0811-2
104. H.R. Drew and S. Pellegrino (eds.): *New Approaches to Structural Mechanics, Shells and Biological Structures*. 2002 ISBN 1-4020-0862-7
105. J.R. Vinson and R.L. Sierakowski: *The Behavior of Structures Composed of Composite Materials*. Second Edition. 2002 ISBN 1-4020-0904-6
106. Not yet published.
107. J.R. Barber: *Elasticity*. Second Edition. 2002 ISBN Hb 1-4020-0964-X; Pb 1-4020-0966-6
108. C. Miehe (ed.): *IUTAM Symposium on Computational Mechanics of Solid Materials at Large Strains*. Proceedings of the IUTAM Symposium held in Stuttgart, Germany, 20-24 August 2001. 2003 ISBN 1-4020-1170-9

SOLID MECHANICS AND ITS APPLICATIONS

Series Editor: G.M.L. Gladwell

109. P. Ståhle and K.G. Sundin (eds.): *IUTAM Symposium on Field Analyses for Determination of Material Parameters – Experimental and Numerical Aspects.* Proceedings of the IUTAM Symposium held in Abisko National Park, Kiruna, Sweden, July 31 – August 4, 2000. 2003 ISBN 1-4020-1283-7
110. N. Sri Namachchivaya and Y.K. Lin (eds.): *IUTAM Symposium on Nonlinear Stochastic Dynamics.* Proceedings of the IUTAM Symposium held in Monticello, IL, USA, 26 – 30 August, 2000. 2003 ISBN 1-4020-1471-6
111. H. Sobieckzky (ed.): *IUTAM Symposium Transsonicum IV*. Proceedings of the IUTAM Symposium held in Göttingen, Germany, 2–6 September 2002, 2003 ISBN 1-4020-1608-5
112. J.-C. Samin and P. Fisette: *Symbolic Modeling of Multibody Systems*. 2003 ISBN 1-4020-1629-8
113. A.B. Movchan (ed.): *IUTAM Symposium on Asymptotics, Singularities and Homogenisation in Problems of Mechanics.* Proceedings of the IUTAM Symposium held in Liverpool, United Kingdom, 8-11 July 2002. 2003 ISBN 1-4020-1780-4
114. S. Ahzi, M. Cherkaoui, M.A. Khaleel, H.M. Zbib, M.A. Zikry and B. LaMatina (eds.): *IUTAM Symposium on Multiscale Modeling and Characterization of Elastic-Inelastic Behavior of Engineering Materials.* Proceedings of the IUTAM Symposium held in Marrakech, Morocco, 20-25 October 2002. 2004 ISBN 1-4020-1861-4
115. H. Kitagawa and Y. Shibutani (eds.): *IUTAM Symposium on Mesoscopic Dynamics of Fracture Process and Materials Strength.* Proceedings of the IUTAM Symposium held in Osaka, Japan, 6-11 July 2003. Volume in celebration of Professor Kitagawa's retirement. 2004 ISBN 1-4020-2037-6
116. E.H. Dowell, R.L. Clark, D. Cox, H.C. Curtiss, Jr., K.C. Hall, D.A. Peters, R.H. Scanlan, E. Simiu, F. Sisto and D. Tang: *A Modern Course in Aeroelasticity*. 4th Edition, 2004 ISBN 1-4020-2039-2
117. T. Burczyński and A. Osyczka (eds.): *IUTAM Symposium on Evolutionary Methods in Mechanics.* Proceedings of the IUTAM Symposium held in Cracow, Poland, 24-27 September 2002. 2004 ISBN 1-4020-2266-2
118. D. Ieşan: *Thermoelastic Models of Continua*. 2004 ISBN 1-4020-2309-X
119. G.M.L. Gladwell: *Inverse Problems in Vibration*. Second Edition. 2004 ISBN 1-4020-2670-6
120. J.R. Vinson: *Plate and Panel Structures of Isotropic, Composite and Piezoelectric Materials, Including Sandwich Construction*. 2005 ISBN 1-4020-3110-6
121. *Forthcoming*
122. G. Rega and F. Vestroni (eds.): *IUTAM Symposium on Chaotic Dynamics and Control of Systems and Processes in Mechanics*. Proceedings of the IUTAM Symposium held in Rome, Italy, 8–13 June 2003. 2005 ISBN 1-4020-3267-6